frontiers | Research Topics

AI empowered cerebro-cardiovascular health engineering

Edited by
Lisheng Xu, Dingchang Zheng, Jianbao Zhang,
Fei Chen and Rong Liu

Coordinated by
Chunsheng Li and Wenjun Tan

Published in
Frontiers in Physiology

ISSN 1664-8714
ISBN 978-2-8325-4219-4
DOI 10.3389/978-2-8325-4219-4

About Frontiers

Frontiers is more than just an open access publisher of scholarly articles: it is a pioneering approach to the world of academia, radically improving the way scholarly research is managed. The grand vision of Frontiers is a world where all people have an equal opportunity to seek, share and generate knowledge. Frontiers provides immediate and permanent online open access to all its publications, but this alone is not enough to realize our grand goals.

Frontiers journal series

The Frontiers journal series is a multi-tier and interdisciplinary set of open-access, online journals, promising a paradigm shift from the current review, selection and dissemination processes in academic publishing. All Frontiers journals are driven by researchers for researchers; therefore, they constitute a service to the scholarly community. At the same time, the *Frontiers journal series* operates on a revolutionary invention, the tiered publishing system, initially addressing specific communities of scholars, and gradually climbing up to broader public understanding, thus serving the interests of the lay society, too.

Dedication to quality

Each Frontiers article is a landmark of the highest quality, thanks to genuinely collaborative interactions between authors and review editors, who include some of the world's best academicians. Research must be certified by peers before entering a stream of knowledge that may eventually reach the public - and shape society; therefore, Frontiers only applies the most rigorous and unbiased reviews. Frontiers revolutionizes research publishing by freely delivering the most outstanding research, evaluated with no bias from both the academic and social point of view. By applying the most advanced information technologies, Frontiers is catapulting scholarly publishing into a new generation.

What are Frontiers Research Topics?

Frontiers Research Topics are very popular trademarks of the *Frontiers journals series*: they are collections of at least ten articles, all centered on a particular subject. With their unique mix of varied contributions from Original Research to Review Articles, Frontiers Research Topics unify the most influential researchers, the latest key findings and historical advances in a hot research area.

Find out more on how to host your own Frontiers Research Topic or contribute to one as an author by contacting the Frontiers editorial office: frontiersin.org/about/contact

AI empowered cerebro-cardiovascular health engineering

Topic editors
Lisheng Xu — Northeastern University, China
Dingchang Zheng — Coventry University, United Kingdom
Jianbao Zhang — Xi'an Jiaotong University, China
Fei Chen — Southern University of Science and Technology, China
Rong Liu — Dalian University of Technology, China

Topic coordinators
Chunsheng Li — Shenyang University of Technology, China
Wenjun Tan — Northeastern University, China

Citation
Xu, L., Zheng, D., Zhang, J., Chen, F., Liu, R., Li, C., Tan, W., eds. (2024). *AI empowered cerebro-cardiovascular health engineering*. Lausanne: Frontiers Media SA. doi: 10.3389/978-2-8325-4219-4

Table of contents

frontiers | Frontiers in Physiology

TYPE Editorial
PUBLISHED 12 December 2023
DOI 10.3389/fphys.2023.1335573

OPEN ACCESS

EDITED AND REVIEWED BY
Raimond L. Winslow,
Northeastern University, United States

*CORRESPONDENCE
Lisheng Xu,
xuls@bmie.neu.edu.cn

RECEIVED 09 November 2023
ACCEPTED 05 December 2023
PUBLISHED 12 December 2023

CITATION
Xu L, Guo Z, Zheng D, Zhang J, Chen F, Liu R, Li C and Tan W (2023), Editorial: AI empowered cerebro-cardiovascular health engineering.
Front. Physiol. 14:1335573.
doi: 10.3389/fphys.2023.1335573

Editorial: AI empowered cerebro-cardiovascular health engineering

Lisheng Xu[1,2]*, Zengzhi Guo[1,2], Dingchang Zheng[3], Jianbao Zhang[4], Fei Chen[5], Rong Liu[6], Chunsheng Li[7] and Wenjun Tan[2,8]

[1]College of Medicine and Biological Information Engineering, Northeastern University, Shenyang, China, [2]Key Laboratory of Medical Image Computing, Ministry of Education, Shenyang, China, [3]Research Centre of Intelligent Healthcare, Coventry University, Coventry, United Kingdom, [4]Department of Life Science and Technology, Xi'an Jiaotong University, Xi'an, China, [5]Department of Electrical and Electronic Engineering, Southern University of Science and Technology, Shenzhen, China, [6]School of Biomedical Engineering, Dalian University of Technology, Dalian, China, [7]Department of Biomedical Engineering, Shenyang University of Technology, Shenyang, China, [8]School of Computer Science and Engineering, Northeastern University, Shenyang, China

KEYWORDS

artificial intelligence, neurophysiological signal and image, signal processing, wearable device, cerebro-cardiovascular health, identification and modeling, diagnosis and treatment, rehabilitation

Editorial on the Research Topic
AI empowered cerebro-cardiovascular health engineering

Introduction

Cerebrovascular and cardiovascular diseases continue to pose significant challenges, contributing significantly to disabilities and mortality rates worldwide (R.L. Sacco et al., 2016). In recent years, artificial intelligence (AI) has emerged as a powerful tool in the realm of cerebrovascular and cardiovascular disease treatment. Its ability to improve decision-making, diagnosis, and treatment processes by analyzing extensive patient data sets has revolutionized medical practices in these fields. This transformative impact is made possible by the rapid advancements in machine learning, deep learning, computational power, and mathematical algorithms, enabling the swift and efficient analysis of vast datasets. Therefore, the integration of AI into cerebrovascular and cardiovascular healthcare has attracted considerable attention among healthcare professionals. Physicians are seeking increasing support from AI tools which improve disease diagnosis, intervention guidance, and therapy monitoring.

This Research Topic "*AI Empowered Cerebro-Cardiovascular Health Engineering*" focuses on recent advancements in AI techniques for enhancing the diagnosis, monitoring, and treatment of cerebrovascular and cardiovascular diseases, including but not limited to noninvasive acquisition methods, accurate diagnosis techniques, personalized therapy approaches, early prediction models, intelligent screening processes, and neurological and cardiovascular rehabilitation strategies. In this Editorial Article, we provide a comprehensive summary of the contributions from the publications within

this Research Topic, shedding light on the cutting-edge developments that are shaping the future of cerebrovascular and cardiovascular healthcare through the power of AI.

Diagnosis of cardiovascular diseases

Screening for cardiovascular disease by the auscultation of heart sound auscultation is a simple, and effective method. Signal processing and AI techniques have been widely used in analyzing heart sounds (Herzig et al., 2014). Li et al. proposed a new heart sound classification method based on improved mel-frequency cepstrum coefficient features and deep residual learning method that achieved an accuracy of 94.4%. This study contributed a more accurate and effective approach to analyzing heart sounds, thus aiding the diagnosis of cardiovascular diseases.

Congenital heart disease (CHD) is one of the leading causes of death (Meras et al., 2021). TrueVue, TrueVue Light, and TrueVue Glass are innovative three-dimensional (3D) echocardiographic techniques that can provide radiation-free visualization of cardiac anatomical structures (Genovese et al., 2019). Sun et al. explored their individual advantages and limitations and summarized their application methods for CHDs. This research demonstrated that the combined use of TrueVue, TrueVue Light, and TrueVue Glass improved the accuracy of CHD evaluation and treatment than the traditional imaging techniques.

Heart failure (HF) results from ventricular filling or ejection dysfunction (Hao et al., 2019). Ballistocardiography (BCG) has been utilized for in-home detection of various cardiac diseases recently (Wen et al., 2019). Feng et al. proposed a machine learning-aided scheme based on BCG signals for HF detection, enabling comprehensive exploration of the relationship between the heart and the lung systems. Experimental results demonstrated that the proposed scheme could significantly improve the accuracy and robustness of in-home HF detection.

Early detection of abnormal electrocardiogram (ECG) patterns is an important method for preventing, identifying, and diagnosing cardiovascular diseases (Dong and Zhu, 2004). Shan et al. proposed an ECG anomaly detection framework (ECG-AAE) based on an adversarial autoencoder and temporal convolutional network. They also employed the adjournment network to solve the ECG data imbalance problem. ECG-AAE could effectively improve the detection rate of abnormal ECG patterns than other popular outlier detection methods while ensuring accuracy.

Coronary artery segmentation is essential for helping doctors to identify and segment the regions of interest. However, automatic segmentation of coronary arteries poses challenges due to issues like over-segmentation or omission, often stemming from the small size and poor distribution of contrast medium (Kroft et al., 2007). Wang et al. proposed a novel automatic method, DR-LCT-UNet, to improve the performance of coronary artery segmentation by preserving unobtrusive features through dense residual connection and focusing on local contextual information. The dice similarity coefficient, Recall, and Precision of DR-LCT-UNet outperformed other comparison methods.

The central aortic pressure waveform (CAPW) contains valuable information about the cardiovascular system, making it useful for predicting and diagnosing cardiovascular diseases (Flores Geronimo et al., 2021). Sun et al. proposed a novel method to approximate the actual flow waveform with a personalized flow waveform and to examine the feasibility of decomposing the CAPW for quantifying wave reflection. This study proposed a more accurate method based on the characteristics of the CAPW to estimate wave reflection indices than the traditional triangular and lognormal flow methods.

Diagnosis of cerebrovascular diseases

Intracranial pressure (ICP), defined as the pressure within the craniospinal compartment, is an important physiological parameter reflecting the biomechanical status of the brain (Czosnyka and Pickard, 2004). The photoplethysmography (PPG) technology has been applied in the daily monitoring of various physiological parameters. Liu et al. developed a computational model of intracranial PPG signals for the first time and investigated the effect of ICP changes on the waveforms of intracranial PPG signals in different cerebral perfusion territories. This research demonstrated that ICP values could significantly change the value-relevant (maximum, minimum, mean, and amplitude) waveform features of PPG signals measured from different cerebral perfusion territories.

Treatment of cardiovascular diseases

Functional single ventricle (FSV) is a complex congenital malformation with only one fully functional ventricle. The Y-shaped conduit total cavopulmonary connection (YCPC) was a theoretically efficient procedure for the treatment of FSV. However, the theoretical effectiveness of TCPC significantly differs from its postoperative efficacy (Trusty et al., 2016). To bridge this gap, Zhang et al. applied preoperative computed tomography angiography and computational fluid dynamics simulation to predict and verify the efficacy of YCPC. This approach has effectively improved the applicability of clinical applications of YCPC.

Left atrial appendage occlusion (LAAO) was used as a new approach for stroke prevention in patients with atrial fibrillation (AF) (Turagam et al., 2020). 3D Auto LAA is an AI tool designed for the automatic identification of the LAA and measuring important parameters related to surgery. Sun et al. were the first to combine TrueVue Glass and 3D Auto LAA to evaluate AF patients undergoing LAAO and explore their clinical value and technical advantages. They found that it provided a more accurate and efficient assessment of LAA anatomy and physiological parameters for LAAO, surpassing other commonly used imaging techniques.

Abdominal aortic aneurysm (AAA) is a degenerative disease that causes significant health problems in humans (Kugo et al., 2019). Artemisia annua L. (A. annua) is a traditional herbal remedy that has been widely used in cardiovascular disease. Molecular docking, a statistical simulation method, focuses on the interaction between molecules and predicts their binding mode and affinity (Wang and Zhu, 2016). Jia et al. systematically summarized the molecular targets of A. annua in the treatment

of AAA using network pharmacology combined with molecular docking technology. The molecular docking results revealed that the top five active components of A. annua had a good affinity for core disease targets and played a central role in treating AAA. The results showed that the low binding energy molecular docking results provided valuable information for the development of drugs to treat AAA.

Treatment of neurological diseases

Epilepsy is the most common chronic neurological disease. Intracranial electroencephalography (EEG) signal provides precise anatomical information about the selective engagement of neuronal populations at the millimeter scale and stereo- EEG is one kind of Intracranial EEG (Parvizi and Kastner, 2018). EEG phase-amplitude coupling (PAC), the amplitude of high-frequency oscillations modulated by the phase of low-frequency oscillations (LFOs), is a useful biomarker to localize epileptogenic tissue (Guirgis et al., 2015). Li et al. proposed a novel approach for generating complex-valued PAC with both the coupling strength and the coupled phase of LFO to identify pathological PAC in Stereo-EEG from patients with epilepsy. Their proposed method held promise for identifying more accurate epileptic brain activity for potential surgical intervention. In a separate contribution, Liu and Li proposed a novel approach for localizing neuromodulatory targets, which used intracranial EEG and multi-unit computational models to simulate the dynamic behavior of epileptic networks through external stimulation. This study provided a new tool for localizing patient-specific targets for neuromodulation therapy.

The innervation zone (IZ) of a muscle is the region where muscle fibers are innervated by motor axon terminals. IZ estimation is important for treating patients with neurological injuries such as stroke and cerebral palsy (Zhang et al., 2021). Huang et al. investigated methods to reliably and automatically estimate the IZ from monopolar M-wave recordings and found that the PCA-based method demonstrated the most consistency with manual detectionthan other methods. This study has significant clinical value for the neurological rehabilitation of patients.

Neurological and cardiovascular rehabilitation

Even after treatment, both cardiovascular and cerebrovascular diseases can result in motor or cognitive dysfunction, requiring a long period of rehabilitation. A rehabilitation process combining motor and cognitive training has the potential to enhance the chance of recovery and rebuild the action ability. 3D gaming and virtual reality have been employed to make the process more immersive (Nasri et al., 2020). Chen et al. proposed an interactive game utilizing real-time skeleton-based hand gesture recognition to assist rehabilitation exercises. This approach improved the hand-eye coordination of the patients during a game-like experience. A lightweight residual graph convolutional architecture was proposed for hand gesture recognition. Most of the participants in this study showed an improvement in their passing rate of the game during the test process.

Risk prediction of cerebrovascular and cardiovascular diseases

Pre-eclampsia (PE) is a type of hypertensive disorder that can occur during pregnancy (Duhig et al., 2019). Li et al. developed and validated a predictive model for predicting the risk of PE. The model was further analyzed in two subgroups: early-onset pre-eclampsia and late-onset pre-eclampsia at prenatal visits at different gestational weeks. The overall accuracy of the model reached 86%. This predictive model for PE is of great significance in giving targeted clinical predictions and recommendations, ultimately contributing to the improvement of maternal and infant conditions.

Myocardial infarction (MI) is a prevalent cardiovascular disease (R. Nasimov et al., 2020). Zhou et al. developed an algorithm using case data to determine the relationship between the physiological indicators of MI patients and their prognosis. The patient prognostic risk prediction model had an impressive accuracy of 92.2%. The results demonstrated that the prediction model could offer an effective solution for clinical disease prognostic risk assessment, leading to improved clinical outcomes.

In summary, this Research Topic presents the most advancements in AI applications within the fields of cerebrovascular and cardiovascular healthcare. These studies represent a significant stride in our understanding of how AI technology can profoundly improve the diagnosis, treatment, risk prediction, and rehabilitation of cerebrovascular or cardiovascular disease. We appreciate the efforts of all authors for their invaluable contributions, which have immensely enriched this Research Topic. Furthermore, we express our gratitude to the diligent reviewers and editors for their tremendous efforts in ensuring the quality of rigor of the published work. We sincerely hope that readers will find this Research Topic to be both insightful and valuable, offering a comprehensive overview of the transformative potential of AI in revolutionizing cerebrovascular and cardiovascular healthcare.

Author contributions

LX: Funding acquisition, Writing–original draft, Writing–review and editing. ZG: Writing–original draft, Writing–review and editing. DZ: Supervision, Writing–review and editing, Visualization. JZ: Writing–review and editing, Visualization. FC: Writing–review and editing, Resources. RL: Writing–review and editing, Resources. CL: Writing–review and editing, Visualization. WT: Writing–review and editing, Visualization.

Funding

The author(s) declare financial support was received for the research, authorship, and/or publication of this article. This work was supported by the National Natural Science Foundation of China under Grant 62273082.

Conflict of interest

The authors declare that the research was conducted in the absence of any commercial or financial relationships that could be construed as a potential conflict of interest.

The author(s) declared that they were an editorial board member of Frontiers, at the time of submission. This had no impact on the peer review process and the final decision.

Publisher's note

References

Czosnyka, M., and Pickard, J. D. (2004). Monitoring and interpretation of intracranial pressure. *J. Neurology, Neurosurg. Psychiatry* 75, 813–821. doi:10.1136/jnnp.2003.033126

Dong, J., and Zhu, H. H. (2004). Mobile ECG detector through GPRS/Internet. *Proc. IEEE Symp. Comput. Med. Syst.* 17, 485–489. doi:10.1109/cbms.2004.1311761

Duhig, K. E., Myers, J., Seed, P. T., Sparkes, J., Lowe, J., Hunter, R. M., et al. (2019). Placental growth factor testing to assess women with suspected pre-eclampsia: a multicentre, pragmatic, stepped-wedge cluster-randomised controlledtrial. *Lancet* 393, 1807–1818. doi:10.1016/S0140-6736(18)33212-4

Flores Geronimo, J., Corvera Poire, E., Chowienczyk, P., and Alastruey, J. (2021). Estimating central pulse pressure from blood flow by identifying the main physical determinants of pulse pressure amplification. *Front. Physiol.* 90, 608098. doi:10.3389/fphys.2021.608098

Genovese, D., Addetia, K., Kebed, K., Kruse, E., Yamat, M., Narang, A., et al. (2019). First clinical experience with 3-dimensional echocardiographic transillumination rendering. *JACC. Cardiovasc. Imaging* 12, 1868–1871. doi:10.1016/j.jcmg.2018.12.012

Guirgis, M., Chinvarun, Y., del Campo, M., Carlen, P. L., and Bardakjian, B. L. (2015). Defining regions of interest using cross-frequency coupling in extratemporal lobe epilepsy patients. *J. Neural Eng.* 12, 026011. doi:10.1088/1741-2560/12/2/026011

Hao, G., Wang, X., Chen, Z., Zhang, L., Zhang, Y., Wei, B., et al. (2019). Prevalence of heart failure and left ventricular dysfunction in China: the China hypertension survey, 2012–2015. *Eur. J. Heart Fail.* 21, 1329–1337. doi:10.1002/ejhf.1629

Kroft, L. J. M., De Roos, A., and Geleijns, J. (2007). Artifacts in ECG-synchronized MDCT coronary angiography. *Am. J. Roentgenol.* 189 (3), 581–591. doi:10.2214/AJR.07.2138

Kugo, H., Moriyama, T., and Zaima, N. (2019). The role of perivascular adipose tissue in the appearance of ectopic adipocytes in the abdominal aortic aneurysmal wall. *Adipocyte* 8, 229–239. doi:10.1080/21623945.2019.1636625

Meras, P., Riesgo-Gil, F., Rybicka, J., Barradas-Pires, A., Smith, J., Kempny, A., et al. (2021). Heart transplantation at a single tertiary adult congenital heart disease centre: too little, too late? *Int. J. Cardiol.* 322, 107–113. doi:10.1016/j.ijcard.2020.08.047

Nasimov, R., Muminov, B., Mirzahalilov, S., and Nasimova, N. (2020). "A new approach to classifying myocardial infarction and cardiomyopathy using deep learning," in *2020 international conference on information science and communications technologies (ICISCT)*, 1–5. doi:10.1109/ICISCT50599.2020.9351386

Nasri, N., Ortsescolano, S., and Cazorla, M. (2020). An semg-controlled 3d game for rehabilitation therapies: real-time time hand gesture recognition using deep learning techniques. *Sensors* 20, E6451. doi:10.3390/s20226451

Parvizi, J., and Kastner, S. (2018). Promises and limitations of human intracranial electroencephalography. *Nat. Neurosci.* 21, 474–483. doi:10.1038/s41593-018-0108-2

Sacco, R. L., Roth, G. A., Reddy, K. S., Arnett, D. K., Bonita, R., Gaziano, T. A., et al. (2016). The heart of 25 by 25: achieving the goal of reducing global and regional premature deaths from cardiovascular diseases and stroke: a modeling study from the American heart association and world heart federation. *Glob. Heart* 11, 251–264. doi:10.1016/j.gheart.2016.04.002

Trusty, P. M., Restrepo, M., Kanter, K. R., Yoganathan, A. P., Fogel, M. A., and Slesnick, T. C. (2016). A pulsatile hemodynamic evaluation of the commercially available bifurcated Y-graft Fontan modification and comparison with the lateral tunnel and extracardiac conduits. *J. Thorac. Cardiovasc. Surg.* 151, 1529–1536. doi:10.1016/j.jtcvs.2016.03.019

Turagam, M. K., Osmancik, P., Neuzil, P., Dukkipati, S. R., and Reddy, V. Y. (2020). Left atrial appendage closure versus oral anticoagulants in atrial fibrillation: a meta-analysis of randomized trials. *J. Am. Coll. Cardiol.* 76 (23), 2795–2797. doi:10.1016/j.jacc.2020.08.089

Wang, G., and Zhu, W. (2016). Molecular docking for drug discovery and development: a widely used approach but far from perfect. *Future Med. Chem.* 8, 1707–1710. doi:10.4155/fmc-2016-0143

Wen, X., Yanqi, H., Xiaomei, W., and Biyong, Z. (2019). A feasible feature extraction method for atrial fibrillation detection from BCG. *IEEE J. Biomed. Health Inf.* 24, 1093–1103. doi:10.1109/jbhi.2019.2927165

Zhang, C., Gutierrez-Verduzco, M., Francisco, G. E., Ping, Z., Sheng, L., Yingchun, Z., et al. (2021). Improving botulinum toxin efficiency in treating post-stroke spasticity using 3D innervation zone imaging. *Int. J. Neural Syst.* 31, 2150007. doi:10.1142/S0129065721500076

frontiers | Frontiers in Physiology

TYPE Original Research
PUBLISHED 02 September 2022
DOI 10.3389/fphys.2022.961724

OPEN ACCESS

EDITED BY
Lisheng Xu,
Northeastern University, China

REVIEWED BY
Chunsheng Li,
Shenyang University of Technology, China
Yang Yao,
Northeastern University, China
Cai Chen,
Shandong Institute of Advanced Technology (CAS), China

*CORRESPONDENCE
Shijie Chang,
sjchang@cmu.edu.cn

†These authors have contributed equally to this work

SPECIALTY SECTION
This article was submitted to Computational Physiology and Medicine, a section of the journal Frontiers in Physiology

RECEIVED 05 June 2022
ACCEPTED 02 August 2022
PUBLISHED 02 September 2022

CITATION
Shan L, Li Y, Jiang H, Zhou P, Niu J, Liu R, Wei Y, Peng J, Yu H, Sha X and Chang S (2022), Abnormal ECG detection based on an adversarial autoencoder. *Front. Physiol.* 13:961724. doi: 10.3389/fphys.2022.961724

Abnormal ECG detection based on an adversarial autoencoder

Lianfeng Shan[1†], Yu Li[2†], Hua Jiang[3], Peng Zhou[2], Jing Niu[2], Ran Liu[2], Yuanyuan Wei[2], Jiao Peng[2], Huizhen Yu[2], Xianzheng Sha[2] and Shijie Chang[2*]

[1]Department of Intelligent Computation, School of Intelligent Medicine, China Medical University, Shenyang, China, [2]Division of Biomedical Engineering, School of Intelligent Medicine, China Medical University, Shenyang, China, [3]Department of Cardiovascular Medicine, The First Affiliated Hospital of China Medical University, Shenyang, China

Automatic detection and alarm of abnormal electrocardiogram (ECG) events play an important role in an ECG monitor system; however, popular classification models based on supervised learning fail to detect abnormal ECG effectively. Thus, we propose an ECG anomaly detection framework (ECG-AAE) based on an adversarial autoencoder and temporal convolutional network (TCN) which consists of three modules (autoencoder, discriminator, and outlier detector). The ECG-AAE framework is trained only with normal ECG data. Normal ECG signals could be mapped into latent feature space and then reconstructed as the original ECG signal back in our model, while abnormal ECG signals could not. Here, the TCN is employed to extract features of normal ECG data. Then, our model is evaluated on an MIT-BIH arrhythmia dataset and CMUH dataset, with an accuracy, precision, recall, F1-score, and AUC of 0.9673, 0.9854, 0.9486, 0.9666, and 0.9672 and of 0.9358, 0.9816, 0.8882, 0.9325, and 0.9358, respectively. The result indicates that the ECG-AAE can detect abnormal ECG efficiently, with its performance better than other popular outlier detection methods.

KEYWORDS

outlier detection (OD), autoencoder (AE), generative adversarial network (GANs), ECG, temporal convolutional network (TCN)

1 Introduction

Cardiovascular diseases (CVDs) are leading causes of human death (R.L. Sacco et al., 2016), and ECG is an important method of diagnosing CVDs. Earlier detection of abnormal ECG is the key step in prevention, identification, and diagnosis of CVDs. Portable ECG could detect sudden abnormal ECG events in the early stage (Dong and Zhu, 2004) and activate warning; it is expected to reduce the mortality rate. Therefore, automatic identification of abnormal ECG events is the first important part of an ECG monitoring system.

Currently, popular artificial intelligence (AI) ECG diagnosis methods, including machine learning (feature extraction and classifiers) and deep networks, always detect abnormal ECG events using classification models. In machine learning, self-organizing map (SOM) (M.R. Risk et al., 1997), C-means clustering (Özbay et al.,

2011), etc. are some of the successful machine learning methods for ECG classification. They extract features, such as wavelet coefficients (P. De Chazal et al., 2000) and autoregressive coefficients (N. Srinivasan et al., 2002), as ECG presentation. Other research studies focus on deep learning for ECG analysis, including convolutional neural networks (CNNs) (U.R. Acharya et al., 2017) and recurrent neural networks (RNNs) (H.M. Lynn et al., 2019). Xia used a deep convolutional neural network (DCNN) (Xia et al., 2018) for atrial fibrillation detection from short ECG signals (<5s) without any designed feature extraction procedure. Martin used long a short-term memory network (LSTM) (H. Martin et al., 2021) to detect myocardial infarction from a single lead ECG signal. Onan, 2020 proposed a CNN-LSTM framework for sentiment analysis of product review on Twitter. Onan and Tocoglu (2021) proposed a three-layer stacked bidirectional LSTM architecture to identify sarcastic text documents. Deep ECG (C. Li et al., 2021) takes ECG images as inputs and performs arrhythmia classification using the DCNN and transfer learning. Furthermore, a new method combining a recurrence plot (RP) and deep learning in two stages (B.M. Mathunjwa et al., 2021) is proposed to detect arrhythmias.

These aforementioned supervised learning ECG interpreting methods have achieved sound performance in previous studies. But these classification frameworks require the dataset to include all types of heart disease data with accurate manual annotation by professional doctors. The clinical ECG data are always imbalanced with fewer abnormal ECG samples, which makes it difficult to establish an effective classification model. Moreover, it is difficult to establish a large dataset including all types of abnormal ECG for clinical purposes in practice. Therefore, the sensitivity and specificity of abnormal ECG detection cannot meet clinical requirements (O. Faust et al., 2018). An outlier detection method (G. Pang et al., 2021) is more suitable for abnormal ECG in an early warning system, only based on normal data in clinical applications.

The outlier detection methods are unsupervised machine learning methods including clustering and semi-supervision including deep learning. In unsupervised methods, statistical methods usually focus on modeling the distribution of normal categories by learning the parameters of the probability model, to identify abnormal categories as outliers with low probability. The distance-based outlier detection methods assume that the normal categories are close to each other, while the abnormal samples are far away from the normal ones. Thus, outliers could be identified by calculating the distance between the abnormal and normal samples. Bin Yao and Hutchison (2014) proposed a density-based local outlier detection method (LOF) for uncertain data. H. Shibuya and Maeda (2016) developed an anomaly detection method based on multidimensional time-series sensor data and using normal state models. Principal component analysis (Li and Wen, 2014) could be used for linear models; and the Gaussian mixture model (GMM) (Dai and Gao, 2013), isolation forest (F.T. Liu et al., 2008), and one-class support vector machine (OC-SVM) (B. Schölkopf et al., 2000) are used in actual outlier detection applications. But these machine learning algorithms often require the manual design of effective features.

Performance of an outlier detection method based on deep learning has been proved well, including Auto-Encoder (Zhou and Paffenroth, 2017), LSTM (P. Malhotra et al., 2015), and VAE (Wang et al., 2020), and widely used in AI-aided diagnosis (T. Fernando et al., 2021) such as X-ray film, MRI, CT, and other medical images, and in the detection of EEG, ECG, and other timing signals as well. Y. Xia et al. (2015) eliminated abnormal data from noisy data by reducing reconstruction errors of the autoencoder, and applying gradients of the autoencoder to make reconstruction errors discriminatory to positive samples. By using deep neural networks (autoencoders) as feature extractors, a deep hybrid model (DHM) has been applied for outlier detection to input extracted features into traditional outlier detection algorithms, such as OC-SVM (Mo, 2016). L. Ruff et al. (2018) used deep one-class classification for end-to-end outlier detection, effectively customizing trainable targets for outlier detection to extract features. K. Li et al. (2012) proposed a transfer learning framework for detecting abnormal ECG; however, this method requires manual coding of features and relies on labeled data for all different types of abnormalities. Due to diversity of diseases and different waveforms collected from different abnormal diseases, such data are not easy to obtain. Time series outlier detection technology is also used in ECG signal processing; Lemos and Tierra-Criollo, 2008; Chauhan and Vig, 2015 proposed an outlier detection method based on LSTM. An abnormal condition is considered when the difference between the predicted value of LSTM and normal value exceeds a given threshold. Latif et al. (2018) used a recurrent neural network (RNN) to detect abnormal heartbeats in the PCG signal detection of the heart sound, which needs a large amount of calculation. K. Wang et al. (2016) used an autoencoder to reconstruct normal ECG data, determine the threshold according to the reconstruction error, and finally, to detect the test set.

Recently, a GAN-based framework has been applied to outlier detection (T. Schlegl et al., 2017). The model generates new data according to the input; if the input was similar to the training data (as normal data), the output would be similar to the input, otherwise, the input would be an outlier. T. Schlegl et al. (2017) used a GAN-based model (AnoGan) to identify anomalies in medical images. However, the aforementioned methods have the problems of overfitting (C. Esteban et al., 2017) or instability (D. Li et al., 2019) when they deal with abnormal ECG detection problems.

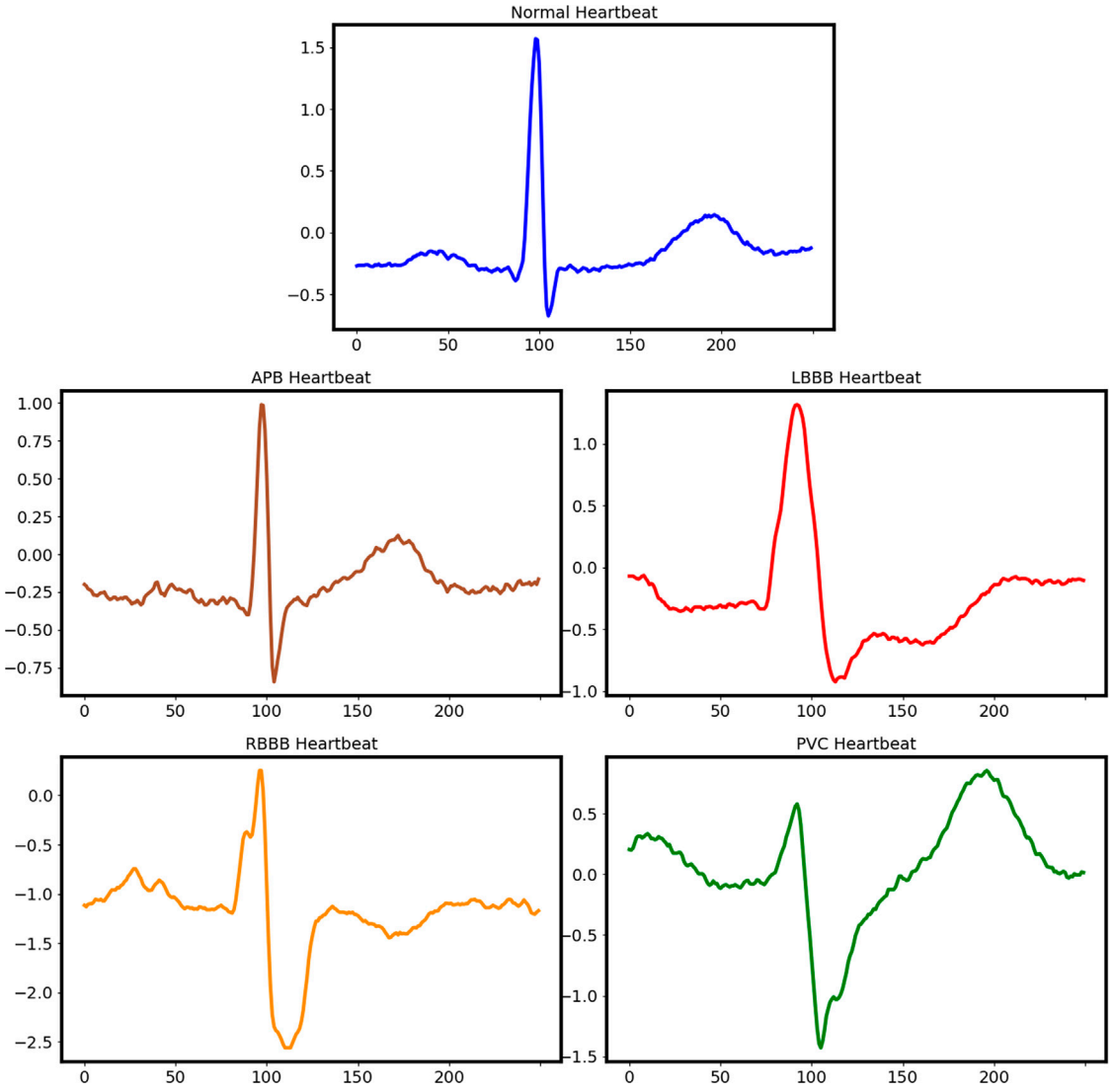

FIGURE 1
Typical sketch of normal and abnormal heartbeats.

An autoencoder is another method of simply "memorizing" the training data and reproducing them. The parameters of the intermediate hidden layer would completely fit the training set, and the content of its memory will be completely output at the time of the output, resulting in identity mapping of the neural network and data overfitting. Problems such as instability and poor controllability occur with the latent model based on the GAN method.

In this study, we proposed a novel method named ECG-AAE for detecting abnormal ECG events, based on an adversarial autoencoder and TCN (L. Sun et al., 2015). It consists of three parts: 1) an autoencoder, 2) a discriminator, and 3) an outlier detector. Our method was evaluated on the MIT-BIH and our CMUH datasets and compared with several other popular outlier detection methods.

2 Materials

2.1 Electrocardiogram datasets

1) Massachusetts Institute of Technology Arrhythmia Dataset (MIT-BIH). The dataset consists of 48 double-lead ECG recordings from 47 subjects; each set lasts 30 min at a

TABLE 1 Number of heartbeats involved in each dataset and the division of datasets.

Dataset	Type	Type of heartbeats	Number of heartbeats	Number of cases	Sample size	Number of training set	Number of test set
MIT-BIH	Normal	N	74,962	40	15,000	10,000	5,000
	Abnormal	A	2,545	—	5,000	0	5,000
		L	8,068	—			
		R	7,254	—			
		V	7,034	—			
		Total	99,863	47	20,000	10,000	10,000
CMUH	Normal	N	20,000	20,000	15,000	10,000	5,000
	Abnormal	A	6,811	6,811	5,000	0	5,000
		L	1,247	1,247			
		R	8,268	8,268			
		V	7,847	7,847			
		Total	44,173	44,173	20,000	10,000	10,000

sample rate of 360 Hz, with approximately 110,000 beats. A set of beat labels is equipped at the peak of R.

2) A CMUH dataset supported by the First Affiliated Hospital of China Medical University. The dataset contains 12-lead ECG records of inpatients in the First Affiliated Hospital of China Medical University from January 2013 to December 2017, with a sampling rate of 560 Hz.

Two or three cardiologists annotated all heartbeats for both datasets independently. Only lead II ECG signals are used in this study.

2.2 Data preprocessing

A total of four types of arrhythmia and normal beats are selected from datasets: right bundle branch block (R), left bundle branch block (L), atrial premature beat (A), ventricular premature beat (V), and normal sinus rhythm (N). ECG signals are split into single heartbeats which are normalized to a range of [−1, 1] for network training. Five typical heartbeats are shown in Figure 1.

2.3 MIT-BIH dataset

In this study, 45 lead II signal records are selected from the MIT-BIH dataset (records 102, 104, and 114 were excluded, as they do not include the lead II data or the type of heart disease in our experiments). Wavelet transform is used to reduce noise and baseline drift (Alfaouri and Daqrouq, 2008). Then, the ECG data are split into single heartbeats using the marked R peak location. A total of 250 points (100 points before the R peak and 150 points after the R peak) are included in a heartbeat.

2.4 CMUH dataset

ECG data of 44,173 people from the CMUH dataset have been selected for this study. Data are resampled at 360 Hz to maintain consistency with MIT-BIH data. The beat segmentation method is the same as the one mentioned previously.

For each dataset, 10,000 normal ECG data are randomly selected as the training set, and 5,000 normal ECG data and 5,000 abnormal ECG data are randomly selected as the test set, as shown in Table 1.

3 Methods

3.1 ECG-AAE framework

The ECG-AAE framework consists of three parts: 1) an autoencoder, 2) a discriminator, and 3) an outlier detector, as shown in Figure 2. The autoencoder tries to minimize reconstruction errors to generate ECG signals similar to input signals. The discriminator uses reconstructed and original data as the input, and is trained to distinguish normal data from reconstructed data. Both the autoencoder and discriminator update simultaneously to improve the reconstruction performance of the autoencoder.

Finally, the combination of reconstruction errors and discriminant scores (probability output of discriminator) is used to evaluate normal ECG. Test data are mapped back to

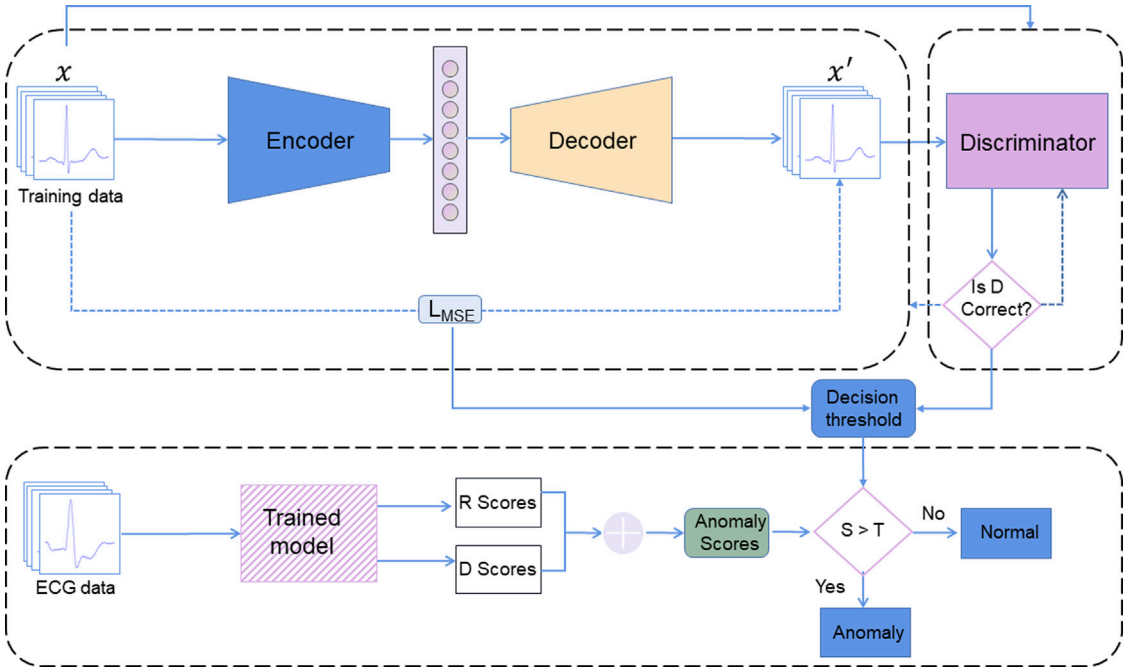

FIGURE 2
ECG-AAE framework consists of three parts: (1) an autoencoder, (2) a discriminator, and (3) an outlier detector. Here, R score is the reconstruction error score; D score is the discrimination score; S is the anomaly scores (the sum of R score and D score). T is the threshold of outlier data.

potential space, and loss between reconstructed test samples and actual test samples has been applied to calculate the corresponding reconstruction loss.

A detailed network of the ECG-AAE is shown in Table 2. The encoder is composed of three TCN blocks, three MaxPooling1D layers, a flatten layer, and a dense layer. The decoder is composed of a dense layer, three TCN blocks, three UpSampling1D layers, and a Conv1D layer. The discriminator is composed of three TCN blocks, three MaxPooling1D layers, a flatten layer, and two dense layers. The activation function for the last dense layer is sigmoid. A large discriminator can make the data overflow easily, while a shallow autoencoder cannot generate enough real data to defeat the discriminator. A small number of hidden units is chosen as the starting point, and the number of hidden units has been gradually increased in each successive layer, which is effective for the training of the model in this study. Also, three TCN blocks are used in the encoder, decoder, and discriminator.

In this study, stochastic gradient descent (Adam) (Kingma and Ba, 2015) is adopted to conduct alternating update training for each lost component, and parameters of the network model are obtained through training and learning.

3.2 Temporal convolutional network

Atemporal convolutional network (TCN) (L. Sun et al., 2015) could capture long-term dependence in an ECG sequence more effectively. A TCN block is superimposed by two causal convolution layers with the same expansion factor, followed by normalization, ReLU, and dropout layers, as shown in Figure 3.

The TCN is used to extract features of ECG time series data. The TCN module has shown competitiveness in many sequence-related modeling tasks (W. Zhao et al., 2019). It can capture dependencies in sequences more effectively than recurrent neural networks (Graves et al., 2013; Z. Huang et al., 2015; J. Chung et al., 2014). The TCN convolution kernel is shared in the same layer, with lower requirement memory.

The TCN is mainly composed of dilated causal convolution. Figure 4 shows a simple structure of TCNs, where x_i represents the characteristics of the ith moment. Expanded convolution enables input interval sampling during convolution, and the sampling rate is controlled by d. The parameter $d = 1$ in the bottom layer means that every point is sampled as input, and $d = 2$ in the middle layer means that every two points are sampled as input. Generally, the higher the level, the larger will be the value

TABLE 2 Detailed overview of the proposed ECG-AAE model.

Modules	Layers	Types	Activation function	Output shapes	Kernel size	No. of filters
Encoder	0	Input	—	250 × 1	—	—
	1	TCN block	ReLU	250 × 32	9	32
	2	MaxPooling1D	—	50 × 32	—	—
	3	TCN block	ReLU	50 × 16	9	16
	4	MaxPooling1D	—	10 × 16	—	—
	5	TCN block	ReLU	10 × 8	9	8
	6	MaxPooling1D	—	2 × 8	—	—
	7	Flatten	—	16	—	—
	8	Dense	ReLU -	8	—	—
Decoder	0	Input	—	8	—	—
	1	Dense	ReLU	16	—	—
	2	Reshape	—	2 × 8	—	—
	3	UpSampling1D	—	10 × 8	—	—
	4	TCN block	ReLU	10 × 8	9	8
	5	UpSampling1D	—	50 × 16	—	—
	6	TCN block	ReLU	50 × 16	9	16
	7	UpSampling1D	—	250 × 16	—	—
	8	TCN block	ReLU	250 × 32	9	32
	9	Conv1D	ReLU	250 × 1	9	1
Discriminator	0	Input	—	250 × 1	—	—
	1	TCN block	ReLU	250 × 32	9	32
	2	MaxPooling1D	—	50 × 32	—	—
	3	TCN block	ReLU	50 × 16	9	16
	4	MaxPooling1D	—	10 × 16	—	—
	5	TCN block	ReLU	10 × 8	9	8
	6	MaxPooling1D	—	2 × 8	—	—
	7	Flatten	—	16	—	—
	8	Dense	ReLU	8	—	—
	9	Dense	sigmoid	1		

of d used, with the size of the effective window of dilated convolution increasing exponentially with the number of levels. Convolution networks can obtain a larger receptive field with fewer layers.

The TCN uses a residual block structure which is similar to that in ResNet to solve problems such as a deeper network structure causing gradient disappearance, to make the model more generic. A residual block superimposes multiple causal convolutional layers with the same expansion factor, followed by normalization, ReLU, and dropout. In this study, a residual block containing two layers of convolution and nonlinear mapping is constructed, and normalization and dropout to each layer are added to regularize the network, as shown in Figure 3.

3.3 Autoencoder module

An autoencoder module consists of three parts: an encoder, a hidden layer, and a decoder. Only normal ECG data are used for training. First, input data x are compressed and encoded into the hidden layer data, and then hidden layer data are decoded to obtain reconstructed ECG data X' . The loss function during training is the reconstruction error between input data x and output data X':

$$\mathrm{Loss}\left(X, X'\right) = \left\|X - X'\right\|^2 \tag{1}$$

The encoder and decoder are optimized to minimize reconstruction errors of normal ECG using training data X.

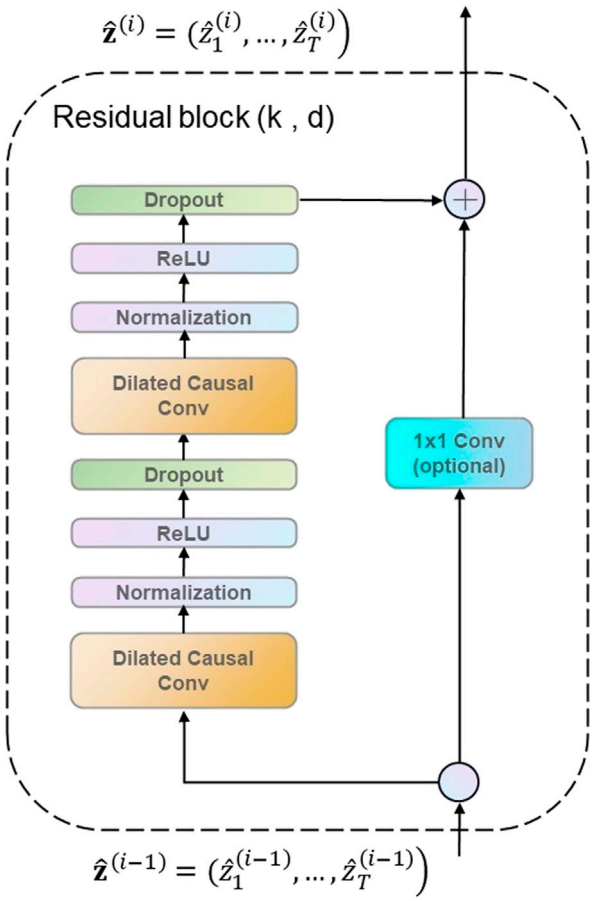

FIGURE 3
Residual block.

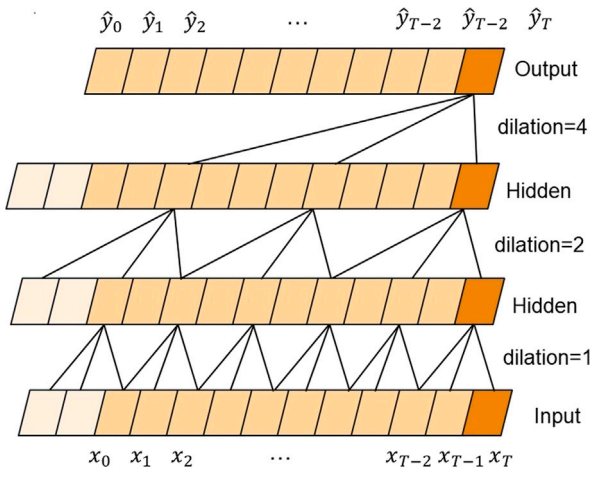

FIGURE 4
Stacked convolutional layers in the TCN.

The activation functions of the encoder and decoded neural networks are shown as follows:

$$Z = \delta(WX + b) \tag{2}$$

$$X' = \delta'(W'Z + b') \tag{3}$$

where, δ and δ' are non-linear exciting functions, and W, b, W', and b' are weights and offsets of linear transformations.

Minimizing the loss function to optimize the parameters in the encoder and decoder is equivalent to a nonlinear optimization problem:

$$\min_{\delta,w,b} \mathrm{Loss}(X, X') = \left\| X - \delta'(\delta(WX + b)) + b' \right\|^2 \tag{4}$$

3.4 Discriminator module

The discriminator (D) is to distinguish reconstructed ECG data X′ generated by the autoencoder (AE) from real data X during the training process, and to make reconstructed data similar to the input data. Thus, the autoencoder tries to minimize the reconstruction error, while the discriminator tries to maximize it. During training, the two modules optimize themselves and improve refactoring and discrimination. The autoencoder is trained to minimize the difference between reconstructed and input samples, and the discriminator is trained to maximize confidence in discriminating the difference between reconstructed and real samples. After training, the discriminator assigns correct labels to real and fake ECG data as sensitively as possible, while the autoencoder generates real ECG data as much as possible to deceive the discriminator, and the two reach a balance (D. Li et al., 2019). The conditional autoencoder and discriminator are trained following a two-player minimax game:

$$\min_{AE}\max_{D} V(D, AE) = \varepsilon_{x\sim Pdata(X)}[\log D(x)] + \varepsilon_{x\sim Pz(Z)}[\log(1 - D(AE))] \tag{5}$$

3.5 Outlier detection module

The combination of reconstruction errors and discriminant scores is used to define the abnormal score. Reconstruction loss R(x) makes a higher score on abnormal ECG data and a lower score on normal ECG data. The discrimination score D(x) produces lower scores on abnormal ECG data and higher scores on normal ECG data.

Therefore, the anomaly score a(x) formula is expressed as

$$a(x) = (1 - \lambda)R(x) + \lambda\frac{1}{D(x)} \tag{6}$$

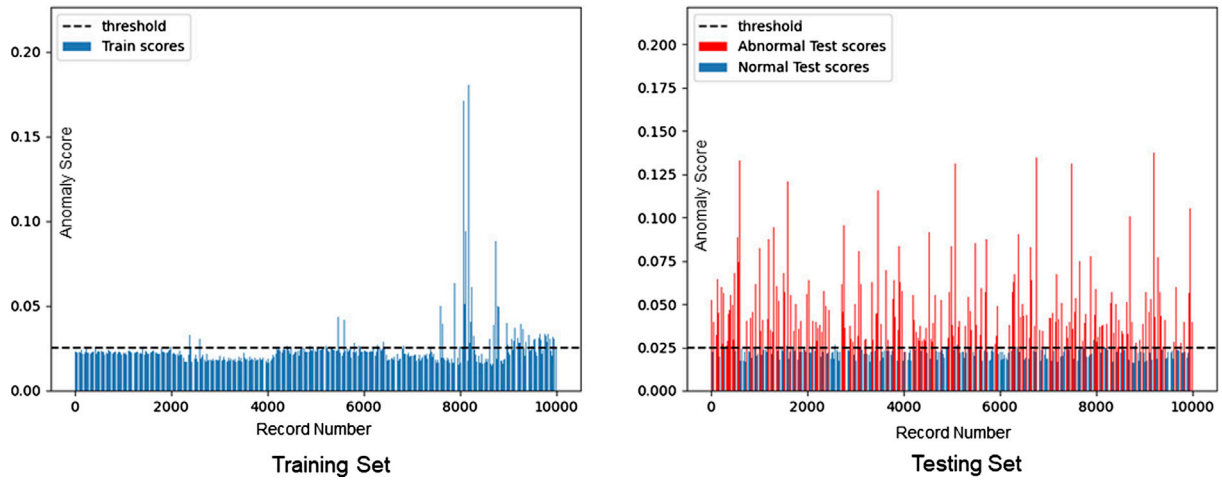

FIGURE 5
Distribution of anomaly scores of the MIT-BIH training set (T = 0.025).

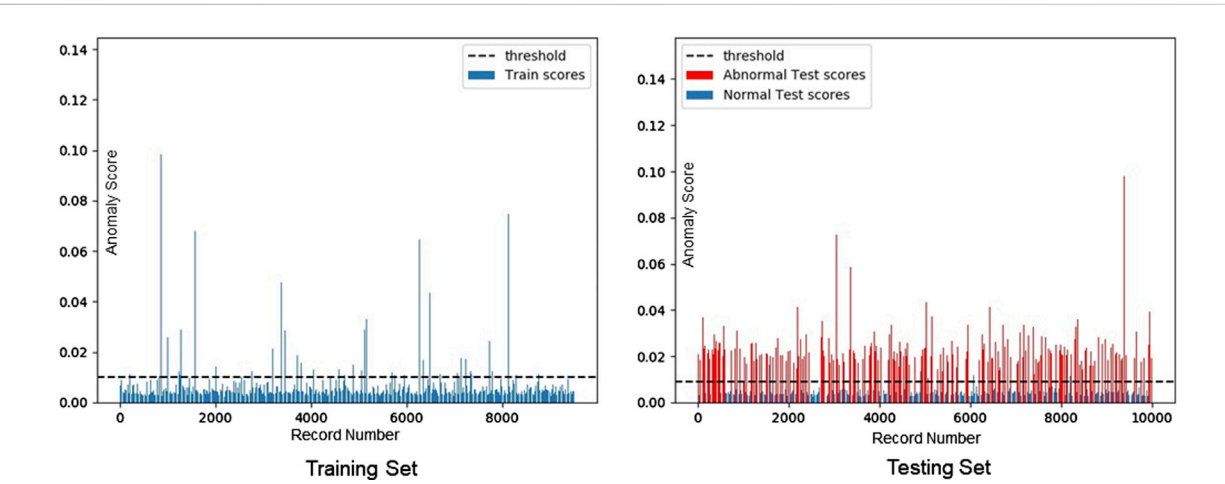

FIGURE 6
Distribution of anomaly scores of the CMUH training set (T = 0.01).

$\lambda = 0$, according to our experience. The threshold is decided following one standard deviation above the mean. ECG data with a (x) greater than the threshold are abnormal.

4 Results

4.1 Evaluation indexes

Accuracy (ACC), precision (Pre), recall (Rec), F1-score (F_1), and AUC value (area under the ROC curve) are used to evaluate the performance of our ECG-AAE and compare it with other methods. In the confusion matrix, abnormal ECG is defined as positive, normal ECG is defined as negative, and true positive (TP), true negative (TN), false positive (FP), and false negative (FN) are calculated.

$$ACC = \frac{TP + TN}{TP + TN + FP + FN}$$

$$Pre = \frac{TP}{TP + FP}$$

$$Rec = \frac{TP}{TP + FN}$$

$$F_1 = 2 \times \frac{Pre \times Rec}{Pre + Rec}$$

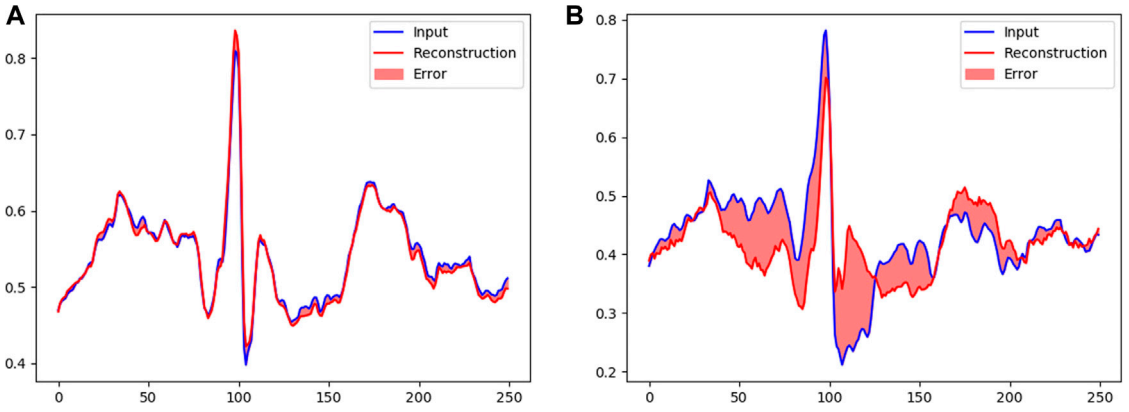

FIGURE 7
Reconstruction of ECG data: **(A)** normal and **(B)** abnormal.

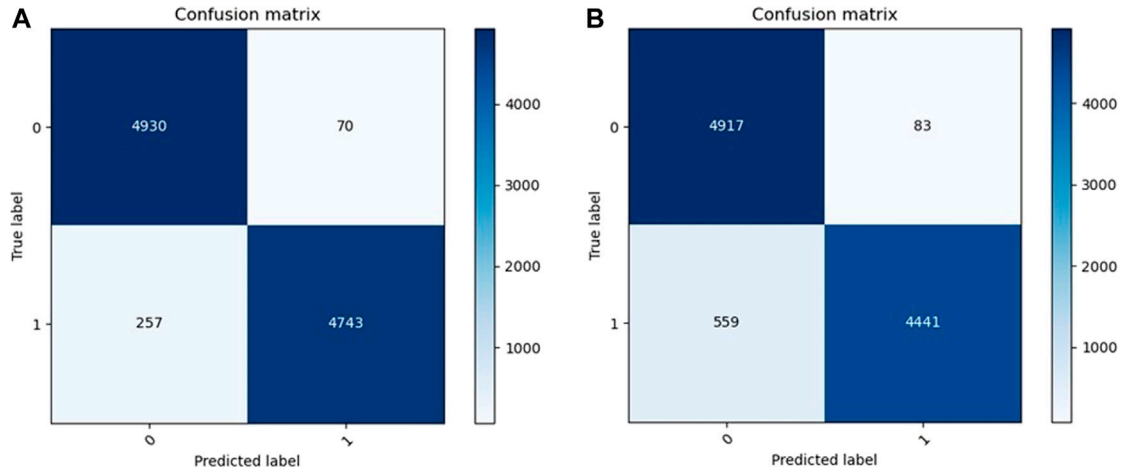

FIGURE 8
Confusion matrix of **(A)** MIT-BIH dataset and **(B)** CMUH dataset (1 = normal 0 = abnormal).

In clinical practice, the precision rate represents the proportion of patients with true ECG abnormalities, while recall rate represents the proportion of patients with true ECG abnormalities. The high-precision detection model could prevent misdiagnosis, while the detection model with a high recall rate could avoid missed diagnosis. The F1-score is a weighted harmonic average of the recall rate and accuracy rate; the F1-score and AUC value are used as the main indicators to measure the performance of outlier detection in this study.

The experiment was implemented on a workstation (Dell T7600, Xeron 2,650 × 2, 256 GB RAM, 1080Ti×2), with Linux 18.04, Python 3.6, Keras 2.3.1, and TensorFlow 2.0.

4.1.1 Experiment 1

Both MIT-BIH and CMUH datasets have been used to verify the performance of our framework. The threshold value is selected as one standard deviation above the mean according to the abnormal score in the training set. T values of MIT-BIH and CMUH datasets can be obtained as 0.025 and 0.01, respectively. When the training set includes normal data only, its abnormal scores are within the range of the threshold T (Figures 5A, 6A), while, in the test dataset including both normal and abnormal ECG data, the abnormal scores are less than the threshold T for normal ECG data, but are greater than the threshold T (Figures 5B, 6B) for abnormal ECG data.

TABLE 3 Average classification performance for different methods on the MIT-BIH dataset.

Methods	Acc ±SD	Pre ±SD	Rec ±SD	F1-score ± SD	AUC ±SD
OURS	**0.9673 ± 0.0005**	0.9854 ± 0.0003	0.9486 ± 0.0001	**0.9666 ± 0.0014**	**0.9672 ± 0.0015**
AnoGAN (Schlegl et al.)	0.9257 ± 0.0101	0.8829 ± 0.0167	0.9876 ± 0.0027	0.9323 ± 0.0085	0.9283 ± 0.0101
AE (K.Wang et al.)	0.9282 ± 0.0180	0.8733 ± 0.2042	**0.9902 ± 0.0233**	0.9281 ± 0.1490	0.9233 ± 0.0049
VAE (X.Wang et al.)	0.8048 ± 0.0028	0.7196 ± 0.0029	0.9874 ± 0.0002	0.8325 ± 0.0157	0.8013 ± 0.0028
Stack LSTM (Chauhan et al.)	0.8875 ± 0.0017	0.8313 ± 0.0021	0.9740 ± 0.0007	0.8970 ± 0.0019	0.8882 ± 0.0052
GRU (Cowton et al.)	0.8764 ± 0.0040	0.8128 ± 0.0064	0.9746 ± 0.0017	0.8864 ± 0.0031	0.8751 ± 0.0040
RNN (Latif et al.)	0.8568 ± 0.0031	0.7826 ± 0.0040	0.9798 ± 0.0003	0.8702 ± 0.0024	0.8538 ± 0.0031
DEEP-SVDD (Ruff et al.)	0.8039 ± 0.0035	0.7221 ± 0.0037	0.8342 ± 0.0002	0.8342 ± 0.0025	0.8037 ± 0.0033
AE + OCSVM (Mo et al.)	0.8624 ± 0.0036	0.7965 ± 0.0046	0.9788 ± 0.0003	0.8783 ± 0.0029	0.8644 ± 0.0050
DAGMM (Song et al.)	0.7646 ± 0.0007	**0.9992 ± 0.0008**	0.5304 ± 0.0004	0.6930 ± 0.0019	0.7650 ± 0.0019
GMM (Dai et al.)	0.6462 ± 0.0463	0.9986 ± 0.1603	0.2924 ± 0.0068	0.4524 ± 0.0274	0.6460 ± 0.0042
OCSVM (Schölkopf et al.)	0.8376 ± 0.0009	0.9982 ± 0.0006	0.6760 ± 0.0005	0.8061 ± 0.0018	0.8374 ± 0.0019
iForest (Liu et al.)	0.6521 ± 0.0106	0.9987 ± 0.2119	0.3046 ± 0.3468	0.4668 ± 0.1334	0.6521 ± 0.0106
LOF (Bin Yao et al.)	0.5050 ± 0.0006	0.5027 ± 0.0007	0.9170 ± 0.0025	0.6494 ± 0.0018	0.5050 ± 0.0020

SD, standard deviation.
The bold values mean maximum.

TABLE 4 Average classification performance for different methods on the CMUH dataset.

Methods	Acc ± SD	Pre ± SD	Rec ± SD	F1-score ± SD	AUC ± SD
OURS	**0.9358 ± 0.0004**	0.9816 ± 0.0002	0.8882 ± 0.0010	**0.9325 ± 0.0008**	**0.9358 ± 0.00010**
AnoGAN (Schlegl et al.)	0.8985 ± 0.0092	0.8396 ± 0.0128	0.9852 ± 0.0018	0.9066 ± 0.0078	0.8985 ± 0.0092
AE (K.Wang et al.)	0.9103 ± 0.0181	0.8504 ± 0.0253	**0.9946 ± 0.0012**	0.9169 ± 0.0148	0.9098 ± 0.0181
VAE (X.Wang et al.)	0.7744 ± 0.0040	0.6885 ± 0.0039	0.9910 ± 0.0015	0.8125 ± 0.0027	0.7713 ± 0.0041
Stack LSTM (Chauhan et al.)	0.8754 ± 0.0033	0.8097 ± 0.0051	0.9772 ± 0.0019	0.8856 ± 0.0025	0.8738 ± 0.0033
GRU (Cowton et al.)	0.8779 ± 0.0038	0.8156 ± 0.0052	0.9748 ± 0.0019	0.8881 ± 0.0030	0.8772 ± 0.0038
RNN (Latif et al.)	0.8221 ± 0.0037	0.7414 ± 0.0041	0.9860 ± 0.0021	0.8464 ± 0.0026	0.8210 ± 0.0037
DEEP-SVDD (Ruff et al.)	0.7649 ± 0.0050	0.6794 ± 0.0047	0.9908 ± 0.0017	0.8061 ± 0.0032	0.7616 ± 0.0050
AE + OCSVM (Mo et al.)	0.8245 ± 0.0030	0.7436 ± 0.0034	0.9864 ± 0.0022	0.8479 ± 0.0021	0.8231 ± 0.0030
DAGMM (Song et al.)	0.7260 ± 0.0012	0.9991 ± 0.0004	0.4520 ± 0.0024	0.6224 ± 0.0023	0.7258 ± 0.0012
GMM (Dai et al.)	0.6057 ± 0.0037	**1.0000 ± 0.0005**	0.2148 ± 0.0074	0.3536 ± 0.0101	0.6074 ± 0.0037
OCSVM (Schölkopf et al.)	0.7600 ± 0.0024	0.9985 ± 0.0010	0.5208 ± 0.0048	0.6845 ± 0.0041	0.7600 ± 0.0024
iForest (Liu et al.)	0.6303 ± 0.0043	**1.0000 ± 0.0009**	0.2606 ± 0.0086	0.4135 ± 0.0107	0.6303 ± 0.0043
LOF (Bin Yao et al.)	0.5767 ± 0.0059	**1.0000 ± 0.0010**	0.1700 ± 0.0117	0.2906 ± 0.0174	0.5850 ± 0.0059

SD, standard deviation.
The bold values mean maximum.

An example of normal and abnormal ECG data reconstructed by our model is shown in Figure 7. For normal ECG data, reconstructed data are continuous, and the shape of the reconstructed waveform is basically the same as the input one, with an error range of 0.0063 ± 0.0098. For abnormal ECG data, the shape of the reconstructed waveform differs greatly from that of the input waveform. Although the reconstructed data are continuous, the error range reaches 0.0289 ± 0.0264.

The confusion matrixes of detection results are shown in Figure 8. In the MIT-BIH dataset, 4,930 abnormal ECGs were detected, and 257 normal ECGs were predicted as abnormal. In our CMUH dataset, 4,917 abnormal ECG data were detected, and 559 normal ECGs were predicted as abnormal. The accuracy, recall, F1 score, and AUC of our model are 0.9673, 0.9854, 0.9486, 0.9666, and 0.9672, and 0.9358, 0.9816, 0.8882, 0.9325, and 0.9358, respectively.

4.1.2 Experiment 2

Our method was compared with 13 popular outlier detection methods using MIT datasets, as shown in Table 3. Among the five

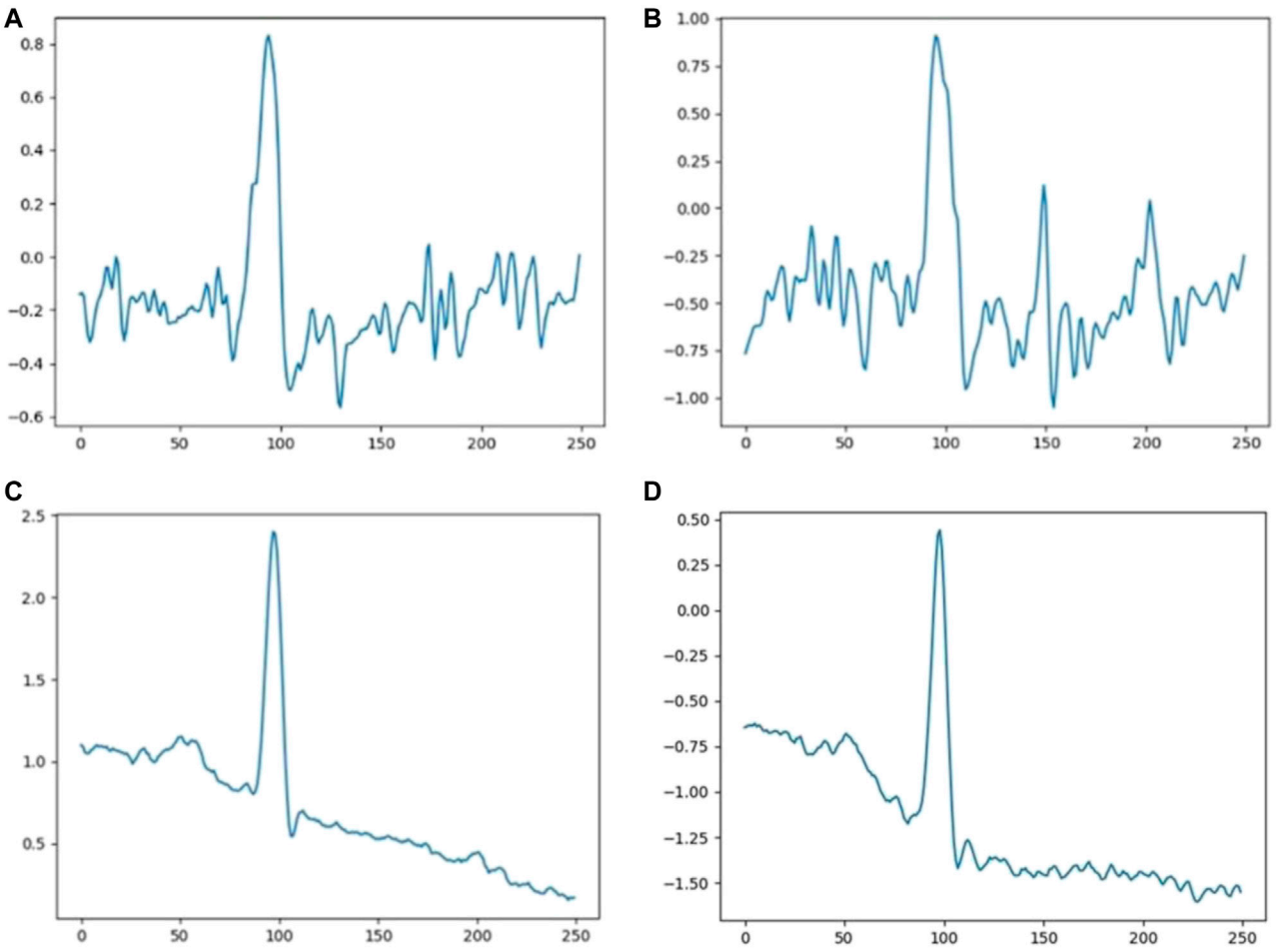

FIGURE 9
Analysis of the predication error **(A,B)** noise interference ECG, **(C,D)** baseline drift ECG.

evaluation indicators, our model achieves the highest score of 0.9673 in accuracy. DAGMM achieves the highest score of 0.9992 in precision, but its recall is 0.5304. This shows that DAGMM tries to predict the sample as a positive sample when it is "more certain," but misses many unsure positive samples due to its excessive conservativeness. The AE achieves the highest recall score of 0.9902, but the precision is 0.8829, indicating that the AE produces more false positives. The ECG-AAE model achieves the highest scores of 0.9673, 0.9666, and 0.9672 in accuracy, F1-score, and AUC value, respectively, better than other models.

4.1.3 Experiment 3

We further verify the robustness and generalization of the model with our CMUH dataset, as shown in Table 4.

Our model achieves the highest scores of 0.9358, 0.9325, and 0.9358 in accuracy, F1-score, and AUC, respectively. GMM, iForest, and LOF models achieve the highest score of 1.000 in precision, but the recall was lower. The AE achieves the highest recall of 0.9946, but the F1-score and AUC value are lower.

5 Discussion

To solve problems that the classification model cannot effectively detect in abnormal ECGs, we propose the ECG-AAE, a framework for detecting abnormal ECG signals. Its performance is verified and compared with the AE, AnoGAN, and other 11 popular outlier detection methods on the MIT-BIH arrhythmia dataset and our CMUH dataset.

The four kinds of machine learning outlier detection algorithms with low performance scores were GMM (Dai and Gao, 2013), OCSVM (B. Schölkopf et al., 2000), iForest (F.T. Liu et al., 2008), and LOF (S.H. Bin Yao and Hutchison, 2014). Among them, GMM enjoys the best performance, whose AUC values are 0.6460 and 0.6074 on the MIT-BIH and CMUH

datasets respectively; LOF, the worst model, shows AUC values are 0.5050 and 0.5850, respectively. It suggests that the machine learning methods might not be the best choice for abnormal ECG detection; they may not extract abnormal ECG effectively. Moreover, the subsequent classifiers could not fit the boundary functions in high-dimension feature space, while, the deep learning models could make ECG feature extraction more elastic to fit the nonlinear feature distribution, and finally improve the detection rate of abnormal ECG while ensuring accuracy.

Among deep learning models, generative models based on AE or GAN are better than hybrid models of machine learning and deep learning (e.g., AE + OCSVM (Mo, 2016) deep-SVDD (L. Ruff et al., 2018), DAGMM (Q. Song et al., 2018), RNN and its variants, LSTM, GRU, and other recurrent neural network models). The autoencoder Cowton et al., (K. Wang et al., 2016) encodes one-dimensional signal data into a lower dimension to learn the general distribution of data and then decodes to a higher dimension to reconstruct data. In this experiment, the AE performs well on both the MIT-BIH and CMUH datasets.

The ECG-AAE combines the autoencoder and discriminator, and it uses the autoencoder to realize reconstruction of the ECG and the discriminator to improve the generation ability of the autoencoder. The TCN could obtain ECG features at different scales with different receptive fields, which helps accurately reconstruct the normal ECG. In addition, the TCN avoids problems of gradient disappearance or gradient explosion. We use the combination of reconstruction errors and discriminant scores as the anomaly score, which effectively reduces the impact of the AE overfitting and instability of the GAN model. Compared with methods dealing with two leads or more, Liu F (2020) provided an accuracy of 97.3% in ECG anomaly detection; Thill et al. (2021 designed a temporal convolutional network autoencoder (TCN-AE) based on dilated convolutions for time series data.

Experiments 2 and 3 suggest that the CMUH dataset is about 0.3% lower than the MIT-BIH dataset on each model. The reason is that all the heartbeats in the MIT-BIH dataset are only from 48 people. These independent heartbeats are obtained through heartbeat segmentation, with very similar characteristics which are not enough for generalization, while each heartbeat in our CMUH dataset comes from a signal person, which is more in line with reality.

False positive data are largely affected by noise interference, as shown in Figures 9A,B. At the same time, false negative data in the experiment have also been analyzed with the finding that a baseline exists in most cases, as shown in Figures 9C,D. The ECG-AAE model can tolerate noise and baseline drift of conventional static ECG, but the form of input data in these error cases is quite different from that of normal ECG data. This situation might occur when patients move in a large range. Although noise filtering and baseline drift are carried out in the data preprocessing stage, an ideal effect is not achieved on the ECG data with large variation, which leads to a false positive and negative output of the model. In clinical practice, false positives and negatives can be avoided by analyzing several continuous heartbeats, and when the several continuous heartbeats are judged to be abnormal ECGs, abnormal ECGs can be diagnosed.

6 Conclusion

Detection and early warning of sudden abnormal ECG is an important procedure in an ECG monitoring and alarm system. The ECG-AAE framework proposed in this study could efficiently detect abnormal ECG signals, and provide better performance on several indicators in our tests. It also suggests that outlier detection performs better than the classical classification framework in clinical practices. As far as we know, this is the first study to combine the adjournment network of abnormal ECG detection, which solves all types of abnormal ECG data and data balance problems and effectively improves the detection rate of abnormal ECG in the open set condition while ensuring accuracy.

Data availability statement

The original contributions presented in the study are included in the article/Supplementary Material; further inquiries can be directed to the corresponding author.

Author contributions

LS and YL contributed equally to design of the study, performed the statistical analysis, and wrote the first draft of the manuscript. HJ organized the dataset and interpreted our ECG data. PZ contributed to debug the program. JN, RL, YW, JP, and HY organized the dataset. SC contributed to the concept and revised the manuscript. All authors contributed to approve the submitted version.

Funding

This work was supported by Liaoning Natural Science Funds for Medicine and Engineering Interdisciplines 2021 (1600779161987) and Big Data Research for Health Science of China Medical University (Key Project No. 6).

Conflict of interest

The authors declare that the research was conducted in the absence of any commercial or financial relationships that could be construed as a potential conflict of interest.

Publisher's note

References

Acharya, U. R., Fujita, H., Oh, S. L., Hagiwara, Y., Tan, J. H., and Adam, M. (2017). Application of deep convolutional neural network for automated detection of myocardial infarction using ECG signals. *Inf. Sci. (N. Y).* 415-416, 190–198. doi:10.1016/j.ins.2017.06.027

Alfaouri, M., and Daqrouq, K. (2008). ECG signal denoising by wavelet transform thresholding. *Am. J. Appl. Sci.* 5 (3), 276–281. doi:10.3844/ajassp.2008.276.281

Bin Yao, S. H., and Hutchison, D. (2014). *Density-based local outlier detection on uncertain data*. doi:10.11896/j.issn.1002-137X.2015.5.046

Chauhan, S., and Vig, L. (2015). Anomaly detection in ECG time signals via deep long short-term memory networks. *Proc. 2015 IEEE Int. Conf. Data Sci. Adv. Anal. DSAA* 2016. doi:10.1109/DSAA.2015.7344872

Chung, J., Gulcehre, C., Cho, K., and Bengio, Y. (2014). *Empirical evaluation of gated recurrent neural networks on sequence modeling*. Available at: http://arxiv.org/abs/1412.3555.

Cowton, J., Kyriazakis, I., Plötz, T., and Bacardit, J. (2018). A combined deep learning GRU-autoencoder for the early detection of respiratory disease in pigs using multiple environmental sensors. *Sensors Switz.*, E2521. doi:10.3390/s18082521

Dai, X., and Gao, Z. (2013). From model, signal to knowledge: A data-driven perspective of fault detection and diagnosis. *IEEE Trans. Ind. Inf.* 9, 2226–2238. doi:10.1109/TII.2013.2243743

De Chazal, P., Celler, B. G., and Reilly, R. B. (2000). Using wavelet coefficients for the classification of the electrocardiogram. *Annu. Int. Conf. IEEE Eng. Med. Biol. - Proc.* 1, 64–67. doi:10.1109/IEMBS.2000.900669

Dong, J., and Zhu, H. H. (2004). Mobile ECG detector through GPRS/Internet. *Proc. IEEE Symp. Comput. Med. Syst.* 17, 485–489. doi:10.1109/cbms.2004.1311761

Esteban, C., Hyland, S. L., and Rätsch, G. (2017). *Real-valued (medical) time series generation with recurrent conditional GANs*. Available at: http://arxiv.org/abs/1706.02633.

Faust, O., Hagiwara, Y., Hong, T. J., Lih, O. S., and Acharya, U. R. (2018). Deep learning for healthcare applications based on physiological signals: A review. *Comput. Methods Programs Biomed.* 161, 1–13. doi:10.1016/j.cmpb.2018.04.005

Fernando, T., Gammulle, H., Denman, S., Sridharan, S., and Fookes, C. (2021). Deep learning for medical anomaly detection – a survey. *ACM Comput. Surv.* 54, 1–37. doi:10.1145/3464423

Graves, A., Mohamed, A., and Hinton, G. (2013). *Speech recognition with deep recurrent neural networks*, 3. Department of Computer Science, University of Toronto, 45–49. Dep. Comput. Sci. Univ. Toronto. Available at: https://ieeexplore.ieee.org/document/6638947.

Huang, Z., Xu, W., and Yu, K. (2015). *Bidirectional LSTM-CRF models for sequence tagging*. Available at: http://arxiv.org/abs/1508.01991.

Kingma, D. P., and Ba, J. L. (2015). Adam: A method for stochastic optimization, 3rd. *Int. Conf. Learn. Represent. ICLR 2015 - Conf. Track Proc.*, 1–15.

Latif, S., Usman, M., Rana, R., and Qadir, J. (2018). Phonocardiographic sensing using deep learning for abnormal heartbeat detection. *IEEE Sens. J.* 18, 9393–9400. doi:10.1109/JSEN.2018.2870759

Lemos, C. W. M., and Tierra-Criollo, C. J. (2008). ECG anomalies identification using a time series novelty. *Detect. Tech.* 18, 766–769. doi:10.1007/978-3-540-74471-9

Li, C., Zhao, H., Lu, W., Leng, X., and Xiang, J. (2021). DeepECG: Image-based electrocardiogram interpretation with deep convolutional neural networks. *Biomed. Signal Process. Control* 69, 102824. doi:10.1016/j.bspc.2021.102824

Li, D., Chen, D., Jin, B., Shi, L., Goh, J., and Ng, S. K. (2019). MAD-GAN: Multivariate anomaly detection for time series data with generative adversarial networks. *Lect. Notes Comput. Sci. Incl. Subser. Lect. Notes Artif. Intell. Lect. Notes Bioinforma. 11730 LNCS*, 703–716. doi:10.1007/978-3-030-30490-4_56

Li, K., Du, N., and Zhang, A. (2012). Detecting ECG abnormalities via transductive transfer learning. *ACM Conf. Bioinforma. Comput. Biol. Biomed. BCB* 2012, 210–217. doi:10.1145/2382936.2382963

Li, S., and Wen, J. (2014). A model-based fault detection and diagnostic methodology based on PCA method and wavelet transform. *Energy Build.* 68, 63–71. doi:10.1016/j.enbuild.2013.08.044

Liu, F. T., Ting, K. M., and Zhou, Z. H. (2008). Isolation forest. *Proc. - IEEE Int. Conf. Data Min. ICDM.*, 413–422. doi:10.1109/ICDM.2008.17

Lynn, H. M., Pan, S. B., and Kim, P. (2019). A deep bidirectional GRU network model for biometric electrocardiogram classification based on recurrent neural networks. *IEEE Access* 7, 145395–145405. doi:10.1109/ACCESS.2019.2939947

Malhotra, P., Vig, L., Shroff, G., and Agarwal, P. (2015). Long short term memory networks for anomaly detection in time series, 23rd eur. Symp. Artif. Neural networks. *Comput. Intell. Mach. Learn. ESANN 2015 - Proc.*, 89–94.

Martin, H., Izquierdo, W., Cabrerizo, M., Cabrera, A., and Adjouadi, M. (2021). Near real-time single-beat myocardial infarction detection from single-lead electrocardiogram using Long Short-Term Memory Neural Network. *Biomed. Signal Process. Control* 68, 102683. doi:10.1016/j.bspc.2021.102683

Mathunjwa, B. M., Lin, Y. T., Lin, C. H., Abbod, M. F., and Shieh, J. S. (2021). ECG arrhythmia classification by using a recurrence plot and convolutional neural network. *Biomed. Signal Process. Control* 64, 102262. doi:10.1016/j.bspc.2020.102262

Mo, J. (2016). *Detecting anomalous data using auto-encoders*. doi:10.18178/ijmlc.2016.6.1.565

Mogren, O. (2016). *C-RNN-GAN: Continuous recurrent neural networks with adversarial training*. Available at: http://arxiv.org/abs/1611.09904.

Onan, A. (2020). Sentiment analysis on product reviews based on weighted word embeddings and deep neural networks. *Concurr. Comput. Pract. Exper.* 33, 1–12. doi:10.1002/cpe.5909

Onan, A., and Tocoglu, M. A. (2021). A term weighted neural language model and stacked bidirectional LSTM based framework for sarcasm identification. *IEEE Access* 9, 7701–7722. doi:10.1109/ACCESS.2021.3049734

Özbay, Y., Ceylan, R., and Karlik, B. (2011). Integration of type-2 fuzzy clustering and wavelet transform in a neural network based ECG classifier. *Expert Syst. Appl.* 38, 1004–1010. doi:10.1016/j.eswa.2010.07.118

Pang, G., Shen, C., Cao, L., and Van Den Hengel, A. (2021). Deep learning for anomaly detection: A review. *ACM Comput. Surv.* 54, 1–38. doi:10.1145/3439950

Risk, M. R., Sobh, J. F., and Saul, J. P. (1997). Beat detection and classification of ECG using self organizing maps. *Annu. Int. Conf. IEEE Eng. Med. Biol. - Proc.* 1, 89–91. doi:10.1109/iembs.1997.754471

Ruff, L., Vandermeulen, R. A., Binder, A., Emmanuel, M., and Kloft, M. (2018). *Deep one-class classification deep one-class classification*.

Sacco, R. L., Roth, G. A., Reddy, K. S., Arnett, D. K., Bonita, R., Gaziano, T. A., et al. (2016). The heart of 25 by 25: Achieving the goal of reducing global and regional premature deaths from cardiovascular diseases and stroke: A modeling study from the American heart association and world heart federation. *Glob. Heart* 11, 251–264. doi:10.1016/j.gheart.2016.04.002

Schlegl, T., Seeböck, P., Waldstein, S. M., Schmidt-Erfurth, U., and Langs, G. (2017). Unsupervised anomaly detection with generative adversarial networks to guide marker discovery. *Lect. Notes Comput. Sci. Incl. Subser. Lect. Notes Artif. Intell. Lect. Notes Bioinforma. 10265 LNCS*, 146–157. doi:10.1007/978-3-319-59050-9_12

Schölkopf, B., Williamson, R., Smola, A., Shawe-Taylor, J., and Piatt, J. (2000). Support vector method for novelty detection. *Adv. Neural Inf. Process. Syst.*, 582–588.

Shibuya, H., and Maeda, S. (2016). Anomaly detection method based on fast local subspace classifier. *Electron. Comm. Jpn.* 99, 32–41. doi:10.1002/ecj.11770

Song, Q., Zong, B., Wu, Y., Tang, L. A., Zhang, H., Jiang, G., et al. (2018). TGNet: Learning to rank nodes in temporal graphs. *Int. Conf. Inf. Knowl. Manag. Proc.*, 97–106. doi:10.1145/3269206.3271698

Srinivasan, N., Ge, D. F., and Krishnan, S. M. (2002). Autoregressive modeling and classification of cardiac arrhythmias. *Annu. Int. Conf. IEEE Eng. Med. Biol. - Proc.* 2, 1405–1406. doi:10.1109/IEMBS.2002.1106452

Sun, L., Jia, K., Yeung, D. Y., and Shi, B. E. (2015). "Human action recognition using factorized spatio-temporal convolutional networks," in Proc. IEEE Int. Conf. Comput. Vis. 2015 Inter, 4597–4605. doi:10.1109/ICCV.2015.522

Thill, M., Konen, W., Wang, H., and Back, T. (2021). Temporal convolutional autoencoder for unsupervised anomaly detection in time series. *Appl. Soft Comput.* 2021 (3), 107751. doi:10.1016/j.asoc.2021.107751

Wang, K., Zhao, Y., Xiong, Q., Fan, M., Sun, G., Ma, L., et al. (2016). Research on healthy anomaly detection model based on deep learning from multiple time-series physiological signals. *Sci. Program.* 2016, 1–9. doi:10.1155/2016/5642856

Wang, X., Du, Y., Lin, S., Cui, P., Shen, Y., and Yang, Y. (2020). adVAE: A self-adversarial variational autoencoder with Gaussian anomaly prior knowledge for anomaly detection. *Knowl. Based. Syst.* 190, 105187. doi:10.1016/j.knosys.2019.105187

Xia, Y., Cao, X., Wen, F., Hua, G., and Sun, J. (2015). "Learning discriminative reconstructions for unsupervised outlier removal," in Proc. IEEE Int. Conf. Comput. Vis. 2015 Inter, 1511–1519. doi:10.1109/ICCV.2015.177

Xia, Y., Wulan, N., Wang, K., and Zhang, H. (2018). Detecting atrial fibrillation by deep convolutional neural networks. *Comput. Biol. Med.* 93, 84–92. doi:10.1016/j.compbiomed.2017.12.007

Zhao, W., Gao, Y., Ji, T., Wan, X., Ye, F., and Bai, G. (2019). Deep temporal convolutional networks for short-term traffic flow forecasting. *IEEE Access* 7, 114496–114507. doi:10.1109/ACCESS.2019.2935504

Zhou, C., and Paffenroth, R. C. (2017). Anomaly detection with robust deep autoencoders. *Proc. ACM SIGKDD Int. Conf. Knowl. Discov. Data Min. Part* F1296, 665–674. doi:10.1145/3097983.3098052

frontiers | Frontiers in Physiology

TYPE Original Research
PUBLISHED 06 September 2022
DOI 10.3389/fphys.2022.1000007

OPEN ACCESS

EDITED BY
Lisheng Xu,
Northeastern University, China

REVIEWED BY
Yong Zhang,
Northern Theater General Hospital, China
Haibo Song,
West China Hospital, Sichuan University, China
Wu Weichun,
Chinese Academy of Medical Sciences and Peking Union Medical College, China

*CORRESPONDENCE
Weidong Ren,
rwd0410@163.com

SPECIALTY SECTION
This article was submitted to Computational Physiology and Medicine, a section of the journal Frontiers in Physiology

RECEIVED 21 July 2022
ACCEPTED 16 August 2022
PUBLISHED 06 September 2022

CITATION
Sun F, Sun A, Chen Y, Xiao Y, Zhang X, Qiao W, Tan X, Liang Y, Li D, Yang S and Ren W (2022), Novel TrueVue series of 3D echocardiography: Revealing the pathological morphology of congenital heart disease.
Front. Physiol. 13:1000007.
doi: 10.3389/fphys.2022.1000007

Novel TrueVue series of 3D echocardiography: Revealing the pathological morphology of congenital heart disease

Feifei Sun[1], Aijiao Sun[1], Yixin Chen[1], Yangjie Xiao[1], Xintong Zhang[1], Wei Qiao[1], Xueying Tan[1], Yanxiao Liang[2], Dongyu Li[2], Shu Yang[3] and Weidong Ren[1]*

[1]Department of Ultrasound, Shengjing Hospital of China Medical University, Shenyang, China, [2]Department of Cardiac Surgery, Shengjing Hospital of China Medical University, Shenyang, China, [3]Department of Ultrasound, Philips Medical Technology, Shenyang, China

Aims: This study explored the advantages and limitations of novel series of three-dimensional (3D) echocardiographic techniques and summarized their application methods for congenital heart diseases (CHDs).

Method and result: Two-dimensional (2D), traditional 3D echocardiography, and TrueVue plus light and/or Glass novel 3D technologies were performed on 62 patients with CHD, and a clinical survey was designed to judge whether the novel 3D images were more helpful for understanding the cardiac condition and guide treatment than traditional 3D images. TrueVue increased the visual resolution and simulated the true texture of cardiac tissue, significantly improving the display ability of abnormal anatomical structures in CHDs. TrueVue Glass displayed the blood channel and the internal structure of cardiac cavity more intuitively, indicating a new observation aspect not shown by conventional echocardiography. The clinical survey results showed that the new 3D imaging methods effectively increased the diagnostic confidence of echocardiographers, enabled surgeons to better understand the details of lesions, promoted efficient communication, and improved the confidence of both doctors and patients in treatment.

Conclusion: The combined application of TrueVue, TrueVue Light, and TrueVue Glass more closely simulated real anatomical features, showed more comprehensive and subtle blood flow in the lumen, not only increased the visual effect but also provided more useful diagnostic information, improved the accuracy of evaluation and treatment of CHD when compared to traditional imaging techniques, indicating that this combined application has significant clinical value.

Abbreviations: 2DE, Two-dimension echocardiography; 3DE, Three-dimensional echocardiography; AI, Artificial intelligence; ASD, Atrial septal defect; AV, Aortic valve; CHD, Congenital heart disease; DOMV, Double orifice mitral valve; CAVSD, Complete atrioventricular septal defect; MV, Mitral valve; PDA, Patent ductus arteriosus; PS, Pulmonary artery stenosis; TEE, Transesophageal echocardiography; TTE, Transthoracic echocardiography; VSD, Ventricular septal defect.

KEYWORDS

heart defects, congenital abnormalities, echocardiography, real-time three-dimensional, ultrasonic imaging

Introduction

Congenital heart disease (CHD) may be caused by developmental disorders during the cardiac embryonic period or unclosed channels after birth and is an important cause of death for children and adults (Meras et al., 2021). Real-time three-dimensional echocardiography (3DE) can visually and stereoscopically display some congenital malformation, providing supplementary information for the diagnostic evaluation of various CHDs. However, traditional 3DE is affected by many factors, such as limited image quality and a monotonous imaging mode (Cossor et al., 2015; Simpson et al., 2017). It has been considered that it cannot be used as an independent diagnostic tool, and reliance on 2D dynamic scanning remains prevalent (Fabricius et al., 2004; van den Bosch et al., 2006; Simpson et al., 2017). Recently, the advent of the TrueVue, TrueVue Light, and TrueVue Glass series of novel rendering technologies (from Philips company) provides more comprehensive, advanced 3D diagnostic evidence for evaluating abnormal cardiac anatomical structures (Genovese et al., 2019; Kern et al., 2019; Vainrib et al., 2019; Vairo et al., 2019). Especially for the artificial intelligence (AI) technology-assisted TrueVue Glass imaging mode, which released globally in the second half of 2020, there are few applied studies of these technologies, and they are mainly limited to transesophageal echocardiography (TEE) (Karagodin et al., 2020); to our knowledge, there has been no systematic exploration of their application for CHD. This study is the first to jointly apply the TrueVue, TrueVue Light, and TrueVue Glass series of advanced 3DE to diagnose and evaluate CHD and explore their application methods and practical value. In addition, a questionnaire was employed to evaluate the merit of these novel tools to echocardiographers, cardiac surgeons, and patients.

Materials and methods

Patients' data collection

This study included 62 patients, who underwent echocardiographic evaluation in our hospital for cardiac-related clinical symptoms or signs and were diagnosed with CHD from August 2020 to May 2021, including 30 males and 32 females, with a mean age of 15.56 ± 14.71 years (range: 3 days to 56 years). This study does not establish strict exclusion criteria, even if the quality of the 2D image is not very satisfactory. For the original 2D image quality is not ideal, we also try to compare the imaging effect and the improvement of the diagnostic value after the conversion to the new 3D imaging mode, in order to objectively evaluate the actual value of these new imaging technologies. Therefore, TTE was performed in 41 cases and TEE was performed in 21 cases. TEE examiners excluded contraindications. All patients or their legal guardians signed an informed consent form. This study was approved by the Ethics Committee of China Medical University. The study protocol conforms to the ethical guidelines of the 1975 Declaration of Helsinki as reflected in *a priori* approval by the institution's human research committee.

Novel three-dimensional echocardiography image acquisition

Imaging was obtained via Philips EPIQ system, CVx equipment (Philips, Andover, MA), with the appropriate 3D probes, including X5-1 or X7-2 for transthoracic echocardiography (TTE) or X8-2t for TEE. Each imaging mode was set to store continuous four cardiac cycles. After the 2D image was satisfactorily obtained, traditional 3D acquisition modes were initiated, such as Live 3D, Full Volume, or 3D Zoom to obtain real-time 3D images (Sun et al., 2017), and six-sided cutting (Box Crop), free surface cutting (Plane Crop), frontal cutting (Face Crop), quick cutting (Quick Crop), or intelligent cutting (iCrop) were used to highlight the target lesion. TrueVue was then initiated to obtain a high-definition photorealistic stereoscopic image. After clicking "Touch", the 3D image appears not only on the monitor, but also on the operation panel at the bottom of the monitor; then, the user can click directly on the operation panel to add a light source at a specific location, move the position of the light source, adjust the depth, and/or touch to adjust the image angle and size to obtain a more vivid image. Engaging the Glass mode provides a transparent image of the heart. These 3D image modes can be optimized for grayscale, brightness, smoothness, contrast, or transparency according to the target structure characteristics.

Clinical survey

We randomly selected 10 sonographers (the average age is 35.6 ± 10.73 years) as the echocardiographer group, eight doctors (40 ± 8.9 years) who specialize in cardiac intervention or thoracotomy surgery as the cardiac surgeon group (no limitation on working years, including doctors who have worked for 1–25 years, the overall average age is 37.6 ± 9.7 years), six cardiologists specializing in CHD interventional

TABLE 1 Scoring results of each group for three-dimensional echocardiography.

Compared with 2DE, the imaging effects of the 3DE showed (N = 62[a])	Echocardiographers (n = 10)			Surgeons (n = 8)			Cardiologists (n = 6)			Patients or their parents (n = 20)		
	Likert score*			Likert score*			Likert score*			Likert score*		
	Conventional 3DE	New series of 3DE	p value	Conventional 3DE	New series of 3DE	p value	Conventional 3DE	New series of 3DE	p value	Conventional 3DE	New series of 3DE	p value
Display the details of the lesion is more vivid and clearer	3 (2, 3)	4 (3, 5)	**<0.0001**	3 (1, 3)	5 (4, 5)	**<0.0001**	3 (2, 3)	5 (4, 5)	**<0.0001**	NC	NC	NC
The boundaries of the septal defect are clearly shown, and the 3D images are very similar to those seen intraoperatively[b]	3 (3, 4)	5 (4, 5)	**0.0001**	3 (2, 3)	5 (4, 5)	**<0.0001**	2 (2, 3)	5 (4, 5)	**<0.0001**	NC	NC	NC
After 3D combined with color Doppler, the entire length and stereoscopic extent of the abnormal shunt passing through the defect is displayed more clearly and accurately[b]	2 (2, 3)	5 (4, 5)	**<0.0001**	2 (1, 3)	5 (4, 5)	**<0.0001**	2 (1, 3)	4 (4, 5)	**<0.0001**	NC	NC	NC
The determination of the location, number and extent of congenital leaflet clefts is more rapid and effective[c]	2 (2, 3)	5 (4, 5)	**<0.0001**	2 (1, 3)	5 (4, 5)	**0.001**	2 (1, 3)	4 (4, 5)	**<0.0001**	NC	NC	NC
Can provide valuable stereoscopic images of the PV, including leaflet number and activity status[d]	2 (1, 2)	4 (3, 5)	**0.003**	2 (1, 2)	4 (3, 5)	**<0.0001**	2 (1, 2)	4 (3, 5)	**0.001**	NC	NC	NC
The entire pathway of blood flow in the lumen of an abnormally located vessel can be seen more clearly	2 (1.2, 2)	5 (3.5, 5)	**<0.0001**	2 (1, 3)	4 (4, 5)	**<0.0001**	2 (1.3, 2)	4 (3, 5)	**0.002**	NC	NC	NC
The number and connection characteristics of the abnormal atrioventricular valves can be clearly demonstrated[e]	2 (2, 3)	4 (4, 5)	**0.004**	3 (2, 3)	5 (4, 5)	**<0.0001**	3 (2, 3)	4 (4, 5)	**0.02**	NC	NC	NC
More helpful in the perception of the level and depth of the lesion	3 (2, 3)	5 (4, 5)	**<0.0001**	3 (2, 3)	4 (3, 5)	**<0.0001**	2 (1, 2)	4 (3, 5)	**0.004**	NC	NC	NC
A quicker diagnosis was made with the aid of 3D imaging	4 (3, 4)	5 (4, 5)	**0.04**	4 (3, 4)	5 (4, 5)	0.13	3 (2, 4)	5 (4, 5)	**0.002**	NC	NC	NC
The pathological pattern of the abnormal anatomy is well understood and grasped prior to surgery	3 (2, 5)	5 (4, 5)	**<0.0001**	3 (3, 4)	5 (4, 5)	**0.04**	4 (3, 4)	5 (4, 5)	0.27	2 (2, 3)	4 (4, 5)	**<0.0001**
Communication efficiency is enhanced by showing the patient or guardians the 3D image of the lesion	4 (3, 4)	5 (4, 5)	**0.04**	3 (3, 4)	5 (4, 5)	**<0.0001**	2 (1, 3)	4 (3, 5)	**<0.0001**	3 (2, 3)	4 (3, 5)	**0.002**
Increased my confidence in diagnosis and/or the success of the operation	3 (3, 4)	5 (4, 5)	**<0.0001**	2 (2, 3)	5 (4, 5)	**0.001**	2 (2, 3)	4 (4, 5)	**<0.0001**	2 (2, 3)	4 (3.5, 5)	**<0.0001**
Overall Score	2 (2, 3)	5 (3, 5)	**<0.0001**	3 (2, 3)	5 (4, 5)	**<0.0001**	2 (1, 3)	4 (4, 5)	**<0.0001**	2 (2, 3)	4 (4, 5)	**<0.0001**

[a]Each observer randomly evaluated the images and videos from the database for each case, during the evaluation process, the images were transformed and post-processed with the assistance of "doctors experienced in new 3DE" to achieve near-ideal image quality.

[b]This question applies only to cases of atrial septal defects and ventricular septal defects.

[c]This question applies only to patients with mitral valve cleft.

[d]This question applies only to patients with pulmonary valve stenosis.

[e]This question is only applicable in cases of complete atrioventricular septal defects.

*A 5-point scoring system, 1 indicating strongly disagree and 5 indicating strongly agree. Scores are expressed as median (IQR). p less than 0.05 was considered statistically significant. 2DE, two-dimensional echocardiography; 3D, three-dimensional; NC, no collection; PV, pulmonary valve.

Bolded values in the p column represent statistically significant results.

10.3389/fphys.2022.1000007

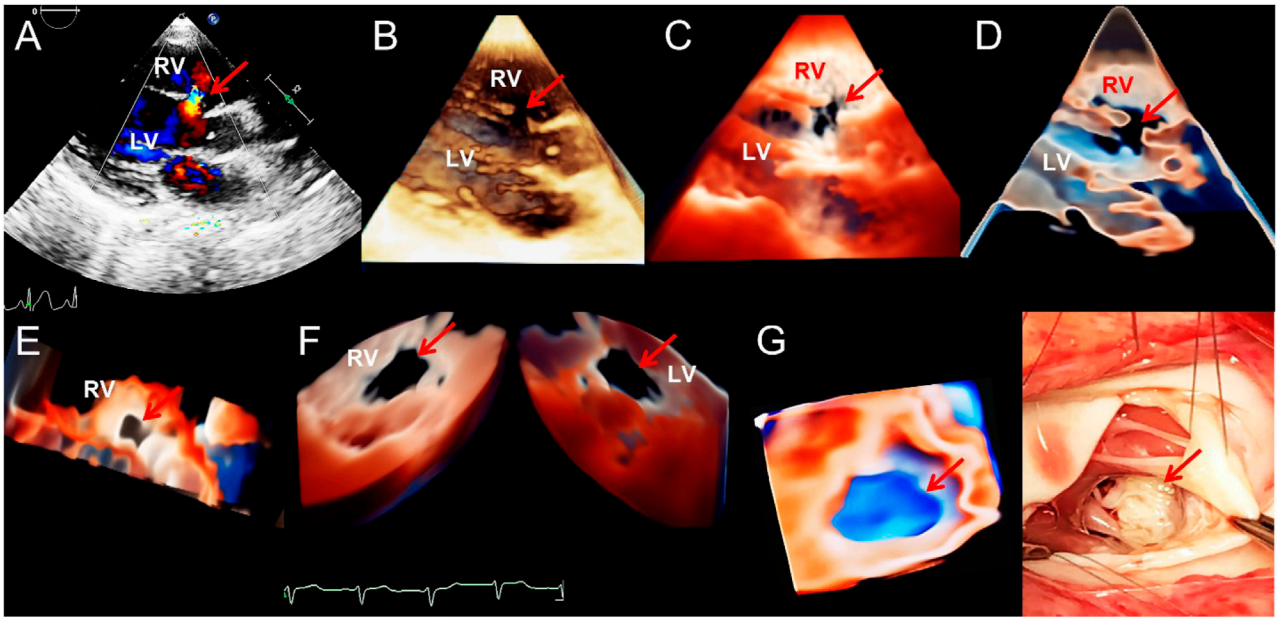

FIGURE 1
Transthoracic echocardiogram showing ventricular septal defect. **(A–D)**. On long axis section of the left ventricle, the 2D, traditional 3D, TrueVue Light, and TrueVue Glass images indicate the defects of the peri-membranous part of the interventricular septum (5 mm × 10 mm, arrows), respectively. **(E)**. In the same patient as A-D, looking down the defect from the right ventricle directly through a single view. **(F)**. In another patient with a large (22 mm × 14 mm) peri-membranous ventricularseptal defect, the "Dual Volume" imaging mode in TrueVue was used to observe the defects (arrows) directly from the right and left ventricles simultaneously. **(G)**. It is the same patient as in Figure **(F)**, showing the three-dimensional shape of the defect displayed by using TrueVue Glass to simulate the "surgical view"(left, arrow), and the comparison of the doctor's field of vision during cardiac surgery (right, arrow). In surgery, after lifting the tricuspid valve, the mitral valve can be seen through the septal defect. 2D, two-dimensional; 3D, three-dimensional; LV, left ventricle; RV, right ventricle.

techniques (unlimited years of experience, including worked for 1–30 years, mean age 32.5 ± 11.3 years), and 20 patients with CHD (or a parent of a child under 14 years) who underwent the novel 3D echocardiographic examinations to fill out a short questionnaire evaluating their experience, they were all provided score [using Likert score system (Harake et al., 2020)] the elements after viewing/manipulate the new series of 3D images/videos by comparing with the traditional 3D for 30 cases randomly selected from the database (Table 1). None of the participants had prior experience with the TrueVue series of technologies. The cases selected for evaluation should be avoided as far as possible to be biased towards those images that will be improved by new rendering display. Instead, we chose a collection of various congenital heart diseases that we encountered randomly during a certain period of clinical work.

Statistics

Using SPSS 25.0 software (IBM Inc., Armonk, New York, United States), categorical data are expressed as number of cases (percentage), for analysis of the Likert responses to the question design, data were tested for normality using the Kolmogorov–Smirnov test. Results are reported as mean ± standard deviation and median [first interquartile range (IQR), third interquartile range] for normally distributed and non-normally distributed data, respectively. Continuous normally-distributed data were compared using Student's *t*-test. Non-Gaussian data were compared using the Mann-Whitney test. Comparisons among the participant groups were performed using analysis of variance, the Kruskal-Wallis test, or the Chi square test as appropriate, and $p < 0.05$ was considered statistically significant.

Results

Patient demographics

The advanced novel 3D echocardiography classified the 62 patients as follows: 18 (29.0%) with ventricular septal defect (VSD); 17 (27.4%) with atrial septal defect (ASD); 9 (14.5%) with patent ductus arteriosus (PDA); 5 (8.1%) with

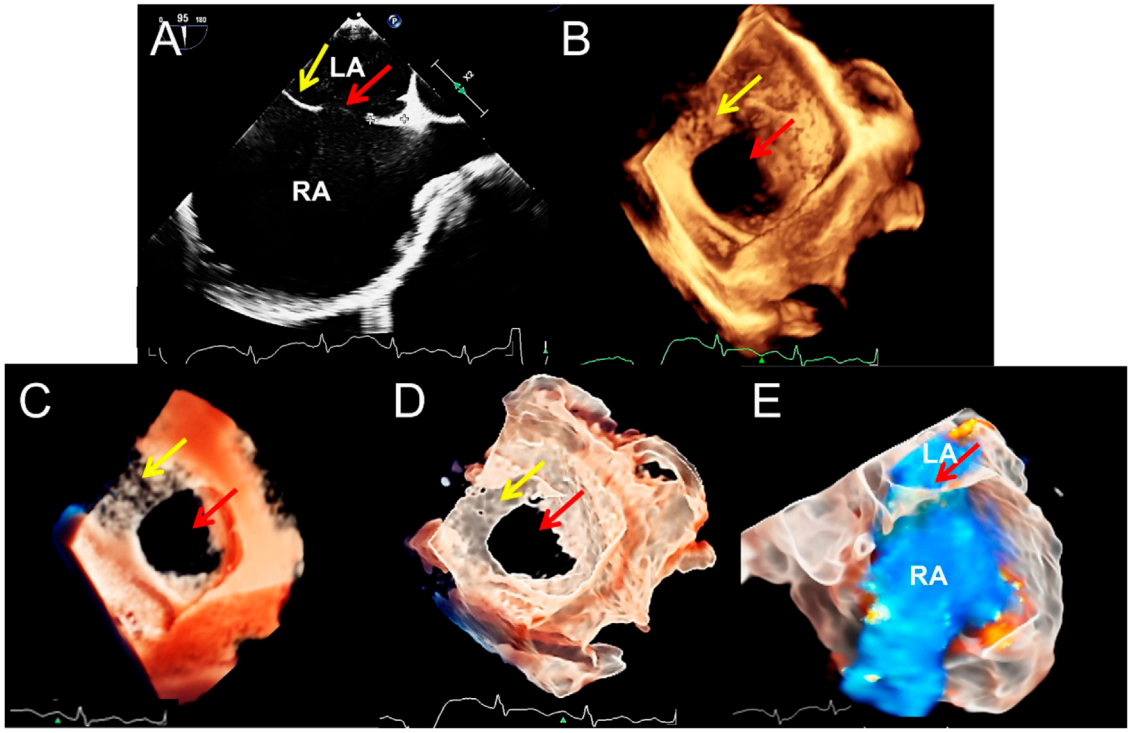

FIGURE 2
Transesophageal echocardiography of double atrial-superior and inferior vena cava section to diagnose atrial septal defect. **(A–D)**. The 2D, traditional 3D, TrueVue Light, and TrueVue Glass show the secondary type of atrial septal defect (25 mm × 23 mm, red arrows) and the upper soft, thin rim (yellow arrows), respectively. Figure **(B–D)** is a direct view of the atrial septum from the left atrium perspective. **(E)**. TrueVue Glass shows the spatial path of the atrial shunt from left to right. 2D, two-dimensional; 3D, three-dimensional; LA, left atrium; RA, right atrium.

aortic valve malformation; 4 (6.5%) with mitral valve cleft; 3 (4.8%) with pulmonary artery stenosis; 2 (3.2%) with complete atrioventricular septal defect (CAVSD); 2 (3.2%) with double orifice mitral valve (DOMV); and one case (1.6%) each of pulmonary artery sling, and ventricular diverticulum. Of the total patients, 55 (88.7%) underwent cardiac surgery, including conventional thoracotomy or interventional cardiac procedures, wherein the results of the ultrasound diagnosis were confirmed.

Novel three-dimensional echocardiographic analysis

For patients undergoing innovative 3D imaging, 55 cases (88.7%) obtained satisfactory TrueVue images, and 59 (95.2%) obtained satisfactory TrueVue Glass images. For patients who underwent TTE, the overall satisfaction ratio with 3D images was 87.8% (36/41). For TEE, the overall satisfaction ratio was 100% (21/21). The standard for satisfactory image quality is to provide a clear and obvious evidence for diagnosis. Dissatisfaction with the quality of transthoracic ultrasound images is mainly due to obesity or excessive lung gas. During the TrueVue imaging of the patients with VSD, placing the light source below the defect made the shape and edge of the defect extremely eye-catching when compared with that of traditional 3D ultrasound, especially for the diagnosis of a small perimembranous ventricular defect (Figure 1). While in the patients with an ASD, placing the light source over the defect displayed the soft edge more clearly and accurately than traditional 3D imaging. After switching to the TrueVue Glass mode and appropriately increasing the transparency, the overall path and spatial range of the shunt through the defects was observed (Figure 2; Supplementary Movie S1). For the patients with PDA, TrueVue Glass plus color Doppler technology better displayed the origin, course, and inner diameter of the shunt of the whole heart cycle in the pulmonary artery through the transparent tube wall structure than traditional 3D or TrueVue imaging modes (Supplementary Movie S2), especially in the synchronous double-sided view (dual volume mode) (Supplementary Figure S1). For the patients with bicuspid aortic valve (BAV) malformation, the valve displayed by TrueVue more closely simulated the real anatomical texture features and showed the crest-like raised

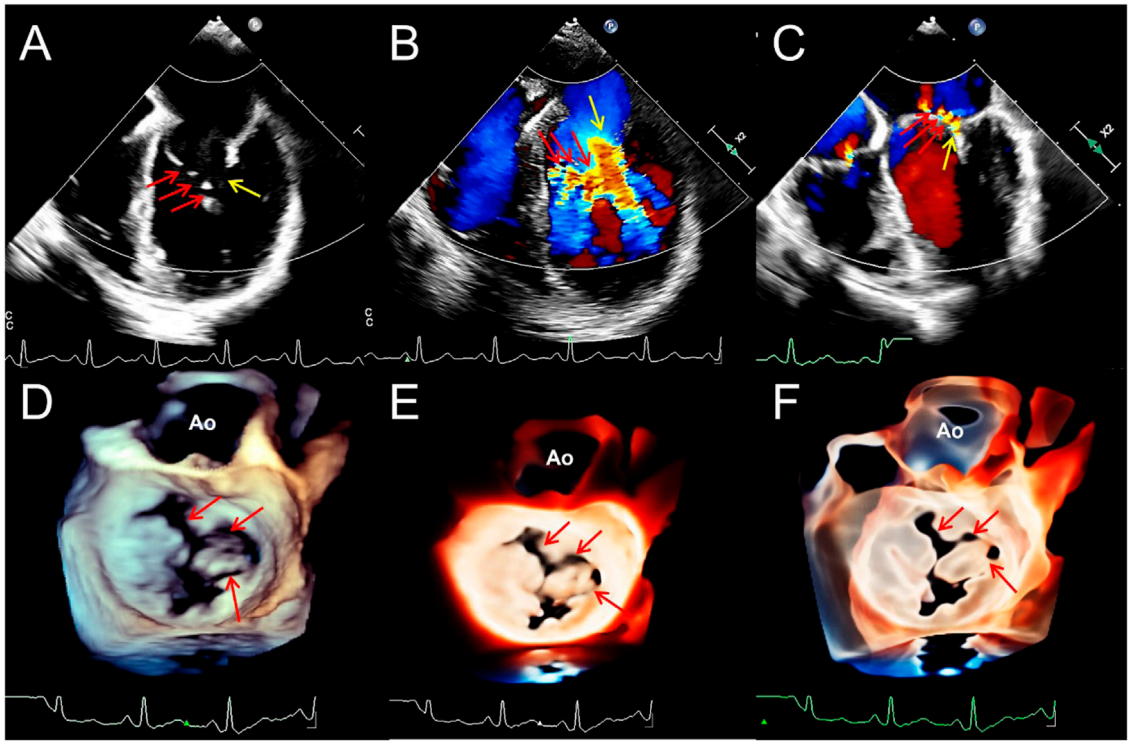

FIGURE 3
Transesophageal echocardiography reveals multiple mitral valve clefts. **(A)**. 2D echocardiography four-chamber view showing multiple loss of echo in the anterior leaflet of mitral valve (MV) (the sizes of the clefts from A1 to A3 area are 3.1, 4.6, and 3.4 mm respectively, red arrows). The yellow arrow points to the junction between the anterior and posterior leaflets. **(B,C)**. Blood flows into the left ventricle during diastole (red arrows) and regurgitation jets into left atrium during systole (red arrows) from the clefts. Yellow arrows represent the blood flow signals of the normal MV orifices. **(D–F)**. From a surgical perspective, traditional 3D, TrueVue Light, and TrueVue Glass show three irregular clefts (the range of the clefts from A1 to A3 area are 2.5–5.4, 2.5–4.3, and 2.0–3.3 mm, respectively) from the perspective of the left atrium, and all are complete cleft to the annulus. 2D, two-dimensional; 3D, three-dimensional; AO, Aorta; A1, A1 scallop of MV; A3, A3 scallop of MV.

fusion structure between the two valves (Supplementary Figure S2). Although both 2D and 3D imaging modes can diagnose BAV, the new imaging mode displays images that are closer to real anatomy and will make communication with surgeons and patients easier and more efficient. For complex mitral clefts, observation of the position, number, shape, and size of the clefts was significantly improved on the TrueVue Light and Glass compared with traditional technologies; furthermore, Glass imaging was more advantageous for irregularly shaped clefts boundaries (Figure 3). In patients with pulmonary artery stenosis, 2D, traditional 3DE, and TrueVue showed echo enhancement, restricted opening of the pulmonary valve, and the turbulence signal when blood passed through the stenotic position. However, in the TrueVue Glass mode, the open state of the flap was clearly displayed according to the light transmittance, and because of the transparence of the surrounding tissue, a segment of the right ventricular outflow tract or the main pulmonary artery was revealed, enabling identification of the location of the opening margin for the pulmonary valve more easily and accurately (Supplementary Figure S3). When CAVSD were suspected on 2DE, TrueVue Light made it easier to determine the number of annulus, while TrueVue Glass showed several bridge lobes of the common atrioventricular valve (Figure 4). For patients with a rare congenital DOMV, novel 3D images not only illustrated the two-orifice structure, but also showed the thickness and arrangement of the chordae and papillary muscles (Figure 5). Pulmonary artery sling is difficult to be observed on 2D and traditional 3DE image, and there was little improvement over traditional 3DE when converting to TrueVue Light, TrueVue Glass displayed an unprecedented visual perspective of the abnormal left pulmonary artery (Figure 6). Finally, in the patient with rare ventricular diverticulum, placing the light source of TrueVue at the entrance of the diverticulum significantly improved the clarity of the patient's finger-shaped diverticulum through the shadow effect when compared with the image of traditional 3DE. Meanwhile, TrueVue Glass shielded the structure around the diverticulum, so that only the shape of the diverticulum was directly indicated (Figure 6), with the addition of color Doppler,

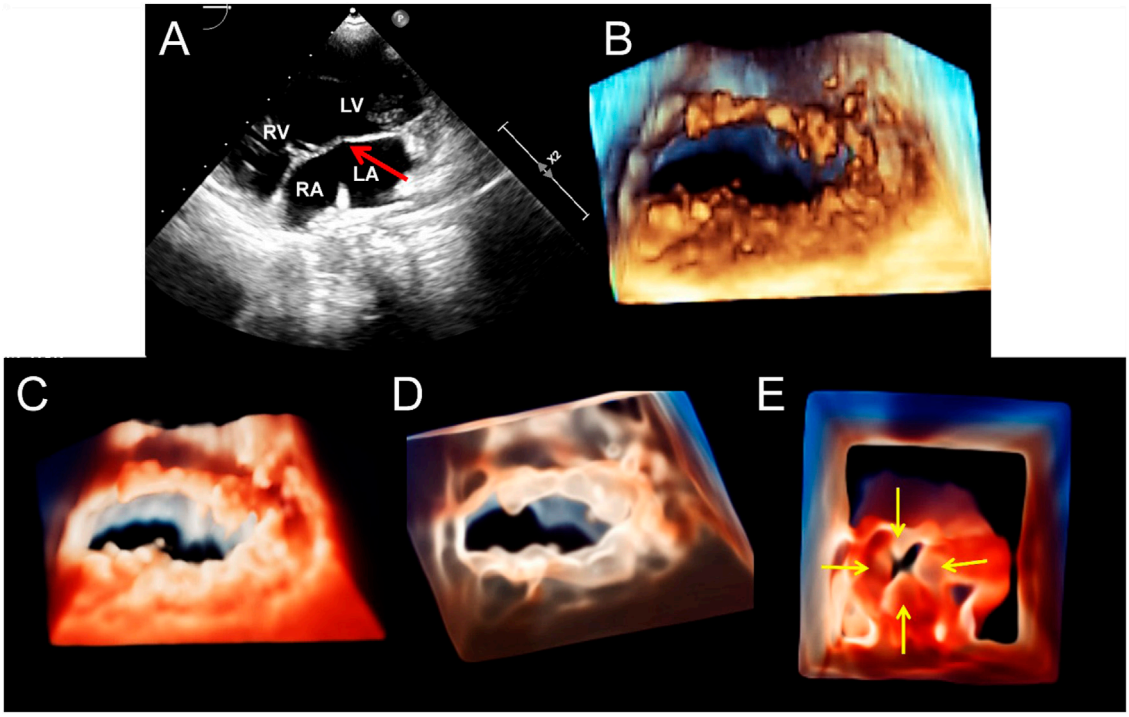

FIGURE 4
Transthoracic echocardiography shows complete atrioventricular septal defect. **(A)**. The four-chamber view of a 2D echocardiography shows only one atrioventricular valve (arrow), combined with a large defect of the lower part of the atrial septum and large ventricular septal defect. **(B–D)**. Traditional 3D, TrueVue, and TrueVue Glass show a single atrioventricular annulus and a group of atrioventricular valves open from the atrium view in diastole. **(E)**. TrueVue Glass shows the systolic phase with atrioventricular valve closed as a single annulus and four lobes from the perspective of the atrium, which are left, right, anterior, and posterior bridge lobes (arrows), confirmed to be a complete atrioventricular septal defect deformity. 2D, two-dimensional; 3D, three-dimensional. LA, left atrium; RA, right atrium; LV, left ventricle; RV, right ventricle.

the blood flow in and out of the diverticulum with the cardiac cycle clearly appears (Supplementary Movie S3).

Clinical rating and scoring survey results

Survey Data results showed that the novel 3D imaging methods effectively increased the diagnostic confidence of echocardiographers, enabled surgeons and patients to better understand the details of lesions, promoted the efficiency of communication, and improved the confidence of both doctors and patients in treatment ($p < 0.0001$) (Table 1).

Discussion

TrueVue is a new, high definition 3D rendering mode whose spatial image gradually transitions from light-pink to orange-red to represent the surface to deep structures and simulate the real texture of heart tissue, enabling a hierarchical and realistic view of a variety of structures (Genovese et al., 2019; Kern et al., 2019; Vainrib et al., 2019; Vairo et al., 2019; Merino Argos et al., 2020). On the other hand, the recent novel TrueVue Glass intelligent hides the myocardium and tissue surrounding the heart that contains little blood automatically, transforming the image into a translucent mode to achieve a clear spatial relationship between the internal structure and the geometry of the heart chamber and vessels structure, information that has never been provided by conventional cardiac ultrasonic images after birth (Karagodin et al., 2020). TrueVue's raw stereo data acquisition and cutting methods are similar to those of traditional 3D, no additional operational steps are added. With TrueVue Light, that is, using a touch screen to retract and/or rotate the TrueVue or TrueVue Glass image and adding a movable virtual light source (Genovese et al., 2019), the area of interest can be illuminated or darkened by adjusting the observation angle and the position and depth of the light source to improve the display ability and detail effects, which enables doctors to have a clearer understanding of the overall anatomical structure of the heart.

Although traditional 3DE can display some congenital malformations, there remain shortcomings in the resolution of small structures and the display of deeper organizational structures (Ge, 2010; Khoshhal, 2013; Charakida et al., 2014; Cossor et al., 2015). Therefore, the preoperative evaluation and

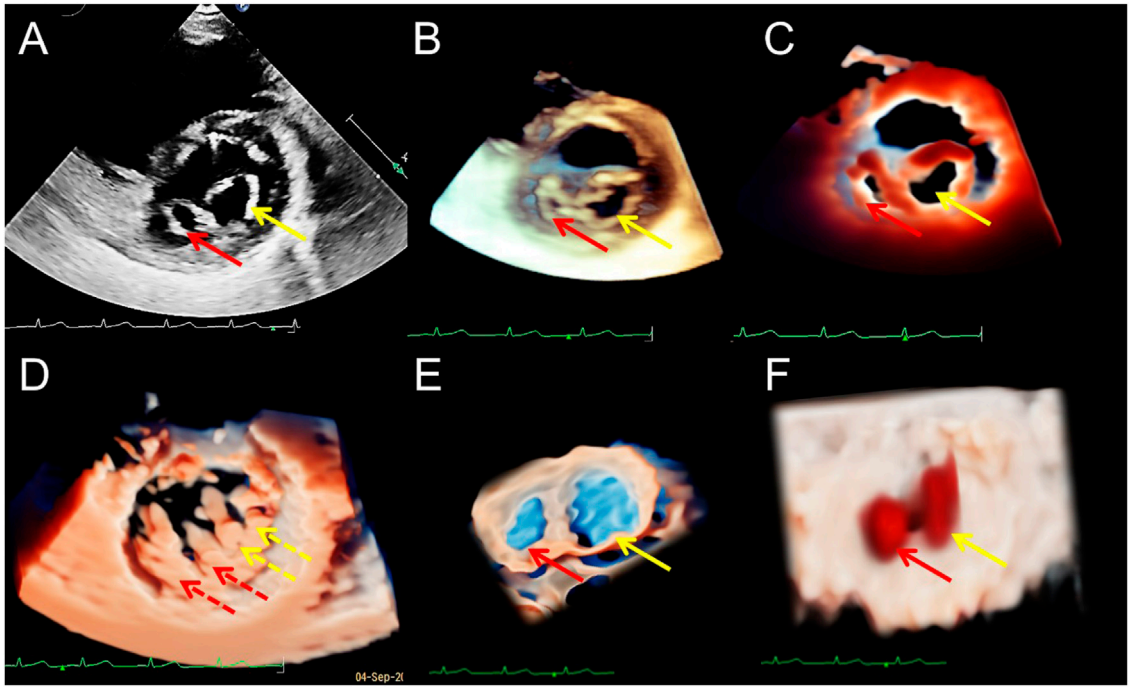

FIGURE 5
Transthoracic echocardiography of the short-axis view of the mitral valve (MV) showing the double orifice MV (arrows). **(A)**. 2D display of asymmetric orifices; **(B,C)**. Traditional 3D and TrueVue show the spatial shape of the orifices; **(D)**. TrueVue shows the abnormal multiple papillary muscles and the tendons connected to them from the perspective of the left ventricle; the red dotted arrows represent the additional structure corresponding to the small orifice, and the yellow dotted arrows represents the additional structure corresponding to the large orifice. TrueVue Glass **(E)** plus color Doppler **(F)** directly visualizes the two orifices of the MV from the left atrium side (surgical view) and the two blood streams entering the left ventricle during diastole. The red and yellow solid line arrows in **(A–C,E,F)** indicate two asymmetric orifices of MV, respectively. 2D, two-dimensional; 3D, three-dimensional.

intraoperative guidance of CHD may require other relatively expensive and time-consuming imaging techniques (Silvestry et al., 2014; Jone et al., 2016; Isorni et al., 2020). The novel TrueVue, TrueVue Light, and TrueVue Glass series of 3DE overcome these deficiencies to some extent, providing more detailed and accurate information for CHD both in the preoperative diagnosis and postoperative follow-up.

Although the diagnostic value of traditional 3DE has been confirmed for relatively common septal defects (Saric et al., 2010; Charakida et al., 2014; Cossor et al., 2015; Hadeed et al., 2016), TrueVue plus a light source makes not only the defect boundary clearer, but also makes the range for the soft rim more visible. In TrueVue Glass, adjusting the transparency highlights the origin and extent of an atrial or ventricular shunt. For PDAs, TrueVue Glass with color allows us to observe the pattern of abnormal blood flow, especially when using the "dual" mode, where we can see that the shunt bundle in the deep pulmonary artery may be more extensive than the surface flow seen in the 2D view. These images can help us judge the PDA typing and degree, because even if the opening width is the same, the shunt of the "window-type" may be much greater than that of the long "tube-type" (Youssef et al., 2020; Sehgal et al., 2021).

For malformations of the thin cardiac valves, traditional 3D images are closely dependent on the quality of 2D images; however, while they are often used to evaluate the relatively large and morphologically regular mitral valves (Sun et al., 2017; Kalçık et al., 2021), their diagnostic value for pulmonary valves is considered to be very limited and thus have not been routinely used (Anwar et al., 2007; Valente et al., 2014). TrueVue Light imaging is advantageous for the mitral and aortic valves. Moreover, although the image quality is improved for the pulmonary valve, the display is still restricted when the quality of the original 2D image is poor, which is not enough to provide sonographers with sufficient diagnostic confidence, especially for infants or for TTE screening. Under these circumstances, the application of TrueVue Glass may be helpful, as its display of the location, number, width, and overall morphology of the mitral valve multiple clefts and pulmonary stenosis is significantly improved, and it provides a clear surgical field of view. In endocardial cushion malformation, it is often difficult to distinguish between "transitional" or complete "single common annulus" on 2D ultrasound (Nina et al., 2019). TrueVue Light imaging makes it quite easy to determine the number of annulus and the

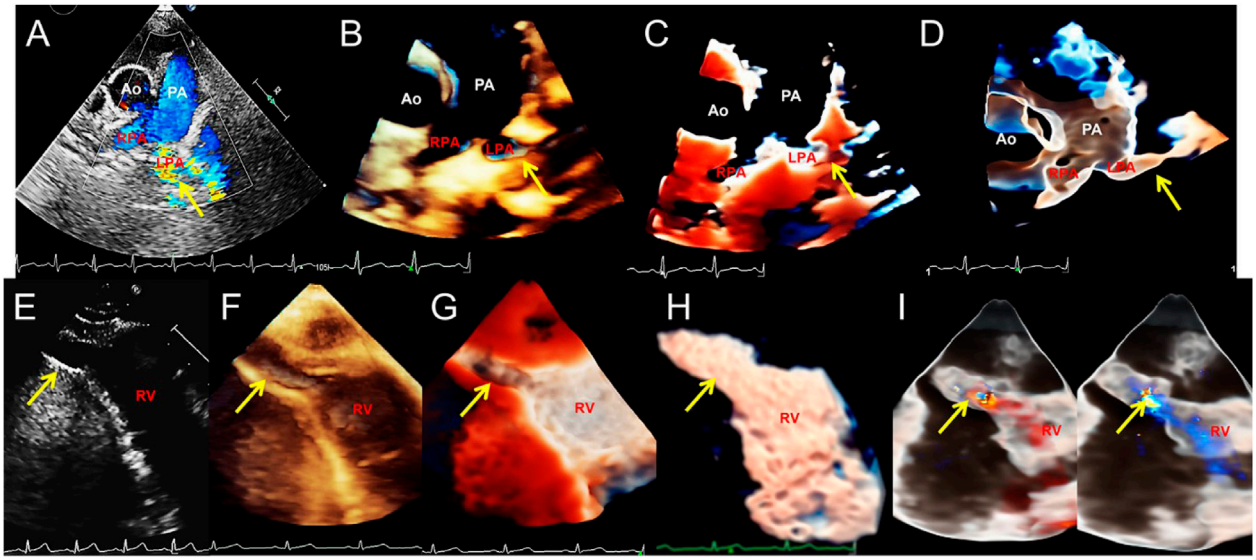

FIGURE 6
Transthoracic echocardiography shows pulmonary artery sling and right ventricular diverticulum. **(A–D)**. Transthoracic echocardiography showing the pulmonary artery sling on the short-axis section of the great artery. 2D, traditional 3D, TrueVue Light, and TrueVue Glass show abnormal orientation of the left pulmonary artery, which originate from a lower position, bypassing the rear of the trachea and then reflexed to the left, with local stenosis showing increased blood flow speed (arrows). **(E–H)**. 2D, traditional 3D, TrueVue Light, and TrueVue Glass show the diverticula (the end-systolic volume is 15 mm × 9 mm × 9 mm, and the end-diastolic volume is 24 mm × 14 mm × 14 mm, arrows) at the apex of the RV (arrows). **(I)**. TrueVue Glass with color Doppler shows that blood in the right ventricle enters the diverticulum during diastole (left), and blood flow in the diverticulum returns to the right ventricle during systole (right). 2D, two-dimensional; 3D, three-dimensional; Ao, aorta; PA, pulmonary artery; LPA, left pulmonary artery; RPA, right pulmonary artery; RV, right ventricle.

morphology of the atrioventricular valve. The shape and outline of the thin bridge leaflet in CAVSD can be clearly displayed when TrueVue Glass is also applied. DOMV is often accompanied by multiple sets of papillary muscle malformations (Karas et al., 2003; Erkol et al., 2009). Traditional 2D and 3D ultrasound can exactly diagnose the existence of the double orifice, but it is often difficult to display the additional structure of the mitral valve apparatus. The TrueVue Light more clearly illuminates the structural characteristics connecting the chordae tendineae to the corresponding papillary muscles.

This is exactly the issue with 3D rendering techniques: they often "look good" but misrepresent the anatomic details; especially with thin structures. The new Glass imaging mode has obvious visual enhancement effects on the ability to display thin structures, such as the atrial septum and thin valves, to a certain extent, improving the problem of false echo loss in traditional ultrasound.

Rare pulmonary artery sling imaging has certain difficulties in 2D and traditional 3DE, usually need time-consuming and laborious to confirm the diagnosis through the 3D reconstruction of enhanced computed tomography (CT), and the children under examination are not easy to cooperate well (Sezer et al., 2019; Xu et al., 2020). TrueVue Glass has an obvious advantage in the diagnosis of pulmonary artery sling, and it is the first time that an innovative 3D ultrasound technology has been used to diagnose such rare cardiovascular malformations. Rare ventricular diverticulum, with its narrow entrance and long shape, may be easily missed or misdiagnosed as a paracardiac vessel on 2D ultrasound (Sozzi et al., 2017; Wang et al., 2021). The TrueVue Light highlights the interior space features of the diverticulum. TrueVue Glass further presents the outer contour of the diverticulum directly. Previously, this contour could only be seen with 3D reconstruction of enhanced CT.

Because the content and features of the diagnostic concerns of different diseases are significantly different when applying ultrasound imaging, we will ask more targeted questions for different diseases during the questionnaire process, also because the diagnostic advantages of these new 3D imaging technologies will be more obvious for certain types of CHD. At the same time, considering that the patient's feelings are equally important in the evaluation and treatment of CHD, including a full understanding of the characteristics and extent of their disease and the surgical procedure explained by the doctor, we ask some of the patients or their guardians to observe the conventional and new 3D display of the lesion through the doctor's explanation of the characteristics of their disease. However, since they are not professionally trained in medicine, they will only answer a small part of the questions related to their medical procedure.

Although the true resolution of the above-mentioned new series of 3D images has not been improved digitally, these new imaging modes plus light and shadow effects have significantly improved the visual effects and diagnostic efficiency of the characteristics of CHDs. Although traditional 2D and 3DE can also help us complete most of the ultrasonic diagnosis of CHD, it is time-consuming and labor-intensive, especially in some special diseases. The innovative TrueVue combined with Light and Glass 3D imaging technology provides us with more reliable reference information. In particular, the layered sense by the photorealistic light source addition, and the outer contour imaging of the heart cavity displayed by the application of Glass (such as the shape of the left atrial appendage (Karagodin et al., 2020) and the rare cardiac diverticulum, etc.) are new image forms and diagnostic information that have never been obtained by traditional postpartum cardiac ultrasound diagnostic technology, which improve and correct the diagnosis more efficiently.

Limitations

The TrueVue, TrueVue Light, and TrueVue Glass series of 3D cardiac ultrasound technologies have achieved satisfactory results in some research fields, but there are some limitations and deficiencies. This innovative series of 3DE improved the visual clarity of image details to a certain extent, but in cases where the 2D image was very dissatisfied displayed, it was still difficult to obtain a satisfying 3D image, especially in TrueVue mode. Moreover, the application of TrueVue plus light and Glass have requirements for the operator, who should have mastery of the overall and partial anatomy of the heart and be able to apply the tools of the machine for image processing. It also requires the operator to be an "artist," able to flexibly use the visual effects produced by the light source to display the abnormal anatomical structure. Therefore, a certain learning curve to obtain optimal rendered images is required, and for doctors with traditional 3DE operation experience, it is easy to master the methods and skills of the new series of 3DE operations. Furthermore, the extensive post-processing increases the possibility of artificial creation or loss of defects based on variations in both scan quality and post-processing technique. At present, as the 3DE of the TrueVue series, especially TrueVue Glass, is a recently launched novel tools, there are few published reports about them. In addition, although our research is one with the largest sample size reporting on the application of the above-mentioned new tools, it discusses limited types of CHDs. Therefore, further studies are needed to explore their application value and experience.

Conclusion

This study showed the excellent applicability of TrueVue, TrueVue Light, and TrueVue Glass as diagnostic tools for patients with suspected CHD. Compared with 2D and traditional 3DE, the TrueVue, TrueVue Light, TrueVue Glass series of novel 3DE technologies' display of abnormal structures in patients with CHD more closely simulate real anatomical features and make the outer contours of the heart chambers, the thin valves and blood flow in the lumen more comprehensive and clearer. These technologies provide us with a wealth of evidence for the diagnosis and treatment of CHD and are a revolution in the ultrasonic diagnosis method of CHD.

Data availability statement

The original contributions presented in the study are included in the article/Supplementary Material, further inquiries can be directed to the corresponding author.

Ethics statement

The studies involving human participants were reviewed and approved by Shengjing Hospital of China Medical University. Written informed consent to participate in this study was provided by the participants' legal guardian/next of kin.

Author contributions

FS and WR accomplish the conception and design of this research. YC, YX, XZ, WQ, YL, DL, and SY took part in analysis and interpretation of data. FS, AS, and XT participated in drafting of the manuscript or revising it critically for important intellectual content. WR finally approved the manuscript submitted.

Funding

This study was supported by grants from Young Scientists Fund of the National Natural Science Foundation of China (81901763); Liaoning Province Medical-Industrial Crossover Joint Fund (2022-YGJC-55); Young and Middle-aged Scientific and Technological Innovation Talent Support Project of Shenyang City (RC210226); 345 Talent Project (M0282); Double First-class New Medical Technology Project of China Medical University (112/3111210415) and The Second Clinical College of China Medical University Educational Innovation (Open) Project (SJKF-2022YB04). The funding assisted in the collection of clinical data and publication fees.

Acknowledgments

We thank Drs Jiahui Yu, Qiaojin Zheng, Weiping Song, and Saofeng Wu for their contributions in collecting patient data, and Editage company for their professional help in the language editing process.

Conflict of interest

The authors declare that the research was conducted in the absence of any commercial or financial relationships that could be construed as a potential conflict of interest.

Publisher's note

Supplementary material

The Supplementary Material for this article can be found online at: https://www.frontiersin.org/articles/10.3389/fphys.2022.1000007/full#supplementary-material

SUPPLEMENTARY FIGURE S1
The diagnosis of patent ductus arteriosus by transthoracic echocardiographic short-axis section of the great artery. . 2D, traditional 3D and TrueVue Light plus color Doppler showing the shunt from the aorta to the main pulmonary artery (3 mm, arrows). **(D)**. TrueVue Glass "dual volume" shows the ventral and dorsal flow of the pulmonary artery, with shunt signals from the ducts more dorsal in space (arrows). 2D, two-dimensional; 3D, three-dimensional.

SUPPLEMENTARY FIGURE S2
Transesophageal echocardiography showed bicuspid aortic valve malformation. . 2D, traditional 3D, TrueVue Light, and TrueVue Glass show the fusion crest by the left coronary and non-coronary leaflet (arrows) from the left ventricular outflow tract side perspective, respectively. 2D, two-dimensional; 3D, three-dimensional.

SUPPLEMENTARY FIGURE S3
. 2D transthoracic echocardiographic short-axis view of the great artery demonstrating a marked acceleration of blood flow (arrow) through the pulmonary valve. **(B)**. Conventional 3D imaging from the right ventricular outflow tract demonstrates a trilobed pulmonary valve with thickened fusion at the valve tip (arrow). **(C)**. TrueVue shows the thickened tip of the pulmonary valve (arrow), but the thin lobes show pseudo-echogenic loss. **(D)**. TrueVue Glass shows thin valves and inadequately opening valves (arrow) during systole. Figures **(B-D)** are from the perspective of the right ventricular outflow tract. 2D, two-dimensional; 3D, three-dimensional.

SUPPLEMENTARY MOVIE S1
TrueVue Glass plus color Doppler shows left atrial blood flow through the atrial septal defect (arrow) into the right atrium on two-atrial section of transesophageal echocardiography. LA, left atrium; RA, right atrium.

SUPPLEMENTARY MOVIE S2
The TrueVue Glass plus color Doppler shows the flow from the aortic arch into the pulmonary artery through an open ductal artery (arrow) on supra sternal fossa section by thoracic echocardiography. AoA, aortic arch; PA, pulmonary artery.

SUPPLEMENTARY MOVIE S3
The TrueVue Glass plus color Doppler shows blood shuttling between the right ventricle and diverticulum (arrow) during the systolic and diastolic phases of the heart. RV, right ventricle.

References

Anwar, A. M., Soliman, O., Bosch, A. E. V. D., Mcghie, J. S., Meijboom, F. J., ten Cate, F. J., et al. (2007). Assessment of pulmonary valve and right ventricular outflow tract with real-time three-dimensional echocardiography. *Int. J. Cardiovasc. Imaging* 23, 167–175. doi:10.1007/s10554-006-9142-3

Charakida, M., Pushparajah, K., Anderson, D., and Simpson, J. M. (2014). Insights gained from three-dimensional imaging modalities for closure of ventricular septal defects. *Circ. Cardiovasc. Imaging* 7, 954–961. doi:10.1161/CIRCIMAGING.114.002502

Cossor, W., Cui, V. W., and Roberson, D. A. (2015). Three-dimensional echocardiographic en face views of ventricular septal defects: Feasibility, accuracy, imaging protocols and reference image collection. *J. Am. Soc. Echocardiogr.* 28, 1020–1029. doi:10.1016/j.echo.2015.05.014

Erkol, A., Karagoz, A., Ozkan, A., Koca, F., Yilmaz, F., Sonmez, K., et al. (2009). Double-orifice mitral valve associated with bicuspid aortic valve: A rare case of incomplete form of shone's complex. *Eur. J. Echocardiogr.* 10, 801–803. doi:10.1093/ejechocard/jep067

Fabricius, A., Walther, T., Falk, V., and Mohr, F. (2004). Three-dimensional echocardiography for planning of mitral valve surgery: Current applicability? *Ann. Thorac. Surg.* 78, 575–578. doi:10.1016/j.athoracsur.2003.10.031

Ge, S. (2010). How can we best image congenital heart defects? Are two-dimensional and three-dimensional echocardiography competitive or complementary? *J. Am. Soc. Echocardiogr.* 23, 722–725. doi:10.1016/j.echo.2010.05.018

Genovese, D., Addetia, K., Kebed, K., Kruse, E., Yamat, M., Narang, A., et al. (2019). First clinical experience with 3-dimensional echocardiographic transillumination rendering. *JACC. Cardiovasc. Imaging* 12, 1868–1871. doi:10.1016/j.jcmg.2018.12.012

Hadeed, K., Hascoet, S., Amadieu, R., Karsenty, C., Cuttone, F., Leobon, B., et al. (2016). Assessment of ventricular septal defect size and morphology by three-dimensional transthoracic echocardiography. *J. Am. Soc. Echocardiogr.* 29, 777–785. doi:10.1016/j.echo.2016.04.012

Harake, D., Gnanappa, G. K., Alvarez, S. G. V., Whittle, A., Punithakumar, K., Boechler, P., et al. (2020). Stereoscopic display is superior to conventional display for three-dimensional echocardiography of congenital heart anatomy. *J. Am. Soc. Echocardiogr.* 33, 1297–1305. doi:10.1016/j.echo.2020.06.016

Isorni, M. A., Moisson, L., Moussa, N. B., Monnot, S., Raimondi, F., Roussin, R., et al. (2020). 4D flow cardiac magnetic resonance in children and adults with congenital heart disease: Clinical experience in a high volume center. *Int. J. Cardiol.* 320, 168–177. doi:10.1016/j.ijcard.2020.07.021

Jone, P. N., Ross, M. M., Bracken, J. A., Mulvahill, M. J., Di Maria, M. V., and Fagan, T. E. (2016). Feasibility and safety of using a fused echocardiography/fluoroscopy imaging system in patients with congenital heart disease. *J. Am. Soc. Echocardiogr.* 29, 513–521. doi:10.1016/j.echo.2016.03.014

Kalçık, M., Özkan, M., Gündüz, S., Gürsoy, M., Yesin, M., Bayam, E., et al. (2021). Normal reference values for mechanical mitral prosthetic valve inner diameters and areas assessed by two-dimensional and real-time three-dimensional transesophageal echocardiography. *Int. J. Cardiovasc. Imaging* 37, 547–557. doi:10.1007/s10554-020-02039-5

Karagodin, I., Addetia, K., Singh, A., Dow, A., Rivera, L., DeCara, J. M., et al. (2020). Improved delineation of cardiac pathology using a novel three-dimensional echocardiographic tissue transparency tool. *J. Am. Soc. Echocardiogr.* 33, 1316–1323. doi:10.1016/j.echo.2020.08.005

Karas, S., Barbetseas, J., Lambrou, S., Parissis, J., Metzikof, D., and Toutouzas, P. (2003). Well-functioning double-orifice mitral valve in a young adult. *J. Clin. Ultrasound.* 31, 170–173. doi:10.1002/jcu.10142

Kern, M. C., Janardhanan, R., Kelly, T., Fox, K. A., Klewer, S. E., and Seckeler, M. D. (2019). Multimodality imaging for diagnosis and procedural planning for a ruptured sinus of Valsalva aneurysm. *J. Cardiovasc. Comput. Tomogr.* 14, e139–e142. doi:10.1016/j.jcct.2019.09.018

Khoshhal, S. (2013). Feasibility and effectiveness of three-dimensional echocardiography in diagnosing congenital heart diseases. *Pediatr. Cardiol.* 34, 1525–1531. doi:10.1007/s00246-013-0718-0

Meras, P., Riesgo-Gil, F., Rybicka, J., Barradas-Pires, A., Smith, J., Kempny, A., et al. (2021). Heart transplantation at a single tertiary adult congenital heart disease centre: Too little, too late? *Int. J. Cardiol.* 322, 107–113. doi:10.1016/j.ijcard.2020.08.047

Merino Argos, C., Lopez Fernandez, T., and Valbuena Lopez, C. (2020). Severe stenosis due to prosthetic thrombosis evaluated with TrueVue. *Rev. Esp. Cardiol.* 73, 499. doi:10.1016/j.rec.2019.07.015

Nina, H., Thomas, H., Torsten, M., Wierup, P., Maynard, C., and Ramgren Johansson, J. (2019). Comprehensive echocardiographic imaging of atrioventricular valves in children with atrioventricular septal defect: Accuracy of 2D and 3D imaging and reasons for disagreement. *Anatol. J. Cardiol.* 21, 214–221. doi:10.14744/AnatolJCardiol.2019.49376

Saric, M., Perk, G., Purgess, J. R., and Kronzon, I. (2010). Imaging atrial septal defects by real-time three-dimensional transesophageal echocardiography: Step-by-step approach. *J. Am. Soc. Echocardiogr.* 23, 1128–1135. doi:10.1016/j.echo.2010.08.008

Sehgal, A., Nitzan, I., Krishnamurthy, M., Pharande, P., and Tan, K. (2021). Toward rational management of patent ductus arteriosus: Ductal disease staging and first line paracetamol. *J. Matern-Fetal Neo Med.* 34 (23), 3940–3945. doi:10.1080/14767058.2019.1702949

Sezer, S., Acar, D., Ekiz, A., Kaya, B., Bornaun, H., and Aslan, H. (2019). Prenatal diagnosis of left pulmonary artery sling and review of literature. *Echocardiography* 36, 1001–1004. doi:10.1111/echo.14325

Silvestry, F. E., Kadakia, M. B., Willhide, J., and Herrmann, H. C. (2014). Initial experience with a novel real-time three-dimensional intracardiac ultrasound system to guide percutaneous cardiac structural interventions: A phase 1 feasibility study of volume intracardiac echocardiography in the assessment of patients with structural heart disease undergoing percutaneous transcatheter therapy. *J. Am. Soc. Echocardiogr.* 27, 978–983. doi:10.1016/j.echo.2014.04.022

Simpson, J., Lopez, L., Acar, P., Friedberg, M., Khoo, N., Ko, H., et al. (2017). Three-dimensional echocardiography in congenital heart disease: An expert consensus document from the European association of cardiovascular imaging and the American society of echocardiography. *J. Am. Soc. Echocardiogr.* 30, 1–27.

Sozzi, F., Hugues, N., Civaia, F., Alexandrescu, C., and Iacuzio, L. (2017). Multimodality imaging of a congenital diverticulum of the left ventricular outflow tract. *Eur. Heart J. Cardiovasc. Imaging* 18, 144. doi:10.1093/ehjci/jew170

Sun, F., Chen, Y., Ren, W., Zhang, Y., Wu, D., Chen, X., et al. (2017). Four-tiered echocardiographic analysis approach for congenital mitral valve malformations: Four years of experience. *Int. J. Cardiol.* 227, 602–610. doi:10.1016/j.ijcard.2016.10.090

Vainrib, A. F., Bamira, D., Aizer, A., Chinitz, L. A., Loulmet, D., Benenstein, R. J., et al. (2019). Photorealistic imaging of left atrial appendage occlusion/exclusion. *Echocardiography* 36, 1601–1604. doi:10.1111/echo.14438

Vairo, A., Marro, M., De Ferrari, G. M., Rinaldi, M., and Salizzoni, S. (2019). Use of a photo-realism 3D rendering technique to enhance echocardiographic visualization of the anatomical details during beating-heart mitral valve repair. *Echocardiography* 36, 2090–2093. doi:10.1111/echo.14515

Valente, A., Cook, S., Festa, P., Ko, H., Krishnamurthy, R., Taylor, A., et al. (2014). Multimodality imaging guidelines for patients with repaired tetralogy of fallot: A report from the AmericanSsociety of echocardiography: Developed in collaboration with the society for cardiovascular magnetic resonance and the society for pediatric radiology. *J. Am. Soc. Echocardiogr.* 27, 111–141. doi:10.1016/j.echo.2013.11.009

van den Bosch, A., Ten Harkel, D., McGhie, J., Roos-Hesselink, J., Simoons, M., Bogers, A., et al. (2006). Surgical validation of real-time transthoracic 3D echocardiographic assessment of atrioventricular septal defects. *Int. J. Cardiol.* 112, 213–218. doi:10.1016/j.ijcard.2005.09.012

Wang, Y., Liu, C., Yin, A., Zhao, X., He, W., Xiong, Y., et al. (2021). Prenatal diagnosis of fetal right ventricular diverticulum with massive pericardial effusion in one of monochorionic diamniotic twins: A case report with a favorable outcome following *in utero* pericardiocentesis. *J. Int. Med. Res.* 49, 300060520986668. doi:10.1177/0300060520986668

Xu, L., Wang, L., Gai, Y., Ma, Q., Xiang, G., Ouyang, C., et al. (2020). Prenatal sonographic diagnosis of partial left pulmonary artery sling: A rare case report. *J. Clin. Ultrasound.* 49, 257–261. doi:10.1002/jcu.22913

Youssef, D., Flores, M., Ebrahim, E., Eshak, K., Westerink, J., Chaudhuri, D., et al. (2020). Assessing the clinical significance of echocardiograms in determining treatment of patent ductus arteriosus in neonates. *J. Neonatal. Perinat. Med.* 13, 345–350. doi:10.3233/NPM-170122

frontiers | Frontiers in Physiology

TYPE Original Research
PUBLISHED 29 September 2022
DOI 10.3389/fphys.2022.991990

OPEN ACCESS

EDITED BY
Lisheng Xu,
Northeastern University, China

REVIEWED BY
Peng Li,
Southern Medical University, China
Ernst Wellnhofer,
CharitÃ© UniversitÃ¤tsmedizin Berlin, Germany
Rajiv Rampat,
William Harvey Hospital, United Kingdom
Yuhang Xu,
Coventry University, United Kingdom

*CORRESPONDENCE
Lin Yang,
aiyzwll@aliyun.com

SPECIALTY SECTION
This article was submitted to Computational Physiology and Medicine, a section of the journal Frontiers in Physiology

RECEIVED 12 July 2022
ACCEPTED 17 August 2022
PUBLISHED 29 September 2022

CITATION
Zhou X, Li X, Zhang Z, Han Q, Deng H, Jiang Y, Tang C and Yang L (2022), Support vector machine deep mining of electronic medical records to predict the prognosis of severe acute myocardial infarction.
Front. Physiol. 13:991990.
doi: 10.3389/fphys.2022.991990

Support vector machine deep mining of electronic medical records to predict the prognosis of severe acute myocardial infarction

Xingyu Zhou[1,2], Xianying Li[1], Zijun Zhang[1], Qinrong Han[1], Huijiao Deng[1], Yi Jiang[1], Chunxiao Tang[1] and Lin Yang[2,1]*

[1]Zhuhai Campus of Zunyi Medical University, Zhuhai, China, [2]Key Laboratory of Human-Machine Intelligence-Synergy Systems, Shenzhen Institutes of Advanced Technology, Chinese Academy of Sciences (CAS), Shenzhen, China

Cardiovascular disease is currently one of the most important diseases causing death in China and the world, and acute myocardial infarction is a major cause of cardiovascular disease. This study provides an analytical technique for predicting the prognosis of patients with severe acute myocardial infarction using a support vector machine (SVM) technique based on information gleaned from electronic medical records in the Medical Information Marketplace for Intensive Care (MIMIC)-III database. The MIMIC-III database provided 4785 electronic medical records data for inclusion in the model development after screening 7070 electronic medical records of patients admitted to the intensive care unit for treatment of acute myocardial infarction. Adopting the APS-III score as the criterion for identifying anticipated risk, the dimensions of data information incorporated into the mathematical model design were found using correlation coefficient matrix heatmaps and ordered logistic analysis. An automated prognostic risk-prediction model was developed using SVM, and the fit was evaluated by 5× cross-validation. We used a grid search method to further optimize the parameters and improve the model fit. The excellent generalization ability of SVM was fully verified by calculating the 95% confidence interval of the area under the receiver operating characteristic curve (AUC) for six algorithms (linear discriminant, tree, Kernel Naive Bayes, RUSBoost, KNN, and SVM). Compared to the remaining five models, its confidence interval was the narrowest with higher fitting accuracy and better performance. The patient prognostic risk prediction model constructed using SVM had a relatively impressive accuracy (92.2%) and AUC value (0.98). In this study, a model was designed for fitting that can maximize the potential information to be gleaned in the electronic medical records data. It was demonstrated that SVM models based on electronic medical records data can offer an effective solution for clinical disease prognostic risk assessment and improved clinical outcomes and have great potential for clinical application in the clinical treatment of myocardial infarction.

KEYWORDS

cardiology, electronic medical records, machine learning, support vector machine, ICU

1 Introduction

Cardiovascular disease is currently one of the most critical diseases causing death and disability worldwide, and it places a significant burden of disease on the population around the world. (Vos et al., 2020). Acute myocardial infarction is ischemic necrosis of myocardial cells and can occur during the natural course of coronary atherosclerosis as an acute coronary syndrome (Reed et al., 2017). As one of the most common cardiovascular diseases, myocardial infarction (MI) is a condition of widespread myocardial necrosis caused by interruption of coronary artery blood supply, resulting in persistent ischemia in the blood supply area, usually complicated by heart failure, heart rupture, and cardiogenic shock. In recent years, the incidence of MI has rapidly increased, and the age composition of MI patients is showing a younger trend, seriously threatening the life and health of human beings. (R. Nasimov et al., 2020). It is estimated that >3 million people suffer an acute ST-segment–elevation MI (STEMI) and >4 million people suffer a non–ST-segment–elevation MI each year. (G. A. Roth et al., 2020). Patients with MI are also at progressively greater risk of re-infarction after discharge from the hospital, and re-infarction or multiple infarctions are a major cause of death in patients with MI (Mal et al., 2019). As a result, it is critical to minimize the mortality rate of MI patients as well as the rate of re-infarction after discharge from the hospital (Nordenskjöld et al., 2019). An accurate evaluation of the prognosis of MI patients may assist health care professionals in devising more appropriate treatment and care plans and in providing more reasonable diagnostic and rehabilitation care in order to enhance the survival rate of MI patients and their quality of life (Than et al., 2019).

The flourishing development of computer technology has played a significant role in enhancing modern health care management, optimizing the allocation of resources, improving efficiency, and reducing medical costs since the third industrial revolution and the gradual maturation of the Internet in the new era. Machine learning algorithms are constantly evolving and have shown effective in medical prediction (Johnson et al., 2021). Machine learning–based predictive models can help less experienced doctors diagnose diseases and improve survival rates by overcoming the drawbacks of relying solely on doctors' personal subjective experience (He et al., 2022). Prognostic predictive models can also assist health care professionals in developing more reasonable care plans and improving survival rates. Furthermore, electronic medical records (EMRs), which contain medical data, have good guarantee, especially when it comes to using data mining techniques to analyze and process pertinent medical records data (Okamoto et al., 2020). Compared to traditional paper medical records, EMRs can record more information and are easier to keep. As a result, more and more hospitals are choosing to use EMRs to preserve patient-related information. Through appropriate data mining methods, the large amount of information contained in EMRs can be extracted more easily (Ayaad et al., 2019). Machine learning can be used to efficiently use information from electronic medical records in order to achieve a more personalized medicine perspective (Latif et al., 2020).

In this paper, we propose an approach based on a support vector machine (SVM) technique, which can overcome the problems of non-linearity, high dimensionality, and local minima (Hossain et al., 2021) and has a good generalization ability. The support vector machine approach is based on the VC dimensional theory of statistical learning theory and the principle of structural risk minimization, which seeks the best compromise between model complexity and learning ability based on limited sample information in order to obtain the best generalization ability. SVM requires a relatively small number of samples, which is good at coping with the situation of linear indistinguishability of sample data, and also can effectively avoid overfitting to a certain extent. Compared to algorithms such as ordered logstic regression, which are most commonly used in traditional prediction methods, SVMs are structured and stable and have a high generalisation capability. We developed an algorithm that can be used to find out the relationship between the physiological indicators of MI patients and their prognosis using case data screened from the Medical Information Marketplace for Intensive Care (MIMIC)-III database. The model may be used to forecast the prognosis of MI patients, and it can be used in conjunction with the Acute Physiology Score III (APS-III) to precisely assess the prognosis of MI patients (Huang et al., 2021), assuring its dependability. The prediction model constructed in this study can be applied to clinical research. At the same time, however, it can also provide assistance to doctors during diagnosis; may improve their work efficiency; and could alleviate the current situation of medical resources tension in various hospitals, which is of great significance to the treatment and prognosis of MI Figure 1.

The paper is structured as follows. Section 2 of this paper describes the public database required to conduct this experiment and the application of SVM for predictive model building. Section 3 focuses on the evaluation of the model effects in this study. Section 4 of this study synthesizes the current state of research at home and abroad, and provides an objective discussion based on the areas for improvement of this experiment. Section 5 of this study draw a conclusion of the paper and provides future research directions.

2 Materials and methods

2.1 Data sources

In this study, data analysis and model construction were performed based on sample data from the MIMIC-III database (Wang et al., 2020; Goldberger et al., 2000). In recent years, EMRs have gradually replaced traditional paper charts for recording patient information and have many advantages, such as ease of storage, accuracy of data, and ease of extraction and analysis. MIMIC-III is a large, freely accessible single-center database (Johnson et al., 2016). Developed at the Massachusetts Institute of Technology, it integrates clinical data from patients admitted to the intensive care unit (ICU) at Beth Israel Deaconess Medical Center and is widely used by researchers internationally (Singh and Mayo, 2018; Scherpf et al., 2019).

To protect the security of private patient data, the MIMIC-III database is de-identified using structured data cleansing and date conversion in line with United States Health Insurance Portability and Accountability Act (HIPAA) requirements. All identifiable data element fields listed in HIPAA, such as patient name, phone number, address, and date, are removed throughout the de-identification process for structured data. The removal of protected health information, such as diagnostic reports and medical prescriptions, from strings is completed using a de-identification system based on extensive dictionary look-ups and regular expression patterns. The MIMIC-III database is available as a collection of comma-separated value files and not only has a large sample size and variety of samples but also good reliability (Gentimis et al., 2017).

The researchers responsible for data collection in this project completed a HIPAA-required Protecting Human Research Participants course, signed a data use agreement, and passed the PhysioNet accreditation.

2.2 Data acquisition and filtering

To select patients for inclusion, We searched the MIMIC-III database using the keyword "MIMICiii.d_icd_diagnoses where long_title like '%yocardial infarctio%' in the table diagnoses_icd." We obtained information on all patients admitted to the ICU due to a MI from the MIMIC-III database. We retrieved materialized views MIMICiii.apsiii to obtain a prognostic evaluation of the patient in question. We also retrieved tables of admissions, chart events, laboratory events, microbiology events, and prescriptions to obtain patient-related monitoring data. A total of 7070 relevant data were gathered.

Patients with a high number of missing indicators or EMR data that were incomplete, patients who died while receiving in-hospital care, and patients who suffered a huge number of problems or for whom an MI was just one of many conditions were excluded. A total of 4785 relevant data were finally included.

2.3 Data content

Relevant personal information about the patient included length of stay, time treated in the ICU, height, weight, type of health insurance the patient had, and ethnicity. Patient laboratory tests of interest included glucose, triglycerides, N-terminal prenatremic peptide, potassium, platelets, total cholesterol, troponin I, high-density lipoprotein, creatine kinase, troponin T, low-density lipoprotein, C-reactive protein, and creatine kinase isoenzyme. We also considered the following patient pathogenic microbial infections: number of *Staphylococcus aureus* flora, number of *Escherichia coli* flora, and number of *Streptococcus pneumoniae* flora.

Finally, we recorded the total dose of different drugs administered during treatment, including aspirin, heparin, atorvastatin, *mycoplasma*, and nitroglycerin. The prognostic model score for patients was the APS-III score.

2.4 Details of the proprietary software

In this study, the software used to construct the model was MatLab (R2021a 9.10.0.1602886; The MathWorks, Inc. Natick, MA, United States). To describe the correlation between features, a correlation coefficient matrix heatmap was drawn using the R language (version 4.1.3; The R Foundation for Statistical Computing, Vienna, Austria).

2.5 Theory/calculation

2.5.1 Prognosis evaluation method

The concept of objective evaluation of critically ill patients' conditions has become widely accepted by clinical workers alike as an important tool in their daily work, and various scores were widely used in clinical applications of this study. In the MIMIC-III database, in addition to the APS-III scale (Knaus et al., 1991) there exist such scales as the Oxford Acute Severity of Illness Score (OASIS) (Holland and Moss, 2017), Sepsis-related Organ Failure Assessment (SOFA) (Lambden et al., 2019), Logistic Organ Dysfunction Score (LODS) (Marshall, 2020), Scale for Assessing Positive Symptoms (SAPS) (Le Gall et al., 1993), and many other scales used in critical care medicine.

Compared to the above-mentioned scales, the APS-III scale—as one of the widely used tools for critical illness assessment—has been shown in many studies to be significantly associated with patient survival evaluation (Pathmanathan, 2005). The APS-III scale was designed to reflect individual differences in acute physiological status, age,

and chronic disease status (Godinjak, 2016; Sadaka et al., 2017). Excellent predictive results have been achieved in evaluating the effectiveness of medical measures, predicting patient prognosis, making predictions about the risk of death in individuals and groups, classifying patients according to their condition, and comparing treatment outcomes (Moreno and Nassar Júnior, 2017).

The APS-III scale has been widely used in the medical community as an important tool for predicting the risk of death prediction in ICU patients. In a recent study on prognosis prediction of ICU patients (Zhang et al., 2022), the results showed that the independent receiver operating characteristic curve (ROC) curve results of the APS-III scale were superior compared to those of the SAPS-II, LODS, OASIS, and SOFA scales, indicating that the former has a more promising accuracy in the prognosis prediction of critically ill patients. Thus, the results of the APS-III scale were used to evaluate the prognosis of patients in this study Figure 2.

2.5.2 Feature extraction and analysis

Redundant or less relevant variable features often exist in multidimensional data, which affects the accuracy of machine learning output (Ho et al., 2019). Feature selection can solve this drawback, reduce the burden of machine learning, and improve the generalization performance, prediction performance and operational efficiency of the algorithm (Chandrashekar and Sahin, 2014).

Correlation analysis between features and APS-III can select features that are meaningful for classification prediction results from all features of sample data, so as to exclude the interference of chance factors in the data. Therefore, in this paper, the correlation coefficients between features and APS-III are calculated and the heat map of the correlation coefficient matrix is drawn to investigate whether there is a correlation between features and APS-III, and the direction and magnitude of the correlation relationship (Haarman et al., 2015).

In this study, first the corrplot package was installed and imported in R language and a dataset in csv format was loaded, then the calculation of the matrix of correlation coefficients between all features was started and two decimal places were retained, and finally the matrix of correlation coefficients was plotted using the corrplot package to create a heat map of the correlation coefficient matrix for all features (as in Figure 3). In the correlation coefficient matrix heatmap, each number represents the correlation coefficient between the corresponding features, and the color shades of the corresponding squares also symbolize the size of the correlation coefficient, i.e., the darker the color, the larger the correlation coefficient, and vice versa. The color of the squares is related to the direction of correlation, with blue representing a positive correlation and red representing a negative correlation. In this study, APS-III was used as a predictor of patient prognosis evaluation. The correlation coefficients between "Length of hospital stay", "Platelets", "C-reactive protein", "Creatine kinase isoenzyme", "Creatine kinase", "Length of stay in ICU", "Triglycerides", "Total dose of atorvastatin ", "total nitroglycerin dose", "*Streptococcus pneumoniae*" and APS-III scores were all low, all <0.2. These indicators were removed in the later model construction. Indicators included in the final model construction were: blood potassium, blood glucose, total cholesterol, troponin I, troponin T, HDL, LDL, N-terminal prenatremic peptide, height, weight, E. coli, total aspirin dose, total *mycoplasma* dose.

2.5.3 SVM

Based on statistical learning theory and the notion of structural risk minimization, Vapnik and others at AT&T Bell Labs introduced SVM for classification and regression investigations (Vapnik, 2000). SVM classifies data by determining the optimum hyperplane for successfully separating a data point class from another (Figure 4). By non-linearly mapping the input space to the high-dimensional feature space, the kernel function can make classification more convenient and effective. The Gaussian radial basis kernel function SVM classification ability is significantly superior to other approaches in the face of non-linear classification issues (Liu et al., 2012), and using SVM on this basis can provide more scientifically accurate results.

The kernel parameter (γ) is the only variable parameter in the space mapped by the Radial Basis Function kernel function, i.e., the value of γ directly influences the distribution of sample data in the kernel space; hence, the optimal value of γ substantially affects the model fit accuracy (Padierna et al., 2018).

The penalty term C is used to limit the model's complexity and accuracy, i.e., to adjust the learning machine's confidence range to the empirical risk in a specific feature subspace, so that the learning machine can generalize as well as possible. The greater the C value, the better the model fits, although this does not guarantee generalization (Tharwat, 2019). In each subspace, there is only 1 optimal penalty term for constraining the entire model; nevertheless, in order to attain high accuracy, this single element must be examined in isolation.

The basis of SVMs is the structural risk minimization (SRM) principle (Shawe-Taylor et al., 1998). The core of the SRM principle is to reduce the complexity of the learning machine, that is the Vapnik-Chervonenkis dimension (VC dimension), while maintaining classification accuracy (experience risks), which allows the expected risk of the learning machine to be controlled over the entire sample set (as in Figure 5). Because the SRM principle's premise is for a specific subspace in the feature space and the data contain different divisions in the non-stop subspace, there are different optimal SVM algorithms in different subspaces; therefore, the SVM kernel parameters and the penalty term

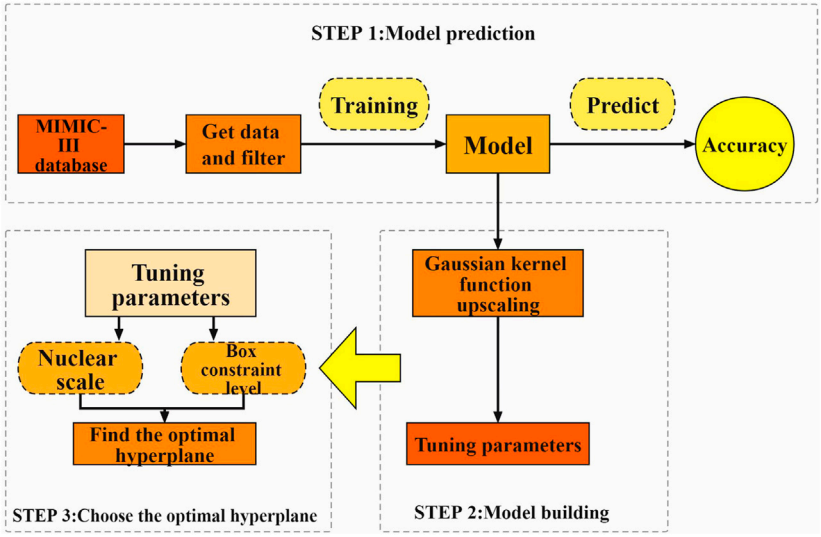

FIGURE 1
The process of acquiring data from a database and constructing a predictive model.

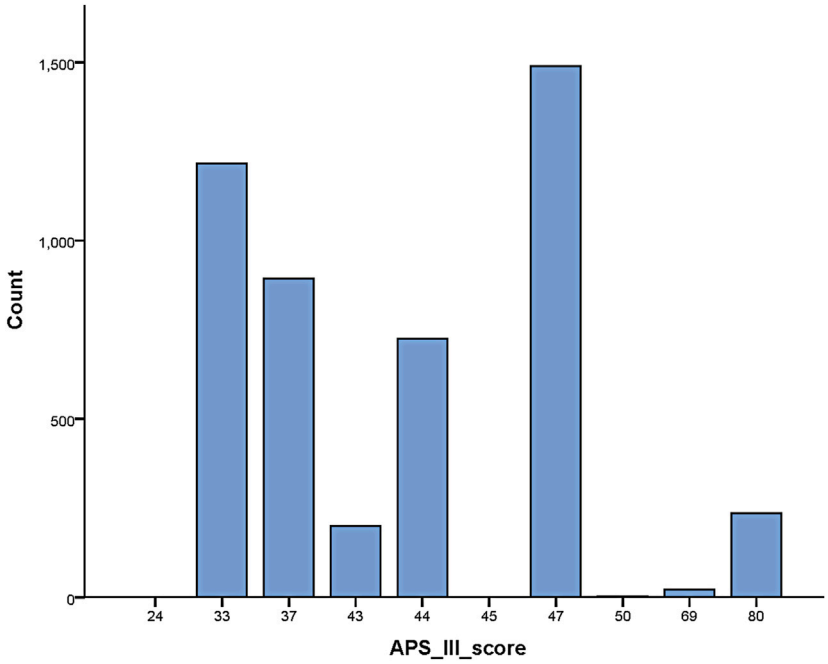

FIGURE 2
APS-III scale scores for patients included in the study.

C must be optimized at the same time. In this study, we used a grid search approach to discover the optimum combination of C and hyperplane, then produced the best-fitting SVM model.

2.5.4 Algorithm steps

SVM is a new type of machine learning algorithm. The ideal hyperplane fulfills the following inequality for a given sample set of variables (x_i, y_i) i = 1,2,. . .,n. In the case of the input variable

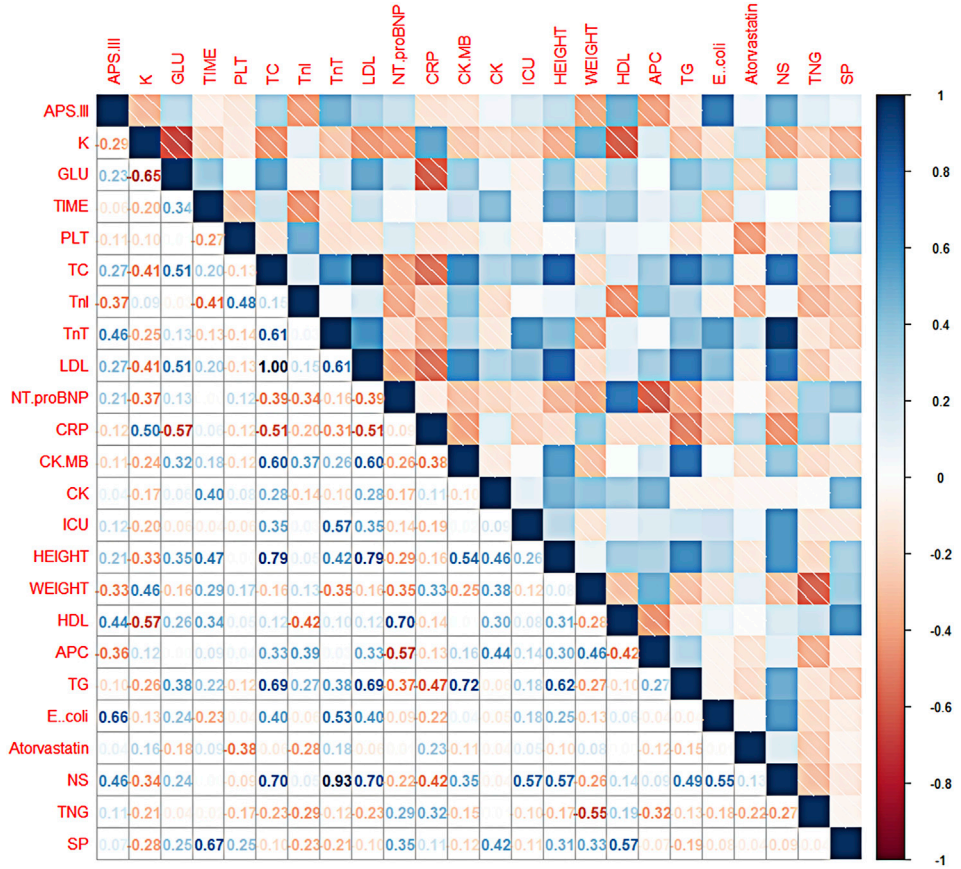

FIGURE 3
Thermalmatrix diagram of correlation coefficients for each feature. Description of the abbreviations in Figure 3: K (blood potassium), GLU (blood glucose), TIME (length of hospital stay), PLT (platelets), TC (total cholesterol), TnI (troponin I), TnT (troponin T), LDL (low-density lipoprotein), Nt. proBNP (N-terminal prenatriuretic peptide), CRP (C-reactive protein), CK. MB (creatine kinase isoenzyme), CK (creatine kinase), ICU (patient's time in ICU), HEIGHT (patient's height), WEIGHT (patient's weight), HDL (high-density lipoprotein), APC (total aspirin dose), TG (triglycerides), E.*coli* (number of *Escherichia coli* flora), Atorvastatin (total atorvastatin dose), NS (total bacteriocin does), TNG (total nitroglycerin dose), SP (*Streptococcus pneumoniae*).

$x_i \in R^d$ and the output variable $y_i \in \{-1, 1\}$, $\varphi(\cdot)$ is a nonlinear function, the optimal hyperplane satisfies the following inequality:

$$y_i\left[w^T\varphi(x_i) + b\right] \geq 1 - \xi_i \tag{1}$$

where w^T is a multidimensional vector, b is a constant, and ξ_i is a slack variable related to the classification error. To maximize the distance between the 2 categories, the above inequality can be rewritten as:

$$min\left[\frac{1}{2}|w|^2 + C\sum_{i=1}^{n}\xi_i\right] \tag{2}$$

where C is a penalty term that adjusts the relaxation variable ξ_i to determine the classification error and also the classification interval $\frac{1}{2}|w|^2$. For non-linear indistinguishable sample points, a kernel function is introduced to map the sample points to a higher dimensional space, thus achieving an effective classification of the sample points.

The radial basis kernel function is expressed as follows:

$$K(x, x') = exp\left(-\frac{\|x - x'\|^2}{2\sigma^2}\right) = exp\left(-\gamma\|x - x'\|^2\right) \tag{3}$$

where the radial basis function (RBF)kernels of two samples, x and x', are represented as eigenvectors in some input space; σ is the bandwidth of the Gaussian radial basis kernel function; γ is the parameter of the Gaussian radial basis kernel function; and exp denotes the exponential function with natural constant e as the base. Also, γ takes the general values $\gamma = \{2^{-15}, 2^{-14}, \ldots, 2^{15}\}$. In this study, by the grid search method, γ is substituted sequentially into the following equation:

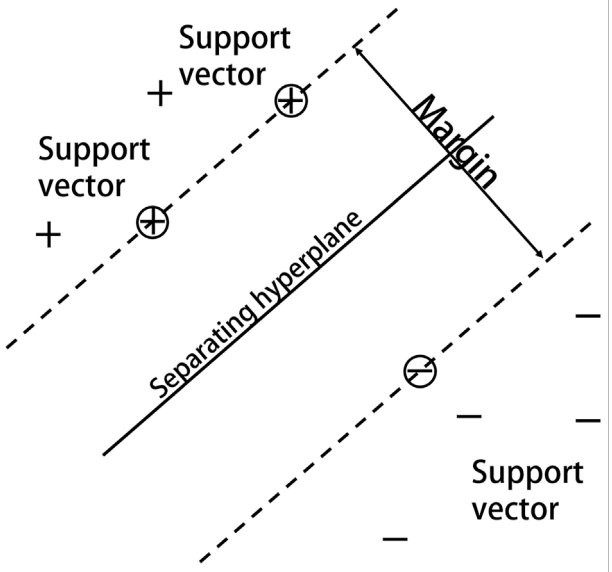

FIGURE 4
SVM schematic.

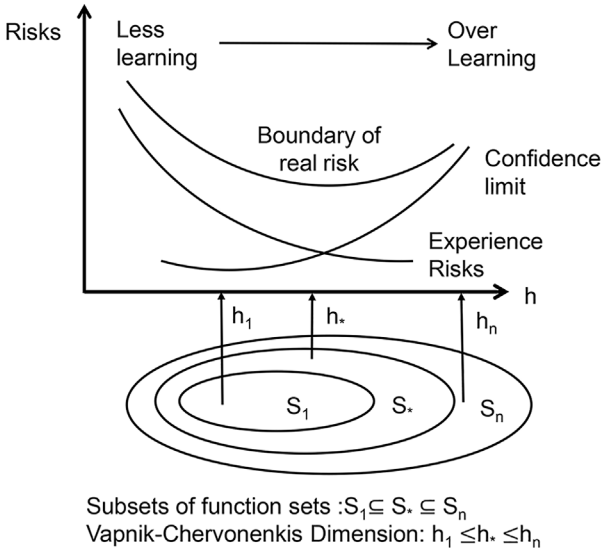

FIGURE 5
Schematic diagram of the principle of structural risk minimization.

$$D_{(c_1,c_2)} = \|\mathrm{m}_1 - m_2^2\| = \frac{1}{l_1^2}\sum_{i=1}^{l_1}\sum_{j=1}^{l_1}\exp\left(-\gamma\left\|x_i^{(1)} - x_j^{(1)}\right\|^2\right) + \frac{1}{l_2^2}\sum_{i=1}^{l_2}\sum_{j=1}^{l_2}\exp\left(-\gamma\left\|x_i^{(2)} - x_j^{(2)}\right\|^2\right) - \frac{1}{l_1 l_2}\sum_{i=1}^{l_1}\sum_{j=1}^{l_2}\exp\left(-\gamma\left\|x_i^{(1)} - x_j^{(2)}\right\|^2\right) \quad (4)$$

The grid search method is an exhaustive search method that divides all of the parameters γ and C to be searched into a grid of the same length in a given space, traverses each grid, and then writes a program to optimize the SVM model using MatLab to find the best combination of parameters with the smallest mean square error (Fayed and Atiya, 2019). Compared to the traditional exhaustive search method, this method is more accurate and easier to use when looking for the best combination of parameters. This work involves the use of cross-validation to evaluate the classification accuracy of the model created for each parameter combination in order to improve its fitting effect and acquire a better generalization capability.

In Formula (4),$D_{(c_1,c_2)}$ is the distance measure obtained from measure learning. The optimal kernel parameter is that which corresponds to the largest kernel space mean distance where m_1 and m_2 are the feature space centroid vectors for the first and second classes of data, respectively. The formula for the particular derivative is as follows:

$$m_1 = \frac{1}{l_1}\sum_{i=1}^{l_1}\Phi\left(x_i^{(1)}\right) \quad (5)$$

$$m_2 = \frac{1}{l_2}\sum_{i=1}^{l_2}\Phi\left(x_i^{(2)}\right) \quad (6)$$

In conclusion, the optimum parameter combination for the following tests in this study is a box constraint level of 30 and a kernel scale value of 250. The soft interval size in SVM, which is stated as the penalty term (C) in RBF, is connected to the box constraint. The lower the value, the lower the penalty, which impacts the model fit, and the higher the value, the higher the penalty, which reduces the model accuracy. It is simple to know that KernelScale = $\sqrt{\frac{1}{\gamma}}$ because KernelScale = $\sqrt{2}\sigma$ (σ is the bandwidth) and Eq. 3 are combined. As a result, the kernel parameters dictate the value of the kernel scale, which affects the model's accuracy.

3 Results

By plotting the correlation coefficient matrix heatmap of all features, the researchers removed indicators with low correlations with APS-III scores. After ensuring the relevance of the data, validation of the accuracy of the model is equally essential. The 5× cross-validation method was used to verify the model accuracy in predicting the prognosis of acute MI disease. The samples in the dataset were separated into five groups, with four groups used to train the model and one used to test it. Five

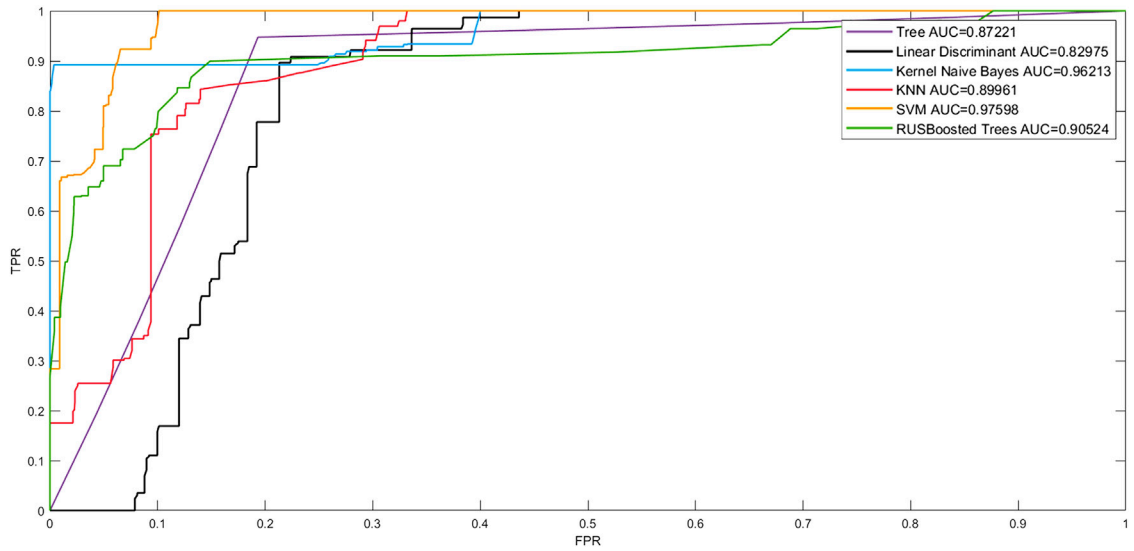

FIGURE 6
ROC curves for the models.

rounds of the above experiments were run, and the average value of the five training results was used to determine the model's accuracy.

The Receiver Operating Character curve (ROC curve), with the false-positive rate (FPR) as the horizontal axis and the true-positive rate (TPR) as the vertical axis, is a commonly used model evaluation metric in the medical field. The area under the ROC curve, or AUC (Area Under ROC Curve), is a visual representation of the model's performance. The number of AUCs is a measure of the model's overall quality, with a greater AUC indicating better model performance. To verify the effectiveness of the model fit in this study, we plotted the linear discriminant, support Vector Machine (SVM) tree, Kernel Naive Bayes, random undersampling boost (RUSBoost), and K-NearestNeighbor (KNN) ROC curves to show the performance of the currently selected training classifiers. As shown in Figure 6, in terms of model classification performance, the SVM algorithm obtained the ROC curve closest to the upper left corner and the largest AUC with an AUC of 0.97598. Kernel Naive Bayes has the second highest AUC value of 0.96213, which proves that the algorithm is also able to meet certain clinical needs in terms of model fitting. However, the best performing model was still the prognostic prediction model constructed by SVM.

For data with a large sample content, the AUC approximates a normal distribution, so the 95% confidence interval (CI) for the AUC can be calculated as described in the CI of the sampling distribution.

The CI is equal to $C \pm se - z_{crit}$, where z_{crit} is the two-tailed critical value of the standard normal distribution.

$$se = \sqrt{\frac{q_0 + (n_1 - 1)q_1 + (n_2 - 1)q_2}{n_1 n_2}}$$

n_1 and n_2 are the sizes of the 2 samples, respectively.

$$q_0 = AUC\,(1 - AUC)\; q_1 = \frac{AUC}{2 - AUC} - AUC^2$$
$$q_2 = \frac{2AUC^2}{1 + AUC} - AUC^2$$

The DeLong test is a relatively common method of AUC significance test. The principle is as follows. Taking two different models as an example, let the two AUCs be A_1 and A_2 respectively.

1 First calculate the difference between the two AUC values.

$$\theta = A_1 - A_2$$

2 Calculate the variances var (A_1) and var (A_2) of A_1 and A_2, and the covariance cov (A_1, A_2) of the two.
3 Calculate the Z-value

$$Z = \frac{\theta}{var\,(A_1) + var\,(A_2) - 2cov\,(A_1, A_2)}$$

4 Finally, take the Z-value distribution as a normal distribution, do a significance test, and get the P value. If the p value is less than 0.05, it means that there is a significant difference between the two AUCs, which is statistically significant, otherwise, it is not significant.

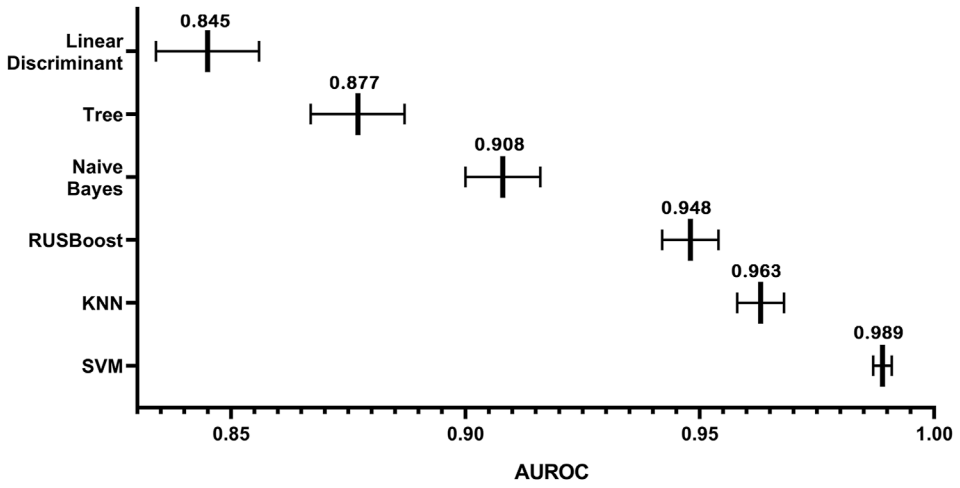

FIGURE 7
Visual overview of the AUC and 95% CI values for each model.

TABLE 1 Conclusion of DeLong test of SVM with other five classifiers.

Classifier	Z-value	*p*-value
KNN	16.536	<2.2e-16
RUBoost	34.198	<2.2e-16
Naïve Bayes	10.448	<2.2e-16
Tree	9.0918	<2.2e-16
Liner Discriminant	28.143	<2.2e-16

In this study, we had a total sample of 4785 cases and used 5× cross-validation to calculate the values of AUC for linear discriminant, tree, Kernel Naive Bayes, RUSBoost, KNN, and SVM, as shown in Figure 7 Using this method, it can be concluded that the algorithm with the highest value of AUC and the narrowest CI is the SVM algorithm. As shown in Table 1, the DeLong test was performed on the ROC of SVM and the ROC of other algorithms, and the obtained *p*-values were all less than 0.05, indicating that there was a significant difference between the AUC of the SVM algorithm and the use of other algorithms, which was statistically significant, further indicating that the model built using the SVM algorithm has better accuracy. The AUC values for linear discriminant, tree, Kernel Naive Bayes, RUSBoost, KNN, and SVM increased sequentially, indicating that the predictive ability of each model increased sequentially and the CI decreased sequentially, which implies that there is a decreasing uncertainty in the prognostic effect of each model in predicting patients with MI. Therefore, we can conclude that when using the existing dataset for prediction model construction, the prediction model constructed by SVM has a more promising fit than the remaining five algorithms.

4 Discussion

The scale-based assessment of patient condition is one of the foundations of our project, but this study has considerable advantages over scale-based assessment. Compared to the current predictive model, scales are time-consuming and difficult to obtain when used alone and can even more difficult to obtain if a patient has specific conditions, such as hearing or vision loss or speech impairment, making it difficult for health care professionals to accurately determine a patient's condition in a timely manner (Arnetz et al., 2008). In this study, using the obtained scales as the basis for the prognosis of the model can largely reduce the process of obtaining the patient's scale scores and can present the findings in a dynamic manner to obtain more accurate and rapid predictions, which can reduce the workload of the clinical staff and help physicians to accurately determine the progress of the disease, thus assisting them in making individualized adjustments to the treatment plan. In other words, the present system will help doctors to make personalized adjustments to treatment plans.

In this study, the biomarkers of our prognostic prediction model are widely used clinically. This may ensure the general applicability of our study results and provides a useful adjunct for clinical treatment. Due to the combination of machine learning and medicine, the large, complex, and multidimensional datasets present in EMRs can be analyzed. For instance, Lee et al. (2021) developed a deep learning–based method used to screen fundus

abnormalities in patients with high specificity and sensitivity. In addition, Zhao et al., using artificial intelligence–based algorithms combined with 12-lead electrocardiogram (ECG) data, developed an accurate early warning system based on ECG data, and the sensitivity of the model was 99%. They also proposed a wearable ECG vest, and smartphones and real-time warning systems coupled with an automatic diagnosis will greatly improve the diagnosis rate for STEMI patients and reduce patient delay times (Zhao et al., 2020).

In recent years, in the context of the era of big data in healthcare, with the development of artificial intelligence technology, more and more researchers are using machine learning, such as K-NearestNeighbor (KNN), the Bayes algorithm, and the decision tree to build predictive models. The KNN method is a lazy learning method that uses instances to discover the K training dataset that is the most similar to the unknown data. Its sample pool size is necessary, which severely restricts its practical application if the sample set is complex or if training samples are not available (Zhang and Zhou, 2007). The Bayesian classification algorithm is a probabilistic statistics-based classification method that considers all qualities and theoretically yields the best solution with the least amount of error. However, the accuracy of its classification may be affected because Bayes' theorem presupposes that the effect of an attribute value on a given class is independent of the values of other attributes, which is frequently false (Manino et al., 2019). A decision tree is a tree-like instance-based inductive classification algorithm that can classify and predict at the same time. However, due to its extreme bifurcation, it is prone to overfitting, and the error can rapidly increase when there are too many categories (Myles et al., 2004). In contrast, SVM, as a supervised learning algorithm, has a rigorous mathematical theoretical support, possesses good interpretability, and does not rely on statistical methods to some extent. SVM's final decision function is determined by only a few vectors, has no significant correlation with sample space dimensionality, and can identify support vectors that are critical to the project (Noble, 2006). SVM has been widely used by the international medical community in recent years to solve the classification regression aspects of biological data, such as in the prognosis prediction of patients with serious diseases like laryngeal cancer (Chen et al., 2007), prostate cancer (Çınar et al., 2009), hepatocellular carcinoma (Ali et al., 2021), and renal cell tumors (Giulietti et al., 2021).

Past studies (Than et al., 2019; Doudesis et al., 2022) used a single physiological condition as an indicator to assess the prognosis of patients or their mortality. However, we believe that the underlying individual circumstances of the patient, as well as their status in society and ethnicity, also largely influence the progression of their disease (Khraim and Carey, 2009). In addition, the different treatment strategies received by different patients during their in-hospital stay also have a significant impact on the prognosis (Anderson and Morrow, 2017). Thus, in this study, we not only included the physical condition of patients in the screening of characteristics but also their health insurance status, height, weight, age, ethnicity, and even the length of time they were treated for in the ICU and the dosage of the injected drugs. The inclusion of multiple dimensions of the patient's condition inevitably allows for a more comprehensive perspective on the progression of said condition. The collection of these characteristics largely facilitates the completeness of the model and allows for an accurate evaluation of the patient from multiple perspectives, which in turn leads to more valid predictive conclusions.

In this study, the data used in this study came from Massachusetts General Hospital in the United States, which limits the model's applicability. More localization is needed to improve the model's applicability so that it can help health care professionals make more accurate predictions about the prognosis of MI patients in the future, assisting in the development of appropriate treatment and care plans and improving the prognosis.

5 Conclusion

We retrieved EMRs from the MIMIC-III database and analyzed them with R to discover that 13 markers, such as blood potassium, blood glucose, and total cholesterol, have a strong link with the prognosis of MI patients. A patient prognostic model was built by comparing plain Bayesian, KNN, linear discriminant, RUSBoost trees, and SVM algorithms, and the prognostic model based on the SVM algorithm was found to have a good fit, with an accuracy rate of 92.2% and an AUC of 0.989, demonstrating that the model still has a certain (necessarily higher) accuracy and conviction compared to other algorithms. SVM feature extraction from EMR data enhances prediction accuracy, and this technology is universally applicable, allowing it to be used for prognostic prediction of different diseases.

Data availability statement

The datasets presented in this study can be found in online repositories. The names of the repository/repositories and accession number(s) can be found below: https://mimic.physionet.org.

Ethics statement

This database was approved by the Massachusetts Institute of Technology (Cambridge, MA) and Beth Israel Deaconess Medical Center (Boston, MA). Initially, consent was obtained for the collection of data. The ethical approval statement and informed consent requirement were waived for this manuscript. According

to national legislation and institutional requirements, written informed consent was not required for participation in this study.

Author contributions

LY: study supervision and funding acquisition. XZ: conduct of the research and investigation process, development of methodology, provision of database, and implementation of the algorithms. XL: Scrubbed data and maintained research data. QH: Analyzed the study data and writing of the initial draft. HD: Graphics and data visualization. YJ: Writing of the initial draft and provision of analysis tools. ZZ: Verification, especially in overall replication of results.

Funding

The study was funded by the National Natural Science Foundation of China (Nos. 81960419, and 81927804) and the College Students Innovation and Entrepreneurship Training Program of Zunyi Medical University (Nos. ZHCX202129 and ZHCY202106).

Acknowledgments

The authors thank Xiaofang Ding and Yuanheng Li for their precious assistance during experiments. The authors would like to thank the Key Laboratory of Human-Machine-Intelligence Synergic System, Shenzhen Institutes of Advanced Technology, Chinese Academy of Sciences.

Conflict of interest

The authors declare that the research was conducted in the absence of any commercial or financial relationships that could be construed as a potential conflict of interest.

Publisher's note

All claims expressed in this article are solely those of the authors and do not necessarily represent those of their affiliated organizations, or those of the publisher, the editors and the reviewers. Any product that may be evaluated in this article, or claim that may be made by its manufacturer, is not guaranteed or endorsed by the publisher.

Supplementary material

The Supplementary Material for this article can be found online at: https://www.frontiersin.org/articles/10.3389/fphys.2022.991990/full#supplementary-material

References

Ali, L., Wajahat, I., Amiri Golilarz, N., Keshtkar, F., and Bukhari, S. A. C. (2021). LDA–GA–SVM: Improved hepatocellular carcinoma prediction through dimensionality reduction and genetically optimized support vector machine. *Neural comput. Appl.* 33, 2783–2792. doi:10.1007/s00521-020-05157-2

Anderson, J. L., and Morrow, D. A. (2017). Acute myocardial infarction. *N. Engl. J. Med.* 376, 2053–2064. doi:10.1056/NEJMra1606915

Arnetz, J. E., Winblad, U., Arnetz, B. B., and Höglund, A. T. (2008). Physicians' and nurses' perceptions of patient involvement in myocardial infarction care. *Eur. J. Cardiovasc. Nurs.* 7, 113–120. doi:10.1016/j.ejcnurse.2007.05.005

Ayaad, O., Alloubani, A., ALhajaa, E. A., Farhan, M., Abuseif, S., Al Hroub, A., et al. (2019). The role of electronic medical records in improving the quality of health care services: comparative study. *Int. J. Med. Inf.* 127, 63–67. doi:10.1016/j.ijmedinf.2019.04.014

Chandrashekar, G., and Sahin, F. (2014). A survey on feature selection methods. *Comput. Electr. Eng.* 40, 16–28. doi:10.1016/j.compeleceng.2013.11.024

Chen, W., Peng, C., Zhu, X., Wan, B., and Wei, D. (2007). "SVM-based identification of pathological voices," in *2007 29th annual international conference of the IEEE engineering in medicine and biology society* (Lyon, France: IEEE), 3786–3789. doi:10.1109/IEMBS.2007.4353156

Çınar, M., Engin, M., Engin, E. Z., and Ziya Ateşçi, Y. (2009). Early prostate cancer diagnosis by using artificial neural networks and support vector machines. *Expert Syst. Appl.* 36, 6357–6361. doi:10.1016/j.eswa.2008.08.010

Doudesis, D., Lee, K. K., Yang, J., Wereski, R., Shah, A. S. V., Tsanas, A., et al. (2022). Validation of the myocardial-ischaemic-injury-index machine learning algorithm to guide the diagnosis of myocardial infarction in a heterogenous population: a prespecified exploratory analysis. *Lancet. Digit. Health* 4, e300–e308. doi:10.1016/S2589-7500(22)00025-5–

Fayed, H. A., and Atiya, A. F. (2019). Speed up grid-search for parameter selection of support vector machines. *Appl. Soft Comput.* 80, 202–210. doi:10.1016/j.asoc.2019.03.037

Gentimis, T., Alnaser, A. J., Durante, A., Cook, K., and Steele, R. (2017). "Predicting Hospital Length of Stay Using Neural Networks on MIMIC III Data," in 2017 IEEE 15th Intl Conf on Dependable, Autonomic and Secure Computing, 15th Intl Conf on Pervasive Intelligence and Computing, 3rd Intl Conf on Big Data Intelligence and Computing and Cyber Science and Technology Congress (DASC/PiCom/DataCom/CyberSciTech), (Orlando, FL: IEEE), 1194–1201. doi:10.1109/DASC-PICom-DataCom-CyberSciTec.2017.191

Giulietti, M., Cecati, M., Sabanovic, B., Scirè, A., Cimadamore, A., Santoni, M., et al. (2021). The role of artificial intelligence in the diagnosis and prognosis of renal cell tumors. *Diagnostics* 11, 206. doi:10.3390/diagnostics11020206

Godinjak, A. G., Iglica, A., Rama, A., Tancica, I., Jusufovic, S., Ajanovic, A., et al. (2016). Predictive value of SAPS II and Apache II scoring systems for patient outcome in a medical intensive care unit. *Acta Med. Acad.* 45, 97–103. doi:10.5644/ama2006-124.165

Goldberger, A. L., Amaral, L. A. N., Glass, L., Hausdorff, J. M., Ivanov, P. Ch., Mark, R. G., et al. (2000). PhysioBank, physio toolkit, and physionet: Components of a new research resource for complex physiologic signals. *Circulation* 101. doi:10.1161/01.CIR.101.23.e215

Haarman, B. C. M., Benno)Riemersma-Van der Lek, R. F., Nolen, W. A., Mendes, R., Drexhage, H. A., et al. (2015). Feature-expression heat maps—a new visual method to explore complex associations between two variable sets. *J. Biomed. Inf.* 53, 156–161. doi:10.1016/j.jbi.2014.10.003

He, Z., Yuan, S., Zhao, J., Du, B., Yuan, Z., Alhudhaif, A., et al. (2022). A novel myocardial infarction localization method using multi-branch DenseNet and spatial matching-based active semi-supervised learning. *Inf. Sci.* 606, 649–668. doi:10.1016/j.ins.2022.05.070

Ho, D. S. W., Schierding, W., Wake, M., Saffery, R., and O'Sullivan, J. (2019). Machine learning SNP based prediction for precision medicine. *Front. Genet.* 10, 267. doi:10.3389/fgene.2019.00267

Holland, E. M., and Moss, T. J. (2017). Acute noncardiovascular illness in the cardiac intensive care unit. *J. Am. Coll. Cardiol.* 69, 1999–2007. doi:10.1016/j.jacc.2017.02.033

Hossain, M. E., Khan, A., Moni, M. A., and Uddin, S. (2021). Use of electronic health data for disease prediction: a comprehensive literature review. *IEEE/ACM Trans. Comput. Biol. Bioinform.* 18, 745–758. doi:10.1109/TCBB.2019.2937862

Huang, W.-C., Xie, H.-J., Fan, H.-T., Yan, M.-H., and Hong, Y.-C. (2021). Comparison of prognosis predictive value of 4 disease severity scoring systems in patients with acute respiratory failure in intensive care unit: a STROBE report. *Medicine* 100, e27380. doi:10.1097/MD.0000000000027380

Johnson, A. E. W., Pollard, T. J., Shen, L., Lehman, L. H., Feng, M., Ghassemi, M., et al. (2016). MIMIC-III, a freely accessible critical care database. *Sci. Data* 3, 160035. doi:10.1038/sdata.2016.35

Johnson, K. B., Wei, W., Weeraratne, D., Frisse, M. E., Misulis, K., Rhee, K., et al. (2021). Precision medicine, AI, and the future of personalized health care. *Clin. Transl. Sci.* 14, 86–93. doi:10.1111/cts.12884

Khraim, F. M., and Carey, M. G. (2009). Predictors of pre-hospital delay among patients with acute myocardial infarction. *Patient Educ. Couns.* 75, 155–161. doi:10.1016/j.pec.2008.09.019

Knaus, W. A., Wagner, D. P., Draper, E. A., Zimmerman, J. E., Bergner, M., Bastos, P. G., et al. (1991). The Apache III prognostic system. Risk prediction of hospital mortality for critically ill hospitalized adults. *Chest* 100, 1619–1636. doi:10.1378/chest.100.6.1619

Lambden, S., Laterre, P. F., Levy, M. M., and Francois, B. (2019). The SOFA score—development, utility and challenges of accurate assessment in clinical trials. *Crit. Care* 23, 374. doi:10.1186/s13054-019-2663-7

Latif, J., Xiao, C., Tu, S., Rehman, S. U., Imran, A., and Bilal, A. (2020). Implementation and use of disease diagnosis systems for electronic medical records based on machine learning: a complete review. *IEEE Access* 8, 150489–150513. doi:10.1109/ACCESS.2020.3016782

Le Gall, J., Lemeshow, S., and Saulnier, F. (1993). A new Simplified Acute Physiology Score (SAPS II) based on a European/North American multicenter study. *JAMA* 270, 2957–2963. doi:10.1001/jama.270.24.2957

Lee, J., Lee, J., Cho, S., Song, J., Lee, M., Kim, S. H., et al. (2021). Development of decision support software for deep learning-based automated retinal disease screening using relatively limited fundus photograph data. *Electronics* 10, 163. doi:10.3390/electronics10020163

Liu, Z., Zuo, M. J., and Xu, H. (2012). "Parameter selection for Gaussian radial basis function in support vector machine classification," in *2012 international conference on quality, reliability, risk, maintenance, and safety engineering* (Chengdu, China: IEEE), 576–581. doi:10.1109/ICQR2MSE.2012.6246300

Mal, K., Awan, I., and Shaukat, F. (2019). Evaluation of risk factors associated with reinfarction: a multicenter observational study. *Cureus* 11, e6063. doi:10.7759/cureus.6063

Manino, E., Tran-Thanh, L., and Jennings, N. R. (2019). On the efficiency of data collection for multiple naïve Bayes classifiers. *Artif. Intell.* 275, 356–378. doi:10.1016/j.artint.2019.06.010

Marshall, J. C. (2020). Measuring organ dysfunction. *Med. Klin. Intensivmed. Notfmed.* 115, 15–20. doi:10.1007/s00063-020-00660-9

Moreno, R. P., and Nassar Júnior, A. P. (2017). Is Apache II a useful tool for clinical research? *Rev. Bras. Ter. Intensiva* 29, 264–267. doi:10.5935/0103-507X.20170046

Myles, A. J., Feudale, R. N., Liu, Y., Woody, N. A., and Brown, S. D. (2004). An introduction to decision tree modeling. *J. Chemom.* 18, 275–285. doi:10.1002/cem.873

Nasimov, R., Muminov, B., Mirzahalilov, S., and Nasimova, N. (2020). "A new approach to classifying myocardial infarction and cardiomyopathy using deep learning," in *2020 international conference on information science and communications technologies (ICISCT)*, 1–5. doi:10.1109/ICISCT50599.2020.9351386

Noble, W. S. (2006). What is a support vector machine? *Nat. Biotechnol.* 24, 1565–1567. doi:10.1038/nbt1206-1565

Nordenskjöld, A. M., Lagerqvist, B., Baron, T., Jernberg, T., Hadziosmanovic, N., Reynolds, H. R., et al. (2019). Reinfarction in patients with myocardial infarction with nonobstructive coronary arteries (MINOCA): coronary findings and prognosis. *Am. J. Med.* 132, 335–346. doi:10.1016/j.amjmed.2018.10.007

Okamoto, K., Yamamoto, T., Santos, L. H. O., Ohtera, S., Sugiyama, O., Yamamoto, G., et al. (2020). Detecting severe incidents from electronic medical records using machine learning methods. *Stud. Health Technol. Inf.* 270, 1247–1248. doi:10.3233/SHTI200385

Padierna, L. C., Carpio, M., Rojas-Domínguez, A., Puga, H., and Fraire, H. (2018). A novel formulation of orthogonal polynomial kernel functions for SVM classifiers: the gegenbauer family. *Pattern Recognit.* 84, 211–225. doi:10.1016/j.patcog.2018.07.010

Pathmanathan, A. (2005). Significance of positive Stenotrophomonas maltophilia culture in acute respiratory tract infection. *Eur. Respir. J.* 25, 911–914. doi:10.1183/09031936.05.00096704

Reed, G. W., Rossi, J. E., and Cannon, C. P. (2017). Acute myocardial infarction. *Lancet* 389, 197–210. doi:10.1016/S0140-6736(16)30677-8

Roth, G. A., Mensah, G. A., Johnson, C. O., Addolorato, G., Ammirati, E., Baddour, L. M., et al. (2020). Global burden of cardiovascular diseases and risk factors 1990–2019: Update from the GBD 2019 study. *J. Am. Coll. Cardiol.* 76 (25), 2982–3021. doi:10.1016/j.jacc.2020.11.010

Sadaka, F., EthmaneAbouElMaali, C., Cytron, M. A., Fowler, K., Javaux, V. M., and O'Brien, J. (2017). Predicting mortality of patients with sepsis: A comparison of APACHE II and APACHE III scoring systems. *J. Clin. Med. Res.* 9, 907–910. doi:10.14740/jocmr3083w

Shawe-Taylor, J., Bartlett, P. L., Williamson, R. C., and Anthony, M. (1998). Structural risk minimization over data-dependent hierarchies. *IEEE Trans. Inf. Theory* 44, 1926–1940. doi:10.1109/18.705570

Scherpf, M., Gräßer, F., Malberg, H., and Zaunseder, S. (2019). Predicting sepsis with a recurrent neural network using the MIMIC III database *Comput. Biol. Med.* 113, 103395. doi:10.1016/j.compbiomed.2019.103395

Singh, K., and Mayo, P. (2018). Transthoracic echocardiography and mortality in sepsis: are we there yet? *Intensive Care Med.* 44, 1342–1343. doi:10.1007/s00134-018-5261-2

Than, M. P., Pickering, J. W., Sandoval, Y., Shah, A. S. V., Tsanas, A., Apple, F. S., et al. (2019). Machine learning to predict the likelihood of acute myocardial infarction. *Circulation* 140, 899–909. doi:10.1161/CIRCULATIONAHA.119.041980

Tharwat, A. (2019). Parameter investigation of support vector machine classifier with kernel functions. *Knowl. Inf. Syst.* 61, 1269–1302. doi:10.1007/s10115-019-01335-4

Vapnik, V. N. (2000). *The nature of statistical learning theory*. New York, NY: Springer. doi:10.1007/978-1-4757-3264-1

Vos, T., Lim, S. S., and Abbafati, C. (2020). Global burden of 369 diseases and injuries in 204 countries and territories, 1990-2019: a systematic analysis for the global burden of disease study 2019. *Lancet* 396, 1204–1222. doi:10.1016/S0140-6736(20)30925-9

Wang, S., McDermott, M. B. A., Chauhan, G., Ghassemi, M., Hughes, M. C., and Naumann, T. (2020). "MIMIC-extract: a data extraction, preprocessing, and representation pipeline for MIMIC-III," in *Proceedings of the ACM conference on health, inference, and learning* (Toronto, Ontario: Canada: ACM), 222–235. doi:10.1145/3368555.3384469

Zhang, L., Huang, T., Xu, F., Li, S., Zheng, S., Lyu, J., et al. (2022). Prediction of prognosis in elderly patients with sepsis based on machine learning (random survival forest). *BMC Emerg. Med.* 22, 26. doi:10.1186/s12873-022-00582-z

Zhang, M.-L., and Zhou, Z.-H. (2007). ML-KNN: a lazy learning approach to multi-label learning. *Pattern Recognit.* 40, 2038–2048. doi:10.1016/j.patcog.2006.12.019

Zhao, Y., Xiong, J., Hou, Y., Zhu, M., Lu, Y., Xu, Y., et al. (2020). Early detection of ST-segment elevated myocardial infarction by artificial intelligence with 12-lead electrocardiogram. *Int. J. Cardiol.* 317, 223–230. doi:10.1016/j.ijcard.2020.04.089

frontiers | Frontiers in Physiology

TYPE Original Research
PUBLISHED 20 October 2022
DOI 10.3389/fphys.2022.1015838

OPEN ACCESS

EDITED BY
Rong Liu,
Dalian University of Technology, China

REVIEWED BY
Yangsong Zhang,
Southwest University of Science and Technology, China
Paulo Ricardo Protachevicz,
University of São Paulo, Brazil

*CORRESPONDENCE
Chunsheng Li,
lichunsheng@sut.edu.cn

SPECIALTY SECTION
This article was submitted to Computational Physiology and Medicine,
a section of the journal Frontiers in Physiology

RECEIVED 10 August 2022
ACCEPTED 10 October 2022
PUBLISHED 20 October 2022

CITATION
Liu Y and Li C (2022), Localizing targets for neuromodulation in drug-resistant epilepsy using intracranial EEG and computational model.
Front. Physiol. 13:1015838.
doi: 10.3389/fphys.2022.1015838

Localizing targets for neuromodulation in drug-resistant epilepsy using intracranial EEG and computational model

Yang Liu and Chunsheng Li*

Department of Biomedical Engineering, School of Electrical Engineering, Shenyang University of Technology, Shenyang, China

Neuromodulation has emerged as a promising technique for the treatment of epilepsy. The target for neuromodulation is critical for the effectiveness of seizure control. About 30% of patients with drug-resistant epilepsy (DRE) fail to achieve seizure freedom after surgical intervention. It is difficult to find effective brain targets for neuromodulation in these patients because brain regions are damaged during surgery. In this study, we propose a novel approach for localizing neuromodulatory targets, which uses intracranial EEG and multi-unit computational models to simulate the dynamic behavior of epileptic networks through external stimulation. First, we validate our method on a multivariate autoregressive model and compare nine different methods of constructing brain networks. Our results show that the directed transfer function with surrogate analysis achieves the best performance. Intracranial EEGs of 11 DRE patients are further analyzed. These patients all underwent surgery. In three seizure-free patients, the localized targets are concordant with the resected regions. For the eight patients without seizure-free outcome, the localized targets in three of them are outside the resected regions. Finally, we provide candidate targets for neuromodulation in these patients without seizure-free outcome based on virtual resected epileptic network. We demonstrate the ability of our approach to locate optimal targets for neuromodulation. We hope that our approach can provide a new tool for localizing patient-specific targets for neuromodulation therapy in DRE.

KEYWORDS

neural computational model, neuromodulation, drug-resistant epilepsy, intracranial EEG, optimal target

1 Introduction

Epilepsy is a neurological disease caused by disorder of the brain network (Terry et al., 2012; Lam et al., 2016). It has the characteristics of recurrent seizures, which often bring irreversible brain damage and affect the normal life of patients with epilepsy (Trinka et al., 2015). About 70% of patients can be cured by taking antiepileptic drugs, and 30% of them

will develop drug-resistant epilepsy (DRE) (Kwan and Brodie, 2000; Stephen et al., 2006; Brodie et al., 2012). Patients with DRE can be treated with surgery (Choi et al., 2008) or neuromodulation (Schulze-Bonhage, 2017; Davis and Gaitanis, 2020; Sisterson and Kokkinos, 2020), such as transcranial magnetic stimulation (TMS) (Davis and Gaitanis, 2020), transcranial focused ultrasound (tFUS) (Lin et al., 2020; Zou et al., 2020). In neuromodulation therapy, different brain regions or nerves can be chosen as target, such as the vagus nerve (Stern et al., 2021), thalamus (Ryvlin and Jehi, 2021), hippocampus (Abouelleil et al., 2022), or localized epileptogenic zone (Tsuboyama et al., 2020; Rincon et al., 2021). Neurologists use intracranial EEG (iEEG), MRI and other methods combined with clinical experience to define the brain regions responsible for seizure generation and resect these regions to prevent seizure. About 30% of patients with DRE failed to achieve seizure freedom after surgical intervention (Janszky et al., 2005; de Tisi et al., 2011). Most of them are not suitable for further surgery because the suspected brain regions have been damaged. Neuromodulation is a promising technique for these non-seizure-free patients. However, to our best knowledge, the reports of localizing neuromodulatory targets for patients who failed to achieve seizure freedom are few.

EEG is widely used in the diagnosis of epilepsy. Comparing with scalp EEG, iEEG electrodes need to be embedded in the patient's skull. The intracranial electrodes are closer to the epileptogenic zone (Kovac et al., 2017), which facilitates subsequent resection of the epileptogenic area. IEEG recording techniques include subdural grids, strips, and depth electrodes. For different epilepsy patients, different iEEG techniques need to be selected (Kovac et al., 2017).

IEEG recordings reflect the characteristics of epileptic networks and have the function of localizing epileptogenic tissues in epilepsy patients (van Diessen et al., 2013; Taylor et al., 2015; Sinha et al., 2017). Network methods can be used to extract the epileptic network, such as Pearson correlation, Granger causality (Coben and Mohammad-Rezazadeh, 2015; Sinha et al., 2017). The coefficients of Pearson correlation represent the correlation between variables. Sinha et al. (2017) calculated the coefficients between different EEG channels and used them as undirected connectivity of the epileptic model. Granger causality explores direct or indirect relationships between variables. Directed transfer function (DTF) computes interactions between input signals in frequency domain (Franaszczuk et al., 1985). A variety of network characteristics can be quantified on the extracted network matrix. One single network feature cannot fully explain all the properties of the network (van Diessen et al., 2013). Different features of network were used in epilepsy studies (Sinha et al., 2017, 2021; Paldino et al., 2019). Seizure is a dynamic process. It is difficult to explore dynamical behaviors of the original signals based on the extracted network matrix. The quantified features of epileptic networks cannot comprehensively describe the dynamics of seizure onset and termination.

Neural computational model can be used to better simulate the dynamical process of seizure (Proix et al., 2018; Saggio et al., 2020; Sip et al., 2022). Richardson proposed a method of combining dynamics and connectomics to explain the abnormal dynamics of epileptic networks (Richardson, 2012). Lopes da Silva et al. (2003) modeled transition states between normal and epileptic states for predicting epileptic pathways. Creaser et al. (2002) modeled the node dynamics and the coupling relationship between nodes, and obtained the transient dynamics during epileptic seizures. Numerous models have been used to explain the physiology of epilepsy or epileptic activity (Wendling et al., 2016). In computational models, the state of the system is commonly changed by adjusting either excitatory or inhibitory parameters, such as Z6 model (Benjamin et al., 2012) and Epileptor model (Proix et al., 2018). In the Z6 model, the values of different excitatory parameters determine whether the system is in normal or epileptic state.

In this paper, we propose a novel approach for localizing targets for neuromodulation in patients with DRE, especially for patients without achieving seizure freedom after surgery. The patient-specific epileptic network is reconstructed using multi-unit computational model. The most effective node for neuromodulation in preventing seizure is localized by introducing external stimulation. The effectiveness of our proposed approach is validated on a multi-variate autoregressive (MVAR) model. Then we validate the approach on a group of DRE patients with iEEG recordings. Finally, the candidate targets for neuromodulation are provided using the proposed approach and virtual resected network of those DRE patients.

2 Methods

2.1 Data and subject description

IEEG recordings from 11 patients were analyzed in this study. The datasets were obtained from the IEEG public website (http://www.ieeg.org), and all patients with DRE had received surgical treatment. Three patients are in seizure-free group with good outcome, who were scored as international league against epilepsy (ILAE) 1 (completely seizure-free) or 2 (no seizures, only auras) (Wieser et al., 2001). The other eight patients are in non-seizure-free group with poor outcome, who were scored as ILAE 3–6 (non-seizure-free). Interictal iEEG recordings of 10 min duration are chosen several hours away from any seizure. The iEEG data are divided into segments of 1 s duration. Each segment overlaps the previous one by 0.5 s. The sampling rate of recordings is 500 Hz. We evaluate the overlapping between the localized target nodes and the resected regions.

2.2 Directed transfer function with surrogate analysis

The directed transfer function (DTF) is a multi-channel directional measurement method based on Granger causality and autoregressive models (Franaszczuk et al., 1985). This method calculates the causal connection matrix between multi-channel EEG signals and measures the causal relationship between channels. The multichannel EEG process in the framework of autoregressive model (AR) can be described by the following equation (Franaszczuk et al., 1985; Kaminski and Blinowska, 1991):

$$\sum_{j=0}^{p} A_j x(t-j) = w(t), \tag{1}$$

where $x(t) = [x_1(t), x_2(t), \ldots, x_N(t)]$ is the vector of EEG N-channel process, p is the order of the model. A_0 is identity matrix, $A_1, A_2, \ldots, A_p$ are the $N \times N$ matrices of model coefficients, $w(t) = [w_1(t), w_2(t), \ldots, w_N(t)]$ is the vector of multivariate zero mean uncorrelated white noise process. We use the order selection criteria of Akaike's Final Prediction Error (FPE) criterion implemented in ARFIT toolbox (Akaike, 1971; Schneider and Neumaier, 2001).

The coefficients A_j can be obtained from (1) by multiplying its both sides by x_{t-s}^T, where x^T is transposed vector of x. We get following equation (Kaminski and Blinowska, 1991):

$$R(-s) + A_1 R(1-s) + \cdots + A_p R(p-s) = 0, \tag{2}$$

where $R(s) = E(x(t), x_{t-s}^T)$ is the covariance matrix with lag s for the vector x, E means expectation value. Applying the z-transform to the both sides of Eq. 1 (Franaszczuk et al., 1985), we have

$$X(z) = H(z)W(z). \tag{3}$$

where $H(z)$ is the transfer function. Set $z^{-1} = e^{-i2\pi f \Delta t}$, where f is the frequency, Δt is the sampling interval. Then we get $H(f)$, where $H_{ij}(f)$ is the directed causal relationship from the node j to the node i.

The directional characteristic of the information flow from node j to node i is defined as following:

$$r_{ij}^2(f) = \frac{|H_{ij}(f)|^2}{\sum_{r=1}^{n} |H_{ir}(f)|^2}. \tag{4}$$

Note that the value of $r_{ij}^2(f)$ is between 0 and 1.

Surrogate data is a statistical method of analyzing nonlinear signals that facilitates the analysis of EEG signals (Dolan and Spano, 2001). We generate surrogate signals by assigning the phase of the EEG signal randomly in 200 times. The strongest 5% of the total possible causal connection are kept for further analysis. The network characteristics in high frequency gamma band are most closely correlated with improved postsurgical outcome (Wilke et al., 2011). Our preliminary study on seizure-free group also showed similar results. In this study, the network analysis focuses on gamma rhythm (31–80 Hz).

2.3 Other methods to build brain network

Besides DTF, there are other ways to build brain networks. The Pearson correlation coefficient (PCC) reflects the linear correlation between iEEG channels. We divide the iEEG into 1 s data segments. The PCC calculates the degree of linear correlation between two variables. It is the ratio of the covariance and standard deviation between two signals, as shown in the following:

$$P_{a,b} = \frac{\mathrm{cov}(a,b)}{\sigma_a \sigma_b}, \tag{5}$$

where $P_{a,b}$ represents the degree of linear correlation between n dimensional signal a and b.

Partial directed coherence (PDC) analyzes the connectivity between multi-channel signals, which is also based on Granger causality. The calculation method of p and A_j is the same as that of DTF. The transfer function $\bar{H}_{ij}(f)$ of PDC is calculated by the following equation (Baccala and Sameshima, 2001):

$$\bar{H}_{ij}(f) = I - \sum_{j=1}^{p} A_j e^{-i2\pi f \Delta t}, \tag{6}$$

where I is the identity matrix.

Isolated effective coherence (iCoh) is similar to PDC. This method computes the interrelationships of directly related nodes, but zeros out all other indirect causal relationships (Pascual-Marqui et al., 2014). When we compute the causal relationship from node j to node i, other nodes except node j and node i are called irrelevant nodes. Node j is the relevant nodes of node i.

The weighted phase lag index (wPLI) measures the phase correlation between signals by weighting the cross-spectrum of the phases of the two signals. First, we need to calculate the phase lag index (PLI) between the signals (Li et al., 2021):

$$PLI = |sgn(\sin(\Delta\theta(t)))|, \tag{7}$$

where sgn represents the sign function, $|\cdot|$ is absolute value, $\Delta\theta(t)$ represents the instantaneous phase difference between the input signal s_1 and the output signal s_2. Then, wPLI is calculated to quantify the phase agreement between the signals (Li et al., 2021),

$$wPLI = \frac{|A_1 A_2 \sin(\Delta\theta(t))|}{|A_1 A_2 \sin(\Delta\theta(t))|}, \tag{8}$$

where A_1 and A_2 are the corresponding amplitudes of the s_1 and s_2, respectively.

Relative entropy is an asymmetric measure (Kullback and Leibler, 1951), also known as Kullback-Leibler divergence (KLDIV), quantifies the difference between two signals. $x(t)$ is divided by 1 s and overlapped by 50%, and then subjected to short-time Fourier transform to obtain $X(n, f)$. The normalized spectrogram is shown in Eq. 9.

$$W_x(n,f) = \frac{|X(n,f)|^2}{\sum_{n,f}|X(n,f)|^2}, \tag{9}$$

Suppose $W_y(n, f)$ is the normalized spectrum of the signal $y(t)$, the KLDIV from $W_x(n, f)$ to $W_y(n, f)$ is as follows:

$$D_{KL}(W_x, W_y) = \sum_{n,f} W_x(n,f)\log\frac{W_x(n,f)}{W_y(n,f)}. \tag{10}$$

KLDIV is asymmetric. When its value is higher, the difference between the signals is larger.

2.4 MVAR model

The electrophysiological activity in short duration can be viewed as a MVAR process. In this study, the MVAR model is written in the following differential form (Baccala and Sameshima, 2001),

$$\begin{cases} X_1(n) = 0.95\sqrt{2}\,X_1(n-1) - 0.9025X_1(n-2) + w_1(n), \\ X_2(n) = 0.5X_1(n-2) + w_2(n), \\ X_3(n) = -0.4X_1(n-3) + w_3(n), \\ X_4(n) = -0.5X_1(n-2) + 0.25\sqrt{2}\,X_4(n-1) + 0.25\sqrt{2}\,X_5(n-1) + w_4(n), \\ X_5(n) = -0.25\sqrt{2}\,X_4(n-1) + 0.25\sqrt{2}\,X_5(n-1) + w_5(n), \end{cases} \tag{11}$$

where X_i, $i = 1, 2, \ldots, 5$, represents the ith node of the network, and w_i, $i = 1, 2, \ldots, 5$, is the white noise. The coefficients between nodes represent the causual relationships of different nodes.

In order to find the method with best performance for constructing epileptic network and validate the effectiveness of our proposed approach, we use a five-node MVAR model to simulate the causal relationship between nodes. The time course of activity assigned on each node is generated by model (11). Simplified MVAR model could be used to simulate epileptic sources (Hosseini et al., 2018). There are both unidirectional and bidirectional connections in model (11). Node X_1 is simulated as epileptic node where seizure starts. Node X_2, X_3 and X_4 are neighbor nodes., and node X_4 has bidirectional connection with node X_5, which represents remote normal tissue.

There are different types of measures to construct the brain network. We choose several commonly used network measures based on causality, coherence, or information theory. We also construct the causal network combining with surrogate analysis to determine which method matches the original network best. We compare nine methods for constructing causal network, including PCC, DTF, DTF with surrogate analysis (DTF-SA), PDC, PDC with surrogate analysis (PDC-SA), iCoh, iCoh with surrogate analysis (iCoh-SA), wPLI and KLDIV. We compute the correlation coefficients between the extracted connectivity matrix and the ground truth of the model (11), which are then normalized by the maximum value. According to the value of the correlation coefficient, we choose the method with the best performance to construct brain network.

2.5 Multi-unit computational model

The Z6 model can simulate the dynamic process of the interaction between nodes due to information transmission during epileptic seizures, and intuitively describe the state transition of nodes. This model contains a fixed point and a limit-cycle. The noise system controls one of two factors in order to control the trajectory of the system. In the noisy system, the deterministic part at the drift coefficient can be expressed by the following single complex equation (Benjamin et al., 2012):

$$\frac{dz}{dt} = f(z) \equiv (a|z|^4 + b|z|^2 + \lambda - 1 + i\omega)z, \tag{12}$$

where z is a complex parameter, $z = x + iy$. a and b are real numbers ($a = -1$, $b = 2$), ω controls the oscillation frequency of the system, λ is the possible attractors of the system. The parameter λ determines the state of the system, and we choose $0 < \lambda < 1$. We can consider λ to be the excitability parameter of the system. When λ approaches 1, the system is more excitable (Benjamin et al., 2012).

The nodes of the brain network have the characteristic of bidirectional functional connectivity, forming a network of interconnected nodes. We extend the equation to a network model with N nodes:

$$\frac{dz_i(t)}{dt} = f(z_i) + \beta\sum_{j\neq i}^{N} KG_{ij}(z_j - z_i) + \alpha w_i(t), \tag{13}$$

where G_{ij} is the normalized information connectivity matrix between nodes, $w(t)$ represents white noise with a mean of 0.0003 and a standard deviation of 0.05 (Sinha et al., 2017), α is the coefficient of noise. β equals 0.02 here. In order to achieve the same order of magnitude as the undirected symmetric information-connected matrix (Benjamin et al., 2012), the normalized matrix G is then multiplied by K = 1,000. The connectivity matrix G describes the topology of the epileptic network, and determines the interaction between each node of the system. When iEEG dataset is analyzed, the patient's epileptic networks are constructed by network measures, which is then used as the matrix G of the computational model. In this case, the dynamic behavior of the model is determined by patient's specific brain network. The model was solved numerically using a fixed step Euler-Maruyama solver with a step size of 0.05.

During the numeric simulation, the network is driven by random noise. The time for a node to change from a stationary state to an oscillating state is called the escape time (T_{es}) (Sinha et al., 2017). T_{es} is used as an indicator for predicting seizure (Benjamin et al., 2012). We use the Z6 model to simulate the epileptic brain as a bi-stability state network (Goodfellow and Glendinning, 2013; Sinha et al., 2017). The probability of a node entering epileptic state is inversely proportional to T_{es} (Petkov et al., 2014; Sinha et al., 2017). It is also proportional to the stability of the system, and the value of T_{es} decreases as the parameter λ increases (Benjamin et al., 2012). The parameters λ

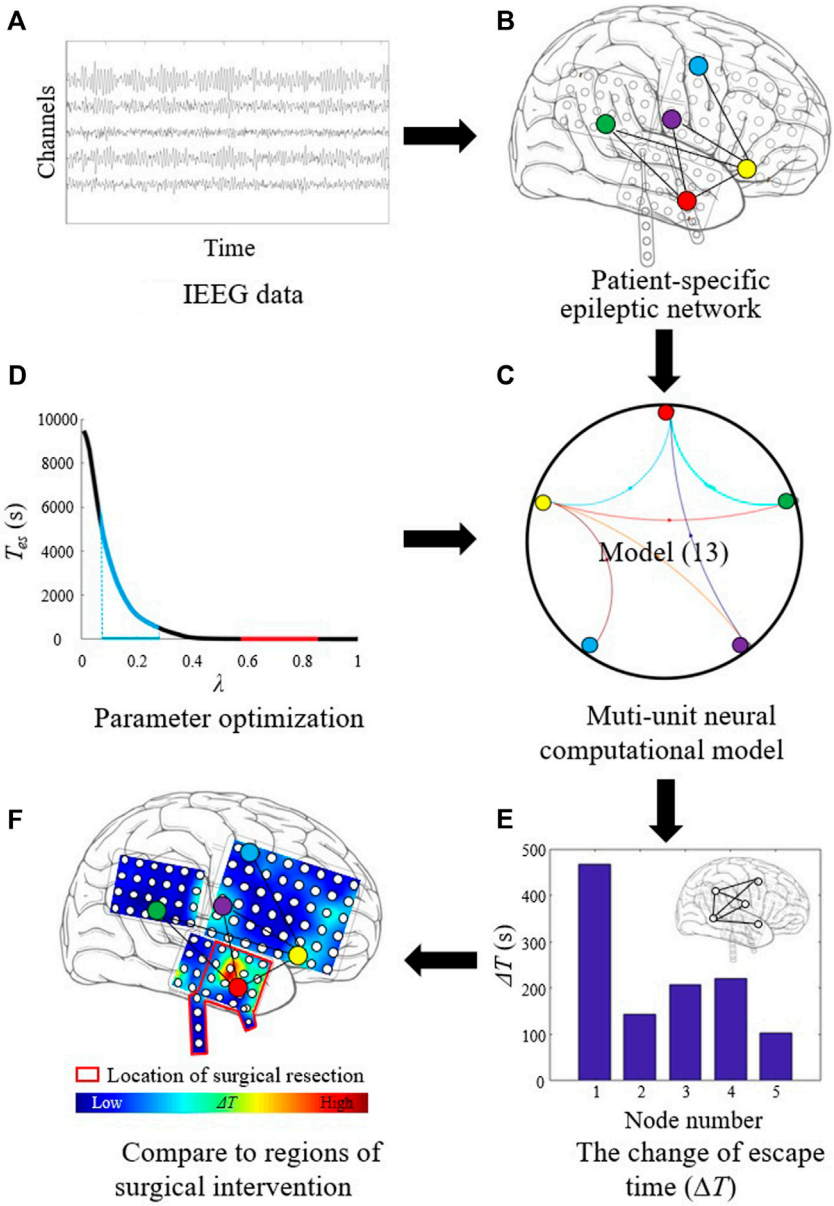

FIGURE 1
Procedure of localizing target for neuromodulation in drug-resistant epilepsy. **(A)** The segmented iEEG recordings. **(B)** Patient-specific epileptic network based on iEEG data. **(C)** Multi-unit neural computational model based on the epileptic network and the Z6 model. **(D)** Parameter optimization for λ. **(E)** Calculating the change of escape time (ΔT) of each node. **(F)** Localizing optimal target with the largest ΔT value.

of all nodes are set to λ_0 or λ_1 on non-target or target nodes, respectively. The optimal λ_0 and λ_1 are chosen by grid search of $\lambda_0 - \lambda_1$ pairs. λ_0 is chosen between 0 and 0.5 in step of 0.05, and λ_1 is chosen between 0.5 and 1 in step of 0.05. The ΔT is calculated at each $\lambda_0 - \lambda_1$ pair. The optimal λ_0 and λ_1 are found when there is the largest standard deviation of ΔT for all pairs. First, we set the λ of all nodes to λ_0, and record the T_{es} as T_0. Then, we change the λ of each target node to λ_1, and record the T_{es} as T_1. The difference between T_0 and T_1 is the change in escape time (ΔT), $\Delta T = |T_0 - T_1|$, represents the effectiveness of the neuromodulation applied on a given node.

2.6 Localizing targets for neuromodulation

The procedure of localizing targets for neuromodulation is shown in Figure 1. First, the segmented iEEG recordings are

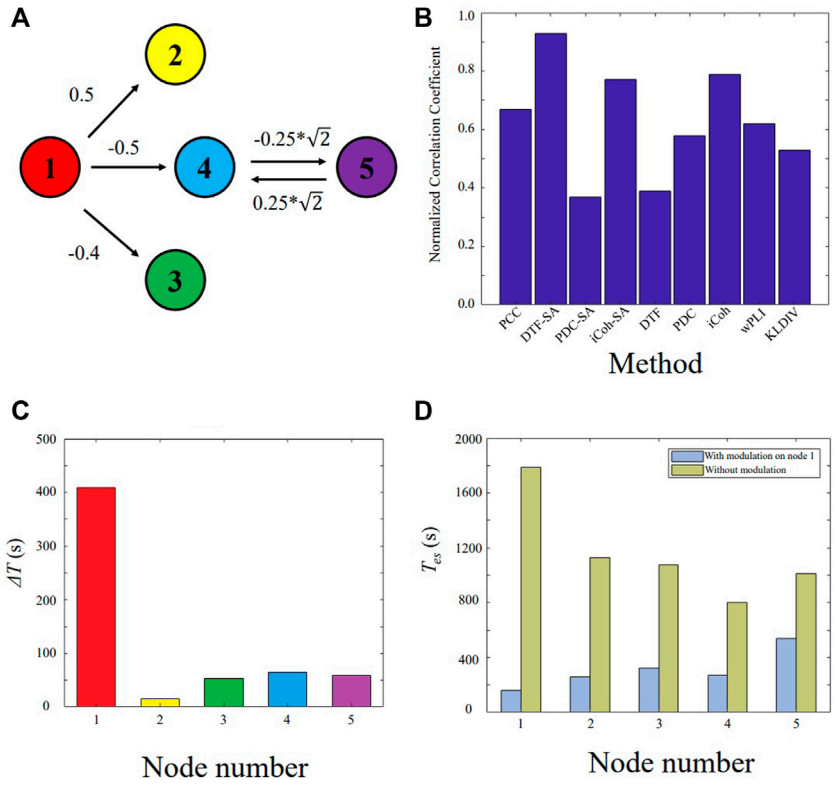

FIGURE 2
Validating the proposed approach on the five-node model. **(A)** Five-node causal network. **(B)** Normalized correlation coefficient between the constructed network and the ground truth. **(C)** ΔT for each node. **(D)** The T_{es} value of the network with and without external modulation.

used, as shown in Figure 1A. The data are processed to construct patient-specific epileptic network (Figure 1B). The epileptic network is in the form of causal connectivity matrix. The multi-unit neural computational model is constructed based on the epileptic network and the Z6 model (Figure 1C). The number of nodes of the multi-unit model is same as the number of channels in iEEG the recordings. The optimal values of λ are determined (Figure 1D). Using the selected parameters, the ΔT of each node is then calculated (Figure 1E). The distribution of ΔT is plotted on patient's head model, and the node with the largest value of ΔT is selected as optimal target. The optimal target is compared with the resected regions of epilepsy patient, as shown in Figure 1F.

2.7 Validation of neuromodulation

We calculated T_{es} of epileptic brain networks in all patients with inhibitory modulation on the localized target nodes and non-target nodes. The Wilcoxon rank sum test was used (Wilcoxon, 1945), and $p < 0.01$ was chosen as significance threshold. The proposed approach was then performed to localize candidate targets for neuromodulation in patients without seizure-free outcome.

3 Result

3.1 Localizing the critical node of MVAR model

The model (11) is shown in Figure 2A. The node X_1 is the main driven force for the model to enter oscillatory state, which is simulated as the epileptogenic node. The normalized correlation coefficients of nine different methods are plotted in Figure 2B. Based on the extracted causal connectivity by DTF-SA method, we localize the target for neuromodulation using our proposed approach. The optimal values of λ_1 and λ_0 is 0.85 and 0.50, respectively. The result of ΔT is shown in Figure 2C, and the node X_1 is with the highest value. The effectiveness of external modulation on the node X_1 is shown in Figure 2D. The T_{es} of the network decreases significantly while the external excitatory stimuli is applied on node X_1.

TABLE 1 Patient information, surgical results, optimal parameters, and target location.

Patient	Dataset ID	Surgical outcome	Target before resection	Parameter λ_0	Distance to resection (mm)	Target after resection	Distance to resection (mm)
P1	Study 038	Seizure free	ITS2	0.25	0.0	-	-
P2	Study 021	Seizure free	RTG15	0.30	0.0	-	-
P3	Study 026	Seizure free	LFG48	0.30	0.0	-	-
P4	Study 028	Not seizure free	LPG7	0.30	28.0	LPG7	28.0
P5	Study 004–2	Not seizure free	RAT4	0.15	0.0	RG20	14.1
P6	Study 016	Not seizure free	RTG24	0.20	0.0	RFG19	45.0
P7	Study 029	Not seizure free	AIT4	0.20	0.0	LT12	30.0
P8	Study 020	Not seizure free	RAG20	0.15	0.0	RAG6	10.0
P9	Study 019	Not seizure free	LT9	0.25	0.0	LF10	48.7
P10	Study 022	Not seizure free	TSG7	0.20	20.0	TSG7	20.0
P11	Study 033	Not seizure free	LTG7	0.35	19.3	LTG7	19.3

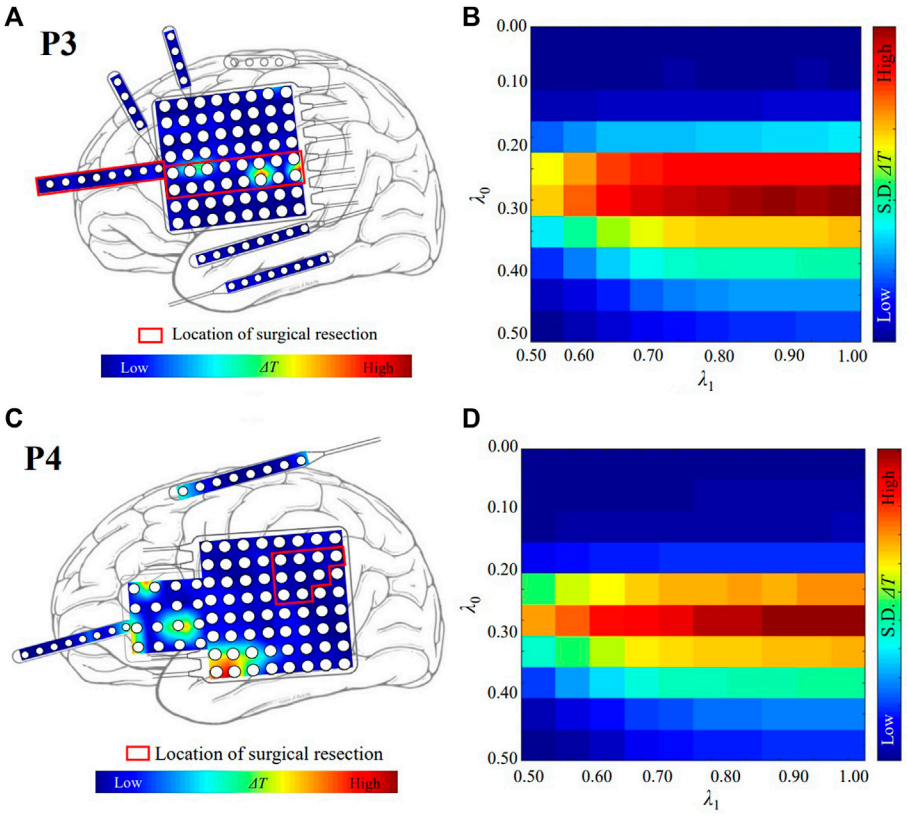

FIGURE 3
The localized targets for neuromodulation of patient P3 and P4. **(A)** The distribution of ΔT for patient P3. The white circles represent the contacts of the electrodes. Red and blue indicate the magnitude of the value of ΔT. The red color indicates that the value of ΔT is large. The blue color indicates that the value of ΔT is small. **(B)** The optimal value of λ for patient P3. λ_0 = 0.30 and λ_1 = 1.00. The red color indicates that the value of standard deviation (S. D.) of ΔT is large. **(C)** The distribution of ΔT for patient P4. **(D)** The optimal value of λ for patient P4. λ_0 = 0.30 and λ_1 = 1.00.

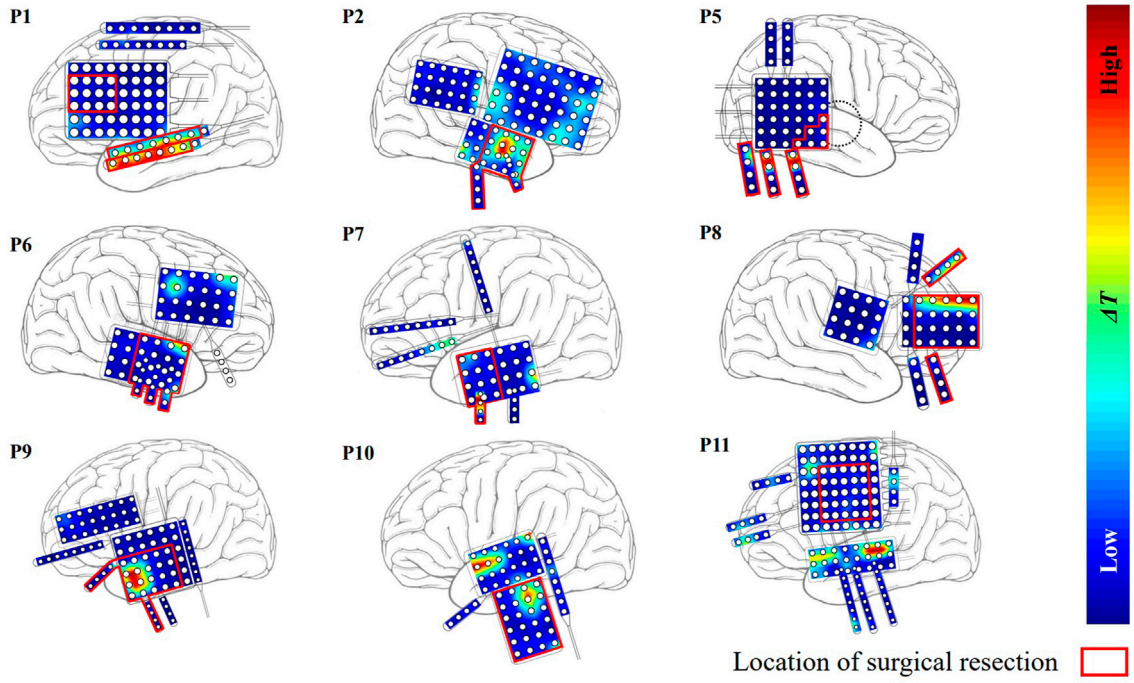

FIGURE 4
The distribution of ΔT for the other nine patients except P3 and P4. Red region indicates that the effect of modulation is strong.

3.2 Localizing targets for neuromodulation using patient data

The localized targets for neuromodulation of 11 patients are listed in Table 1. For patient P1-P3 with seizure-free outcome, the targets are inside the resected regions. In non-seizure-free group, localized targets for patients P4, P10, and P11 are outside the resected regions, and localized targets for patients P5-P9 are inside the surgical resected regions. The mean error distance is 8.4 mm in non-seizure-free group. The values of parameter λ_0 for 11 patients is 0.22 ± 0.08, λ_1 is 0.99 ± 0.01 (mean ± SD).

The localized targets for neuromodulation of patient P3 and P4 are plotted in Figures 3A,C, respectively. Red region indicates the stimulation is effective to suppress seizure in Figures 3A,C. Patient P3 belongs to the seizure-free group. The resected region of this patient was mainly in left lateral frontal cortex. The electrode LFG48 with the highest ΔT is selected as the target, and reside in the resected region (red rectangle), as shown in Figure 3A. Patient P4 belongs to the non-seizure-free group. The resected region was mainly in left parietal cortex. The electrode LPG7 with the highest ΔT is selected as the target, which is 28.0 mm away from the resected region (red rectangle), as shown in Figure 3C. The distribution of ΔT for choosing optimal λ_0–λ_1 pair is plotted in Figures 3B,D. The λ_0 = 0.30 and λ_1 = 1.00 for both patients.

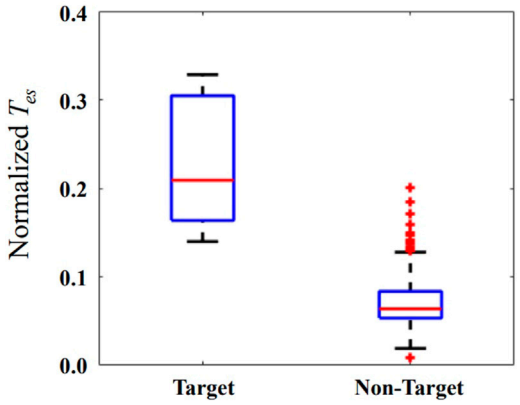

FIGURE 5
The normalized T_{es} when external modulation is applied on the localized target and non-target nodes. The horizontal red bar represents the median, and the blue box represents the rang from first to third quartile, respectively. The horizontal black lines represent the upper and lower limits, and the red plus sign represents outlier data.

The ΔT distributions for the other 9 patients are plotted in Figure 4. Among them, patients P1 and P2 belonged to the seizure-free group. The surgical field in both patients was in the

left temporal lobe. Targets identified by our method that were effective in eliminating epilepsy were located at the surgical field of each of the two patients.

3.3 The effectiveness of neuromodulation

The T_{es} is normalized relative to its minimum and maximum values of each patient. The horizontal red bar represents the median in Figure 5. The median of the T_{es} is 0.21 and 0.06 for target and non-target nodes, respectively. The values of T_{es} on the localized target nodes are significantly longer than the values on non-target nodes ($p < 0.01$). The modulation on the localized target nodes is more effective in suppressing seizure than non-target ones. Outlier data indicate that modulation on some non-target nodes is more (or less) efficient than modulation on other nodes.

We remove the iEEG channels in the resected regions, and reconstruct virtual resected networks for the non-seizure-free patients. In the virtual resected network, the iEEG channels in resected regions are removed. The connectivity matrix G is calculated using other channels, which results in a smaller matrix. The value of λ_0 is set to 0.22 for the non-target of the resected network, and $\lambda_1 = 1$. The localized candidate targets for neuromodulation are listed in Table 1. The mean distance between the new targets and the surgical resected regions is 26.9 mm. The localized targets for Patient P4, P10, and P11 are not changed before and after surgical resection. The mean distance between the new localized targets and the resected regions is 29.6 mm for patient P5-P9.

4 Discussion

Localizing the effective targets is the key to neuromodulation therapy. The proposed approach identified the node X_1 of the MVAR model as optimal target successfully, which is the designed node to drive the model to oscillatory state. The network measures based on correlation, causal effects, phase lag, and information entropy were compared for reconstructing the network. The DTF-SA method showed highest similarity between the reconstructed network and the ground true. Our results could help other study for choosing network measures. We choose the Z6 model as the network node because of the relative low computational cost. Other neural computation models could also be adopted, such as Epileptor model (Proix et al., 2018). The parameter λ_0 of non-target node is the only parameter need to be determined for the network except for connectivity matrix. Our result show that the mean value of λ_0 for non-target nodes is good in most cases when analyzing the iEEG dataset, and the value λ_1 for target node is set to 1, which leads that our proposed approach is easy to use.

Patient P1, P2, and P3 have undergone surgical resection, and achieved good outcome. The epileptogenic tissues are assumed inside the resected regions. Based on the patient-specific epileptic network, all localized targets for those patients reside in the resected regions. Those results indicate that our approach find the target responsible for seizure generation. The localized targets for patient P5-P9 also reside in the resected regions, which is consistent with judgement of neurologist. The epilepsy is a brain network disease. Resection of brain tissue changes the topology of epileptic network, and seizure may start from other brain location. Applying the external stimulation on a given node will result in influence on whole network. In this context, we believe the neuromodulation measure may lead to better outcomes for those patients without seizure-free outcome. The localized targets for patient P4, P10, and P11 are outside the resected regions based on the epileptic network before surgery, and the mean distance from the surgical resected regions is 22.4 mm. After removing the resected nodes, our approach also localizes the targets on the same electrodes. This result reflects that our proposed network is stable on localizing the targets even with the virtual resection.

When applying inhibitory stimulation on the localized target nodes, it can significantly delay the brain network from entering a state of oscillation relative to the non-target nodes, as shown in Figure 5. This demonstrates the effectiveness of the proposed method for preventing epileptic seizures. Neuromodulation is used as a non-destructive means of brain network regulation, such as TMS, tFUS, which have different spatial resolutions (Davis and Gaitanis, 2020; Lin et al., 2020; Zou et al., 2020). Considering the applicability of our proposed method, the number of targets selected for neuromodulation is 1. Selecting 2 or more targets for neuromodulation will have a more obvious modulation effect, but it is not suitable for neuromodulation methods with low spatial resolution, such as TMS.

Our method induces resting-state brain networks into epilepsy *via* stimulation parameters. This approach differs from current neuromodulation treatments. For example, tFUS suppresses seizure by reducing the excitability of the nervous system (Folloni et al., 2019; Lin et al., 2020; Zou et al., 2020). However, in clinical surgery, the traditional method is to find the epilepsy surgery area by evoking electrical stimulation. Combined with the clinical surgical process, we select parameters that can induce the brain network to enter the epileptic state to determine the target of neuromodulation. This choice ensures the practicality of our method.

Furthermore, this approach has limitations. The iEEG recording is an invasive measure mainly for presurgical evaluation of DRE patient. We have not applied this measure on scalp EEG recording. The low coverage of the intracranial electrodes on the epileptogenic zone may result in the inaccurate of constructing epileptic network, which ultimately leads to poor localization of the targets. Validating our method in the real application will further advance the technology. On the one hand, the Z6 model is a noise-driven

computational model that simulates epileptic seizures (Sinha et al., 2017). Due to the randomness and uncertainty of noise, multiple calculations are required to avoid accidental factors. The long computational time is another limitation of our method. On the other hand, we chose the Z6 model to simulate the dynamic process of epileptic seizures. Other neural computational models can also replace the Z6 model, such as the Epileptor model. Therefore it is necessary to choose different and more suitable parameters to simulate the process of neuromodulation.

5 Conclusion

The effective neuromodulation therapy is very important for DRE patients with bad surgical outcome. The DTF with surrogate analysis is more suitable for constructing patient's epileptic network using iEEG recording. Multi-unit computational model can be used to simulate the seizure dynamics, and evaluate the effects of external excitatory and inhibitory stimulation. By using iEEG and computational model, our study provided a new approach to localize the optimal targets for the potential neuromodulation of these patients.

Data availability statement

Publicly available datasets were analyzed in this study. This data can be found here: http://www.ieeg.org.

Author contributions

CL and YL proposed the approach. YL performed the data analysis and model simulation. YL wrote the first draft of the manuscript. CL revised the manuscript. YL and CL approved the submitted version.

Funding

This work was supported by the National Natural Science Foundation of China (61771323) and Research Fund of Liaoning Provincial Natural Science (2021-KF-12-11), Program for Liaoning Innovative Talents in University, Research project of Liaoning Provincial Department of Education (LJGD20200012).

Acknowledgments

We would like to thank Fang Zhou for her help with data analysis.

Conflict of interest

The authors declare that the research was conducted in the absence of any commercial or financial relationships that could be construed as a potential conflict of interest.

Publisher's note

References

Abouelleil, M., Deshpande, N., and Ali, R. (2022). Emerging trends in neuromodulation for treatment of drug-resistant epilepsy. *Front. Pain Res.* 3, 839463. doi:10.3389/fpain.2022.839463

Akaike, H. (1971). Autoregressive model fitting for control. *Ann. Inst. Stat. Math.* 23, 163–180. doi:10.1007/bf02479221

Baccala, L. A., and Sameshima, K. (2001). Partial directed coherence: a new concept in neural structure determination. *Biol. Cybern.* 84, 463–474. doi:10.1007/PL00007990

Benjamin, O., Fitzgerald, T. H., Ashwin, P., Tsaneva-Atanasova, K., Chowdhury, F., Richardson, M. P., et al. (2012). A phenomenological model of seizure initiation suggests network structure may explain seizure frequency in idiopathic generalised epilepsy. *J. Math. Neurosci.* 2, 1. doi:10.1186/2190-8567-2-1

Brodie, M. J., Barry, S. J. E., Bamagous, G. A., Norrie, J. D., and Kwan, P. (2012). Patterns of treatment response in newly diagnosed epilepsy. *Neurology* 78, 1548–1554. doi:10.1212/WNL.0b013e3182563b19

Choi, H., Sell, R. L., Lenert, L., Muenning, P., Goodman, R. R., Gilliam, F. G., et al. (2008). Epilepsy surgery for pharmacoresistant temporal lobe epilepsy: A decision analysis. *JAMA* 300, 2497–2505. doi:10.1001/jama.2008.771

Coben, R., and Mohammad-Rezazadeh, I. (2015). Neural connectivity in epilepsy as measured by Granger causality. *Front. Hum. Neurosci.* 9, 194. doi:10.3389/fnhum.2015.00194

Creaser, J., Lin, C., Ridler, T., Brown, J. T., D'Souza, W., Seneviratne, U., et al. (2002). Domino-like transient dynamics at seizure onset in epilepsy. *PLoS Comput. Biol.* 16, 1008206. doi:10.1371/journal.pcbi.1008206

Davis, P., and Gaitanis, J. (2020). Neuromodulation for the treatment of epilepsy: a review of current approaches and future directions. *Clin. Ther.* 42, 1140–1154. doi:10.1016/j.clinthera.2020.05.017

de Tisi, J., Bell, G. S., Peacock, J. L., McEvoy, A. W., Harkness, W. F. J., Sander, J. W., et al. (2011). The long-term outcome of adult epilepsy surgery, patterns of seizure remission, and relapse: a cohort study. *Lancet* 378, 1388–1395. doi:10.1016/S0140-6736(11)60890-8

Dolan, K. T., and Spano, M. L. (2001). Surrogate for nonlinear time series analysis. *Phys. Rev. E Stat. Nonlin. Soft Matter Phys.* 64, 046128. doi:10.1103/PhysRevE.64.046128

Folloni, D., Verhagen, L., Mars, R. B., Fouragnan, E., Constans, C., Aubry, J., et al. (2019). Manipulation of subcortical and deep cortical activity in the primate brain using transcranial focused ultrasound stimulation. *Neuron* 101, 1109–1116.e5. doi:10.1016/j.neuron.2019.01.019

Franaszczuk, P. J., Blinowska, K. J., and Kowalczyk, M. (1985). The application of parametric multichannel spectral estimates in the study of electrical brain activity. *Biol. Cybern.* 51, 239–247. doi:10.1007/BF00337149

Goodfellow, M., and Glendinning, P. (2013). Mechanisms of intermittent state transitions in a coupled heterogeneous oscillator model of epilepsy. *J. Math. Neurosci.* 3, 17. doi:10.1186/2190-8567-3-17

Hosseini, S. A. H., Sohrabpour, A., and He, B. (2018). Electromagnetic source imaging using simultaneous scalp EEG and intracranial EEG: An emerging tool for interacting with pathological brain networks. *Clin. Neurophysiol.* 129 (1), 168–187. doi:10.1016/j.clinph.2017.10.027

Janszky, J., Janszky, I., Schulz, R., Hoppe, M., Behne, F., Pannek, H. W., et al. (2005). Temporal lobe epilepsy with hippocampal sclerosis: predictors for long-term surgical outcome. *Brain* 128, 395–404. doi:10.1093/brain/awh358

Kaminski, M. J., and Blinowska, K. J. (1991). A new method of the description of the information flow in the brain structures. *Biol. Cybern.* 65 (3), 203–210. doi:10.1007/BF00198091

Kovac, S., Vakharia, V. N., Scott, C., and Diehl, B. (2017). Invasive epilepsy surgery evaluation. *Seizure* 44, 125–136. doi:10.1016/j.seizure.2016.10.016

Kullback, S., and Leibler, R. A. (1951). On information and sufficiency. *Ann. Math. Stat.* 22, 79–86. doi:10.1214/aoms/1177729694

Kwan, P., and Brodie, M. J. (2000). Early identification of refractory epilepsy. *N. Engl. J. Med.* 342, 314–319. doi:10.1056/NEJM200002033420503

Lam, A. D., Zepeda, R., Cole, A. J., and Cash, S. S. (2016). Widespread changes in network activity allow non-invasive detection of mesial temporal lobe seizures. *Brain* 139, 2679–2693. doi:10.1093/brain/aww198

Li, X., Wu, Y., Wei, M., Guo, Y., Yu, Z., Wang, H., et al. (2021). A novel index of functional connectivity: phase lag based on wilcoxon signed rank test. *Cogn. Neurodyn.* 15, 621–636. doi:10.1007/s11571-020-09646-x

Lin, Z., Meng, L., Zou, J., Zhou, W., Huang, X., Xue, S., et al. (2020). Non-invasive ultrasonic neuromodulation of neuronal excitability for treatment of epilepsy. *Theranostics* 10, 5514–5526. doi:10.7150/thno.40520

Lopes da Silva, F., Blanes, W., Kalitzin, S. N., Parra, J., Suffczynski, P., and Velis, D. N. (2003). Epilepsies as dynamical diseases of brain systems: basic models of the transition between normal and epileptic activity. *Epilepsia* 44, 72–83. doi:10.1111/j.0013-9580.2003.12005.x

Paldino, M. J., Golriz, F., Zhang, W., and Chu, Z. D. (2019). Normalization enhances brain network features that predict individual intelligence in children with epilepsy. *PloS One* 14, e0212901. doi:10.1371/journal.pone.0212901

Pascual-Marqui, R. D., Biscay, R. J., Bosch-Bayard, J., Lehmann, D., Kochi, K., Kinoshita, T., et al. (2014). Assessing direct paths of intracortical causal information flow of oscillatory activity with the isolated effective coherence (iCoh). *Front. Hum. Neurosci.* 8, 1, 12. doi:10.3389/fnhum.2014.00448

Proix, T., Jirsa, V. K., Bartolomei, F., Guye, M., and Truccolo, W. (2018). Predicting the spatiotemporal diversity of seizure propagation and termination in human focal epilepsy. *Nat. Commun.* 9, 1088. doi:10.1038/s41467-018-02973-y

Richardson, M. P. (2012). Large scale brain models of epilepsy: dynamics meets connectomics. *J. Neurol. Neurosurg. Psychiatry* 83, 1238–1248. doi:10.1136/jnnp-2011-301944

Rincon, N., Barr, D., and Velez-Ruiz, N. (2021). Neuromodulation in drug resistant epilepsy. *Aging Dis.* 12, 1070–1080. doi:10.14336/AD.2021.0211

Ryvlin, P., and Jehi, L. E. (2021). Neuromodulation for refractory epilepsy. *Epilepsy Curr.* 22, 11–17. doi:10.1177/15357597211065587

Saggio, M. L., Crisp, D., Scott, J. M., Karoly, P., Kuhlmann, L., Nakatani, M., et al. (2020). A taxonomy of seizure dynamotypes. *Elife* 9, 55632. doi:10.7554/eLife.55632

Schneider, T., and Neumaier, A. (2001). Algorithm 808: ARfit – a matlab package for the estimation of parameters and eigenmodes of multivariate autoregressive models. *ACM Trans. Math. Softw.* 27, 58–65. doi:10.1145/382043.382316

Schulze-Bonhage, A. (2017). Brain stimulation as a neuromodulatory epilepsy therapy. *Seizure* 44, 169–175. doi:10.1016/j.seizure.2016.10.026

Sinha, N., Dauwels, J., Kaiser, M., Cash, S. S., Westover, M. B., Wang, Y., et al. (2017). Predicting neurosurgical outcomes in focal epilepsy patients using computational modelling. *Brain* 140, 319–332. doi:10.1093/brain/aww299

Sinha, N., Wang, Y., da Silva, N., Miserocchi, A., McEvoy, A. W., de Tisi, J., et al. (2021). Structural brain network abnormalities and the probability of seizure recurrence after epilepsy surgery. *Neurology* 96, e758–e771. doi:10.1212/WNL.0000000000011315

Sip, V., Guye, M., Bartolomei, F., and Jirsa, V. (2022). Computational modeling of seizure spread on a cortical surface. *J. Comput. Neurosci.* 50, 17–31. doi:10.1007/s10827-021-00802-8

Sisterson, N. D., and Kokkinos, V. (2020). Neuromodulation of epilepsy networks. *Neurosurg. Clin. N. Am.* 31, 459–470. doi:10.1016/j.nec.2020.03.009

Stephen, L. J., Kelly, K., Mohanraj, R., and Brodie, M. J. (2006). Pharmacological outcomes in older people with newly diagnosed epilepsy. *Epilepsy Behav.* 8, 434–437. doi:10.1016/j.yebeh.2005.11.007

Stern, J. M., Spivak, N. M., Becerra, S. A., Kuhn, T. P., Korb, A. S., Kronemyer, D., et al. (2021). Safety of focused ultrasound neuromodulation in humans with temporal lobe epilepsy. *Brain Stimul.* 14, 1022–1031. doi:10.1016/j.brs.2021.06.003

Taylor, P. N., Han, C. E., Schoene-Bake, J., Weber, B., and Kaiser, M. (2015). Structural connectivity changes in temporal lobe epilepsy: spatial features contribute more than topological measures. *Neuroimage. Clin.* 8, 322–328. doi:10.1016/j.nicl.2015.02.004

Terry, J. R., Benjamin, O., and Richardson, M. P. (2012). Seizure generation: the role of nodes and networks. *Epilepsia* 53, e166–e169. doi:10.1111/j.1528-1167.2012.03560.x

Trinka, E., Cock, H., Hesdorffer, D., Rossetti, A. O., Scheffer, I. E., Shinnar, S., et al. (2015). A definition and classification of status epilepticus–report of the ILAE task force on classification of status epilepticus. *Epilepsia* 56, 1515–1523. doi:10.1111/epi.13121

Tsuboyama, M., Kaye, H. L., and Rotenberg, A. (2020). Review of transcranial magnetic stimulation in epilepsy. *Clin. Ther.* 42, 1155–1168. doi:10.1016/j.clinthera.2020.05.016

van Diessen, E., Diederen, S. J. H., Braun, K. P. J., Jansen, F. E., and Stam, C. J. (2013). Functional and structural brain networks in epilepsy: What have we learned? *Epilepsia* 54, 1855–1865. doi:10.1111/epi.12350

Wendling, F., Benquet, P., Bartolomei, F., and Jirsa, V. (2016). Computational models of epileptiform activity. *J. Neurosci. Methods* 260, 233–251. doi:10.1016/j.jneumeth.2015.03.027

Wieser, H. G., Blume, W. T., Fish, D., Goldensohn, E., Hufnagel, A., King, D., et al. (2001). Proposal for a new classification of outcome with respect to epileptic seizures following epilepsy surgery. *Epilepsia* 42, 282–286. doi:10.1046/j.1528-1157.2001.35100.x

Wilcoxon, F. (1945). Individual comparisons by ranking methods. *Biom. Bull.* 1, 80–83. doi:10.2307/3001968

Wilke, C., Worrell, G., and He, B. (2011). Graph analysis of epileptogenic networks in human partial epilepsy. *Epilepsia* 52, 84–93. doi:10.1111/j.1528-1167.2010.02785.x

Zou, J., Meng, L., Lin, Z., Qiao, Y., Tie, C., Wang, Y., et al. (2020). Ultrasound neuromodulation inhibits seizures in acute epileptic monkeys. *iScience* 23, 101066. doi:10.1016/j.isci.2020.101066

frontiers | Frontiers in Physiology

TYPE Original Research
PUBLISHED 20 October 2022
DOI 10.3389/fphys.2022.1034014

OPEN ACCESS

EDITED BY
Lisheng Xu,
Northeastern University, China

REVIEWED BY
Huang Chongquan,
Nanyang Technological University, Singapore
Liu Chang,
Sichuan University, China
Yuning Zhan,
Harbin Medical University Cancer Hospital, China

*CORRESPONDENCE
Shijie Xin,
sjxin@cmu.edu.cn

SPECIALTY SECTION
This article was submitted to Computational Physiology and Medicine, a section of the journal Frontiers in Physiology

RECEIVED 01 September 2022
ACCEPTED 10 October 2022
PUBLISHED 20 October 2022

CITATION
Jia L, Jing Y, Wang D, Cheng S, Fu C, Chu X, Yang C, Jiang B and Xin S (2022), Through network pharmacology and molecular docking to explore the underlying mechanism of Artemisia annua L. treating in abdominal aortic aneurysm.
Front. Physiol. 13:1034014.
doi: 10.3389/fphys.2022.1034014

Through network pharmacology and molecular docking to explore the underlying mechanism of *Artemisia annua* L. treating in abdominal aortic aneurysm

Longyuan Jia[1,2], Yuchen Jing[1,2], Ding Wang[1,2], Shuai Cheng[1,2], Chen Fu[3], Xiangyu Chu[1,2], Chenye Yang[1,2], Bo Jiang[1,2] and Shijie Xin[1,2]*

[1]Department of Vascular Surgery, The First Affiliated Hospital of China Medical University, Shenyang, China, [2]Key Laboratory of Pathogenesis, Prevention, and Therapeutics of Aortic Aneurysm in Liaoning Province, Shenyang, China, [3]Department of Pharmacology, School of Pharmacy, China Medical University, Shenyang, Liaoning, China

Background: Abdominal aortic aneurysm (AAA) is a degenerative disease that causes health problems in humans. However, there are no effective drugs for the treatment of AAA. *Artemisia annua* L. (*A. annua*) is a traditional herbal that has been widely used in cardiovascular disease. Based on network pharmacology and molecular docking technology, this study predicted the practical components and potential mechanisms of *A. annua* inhibiting the occurrence and development of AAA.

Methods: The main active ingredients and targets of *A. annua* were screened through the TCMSP database; the GeneCards, OMIM, PharmGkb, and TTD databases were used to search for the targeted genes of AAA and map them to the targets of the active ingredients to obtain the active ingredient therapy of *A. annua*. The targets of AAA were to construct a protein interaction network through the STRING platform. R software was used to carry out the enrichment analysis of GO and KEGG for relevant targets, and Cytoscape was used to construct the active ingredient-target network prediction model of *A. annua*. Finally, AutoDock Vina was used to verify the results of the active ingredients and critical targets.

Results: The main active ingredients obtained from *A. annua* for the treatment of AAA include quercetin, luteolin, kaempferol, isorhamnetin, and artemetin, as

Abbreviations: AAA, abdominal aortic aneurysm; *A. annua*, *Artemisia annua* L; BP, biological process; CC, cellular component; DL, drug-likeness; GO, gene Ontology; KEGG, Kyoto encyclopedia of genes and Genomes; MF, molecular function; MMP, matrix metalloproteinase; OB, oral bioavailability; OMIM, online Mendelian inheritance in man; PDB, protein data bank; Pharm GKB, pharmacogenomics knowledgebase; PPI, protein-protein interaction; TCMSP, traditional Chinese medicines for systems pharmacology database and analysis platform; TTD, therapeutic target database.

well as 117 effective targets, including RELA, MAPK14, CCND1, MAPK1, AKT1, MYC, MAPK8, TP53, ESR1, FOS, and JUN. The 11 targeted genes might play a key role in disease treatment. Enriched in 2115 GO biological processes, 159 molecular functions, 56 cellular components, and 156 KEGG pathways, inferred that its mechanism of action might be related to PI3K-Akt signaling pathway, fluid shear stress, atherosclerosis, and AGE-RAGE signaling pathway. Molecular docking results showed that the top five active components of *A. annua* had a good affinity for core disease targets and played a central role in treating AAA. The low binding energy molecular docking results provided valuable information for the development of drugs to treat AAA.

Conclusion: Therefore, *A. annua* may have multiple components, multiple targets, and multiple signaling pathways to play a role in treating AAA. *A. annua* may have the potential to treat AAA.

KEYWORDS

abdominal aortic aneurysm, *Artemisia annua* L., molecular docking, network pharmacology, therapeutic targets

Introduction

Abdominal aortic aneurysm (AAA) is mainly characterized by local progressive dilation of the abdominal aorta, the most high-risk vascular degenerative disease in vascular surgery (Kugo et al., 2019). Once AAA ruptures, the mortality rate can reach 80%. After surgical resuscitation, mortality remains high at around 42% (Karthikesalingam et al., 2014). AAA is usually diagnosed when the diameter of the upper abdominal aorta is greater than 30 mm (Moll et al., 2011). Currently, AAA with greater than 55 mm in diameter is mainly treated by surgical intervention, and these surgical interventions are effective ways to prevent abdominal aortic rupture (Powell, 1998; Lavin et al., 2019). In addition to surgical treatment, there is currently a lack of effective drug interventions, especially in the early treatment of AAA (Baxter et al., 2008; Golledge et al., 2017). Therefore, it is vital to explore potential effective drugs.

Chinese traditional medicine is a substantial medical resource. *Artemisia annua* L. (*A. annua*) is a kind of traditional Chinese medicine. With the award of the 2015 Nobel Prize in Physiology or Medicine to a Chinese scientist, Artemisia has attracted global attention (Abba et al., 2018). *Artemisia* and its derivatives are extensively used to treat oncology and cardiovascular diseases (Bora and Sharma, 2011; von Hagens et al., 2017; Abba et al., 2018; Saeed et al., 2019; Aktaş et al., 2020). Several studies have shown that *A. annua* and its derivatives have a particular therapeutic effect on inhibiting atherosclerosis and inflammation (Cao et al., 2020; He et al., 2020; Jiang et al., 2020). Although *A. annua* contains a variety of active ingredients, its therapeutic target and mechanism for AAA treatment are not fully understood.

Network pharmacology, based on bioinformatics and computer technology, integrates a large amount of biological information and data to study the mechanism of action of multi-target drugs from molecules to cells to the body (Hopkins, 2008; Berger and Iyengar, 2009). The strength of network pharmacology lies in analyzing the "drug-component-target-disease" interaction network, systematically discovering drug-disease associations, and revealing the synergistic effects between multi-molecular drugs (Li et al., 2014). Furthermore, molecular docking is a statistical simulation method that focuses on the interaction between molecules and predicts their binding mode and affinity (Wang and Zhu, 2016). The main function of the method is to identify the binding pocket and binding affinity of the drug to the target protein. Therefore, with the help of network pharmacology and molecular docking methods, this study analyzed the role and mechanism of *A. annua* in the treatment of AAA, aiming to provide new ideas for drug treatment of AAA and to facilitate new drug development in the future. The flowchart for this study was shown in Figure 1.

Materials and methods

Database and software

①Drug component target database: Traditional Chinese Medicine Systems Pharmacology Database and Analysis Platform (TCMSP, http://tcmspw.com/tcmsp.php). ②Disease Target Database: GeneCards (https://www.genecards.org/); Online Mendelian Inheritance in Man (OMIM, https://omim.org), Pharmacogenomics Knowledgebase (PharmGKB, https://www.pharmgkb.org/); Therapeutic Target Database (TTD, http://db.idrblab.net/ttd/); ③Protein database, UniProt (https://www.uniprot.org); Protein Data Bank (PDB, http://

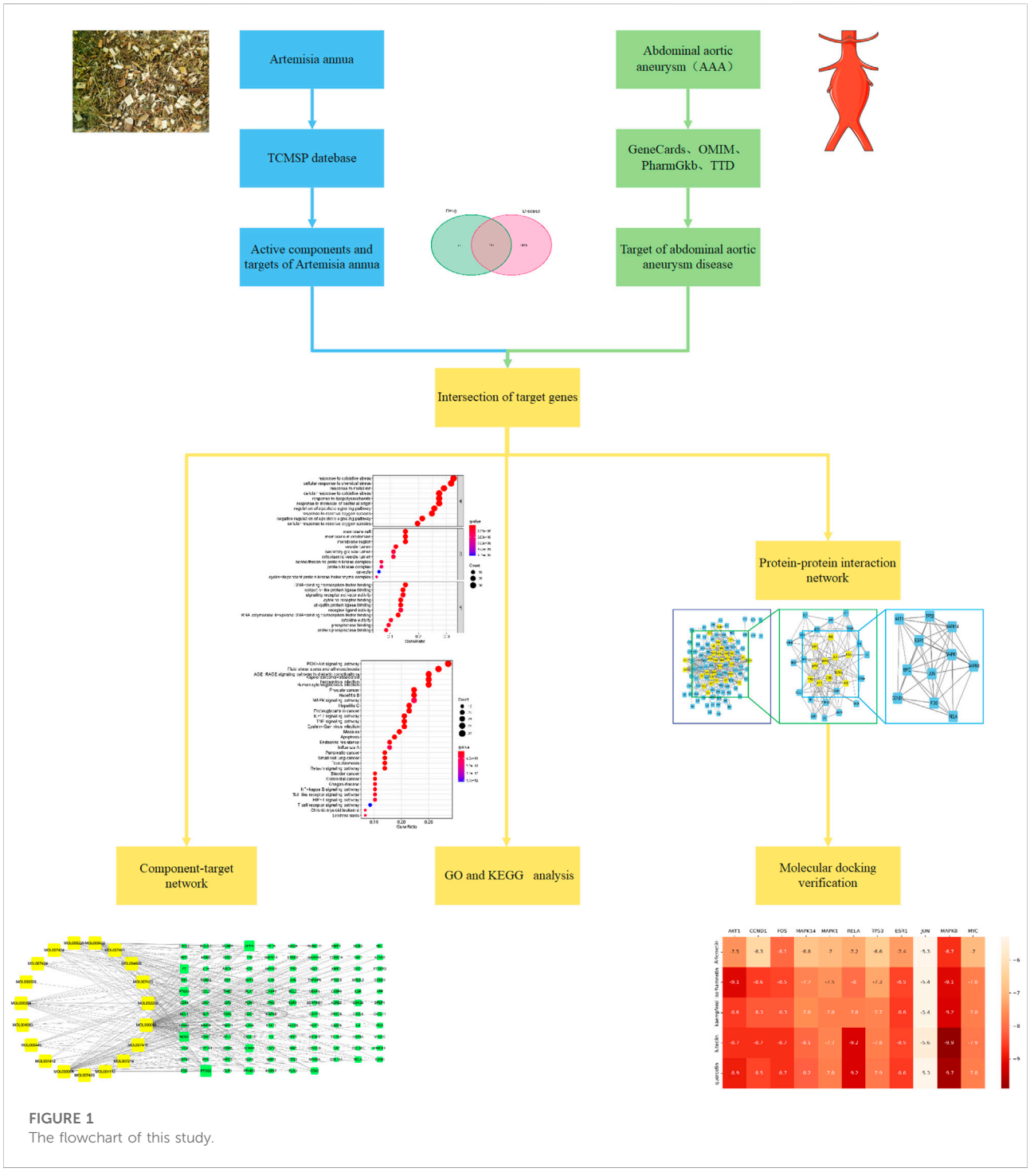

FIGURE 1
The flowchart of this study.

www.rcsb.org/); ④Protein interaction analysis platform, String (https://String-db.org/); ⑤Network analysis and mapping software: Cytoscape 3.8.0;R (R4.0.3 for Windows); ⑥Biological information analysis packet: VennDiagram packet; Bioconductor(https://Bioconduct.org/biolite.r) and its: org.hs.eg.DB, ⑦Molecular Docking Software: AutoDock Vina 4.1, PyMOL 2.4.

Collection of the active components and targets of *A. annua*

All active ingredients in *A. annua* were obtained from TCMSP (https://www.tcmspw.com/tcmsp.PHP). The classification standards were defined based on drug-likeness (DL) greater than or equal to 0.18 and oral bioavailability

(OB) greater than or equal to 30% (Xu et al., 2020). Then, the targets of the selected compounds were obtained from the TCMSP database, and the targeted name was input into Uniprot (http://www.uniprot.org/) to obtain the standardized gene symbol.

Screening of genes related to the treatment of AAA with *A. annua*

In the Genecards, OMIM, PHARGKB, and TDD databases, "abdominal aortic aneurysm" was input as the keyword for retrieval to obtain related AAA targets. The Venn diagram packet was then run in R to obtain compositional targets of *A. annua* intersected with targets related to AAA to screen out the targets related to the treatment of AAA in *A. annua*.

GO and KEGG pathway enrichment analysis

The ClusterProfiler software package in R software (version 4.0.3) was used for Gene Ontology (GO) and Kyoto Encyclopedia of Genes and Genomes (KEGG) pathway enrichment analysis of the intersection genes (Kanehisa and Goto, 2000; Yu et al., 2012). When the q value ≤0.05, GO terms and KEGG pathways were considered to be statistically significant. Then, the top 10 GO terms and the top 30 KEGG pathways for molecular function (MF), cellular component (CC), and biological process (BP) were selected for further analysis.

Construction of the component-target network

The targets of *A. annua* for treating AAA were input into Cytoscape software to construct a "component-target" network (Shannon, 2003). The active components and targets of the drug were represented as "nodes", and the interaction between nodes was defined as "edges".

PPI network construction and core target screening

The intersection gene data were imported into the String database (https://string-db.org/) to obtain the possible intersection points and establish the relationship between the targets (Szklarczyk et al., 2019). The generated files were then imported into Cytoscape software for protein-protein interaction (PPI) maps to describe the relationship between *A. annua* and the intersecting genes of AAA.

Molecular docking

Referring to the previous research literature (Powell, 1998; Hong et al., 2022; Xu et al., 2022), we selected the top 5 active ingredients in *A. annua* as ligands and hub genes from the PPI network as receptors for molecular docking validation. According to the molecular docking method, the 3D structure of the active component was downloaded from PubChem CID, the protein structure guide of the target was downloaded from the PDB database, and the hydrodewatering and hydrogenation of the protein were carried out by using PyMol software (Seeliger and de Groot, 2010; Lill and Danielson, 2011). The component and target protein formats were entered into PDBQT format by AutoDockTools1.5 (Morris et al., 2008). Molecular docking was performed using AutoDock Vina 4.1 software, and the results - were further analyzed by PyMol 2.4 (Trott and Olson, 2010).

Results

Screening of active ingredients and targets of *A. annua* for the treatment of AAA

After the search, screening was carried out under the conditions of OB greater than or equal to 30% and DL greater than or equal to 0.18, and the nontarget components were removed. The 22 potential effective components were obtained (Table 1). Furthermore, we found that 510 potential targets corresponded to 22 potential effective ingredients (Supplementary Table S1).

Targets of *A. annua* for AAA

The related targets of AAA were collected from the GeneCards, OMIM, PharmGkb, and TTD databases. The data were sorted and merged to obtain a total of 2010 disease targets (Supplementary Table S2), as shown in Figure 2A. Then, we intersected the obtained *A. annua* targets with the genes associated with AAA and obtained a Venn diagram of the intersected gene symbols for a total of 117 targets (Supplementary Table S3), as shown in Figure 2B.

GO enrichment analysis

GO enrichment analysis was performed to analyze 117 genes of drug-disease intersection by using the ClusterProfiler package in R software (version 4.0.3). They grouped the functions of the genes into three components: biological processes (BP), cellular component (CC), and molecular function (MF), and enriched 2115 GO BPs, 159 MFs, and 56 CCs (Supplementary Table S4). The top 10 significant items (p-value ≤ 0.05) for each module

TABLE 1 The main active ingredients of *A. annua*.

MOL ID	Molecule name	OB	Dl
MOL002235	Eupatin	50.8	0.41
MOL000354	Isorhamnetin	49.6	0.31
MOL000359	Sitosterol	36.91	0.75
MOL004083	Tamarixetin	32.86	0.31
MOL004112	Patuletin	53.11	0.34
MOL000422	Kaempferol	41.88	0.24
MOL000449	Stigmasterol	43.83	0.76
MOL004609	Areapillin	48.96	0.41
MOL005229	Artemetin	49.55	0.48
MOL000006	Luteolin	36.16	0.25
MOL007274	Skrofulein	30.35	0.3
MOL007389	Artemisitene	54.36	0.31
MOL007400	Vicenin-2_qt	45.84	0.21
MOL007401	Cirsiliol	43.46	0.34
MOL007404	Vitexin_qt	52.18	0.21
MOL007412	DMQT	42.6	0.37
MOL007415	[(2S)-2-[[(2S)-2-(benzoylamino)-3-phenylpropanoyl]amino]-3-phenylpropyl] acetate	58.02	0.52
MOL007423	6,8-di-c-glucosylapigenin_qt	59.85	0.21
MOL007424	Artemisinin	49.88	0.31
MOL007425	Dihydroartemisinin	50.75	0.3
MOL007426	Deoxyartemisinin	54.47	0.26
MOL000098	Quercetin	46.43	0.28

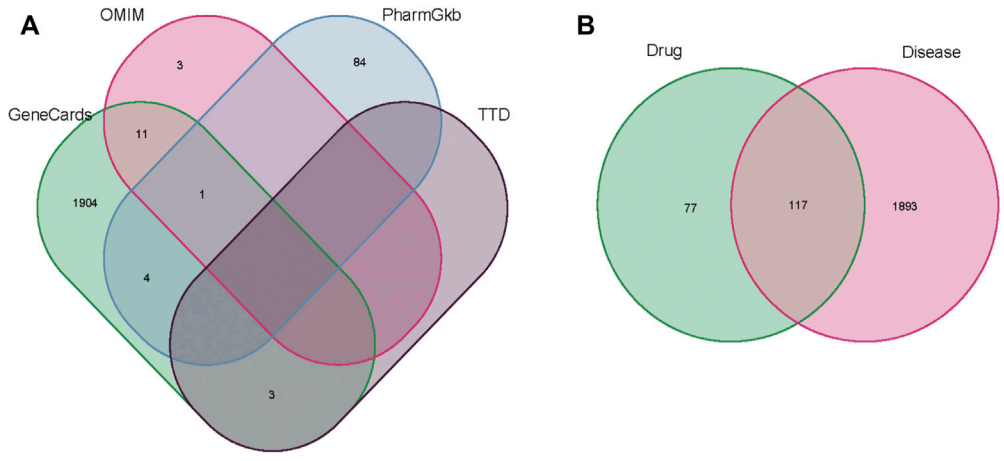

FIGURE 2
(A) The results of the Venn diagram of AAA-related targets in four databases. **(B)** The results of the Venn diagram of drug genes (green) and disease genes (pink).

were shown in Figure 3. The horizontal coordinate indicated the proportion of GO entries, the vertical coordinate representing the name of the enriched entry, and the size of the scatter points represented the number of targets involved in each entry. The higher the significance of the entry, the redder it was. As shown in Figure 3, in biological processes, *A. annua* was mainly associated

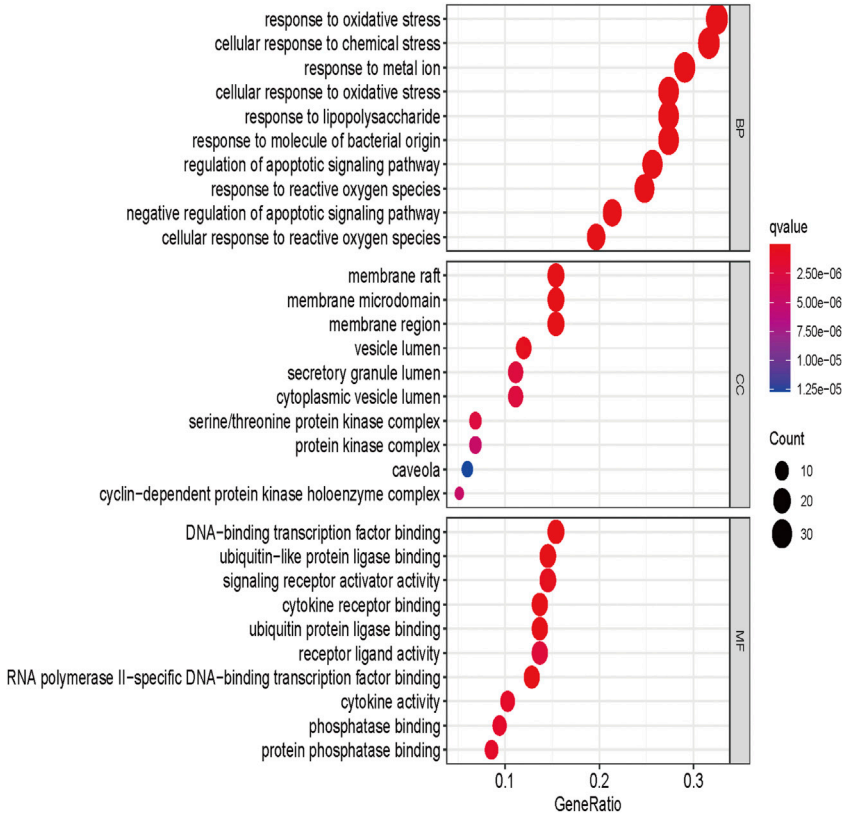

FIGURE 3
GO enrichment analysis of A. annua compound and AAA "intersection target."

with oxidative stress, cellular response to chemical stress, and response to metal ion. Among the cellular components, *A. annua* was primarily associated with membrane raft, membrane microdomain, membrane region, and other cellular components. *A. annua* was mainly related to DNA-binding transcription factor binding, ubiquitin-like protein ligase binding, signaling receptor activator activity, and other molecular functions among the molecular functions.

KEGG enrichment analysis

KEGG enrichment analysis was performed using the ClusterProfiler package (version 4.0.3) in R software for 117 genes targeted at drug-disease crossover. The results of KEGG analysis showed that these genes mainly enriched in 156 KEGG pathways (Supplementary Table S5), and the top 30 items were presented in Figure 4. The results suggested that the active ingredients in *A. annua* might act together through multiple pathways, such as the PI3K-Akt signaling pathway, fluid shear stress, atherosclerosis, and AGE-RAGE signaling pathway in diabetic complications. The size and color of the nodes in the bubble map were determined by the number and *p*-value of the associated genes. The node size indicated how many target genes were associated, and the color from purple to yellow reflected the *p*-value from high to low.

Construction of the *A. annua* component-target network

A total of 117 targets of *A. annua* for treating AAA were input into Cytoscape software to construct a "component-target" network. The active ingredients and targets were represented as "nodes", and the interaction between nodes was defined as "edges". The details were presented in Supplementary Table S6. As shown in Figure 5, yellow represented the active components of *A. annua* in the treatment of AAA, and green represented the potential targets.

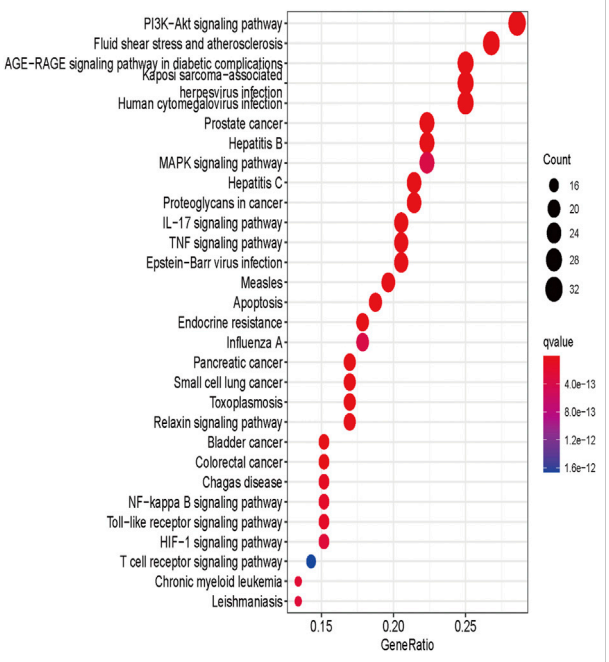

FIGURE 4
KEGG enrichment analysis of A. annua compound and AAA "intersection target."

Construction of the protein-protein interaction network

The 117 targets of *A. annua* for the treatment of AAA were entered into the STRING platform; the parameter was set to *Homo sapiens*, with the highest confidence (0.900), and the rest of the parameters were set to default to build the target protein interaction network, as shown in Figure 6A. It was visualized and analysed by Cytoscape. A node in the PPI network represented each target, and the edges connecting the nodes represented the interaction between the targets. Topological analysis of 117 targets using the plug-in CytoNCA with two median filtering, the first filtering criterion was: betweenness: 31.368076265, closeness: 0.117252968, degree: 6, eigenvector: 0.0489839665, lac: 2.45, network: 3.3304473305. The second screening criterion was: betweenness: 8.080020796, closeness: 0.576923077, degree: 9. eigenvector: 0.145350322, lac: 4.5 network: 5.6, 11 hub genes were screened as shown in Figure 6B. RELA, APK14, CCND1, MAPK1, AKT1, MYC, MAPK8, TP53, ESR1, FOS, and JUN, with 11 nodes and 45 edges, scored as shown in Table 2. Therefore, we considered these 11 genes can serve as potential central genes of *A. annua* in the treatment of AAA.

Molecular docking verification

According to the "component-target" network, quercetin, luteolin, kaempferol, isorhamnetin, and artemetin were the top five active ingredients of *A. annua* in the treatment of AAA, 11 centers for topological analysis of genetic screening for potential *A. annua* center for gene therapy AAA. Therefore, we docked the active ingredients to the hub target genes. We downloaded the 3D structures of the five active ingredients from PubChem and the protein structures of

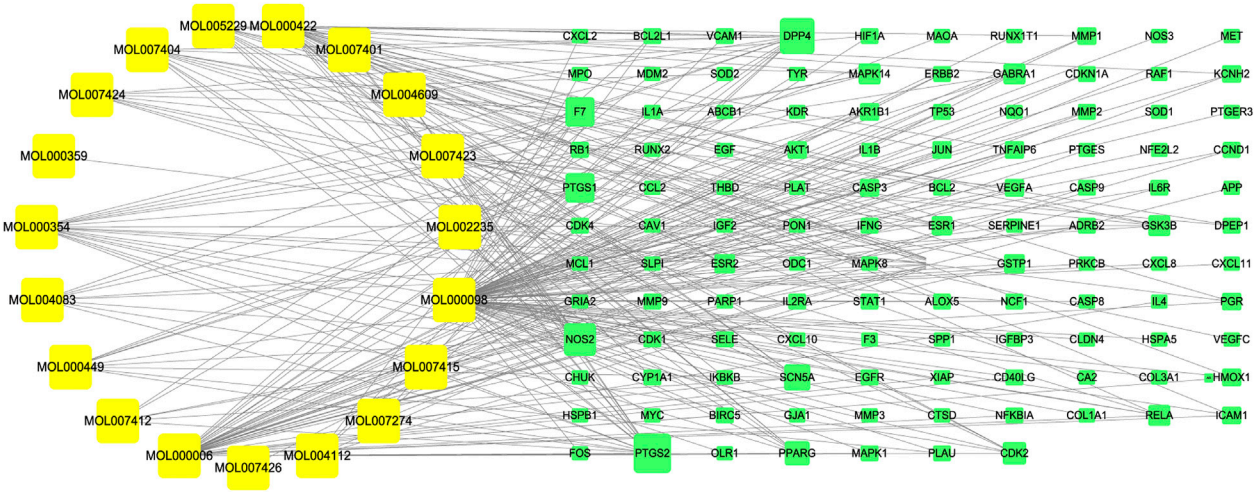

FIGURE 5
"Component-target" network diagram. Yellow represented the active components of A. annua in the treatment of AAA, and green represented the potential targets.

10.3389/fphys.2022.1034014

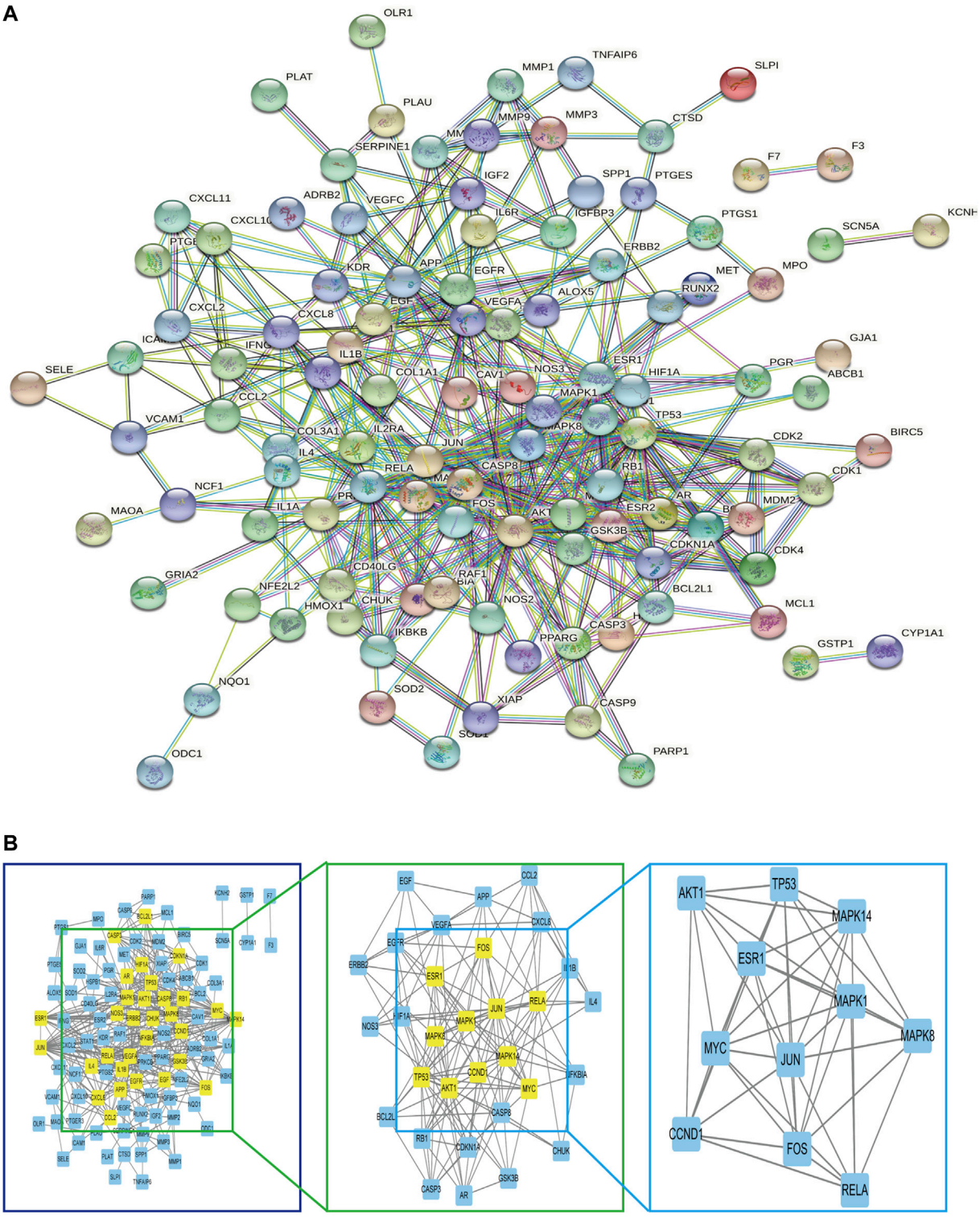

FIGURE 6
(A) Construction of the PPI network. **(B)** Hub genes of **(A)** annua for the treatment of AAA.

TABLE 2 Hub genes of degree value in the PPI network.

name	Betweenness	Closeness	Degree	Eigenvector	LAC	Network
RELA	1.507,142,857	0.769,230,769	7	0.25,598,225	4.571,428,571	5.333,333,333
MYC	2.078,571,429	0.909,090,909	9	0.326,317,787	6.444,444,444	8.172,619,048
MAPK8	0.821,428,571	0.769,230,769	7	0.263,347,566	5.142,857,143	6
FOS	2.078,571,429	0.909,090,909	9	0.326,427,132	6.444,444,444	8.172,619,048
TP53	2.192,857,143	0.909,090,909	9	0.326,792,687	6.444,444,444	8.130,952,381
JUN	3.164,285,714	1	10	0.354,707,539	7	10
MAPK14	1.942,857,143	0.833,333,333	8	0.295,108,497	5.5	6.595,238,095
CCND1	1.257,142,857	0.769,230,769	7	0.263,187,557	4.857,142,857	5.666,666,667
ESR1	2.192,857,143	0.909,090,909	9	0.326,792,687	6.444,444,444	8.130,952,381
MAPK1	1.942,857,143	0.833,333,333	8	0.295,108,497	5.5	6.595,238,095
AKT1	0.821,428,571	0.769,230,769	7	0.26,312,241	5.142,857,143	6

FIGURE 7
Thermal diagram of the molecular docking binding energy. The color from white to red indicated that the binding ability was weak to strong.

eleven hub genes from the PDB database. All active ingredients and hub genes were docked, with binding free energies calculated by running Vina, and the results were presented as a thermal diagram in Figure 7. The binding free energy of less than or equal to −5.0 kcal/mol was regarded as good binding activity between molecules, and the binding free energy of less than or equal to −7 kcal/mol represented a strong binding force between molecules (Morris et al., 2008). The docking results showed that all five active ingredients had good affinity with eleven core disease targets and played a central role in the action of *A. annua* in the treatment of AAA. We showed the top 10 molecular docking maps with low binding energies in Figure 8. The low binding energy molecular docking results provided valuable information for the development of drugs to treat AAA.

Discussion

Since the 2015 Nobel Prize in Physiology or Medicine was awarded to Chinese scientists, *Artemisia* has gained global attention (Efferth et al., 2015). *Artemisia* and its derivatives are used to treat malaria and are widely used to treat various oncological and cardiovascular diseases (Ahmad et al., 2015; Efferth, 2017; Lang et al., 2019; Feng et al., 2020; Jiang et al., 2020; Yin et al., 2020; Meng et al., 2021). As the COVID-19 epidemic rages around the world, some studies have been conducted to fully elucidate the mechanisms behind *A. annua*'s treatment of COVID-19 through network pharmacology and molecular docking techniques (Tang et al., 2022). More studies have been performed to explore the potential mechanisms of *A. annua* and the treatment of chronic hepatitis B and hepatocellular carcinoma (He et al., 2021; Zhang et al., 2021).

10.3389/fphys.2022.1034014

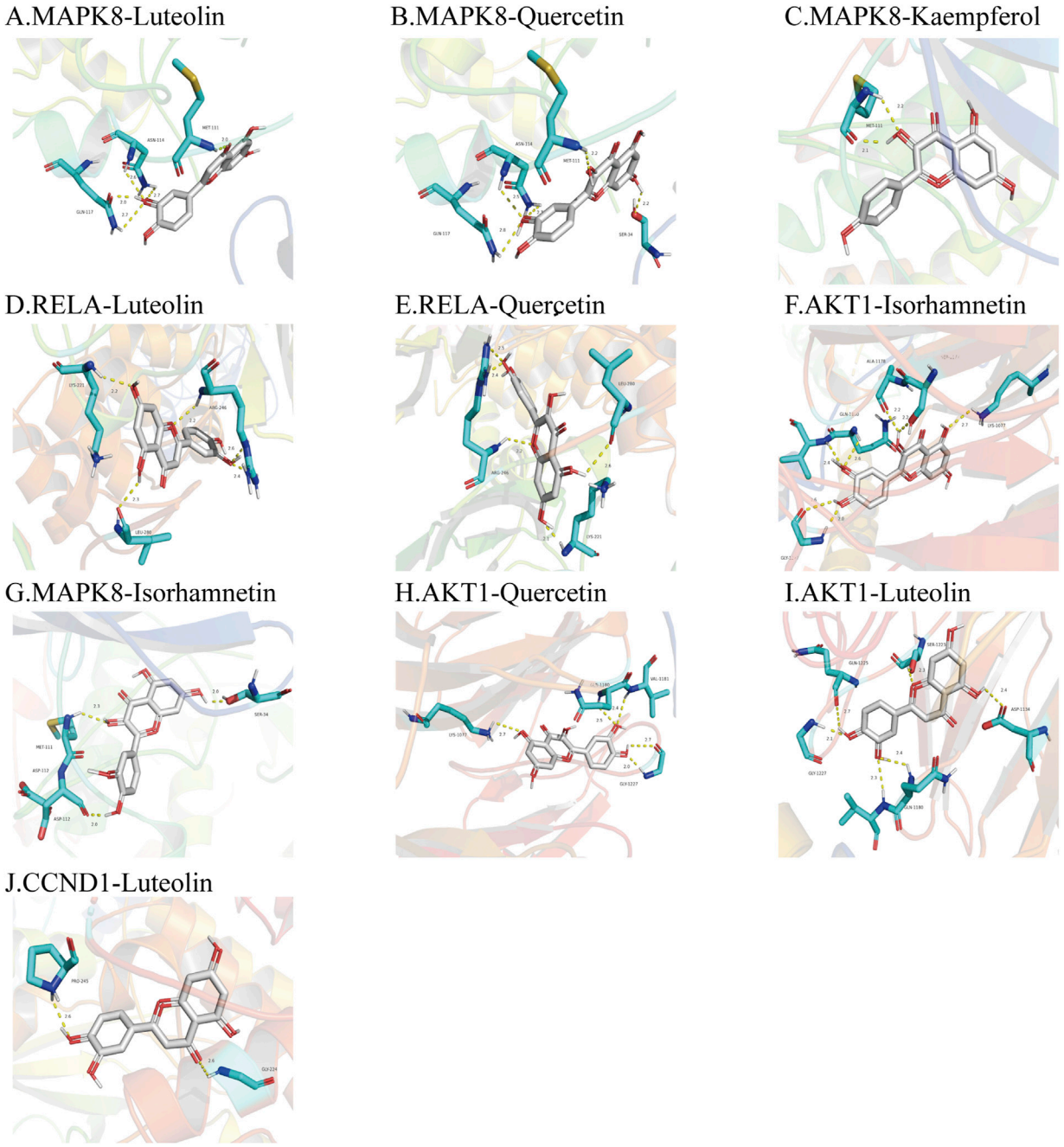

FIGURE 8
Molecular docking diagrams of the top 10 molecular docking maps with low binding energies. The protein active site, binding distance, and molecular docking model between the protein and the main active ingredient were shown in Figure 8. **(A)**. MAPK8-Luteolin (−9.9 kcal/mol); **(B)**. MAPK8-Quercetin (−9.7 kcal/mol); **(C)**. MAPK8-Kaempferol (−9.2 kcal/mol); **(D)**. RELA-Luteolin (−9.2 kcal/mol); **(E)**. RELA-Quercetin (−9.2 kcal/mol); **(F)**. AKT1-Isorhamnetin (−9.1 kcal/mol); **(G)**. MAPK8-Isorhamnetin (−9.1 kcal/mol); **(H)**. AKT1-Quercetin (−8.9 kcal/mol); **(I)**. AKT1-Luteolin (−8.7 kcal/mol); **(J)**. CCND1-Luteolin (−8.7 kcal/mol).

With the development of network pharmacology, traditional medicine based on multi-component, multi-target, and multi-channel treatment of diseases have been paid more attention (Yuan et al., 2017).

Our research screened 22 potentially active ingredients of *A. annua*, including quercetin, luteolin, kaempferol, isorhamnetin, artemetin, and artemisinin. Some ingredients had been proven to affect vascular diseases,

such as AAA. Quercetin, a flavonoid with anti-inflammatory activity, was the most abundant ingredients that could act on AAA and inhibited the development of AAA in mice (Wang et al., 2012). Additionally, quercetin attenuated neovascularization during AAA growth (Wang et al., 2020) and decreased oxidative stress in AAA mouse models (WANG et al., 2014). Luteolin inhibited vascular smooth muscle cells proliferation and migration (Xu et al., 2015; Wu et al., 2018). Kaempferol inhibited diabetic cardiomyopathy in rats through a hypoglycemic effect and upregulation of SIRT1 (Alshehri et al., 2021). Kaempferol attenuated atherosclerosis *via* the PI3K/AKT/Nrf2 pathway (Feng et al., 2021). In addition, some epidemiological studies had found a positive correlation between the consumption of foods containing kaempferol and a reduced risk of many diseases, such as cancer and cardiovascular disease (Calderón-Montaño et al., 2011). Isorhamnetin inhibited oxidative stress (Skalski et al., 2019), and prevented doxorubicin-induced cardiotoxicity (Sun et al., 2013), and isorhamnetin attenuated atherosclerosis through PI3K/AKT activation and HO-1-induced inhibition of macrophage apoptosis (Luo et al., 2015). *Artemetin* had a certain inhibitory effect on atherosclerosis (Kim and Shim, 2019) and also could reduce hypertension proliferation, migration, and inflammation of VSMCs (de Souza et al., 2011; Cao et al., 2015). Therefore, the above results also showed that the effective chemical components in *A. annua* had a certain therapeutic effect on treating AAA.

After our filtering, there are 22 active ingredients in Artemisia annua. The top compound is quercetin with a degree-value of 89, and the last compound with a degree-value of 1. The difference between the two values is too large. We predicted the compounds and targets that play a major role in *A. annua*, and the compounds with high degree-value have higher representativeness while referring to previous studies(Feng et al., 2022; Hong et al., 2022; Xu et al., 2022), we selected the top five compounds for subsequent validation and molecular docking. By screening a total of 117 intersections of a drug-disease gene, the topological analysis of 11 hub genes RELA, APK14, CCND1, MAPK1, AKT1, MYC, MAPK8, TP53, ESR1, FOS, and JUN were finally performed. The molecular docking technique predicted the binding strength between herbal components and targets (Zeng et al., 2019). The results showed that the top 5 active ingredients had a good affinity with 11 core disease targets, and the docking results were less than −5.0 kcal/mol, which further demonstrated that active ingredients and hub genes were critical targets of *A. annua* in the treating of AAA. Among these, MAPK8-Luteolin (−9.9 kcal/mol) had the best binding ability and could be used as a potential drug therapeutic target in the future. More literature had reported that these selected genes were closely related to AAA (DiMusto et al., 2012; Leeper et al., 2013; Ijaz et al., 2017; Hao et al., 2018; Zhang et al., 2018; Zhao et al., 2019; Moran et al., 2020). These genes and their associated pathways might become potential therapeutic targets for AAA treatment. Because there is no reliable high-level clinical evidence of drugs for the treatment of abdominal aortic aneurysms (Golledge, 2019), we do not have a positive control set in our molecular docking. As a result, based on the advantages of *A. annua* in multigene targeting, it is more promising to bring good news to AAA patients.

In addition, KEGG enrichment analysis showed that several pathways, such as the PI3K-Akt signaling pathway, fluid shear stress, atherosclerosis, and the AGE-RAGE signaling pathway, were closely associated with the treatment of AAA by *A. annua*.

The relationship between the above pathways and AAA had been extensively studied. Inhibition of Notch1-mediated inflammation prevented AAA *via* the PI3K/Akt signaling pathway (Ni et al., 2021), and AGE-RAGE stress was associated with the pathogenesis of aortic aneurysms (Prasad, 2019). Daidzein attenuated AAA through the NF-κB, p38-MAPK, and TGF-β1 pathways (Liu et al., 2016). The MAPK (mitogen-activated protein kinase)/ERK pathway was an essential regulator of AAA formation during matrix metalloproteinase (MMP) (Ghosh et al., 2012). Lithium chloride could inhibit AAA by modulating the NF-κB signaling pathway (Xu et al., 2021). Therefore, it was speculated that *A. annua* might inhibit AAA by acting on related signaling pathways or targets.

In summary, the study used network pharmacology and molecular docking technology strategies to predict the significant active compounds and critical targets of *A. annua* in the treatment of AAA and speculated the potential mechanisms from multiple approaches and perspectives. Therefore, *A. annua* might have multiple components, multiple targets, and multiple signaling pathways to play a role in treating AAA. Among them, quercetin corresponds to the most targets and has the strongest activity, and it will be one of the possible potential drugs in the future drug treatment of abdominal aortic aneurysm.

Conclusion

Based on network pharmacology combined with molecular docking technology, this study systematically summarized the molecular targets of *A. annua* in the treatment of AAA, aiming to promote more comprehensive development and research of *A. annua*. The potential molecular mechanism of the active ingredients of *A. annua* in the treatment of AAA could support its subsequent clinical research and be vital for exploring the pharmacological

treatment of AAA. At the same time, the current work also has some shortcomings. This study lacks corresponding experimental verification, which will be further verified in future research. In addition, the loss and incompleteness of some database information will also have a particular impact on the prediction results.

Data availability statement

The original contributions presented in the study are included in the article/Supplementary Material, further inquiries can be directed to the corresponding author.

Author contributions

LJ designed the study and wrote the research. DW, SC, and CF analyzed the results. XC, CY, and YJ designed the letters and figures. BJ and SX reviewed and edited the paper. All authors have read and approved the manuscript writing..

Funding

This study is financially supported by the Natural Science Foundation of China (Grant Number 81974049).

Acknowledgments

Special thanks are due to Qihao Xu for his support and encouragement.

Conflict of interest

The authors declare that the research was conducted in the absence of any commercial or financial relationships that could be construed as a potential conflict of interest.

Publisher's note

Supplementary material

The Supplementary Material for this article can be found online at: https://www.frontiersin.org/articles/10.3389/fphys.2022.1034014/full#supplementary-material

References

Abba, M. L., Patil, N., Leupold, J. H., Saeed, M. E. M., Efferth, T., and Allgayer, H. (2018). Prevention of carcinogenesis and metastasis by Artemisinin-type drugs. *Cancer Lett.* 429, 11–18. doi:10.1016/j.canlet.2018.05.008

Ahmad, L., Semotiuk, A., Zafar, M., Ahmad, M., Sultana, S., Liu, Q.-R., et al. (2015). Ethnopharmacological documentation of medicinal plants used for hypertension among the local communities of DIR Lower, Pakistan. *J. Ethnopharmacol.* 175, 138–146. doi:10.1016/j.jep.2015.09.014

Aktaş, İ., Özmen, Ö., Tutun, H., Yalçın, A., Türk, A., Yalcin, A., et al. (2020). Artemisinin attenuates doxorubicin induced cardiotoxicity and hepatotoxicity in rats. *Biotech. Histochem.* 95, 121–128. doi:10.1080/10520295.2019.1647457

Alshehri, A. S., El-Kott, A. F., Eleawa, S. M., El-Gerbed, M. S. A., Khalifa, H. S., El-Kenawy, A. E., et al. (2021). Kaempferol protects against streptozotocin-induced diabetic cardiomyopathy in rats by a hypoglycemic effect and upregulating SIRT1. *J. Physiol. Pharmacol.* 72 , 339–355. doi:10.26402/jpp.2021.3.04

Baxter, B. T., Terrin, M. C., and Dalman, R. L. (2008). Medical management of small abdominal aortic aneurysms. *Circulation* 117, 1883–1889. doi:10.1161/CIRCULATIONAHA.107.735274

Berger, S. I., and Iyengar, R. (2009). Network analyses in systems pharmacology. *Bioinformatics* 25, 2466–2472. doi:10.1093/bioinformatics/btp465

Bora, K. S., and Sharma, A. (2011). The genus Artemisia: A comprehensive review. *Pharm. Biol.* 49, 101–109. doi:10.3109/13880209.2010.497815

Calderón-Montaño, J. M., Burgos-Morón, E., Pérez-Guerrero, C., and López-Lázaro, M. (2011). A review on the dietary flavonoid kaempferol. *Mini Rev. Med. Chem.* 11, 298–344. doi:10.2174/138955711795305335

Cao, Q., Du, H., Fu, X., Duan, N., Liu, C., and Li, X. (2020). Artemisinin attenuated atherosclerosis in high-fat diet–fed ApoE−/− mice by promoting macrophage autophagy through the AMPK/mTOR/ULK1 pathway. *J. Cardiovasc. Pharmacol.* 75, 321–332. doi:10.1097/FJC.0000000000000794

Cao, Q., Jiang, Y., Shi, J., Xu, C., Liu, X., Yang, T., et al. (2015). Artemisinin inhibits the proliferation, migration, and inflammatory reaction induced by tumor necrosis factor-α in vascular smooth muscle cells through nuclear factor kappa B pathway. *J. Surg. Res.* 194, 667–678. doi:10.1016/j.jss.2014.12.013

de Souza, P., Gasparotto, A., Crestani, S., Stefanello, M. É. A., Marques, M. C. A., da Silva-Santos, J. E., et al. (2011). Hypotensive mechanism of the extracts and artemetin isolated from *Achillea millefolium* L. (Asteraceae) in rats. *Phytomedicine* 18, 819–825. doi:10.1016/j.phymed.2011.02.005

DiMusto, P. D., Lu, G., Ghosh, A., Roelofs, K. J., Sadiq, O., McEvoy, B., et al. (2012). Increased JNK in males compared with females in a rodent model of abdominal aortic aneurysm. *J. Surg. Res.* 176, 687–695. doi:10.1016/j.jss.2011.11.1024

Efferth, T. (2017). From ancient herb to modern drug: Artemisia annua and artemisinin for cancer therapy. *Semin. Cancer Biol.* 46, 65–83. doi:10.1016/j.semcancer.2017.02.009

Efferth, T., Zacchino, S., Georgiev, M. I., Liu, L., Wagner, H., and Panossian, A. (2015). Nobel Prize for artemisinin brings phytotherapy into the spotlight. *Phytomedicine* 22, A1–A3. doi:10.1016/j.phymed.2015.10.003

Feng, S., Wang, T., Fan, L., An, X., Ding, X., Wang, M., et al. (2022). Exploring the potential therapeutic effect of Eucommia ulmoides–Dipsaci Radix herbal pair on osteoporosis based on network pharmacology and molecular docking technology. *RSC Adv.* 12, 2181–2195. doi:10.1039/D1RA05799E

Feng, X., Cao, S., Qiu, F., and Zhang, B. (2020). Traditional application and modern pharmacological research of Artemisia annua L. *Pharmacol. Ther.* 216, 107650. doi:10.1016/j.pharmthera.2020.107650

Feng, Z., Wang, C., Yue, J., Sun, H., Meng, Q., and Wu, J. (2021). Kaempferol-induced GPER upregulation attenuates atherosclerosis via the PI3K/AKT/Nrf2 pathway. *Pharm. Biol.* 59, 1106–1116. doi:10.1080/13880209.2021.1961823

Ghosh, A., DiMusto, P. D., Ehrlichman, L. K., Sadiq, O., McEvoy, B., Futchko, J. S., et al. (2012). The role of extracellular signal-related kinase during abdominal aortic aneurysm formation. *J. Am. Coll. Surg.* 215, 668–680. doi:10.1016/j.jamcollsurg.2012.06.414

Golledge, J. (2019). Abdominal aortic aneurysm: Update on pathogenesis and medical treatments. *Nat. Rev. Cardiol.* 16, 225–242. doi:10.1038/s41569-018-0114-9

Golledge, J., Norman, P. E., Murphy, M. P., and Dalman, R. L. (2017). Challenges and opportunities in limiting abdominal aortic aneurysm growth. *J. Vasc. Surg.* 65, 225–233. doi:10.1016/j.jvs.2016.08.003

Hao, Q., Dong, X., Chen, X., Yan, F., Wang, X., Shi, H., et al. (2018). Angiotensin-converting enzyme 2 inhibits angiotensin II–induced abdominal aortic aneurysms in mice. *Hum. Gene Ther.* 29, 1387–1395. doi:10.1089/hum.2016.144

He, A., Wang, W., Xia, Y., and Niu, X. (2021). A network pharmacology approach to explore the mechanisms of artemisiae scopariae herba for the treatment of chronic hepatitis B. *Evid. Based. Complement. Altern. Med.* 2021, 6614039. doi:10.1155/2021/6614039

He, L.-H., Gao, J.-H., Yu, X.-H., Wen, F.-J., Luo, J.-J., Qin, Y.-S., et al. (2020). Artesunate inhibits atherosclerosis by upregulating vascular smooth muscle cells-derived LPL expression via the KLF2/NRF2/TCF7L2 pathway. *Eur. J. Pharmacol.* 884, 173408. doi:10.1016/j.ejphar.2020.173408

Hong, J., Ding, J., Hong, H., Xu, X., Pan, B., Ruan, Y., et al. (2022). Identifying the Mechanism of Polygoni Cuspidati Rhizoma et Radix in Treating Acute Liver Failure Based on Network Pharmacology and Molecular Docking. *Gastroenterol. Res. Pract.* 2022, e2021066. doi:10.1155/2022/2021066

Hopkins, A. L. (2008). Network pharmacology: The next paradigm in drug discovery. *Nat. Chem. Biol.* 4, 682–690. doi:10.1038/nchembio.118

Ijaz, T., Sun, H., Pinchuk, I. V., Milewicz, D. M., Tilton, R. G., and Brasier, A. R. (2017). Deletion of NF-κB/RelA in angiotensin II-sensitive mesenchymal cells blocks aortic vascular inflammation and abdominal aortic aneurysm formation. *Arterioscler. Thromb. Vasc. Biol.* 37, 1881–1890. doi:10.1161/ATVBAHA.117.309863

Jiang, Y., Du, H., Liu, X., Fu, X., Li, X., and Cao, Q. (2020). Artemisinin alleviates atherosclerotic lesion by reducing macrophage inflammation via regulation of AMPK/NF-κB/NLRP3 inflammasomes pathway. *J. Drug Target.* 28, 70–79. doi:10.1080/1061186X.2019.1616296

Kanehisa, M., and Goto, S. (2000). KEGG: Kyoto Encyclopedia of genes and Genomes. *Nucleic Acids Res.* 28, 27–30. doi:10.1093/nar/28.1.27

Karthikesalingam, A., Holt, P. J., Vidal-Diez, A., Ozdemir, B. A., Poloniecki, J. D., Hinchliffe, R. J., et al. (2014). Mortality from ruptured abdominal aortic aneurysms: Clinical lessons from a comparison of outcomes in england and the USA. *Lancet* 383, 963–969. doi:10.1016/S0140-6736(14)60109-4

Kim, J.-Y., and Shim, S. H. (2019). Anti-Atherosclerotic effects of fruits of vitex rotundifolia and their isolated compounds via inhibition of human LDL and HDL oxidation. *Biomolecules* 9, E727. doi:10.3390/biom9110727

Kugo, H., Moriyama, T., and Zaima, N. (2019). The role of perivascular adipose tissue in the appearance of ectopic adipocytes in the abdominal aortic aneurysmal wall. *Adipocyte* 8, 229–239. doi:10.1080/21623945.2019.1636625

Lang, S. J., Schmiech, M., Hafner, S., Paetz, C., Steinborn, C., Huber, R., et al. (2019). Antitumor activity of an Artemisia annua herbal preparation and identification of active ingredients. *Phytomedicine* 62, 152962. doi:10.1016/j.phymed.2019.152962

Lavin, B., Lacerda, S., Andia, M. E., Lorrio, S., Bakewell, R., Smith, A., et al. (2019). Tropoelastin: An *in vivo* imaging marker of dysfunctional matrix turnover during abdominal aortic dilation. *Cardiovasc. Res.* 116, 995–1005. doi:10.1093/cvr/cvz178

Leeper, N. J., Raiesdana, A., Kojima, Y., Kundu, R. K., Cheng, H., Maegdefessel, L., et al. (2013). Loss of *CDKN2B* promotes p53-dependent smooth muscle cell apoptosis and aneurysm formation. *Arterioscler. Thromb. Vasc. Biol.* 33, e1–e10. doi:10.1161/ATVBAHA.112.300399

Li, S., Fan, T.-P., Jia, W., Lu, A., and Zhang, W. (2014). Network pharmacology in traditional Chinese medicine. *Evid. Based. Complement. Altern. Med.* 2014, 138460. doi:10.1155/2014/138460

Lill, M. A., and Danielson, M. L. (2011). Computer-aided drug design platform using PyMOL. *J. Comput. Aided. Mol. Des.* 25, 13–19. doi:10.1007/s10822-010-9395-8

Liu, Y.-F., Bai, Y.-Q., and Qi, M. (2016). Daidzein attenuates abdominal aortic aneurysm through NF-κB, p38MAPK and TGF-β1 pathways. *Mol. Med. Rep.* 14, 955–962. doi:10.3892/mmr.2016.5304

Luo, Y., Sun, G., Dong, X., Wang, M., Qin, M., Yu, Y., et al. (2015). Isorhamnetin attenuates atherosclerosis by inhibiting macrophage apoptosis via PI3K/AKT activation and HO-1 induction. *PLoS One* 10, e0120259. doi:10.1371/journal.pone.0120259

Meng, Y., Ma, N., Lyu, H., Wong, Y. K., Zhang, X., Zhu, Y., et al. (2021). Recent pharmacological advances in the repurposing of artemisinin drugs. *Med. Res. Rev.* 41, 3156–3181. doi:10.1002/med.21837

Moll, F. L., Powell, J. T., Fraedrich, G., Verzini, F., Haulon, S., Waltham, M., et al. (2011). Management of abdominal aortic aneurysms clinical practice guidelines of the European society for vascular surgery. *Eur. J. Vasc. Endovasc. Surg.* 41, S1–S58. doi:10.1016/j.ejvs.2010.09.011

Moran, C. S., Seto, S.-W., Biros, E., Krishna, S. M., Morton, S. K., Kleinschnitz, C., et al. (2020). Factor XII blockade inhibits aortic dilatation in angiotensin II-infused apolipoprotein E-deficient mice. *Clin. Sci.* 134, 1049–1061. doi:10.1042/CS20191020

Morris, G. M., Huey, R., and Olson, A. J. (2008). Using AutoDock for ligand-receptor docking. *Curr. Protoc. Bioinforma.* 24, Unit 8.14. doi:10.1002/0471250953.bi0814s24

Ni, X.-Q., Zhang, Y.-R., Jia, L.-X., Lu, W.-W., Zhu, Q., Ren, J.-L., et al. (2021). Inhibition of Notch1-mediated inflammation by intermedin protects against abdominal aortic aneurysm via PI3K/Akt signaling pathway. *Aging (Albany NY)* 13, 5164–5184. doi:10.18632/aging.202436

Powell, J. T. (1998). Mortality results for randomised controlled trial of early elective surgery or ultrasonographic surveillance for small abdominal aortic aneurysms. The UK Small Aneurysm Trial Participants. *Lancet* 352, 1649–1655. doi:10.1016/S0140-6736(98)10137-X

Prasad, K. (2019). AGE-RAGE stress play a role in aortic aneurysm: A comprehensive review and novel potential therapeutic target. *Rev. Cardiovasc. Med.* 20, 201–208. doi:10.31083/j.rcm.2019.04.57

Saeed, M. E. M., Breuer, E., Hegazy, M.-E. F., and Efferth, T. (2019). Retrospective study of small pet tumors treated with Artemisia annua and iron. *Int. J. Oncol.* 56, 123–138. doi:10.3892/ijo.2019.4921

Seeliger, D., and de Groot, B. L. (2010). Ligand docking and binding site analysis with PyMOL and Autodock/Vina. *J. Comput. Aided. Mol. Des.* 24, 417–422. doi:10.1007/s10822-010-9352-6

Shannon, P., Markiel, A., Ozier, O., Baliga, N. S., Wang, J. T., Ramage, D., et al. (2003). Cytoscape: A software environment for integrated models of biomolecular interaction networks. *Genome Res.* 13, 2498–2504. doi:10.1101/gr.1239303

Skalski, B., Lis, B., Pecio, Ł., Kontek, B., Olas, B., Żuchowski, J., et al. (2019). Isorhamnetin and its new derivatives isolated from sea buckthorn berries prevent H2O2/Fe - induced oxidative stress and changes in hemostasis. *Food Chem. Toxicol.* 125, 614–620. doi:10.1016/j.fct.2019.02.014

Sun, J., Sun, G., Meng, X., Wang, H., Luo, Y., Qin, M., et al. (2013). Isorhamnetin protects against doxorubicin-induced cardiotoxicity *in vivo* and *in vitro*. *PLoS One* 8, e64526. doi:10.1371/journal.pone.0064526

Szklarczyk, D., Gable, A. L., Lyon, D., Junge, A., Wyder, S., Huerta-Cepas, J., et al. (2019). STRING v11: Protein–protein association networks with increased coverage, supporting functional discovery in genome-wide experimental datasets. *Nucleic Acids Res.* 47, D607–D613. doi:10.1093/nar/gky1131

Tang, Y., Li, X., Yuan, Y., Zhang, H., Zou, Y., Xu, Z., et al. (2022). Network pharmacology-based predictions of active components and pharmacological mechanisms of Artemisia annua L. for the treatment of the novel Corona virus disease 2019 (COVID-19). *BMC Complement. Med. Ther.* 22, 56. doi:10.1186/s12906-022-03523-2

Trott, O., and Olson, A. J. (2010). AutoDock Vina: Improving the speed and accuracy of docking with a new scoring function, efficient optimization and multithreading. *J. Comput. Chem.* 31, 455–461. doi:10.1002/jcc.21334

von Hagens, C., Walter-Sack, I., Goeckenjan, M., Osburg, J., Storch-Hagenlocher, B., Sertel, S., et al. (2017). Prospective open uncontrolled phase I study to define a well-tolerated dose of oral artesunate as add-on therapy in patients with metastatic breast cancer (ARTIC M33/2). *Breast Cancer Res. Treat.* 164, 359–369. doi:10.1007/s10549-017-4261-1

Wang, G., and Zhu, W. (2016). Molecular docking for drug discovery and development: A widely used approach but far from perfect. *Future Med. Chem.* 8, 1707–1710. doi:10.4155/fmc-2016-0143

Wang, L., Cheng, X., Li, H., Qiu, F., Yang, N., Wang, B., et al. (2014). Quercetin reduces oxidative stress and inhibits activation of c-Jun N-terminal kinase/activator protein-1 signaling in an experimental mouse model of abdominal aortic aneurysm. *Mol. Med. Rep.* 9, 435–442. doi:10.3892/mmr.2013.1846

Wang, L., Wang, B., Li, H., Lu, H., Qiu, F., Xiong, L., et al. (2012). Quercetin, a flavonoid with anti-inflammatory activity, suppresses the development of abdominal aortic aneurysms in mice. *Eur. J. Pharmacol.* 690, 133–141. doi:10.1016/j.ejphar.2012.06.018

Wang, L., Wu, H., Xiong, L., Liu, X., Yang, N., Luo, L., et al. (2020). Quercetin downregulates cyclooxygenase-2 expression and HIF-1α/VEGF signaling-related angiogenesis in a mouse model of abdominal aortic aneurysm. *Biomed. Res. Int.* 2020, 9485398. doi:10.1155/2020/9485398

Wu, Y.-T., Chen, L., Tan, Z.-B., Fan, H.-J., Xie, L.-P., Zhang, W.-T., et al. (2018). Luteolin inhibits vascular smooth muscle cell proliferation and migration by inhibiting TGFBR1 signaling. *Front. Pharmacol.* 9, 1059. doi:10.3389/fphar.2018.01059

Xu, B., Dan, W., Zhang, X., Wang, H., Cao, L., Li, S., et al. (2022). Gene differential expression and interaction networks illustrate the biomarkers and molecular biological mechanisms of unsaponifiable matter in kanglaite injection for pancreatic ductal adenocarcinoma. *Biomed. Res. Int.* 2022, e6229462. doi:10.1155/2022/6229462

Xu, J., Wang, F., Guo, J., Xu, C., Cao, Y., Fang, Z., et al. (2020). Pharmacological mechanisms underlying the neuroprotective effects of alpinia oxyphylla miq. On alzheimer's disease. *Int. J. Mol. Sci.* 21, 2071. doi:10.3390/ijms21062071

Xu, T., Wang, S., Li, X., Li, X., Qu, K., Tong, H., et al. (2021). Lithium chloride represses abdominal aortic aneurysm via regulating GSK3β/SIRT1/NF-κB signaling pathway. *Free Radic. Biol. Med.* 166, 1–10. doi:10.1016/j.freeradbiomed.2021.02.007

Xu, T., Zhu, H., Li, D., Lang, Y., Cao, L., Liu, Y., et al. (2015). Luteolin inhibits angiotensin II-stimulated VSMC proliferation and migration through downregulation of akt phosphorylation. *Evid. Based. Complement. Altern. Med.* 2015, 931782. doi:10.1155/2015/931782

Yin, X., Liu, Y., Qin, J., Wu, Y., Huang, J., Zhao, Q., et al. (2020). Artesunate suppresses the proliferation and development of estrogen receptor-α-positive endometrial cancer in HAND2-dependent pathway. *Front. Cell Dev. Biol.* 8, 606969. doi:10.3389/fcell.2020.606969

Yu, G., Wang, L.-G., Han, Y., and He, Q.-Y. (2012). clusterProfiler: an R Package for comparing biological themes among gene clusters. *OMICS* 16, 284–287. doi:10.1089/omi.2011.0118

Yuan, H., Ma, Q., Cui, H., Liu, G., Zhao, X., Li, W., et al. (2017). How can synergism of traditional medicines benefit from network pharmacology? *Molecules* 22, E1135. doi:10.3390/molecules22071135

Zeng, Q., Li, L., Jin, Y., Chen, Z., Duan, L., Cao, M., et al. (2019). A network pharmacology approach to reveal the underlying mechanisms of paeonia lactiflora pall. On the treatment of alzheimer's disease. *Evid. Based. Complement. Altern. Med.* 2019, 8706589. doi:10.1155/2019/8706589

Zhang, S., Kan, X., Li, Y., Li, P., Zhang, C., Li, G., et al. (2018). Deficiency of γδT cells protects against abdominal aortic aneurysms by regulating phosphoinositide 3-kinase/AKT signaling. *J. Vasc. Surg.* 67, 899–908. e1. doi:10.1016/j.jvs.2016.03.474

Zhang, S., Mo, Z., Zhang, S., and Li, X. (2021). A network pharmacology approach to reveal the underlying mechanisms of Artemisia annua on the treatment of hepatocellular carcinoma. *Evid. Based. Complement. Altern. Med.* 2021, 8947304. doi:10.1155/2021/8947304

Zhao, L., Ouyang, Y., Bai, Y., Gong, J., and Liao, H. (2019). miR-155-5p inhibits the viability of vascular smooth muscle cell via targeting FOS and ZIC3 to promote aneurysm formation. *Eur. J. Pharmacol.* 853, 145–152. doi:10.1016/j.ejphar.2019.03.030

frontiers | Frontiers in Physiology

TYPE Original Research
PUBLISHED 26 October 2022
DOI 10.3389/fphys.2022.1035726

OPEN ACCESS

EDITED BY
Lisheng Xu,
Northeastern University, China

REVIEWED BY
Shan Chang,
Jiangsu University of Technology, China
Li Yang,
Beijing Chaoyang District Maternal and Child Healthcare Hospital, China

*CORRESPONDENCE
Qi Xu,
xuqi_0612@163.com
Lin Yang,
yanglin@bjut.edu.cn

†These authors have contributed equally to this work and share first authorship

SPECIALTY SECTION
This article was submitted to Computational Physiology and Medicine, a section of the journal Frontiers in Physiology

RECEIVED 03 September 2022
ACCEPTED 10 October 2022
PUBLISHED 26 October 2022

CITATION
Li Z, Xu Q, Sun G, Jia R, Yang L, Liu G, Hao D, Zhang S, Yang Y, Li X, Zhang X and Lian C (2022), Dynamic gestational week prediction model for pre-eclampsia based on ID3 algorithm. *Front. Physiol.* 13:1035726. doi: 10.3389/fphys.2022.1035726

Dynamic gestational week prediction model for pre-eclampsia based on ID3 algorithm

Ziwei Li[1†], Qi Xu[2*†], Ge Sun[1,2], Runqing Jia[1], Lin Yang[1,2*], Guoli Liu[3], Dongmei Hao[1,2], Song Zhang[1,2], Yimin Yang[1,2], Xuwen Li[1,2], Xinyu Zhang[1,2] and Cuiting Lian[1,2]

[1]Faculty of Environment and Life Sciences, Beijing University of Technology, Beijing, China, [2]Intelligent Physiological Measurement and Clinical Translation, Beijing International Base for Scientific and Technological Cooperation, Beijing, China, [3]Department of Obstetrics, Peking University People's Hospital, Beijing, China

Pre-eclampsia (PE) is a type of hypertensive disorder during pregnancy, which is a serious threat to the life of mother and fetus. It is a placenta-derived disease that results in placental damage and necrosis due to systemic small vessel spasms that cause pathological changes such as ischemia and hypoxia and oxidative stress, which leads to fetal and maternal damage. In this study, four types of risk factors, namely, clinical epidemiology, hemodynamics, basic biochemistry, and biomarkers, were used for the initial selection of model parameters related to PE, and factors that were easily available and clinically recognized as being associated with a higher risk of PE were selected based on hospital medical record data. The model parameters were then further analyzed and screened in two subgroups: early-onset pre-eclampsia (EOPE) and late-onset pre-eclampsia (LOPE). Dynamic gestational week prediction model for PE using decision tree ID3 algorithm in machine learning. Performance of the model was: macro average (precision = 76%, recall = 73%, F1-score = 75%), weighted average (precision = 88%, recall = 89%, F1-score = 89%) and overall accuracy is 86%. In this study, the addition of the dynamic timeline parameter "gestational week" made the model more convenient for clinical application and achieved effective PE subgroup prediction.

KEYWORDS

hypertensive disorders of pregnancy, pre-eclampsia, decision tree, prediction model, dynamic

1 Introduction

Hypertensive disorders in pregnancy (HDP) are conditions in which pregnancy and hypertension coexist, with a prevalence of approximately 5%–12% (Mahendra et al., 2021). The pathogenesis of HDP is complex and multifactorial, and although some research has been done, its etiology is still unclear and no effective predictive method has been established. HDP is a multi-causal disease whose pathogenesis is related to impaired

placental angiogenesis, placental oxidative stress and abnormal maternal immune response. It is not only hypertension and proteinuria, but especially with the involvement of the heart, lungs, liver and kidneys, the blood, digestive and nervous systems, but also the placenta and the fetus. The disease includes five subtypes: hypertension in pregnancy, PE, eclampsia, chronic hypertension complicated by pre-eclampsia and chronic hypertension in pregnancy (Duhig et al., 2019). PE is one of the more severe of the above sub-types in its pathogenesis. Patients with suspected preeclampsia are diagnosed when any of the following points are met: new onset of hypertension or exacerbation of preexisting hypertension, positive urine test for urine protein, epigastric or right upper abdominal pain, headache with visual disturbance, fetal growth restriction or abnormal maternal blood tests (e.g., thrombocytopenia or liver and kidney dysfunction) (Li et al., 2021). The clinical management of preeclampsia is a complex task for the following reasons: (A) Complex pathogenic background: preeclampsia is a multifactorial-multi-mechanism-multi-pathway pathogenic syndrome. (B) Complex symptom presentation: The degree and presentation of hypertensive symptoms in preeclamptic patients are complex, and the first symptoms are diverse. In traditional medical diagnosis, physicians can only rely on the information of the target patient as well as their own experience and knowledge base to make judgments, which has some limitations. The machine learning approach, however, can better assist in diagnosis. Termination of pregnancy before 34 weeks of gestation due to pre-eclampsia is de-fined as EOPE, and termination at ≥34 weeks of gestation is defined as LOPE (Raymond and Peterson, 2011). Risk factors associated with PE can be divided into various aspects such as clinical epidemiology, hemodynamics, underlying biochemical factors, and biomarkers in pregnant women. If the high-risk risk factors in the development of PE are clarified and a com-prehensive multifactorial dynamic study is performed, the impact and significance of preeclampsia prediction and prevention are very important.

Tan et al. (2020) established a prediction model for severe maternal outcomes in pregnant women with PE by using a multivariable logistic regression model. The model has a good predictive ability by internal validation. Further external validation is required to clarify the clinical applicability of this model. Beth et al. (2014) developed the miniPIERS risk prediction model to provide a simple, evidence-based tool to identify pregnant women in LMICs at increased risk of death or major hypertensive-related complications. The miniPIERS model shows reasonable ability to identify women at increased risk of adverse maternal outcomes associated with the HDP. Saleh et al. (2021) propose a simple clinical prediction model with good discriminative performance to predict the risk of a composite outcome of PE-related maternal and fetal complications within 7, 14, and 30 days of testing in women with suspected or confirmed PE. The clinical pre-diction models with good identification performance can be used to predict PE-related complications. Ziad et al. (2020) using births from 2011 to 2012, multivariable logistic regression incorporated established maternal risk factors to develop and internally vali-date the WS (Western Sydney) model. The WS model was then externally validated using births from 2013 to 2014, assessing its discrimination and calibration. The model achieved modest performance for prediction of PE in nulliparous women but did not outperform the NICE approach.

Placental growth factor (PlGF), a member of the vascular endothelial growth fac-tor family, is a pro-angiogenic factor serum marker with important functions in regulating placental trophoblast and endothelial cell function (Duhig et al., 2020). PlGF levels are usually measured at the first antenatal visit, 11–13 weeks of gestation, 19–24 weeks of gestation, and 30–34 weeks of gestation as a way to assess the risk of developing preeclampsia. However, the pathogenesis of preeclampsia has not been elucidated, and there is a lack of effective clinical means to prevent it. Its multifactorial predisposition, multiple pathways of pathogenesis and individual differences all determine that a single index is not a good predictor of preeclampsia. Researchers have also combined maternal characteristics and the biomarker PlGF to make relevant predictions. Knudsen et al. (2012) demonstrated the potential of the biomarker PlGF as an aid in the diagnosis of PE: the highest clinical sensitivity was calculated using a threshold value based on the fifth percentile of PlGF concentrations in reference pregnancies within a defined gestational week, and the single biomarker PlGF had the same diagnostic performance compared to the ratio of the two biomarkers, simplifying the test results and reducing costs, with some economic benefits. Black et al. (2020) used the Fetal Medicine Foundation algorithm to combine Maternal own condition, mean arterial pressure, mean uterine artery pulsatility index, and median multiples of PlGF parameters for combined screening of mid-pregnancy PE. Stepan et al. (2020) combined information from ultrasound, mean arterial pressure, clinical features and PlGF to improve the prediction of PE in early pregnancy. Poon et al. (2009) used a logistic regression analysis algorithm combining mean arterial pressure, uterine artery pulsatility index, PAPP-A and PlGF for the prediction of preeclampsia and its subtypes. Mendoza et al. (2021) Combined screening for PE and its subtypes in early pregnancy with physical indicators and biomarkers. Sufriyana et al. (2020) predicted PE by maternal characteristics, uterine motility Doppler measurements, sFlt-1 and PlGF in mid and late pregnancy. sFlt-1 and PlGF in mid- and late-trimester, using machine learning-related algorithms to predict PE.

The aim of this study was to develop and validate a model for predicting the risk of PE for uncomplicated pregnancies. The model can be used at prenatal visits at different gestational weeks to predict whether a pregnant woman is likely to have PE and if so whether she has EOPE or LOPE.

TABLE 1 Classification of PE risk factors.

Category		Factors
Static parameters	Qualitative factors	First birth, multiple births, spontaneous miscarriage history, history of hypertension in pregnancy, history of diabetes mellitus, family history of hypertension, family history of diabetes mellitus, gestational diabetes mellitus, pregestational diabetes mellitus, pregnancy with immune system diseases, pregnancy with hematologic diseases, pregnancy with thyroid diseases
	Quantitative factors	Height, age, preconception body mass index
Dynamic parameters	Epidemiological factors	body mass index during pregnancy
	Hemodynamic factors	Systolic blood pressure (SBP), diastolic blood pressure (DBP), pulse pressure (PP), mean arterial pressure (MAP), pulse waveform area parameters(K), cardiac output (CO), cardiac index (CI), total peripheral resistance (TPR)
	Basic biochemical factors	Hematocrit (HCT), mean platelet volume (MPV), platelet count (PLT), alanine aminotransferase (ALT), aspartate aminotransferase (AST), creatinine (CRE), uric acid (UA)
	Biomarker factors	PlGF

2 Materials and methods

The study data were obtained from clinical epidemiological data, hemodynamic data, data on underlying biochemical data, and biomarker data. Radial artery and fingertip volumetric pulse waveform information collected from 2015 to 2016 at Beijing Haidian District Maternal and Child Health Hospital and from 2006 to 2008 at Beijing Maternity Hospital for detecting gestational weeks of 10–40 weeks. The clinical epidemiological data, hemodynamic data, data on underlying biochemical data, and biomarker data, and PlGF parameter information were collected from July 2015 to 2017 at Peking University People's Hospital for the detection of gestational weeks 10–40 weeks. And PlGF testing was mainly focused on about 15–26 weeks. The study subjects were included in the following conditions: pregnant women were not on long-term oral medication; The fetus was free of malformations.

The study population was 80 pregnant women with EOPE (96 tests), 219 pregnant women with LOPE (371 tests) and 633 pregnant women without HDP (1,351 tests). Pregnant women with EOPE were included in the EOPE group, those with LOPE in the LOPE group, and those without HDP in the control group.

2.1 Model parameter filtering

Risk factors for PE mainly include clinical epidemiological factors, hemodynamic factors, basic biochemical factors and biomarker factors. In order to analyze the correlation dynamics of each model parameter before the construction of the dynamic gestation prediction model of PE, and according to whether the factors themselves change with the gestational age, the risk factors initially screened out are divided into static parameters that do not change with the gestational age and dynamic parameters that change with the gestational age. This is shown in Table 1.

The characteristic parameters of pulse wave were obtained by detecting the pulse wave of radial artery. Radial artery pulse wave detection at the Beijing Obstetrics and Gynecology Hospital was obtained by MP HDP detection instrument developed by Beijing Yes Medical Devices Co., Ltd. The eight-channel PowerLab data acquisition system, LabChart 8 software and strain gauge pressure sensor were used to collect radial artery pulse wave at the Beijing Haidian Maternal and Child Health Hospital. Biochemical parameters were obtained by blood routine examination and biochemical examination. SPSS 23.0 software was used for statistical basic analysis and decision tree was used to construct the predictive model of PE in Jupyter Notebook.

2.1.1 Static parameter filtering

For the screening of static parameters that do not change with the gestational age, the basic information statistics of qualitative and quantitative parameters are used. In order to describe the difference between the parameters in the EOPE group and the LOPE group and the same control group. A chi-square test was performed on 12 qualitative factors. Odds ratio (OR) > 1, indicating that the risk of this factor associated with PE was high, and $p < 0.05$ was statistically significant. While the independent sample t test for three quantitative factors was expressed as mean ± standard deviation, and $p < 0.05$ was statistically significant. The specific analysis of static parameters of pregnant women in the EOPE group, LOPE group and the same control group that do not change with gestational age is shown in Tables 2, 3.

The static parameters of 80 cases of EOPE group and 633 control groups that did not change with gestational age were as follows: multiple pregnancies, history of spontaneous abortion, and history of hypertensive disease during pregnancy were qualitative parameters, and the proportion of all in the EOPE subgroup was higher than that of the control group, OR>1 and $p < 0.05$, indicating that these factors were high-risk and statistically significant; preconception body mass index

TABLE 2 Analysis of factors that do not change with gestational age in EOPE subgroup and control.

Parameter	EOPE subgroup	Control group	OR
Number	80	633	—
First birth	56 (70.0%)	515 (81.4%)	0.535
Multiple births	7 (8.8%)**	4 (0.6%)	15.079
Spontaneous miscarriage history	39 (48.8%)**	141 (22.3%)	3.319
History of hypertension in pregnancy	2 (2.5%)*	1 (0.2%)	16.205
History of diabetes mellitus	2 (2.5%)	10 (1.6%)	1.597
Family history of hypertension	15 (18.8%)	105 (16.6%)	1.160
Family history of diabetes mellitus	2 (2.5%)	32 (5.1%)	0.482
Gestational diabetes mellitus	2 (2.5%)	37 (5.8%)	0.413
Pregestational diabetes mellitus	0	2 (0.3%)	0.997
Pregnancy with immune system diseases	2 (2.5%)	14 (2.2%)	1.134
Pregnancy with hematologic diseases	2 (2.5%)	20 (3.2%)	0.786
Pregnancy with thyroid diseases	2 (2.5%)	30 (4.7%)	0.515
Age	30.650 ± 4.543	30.220 ± 3.742	—
Height(m)	1.618 ± 0.051	1.624 ± 0.048	—
Preconception body mass index	55.734 ± 8.588**	21.140 ± 3.101	—

Notes: *for $p < 0.05$, ** for $p < 0.001$. $p < 0.001$ has significant difference.

TABLE 3 Analysis of factors that do not change with gestational age in LOPE subgroup and control group.

Parameter	LOPE subgroup	Control group	OR
Number	219	633	—
First birth	172 (78.5%)	515 (81.4%)	0.839
Multiple births	12 (5.5%)**	4 (0.6%)	9.116
Spontaneous miscarriage history	90 (41.1%)**	141 (22.3%)	2.434
History of hypertension in pregnancy	6 (2.7%)**	1 (0.2%)	17.803
History of diabetes mellitus	7 (3.2%)	10 (1.6%)	2.057
Family history of hypertension	51 (23.3%)*	105 (16.6%)	1.527
Family history of diabetes mellitus	24 (11.0%)*	32 (5.1%)	2.312
Gestational diabetes mellitus	12 (5.5%)	37 (5.8%)	0.934
Pregestational diabetes mellitus	1 (0.5%)	2 (0.3%)	1.447
Pregnancy with immune system diseases	9 (4.1%)	14 (2.2%)	1.895
Pregnancy with hematologic diseases	2 (0.9%)	20 (3.2%)	0.282
Pregnancy with thyroid disease	8 (3.7%)	30 (4.7%)	0.762
Age	30.350 ± 4.300	30.220 ± 3.742	—
Height(m)	1.619 ± 0.053	1.624 ± 0.048	—
Preconception body mass index	23.239 ± 3.916**	21.140 ± 3.101	—

Notes: *for $p < 0.05$, ** for $p < 0.001$. $p < 0.001$ has significant difference.

was a quantitative parameter, which was significantly higher than that of the control group in the EOPE subgroup, and $p < 0.001$ was statistically significant, as shown in Table 2. Multiple pregnancies, a history of spontaneous miscarriage, a history of hypertensive disorders during pregnancy, and a history of preconception body mass index as static parameters in the EOPE subgroup are consistent with clinical needs and previous studies.

Static parameter analysis of 219 patients in the LOPE group and 633 control groups that did not change with gestational age: multiple pregnancies, natural abortion history, gestational hypertension disease history, hypertension family history, and

diabetes family history, the proportion of the LOPE group was higher than that of the control group. OR >1 and $p < 0.05$ indicated that the risk of factors was high and statistically significant; preconception BMI was a quantitative parameter, which was significantly higher than that of the control group in the LOPE group, and $p < 0.001$ was statistically significant, as shown in Table 3. The inclusion of multiple pregnancies, history of spontaneous abortion, history of hypertensive disease during pregnancy, family history of hypertension, family history of diabetes and preconception body mass index as static parameters of the LOPE subgroup has certain significance from the perspective of clinical and related research (Knudsen et al., 2012; Black et al., 2020; Duhig et al., 2020).

2.1.2 Dynamic parameter filtering

For the screening of dynamic parameters that change with gestational age, the control variable analysis is mainly carried out. This study mainly constructs a dynamic gestational age prediction model, and the selection of dynamic parameters that change with gestational age takes into account the improvement of the dynamic model effect, etc., and the clinical epidemiological factors that change with gestational age mentioned in Table 1 above: gestational body mass index and one of the effective biomarkers (PlGF) These two dynamic parameters, which are relatively small in this study, are directly included in the model, and are also consistent with clinical needs and previous studies (Rantakallio et al., 2021). The purpose of combining hemodynamic factors is that hemodynamic alterations are important factors in the development and progression of preeclampsia in patients with preeclampsia due to various pathophysiological alterations resulting in blood concentration, decreased blood volume, and increased peripheral resistance. Blood pressure is the combined result of the interaction of hemodynamic parameters. SBP and DBP are obtained from clinical history data, and PP indicates that pulse pressure difference is related to both SBP and DBP. MAP is the mean value of arterial blood pressure during a cardiac cycle, CI mainly reflects cardiac function-related conditions, CO is a very important blood flow parameter to assess cardiovascular function, and TPR can measure small vessel spasm.

For a total of 15 parameters of hemodynamic factor(H) and basal biochemical factor(B) in Table 1 that change with gestational age, the control variables were analyzed in two groups, that is, the probability of parameter combination was calculated by logistic regression to control the parameters of other classes within a fixed range, and the two types of parameters were then independently sampled *t*-tested and outliers analyzed at different gestational stages.

Finally, the parameters for inclusion in the prediction model of each dynamic subgroup were finally determined based on the actual needs of clinical and related studies. Finally, the parameters for inclusion in the prediction model of each dynamic subgroup were finally determined based on the actual needs of clinical and related studies. From the perspective of clinical and related research, further group analysis of gestational segments was carried out at 20 weeks and 34 weeks in the first and third trimesters of each group, namely the second-trimester-E group (ST-EG) and the second-trimester-L group (ST-LG), as well as the late-trimester-E group (LT-EG) and the late-trimester-L group (LT-LG) (Meah et al., 2016). If there are multiple tests in the group, the data of the later and earlier detection of the second and late trimesters of pregnancy are taken respectively to focus on the changes in the parameters of the second half of the late trimester and the first half of the late trimester affect whether the final pregnant woman is ill. The sensitivity analysis of the EOEP subgroup and the LOPE subgroup for the H and B parameters of each gestational segment is shown in Tables 4, 5, and the values of each parameter represent the mean of the *t* test of the independent samples.

The results in Tables 4, 5 showed that the H and B parameters of each gestational segment met the conditions of sensitive parameters in the LOPE subgroup, that is, the prediction of disease outcomes was more sensitive, and the platelet count of the EOPE subgroup did not meet the sensitive parameter conditions, possibly because the amount of data in the EOPE subgroup was relatively small and did not reflect significant differences or abnormalities. However, the two are themselves dynamic parameters.

In this study, the H and B parameters are put into the prediction model of each dynamic subgroup. In addition to the model parameters summarized above, the gestational age as a timeline parameter is also directly incorporated into the prediction model to form a dynamic model. Conditions met for sensitive parameters: independent samples *t*-test for parameters, that is, $p < 0.05$ between groups in the disease and control groups or parameters outside the range of normal values.

2.1.3 Final parameters

Through the filtering of dynamic and static parameters, the parameters identified for inclusion in this study are shown in Table 6.

2.2 Machine learning model

The study used an algorithm from decision trees called the Iterative Dichotomiser (ID3) algorithm (Quilan, 1986). The algorithm is a classification prediction algorithm proposed by J. Ross Quinlan at the University of Sydney in 1975. The ID3 algorithm calculates the information gain of each label by selecting the attribute with the highest information gain as the classification criterion for each division, and repeats the process until a perfect decision tree can be generated.

Information entropy is a metric to measure the purity of a sample set. Suppose that the proportion of the class *k* sample in

TABLE 4 Sensitivity analysis of H and B parameters in EOPE subgroup and control group.

Parameter	Group	ETG	ST-EG	ST-LG	LT -EG	LT-LG
SBP	EOPE subgroup	114.438	124.286*	120.000*	118.385*	148.963*#
	Control group	115.547	112.313	109.252	108.252[1]	110.013
DBP	EOPE subgroup	75.438	77.857*	77.316*	75.538*	96.074*#
	Control group	73.795	70.270	68.454	68.034	69.479
PP	EOPE subgroup	39.000	46.429	42.684	42.846	52.889*#
	Control group	41.752	42.043	40.797	40.218	40.534
MAP	EOPE subgroup	91.553	95.680*	93.128*	91.603*	117.952*
	Control group	90.336	86.029	83.583	84.195	84.453
K	EOPE subgroup	0.414#	0.387	0.373	0.385*	0.415*#
	Control group	0.401#	0.380	0.375	0.373	0.403#
CO	EOPE subgroup	4.071	5.286	5.181	5.215	5.273*
	Control group	4.320	4.795	4.876	4.969	4.302
CI	EOPE subgroup	2.573	3.088	3.203	3.174	2.960*
	Control group	2.781	3.048	3.006	3.000	2.547
TPR	EOPE subgroup	1.494#	1.121#	1.112	1.410*#	1.105
	Control group	1.331#	1.136#	1.088	1.079	1.267#
HCT	EOPE subgroup	37.321	38.512*	38.329*	35.985	37.654
	Control group	37.591	35.246	35.197	36.129	36.175
MPV	EOPE subgroup	8.902	9.106	9.692	9.678	10.477*
	Control group	8.986	9.277	9.615	9.664	9.203
PLT	EOPE subgroup	228.482	241.275	192.046	180.378	180.923
	Control group	222.409	221.554	205.166	196.200	199.134
ALT	EOPE subgroup	19.669	20.446	21.886	23.333*	23.500
	Control group	23.786	21.423	22.692	21.814	22.765
AST	EOPE subgroup	21.206	21.964	22.694	23.889*	24.000
	Control group	23.710	22.497	23.175	22.735	23.563
CRE	EOPE subgroup	47.761	62.517	62.098	76.275*	56.395
	Control group	52.227	61.248	65.818	49.743	54.863
UA	EOPE subgroup	212.681	231.447	232.684*	335.053*	276.247
	Control group	200.542	240.577	246.082	228.289	263.255

Notes: * indicates $p < 0.05$ between groups, # indicates outside the normal range.

the sample set D is $p_k\,(k = 1, 2, 3 \ldots |y|)$, then the entropy of the information D is:

$$Ent\,(D) = -\sum_{k=1}^{|y|} p_k log_2 p_k$$

Assuming that the discrete attribute a has v possible values, if a is used to divide the data set D, v branch nodes are generated, wherein the v branch node contains all the samples in D with the value of a^v on the property a, denoted as D^v. According to Equation, the information entropy of D^v is calculated, and the number of samples contained in different branch nodes is taken into account, and the branch nodes are given weights $\frac{|D^v|}{|D|}$, that is, the greater the influence of branch nodes with more sample numbers, so the information gain obtained by dividing sample D by the a attribute is:

$$Gain\,(D, a) = Ent\,(D) - \sum_{v=1}^{V} \frac{|D^v|}{|D|} Ent\,(D^v)$$

The process of the algorithm is as follows:

1) Classification training starts from the root node, calculates the information gain of all possible features, and selects the feature with the largest information gain as the partition feature of the node;
2) Child nodes are established from different values for the feature;
3) Recursive step 1 to step 2 of the child nodes to construct the decision tree;
4) A final decision tree is obtained until no features can be selected or the categories are identical.

TABLE 5 Sensitivity analysis of H and B parameters in LOPE subgroup and control group.

Parameter	Group	ETG	ST-EG	ST-LG	LT-EG	LT-LG
SBP	LOPE subgroup	114.118	120.226*	120.039*	127.897*	136.083*
	Control group	115.575	112.009	109.117	110.067	109.280
DBP	LOPE subgroup	73.647	76.547*	74.471*	80.971*	90.861*#
	Control group	73.856	70.164	68.400	69.537	68.986
PP	LOPE subgroup	40.471	43.679	45.569*	46.926*	45.222*
	Control group	41.719	41.845	40.717	40.530	40.294
MAP	LOPE subgroup	90.119	92.526*	91.526*	98.891*	108.468*
	Control group	90.369	85.847	83.510	84.510	84.928
K	LOPE subgroup	0.407#	0.374	0.379	0.383*	0.387
	Control group	0.401#	0.380	0.375	0.373	0.397
CO	LOPE subgroup	4.313	4.900	5.248	5.424*	5.206*
	Control group	4.322	4.796	4.867	4.968	4.458
CI	LOPE subgroup	2.774	3.183	3.195	3.201*	2.927*
	Control group	2.782	3.055	3.005	3.003	2.627
TPR	LOPE subgroup	1.347#	1.149	1.118	1.152	1.339#
	Control group	1.331#	1.134	1.090	1.080	1.238#
HCT	LOPE subgroup	37.584	36.492*	36.633*	36.976	36.972
	Control group	37.588	35.196	35.173	36.079	36.586
MPV	LOPE subgroup	8.943	9.710*	9.403	9.791	10.297*
	Control group	8.987	9.285	9.600	9.660	9.411
PLT	LOPE subgroup	223.983	201.779*	203.542	193.047	179.028
	Control group	222.049	220.816	205.503	195.800	194.364
ALT	LOPE subgroup	19.394	18.746*	22.673	22.334	23.500
	Control group	23.788	21.506	22.769	21.834	22.888
AST	LOPE subgroup	20.782	19.882*	22.845	23.326	24.000
	Control group	23.708	22.572	23.215	22.754	23.636
CRE	LOPE subgroup	48.396	53.677*	65.454	65.037*	61.924*
	Control group	52.211	61.427	65.848	49.630	55.067
UA	LOPE subgroup	203.576	211.578*	238.838*	304.248*	308.173*
	Control group	200.624	240.662	246.135	228.304	265.950

Notes: * indicates $p < 0.05$ between groups, # indicates outside the normal range.

TABLE 6 Parameters eventually incorporated into the model.

Category	Factors
Static parameters	Multiple births, spontaneous miscarriage history, history of hypertension in pregnancy, history of diabetes mellitus, family history of hypertension, preconception body mass index
Dynamic parameters	gestational week, body mass index during pregnancy, SBP, DBP, PP, MAP, K, CO, CI, TPR, HCT, MPV, PLT, ALT, AST, CRE, UA, and PlGF

TABLE 7 The dataset of the model.

	EOPE	LOPE	Health	Total
Training set	68	255	949	1,272
Test set	28	116	402	546
Total	96	371	1,351	1818

3 Results

The dataset is shown in Table 7. Using 70%/30% random training/test data splitting, repeat this process 20 times and achieve average performance. The model should classify and predict EOPE, LOPE and healthy people.

Precision, recall, and F1-score are used as evaluation indicators for this model. For evaluating performance average across categories, there are two conventional methods, namely macro average and weighted average. Macro averaged performance scores are computed by first computing the scores for the per-category contingency tables and then averaging these per-category scores to compute the global means (Yang et al., 1999). When there is a serious class

TABLE 8 The performance of the model.

	Precision (%)	Recall (%)	F1-score (%)
macro average	76	73	75
weighted average	88	89	89

imbalance in the dataset, the weighted average can be adopted. The performance of the model is shown in Table 8, Overall accuracy of the model is 86%.

4 Discussion

This study describes the importance of predicting PE, and analyzes the status of existing relevant studies comparing risk factors and prediction methods for PE and other deficiencies, thus illustrating the need and importance of this study. This study is mainly based on retrospective analysis and screening of factors that are effective for the risk of developing EOPE as well as LOPE by combining four categories of factors: clinical epidemiological factors, hemodynamic factors, basic biochemical factors and biomarkers. Based on the model parameters obtained from the screening of each subgroup, the decision tree (ID3) algorithm was used to develop dynamic gestational week prediction models for two types of subgroups, EOPE and LOPE, respectively. The core idea of the ID3 algorithm is to measure the selection of attributes in terms of information gain and select the attribute with the greatest information gain after splitting for splitting. The algorithm uses a top-down search to traverse the space of possible decisions. In other words, before dividing each non-leaf node of the decision tree, the information gain of each risk factor incorporated into the model is calculated, and then the risk factor with the greatest information gain is selected for division, because the greater the information gain, the more representative the risk factor is, and the stronger the algorithm's ability to identify early-onset pre-eclampsia. The model structure was optimized and simplified to enhance the clinical applicability of the model in order to achieve detailed and effective prediction using a simpler dynamic periconceptional subgroup model.

There are still many ways to predict PE Carhillon et al. (2005). Showed that measuring umbilical artery flow parameters such as peak systolic velocity/end diastolic (S/D), beat index, and resistance index can predict the occurrence of PE. In urine, there are studies on the use of urine proteomics for the diagnosis and screening of PE (Carty et al., 2011). Proteomic analysis of the cerebrospinal fluid can accurately determine the severity of PE (Norwitz et al., 2011). sFlt-1 is an anti-angiogenic factor serum marker that downregulates and inhibits the bioactivity of PIGF in promoting placental vascular growth. sFlt-1/PlGF ratio is a good predictive value and diagnostic guide for PE when measured jointly by Bian et al. (2019). However, single prediction is one-sided and unstable, Cnossen et al. (2008) performed a separate study of uterine artery Doppler and the results were low for PE-related subtypes The predictive value of PE-related subtypes was low.

In this study, a multifactorial PE subgroup analysis was performed by combining four categories of clinical epidemiological factors, hemodynamic factors, basal biochemical factors and biomarkers, reclassified according to whether they varied with gestational week. Among them, the biomarker PlGF was tested and compared and had a more significant predictive role and value for the EOPE subgroup. The biomarker is an important dynamic parameter, and the current testing gestational weeks of PlGF in this subject are mainly distributed in 15–26 weeks, with less data on testing samples in the rest of the gestational weeks. In order to improve the quality and effectiveness of the full gestational week data model, the clinical data of full gestational week testing of the biomarker PlGF need to be supplemented in the future. The data in this study are based on retrospective analysis and have limitations such as the type of data. To achieve reliable prediction and enhance clinical application, prospective and multicenter studies are needed to demonstrate the clinical utility of predictive parameters.

5 Conclusion

In this study, a multifactorial approach was used for the prediction of dynamic PE-related subgroups, and the model was further refined and incorporated the dynamic timeline parameter "gestational week" for overall dynamic gestational week prediction. It is simpler and more convenient for clinical application, and the model parameters and structure are optimized to achieve effective PE subgroup prediction. This study's model and method for the prediction of PE integrated dynamic gestational week subgroups is of great significance in giving targeted clinical predictions and recommendations for improving maternal and infant conditions.

Data availability statement

The original contributions presented in the study are included in the article/supplementary material, further inquiries can be directed to the corresponding author.

Ethics statement

The studies involving human participants were reviewed and approved by Ethics Committee of Beijing University of Technology. The patients/participants provided their written informed consent to participate in this study. Written informed consent was obtained from the individual(s) for the publication of any potentially identifiable images or data included in this article.

Author contributions

Conceptualization, LY, GS, and QX; methodology, ZL and GS; software, ZL; validation, RJ, YY, and XL; formal analysis, QX; investigation, XZ and CL; resources, GL; data cura-tion, GS and QX; writing—original draft preparation, ZL; writing—review and editing, LY; supervision, LY, RJ, and GL; project administration, DH and SZ; funding acquisition, DH and SZ. All authors have read and agreed to the published version of the manuscript.

Funding

This research was funded by the National Key R&D Program of China (2019YFC0119700), National Natural Science Foundation of China (U20A201163).

Conflict of interest

The authors declare that the research was conducted in the absence of any commercial or financial relationships that could be construed as a potential conflict of interest.

Publisher's note

All claims expressed in this article are solely those of the authors and do not necessarily represent those of their affiliated organizations, or those of the publisher, the editors and the reviewers. Any product that may be evaluated in this article, or claim that may be made by its manufacturer, is not guaranteed or endorsed by the publisher.

References

Beth, A., Jennifer, A., Ansermino, J. M., Hall, D. R., Bhutta, Z. A., Bhutta, S. Z., et al. (2014). A risk prediction model for the assessment and triage of women with hypertensive disorders of pregnancy in low-resourced settings: The miniPIERS (Pre-eclampsia integrated estimate of RiSk) multi-country prospective cohort study. *PLoS Med.* 11, 10015899–e1001613. doi:10.1371/journal.pmed.1001589

Bian, X., Biswas, A., Huang, X., Lee, K. J., Li, T. K. T., Masuyama, H., et al. (2019). Short-term prediction of adverse outcomes using the sFlt-1 (soluble fms-like tyrosine kinase 1)/PlGF (placental growth factor) ratio in asian women with suspected preeclampsia. *Hypertension* 74, 164–172. doi:10.1161/HYPERTENSIONAHA.119.12760

Black, C., Rolnik, D., Al-Amin, A., Kane, S. C., Stolarek, C., White, A., et al. (2020). Prediction of preterm pre-eclampsia at midpregnancy using a multivariable screening algorithm. *Aust. N. Z. J. Obstet. Gynaecol.* 60, 675–682. doi:10.1111/ajo.13113

Carhillon, L., Ziol, M., Challier, J. C., Perrot, N., Uzan, M., Prevot, S., et al. (2005). Doppler and immunohistochemical evaluation of decidual spiral arteries in early pregnancy. *Gynecol. Obstet. Invest.* 59, 24–28. doi:10.1159/000080671

Carty, D., Siwy, J., Brennand, J., Zurbig, P., Mullen, W., Franke, J., et al. (2011). Urinary proteomics for prediction of preeclampsia. *Hypertension* 57, 561–569. doi:10.1161/HYPERTENSIONAHA.110.164285

Cnossen, J., Morris, R., Ter, G., Mol, B. W. J., van der Post, J. A. M., Coomarasamy, A., et al. (2008). Use of uterine artery Doppler ultrasonography to predict preeclampsia and intrauterine growth restriction: A systematic review and bivariable meta-analysis. *Can. Med. Assoc. J.* 178, 701–711. doi:10.1503/cmaj.070430

Duhig, K., Webster, L., Sharp, A., Gill, C., Seed, P. T., Shennan, A. H., et al. (2020). Diagnostic accuracy of repeat placental growth factor measurements in women with suspected preeclampsia: A case series study. *Acta Obstet. Gynecol. Scand.* 99, 994–1002. doi:10.1111/aogs.13818

Duhig, K. E., Myers, J., Seed, P. T., Sparkes, J., Lowe, J., Hunter, R. M., et al. (2019). Placental growth factor testing to assess women with suspected pre-eclampsia: A multicentre, pragmatic, stepped-wedge cluster-randomised controlledtrial. *Lancet* 393, 1807–1818. doi:10.1016/S0140-6736(18)33212-4

Knudsen, U., Kronborg, C., von Dadelszen, P., Kupfer, K., Lee, S. W., Vittinghus, E., et al. (2012). A single rapid point-of-care placental growth factor determination as an aid in the diagnosis of preeclampsia. *Pregnancy Hypertens.* 2, 8–15. doi:10.1016/j.preghy.2011.08.117

Li, F., Qin, J., Zhang, S., and Chen, L. (2021). Prevalence of hypertensive disorders in pregnancy in China: A systematic review and meta-analysis. *Pregnancy Hypertens.* 24, 13–21. doi:10.1016/j.preghy.2021.02.001

Mahendra, V., Clark, S., and Suresh, M. S. (2021). Neuropathophysiology of preeclampsia and eclampsia: A review of cerebral hemodynamic principles in hypertensive disorders of pregnancy. *Pregnancy Hypertens.* 23, 104–111. doi:10.1016/j.preghy.2020.10.013

Meah, L., Cockcroft, J., Backx, K., Shave, R., and Stohr, E. J. (2016). Cardiac output and related haemodynamics during pregnancy: A series of meta-analyses. *Heart* 102, 518–526. doi:10.1136/heartjnl-2015-308476

Mendoza, M., Garcia-Manau, P., Arevalo, S., Aviles, M., Serrano, B., Sanchez-Duran, M. A., et al. (2021). Diagnostic accuracy of first-trimester combined screening for early-onset and preterm pre-eclampsia at 8-10 compared with 11-13 weeks' gestation. *Ultrasound Obstet. Gynecol.* 57, 84–90. doi:10.1002/uog.22071

Norwitz, E., Tsen, L., Park, J., Fitzpatrick, P. A., Dorfman, D. M., Saade, G. R., et al. (2011). Discriminatory proteomic biomarker analysis identifies free hemoglobin in the cerebrospinal fluid of women with severe preeclampsia. *Am. J. Obstet. Gynecol.* 193, 957–964. doi:10.1016/j.ajog.2005.06.055

Poon, L., Kametas, N., Maiz, N., Akolekar, R., and Nicolaides, K. H. (2009). First-trimester prediction of hypertensive disorders in pregnancy. *Hypertension* 53, 812–818. doi:10.1161/HYPERTENSIONAHA.108.127977

Quilan, J. (1986). Induction of decision trees. *Mach. Learn.* 4, 81–106. doi:10.1007/bf00116251

Rantakallio, J., Nevalainen, J., West, S. I., Ollila, M. M., Puukka, K., Bloigu, A. H., et al. (2021). Association of self-reported polycystic ovary syndrome, obesity, and weight gain from adolescence to adulthood with hypertensive disorders of pregnancy: A community-based approach. *Hypertension* 77, 1010–1019. doi:10.1161/HYPERTENSIONAHA.120.15702

Raymond, D., and Peterson, E. (2011). A critical review of early-onset and late-onset preeclampsia. *Obstet. Gynecol. Surv.* 66, 497–506. doi:10.1097/OGX.0b013e3182331028

Saleh, L., Alblas, M. M., Nieboer, D., Neuman, R. I., Vergouwe, Y., Brusse, I. A., et al. (2021). Prediction of pre-eclampsia-related complications in women with suspected or confirmed pre-eclampsia: Development and internal validation of clinical prediction model. *Ultrasound Obstet. Gynecol.* 58, 698–704. doi:10.1002/uog.23142

Stepan, H., Hund, M., and Andraczek, T. (2020). Combining biomarkers to predict pregnancy complications and redefine preeclampsia the angiogenic-placental syndrome. *Hypertension* 75, 918–926. doi:10.1161/HYPERTENSIONAHA.119.13763

Sufriyana, H., Wu, Y., and Su, E. (2020). Prediction of preeclampsia and intrauterine growth restriction: Development of machine learning models on a prospective cohort. *JMIR Med. Inf.* 8, 15411. doi:10.2196/15411

Tan, J., Yang, M., Liao, Y., Qi, Y., Ren, Y., Liu, C., et al. (2020). Development and validation of a prediction model on severe maternal, outcomes among pregnant women with pre-eclampsia: A 10-year cohort study. *Sci. Rep.* 10, 15590. doi:10.1038/s41598-020-72527-0

Yang, Y., Fischer, P., Leu, S. J., Zhu, M., Woods, V. L., Jr, and Chen, P. P. (1999). Possible presence of enhancing antibodies in idiopathic thrombocytopenic purpura. *Br. J. Haematol.* 1, 69–80. doi:10.1046/j.1365-2141.1999.01144.x

Ziad, T., Malcolm, H., Jenkins, G., Mahmoud, I., Ray, J. G., Askie, L. M., et al. (2020). Prediction of pre-eclampsia in nulliparous women using routinely collected maternal characteristics: A model development and validation study. *BMC Pregnancy Childbirth* 20, 23–14. doi:10.1186/s12884-019-2712-x

frontiers | Frontiers in Physiology

TYPE Original Research
PUBLISHED 26 October 2022
DOI 10.3389/fphys.2022.1028907

OPEN ACCESS

EDITED BY
Dingchang Zheng,
Coventry University, United Kingdom

REVIEWED BY
Jing Guo,
Guangdong University of Technology, China
Le Sun,
Nanjing University of Information Science and Technology, China

*CORRESPONDENCE
Shuying Zhao,
zhaoshuying@ise.neu.edu.cn

SPECIALTY SECTION
This article was submitted to Computational Physiology and Medicine, a section of the journal Frontiers in Physiology

RECEIVED 26 August 2022
ACCEPTED 07 October 2022
PUBLISHED 26 October 2022

CITATION
Chen J, Zhao S, Meng H, Cheng X and Tan W (2022), An interactive game for rehabilitation based on real-time hand gesture recognition.
Front. Physiol. 13:1028907.
doi: 10.3389/fphys.2022.1028907

An interactive game for rehabilitation based on real-time hand gesture recognition

Jiang Chen[1], Shuying Zhao[1]*, Huaning Meng[1], Xu Cheng[2] and Wenjun Tan[3]

[1]College of Information Science and Engineering, Northeastern University, Shenyang, China, [2]College of Economics and Management, Shenyang Agricultural University, Shenyang, China, [3]Key Laboratory of Intelligent Computing in Medical Image, Ministry of Education, Northeastern University, Shenyang, China

Currently, cardiovascular and cerebrovascular diseases have become serious global health problems related to their high incidence and fatality rate. Some patients with cardiovascular cerebro-cardiovascular diseases even may face motor or cognitive dysfunction after surgery. In recent years, human–computer interactive systems with artificial intelligence have become an important part of human well-being because they enable novel forms of rehabilitation therapies. We propose an interactive game utilizing real-time skeleton-based hand gesture recognition, which aims to assist rehabilitation exercises by improving the hand-eye coordination of the patients during a game-like experience. For this purpose, we propose a lightweight residual graph convolutional architecture for hand gesture recognition. Furthermore, we designed the whole system using the proposed gesture recognition module and some third-party modules. Finally, some participants were invited to test our system and most of them showed an improvement in their passing rate of the game during the test process.

KEYWORDS

hand gesture recognition, graph convolutional network, residual mechanism, rehabilitation, human–computer interaction

1 Introduction

We have previously reported research in the field of tech-assisted rehabilitation (Liu et al., 2019; Tan et al., 2021; Sun and Wu, 2022). Cardiovascular and cerebrovascular diseases have become serious global health problems because of their high incidence and fatality rate. Cardiovascular disease is the leading cause of death, accounting for about 34% of all deaths worldwide (Anteneh et al., 2021), followed by stroke, a typical cerebrovascular disease, accounting for 11.6% (Kisa et al., 2021). Even after treatment, both cardiovascular and cerebrovascular disease may lead to motor or cognitive dysfunction, which needs a long period of rehabilitation (Berthier, 2005; Pattanshetty et al., 2015). Aerobic and strength training programs can improve cognitive performance even during the chronic stroke phase (Oberlin et al., 2017). For patients, a rehabilitation process combining motor and cognitive training

has the potential to enhance their chance of recovery and rebuild their ability to take care of themselves.

In the last few years, an increasing trend in the innovation of rehabilitation methods using new technology to make rehabilitation processes more efficient has emerged. A good rehabilitation method should be user-friendly and interesting, so that patients may engage in the process and have a good time. Human–computer interactive systems free the patients from having to travel to rehabilitation clinics and offer them an opportunity to do these exercises at home. Because patients might perform the exercises casually or incorrectly in a home-based environment, many advances in technology have been leveraged to make the process more immersive, such as 3D gaming (Nasri et al., 2020) and virtual reality (VR) (Rincon et al., 2016).

This article proposes an interactive game controlled by 10 hand gestures for people, who suffer from limitations in daily life caused by aging or a health condition and thus want to strengthen their hand–eye coordination or do brain exercises. Our contributions can be summarized as follows:

- A rehabilitation game that leverages artificial intelligence (AI) (hand gesture recognition and character recognition).
- A network architecture for real-time skeleton-based hand gesture recognition.

The article is organized as follows: Section 2 reviews the state-of-the-art rehabilitation methods with technological assistance and hand gesture recognition approaches. Section 3 describes the details of the interactive game. This section also describes the network architecture and introduces the whole system we designed to keep the application more reliable. Section 4 presents more details about the experimental process and the results obtained. In Section 5, we report the study conclusions and provide future research directions.

2 Related work

2.1 Rehabilitation system

Conventional rehabilitation utilizes methods including the mini-mental state examination (MMSE), neurobehavioral cognitive status examination, Loewenstein occupation therapy cognitive assessment, and Wechsler memory scale to train and evaluate rehabilitation. Some of these use real cards to train the patients and often ask them to choose the correct card or sort them in order. These approaches require a long intervention cycle and are difficult for patients to maintain good exercise independence for a long time.

With the development of computer technology, the PC has become an auxiliary tool in cognitive rehabilitation training. In the beginning, it only used simple interactive logic to guide patients through rehabilitation (Hofmann et al., 1996a). In 1996, Hofmann's team introduced computer graphics into cognitive training (Hofmann et al., 1996b), making the program more interactive with colored images. The rapid development of computer graphics and human–computer interactions has led to more visual and audio usage in rehabilitation systems. The newest rehabilitation methods leverage AI and VR technology. A system with AI can recognize a patient's behavior, such as hand gestures through vision or sensor data, which makes human–computer interactions more natural and convenient. Relatively, a system with VR allows patients to do rehabilitation exercises in any location, with an insignificant difference from the real world.

2.2 Hand gesture recognition

According to the type of input, methods of hand gesture recognition can be classified into two categories: image-based methods and hand skeleton-based methods. The former adopts image sequences, whereas the latter uses sequences of hand joints as input. Compared with image-based methods, hand skeleton-based methods relieve the difficulty in recognizing a cluttered background, and requires lower computation cost, thus enabling real-time hand gesture recognition to be installed on small devices (Zhang et al., 2020). However, a skeleton-based approach needs additional tools to extract the hand skeleton accurately.

According to the method used to extract features, hand gesture recognition methods can also be classified into two categories: hand-crafted feature-based methods and end-to-end-based methods. The former encodes the input data into handcrafted features, such as joint angle similarities (Ohn-Bar and Trivedi, 2013) and time sequence similarity (Plouffe and Cretu, 2016). The former encodes the sequences of joints into embedding vectors and often feeds them into deep-learning architecture, like recurrent neural networks (RNNs) or convolutional neural networks (CNNs), to extract deep features. Graph convolutional network (GCN) also has an important role in skeleton-based hand gesture recognition. Many studies have demonstrated the effectiveness of GCN using the skeleton as a graph structure (Yan et al., 2018; Zhang et al., 2020).

3 Methods and materials

3.1 Graph convolutional network architecture

Because the input data were acquired as a sequence of 21 hand joints, which is a natural graph structure, we chose

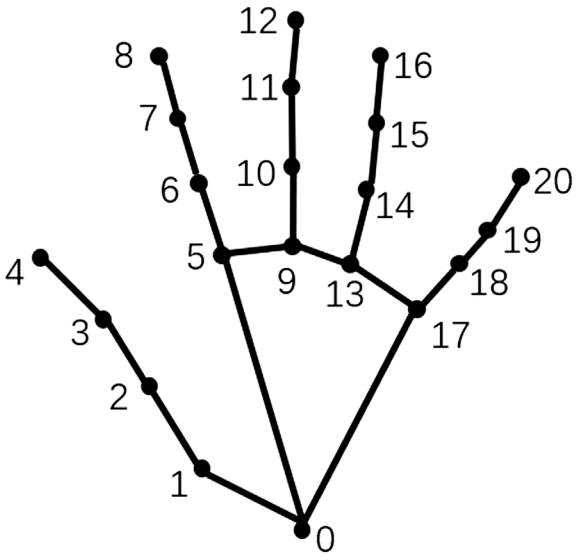

FIGURE 1
The hand skeleton graph. The nodes denote the hand joints and the edges denote the connections.

to work with a graph convolutional network. For each hand with N joints, we defined a skeleton graph $G(V, E)$, where $V = \{v_i | i = 0, 1, \ldots, N-1\}$ is the set of nodes (v_i denotes the j-th joint) and $E = \{e_{i,j} | i, j \in V\}$ is the set of edges. In our system, we set $N = 21$.

The topological relationship of nodes in the hand skeleton graph is illustrated in Figure 1. The edge-connecting nodes v_i and v_j mean node v_i and v_j have connected joints in the hand skeleton tree. It also means that nodes v_i and v_j are adjacent. The graph convolution propagation rule of the graph G can be described with the following formula:

$$\boldsymbol{F}^{(l+1)} = \boldsymbol{\sigma}\left(\boldsymbol{A}^{s}\boldsymbol{W}_{s}^{(l)}\boldsymbol{F}^{(l)}\right), \boldsymbol{A}^{s} = \boldsymbol{D}_{s}^{-1/2}\boldsymbol{A}^{s}\boldsymbol{D}_{s}^{-1/2}, \quad (1)$$

where $\mathbf{A}^{s}$ is the normalized adjacent matrix of G, $\mathbf{W}_{s}^{(l)}$ of the size $C_{\text{out}} \times C_{\text{in}} \times 1 \times 1$ is a weight matrix to be trained (Cout and Cin are the numbers of input and output channels), $\mathbf{F}^{(l)}$ denotes the output of the l-th layer, $\sigma(\cdot)$ is the activation function of the graph convolutional layer, and $\mathbf{D}_{s}$ is the degree matrix of $\mathbf{A}^{s}$.

Before sending the data into the model, we preprocessed the data by setting the origin of the coordinates in the palm (midpoint between v_0 and v_9), making the data more evenly distributed. To prevent overfitting, the input hand data are randomly rotated as a data augmentation approach. The rotation angle $\theta \sim N(0, \pi/10)$.

Figure 2 illustrates our proposed neural network architecture for hand gesture recognition. In this model, we implemented one graph convolutional layer with 64 channels to transform the input 3-channel data into a 64-channel vector. This was followed by two graph convolutional units with the residual mechanism, which requires making a straight connection between the input and output of every unit (Figure 2). This is effective at resolving gradient disappearance. Each unit has two layers of graph convolution with 64 channels of output. Finally, we fed the feature vector into a graph convolutional layer with 10 channels to match the number of gesture categories. We used softmax to calculate the probability of each class. The architecture described is shown in Figure 2.

3.2 Rehabilitation game experience

We created an interactive game controlled by hand gestures. This game utilizes a camera to recognize the hand behavior of the player and motivate the player to do air writing. It provides a hand–brain combined exercise and facilitates the rehabilitation process.

At the beginning of the game, two hand gestures were given by the computer to control an invisible pen to draw in the air (by generating a line or undoing a line). The player is required to control the pen correctly to complete a Chinese character. The system displays the player's finger movements as they write and show the recognition result after they finish handwriting (Figure 3).

3.3 Design of the rehabilitation system

The system obtains visual images from the computer camera and communicates with users through an interface. The backend of the system is composed of a hand joint

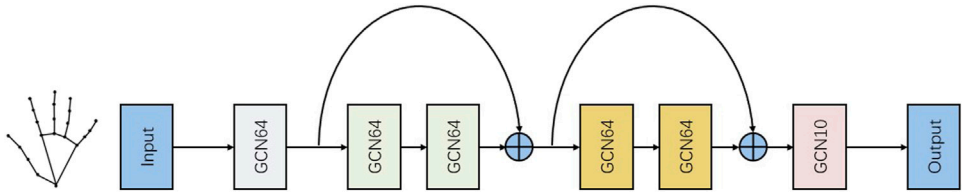

FIGURE 2
Illustration of our graph convolutional network architecture. The input is the coordinates of 21 hand joints. The two side paths that both bypass two 64-channel GCN, bring residual mechanism to our architecture.

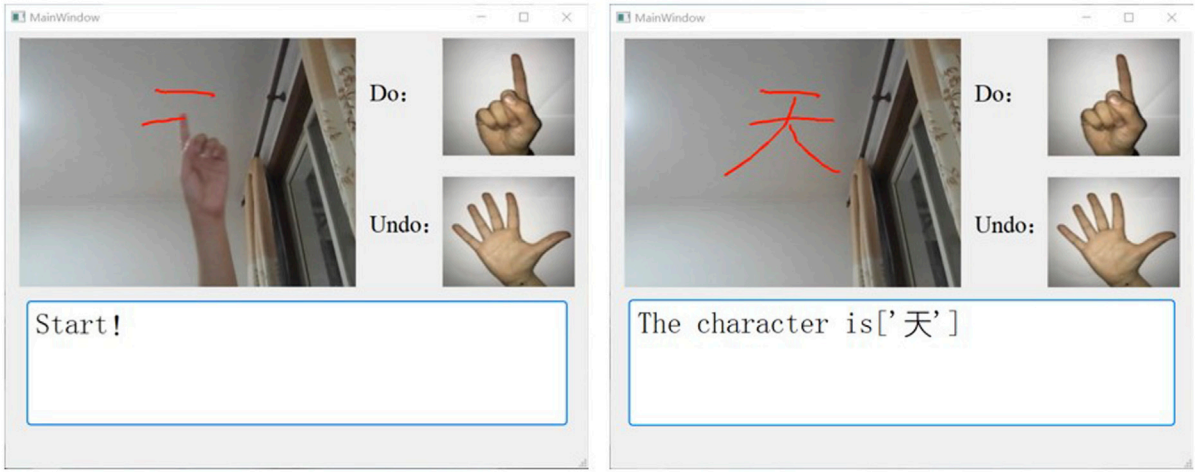

FIGURE 3
Illustration of one example of the rehabilitation game experience. **(A)** shows the process of writing in the air. **(B)** shows the result of the character recognition.

detection module, a gesture recognition module, a trajectory processing module, and a character recognition module. The visual image is first sent to the hand joint detection module and transformed into 3D coordinates of 21 hand joints. Then, the gesture recognition module identifies the specific gesture category. The trajectory processing module controls the generation of handwriting according to the hand behavior of the player. After that, it also performs Bezier smoothing and then passes the image with the completed character to the next module. Finally, the character recognition module recognizes the image with the character and delivers them back to the interactive interface, which will guide the player to interact further *via* the camera. The system described is shown in Figure 4.

4 Experiments and results

In this section, we evaluate the performance of our model for skeleton-based action recognition. We used the American Sign Language Digits Dataset (Mavi, 2020) in our experiments. This consists of 2062 RGB pictures labeled by 10 gesture classes (from gesture "0" to "9"). These pictures are taken from 218 different students, making the hand features to be learned more diverse. We implemented a 5-fold cross-validation technique in our experiments, and they were conducted *via* a GeForce GTX 1650 GPU. Some examples of the dataset images are shown in Figure 5.

We used cross-entropy as a loss function. The models were learned using a stochastic gradient descent with a learning rate of

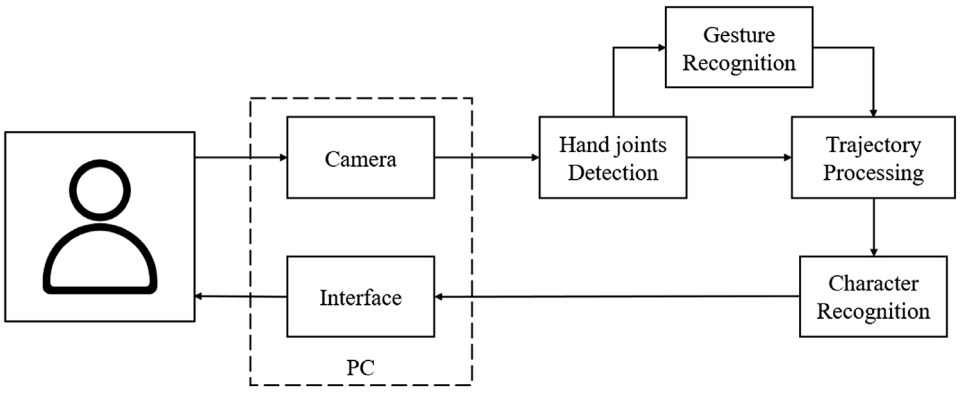

FIGURE 4
Designed diagram of the proposed system. Each block denotes a single module in our system. The two modules in the dotted box belong to a PC.

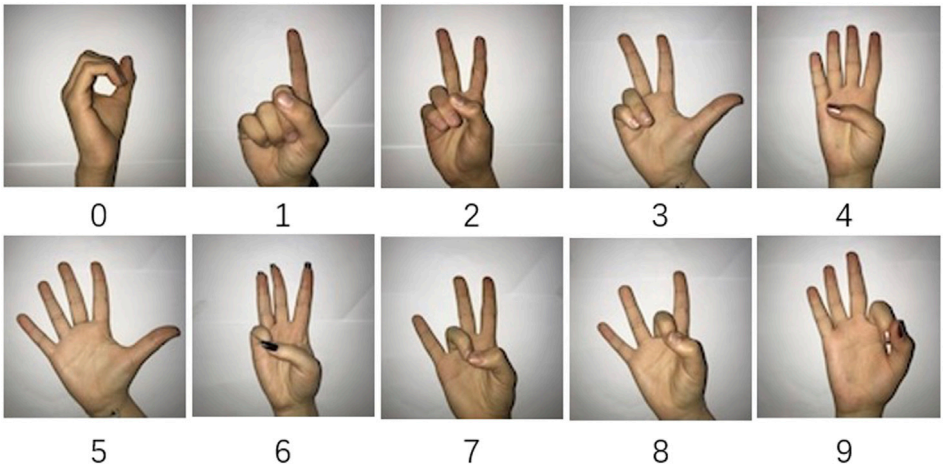

FIGURE 5
Samples of the dataset. It consists of 2062 RGB pictures labeled by 10 gesture classes (from gesture "0" to "9").

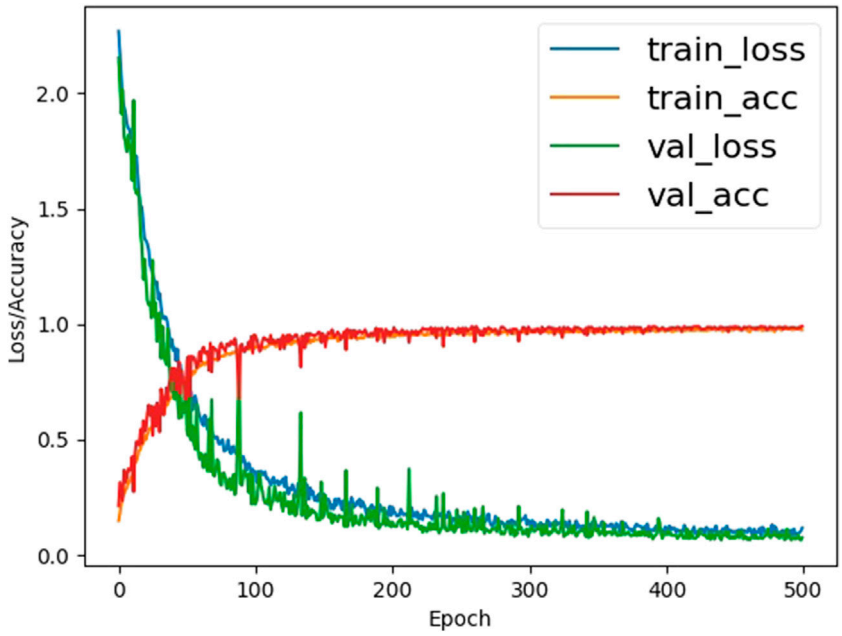

FIGURE 6
Loss and accuracy graph of the training process. The horizontal axis represents epoch and the vertical axis represents loss and accuracy value.

0.001. We decayed the learning rate to 0.9 after every 30 epochs. To restrain extreme weights, we implemented L1 regularization with a parameter of 5e-3 and a weight decay (L2 regularization) with a parameter of 1e-4.

Our cross-validation strategy is as follows: in each round, we used 4 folds of data for training and 1 fold of data for validation. This process lasts for 5 rounds during each epoch to ensure every fold is chosen as validation data at least once. In this case, the loss and accuracy of one epoch are calculated as the average loss and accuracy of 5 rounds. The model is trained for 500 epochs. During the training period, both the train loss and validation loss decrease continuously, indicating the network is trained properly. After about 200 epochs, the loss value becomes stable. The validation accuracy peaked at 99.03%, with an insignificant difference in training

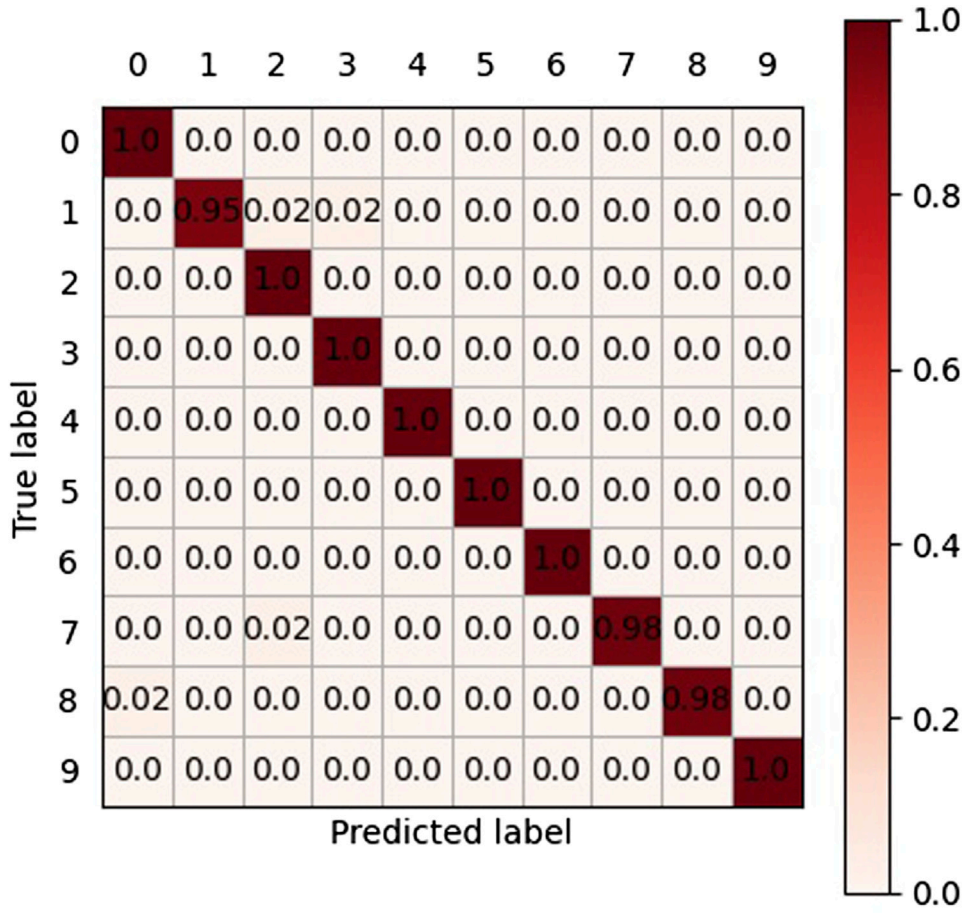

FIGURE 7
Chaotic matrix of all the samples in the test experiment. The diagonal values of the matrix are the rates of correct classifications, while the non-diagonal values are the rates of wrong classifications.

accuracy (Figure 6). As shown in the confusion matrix (Figure 7) we recorded, the system was reasonably capable of classifying different hand gestures from "0" to "9."

An ablation experiment was performed to better show the effect of the residual mechanism in our architecture (Table 1). The difference between the Naive model and Residual model was whether there was a forward path from the input to the output of each graph convolution unit. The FPS indicates how many frames can be processed per second. According to the results, the residual module improved the recognition accuracy by 1% while maintaining a fast processing speed and a small size. The architecture is relatively lightweight because the prediction cost of each gesture is about 6 ms and the size of the model is only 72.5 KB. This enables the game to support many small devices, which usually do not have enough memory, and to calculate the performance required to support an AI application.

TABLE 1 Ablation study.

Methods	Acc (%)	FPS (/s)	Size (KB)
Naive model	98.03	178.51	72.50
+ Residual	99.03	178.32	72.50

TABLE 2 Comparisons with state-of-the-art models.

Model	Acc (%)	Size
CNN (Mavi, 2020)	98.00	17.2 MB
MobileNetV2 (Dayal et al., 2021)	98.50	8.5 MB
CNN (Dayal et al., 2021)	99.10	4 MB
Ours	99.03	72.5 KB

TABLE 3 Passing rates and opinions of participants.

	Passing rate (%)					Opinion
	Round 1	Round 2	Round 3	Round 4	Round 5	
Subject 1	0.58	0.58	0.75	0.67	0.75	Handwriting in the air is difficult
Subject 2	0.50	0.50	0.58	0.58	0.50	The word recognition seems not to work well
Subject 3	0.75	0.67	0.67	0.75	0.92	It is difficult to control the pen trajectory as I want
Subject 4	0.58	0.50	0.75	0.67	0.67	It is interesting

Comparisons have been made between our model and other state-of-the-art models (Table 2). The first CNN (Mavi, 2020) is a convolution network with more convolution layers than MVGG-5 and less than MVGG-9 architecture. MobileNetV2 (Dayal et al., 2021) is a state-of-the-art lightweight CNN. The second CNN (Dayal et al., 2021) is a memory-efficient convolution network based on a bottleneck module, specifically designed for edge computing systems. According to Table 2, using the same dataset, the accuracy of our model is comparable to state-of-the-art models, although our model has a significant advantage in model size.

The system has been tested by four participants. All subjects were given instructions before playing and were allowed to play several rounds to become familiar with the rules. The participants were required to write 12 characters correctly in each round of the test by using their hand behavior in front of the system camera. They needed to write the indicated character as clearly as possible to ensure it could be recognized by the word recognition module. There were several minutes of rest between every two rounds. Their passing rates in each round and their opinions on the game experience are recorded in Table 3. According to the results, most of the subjects showed an improvement in the passing rate during five rounds of testing. However, it seems to be hard to reach a passing rate of 100% because of difficulty in writing in the air and some problems in the third-party word recognition module, which can be substituted and improved. Despite this, all the subjects agreed that the game experience was smooth and interesting.

5 Conclusion

This work proposes an interactive game and a human–computer interaction system for rehabilitation usage. We also propose a new residual graph convolution structure for skeleton-based gesture recognition. The model was trained for the recognition of 10 static hand gestures and was evaluated after the experiments. The system achieved 99.03% validation accuracy and maintained a relatively small size of 72.5 KB. The experimental results demonstrated that our model was sufficiently accurate as a gesture recognition system and that the game has the potential to be extended for rehabilitation usage. Four participants were invited to test this interactive game, and most subjects showed an improvement and interest during the test.

We should consider more motivational rewards and better hand gesture recognition models for the rehabilitation game. Additionally, the interactive process should be enhanced to be more smooth and interesting.

Data availability statement

Publicly available datasets were analyzed in this study. These data can be found at: https://github.com/ardamavi/Sign-Language-Digits-Dataset/.

Author contributions

Authors contributed as follows: study conception, JC; application conception, SZ; study supervision and funding acquisition, SZ and WT; methodology, JC; software, JC and HM; validation, HM; investigation, JC and WT; resources, SZ and WT; writing of the original draft, JC; review and editing, XC; visualization, JC. All authors have read and agreed to the published version of the manuscript.

Funding

This work was supported by the National Natural Science Foundation of China (61971118 and 71902121), Science and Technology Plan of Liaoning Province (2021JH1/10400051), and Fundamental Research Funds for the Central Universities (N2216014).)

Acknowledgments

In the process of experiment and writing, the contributors get a lot of writing suggestions and work guidance from editors and readers, which helps us to make the content more rigorous and

easier to understand. Here, we would like to express our most sincere thanks to you.

Conflict of interest

The authors declare that the research was conducted in the absence of any commercial or financial relationships that could be construed as a potential conflict of interest.

Publisher's note

References

Anteneh, Z., Lorkowski, S., and Banik, P. (2021). Global burden of cardiovascular diseases and risk factors, 1990–2019: Update from the GBD 2019 study. *J. Am. Coll. Cardiol.* 76 (25), 2982–3021. doi:10.1016/j.jacc.2020.11.010

Berthier, M. (2005). Poststroke aphasia: Epidemiology, pathophysiology and treatment. *Drugs Aging* 22, 163–182. doi:10.2165/00002512-200522020-00006

Dayal, A., Paluru, N., Cenkeramaddi, L. R., Soumya, J., and Yalavarthy, P. (2021). Design and implementation of deep learning based contactless authentication system using hand gestures. *Electronics* 10, 182. doi:10.3390/electronics10020182

Hofmann, M., Hock, C., Kühler, A., MüllerSpahn, F., and Kuhler, A. (1996a). Interactive computer-based cognitive training in patients with alzheimer's disease. *J. Psychiatr. Res.* 30 (6), 493–501. doi:10.1016/s0022-3956(96)00036-2

Hofmann, M., Hock, C., and Müller-Spahn, F. (1996b). Computer-based cognitive training in Alzheimer's disease patients. *Ann. N. Y. Acad. Sci.* 777, 249–254. doi:10.1111/j.1749-6632.1996.tb34427.x

Kisa, A., Kisa, S., Collaborators, G. B. D., Oancea, B., Abu-Zaid, A., and Samy, A. (2021). Global, regional, and national burden of stroke and its risk factors, 1990–2019: A systematic analysis for the global burden of disease study 2019. *Lancet Neurology* 20(10), 795-820. doi:10.1016/S1474-4422(21)00252-0

Liu, Y., Tan, W., Chen, C., Liu, C., Yang, J., and Zhang, Y. (2019). A review of the application of virtual reality technology in the diagnosis and treatment of cognitive impairment. *Front. Aging Neurosci.* 11, 280. doi:10.3389/fnagi.2019.00280

Mavi, A. (2020). A new dataset and proposed convolutional neural network architecture for classification of American Sign Language Digits. arXiv: 2011.08927 [cs.CV] https://arxiv.org/abs/2011.08927.

Nasri, N., Ortsescolano, S., and Cazorla, M. (2020). An semg-controlled 3d game for rehabilitation therapies: Real-time time hand gesture recognition using deep learning techniques. *Sensors* 20, E6451. doi:10.3390/s20226451

Oberlin, L. E., Waiwood, A. M., Cumming, T. B., Marsland, A. L., Bernhardt, J., and Erickson, K. I. (2017). Effects of physical activity on poststroke cognitive function: A meta-analysis of randomized controlled trials. *Stroke* 48 (11), 3093–3100. doi:10.1161/STROKEAHA.117.017319

Ohn-Bar, E., and Trivedi, M. M. (2013). "Joint angles similarities and HOG2 for action recognition." In Proceedings of the 2013 IEEE Conference on Computer Vision and Pattern Recognition Workshops. IEEE, Portland, OR, USA, doi:10.1109/CVPRW.2013.76

Pattanshetty, D., Cook, D., Malik, S., and Dunlap, M. (2015). Patients with HF show high degrees of moderate to severe cognitive impairment despite normal MMSE testing. *J. Cardiac Fail.* 21, S3–S4. doi:10.1016/j.cardfail.2015.06.053

Plouffe, G., and Cretu, A. M. (2016). Static and dynamic hand gesture recognition in depth data using dynamic time warping. *IEEE Trans. Instrum. Meas.* 65 (2), 305–316. doi:10.1109/tim.2015.2498560

Rincon, A., Yamasaki, H., and Shimoda, S. (2016). "Design of a video game for rehabilitation using motion capture, EMG analysis and virtual reality." In Proceedings of the 2016 Int. Conf. Electron. Commun. Comput. (CONIELECOMP). Cholula, Mexico, 198–204. doi:10.1109/CONIELECOMP.2016.7438575

Sun, L., and Wu, J. (2022). A scalable and transferable federated learning system for classifying healthcare sensor data. *IEEE J. Biomed. Health Inf.*, 1. doi:10.1109/JBHI.2022.3171402

Tan, W., Xu, Y., Pan, L., Liu, C., Li, Y., and Du, Y., (2021). A method of VR-EEG scene cognitive rehabilitation training. *Health Inf. Sci. Syst.* 9 (1), 4. doi:10.1007/s13755-020-00132-6

Yan, S., Xiong, Y., and Lin, D. (2018). "Spatial temporal graph convolutional networks for skeleton-based action recognition." In Proceedings of the AAAI Conf. Artif. Intell., New Orleans, LA, U.S.A. doi:10.1609/aaai.v32i1.12328

Zhang, W., Lin, Z., Cheng, J., Ma, C., Deng, X., and Wang, H. (2020). STA-GCN: Two-stream graph convolutional network with spatial–temporal attention for hand gesture recognition. *Vis. Comput.* 36, 2433–2444. doi:10.1007/s00371-020-01955-w

frontiers | Frontiers in Physiology

TYPE Original Research
PUBLISHED 09 November 2022
DOI 10.3389/fphys.2022.1043551

OPEN ACCESS

EDITED BY
Lisheng Xu,
Northeastern University, China

REVIEWED BY
Jianqiang Li,
First Affiliated Hospital of Harbin Medical University, China
Jing Han,
Capital Medical University, China
Lin Liu,
Henan Provincial People's Hospital, China

*CORRESPONDENCE
Feifei Sun,
sffecho0120@163.com

SPECIALTY SECTION
This article was submitted to Computational Physiology and Medicine, a section of the journal Frontiers in Physiology

RECEIVED 13 September 2022
ACCEPTED 27 October 2022
PUBLISHED 09 November 2022

CITATION
Sun A, Ren S, Xiao Y, Chen Y, Wang N, Li C, Tan X, Pan Y, Sun F and Ren W (2022), Real-time 3D echocardiographic transilluminated imaging combined with artificially intelligent left atrial appendage measurement for atrial fibrillation interventional procedures. *Front. Physiol.* 13:1043551. doi: 10.3389/fphys.2022.1043551

Real-time 3D echocardiographic transilluminated imaging combined with artificially intelligent left atrial appendage measurement for atrial fibrillation interventional procedures

Aijiao Sun[1], Sihua Ren[2], Yangjie Xiao[1], Yixin Chen[1], Nan Wang[1], Chendi Li[1], Xueying Tan[1], Yilong Pan[3], Feifei Sun[1]* and Weidong Ren[1]

[1]Department of Ultrasound, Shengjing Hospital of China Medical University, Shenyang, China, [2]Department of Radiology, The First Affiliated Hospital of China Medical University, Shenyang, China, [3]Department of Cardiology, Shengjing Hospital of China Medical University, Shenyang, China

Aims: This study investigated the feasibility and accuracy of real-time three-dimensional (3D) echocardiographic transilluminated imaging (TrueVue Glass) in left atrial appendage (LAA) anatomical morphology and artificial intelligence (AI)-assisted 3D automated LAA measurement (3D Auto LAA) software in the preoperative evaluation of LAA occlusion (LAAO) in patients with atrial fibrillation (AF).

Method and results: Thirty-seven patients with AF were selected. Two-dimensional (2D) and real-time 3D transesophageal echocardiography (RT3D-TEE) were performed preoperatively, using conventional 3D, the new 3D TrueVue Glass mode, and cardiac computed tomography angiography (CCTA) to assess and type the morphology of LAA. Physiological parameters were measured using traditional 2D and 3D manual (3D Manual LAA), 3D Auto LAA, and CCTA. TrueVue Glass for LAA outer contour display was compared with CCTA. Comparisons were based on correlation and consistency in measuring the maximum diameter (LZ max), minimum diameter (LZ min), area (LZ area), and circumference (LZ cir) of LAA landing zone (LZ). Times and variabilities were compared. The concordance rate for external shape of LAA was 97.14% between TrueVue Glass and CCTA. 3D Auto LAA and 3D Manual LAA have a stronger correlation and higher consistency in all parameters. 3D Auto LAA showed higher intra- and interobserver reproducibility and allowed

Abbreviations: 2D, two-dimensional; 3D, three-dimensional; 3D auto LAA, three-dimensional automated left atrial appendage measurement; AI, artificial intelligence; AF, atrial fibrillation; CCTA, cardiac computed tomographic angiography; LAAO, left atrial appendage occlusion; LZ, landing zone; RT3D, real-time three-dimensional; TEE, transesophageal echocardiography.

quicker analysis ($p < 0.05$). LAAO was performed in 35 patients (94.59%), and none of which had serious adverse events.

Conclusion: TrueVue Glass is the first non-invasive and radiation-free visualization of the overall external contour of LAA and its adjacent structures. 3D Auto LAA simplifies the measurement, making the preoperative assessment more efficient and convenient while ensuring the accuracy and reproducibility. A combination of the two is feasible for accurate and rapid assessment of LAA anatomy and physiology in AF patients and has practical application in LAAO.

KEYWORDS

3D Auto LAA, artificial intelligence-AI, left atrial appendage occlusion, real-time three-dimensional, transesophageal echocardiography, TrueVue Glass

1 Introduction

Left atrial appendage occlusion (LAAO) has gained widespread acceptance and use as a new tool for stroke prevention in patients with atrial fibrillation (AF) (Holmes et al., 2019; Turagam et al., 2020). The 2020 European Society of Cardiology and European Association for Cardiothoracic Surgery guidelines for the diagnosis and management of AF give LAAO a class II b recommendation and a level of evidence of B (Hindricks et al., 2021). The anatomical structure of the LAA varies significantly among individuals, and thus the successful performance of LAAO depends on the accurate preoperative assessment of the morphology, size, and physiological status of the LAA (Korsholm et al., 2020). Currently, transesophageal echocardiography (TEE) and cardiac computed tomography angiography (CCTA) are the main methods for preoperative evaluation of the LAA. The main advantages of conventional two-dimensional (2D) and real-time three-dimensional (RT3D) TEE are that the spatial resolutions are significantly higher than that of transthoracic echocardiography, enabling TEE to clearly and dynamically display the internal structure of the LAA, identify the thrombus and comb muscles, and provide more accurate measurements. However, the assessment of the overall morphology can only be made based on lateral-view LAA cross-sectional images. In contrast, CCTA often must be combined with contrast-enhanced imaging; its main application value is in displaying the external contour of the LAA (Glikson et al., 2020; Korsholm et al., 2020). However, 3D image reconstruction is required to obtain LAA shape images, and LAA morphology changes cannot be shown with the cardiac cycle in real time, making this method time-consuming, laborious, and requiring high human interference. Previously, some researchers considered 2D-TEE as the gold standard for the preoperative measurement of relevant morphological parameters in LAAO, but with the rapid development of three-dimensional ultrasound, an increasing number of studies have shown that the results of RT3D-TEE are more accurate and reliable and correlate better with the implanted occluder, making it more suitable as a key reference for the selection of occluder models for LAAO patients (Morcos et al., 2018; Streb et al., 2019). However, in addition to its inability to directly display the overall external contour of the LAA, conventional RT3D-TEE still has several limitations such as cumbersome and time-consuming operation procedures when measuring the anatomical and physiological parameters of the LAA (Morais et al., 2022). Recently introduced advanced 3D echocardiographic imaging and measurement technologies, referred to as TrueVue Glass and 3D automated LAA (3D Auto LAA) measurement, are expected to solve the aforementioned problems. TrueVue Glass is a new 3D rendering mode that can intelligently render the contours of the heart chambers and vascular chambers containing blood flow and the heart valve structure, automatically shield substantial structures around the heart, and provide a new perspective for the ultrasonic diagnosis and evaluation of heart diseases (Karagodin et al., 2020). In contrast, 3D Auto LAA is an artificial intelligence (AI)-assisted automatic measurement technology that can automatically identify the ostium of the LAA after cutting and measure important parameters related to surgery such as the maximum diameter, minimum diameter, area, and circumference. To the best of our knowledge, their combined application in LAAO has not been systematically explored. In this study, for the first time, 3D Auto LAA was performed in association with TrueVue Glass for the examination and evaluation of AF patients undergoing LAAO and compared with other commonly used imaging techniques to explore the clinical value and technical advantages of these new methods.

2 Materials and methods

2.1 Study population

Thirty-seven patients with AF who were proposed to undergo LAAO from July 2020 to May 2022 at the Cardiology Center of China Medical University were included in this study,

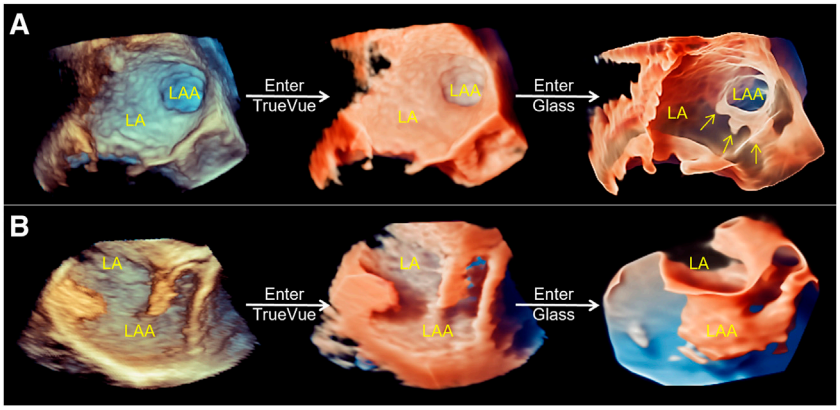

FIGURE 1
Schematic of process of the conversion of conventional real-time 3D transesophageal echocardiography to TrueVue Glass. **(A)**. From left to right, conventional 3D, TrueVue and TrueVue Glass imaging modes of the LAA at the entrance of the left atrium are shown. The TrueVue Glass (right) shows the three lobular structures at the blind end of the LAA (arrows) **(B)**. From left to right, conventional 3D, TrueVue and TrueVue Glass imaging of the LAA in lateral view are shown. 3D, three-dimensional; LA, left atrium; LAA, left atrium appendage.

and all patients underwent 2D-TEE, RT3D-TEE, and CCTA preoperatively. The inclusion criteria are as follows: AF thrombotic risk score (CHA_2DS_2-VASc score) ≥ 2, while meeting one of the following conditions unsuitable for or unwilling to be subjected to long-term standardized anticoagulation; stroke or embolism occurring based on long-term standardized anticoagulation; bleeding risk score (HAS-BLED score) ≥ 3; and need for combined antiplatelet drug therapy. The exclusion criteria are 1) contraindication to TEE; 2) suspicious or definite thrombus in the LAA on preoperative TEE or CCTA; 3) presence of severe cardiac structural abnormalities or valvular disease requiring surgical treatment; 4) New York Heart Association cardiac function class IV; and 5) presence of recent active bleeding. This study was approved by our Institutional Ethics Committee and was conducted in accordance with the ethical principles for medical research involving human subjects established by the Declaration of Helsinki, protecting the privacy of all participants and the confidentiality of personal information.

2.2 Transesophageal echocardiography image acquisition and preoperative evaluation of left atrial appendage

In this study, a Philips CVx 3D ultrasound system (Philips Medical Systems, Andover, MA, United States) equipped with X7-2t and X8-2t transesophageal ultrasound probes was used for the 2D and 3D TEE examinations. All patients underwent TEE examinations and data acquisition after pharyngeal anesthesia, and 3–5 cardiac cycles were applied to store the images.

2.2.1 2D-transesophageal echocardiography and RT3D-transesophageal echocardiography image acquisition

2D-TEE was used to observe the morphology of the LAA, particularly the internal commissural muscle and blind end lobes in multiple angles and views, and to clarify the presence of thrombus and its relationship with surrounding adjacent structures. And 2D data acquisition was performed at 0°, 45°, 90°, and 135°. The 2D image depth, gain, and other parameters are adjusted to produce the best display output from the LAA display, and 3D Zoom mode is selected for 3D data acquisition of the complete structure of the LAA. The acquired LAA 3D data set is entered into TrueVue Glass mode *via* the instrument touch panel (first "TrueVue" is clicked upon, and then "Glass" is clicked upon to enter TrueVue Glass mode), and parameters, such as transparency, smoothness, contrast, and gain, are adjusted appropriately. The external contours of the LAA are clearly displayed using a suitable image cutting method (cutting tools as before (Sun et al., 2022)) (Figure 1).

2.2.2 Preoperative evaluation of left atrial appendage occlusion related parameters for 2D-Transesophageal echocardiography and RT3D-Transesophageal echocardiography

The inner diameter of the LAA landing zone (LZ) was measured at 0°, 45°, 90°, and 135° at the end of the left ventricular systole (starting from the left circumflex coronary artery to 1–2 cm below the contralateral left superior pulmonary vein crest). The maximum value of the inner diameter in the four angles was labeled LZ max, and the minimum value was labeled LZ min of 2D-TEE (Figure 2A). LAA anatomical parameter data measure of RT3D-TEE was performed online, including in the

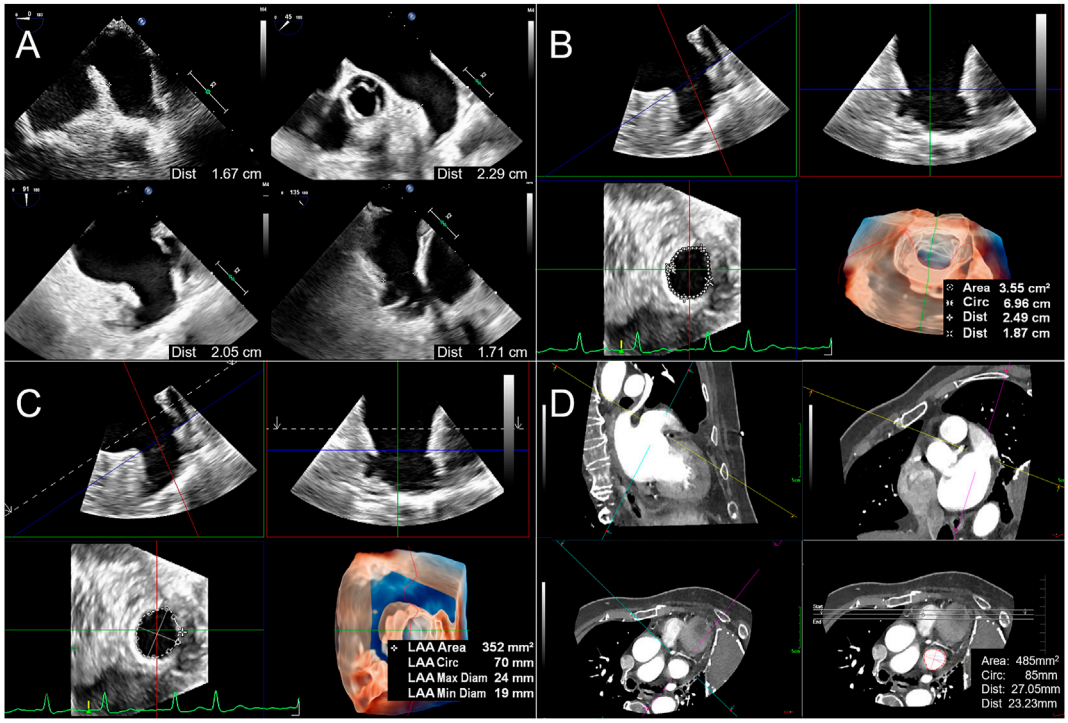

FIGURE 2
Flow chart of LAA parameter measurements before percutaneous left atrial appendage occlusion. **(A)**. For 2D TEE method, the LAA LZ diameters (LZ is defined as the point from the left circumflex artery to 1–2 cm below the contralateral left superior pulmonary vein crest) are measured at 0°, 45°, 90°, and 135 at end-systole, respectively. **(B)**. When applying 3D Manual LAA method, enter MultiVue mode on the basis of LAA 3D Zoom image, and at the end of systole, adjust the LZ positioning line (blue line) in the LAA sagittal plane (upper left), coronal plane (upper right), obtain the LAA LZ cross-section (lower left), and manually measure the LAA LZ maximum diameter (the first Dist value obtained), minimum diameter (the second Dist value), area and circumference (Circ). The lower right figure shows 3D downward view of the LAA LZ and the measurement results. **(C)**. After positioning the LAA LZ in the same way as 3D Manual LAA, the above parameters are automatically obtained by clicking "3D Auto LAA" (lower right). **(D)**. When using CCTA, measurement method is similar to 3D Manual LAA by adjusting the LZ positioning lines (yellow lines) in the sagittal plane (upper left) and coronal plane (upper right) of the LAA, obtaining the LAA LZ cross-section (lower left) and then manually measuring the above parameters in sequence (lower right). 3D Auto LAA, three-dimensional automated left atrial appendage; 3D Manual LAA, three-dimensional manual left atrial appendage; CCTA, cardiac computed tomographic angiography; LAA, left atrium appendage; LZ, landing zone.

traditional 3D manual measurement method (3D Manual LAA) and intelligent measurement method (3D Auto LAA). 3D Manual LAA measurement method: The appropriate LAA 3D Zoom image was selected, and MultiVue mode was entered. The end-systolic phase of left ventricle was selected, and the blue line (LAA LZ cross-sectional positioning line) in the sagittal and coronal planes of LAA, thus enabling the LAA LZ ostium to be obtained. In this plane, the LAA LZ maximum diameter (LZ max), minimum diameter (LZ min), area (LZ area), and circumference (LZ cir) are manually measured (Figure 2B). 3D Auto LAA measurement method: 3D Auto LAA can automatically identify the endocardium, after adjusting the LAA LZ in MultiVue mode as shown in 3D Manual LAA, the above anatomical and physiological parameters of the LAA LZ can be automatically obtained with a single click on "3D Auto LAA" (Figure 2C). Manual adjustment to identify unsatisfactory loci when needed is allowed.

2.3 Cardiac computed tomography angiography image acquisition and measurements

An IQon-Spectral CT instrument from Philips was used for cardiac enhancement imaging and to display the external morphology of the LAA *via* 3D reconstruction. In the LAA measurement method, which is similar to conventional RT3D-TEE, the LAA LZ is manually adjusted from three mutually perpendicular planes, and the LZ max, LZ min, LZ area, and LZ cir parameters are measured separately (Figure 2D).

2.4 Comparison of time

The time taken to measure the LAA by each of the aforementioned methods (specifically, the time period from

loading and displaying data on the workstation to extraction for all clinical indicators) is recorded.

2.5 left atrial appendage morphological determination

The international anatomical morphology classification of LAA into four types is as follows (Wang et al., 2010): 1) chicken-wing type: LAA has the main leaf with a clear bend at its proximal or middle part and may have secondary lobes; 2) windsock type: LAA has no clear bend, has a sufficiently long main leaf, and can vary according to the position and number of secondary and tertiary leaves issued; 3) cactus type: LAA has no clear bend and is characterized by a dominant primary leaf, with secondary leaves extending upward or downward, and 2–3 secondary leaves at the tip of one primary leaf; and 4) cauliflower type: LAA without obvious curvature and with limited overall length, lack of primary leaves, more complex internal structure, and irregular shape of LAA mouth.

2.6 Procedural strategy for left atrial appendage occlusion

The patient is delivered with a sheath and guidewire *via* the femoral vein under general anesthesia, followed by penetration of the guidewire through the interatrial septum under X-ray fluoroscopy, TEE, or intracardiac echocardiography guidance and delivery to the LAA for contrast observation. The choice of the occluder model is recommended to be 4–6 mm larger than the maximum LZ diameter measured by intraoperative fluoroscopy or TEE. After the initial implantation is completed, it is judged that the occluder is appropriately positioned: there is no residual shunt or shunt bundle width <5 mm around it, pull test is stable, compression ratio is appropriate, and release principle is satisfied before it is fully deployed (Vainrib et al., 2018), while observations are made based on whether adverse events such as pericardial effusion and compression of surrounding tissue structures have occurred. The procedure is ended after it is determined that there are no abnormalities.

2.7 Reproducibility verification and follow-up

To determine the reproducibility of the different methods of preoperatively measuring the parameters of LAA, measurements were repeated one month later in 10 randomly selected patients by the same observer and by a different observer. During the repeat analysis, the observers were unaware of all previous measurements and clinical details. TEE follow-up was applied approximately 45 days, 3 months and 6 months after surgery to observe the morphology and position of the occluder and the occurrence of adverse events such as residual shunts and device-related thrombosis around the blocker.

TABLE 1 Baseline clinical characteristics of study population (n = 35).

Parameter	Value
Men, n (%)	19 (54.29%)
Age, years	61.20 ± 9.98
Medical history	
Paroxysmal AF, n (%)	23 (65.71%)
Nonparoxysmal AF, n (%)	12 (34.29%)
Hypertension, n (%)	25 (71.43%)
Diabetes mellitus, n (%)	12 (34.29%)
Coronary Heart Disease, n (%)	5 (14.29%)
Prior stroke/TIA, n (%)	4 (11.43%)
CHA_2DS_2-VASc score	3.20 ± 1.32
HAS-BLED score	2.17 ± 0.92

All data are presented as number (%) or mean ± SD. AF, atrial fibrillation; TIA, transient ischemic attack. CHA_2DS_2-VASc score is a scoring for stroke risk assessment in patients with atrial fibrillation (C: 1 point for Congestive heart failure; H: 1 point for Hypertension; A2: 2 points for Age ≥75 years; D: 1 point for Diabetes; S2: 2 points for thromboembolism, Stroke, or transient ischemic attack; V: 1 point for Vascular disease; A: 1 point for Age of 65–74 years; S: sex category, 1 point for female). HAS-BLED score is a scoring scale for bleeding risk in patients with atrial fibrillation (For the presence of Hypertension, Abnormal renal/liver function, Stroke, Bleeding history, Labile INRs, Elderly (>65 years), or Drugs/alcohol, 1 point was recorded).

2.8 Statistics

Statistical analysis was performed using SPSS Statistics version 26.0 (IBM Inc., Armonk, New York). The normal distribution of continuous quantitative variables was assessed *via* the Kolmogorov–Smirnov test. Continuous variables are presented as mean ± standard deviation or median (first interquartile range [IQR], third interquartile range) for skewed variables, and categorical variables are presented as counts and percentages. A comparison of the results obtained by the different methods of measuring the preoperative anatomical parameters of LAA was performed *via* paired-sample Wilcoxon signed-rank test and using the Pearson correlation and intraclass correlation coefficient (ICC). The ICC was used to determine the intra- and interobserver variability, and 95% confidence intervals (CI) were calculated. It is generally accepted that an ICC below 0.4 indicates poor agreement (reliability) and above 0.75 indicates high agreement (reliability). One-way analysis of variance was then used to compare the differences in the times taken to measure LAA using the different measurement methods, where $p < 0.05$ was considered statistically significant.

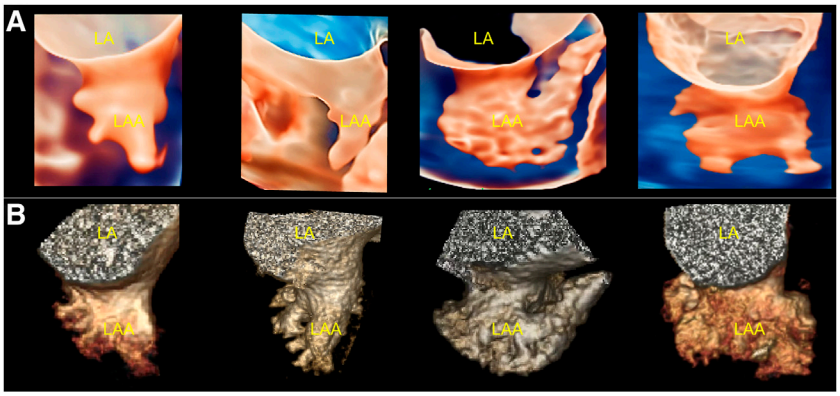

FIGURE 3
Comparison of TrueVue Glass and CCTA for displaying different morphologies of LAA. **(A)**. From left to right, TrueVue Glass shows cactus, windsock, chicken-wing, and cauliflower type of LAA **(B)**. From left to right, CCTA display of the above morphological types of LAA are shown. CCTA, cardiac computed tomographic angiography; LA, left atrium; LAA, left atrium appendage.

3 Results

Patient demographics: Of the 37 AF patients, 35 (94.59%) had successful final LAAO surgery, whereas two had their procedures terminated because of intra-LAA thrombosis on preoperative TEE. The basic patient characteristics are presented in Table 1.

3.1 Comparison of left atrial appendage morphology by TrueVue Glass and cardiac computed tomography angiography

From all patients, stereo morphological information of the LAA was obtained using TrueVue Glass and CCTA images. Additionally, systolic and diastolic changes in the LAA with cardiac pulsation can be observed in real time using TrueVue Glass (Supplementary Movie S1). TrueVue Glass revealed 11/35 (31.43%) cases of cactus type, 10/35 (28.57%) cases of windsock type, 9/35 (25.71%) cases of chicken-wing type, and 5/35 (14.29%) cases of cauliflower type. For comparison, CCTA revealed 12/35 (34.29%) cases of cactus type, 9/35 (25.71%) cases of windsock type, 9/35 (25.71%) cases of chicken-wing type, and 5/35 (14.29%) cases of cauliflower type. One case was determined by TrueVue Glass to be windsock type and CCTA to be cactus type; the compliance rate was 34/35 (97.14%) (Figure 3). In addition, some patients with AF showed spontaneous echo contrast because of the enlarged left atrium and LAA; the flowing cloudy stereomorphic features could be observed using TrueVue Glass (Supplementary Movie S2).

3.2 Comparison of 3D auto LAA with 2D-Transesophageal echocardiography, 3D manual left atrial appendage, and cardiac computed tomography angiography

3D Auto LAA was feasible for all patients, although 19 patients (54.29%) required fine-tuning of the recognition position by hand at the time of analysis.

The variability, correlation, and agreement between 3D Auto LAA and other measurement methods are presented in Table 2. There were no significant differences in LZ max and LZ min between 3D Auto LAA and 2D-TEE ($p > 0.05$), whereas there were significant differences in LZ max and LZ min between 3D Auto LAA and 3D Manual LAA ($p < 0.05$). In contrast, there were no significant differences in LZ area and LZ cir between 3D Auto LAA and 3D Manual LAA ($p > 0.05$). There were significant differences in LZ max, LZ min, LZ area, and LZ cir between 3D Auto LAA and CCTA ($p < 0.05$). 3D Auto LAA and 3D Manual LAA have a stronger correlation and higher consistency in all parameters, particularly for LZ area and LZ cir.

3.3 Analysis time

Figure 4 shows the times taken to measure the LAA preoperative parameters for the different operating mode approaches that were evaluated. The time taken to measure LAA using 2D-TEE, 3D Manual LAA, 3D Auto LAA, and CCTA was 240.95 ± 0.20 s, 143.64 ± 0.31 s, 85.96 ± 0.42 s, and 246.33 ± 0.57 s, respectively. Except for 2D-TEE and CCTA, there were significant differences in operation time between the measurement modes ($p < 0.05$).

TABLE 2 Comparison of 2D-TEE, 3D Manual LAA, 3D Auto LAA and CCTA for preoperative measurements of parameters related to left atrial appendage occlusion.

	LZ max (mm)	LZ min (mm)	LZ area (mm^2)	LZ cir (mm)
2D-TEE	21.35 (18.65, 22.88)	17.70 (14.75, 19.60)	NA	NA
3D Manual LAA	22.85 (19.83, 25.28)[a]	17.70 (15.03, 20.80)[a]	341.00 (206.25, 405.00)	67.05 (54.38, 74.05)
3D Auto LAA	21.50 (18.75, 24.00)	17.00 (13.50, 20.00)	332.50 (184.75, 375.00)	68.00 (56.00, 73.50)
CCTA	25.20 (21.03, 27.13)[a]	19.65 (17.78, 21.23)[a]	394.50 (302.75, 486.50)[a]	74.35 (65.20, 82.43)[a]
SCC (*p*-value)[b]	0.82 (<0.001)	0.73 (<0.01)	NA	NA
ICC (*p*-value)[b]	0.78 (<0.001)	0.66 (<0.01)	NA	NA
SCC (*p*-value)[c]	0.94 (<0.001)	0.95 (<0.001)	0.96 (<0.001)	0.96 (<0.001)
ICC (*p*-value)[c]	0.91 (<0.001)	0.89 (<0.001)	0.96 (<0.001)	0.96 (<0.001)
SCC (*p*-value)[d]	0.62 (0.02)	0.25 (0.40)	0.71 (0.01)	0.67 (0.01)
ICC (*p*-value)[d]	0.51 (0.01)	0.17 (0.20)	0.55 (<0.01)	0.55 (<0.01)

LZ max, LZ min, LZ area, and LZ cir are expressed as median (25th percentile, 75th percentile). 2D-TEE, two-dimensional transesophageal echocardiography; 3D Auto LAA, three-dimensional automated left atrial appendage; 3D Manual LAA, three-dimensional manual left atrial appendage; CCTA, cardiac computed tomographic angiography; ICC, intraclass correlation coefficient; LZ area, landing zone area; LZ cir, landing zone circumference; LZ max, landing zone maximum diameters; LZ min, landing zone minimum diameters; SCC, spearman correlation coefficient.

[a]$p < 0.05$ vs. 3D Auto LAA in difference.

[b]comparison results between 3D Auto LAA and 2D-TEE.

[c]comparison results between 3D Auto LAA and 3D Manual LAA.

[d]comparison results between 3D Auto LAA and CCTA.

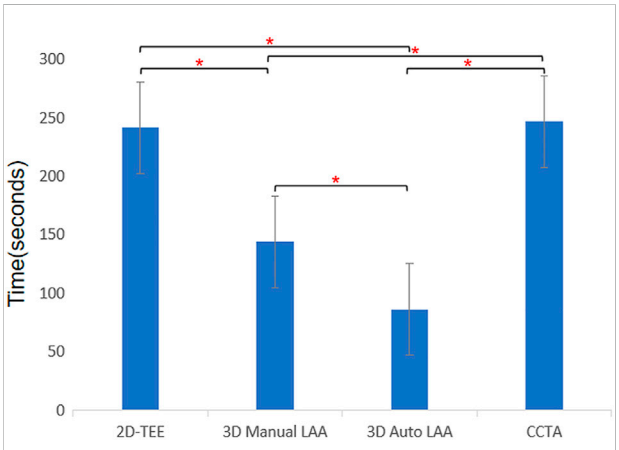

FIGURE 4
Times consumption of different methods for measuring morphological parameters of left atrium appendage. 2D-TEE, two-dimensional transesophageal echocardiography; 3D Auto LAA, three-dimensional automated left atrial appendage; 3D Manual LAA, three-dimensional manual left atrial appendage; CCTA, cardiac computed tomographic angiography; * *p*-value < 0.05.

3.4 Reproducibility verification and follow-up

Table 3 summarizes the intra- and interobserver variability of the different methods for preoperatively measuring the parameters of LAA. The results showed that 3D Auto LAA achieved higher interobserver and intraobserver

TABLE 3 Intra- and interobserver variability of 2D-TEE, 3D Manual LAA, 3D Auto LAA and CCTA.

	Intraobserver, ICC (95% CI)	Interobserver, ICC (95% CI)
2D-TEE		
LZ max	0.78 (0.36–0.94)	0.64 (0.03–0.90)
LZ min	0.67 (0.16–0.91)	0.15 (-0.36–0.66)
3D Manual LAA		
LZ max	0.72 (0.25–0.92)	0.64 (0.09–0.90)
LZ min	0.78 (0.35–0.94)	0.58 (-0.07–0.88)
LZ area	0.82 (0.42–0.95)	0.81 (0.44–0.95)
LZ cir	0.82 (0.42–0.95)	0.82 (0.47–0.95)
3D Auto LAA		
LZ max	0.81 (0.44–0.95)	0.72 (0.25–0.92)
LZ min	0.84 (0.51–0.96)	0.76 (0.33–0.93)
LZ area	0.87 (0.56–0.97)	0.86 (0.54–0.96)
LZ cir	0.87 (0.55–0.97)	0.83 (0.47–0.95)
CCTA		
LZ max	0.75 (-0.04–0.94)	0.50 (-0.19–0.85)
LZ min	0.50 (-0.14–0.85)	0.43 (-0.30–0.82)
LZ area	0.59 (0.04–0.88)	0.62 (-0.01–0.89)
LZ cir	0.59 (0.04–0.88)	0.49 (-0.21–0.85)

2D-TEE, two-dimensional transesophageal echocardiography; 3D Auto LAA, three-dimensional automated left atrial appendage; 3D Manual LAA, three-dimensional manual left atrial appendage; CCTA, cardiac computed tomographic angiography; ICC, intraclass correlation coefficient; LZ area, landing zone area; LZ cir, landing zone circumference; LZ max, landing zone maximum diameters; LZ min, landing zone minimum diameters.

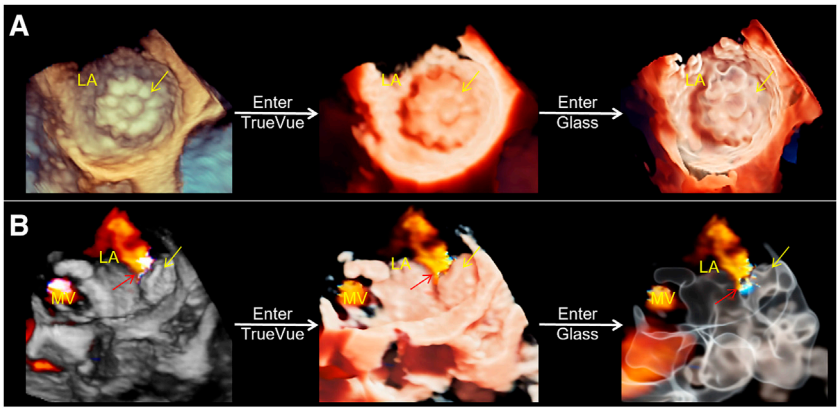

FIGURE 5
Three-dimensional transesophageal echocardiography plus color Doppler for outcome assessment after left atrial appendage occlusion. **(A)**. From left to right, conventional 3D, TrueVue and TrueVue Glass direct views of the left atrium appendage occluder (yellow arrows) are displayed. **(B)**. From left to right, conventional 3D, TrueVue and TrueVue Glass with color Doppler showing the residual shunt (red arrows) around the occluder (yellow arrows), among them, TrueVue Glass showing the origin and path of the shunt more entirely. LA, left atrium; MV, mitral valve.

reproducibility compared with those of 2D-TEE, 3D Manual LAA, and CCTA. At 45 days postoperatively, thirty-five patients were followed up with TEE (Figure 5A), and residual shunts around the occluder were found in six cases (17.14%), none of which exceeded 5 mm (considered to be ineffective shunts), and none of which had serious adverse events such as pericardial tamponade and device dislodgement. The application of conventional 2D, 3D-TEE, and TrueVue Glass all enable the diagnosis of residual shunts with no difference in diagnostic rates, but TrueVue Glass imaging allows the observation of the overall path of the shunt, including the overall spatial situation of the origin and travel of abnormal blood flow, through increased transparency (Figure 5B). At the 3-month postoperative follow-up, the residual shunts around the occluder disappeared in the six patients mentioned above. Thirty-four patients (97.14%) completed the 6-month postoperative follow-up and none of which had serious adverse events.

4 Discussion

The main findings of this study include 1) TrueVue Glass is feasible for the stereoscopic display for the overall external contour of the LAA and adjacent structures, and has a high consistency with CCTA; 2) TrueVue Glass can also be used in the postoperative follow-up of LAAO patients to achieve a visual and integrated visualization of the residual shunt in and around the occluder; 3) AI-assisted automated LAA measurements are feasible, more efficient and reproducible than other previously used techniques. 3D Auto LAA results showed higher correlation with 3D Manual LAA method, which is generally considered to be more accurate, and there is no statistical difference between them in terms of important anatomical and physiological parameters of the LAA.

TrueVue Glass imaging is a new 3D cardiac ultrasound rendering mode that has been introduced in recent years (Karagodin et al., 2020; Sun et al., 2021). It automatically hides surrounding cardiac tissues through a one-click operation and presents the heart chambers and small and large vessel chambers containing blood flow in a crystal-clear visualization. It breaks through the limitations of conventional echocardiographic display, providing a new perspective not previously offered by 3D cardiac ultrasound, particularly for the overall external contour of the LAA, which is comparable to that of enhanced CT, and is a non-invasive, real-time dynamic imaging method.

The significant differences in LAA morphology pose several challenges for LAAO to proceed, especially the chicken-wing-type LAA, which is a particular challenge for LAAO (Freixa et al., 2013; Korsholm et al., 2018). Combined with recent studies (Hahn et al., 2022), the preoperative application of TrueVue Glass for LAAO can provide new information to support the assessment of the anatomical morphology of the LAA, i.e., the overall contour of the LAA and its adjacent structures from the outside. Karagodin et al. applied this technique to observe an LAA and confirmed that it could clearly show the LAA boundary contour and lobing, but the morphology of the LAA was displayed only from the lateral view, without further 3D display of the overall shape. This outcome was similar to the traditional 3D observation view and was not compared with CT results (Karagodin et al., 2020). In our study, the display rate of the overall contour morphology of the LAA by TrueVue Glass was 100%, and the results were basically consistent with the CCTA display results. Additionally, the spatial position

relationship and hemodynamics of the surrounding structures, such as the left atrium, mitral valve, and aortic valve, could be displayed. To demonstrate, the anatomical features of the beating heart were displayed in a physiological state in real time (Supplementary Movie S1).

In the TrueVue Glass mode, a color doppler can be added, and after effective adjustment of transparency, the complete origin and path of the blood flow bundle can be observed through transparent tissue, thus locating more comprehensively and precisely any leaks around the LAAO postoperative occluder. Thus, the display of color blood flow is more comprehensive and clearer. In a past study, Tamborini et al. used TrueVue Glass in patients undergoing mitral valve repair and clearly observed the advantages of this method vs. conventional RT3D-TEE imaging in depicting the preoperative regurgitant orifice boundary and identifying the residual shunt after surgery, confirming the value of this technology in interventional procedures for various cardiac diseases (Tamborini et al., 2021). In our study, this advanced 3D cardiac ultrasound technology was systematically applied to the preoperative and postoperative real-time imaging evaluation of LAAO in patients with various forms of LAA, to observe whether the morphology and position of the occluder are normal and to qualify, locate, and quantify any residual leakages around the occluder, providing a basis for individualized treatment planning after surgery. Although the application of TrueVue Glass in this study did not differ from conventional RT3D-TEE in terms of the diagnostic rate of residual shunts, TrueVue Glass revealed a more realistic, comprehensive, and clearer overall path for residual shunts, improving diagnostic efficacy and communication with clinicians.

The advantages of TrueVue Glass over CCTA are three-fold. First, it is based on simple post-processing of conventional RT3D-TEE data and does not require additional examination of the patient. Second, it avoids damage to the patient caused by radiation or contrast allergy and avoids contraindications to CCTA imaging. Finally, it facilitates real-time dynamic imaging and provides timely diagnosis and evaluation of the patient at the bedside. This, with the gradual improvement of TrueVue Glass resolution and other parameters, is expected to replace the need for CT examination for LAAO surgery, to achieve a single ultrasound examination that completes the collection of information on various aspects of LAA anatomical morphology and physiological function and parameter measurement.

In our study, the LAA morphological classification of one patient was inconsistent with the CCTA results. The reason for this was inferred to be the poor quality of the original ultrasound image acquisition and the limitations of TrueVue Glass in resolving minute details, which resulted in the poor display of small LAA fractions located in the far field of the image. These inadequacies may have led to the difference in the identification of the overall morphological classification. Meanwhile, the LAA fractions of most patients were matched with the CT results commonly used in current clinical practice, and thus we considered the effect of the difference for this one patient to be minor.

To the best of our knowledge, this is the first study to explore the clinical application of 3D Auto LAA. This technique is a new three-dimensional fully automated LAA parameter measurement method based on TEE images, which can automatically track the endothelial border according to the shape of the LAA LZ of the patient and measure all important surgical reference indicators of the LAA LZ. If necessary, the examiner can make overall or local adjustments to the endothelial border to make the measurement results more accurate. The results of this study show that 3D Auto LAA reduces the number of manual tracing steps during traditional 3D measurements, resulting in a more convenient process, a significant reduction in analysis time (including when manual adjustments are required), and satisfactory reproducibility. Similar to other studies, the application of automated measurement techniques combined with manual fine-tuning allows for accurate measurements with higher repeatability (Queirós et al., 2018; Morais et al., 2022).

In this study, the measurements of the LZ max, LZ min, LZ area, and LZ cir of LAA by 3D Auto LAA correlated more strongly and agreed better with 3D Manual LAA than with 2D-TEE and CCTA, probably because both were usually measured based on the same raw 3D data. However, the differences between the two on LZ max and LZ min measurements of the LAA were significant. In contrast, there were no significant differences between the two on LZ area and LZ cir measurements, probably because of the diversity of LAA orifice morphology such as the oval, teardrop, and foot shape (Glikson et al., 2020). Moreover, the human eye is more prone to bias when measuring the maximum and minimum diameters, whereas it has little influence on the measurement after the LZ area and LZ cir are traced *via* manual or automatic methods. In addition, the parameters of LZ area and LZ cir may be more accurate for the selection of the occluder model compared to LZ max and LZ min. In a past study, Al-Kassou et al. (2017) showed that using the diameter derived from the LZ area and LZ cir as a reference indicator for the occluder model is more relevant to the final choice of the occluder model. Kong et al. also showed (Kong et al., 2020) that the diameter derived from the LAA circumference is more suitable as a reference indicator for the occluder model because it is more stable compared to other indicators.

In addition, although there were no significant differences between 3D Auto LAA and 2D-TEE in terms of the measured LZ max after multi-angle measurements in this study, numerically, the 3D Auto LAA measurements were still greater than 2D-TEE. This difference is probably because of the inherent display limitations of 2D-TEE, which sometimes does not take the maximum value from only four angles (Wunderlich et al., 2015; Song et al., 2016; Zhang et al., 2019). These limitations in 2D-TEE

may lead to small device selection, resulting in excessive residual shunts and even dislodgment of the occluder, prolonging surgical time and negatively affecting the surgical outcome. The 3D Auto LAA avoids the above situation by measuring the LAA as a three-dimensional aspect, making the measurement results closer to the real anatomical parameters. X-ray is also observed and measured in a 2D plane and therefore faces limitations similar to those of 2D-TEE. Saw's study showed that X-ray angiography consistently gave the lowest LAA diameters compared to CCTA and TEE and believed that X-ray angiographic measurements should have been omitted (Saw et al., 2016). It has been shown that the correlation between X-ray measurements and the final implanted occluder size of LAAO is the lowest, second to the 2D-TEE reference index, and the best correlation is with the 3D-TEE (Al-Kassou et al., 2017). In a recent expert consensus on LAAO released by EHRA and EAPCI in 2020, it was stated that CCTA measurements were the highest and the most accurate predictor of occluder size when comparing the results of the three imaging techniques (including TEE, CCTA and X-ray angiography) (Glikson et al., 2020). Therefore, a more appropriate radiological index-CCTA than X-ray angiography was chosen for reference in our study. Compared with TEE, which was the previously accepted gold standard for preoperative LAAO examination, CCTA has higher spatial resolution (Bai et al., 2017; Glikson et al., 2020) and in recent years has been suggested to become the new gold standard for the preoperative planning of LAAO (Korsholm et al., 2020). Meanwhile, researchers still believe that the measurement results of conventional 3D-TEE are more informative for the selection of LAAO occluder models (Morcos et al., 2018). Although CCTA also measures the LAA at the 3D level, the results of this study showed that the discrepancy and agreement between its measurements and 3D Auto LAA were poor compared to those of other methods, and the measurements were generally higher than those of TEE, which is consistent with the results of previous studies (Bai et al., 2017; Gilhofer and Saw, 2020; Glikson et al., 2020). This may be because of inherent differences in the imaging principles of the techniques or the fact that the application of CCTA requires the use of contrast agents, which inevitably infiltrate the local myocardium in the contrast-filled space, resulting in a large discrepancy in the measured values.

Therefore, combined with joint 2D and 3D-TEE to observe the presence of thrombus in the LAA from the inside, to observe the distribution and number of lobes of the commissural muscle at the blind end, and to measure the size and functional assessment of the LAA, we can achieve a comprehensive dynamic and accurate evaluation of the physiological structure and function of the LAA. This assessment is more conducive to designing an individualized occluder implantation plan in advance, anticipating possible risks that may be encountered during the implantation process and improving the efficiency and success rate of LAAO. Most of the patients in this study achieved complete closure of LAA, although six patients had residual shunts after surgery, but all of them were ineffective, which further proved the advantages of applying the combined technique.

4.1 Limitations

There are several limitations of our study. First, the sample size of this study was small and the follow-up period is relatively short, and although it initially confirmed the superior role of TrueVue Glass and 3D Auto LAA in LAAO, further validation using a larger sample size and longer follow-up is necessary. Second, although the visualization of the LAA by TEE has basically fulfilled clinical requirements, 3D Auto LAA is still dependent on the quality of the original 2D ultrasound image. When the image quality is poor, or when there are obvious spontaneous echo contrasts within the LAA, it may interfere with the accurate identification of the endothelium by 3D Auto LAA. This interference may result in small measurement values, which require minor manual adjustments of the tracking position by the sonographer. Third, at present, TrueVue Glass and 3D Auto LAA are available only for specific commercial models of ultrasound diagnostic machines and are not universal and comparable with other models of machines, pending further development and expansion.

5 Conclusion

TrueVue Glass, a new advanced 3D ultrasound imaging technology, provides the first real-time dynamic and radiation-free visualization of the entire external stereoscopic profile of the LAA and adjacent structures with a high degree of consistency with CCTA display and a more complete visualization of the occluder surrounding residual shunts during postoperative follow-up. AI-assisted 3D Auto LAA software streamlines the LAA measurement process, making preoperative LAAO evaluation more efficient and convenient while ensuring accurate and reproducible results. The combination of TrueVue Glass and 3D Auto LAA allows for a more accurate and efficient preoperative assessment of LAA anatomy and physiological parameters for LAAO.

Data availability statement

The original contributions presented in the study are included in the article/Supplementary Material, further inquiries can be directed to the corresponding author.

Ethics statement

The studies involving human participants were reviewed and approved by Shengjing Hospital of China Medical University. The patients/participants provided their written informed consent to participate in this study. Written informed consent was obtained from the individual(s) for the publication of any potentially identifiable images or data included in this article.

Author contributions

FS and WR accomplish the conception and design of this research. AS, SR, YX, YC, NW, and XT took part in analysis and interpretation of data. AS and FS participated in drafting of the manuscript or revising it critically for important intellectual content. YP and CL collected and analysed the clinical data. CL obtained the patient's consent. FS finally approved the manuscript submitted.

Funding

This study was supported by grants from the Young Scientists Fund of the National Natural Science Foundation of China (81901763); Liaoning province Medical-Industrial Crossover Joint Fund (2022-YGJC-55); Young and Middle-aged Scientific and Technological Innovation Talent Support Project of Shenyang City (RC210226); 345 Talent Project (M0282); Double First-class New Medical Technology Project of China Medical University (112/3111210415) and The Second Clinical College of China Medical University Educational Innovation (Open) Project (SJKF-2022YB04). The funding assisted in the collection of clinical data and publication fees.

Acknowledgments

We thank Drs Weiping Song, Hong Liu, and Saofeng Wu for their contributions in collecting patient data, and Editage company for their professional help in the language editing process.

Conflict of interest

The authors declare that the research was conducted in the absence of any commercial or financial relationships that could be construed as a potential conflict of interest.

Publisher's note

Supplementary material

The Supplementary Material for this article can be found online at: https://www.frontiersin.org/articles/10.3389/fphys.2022.1043551/full#supplementary-material

SUPPLEMENTARY MOVIE S1
TrueVue Glass shows morphological changes of left atrium appendage with cardiac cycle. LA, left atrium; LAA, left atrium appendage.

SUPPLEMENTARY MOVIE S2
TrueVue Glass shows the autonomic echogenic reflection in left atrium and left atrium appendage of patient with atrial fibrillation (arrows). LA, left atrium; LAA, left atrium appendage; LV, left ventricle.

References

Al-Kassou, B., Tzikas, A., Stock, F., Neikes, F., Völz, A., and Omran, H. (2017). A comparison of two-dimensional and real-time 3D transoesophageal echocardiography and angiography for assessing the left atrial appendage anatomy for sizing a left atrial appendage occlusion system: impact of volume loading. *EuroIntervention* 12 (17), 2083–2091. doi:10.4244/eij-d-15-00543

Bai, W., Chen, Z., Tang, H., Wang, H., Cheng, W., and Rao, L. (2017). Assessment of the left atrial appendage structure and morphology: comparison of real-time three-dimensional transesophageal echocardiography and computed tomography. *Int. J. Cardiovasc. Imaging* 33 (5), 623–633. doi:10.1007/s10554-016-1044-4

Freixa, X., Tzikas, A., Basmadjian, A., Garceau, P., and Ibrahim, R. (2013). The chicken-wing morphology: an anatomical challenge for left atrial appendage occlusion. *J. Interv. Cardiol.* 26 (5), 509–514. doi:10.1111/joic.12055

Gilhofer, T. S., and Saw, J. (2020). Periprocedural imaging for left atrial appendage closure: Computed tomography, transesophageal echocardiography, and intracardiac echocardiography. *Card. Electrophysiol. Clin.* 12 (1), 55–65. doi:10.1016/j.ccep.2019.11.007

Glikson, M., Wolff, R., Hindricks, G., Mandrola, J., Camm, A. J., Lip, G. Y. H., et al. (2020). EHRA/EAPCI expert consensus statement on catheter-based left atrial appendage occlusion - an update. *Europace.* 22 (2), 184. doi:10.1093/europace/euz258

Hahn, R. T., Saric, M., Faletra, F. F., Garg, R., Gillam, L. D., Horton, K., et al. (2022). Recommended standards for the performance of transesophageal echocardiographic screening for structural heart intervention: From the American society of echocardiography. *J. Am. Soc. Echocardiogr.* 35 (1), 1–76. doi:10.1016/j.echo.2021.07.006

Hindricks, G., Potpara, T., Dagres, N., Arbelo, E., Bax, J. J., Blomström-Lundqvist, C., et al. (2021). 2020 ESC Guidelines for the diagnosis and management of atrial fibrillation developed in collaboration with the European Association for Cardio-Thoracic Surgery (EACTS): The Task Force for the diagnosis and management of atrial fibrillation of the European Society of Cardiology (ESC) Developed with the special contribution of the European Heart Rhythm Association (EHRA) of the ESC. *Eur. Heart J.* 42 (5), 373–498. doi:10.1093/eurheartj/ehaa612

Holmes, D. R., Jr., Reddy, V. Y., Gordon, N. T., Delurgio, D., Doshi, S. K., Desai, A. J., et al. (2019). Long-term safety and efficacy in continued access left atrial appendage closure registries. *J. Am. Coll. Cardiol.* 74 (23), 2878–2889. doi:10.1016/j.jacc.2019.09.064

Karagodin, I., Addetia, K., Singh, A., Dow, A., Rivera, L., DeCara, J. M., et al. (2020). Improved delineation of cardiac pathology using a novel three-dimensional echocardiographic tissue transparency tool. *J. Am. Soc. Echocardiogr.* 33 (11), 1316–1323. doi:10.1016/j.echo.2020.08.005

Kong, D., Jiang, Y., Zhang, X., Jin, Q., Dong, L., Zhou, D., et al. (2020). Reference value of perimeter-derived diameter assessed by three-dimensional transesophageal echocardiography in left atrial appendage occluder size selection. *Echocardiography* 37 (11), 1828–1837. doi:10.1111/echo.14705

Korsholm, K., Berti, S., Iriart, X., Saw, J., Wang, D. D., Cochet, H., et al. (2020). Expert recommendations on cardiac computed tomography for planning transcatheter left atrial appendage occlusion. *JACC. Cardiovasc. Interv.* 13 (3), 277–292. doi:10.1016/j.jcin.2019.08.054

Korsholm, K., Jensen, J. M., and Nielsen-Kudsk, J. E. (2018). Cardiac computed tomography for left atrial appendage occlusion: Acquisition, analysis, advantages, and limitations. *Interv. Cardiol. Clin.* 7 (2), 229–242. doi:10.1016/j.iccl.2017.12.004

Morais, P., Fan, Y., Queirós, S., D'Hooge, J., Lee, A. P., and Vilaça, J. L. (2022). Feasibility and accuracy of automated three-dimensional echocardiographic analysis of left atrial appendage for transcatheter closure. *J. Am. Soc. Echocardiogr.* 35 (1), 124–133. doi:10.1016/j.echo.2021.08.023

Morcos, R., Al Taii, H., Bansal, P., Casale, J., Manam, R., Patel, V., et al. (2018). Accuracy of commonly-used imaging modalities in assessing left atrial appendage for interventional closure: Review article. *J. Clin. Med.* 7 (11), E441. doi:10.3390/jcm7110441

Queirós, S., Morais, P., Dubois, C., Voigt, J. U., Fehske, W., Kuhn, A., et al. (2018). Validation of a novel software tool for automatic aortic annular sizing in three-dimensional transesophageal echocardiographic images. *J. Am. Soc. Echocardiogr.* 31 (4), 515–525. doi:10.1016/j.echo.2018.01.007

Saw, J., Fahmy, P., Spencer, R., Prakash, R., McLaughlin, P., Nicolaou, S., et al. (2016). Comparing measurements of CT angiography, TEE, and fluoroscopy of the left atrial appendage for percutaneous closure. *J. Cardiovasc. Electrophysiol.* 27 (4), 414–422. doi:10.1111/jce.12909

Song, H., Zhou, Q., Deng, Q., Chen, J., Zhang, L., Tan, T., et al. (2016). Morphologic assessment of the left atrial appendage in patients with atrial fibrillation by gray values-inverted volume-rendered imaging of three-dimensional transesophageal echocardiography: A comparative study with computed tomography. *J. Am. Soc. Echocardiogr.* 29 (11), 1100–1108. doi:10.1016/j.echo.2016.08.003

Streb, W., Mitręga, K., Podolecki, T., Szymała, M., Leopold-Jadczyk, A., Kukulski, T., et al. (2019). Two-dimensional versus three-dimensional transesophageal echocardiography in percutaneous left atrial appendage occlusion. *Cardiol. J.* 26 (6), 687–695. doi:10.5603/CJ.a2018.0019

Sun, F., Sun, A., Chen, Y., Xiao, Y., Zhang, X., Qiao, W., et al. (2022). Novel TrueVue series of 3D echocardiography: Revealing the pathological morphology of congenital heart disease. *Front. Physiol.* 13, 1000007. doi:10.3389/fphys.2022.1000007

Sun, F., Tan, X., Sun, A., Zhang, X., Liang, Y., and Ren, W. (2021). Rare double orifice mitral valve malformation associated with bicuspid aortic valve in turner syndrome: diagnosed by a series of novel three-dimensional echocardiography and literature review. *BMC Cardiovasc. Disord.* 21 (1), 377. doi:10.1186/s12872-021-02184-2

Tamborini, G., Mantegazza, V., Garlaschè, A., Muratori, M., Fusini, L., Ghulam Ali, S., et al. (2021). Head to head comparison between different 3-dimensional echocardiographic rendering tools in the imaging of percutaneous edge-to-edge mitral valve repair. *J. Cardiovasc. Dev. Dis.* 8 (7), 73. doi:10.3390/jcdd8070073

Turagam, M. K., Osmancik, P., Neuzil, P., Dukkipati, S. R., and Reddy, V. Y. (2020). Left atrial appendage closure versus oral anticoagulants in atrial fibrillation: A meta-analysis of randomized trials. *J. Am. Coll. Cardiol.* 76 (23), 2795–2797. doi:10.1016/j.jacc.2020.08.089

Vainrib, A. F., Harb, S. C., Jaber, W., Benenstein, R. J., Aizer, A., Chinitz, L. A., et al. (2018). Left atrial appendage occlusion/exclusion: Procedural image guidance with transesophageal echocardiography. *J. Am. Soc. Echocardiogr.* 31 (4), 454–474. doi:10.1016/j.echo.2017.09.014

Wang, Y., Di Biase, L., Horton, R. P., Nguyen, T., Morhanty, P., and Natale, A. (2010). Left atrial appendage studied by computed tomography to help planning for appendage closure device placement. *J. Cardiovasc. Electrophysiol.* 21 (9), 973–982. doi:10.1111/j.1540-8167.2010.01814.x

Wunderlich, N. C., Beigel, R., Swaans, M. J., Ho, S. Y., and Siegel, R. J. (2015). Percutaneous interventions for left atrial appendage exclusion: options, assessment, and imaging using 2D and 3D echocardiography. *JACC. Cardiovasc. Imaging* 8 (4), 472–488. doi:10.1016/j.jcmg.2015.02.002

Zhang, L., Cong, T., and Liu, A. (2019). Percutaneous closure of the left atrial appendage: The value of real time 3D transesophageal echocardiography and the intraoperative change in the size of the left atrial appendage. *Echocardiography* 36 (3), 537–545. doi:10.1111/echo.14262

frontiers | Frontiers in Physiology

TYPE Original Research
PUBLISHED 24 November 2022
DOI 10.3389/fphys.2022.1078140

OPEN ACCESS

EDITED BY
Lisheng Xu,
Northeastern University, China

REVIEWED BY
Siyi He,
General Hospital of Western Theater Command, China
Xiangji Yue,
Northeastern University, China

*CORRESPONDENCE
Huishan Wang,
huishanw@126.com

SPECIALTY SECTION
This article was submitted to Computational Physiology and Medicine, a section of the journal Frontiers in Physiology

RECEIVED 24 October 2022
ACCEPTED 14 November 2022
PUBLISHED 24 November 2022

CITATION
Zhang Y, Fang M, Wang Z, Liu Y, Zhang C, Wang Z and Wang H (2022), The prediction and verification of outcome of extracardiac conduits fontan based on computational fluid dynamics simulation.
Front. Physiol. 13:1078140.
doi: 10.3389/fphys.2022.1078140

The prediction and verification of outcome of extracardiac conduits fontan based on computational fluid dynamics simulation

Yong Zhang, Minhua Fang, Zengwei Wang, Yu Liu, Chunzhen Zhang, Zhenlong Wang and Huishan Wang*

Department of Cardiovascular Surgery, General Hospital of Northern Theater Command, Shenyang, Liaoning, China

Objective: This study applied preoperative computed tomography angiography (CTA) and computational fluid dynamics (CFD) simulation to predicte and verify the outcome of Y-shaped extracardiac conduits Fontan for functional single ventricle.

Methods: Based on the preoperative CTA data of functional single ventricle (FSV), 4 types of spatial structures of extracardiac conduits were designed for 4 experimental groups: Group A, a traditional TCPC group (20 mm); Group B, a diameter-preserving Y-shaped TCPC (YCPC) group (branch 10 mm); Group C, YCPC group (branch 12 mm); and Group D, an area-preserving YCPC group (branch14 mm). Four indicators including flow velocity, pressure gradient (PG), energy efficiency and inferior vena cava (IVC) blood flow distribution were compared. The optimal procedure was applied. The radionuclide lung perfusion, CTA, echocardiography, cardiovascular angiography and catheterization were performed postoperatively.

Results: There were the lowest PG, the lowest flow velocity of branches, the highest energy efficiency, and a relatively balanced and stable distribution of IVC flow for group D. Subsequently, the group D, a handcrafted Y-shaped conduit (14 mm) was used for the YCPC procedure. There was no postoperative PG between the conduit and pulmonary artery with normal pressure and resistance. IVC flow was distributed uniformly.

Conclusion: CTA-based CFD provided more guidance for the clinical application of TCPC. A comprehensive surgical design could bring good postoperative outcome. Area-preserving YCPC has more advantages than TCPC and the diameter-preserving YCPC. The study effectively improved the feasibility of clinical applications of YCPC.

Abbreviations: CFD, Computational fluid dynamics; CTA, Computed tomography angiography; FSV, Functional single ventricle; IVC, Inferior vena cava; LPA, Left pulmonary artery; PG, Pressure gradient; RPA, Right pulmonary artery; TCPC, Total cavopulmonary connection; YCPC, Y-shaped conduit total cavopulmonary connection

KEYWORDS

functional single ventricle, total cavopulmonary connection, numerical simulation, fluid dynamics, computed tomography angiography

1 Introduction

Functional single ventricle (FSV) is a type of complex congenital malformations with only one fully functional ventricle. Due to the unique anatomical structure of ventricles, it is not clinically possible to fully reconstruct the two-ventricle series circulation through surgical operations. Only a single-ventricle series circulation can be realized by using the Fontan procedure, which completely separates the parallel systemic and pulmonary circulations to improve the clinical symptoms of hypoxia and eliminates single ventricular volume overload (Piran et al., 2002). However, the Fontan circulation is limited by its single ventricular physiology and can only rely on increasing central venous pressure to maintain pulmonary circulation, which in turn causes increased vascular resistance of multiple organs and decreased blood perfusion. In addition, the uneven distribution of blood flow of the inferior vena cava (IVC) in bilateral lungs leads to a significant increase in the incidence of pulmonary arteriovenous fistula in patients undergoing Fontan procedure (de Zelicourt et al., 2011). Long-term Fontan circulation after surgery often leads to multiple complications such as recurrent pleural effusion, protein-losing enteropathy, liver cirrhosis, and cardiac insufficiency (Dabal et al., 2014). Therefore, the efficiency of single-ventricle circulation and the uniform distribution of IVC flow after Fontan procedure directly affect the life span and quality of life of patients with FSV. Furthermore, studies have shown that different spatial structures connecting the vena cava to the pulmonary artery affect a variety of hydrodynamic parameters and directly affect the efficiency of the Fontan circulation and the uniform distribution of blood flow of the IVC (Soerensen et al., 2007; Kanter et al., 2012; Trusty et al., 2016).

Therefore, how to reduce hemodynamic energy consumption after a Fontan procedure is a problem that needs to be solved urgently in Fontan procedures. Since de Leval (Marsden et al., 2009) proposed total cavopulmonary connection (TCPC) that can produce more linear blood flow in blood vessels and lower the energy consumption in 1988, more and more research centers have carried out relevant studies (de Leval et al., 1988; Sundareswaran et al., 2012; Tang et al., 2013).

Later, a theoretically more efficient procedure that Y-shaped conduit total cavopulmonary connection (YCPC) was proposed. However, Trusty et al. Trusty et al. (2016) found that there were higher resistance and less balanced hepatic flow for commercially available YCPC than TCPC, while Martin et al. Martin et al. (2015) also found handcrafted YCPC might bring unbalanced hepatic flow.

There was still a big gap between the theoretical efficacy of TCPC and its postoperative efficacy. It is our major objective to minimize this gap. We use the computed tomography angiography (CTA) imaging data and computational fluid dynamics (CFD) simulation for surgical patients to obtain preliminary experimental data.

Artificial intelligence (AI) has been applicated in medical image analysis and deep learning for a long time. We try to quantify and score the simulation indicators to select the optimal procedure, which is convenient for machine learning. Based on this experimental basis, we hope to obtain an objective and standardized surgical design with the help of AI in the future. Therefore, this study was designed to predict and verify the outcome of Y-shaped extracardiac conduits Fontan for FSV based on preoperative CTA and CFD.

2 Methods

This study was approved by our institutional ethics committee (IRP approval number: 2020015, 16 April 2020) and patients' guardians have given their consent statement for the publication of this study.

2.1 Image acquisition and geometric model construction

A 17-year-old boy was diagnosed preoperatively with SLL-type congenitally corrected transposition of the great arteries with right ventricular dysplasia and ventricular septal defect. Preoperative cardiovascular computed tomography angiography (CTA) was performed. Subsequently, a TCPC with extracardiac conduits was planned for the patient, and the patient's personalized CTA data (standard Dicom format) was imported into a medical image processing software (Mimics Research, 20.0). First, the images were filtered and denoised to complete image optimization. Then, the nonrelevant images of the heart, spine and aorta were removed. The data for SVC and IVC, pulmonary artery and their branches were preserved to reconstruct three-dimensional images. The branches of pulmonary artery were extended to 50 mm to provide stability.

2.2 CTA-based surgical design

According to the experimental design, 4 types TCPC were designed to connect the extracardiac conduit and the pulmonary artery:

Group A (20 mmT), a conventional TCPC group: The IVC was anastomosed with the pulmonary artery *via* an extracardiac

conduit with a diameter of 20 mm using the conventional method, and the anastomosis was close to the left hilum. The superior vena cava (SVC) was anastomosed with the pulmonary artery, and the anastomosis was close to the right hilum. This design of anastomosis can reduce the competition between blood flows in the SVC and IVC and thus reduce energy consumption.

Group B (20 mmY), a commercially available YCPC group (diameter-preserving 20 mm-10 mm-10 mm): The IVC was connected to the pulmonary artery *via* a Y-graft (extracardiac conduit), and the sum of the diameters (10 mm) of the two branches of the Y-graft was equal to the diameter of the trunk (20 mm); the two branches were anastomosed to the pulmonary artery close to the left hilum and right hilum, respectively, and the SVC was anastomosed to the pulmonary artery between the two branches to avoid energy consumption caused by competition between blood flows.

Group C (12 mmY), an intermediate YCPC group (20 mm-12 mm-12 mm): The trunk diameter of the extracardiac conduit remains unchanged, and the branch diameter (12 mm) was larger than one half the trunk diameter. The anastomosis method was same as that of group B.

Group D (14 mmY), a handcrafted YCPC group (area-preserving 20 mm-14 mm-14 mm): The square of the trunk radius (10 mm) of the extracardiac conduit is approximately equal to the sum of the squares of the radii (7 mm) of two branches, and the anastomosis method was same as that of group B.

2.3 Numerical simulation method and boundary condition settings

Based on the completion of the construction of the three-dimensional geometric model, the geometric models of the four preoperative plans were meshed. Meshing software Hypermesh was used to mesh the computational domains. Hexahedral and tetrahedral meshes were used to test the mesh sensitivity, and the adaptive mesh technology was used for local mesh refinement. (It is recommended to add the results of sensitivity analysis to confirm whether tetrahedral or hexahedral mesh should be used, the number of meshes, and the graph of the computational domain mesh changes before and after mesh adaptation.)

Using the CFD analysis software Fluent and the in-house developed three-component coupling program, the team used the Lagrangian-Euler method to carry out numerical simulation of multiple working conditions and multiple schemes.

Due to its low flow velocity and laminar flow, blood was regarded as an incompressible Newtonian fluid, and the influence of gravity on it was neglected. The walls of artificial blood vessels and pulmonary arteries were assumed to be rigid walls, and no-slip boundary conditions were used. x, y, and z represent the components in the three directions of the rectangular coordinate system. The blood flow satisfies the Navier-Stokes (N-S) equation and the continuity equation:

$$\frac{Dv_x}{Dt} = -\frac{1}{\rho}\frac{\partial P}{\partial x} + \frac{\mu}{\rho}\left(\frac{\partial^2 v_x}{\partial x^2} + \frac{\partial^2 v_x}{\partial y^2} + \frac{\partial^2 v_x}{\partial z^2}\right) \quad (1)$$

$$\frac{Dv_y}{Dt} = -\frac{1}{\rho}\frac{\partial P}{\partial y} + \frac{\mu}{\rho}\left(\frac{\partial^2 v_y}{\partial x^2} + \frac{\partial^2 v_y}{\partial y^2} + \frac{\partial^2 v_y}{\partial z^2}\right) \quad (2)$$

$$\frac{Dv_z}{Dt} = -\frac{1}{\rho}\frac{\partial P}{\partial z} + \frac{\mu}{\rho}\left(\frac{\partial^2 v_z}{\partial x^2} + \frac{\partial^2 v_z}{\partial y^2} + \frac{\partial^2 v_z}{\partial z^2}\right) \quad (3)$$

$$\frac{\partial v_x}{\partial x} + \frac{\partial v_y}{\partial y} + \frac{\partial v_z}{\partial z} = 0 \quad (4)$$

In the equations, ρ represents the density of blood; v_x, v_y, v_z are the components of blood flow velocity; μ is the dynamic viscosity; and P is pressure. The density is 1,060 kg/m^3, and the dynamic viscosity is 0.0035pas.

The flow velocity of the SVC and IVC were extracted from the previous TCPC patient's echocardiography and recorded during a respiratory cycle, and the measured images of the SVC and IVC flows were extracted into a flow curve that changes with the respiratory cycle. The computing cycle was 2.54s, the time step was 0.001 s. The results obtained by the average of 2,540 time steps.

The flow velocity curve was applied to the inlets of the SVC and IVC. The conditions at light, moderate, and heavy exercise were simulated by setting the IVC flow velocity at 2, 3, and 4 times the IVC flow velocity at rest, respectively, and reducing the resistance by 5%, 10%, and 15%, respectively. In addition, the SVC flow velocity for heavy exercise was set 50% higher than the SVC flow velocity at rest, and the SVC flow velocity for light and moderate exercise were set the same as the SVC flow velocity at rest (Marsden et al., 2009).

2.4 Computation of energy efficiency

Based on the energy efficiency formula, the energy efficiency of the flow from inlet to outlet was computed for different levels of exercise. Because of the same SVC and IVC configurations at all inlets and the identical pulmonary artery configurations at all outlets, the difference in energy efficiency was mainly due to the different configurations of the extracardiac conduits. The energy efficiency satisfies the following equation:

$$E_{diss} = -\sum_{i=1}^{N_{in}} \int_{Ai} \left(p + \frac{1}{2}\rho u^2\right)\mathbf{u} \cdot dA - \sum_{i=1}^{N_{out}} \int_{Ai} \left(p + \frac{1}{2}\rho u^2\right)\mathbf{u} \cdot dA, \quad (5)$$

where u is the flow velocity, p is the pressure, ρ is the density, N_{in} and N_{out} are the number of inlets and outlets of the model, respectively, and A_i is the area of the i-th inlet or outlet. Energy

efficiency is the ratio of the second term to the first term in the above equation.

2.5 Particle tracking

This method was used to count the left pulmonary artery (LPA) and right pulmonary artery (RPA) flow of the IVC during a whole respiratory cycle. Assuming that the particles have no mass, and the diffusion effect is ignored, in a single breathing cycle, about 400 particles are released every 0.001 s. The total amount of released particles in the whole cycle is 1016000, and the total amount of captured particles is 936000. The uncapped particles are particles still flowing in the fluid domain at the end of breathing, and the captured particle mass at the LPA and RPA outlets can be counted to obtain the left and right blood diversion ratio.

2.6 Postoperative data collection

The patient had been followed up for 3 years, the radionuclide lung perfusion, CTA, cardiovascular angiography and catheterization were performed 12 months after operation, echocardiography was performed every year.

Radionuclide lung perfusion with technetium-99 m (99 mTc, Atomic High Technology Co., Ltd., Beijing, China)-labeled macroaggregated albumin (MAA, Jiangsu Institute of Nuclear Medicine) was performed to determine the distribution of the patient's IVC flow. The tracer, 99 mTc-labeled MAA, was administered through the dorsal vein of the foot. The distribution of IVC flow to the left and right lungs was compared.

2.6.1 Imaging method

After a slow intravenous injection of 99 mTc-labeled MAA in the supine position, the patient was scanned at eight views, including anteroposterior, left anterior oblique, left lateral, left posterior oblique, posteroanterior, right posterior oblique, right lateral and right anterior oblique views.

2.6.2 Quantitative analysis

The posteroanterior image was used to measure the radionuclide counts in the left and right lungs.

3 Results

We obtained the preoperative CTA data of the patient and then created a model. Different spatial structures were used to connect the extracardiac conduit and pulmonary artery. These spatial structures were divided into 4 groups. The experimental results are described as follows:

3.1 Pressure gradient

The PG was calculated by subtracting the sum of pressures at the left and right pulmonary hilum by the sum of pressure of SVC and IVC, and then divided by 2.

The PG of each group is lower than 1 mmHg at rest, but with the increase of exercise, the PG gradually increases, and in group A, PG can reach 7.07 mmHg under heavy exercise. For Y-shaped conduit, the highest PG is 7.67 mmHg in group B (10 mmY). The increase of branch diameter can effectively reduce the PG under different levels of exercise. The PG in Group D was lowest and the increase rate was the slowest under rest and different levels of exercise (Figure 1). Therefore, if the branch diameter of Y-shaped conduit is not enough, the PG would be higher.

We look for the main source of the PG by the pressure distribution nephogram (Figure 2). In group A, the main source of PG was located between the intersection of SVC and the right hilum. For Y-shaped conduit, PG mainly comes from the bifurcation of conduit. However, the PG gradually decreases with the increase of bifurcation diameter, and the PG almost cannot be found in group D (14 mmY).

3.2 Flow velocity

The flow velocity was calculated at bifurcation of conduit in group B, C and D, and at the same section of T-shaped conduit trunk in group A.

At the inlet of the SVC and IVC in each group were same. At rest and different levels of exercise, group B had a significantly faster flow velocity in the Y-graft branches than other groups. As the branch diameter increased, the branch flow velocity gradually decreased (Group C). The branch flow velocity in Group D was basically same as that of the trunk of the conduit (Figure 3).

Therefore, a smaller branch diameter might be the main reason of the faster flow for Y-shaped conduit.

3.3 Distribution of IVC flow

The distribution of the IVC flow to the LPA and RPA is a main determinant for prognosis of Fontan circulation. We were able to determine those different spatial configurations which significantly changed the distribution of the IVC flow to the LPA and RPA by the particle tracking. We assumed that the ratio of LPA and RPA distribution was 45 to 55 (LPA/RPA) (Marsden et al., 2009).

The conventional surgical method (Group A) alleviated the competition between the SVC and IVC flows, but the misalignment of the anastomosis caused more blood in the IVC flow to the LPA (60%) (Figure 4). However, the distribution percentage of IVC blood in LPA and RPA changed dramatically (LPA, 46.4%-60%) from rest to exercise.

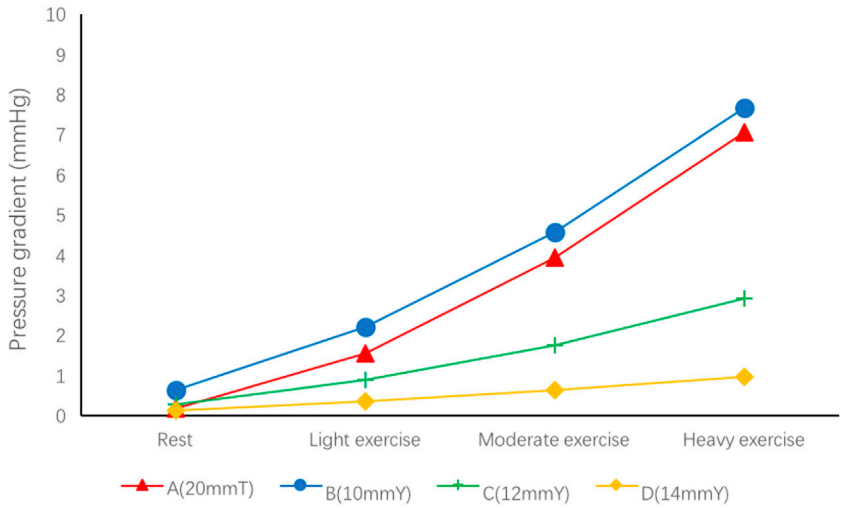

FIGURE 1
Pressure gradient in the four groups of different spatial configurations.

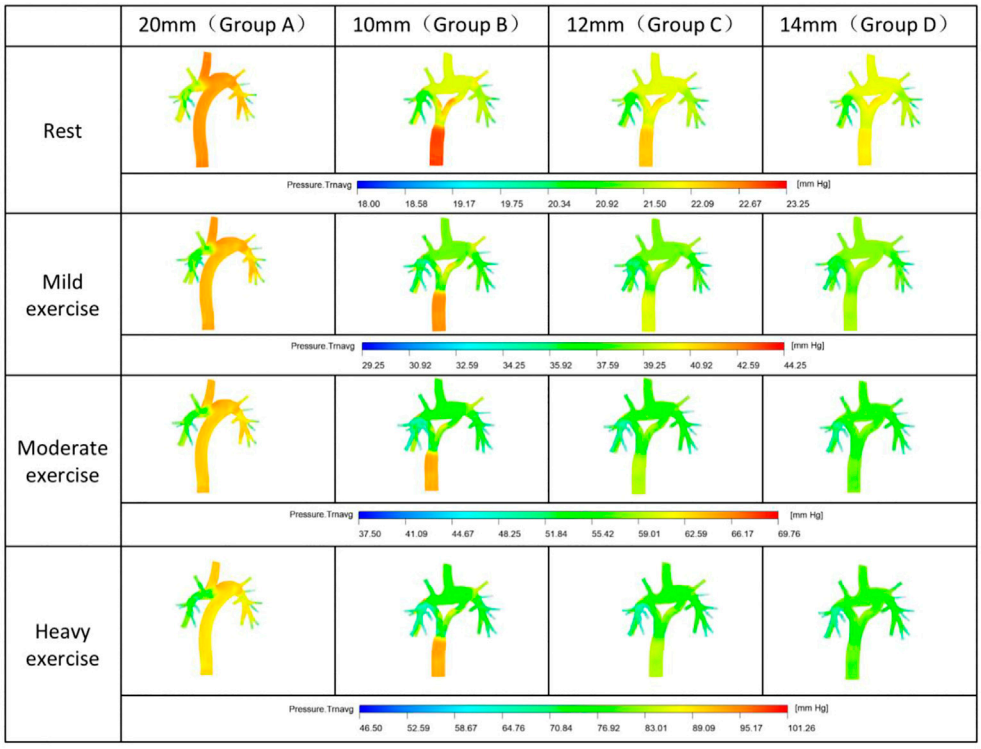

FIGURE 2
Nephogram of pressure distribution.

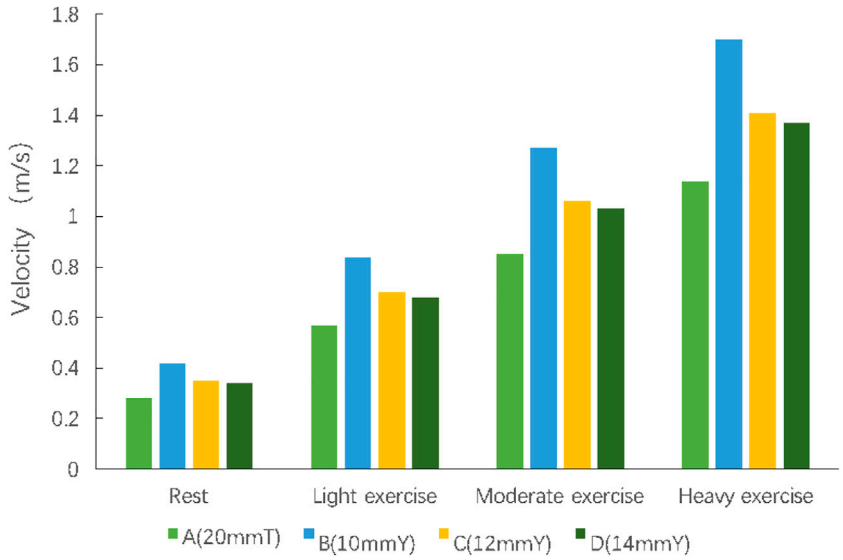

FIGURE 3
The velocity at corresponding section of each group.

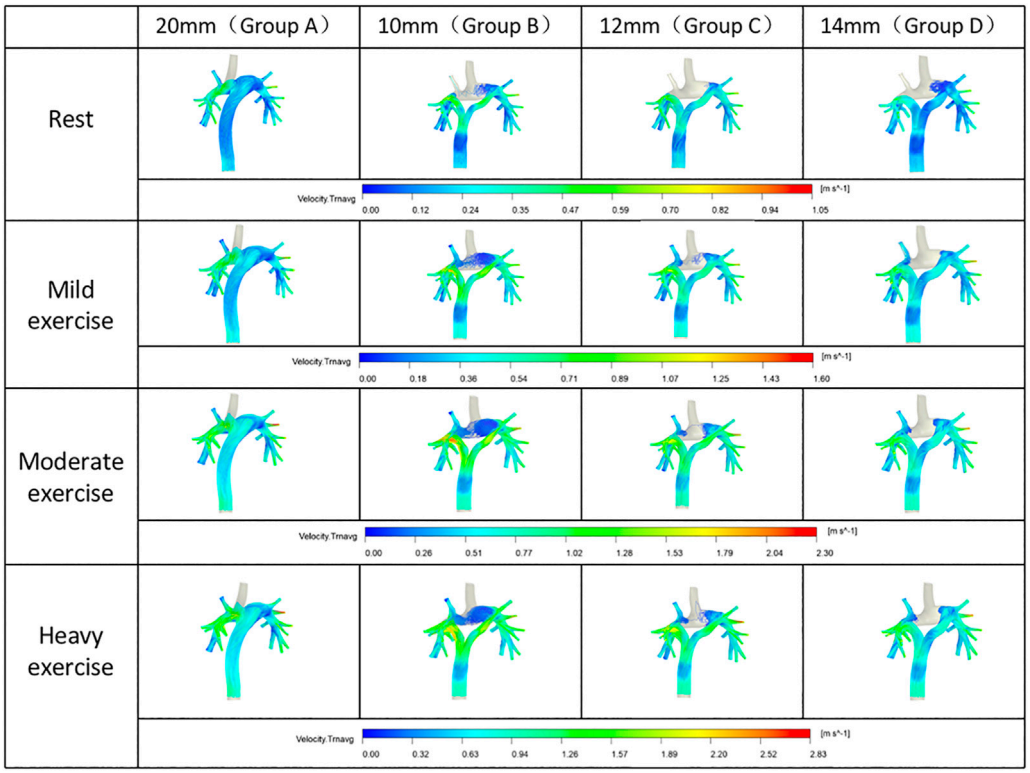

FIGURE 4
Distribution of the inferior vena cava blood flow.

TABLE 1 Distribution of the inferior vena cava blood flow under different levels of exercise.

Percentage (%)	A (20 mm T)		B (10 mm Y)		C (12 mm Y)		D (14 mm Y)	
	L	R	L	R	L	R	L	R
Rest	60	40	43.4	56.6	42	58	40	60
Light exercise	48.2	51.8	42.4	57.6	42.3	57.7	40.3	59.7
Moderate exercise	46.4	53.6	42.8	57.2	41.1	58.9	40.8	59.2
Heavy exercise	47	53	40.7	59.3	40.7	59.3	40.6	59.4

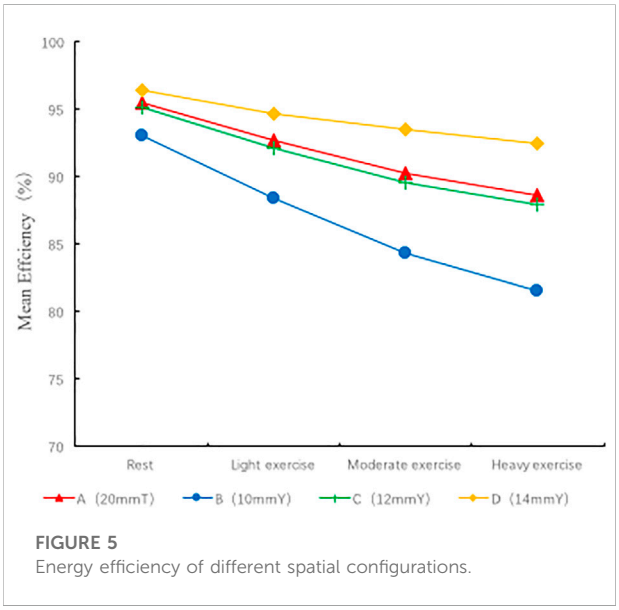

FIGURE 5
Energy efficiency of different spatial configurations.

The IVC flow distribution was more balanced for the group B, while that in group D was the most stable during different levels of exercise (Table 1).

3.4 Energy efficiency

The energy efficiency of each geometric configuration was computed according to the energy efficiency equation (Figure 5). In all models, group B (10 mmY type) was associated with the lowest energy efficiency (93% at rest, 81.5% for heavy exercise), and the energy efficiency was 11.5% lower during heavy exercise than at rest. Compared with the conventional group A (20 mmT), the Y-graft branches (10 mmY) of group B did not significantly improve the energy efficiency of the surgical method. However, the diameter of the Y-graft branches directly affected the overall energy efficiency. As the branch diameter increased, the energy efficiency gradually improved. Group D (14 mmY) was associated with the highest energy efficiency (96.4% at rest, 92.4% for heavy exercise), and the energy efficiency was only 4% during heavy exercise than at rest. The energy efficiency in all groups was significantly lower during exercise than at rest. Therefore, a large diameter of the Y-graft branches can significantly improve the energy efficiency of YCPC, while a smaller branch diameter increases the energy consumption (Figure 5).

3.5 Application of a handcrafted Y-shaped conduit

To facilitate AI learning in the future, we try to quantify the simulation indicators to select the optimal procedure. According to the best to the worst indicators, we score each indicator of 4, 3, 2 and 1 respectively (Table 2).

In the operation design stage, based on Table 2, the group D (14 mm Y) had following advantages: the lowest PG, the lower velocity at bifurcation of Y-shaped conduit, the highest energy efficiency, and a relatively balanced (not the most balanced, but the most stable) IVC flow distribution.

In the application stage, the right branch of the Y-shaped conduit was moved to a position close to the midline because the right superior pulmonary artery could not obtain IVC blood flow. Subsequently, a handcrafted Y-shaped conduit (20 mm-14mm-14 mm) was used for the YCPC procedure under mild hypothermic cardiopulmonary bypass, because the commercially available Y-grafts was diameter-preserving (20 mm-10 mm-10 mm). The procedure went well and postoperative recovery was good (Figure 6).

3.6 Verification

In the postoperative stage, tracheal extubation was conducted on the 7th day after surgery. The patient was discharged from hospital on the 15th day after surgery. The patient had been followed up for 3 years with a good recovery. During the follow-up, the echocardiography, cardiovascular CTA, pulmonary blood perfusion scan, cardiovascular angiography and catheterization were perfomed to verification the outcome (Figure 6).

TABLE 2 The scores of each indicator for 4 groups.

Score	PG	Velocity	Energy efficiency	Balanced IVC flow	Total
A (20 mm T)	2	4	2	1	9
B (10 mm Y)	1	1	1	4	7
C (12 mm Y)	3	2	3	3	11
D (14 mm Y)	4	3	4	2	13

PG, Pressure gradient; IVC, inferior vena cava.

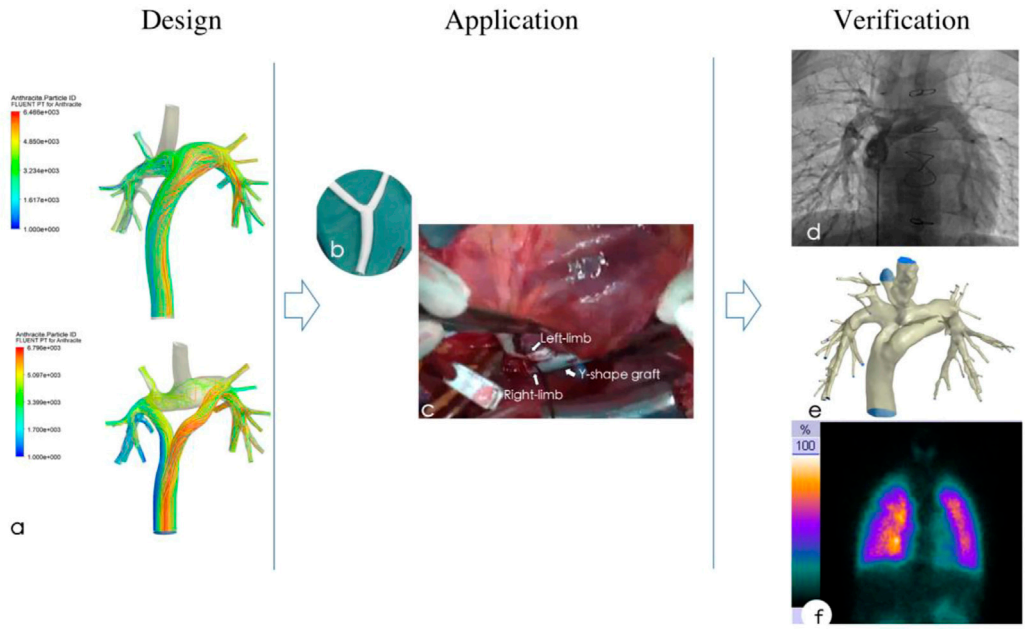

FIGURE 6
Preoperative design based on computational fluid dynamics simulation **(A)**, then a handcrafted Y-shaped conduit **(B)** was applicated for functional single ventricle **(C)**, postoperative catheter angiography **(D)**, CT angiography **(E)** and pulmonary perfusion scan **(F)** showed normal pulmonary pressure and resistance, while IVC flow was distributed uniformly.

3.6.1 Morphology and velocity

The CTA showed that the conduit was in good shape, and there was no stenosis at each anastomosis; And cardiovascular angiography showed that the Y-graft extracardiac conduit made the IVC blood evenly distribute to the LPA and RPA, which brought good blood perfusion in pulmonary (Supplementary Video S1).

The echocardiography was performed every year regularly after the operation, and the velocity of each anastomosis were specifically detected. We recorded them during the follow-up period. Echocardiography showed that the flow velocity at the anastomotic site between the IVC and RPA was 0.35 m/s; The velocity of the anastomosis between the conduit and IVC, LPA and RPA was 0.3 m/s, 0.48 m/s and 0.45 m/s respectively, which was basically consistent with the velocity before operation (0.24–0.41 m/s).

3.6.2 PG

Catheterization showed there is no PG in the conduit and pulmonary, the pressure of vena cava and pulmonary both are 24/16 mmHg, while the pulmonary vascular resistance was 1.18 woods.

3.6.3 Distribution of the IVC

We used the distribution ratio of IVC flow in both lungs to represent the distribution of hepatic blood flow, and achieved good results. Pulmonary blood perfusion scan was used to detect the distribution of the IVC flow to LPA and RPA. The

TABLE 3 Percentage of inferior vena cava flow by radionuclide lung perfusion.

Percentage (%)	Left	Right
Upper	8.1	9.66
Middle	21.79	25.97
Lower	16.82	17.66
Total	46.71	53.29

99 mTc was injected through the dorsal vein of the foot to show the distribution of the IVC flow to LAP and RPA. The results showed that the IVC flow was distributed uniformly to LPA and RPA (46.71 vs. 53.29) and was uniformly distributed to the upper, middle and lower parts of the lung. The result was similar as the preoperative simulation data (Table 3). In addition, the hepatic function (transaminase and bilirubin) was normal at the early stage and during the follow-up period.

4 Discussion

After nearly 50 years of development and improvement of the series of Fontan procedure, its clinical efficacy has continuously improved. In 1988, de Leval de Leval et al. (1988) found that conventional Fontan procedures could easily cause intra-atrial vortexes to increase energy consumption and thus lead to resistance to forward blood flow. Computer simulations has proven the importance of linear blood flow in blood vessels. Thus, TCPC was designed to provide linear flow in blood vessels to improve the conventional Fontan procedures.

With the continuous innovation of technology, data modeling and CFD research based on CT and MR imaging revealed that TCPC is still problematic in high energy consumption and uneven IVC flow split (Sundareswaran et al., 2012; Tang et al., 2013). Some researchers have applied CT-based vascular geometric models in individual patients. From the perspective of fluid mechanics, they proved that the use of a Y-graft extracardiac tube to connect the SVC to the pulmonary arteries and another Y-graft extracardiac tube to connect the pulmonary arteries to the IVC can form a diamond-shaped spatial configuration to optimize the conventional TCPC (Soerensen et al., 2007). Although this design is theoretically feasible and can make blood flow distribution more evenly, it cannot be effectively implemented from a surgical perspective. Moreover, we believe that if the competition between the SVC and IVC flows cannot be avoided, energy consumption can easily be high. Subsequent studies show that split of the blood flow in the IVC into two flows can make the blood evenly distributed and thus increase fluid efficiency and reduce vortex and conduit wall shear force (Kanter et al., 2012; Martin et al., 2015). In theory, YCPC brings two major advantages, decreases in energy consumption and even IVC flow split. Therefore, YCPC may gradually replace conventional TCPC in clinical applications.

The clinical effect of Fontan series surgery is improving, but the two desired theoretical advantages of YCPC design have not been fully realized in clinical application in view of the current studies. There might be higher resistance and less balanced hepatic flow for YCPC than lateral tunnel or extracardiac conduit (Martin et al., 2015; Trusty et al., 2016).

Our center had conducted a long-term and in-depth clinical study on a series of Fontan procedures since 1980. We reported the first group of traditional modified Fontan operation and TCPC of China in 1984 and 1992, respectively (Wang et al., 1984; Wang et al., 1992). The subsequent follow-up studies on pulmonary vascular perfusion and activity tolerance were carried out (Yin et al., 2006; Yin et al., 2009; Yin et al., 2012), and the longest follow-up period was 32 years (Zhang et al., 2020). In 2015, we reported the first group of YCPC of China with good follow-up result of hemodynamics (Wang et al., 2015). We found that the individualized differences of patients significantly affected the postoperative efficacy. Therefore, a good clinical operation design and effect prediction is urgently needed.

In previous studies (Soerensen et al., 2007; Sundareswaran et al., 2009), CFD technology were applied for simulation of the hemodynamics of TCPC, but they were not used for the optimization of spatial structures and prediction of efficacy. Moreover, there were huge defects in their applications, such as incomplete image information of pulmonary arteries. Although many studies have been done, it is impossible to simulate blood flow realistically, and it is impossible to predict the impact of the main branches of the pulmonary artery on blood flow energy consumption, resulting in a significantly poorer clinical prognosis than expected.

Because commercial Y-grafts currently used are diameter-preserving, in order to make the extracardiac conduits more efficient, some international centers (Marsden et al., 2009; Yang et al., 2015) began to use hand-sewn Y-grafts (extracardiac conduits) to ensure the sum of the area of the two branches close to the area of the trunk. In their studies, they found that the efficiency of the diameter-preserving Y-grafts was 88.5%, while the efficiency of area-preserving Y-grafts could reach 90.3%. In the case of exercise, the difference between the efficiencies of diameter-preserving Y-grafts and area-preserving Y-grafts is more obvious. Therefore, we used different Y-graft designs in our study to analyze their differences.

Our study has shown that when compared with TCPC, the YCPC can achieve more evenly distribution of the SVC and IVC flows to the left and right lungs, resulting in a balanced distribution of the IVC flow and promotes the haptic factors to flow into the left and right lungs, and reducing the incidence of

postoperative pulmonary arteriovenous fistula (de Zelicourt et al., 2011). In the application of the Y-grafts, the branch diameter directly affects the branch flow velocity. The diameters of Y-grafts in the diameter-preserving group were 20-10-10 mm. The branch flow velocity increased significantly in the beginning. This in turn leads to an increase in energy consumption. As the branch diameter increases, the rate in the beginning of the branch also decreases, thus reducing the energy consumption of the conduits. In the area-preserving group (20-14-14 mm), the sum of the cross-sectional area of the two branches were approximately equal to the cross-sectional area of the trunk, the flow velocity in the beginning of the branch was gradually reduced to close to that of the trunk. The branch diameter of the Y-graft directly affected the pressure at the inlet of the IVC, and compared with the conventional TCPC group, the pressure at the IVC inlet in the diameter-preserving group (20-10-10 mm) was significantly higher. With increase of the branch diameter, the pressure at the IVC inlet gradually decreased. The pressure at the IVC inlet in the area-preserving group (20-14-14 mm) was close to that in the conventional TCPC group. Overall, compared with the conventional spatial configuration of TCPC, the area-preserving spatial configuration of the YCPC were not significantly different in the pressure at the SVC and IVC inlets and the overall flow velocity but resulted a more even distribution of the IVC flow to the left and right lungs without increasing energy consumption.

We found that smaller branch diameter may be the main reason for the PG in Y-shaped conduit which will bring more energy consumption. Sufficient cross-sectional area of branch brought a higher energy efficiency. This theory might explain why the resistance for commercially available YCPC was higher (Trusty et al., 2016).

4.1 Study limitations

This study is only a preliminary study, providing a possibility for future AI learning. We need more cases and studies to provide objective data for machine learning.

In addition, it has great limitations when addressing clinical application. There are many factors can bring decreased energy efficiency such as wall shear stress, vortex, etc. The mechanism of higher energy efficiency did not be study and discuss in this research. Furthermore, Blood vessels were assumed to be rigid structures, but they are elastic structures that can be deformed. FSI (Fluid Structure Interaction) can simulate the interaction between fluid and solid, so as to simulate dynamic blood vessels, which is closer to the real clinical application. These will be discussed in future studies.

5 Conclusion

By combining the advantages of clinical medicine, radiodiagnostics, and fluid mechanics, we analyzed the optimal spatial configuration of the extracardiac conduit suitable for TCPC. We found that the smaller bifurcation diameter may be the main reason for the higher PG and faster velocity in Y-shaped conduit. A good preoperative design on individual basis based on CFD could bright more balance IVC distribution and higher energy efficiency. This study also provides a theoretical basis for clinical applications of YCPC.

Data availability statement

The original contributions presented in the study are included in the article/Supplementary Material, further inquiries can be directed to the corresponding author.

Ethics statement

The studies involving human participants were reviewed and approved by General Hospital of Northern Theater Command. Written informed consent to participate in this study was provided by the participants' legal guardian/next of kin. Written informed consent was obtained from the minor(s)' legal guardian/next of kin for the publication of any potentially identifiable images or data included in this article.

Author contributions

Drafting article and computational fluid dynamics: YZ; Critical revision of article and approval of article: HW; Surgical design and guidance: ZW; Clinical application: MF and CZ; Perioperative data collection: YL, CZ, and ZW.

Funding

Natural Science Foundation of Liaoning Province (2022-YGJC-12).

Conflict of interest

The authors declare that the research was conducted in the absence of any commercial or financial relationships that could be construed as a potential conflict of interest.

Publisher's note

Supplementary material

The Supplementary Material for this article can be found online at: https://www.frontiersin.org/articles/10.3389/fphys.2022.1078140/full#supplementary-material

SUPPLEMENTARY VIDEO S1

Preoperative design based on computational fluid dynamics simulation and postoperative catheter cardiovascular angiography of Y-shaped conduit total cavopulmonary connection.

References

Dabal, R. J., Kirklin, J. K., Kukreja, M., Brown, R. N., Cleveland, D. C., Eddins, M. C., et al. (2014). The modern fontan operation shows no increase in mortality out to 20 years: A new paradigm. *J. Thorac. Cardiovasc. Surg.* 148 (6), 2517–2523. doi:10.1016/j.jtcvs.2014.07.075

de Leval, M. R., Kilner, P., Gewillig, M., Bull, C., and McGoon, D. C. (1988). Total cavopulmonary connection: A logical alternative to atriopulmonary connection for complex fontan operations. *J. Thorac. Cardiovasc. Surg.* 96 (05), 682–695. doi:10.1016/s0022-5223(19)35174-8

de Zelicourt, D. A., Haggerty, C. M., Sundareswaran, K. S., Whited, B. S., Rossignac, J. R., Kanter, K. R., et al. (2011). Individualized computer-based surgical planning to address pulmonary arteriovenous malformations in patients with a single ventricle with an interrupted inferior vena cava and azygous continuation. *J. Thorac. Cardiovasc. Surg.* 141, 1170–1177. doi:10.1016/j.jtcvs.2010.11.032

Kanter, K. R., Haggerty, M. M., Restrepo, M., de Zelicourt, D. A., Rossignac, J., Parks, W. J., et al. (2012). Preliminary clinical experience with a bifurcated Y-graft Fontan procedure--a feasibility study. *J. Thorac. Cardiovasc. Surg.* 144 (2), 383–389. doi:10.1016/j.jtcvs.2012.05.015

Marsden, A. L., Bernstein, A. J., Reddy, V. M., Shadden, S. C., Spilker, R. L., Chan, F. P., et al. (2009). Evaluation of a novel Y-shaped extracardiac Fontan baffle using computational fluid dynamics. *J. Thorac. Cardiovasc. Surg.* 137 (2), 394–403. doi:10.1016/j.jtcvs.2008.06.043

Martin, M. H., Feinstein, J. A., Chan, F. P., Marsden, A. L., Yang, W., and Reddy, V. M. (2015). Technical feasibility and intermediate outcomes of using a handcrafted, area-preserving, bifurcated Y-graft modification of the Fontan procedure. *J. Thorac. Cardiovasc. Surg.* 149 (1), 239–245. doi:10.1016/j.jtcvs.2014.08.058

Piran, S., Veldtman, G., Siu, S., Webb, G. D., and Liu, P. P. (2002). Heart failure and ventricular dysfunction in patients with single or systemic right ventricles. *Circulation* 105 (10), 1189–1194. doi:10.1161/hc1002.105182

Soerensen, D. D., Pekkan, K., de Zelicourt, D., Sharma, S., Kanter, K., Fogel, M., et al. (2007). Introduction of a new optimized total cavopulmonary connection. *Ann. Thorac. Surg.* 83 (6), 2182–2190. doi:10.1016/j.athoracsur.2006.12.079

Sundareswaran, K. S., Frakes, D. H., Fogel, M. A., Soerensen, D. D., Oshinski, J. N., and Yoganathan, A. P. (2009). Optimum fuzzy filters for phase-contrast magnetic resonance imaging segmentation. *J. Magn. Reson. Imaging* 29 (1), 155–165. doi:10.1002/jmri.21579

Sundareswaran, K. S., Haggerty, C. M., de Zelicourt, D., Dasi, L. P., Pekkan, K., Frakes, D. H., et al. (2012). Visualization of flow structures in Fontan patients using 3-dimensional phase contrast magnetic resonance imaging. *J. Thorac. Cardiovasc. Surg.* 143 (5), 1108–1116. doi:10.1016/j.jtcvs.2011.09.067

Tang, E., Haggerty, C. M., Khiabani, R. H., de Zelicourt, D., Kanter, J., Sotiropoulos, F., et al. (2013). Numerical and experimental investigation of pulsatile hemodynamics in the total cavopulmonary connection. *J. Biomech.* 46 (2), 373–382. doi:10.1016/j.jbiomech.2012.11.003

Trusty, P. M., Restrepo, M., Kanter, K. R., Yoganathan, A. P., Fogel, M. A., and Slesnick, T. C. (2016). A pulsatile hemodynamic evaluation of the commercially available bifurcated Y-graft Fontan modification and comparison with the lateral tunnel and extracardiac conduits. *J. Thorac. Cardiovasc. Surg.* 151, 1529–1536. doi:10.1016/j.jtcvs.2016.03.019

Wang, H., Wang, Z., and Fang, M., (2015). Analysis of postoperative hemodynamic results of Y type extracardiac conduit fontan operation. *Chin. J. Thorac. Cardiovasc Surg.* 031 (009), 553–555. doi:10.3760/cma.j.issn.1001-4497.2015.09.011

Wang, Z., Fei, C., and Zhang, R., (1984). Modified Fontan operation for a univentricular heart. *Zhonghua Wai Ke Za Zhi* 22 (6), 365–367, 384.

Wang, Z., Fei, C., and Zhu, H., (1992). Total cavopulmonary connection operation. *Chin. J. Thorac. Cardiovasc Surg.* 3, 142–144.

Yang, W., Chan, F. P., Reddy, V. M., Marsden, A. L., and Feinstein, J. A. (2015). Flow simulations and validation for the first cohort of patients undergoing the Y-graft Fontan procedure. *J. Thorac. Cardiovasc. Surg.* 149 (1), 247–255. doi:10.1016/j.jtcvs.2014.08.069

Yin, Z., Wang, C., Zhu, H., Zhang, R., Wang, H., and Li, X. (2009). Exercise tolerance in extracardiac total cavopulmonary connection. *Asian cardiovasc. Thorac. Ann.* 17 (1), 39–44. doi:10.1177/0218492309102531

Yin, Z., Wang, H., Wang, Z., Zhu, H., Zhang, R., Hou, M., et al. (2012). Radionuclide and angiographic assessment of pulmonary perfusion after fontan procedure: Comparative interim outcomes. *Ann. Thorac. Surg.* 93 (2), 620–625. doi:10.1016/j.athoracsur.2011.10.001

Yin, Z., Wang, Z., Zhu, H., Zhang, R., Wang, H., and Li, X. (2006). Experimental study of effect of Fontan circuit on pulmonary microcirculation. *Asian cardiovasc. Thorac. Ann.* 14 (3), 183–188. doi:10.1177/021849230601400303

Zhang, Y., Fang, M., Wang, Z., and Wang, H. (2020). Traditional atriopulmonary connection fontan with excellent outcome for 32 years. *Thorac. Cardiovasc. Surg. Rep.* 9 (1), e18–e20. doi:10.1055/s-0040-1708528

frontiers | Frontiers in Physiology

TYPE Original Research
PUBLISHED 22 December 2022
DOI 10.3389/fphys.2022.1084420

OPEN ACCESS

EDITED BY
Lisheng Xu,
Northeastern University, China

REVIEWED BY
Nivitha Varghees V.,
Jyothi Engineering College, India
Hong Tang,
Dalian University of Technology, China

*CORRESPONDENCE
Lingling Wang,
wll@aufe.edu.cn

SPECIALTY SECTION
This article was submitted to Computational Physiology and Medicine, a section of the journal Frontiers in Physiology

RECEIVED 30 October 2022
ACCEPTED 12 December 2022
PUBLISHED 22 December 2022

CITATION
Li F, Zhang Z, Wang L and Liu W (2022), Heart sound classification based on improved mel-frequency spectral coefficients and deep residual learning. *Front. Physiol.* 13:1084420. doi: 10.3389/fphys.2022.1084420

Heart sound classification based on improved mel-frequency spectral coefficients and deep residual learning

Feng Li[1,2], Zheng Zhang[1], Lingling Wang [1]* and Wei Liu[1]

[1]Department of Computer Science and Technology, Anhui University of Finance and Economics, Bengbu, Anhui, China, [2]School of Information Science and Technology, University of Science and Technology of China, Hefei, Anhui, China

Heart sound classification plays a critical role in the early diagnosis of cardiovascular diseases. Although there have been many advances in heart sound classification in the last few years, most of them are still based on conventional segmented features and shallow structure-based classifiers. Therefore, we propose a new heart sound classification method based on improved mel-frequency cepstrum coefficient features and deep residual learning. Firstly, the heart sound signal is preprocessed, and its improved features are computed. Then, these features are used as input features of the neural network. The pathological information in the heart sound signal is further extracted by the deep residual network. Finally, the heart sound signal is classified into different categories according to the features learned by the neural network. This paper presents comprehensive analyses of different network parameters and network connection strategies. The proposed method achieves an accuracy of 94.43% on the dataset in this paper.

KEYWORDS

heart sound classification, cardiovascular, MFCC, deep learning, Resnet

1 Introduction

Cardiovascular disease is a term used to describe a group of diseases, including coronary heart disease, cerebrovascular disease, and rheumatic heart disease. A patient's blood pressure, blood sugar, and lipid levels can be raised by fried foods, fast foods, alcohol, and tobacco, as well as weight gain and obesity, leading to premature death. Prevention of sudden death from cardiovascular disease can be achieved by finding groups at risk for cardiovascular disease and ensuring they receive the proper treatment. It is possible to reduce the risk of sudden death from cardiovascular disease by reducing alcohol consumption, reducing salt intake, eating more fruits and vegetables, and exercising more.

Heart sounds are produced by the heart through rhythmic contraction and diastole. The heart is the powerhouse of the body and it is the most critical organ in the body, responsible for delivering blood to other organs to provide oxygen and other nutrients and to carry away the end products of metabolism so that cells can maintain a normal

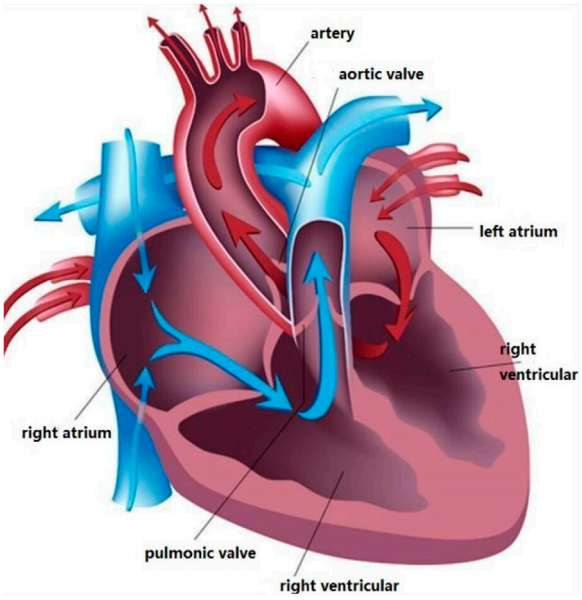

FIGURE 1
The Structure of the human heart.

physiological state. Hearts have four chambers: Left atrium, left ventricle, right atrium, and right ventricle, the details of heart structure are shown in Figure 1. Atrioventricular valves prevent blood from flowing backward between the atria and ventricles Li S. et al. (2020).

A cardiac cycle occurs when one heartbeat precedes the next, producing four heart sounds, which are the first, second, third, and fourth heart sounds. Screening for cardiovascular disease by auscultatory heart sound auscultation is a simple, necessary, and effective method that has been used for over 180 years Liu et al. (2016). The first heart sound marks the beginning of ventricular systole and is characterized by long duration, high intensity, and loud sound. The second heart sound marks the beginning of ventricular diastole and has the characteristics of shorter duration, less intensity, and less sound. After the second heart sound, the third heart sound occurs. It lasts between 0.04 and 0.05 s and has a longer wavelength. About half of young adults and most children hear it, and it does not necessarily indicate abnormality. In the fourth heart sound, a long wave sound precedes the first heart sound and lasts for about 0.04 s. It is mechanical wave caused by the contraction of the atria and the rapid filling of the ventricles with blood flow, also known as an atrial sound. Most healthy adults can record a tiny fourth heart sound on an electrocardiogram, which is difficult to detect on general auscultation. Based on the patient's clinical condition, the physician records the four basic heart sounds and analyzes their differences from the normal situation. It is typically tricky for physicians to determine a patient's condition by heart sound auscultation in clinical practice Jiang and Choi (2006). Industrialization has made sophisticated machines standard medical tools, and electrocardiograms (PCG) are recorded using acoustic instruments to diagnose and treat patients. With the continuous application of PCG, the use of signal processing and artificial intelligence techniques to extract physiological and pathological information from PCG data has gradually become a popular trend Herzig et al. (2014). Benefit from the development of deep learning field in recent years Hinton and Salakhutdinov (2006); Yu et al. (2013); Ranzato et al. (2006); Bengio. (2009); Hinton and Salakhutdinov (2012); Vincent et al. (2010); Silver et al. (2016); Nair and Hinton (2010), a new horizon has been opened for heart sound classification Zhang and Han (2017). CNN is now a mature deep learning framework since it was first proposed in 2006. It has become a widely used approach in computer vision due to its convolutional layer that learns local patterns of images. CNN is also gradually applied to biomedical signal classification and speech semantic

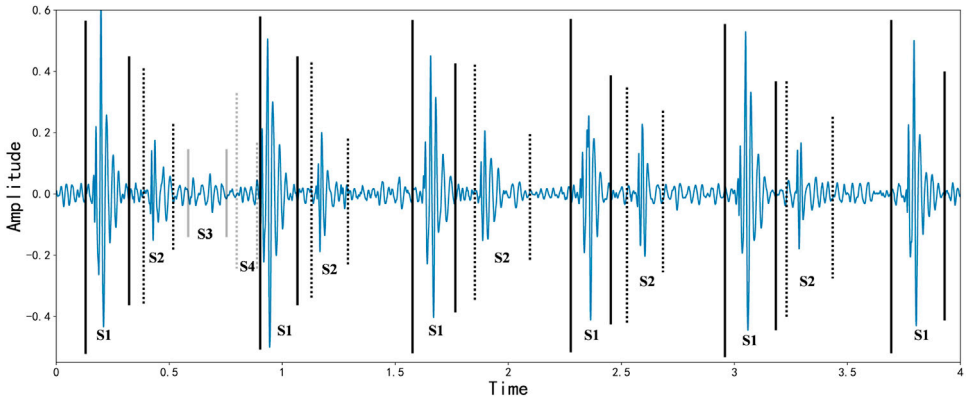

FIGURE 2
Waveform representation of S1, S2, S3, and S4 sounds in systole and diastole intervals, as of Varghees and Ramachandran (2014).

recognition through corresponding audio processing methods, such as transforming human physiological signals into speech spectrograms. Recurrent neural networks (RNN) are a class of neural networks that specialize in processing sequential data. Gated recurrent units (GRU) and long short-term memory (LSTM) are improved versions of RNN, and they provide state-of-the-art performance in many applications, including machine translation, speech recognition, and image captioning Abduh et al. (2019). Heart sound signals are sequential data with strong temporal correlation, so heart sound classification can be efficiently processed by RNN Nogueira et al. (2019); Ismail et al. (2022); Sakib et al. (2019). Figure 2 describes the Waveform representation of S1, S2, S3, and S4 sounds in systole and diastole intervals.

In addition, since some noise in the environment is inevitably collected during the acquisition of heart sounds, this can greatly affect the accuracy of the model classification. Therefore, it is crucial to process the original heart sound signal through feature engineering before feeding it into the neural network for training. There are several commonly used feature extraction methods in heart sound classification tasks, including discrete wavelet transform coefficients (DWT) Mei et al. (2021), and Mel frequency cepstral coefficients (MFCC) Yang and Hsieh (2016). In this paper, the MFCC-based first and second-order difference coefficients are used as the input tensor of the neural network. This feature extraction method reduces the effect of noise on the results and allows the neural network to extract the physiological and pathological features in the heart sound signal, resulting in higher classification accuracy. Compared to traditional heart sound classification algorithms, deep learning techniques avoid the problems of manual intervention, complex processes, and poor generalization. Kui et al. (2021) combined MFSC and CNN for classification of heart sounds. Li et al. (2021) used Short Time Fourier Transform (SFTF) based features as input to CNN. Tschannen et al. (2016) used Wavelet-based features and CNN. Li F. et al. (2020) extracted 497 features from time series as input to the CNN. Er (2021) proposed Local Binary Pattern (LBP) and Local Ternary (LTP) pattern features as input to the CNN. Wu et al. (2019) used MFCC as input to the CNN. Lack of large authoritative open heart sound datasets restricts the performance of the model. To address this concern, this paper incorporates three of the most widely used heart sound datasets. It helps to radically improve the performance of the deep learning model. Although the performance of the above methods has been greatly improved compared to traditional machine learning methods, most of these are shallow structures and the features used are insufficient to fully express the information of heart sounds. In this study, we select improved MFCC as input features to more comprehensively represent the static and dynamic characteristics of the heart sound signal. Additionally, we use a residual neural network which alleviates gradient disappearance and degradation during training. Figure 3 summarizes the motivation of our study.

The rest of the paper is structured as follows: Section 2 discusses recent research trends and essential methods related to heart sound classification. Section 3 describes in detail the preprocessing and feature engineering of heart sound audio and introduces the deep residual neural network structure used in this paper and analyzes in detail the more critical convolution and residual principles. In Section 4, we describe the three datasets used in this paper in detail. We split 20% of the dataset as the testing set. All metrics are the results of the testing set. Additionally, we make a comparison between MFCC, $\triangle$MFCC, $\triangle^2$MFCC, and improved MFCC to further explain what the improvements are for a better understanding of the superiority of the methods in this paper, RNNs and CNNs are used for comparison and we show models' loss and accuracy during training. We also list references with other methods used for comparison. Section 5 summarizes our study, and our proposed method is feasible for the heart sound classification task.

2 Related work

At present, heart sound auscultation technology is one of the leading clinical diagnostic tools for treating cardiovascular diseases, with the characteristics of non-invasive, efficient, convenient, and can obtain physiological and pathological information about the heart, but due to the complex clinical diagnostic conditions, there is a lot of noise pollution, a lack of experience in physicians are often disturbed by the noise of the environment, resulting in an inaccurate diagnoses of the condition. In 1929, the German doctor Werner used a catheter to deliver drugs to the heart, opening the door to the use of physical models to study cardiovascular disease; in the 1970s, Dr. Marcus in the United States used angiography to observe the causes of cardiovascular disease, overturning long-held misconceptions about heart disease; in the 1980s, the earliest cardiac defibrillators came into clinical use at Johns Hopkins University, and the earliest telemetry systems were developed so that Doctors coule observe the vital signs of heart disease patients from a distance; in recent years, with the development of technology, devices similar to comprehensive ECG heart sound analyzers and intelligent electronic stethoscopes have been put into clinical use, but due to the inevitable factors in the use process, the collected heart sound signals will contain various types of noise to varying degrees, affecting the final diagnostic results. At present, digital filters, wavelet decomposition and empirical modal decomposition are widely used for digital denoising of heart sound signals. In recent years, with the rise of artificial intelligence, big data, and other technologies, more accurate and effective heart sound detection methods are expected to be realized.

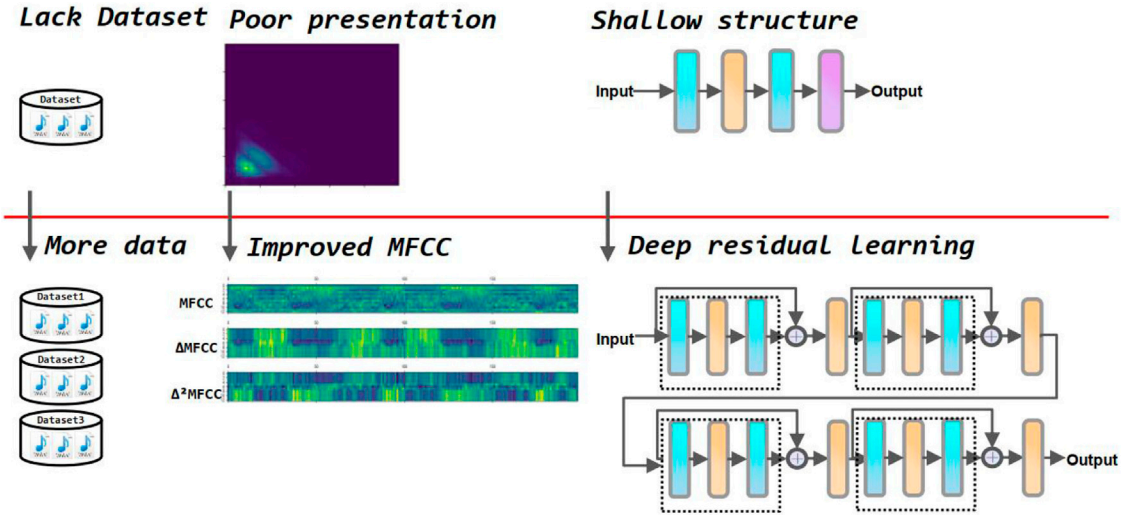

FIGURE 3
Motivation of the proposed method.

The dataset is one of the fundamental issues affecting the results, and heart sound classification is no exception. In general, the larger the data set, the more specialized the distribution, and the more extensive the heart sound data, the more overfitting of the model can be avoided, and the generalizability of the model can be increased. According to a survey Milani et al. (2022), using deep learning techniques for heart sound classification tasks remains challenging due to the lack of a large authoritative open heart sound dataset. In this paper, the Physio heart sound dataset Liu et al. (2016), Pascal heart sound dataset Gomes et al. (2013) and Yaseen heart sound dataset Son and Kwon (2018) were used to construct more extensive, less noisy, and more reliable heart sound dataset. Positive and negative sample imbalances can affect the performance of the model. It is assumed that the distribution of positive and negative samples in the feature space is unbalanced. When the neural network tries to learn the mapping relationship model. It predicts that more samples will bring less loss in most feature space regions. Eventually, this causes the model to fail, and the predicted values are always concentrated near the labels with more samples. That is, the model has very high accuracy on the training set, but a low accuracy on the validation and test sets. It significantly reduces the generalizability of the model. To solve such problems, researchers usually sample the heart sound data and perform slicing operations Baghel et al. (2020); Baydoun et al. (2020) to ensure the balance between the different labels of the samples. Wang et al. (2021) used a weighted improvement of the classifier to reduce the impact of the unbalanced dataset on training. In this paper, the pre-processing of heart sound audio is used to perform cuts and enhance a smaller number of samples to avoid the problem of sample imbalance.

In general, binary classification, multiple classification and regression are often used in classification problems, and how the classification task is chosen can also affect the classification results to some extent. For sequence data with considerable background noise such as heart sounds, the impact of the acquisition process on the real heart sounds must be considered according to the actual situation of the data set. In the current studies of heart sound classification, most of the tasks are dichotomous, normal heart sounds and abnormal heart sounds. Few experiments have classified specific situations such as aortic stenosis and mitral valve insufficiency based on medical knowledge. Demir et al. (2019) used deep convolution neural networks to perform a four classification task on a Kaggle dataset, as well as Oh et al. (2020) performed a quintuple classification task on a heart sound dataset. In this paper, heart sound datasets from three different platforms are considered, considering the inevitable noise generated during the acquisition process due to hardware limitations. Since some cannot identify the heart sound signals, three classification tasks are performed for heart sounds, namely normal, abnormal and noisy, and this selection of classification tasks is closer to the actual situation. It also helps to further improve the accuracy and practical application of heart sound classification.

Many researcher have used deep learning techniques to solve heart sound classification problems. Kui et al. (2021) investigated the effect of discrete cosine transform (DCT) on classification results during MFCC signal extraction. MFSC is an intermediate state in the MFCC extraction process, which omits the step of DCT. CNN is essentially a non-linear transformation of the data, and since DCT is essentially a linear transformation, this operation results in the absence of pathological information in

the heart sound signal, so MFSC is feasible for heart sound classification using deep learning techniques. Krishnan et al. (2020) obtained an accuracy of 85.74% by directly using the unsegmented PCG signal as the input to the CNN. Zeinali and Niaki (2022) used a heart sound audio signal processing algorithm to convert one-dimensional temporal features into two-dimensional spectral features. This proposed method achieved 87.0% accuracy in a heart sound triple classification task. Tian et al. (2022) directly trained the neural network using raw data without using feature engineering from the PhysioNet dataset to perform a binary classification task on PCG to distinguish between normal and abnormal heart sounds. Wang et al. (2021) extracted five classes of features by segmenting the PCG signal. and used a recursive feature elimination method to obtain suitable input features, and proposed an XGBoost-based and LSTM combination for heart sound classification, and obtained an accuracy of 90.0% on the test set. Li et al. (2021) segmented the original heart sound signal and then calculated its frequency domain features by short-time Fourier transform. For training, they proposed 2D-CNN and achieved an accuracy of 85.70%. Er (2021) extracted the local binary pattern (LBP) of heart sounds using local three-valued pattern (LTP) and trained it with 1D-CNN with an accuracy of 90% on the PhysioNet dataset. Ren et al. (2022) used the attention mechanism to explore the interpretable heart sound classification algorithm for heart sound triple classification task on PhysioNet dataset and obtained an unweighted average recall of 51.2%. Iqtidar et al. (2021) obtained 98.3% accuracy on heart sound double classification problem using MFCC based 1D adaptive local ternary model and support vector machine. Lahmiri and Bekiros (2022) used discrete wavelet transform with support vector machine optimized through bayesian optimization obtained 89.26% accuracy. In the heart-tone classification task mentioned above, neural networks with MFCC-based features perform better. To further enhance the advantages of MFCC features in expressing heart sound signals, this paper calculates first-order and second-order difference coefficients for expressing the dynamic properties of heart sound signals.

3 Proposed methodology

This section describes the heart sound classification algorithm proposed in this paper in three parts. The first step is data set fusion, which filters, downsamples, and cuts the original heart sounds. The second step is feature engineering, extracting standard MFCC, first-order MFCC, and second-order MFCC, and fusing them into input feature vectors. In the third step, a deep residual neural network is constructed, and feature vectors are input for training. Finally, the test samples are predicted using the trained model, and the accuracy is counted. Figure 4 shows the workflow of this paper. The innovation of the methodology as threefold: 1) Using the authoritative heart sound datasets from three different sources, which helps to radically improve the performance of the deep learning model. 2) Selecting improved MFCC as input features to more comprehensively represent the static and dynamic characteristics of the heart sound signal. 3) Using a residual neural network, which alleviates gradient disappearance and degradation during training.

3.1 Dataset fusion

The label classification standards of the datasets selected in this paper are different. Before entering the data into the neural network, the labels must be unified, and data pre-processing is performed on all files. making full use of heart sound datasets from different sources helps to improve the generalization of the model further. According to the characteristics of the label types of the dataset, this paper divides the labels of the fused heart sound data into three categories: normal, abnormal, and noise.

3.1.1 Digital filtering

In collecting heart sound audio, due to hardware limitations and the influence of the background environment, many noises will inevitably be collected in the audio. To reduce the impact of noise on neural network training, this paper filtered the heart sound audio. To preserve the low frequency components of heart sounds that contains important physiological information, this paper sends the heart sound audio into the fifth-order 400 hz Butterworth low-pass filter to filter out the high-frequency murmurs in the heart sound signal.

3.1.2 Down sampling

To reduce the computational complexity of the model and ensure that the heart sound data from different sources can generate the same size feature map in the subsequent feature engineering, all audio signals are down-sampled to 2000 hz.

3.1.3 Audio cutting

Considering the significant difference in length between heart sound audios, this paper cuts the audio in units of 2 s to use the existing heart sound audio and unified audio length as much as possible. On the other hand, considering the solid temporal correlation of pathological features in heart sound audio, heart sound audio with too short duration is difficult to express the pathological features of heart sound, so this paper discarded heart sound audio with less than 2 s.

3.2 Feature engineering

In most cases, deep learning models cannot learn from completely arbitrary data, so it is essential to extract heart

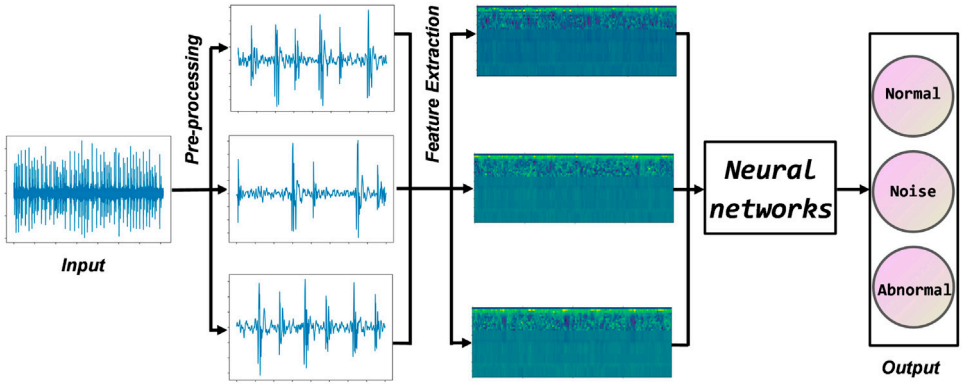

FIGURE 4
Flow chart of the proposed method.

sound features by hard coding through feature engineering. To obtain an effective pathological feature representation of cardiovascular disease, this paper used an improved feature extraction algorithm based on MFCC Deng et al. (2020). The human ear's perception of frequency is logarithmic. It is sensitive to changes in low-frequency bands and insensitive to changes in high-frequency bands. The use of linearly distributed spectrograms in feature engineering affected the model's performance. MFCC reflects the non-linear relationship between the human ear and the sound frequency, which can effectively extract the pathological features in the heart sound audio. The calculation formula of the MFCC is shown as follows

$$\mathrm{Mel}(f) = 2595\lg(1 + f/700) \tag{1}$$

where lg is defined as the base 10 logarithm.

3.2.1 Signal pre-emphasis

In processing the heart sound signals, the high-frequency signal generated during cardiovascular exercise is inadequate, and the low-frequency signal is adequeate. The reason for this phenomenon can explain from the physical level. In the process of sound energy propagation in the medium, the higher the frequency, the more it is easy to be lost, and pre-emphasis makes up for the loss of high frequency and protects the original heart sound signal. In this paper, the heart sound signal. is passed through a high-pass filter to narrow the intensity gap between the high and low-frequency components of the signal. The specific operation of the signal x[n] is shown as follows

$$y[n] = x[n] - \alpha x[n-1] \tag{2}$$

where α usually takes a value close to 1.

3.2.2 Framing windowing

To obtain the distribution of each element of frequency in the heart sound audio, it is necessary to perform Fourier transform on the audio signal, and the Fourier transform requires that the input signal must be stable, so the audio signal needs to be framed and windowed first. Framing is to divide the original signal into several small blocks according to time, and one block is called a frame. In framing process, the original signal will have a spectrum leakage phenomenon. The spectrum corresponding to the original signal and the signal after framing are very different. The Hamming window can effectively overcome the leakage phenomenon Astuti et al. (2012). The Hamming window function W(n) is shown as follows

$$W(n) = (1-\alpha) - \alpha\cos(2\pi n/(N-1)), 0 \le n \le N-1 \tag{3}$$

where the α value is 0.46 by suggested in Trang et al. (2014).

3.2.3 Get power spectrum

After framing and windowing, this paper used discrete Fourier transform (DFT) on the data to transform the time-domain signal into a frequency-domain signal to obtain the spectrum X(k) is shown as follows

$$X(k) = \sum_{n=0}^{N-1} x(n)e^{-j2\pi nk/N}, 0 \le n, k \le N-1 \tag{4}$$

The power spectrum P(k) is equal to the signal spectrum X(k) as the square of its modulus, as shown in Eq. 5. The power spectrum expresses the energy characteristics of the heart sound signal more accurately, retains some amplitude elements in the heart sound spectrum, and discards the phase characteristics of the heart sound spectrum is described as follows

$$P(k) = \frac{1}{N}|X(k)|^2 \tag{5}$$

3.2.4 Mel filter bank

A normal human ear is able to hear sounds with frequencies from 20 Hz to 20,000 Hz. The range of 20 Hz to 20,000 Hz is

called the audible frequency range. The sounds we hear comprise of various frequencies. The Mel filter bank is represented as a group of triangular filters on the image. Usually a set contains 20 to 40 ascending triangular filters, and the starting position of each triangular filter is at the midpoint of the previous triangular filter, and because it has a linear frequency in the Mel scale, it is called a Mel filter bank. At each frequency, calculate the product of P(k) and filter Hm(k). Defining a triangular filter bank with Mel filters, the frequency response Hm(k) of the triangular filter is calculated as follows

$$H_m(k) = \begin{cases} 0, & k < f(m-1) \\ \dfrac{k - f(m-1)}{f(m) - f(m-1)}, & f(m-1) \le k \le f(m) \\ \dfrac{f(m+1) - k}{f(m+1) - f(m)}, & f(m) \le k \le f(m+1) \\ 0, & k > f(m+1) \end{cases} \tag{6}$$

where m represents the serial number of the filter, and f (m-1), f(m), and f (m+1) correspond to the starting point, middle point, and end point of the filter, respectively. In calculations, the values of m take 1, 2, . . . , 13. For a Mel triangular filter, f(m) represents the center frequency of the Mel trangular filter, f (m-1) represents the start of the Mel trangular filter, and f (m+1) represents the end of the Mel trangular filter. Summing the whole of Hm(k), we can obtain Eq. 7, and the value of M is 13.

$$\sum_{m=0}^{M-1} H_m(k) = 1 \tag{7}$$

3.2.5 Log spectrum

The logarithmic energy spectrum S(m) at each frame is obtained by using the logarithmic operation is shown as follows

$$S(m) = \ln\left[\sum_{k=0}^{N-1} P(k) H_m(k)\right], 0 \le m \le M \tag{8}$$

where lg is defined as the base e logarithm.

3.2.6 Discrete cosine transform

The discrete cosine transform (DCT) is performed on the above log spectrum to obtain the Mel cepstral coefficient C(n), which is the MFCC feature, The corresponding equation is described as follows.

$$C(n) = \sum_{m=0}^{N-1} S(m) \cos\left(\pi n (m - 0.5)/M\right), \quad n = 1, 2, \ldots, L \tag{9}$$

3.2.7 Dynamic feature extraction

MFCC reflects the static information of the heart sound signal, and the dynamic information of the heart sound signal also contains rich pathological features, which can be used to improve the classification accuracy further. To reflect the dynamic information of the heart sound signal, this paper extracts the first-order difference coefficient D(n) and the second-order difference coefficient D2(n) based on MFCC. The calculation formulas are described as follows

$$D(n) = \frac{1}{\sqrt{\sum_{i=-k}^{i=k} i^2}} \sum_{i=-k}^{i=k} i \cdot C(n+i) \tag{10}$$

$$D_2(n) = \frac{1}{\sqrt{2\sum_{i=-k}^{i=k} i^2}} \sum_{i=-k}^{i=k} i \cdot D(n+i) \tag{11}$$

where the value of k is taken as 2, and C (n + i) is a frame of MFCC coefficient. Figure 5 shows 2D visualization of them, where MFCC is the result of Eq. 9, △MFCC is the result of Eq. 10, and △^{2}MFCC is the result of Eq. 11. The size of them are all (199,13), we use them to construct a (199,39) feature as the input of neural network.

3.3 Resnet

The network structure in this paper is shown in Figure 6.

Convolutional neural network (CNN) can learn valuable features in large-scale heart sound spectrograms developed from traditional artificial neural networks, CNN not only have the traditional fully connected neural network characteristics, but also have many differences and improvements based on them. Convolutional neural networks work on the basic principle of converting the original data into a two-dimensional matrix format, which is superior to traditional artificial neural networks in terms of the performance of extracting image feature values. In CNN, the initial convolutional layer functions similarly to an edge detector and can be used to identify low-level features. Although the network near the convolutional layer is more complex or abstract, because of the CNN weight sharing property, its network requires fewer parameters to train than the fully connected to the feature space. It shows that when the network layers, each layer output at the same time, the number of dimensions required for the stage CNN to process the same data is much lower than the whole connected to the feature space fully. Compared with other feature extraction methods, CNN has a simple structure, fitting ability and trainability. The principle of convolution calculation in CNN is shown in Figure 7.

Batch Normalization (BN) was originally designed to solve Internal Covariate Shift (ICS), which is a phenomenon where the internal node data distribution changes due to parameter changes in the network. ICS has a greater negative impact on deeper neural networks. Data distribution change times increase with the number of neural network layers. It makes the network harder to train and more sensitive to overfitting. BN layer adjusts their distribution by normalizing each batch of data, the principle of which is shown in Figure 8. Using the BN layer not only

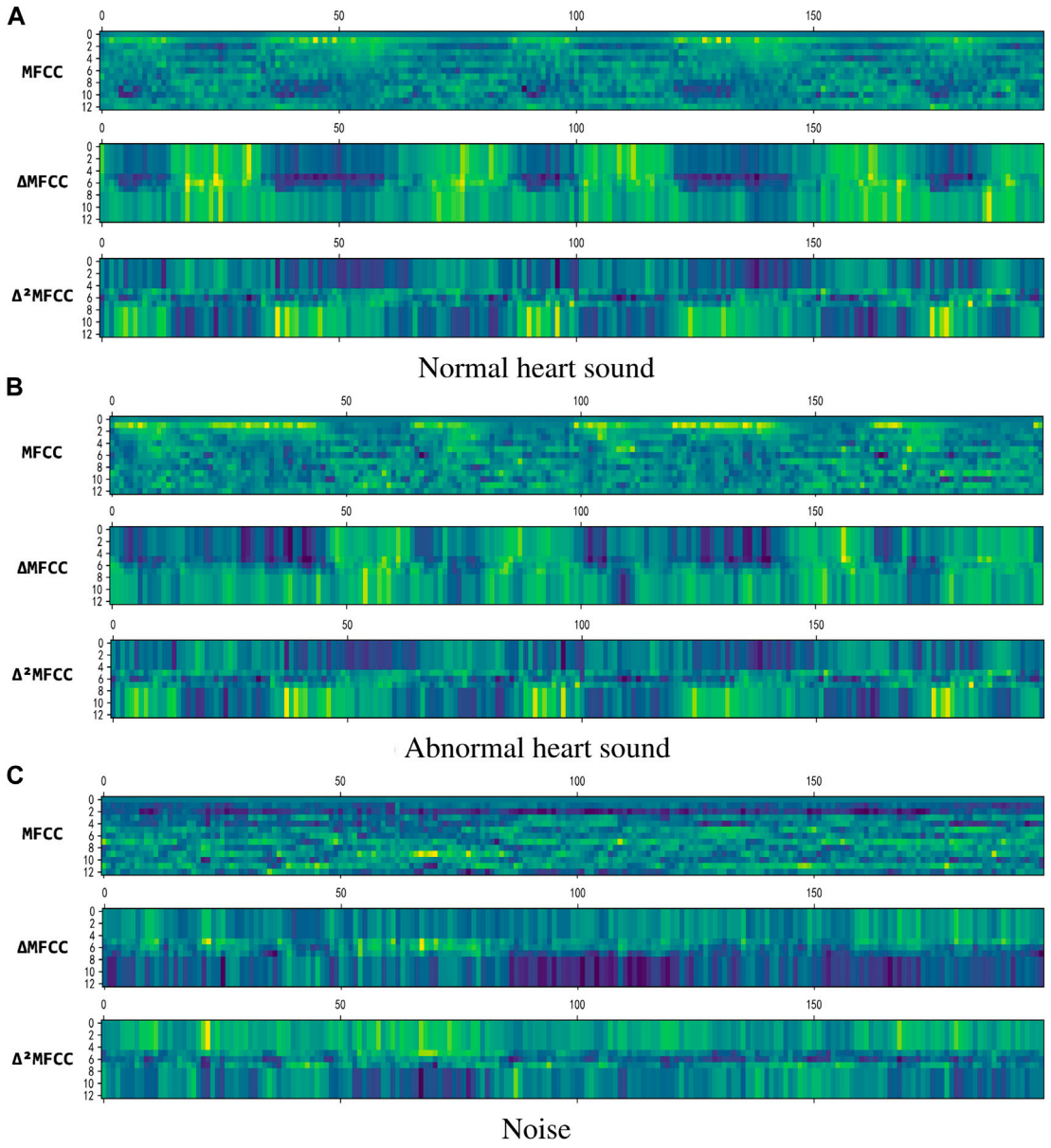

FIGURE 5
2D visualization of the features. **(A)** Normal heart sound. **(B)** Abnormal heart sound. **(C)** Noise

reduces the training time, but also make the model converge faster, and better control the problems of gradient disappearance and gradient explosion at the same time Ioffe and Szegedy (2015). The BN is calculated as follows

$$\hat{x}_l = \frac{x_i - \mu_B}{\sqrt{\sigma_B^2 + \epsilon}} \tag{12}$$

where μ_B is the mean of each batch of data, σ_B^2 is the variance of each batch of data, and ϵ is called the smoothing term, which ensures numerical stability in the operation by stopping the division by zero values.

The residual neural network was proposed initially by He et al. (2016). The degeneration phenomenon refers to the substantial decrease in model accuracy that occurs without warning as the depth of the network continues to increase. The degeneracy phenomenon makes us reflect on non-linear transformation, which significantly improves data classification. However, as the depth of the network continues to increase, we have gone too far in the non-linear transformation to achieve linear transformation surprisingly. Bottlenecks can quickly occur when training the data using CNN, and this paper introduces a residual module to address this phenomenon. It is no

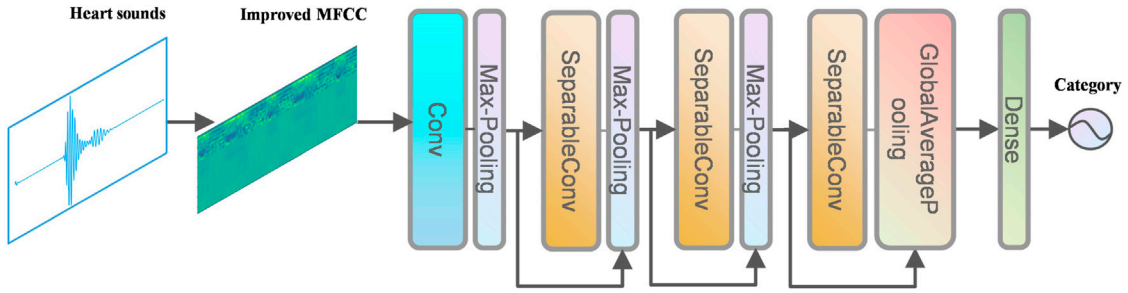

FIGURE 6
Structure of Resnet.

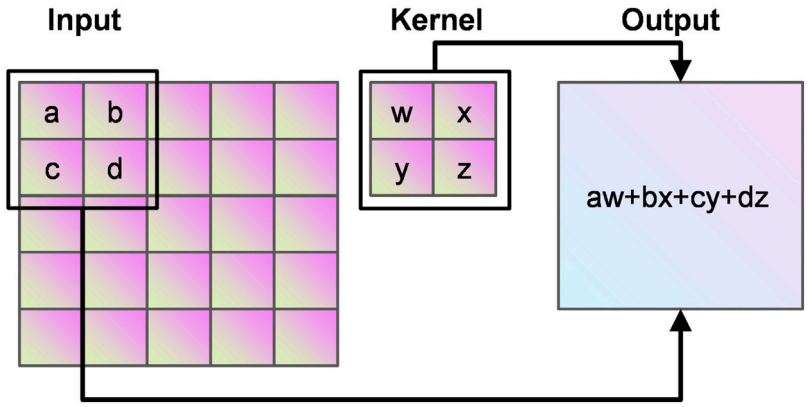

FIGURE 7
Principle of convolution.

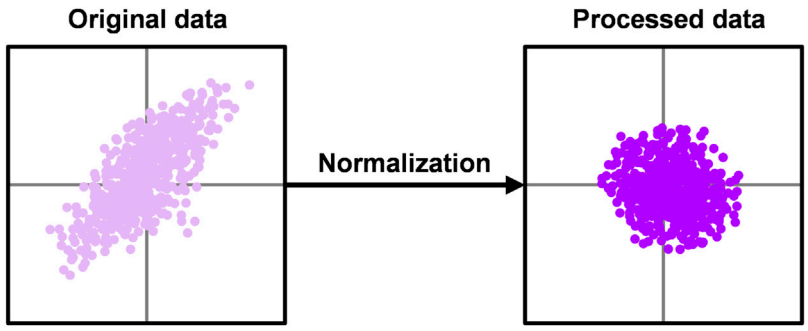

FIGURE 8
Principle of batch normalization.

exaggeration to say that half of the neural networks used in computer vision today are based on Resnet and his variants.

The principle of the residual structure constructed in this paper is shown in Figure 9. A layer of the network can usually be viewed as y = H(x), and a residual block of the residual network is: H(x) = F(x) + x, then F(x) = H(x)—x, and y = x is the observed value and H(x) is the predicted value, so H(x)—x is the residual, that is, F(x) is the residual, so it is called the residual network.

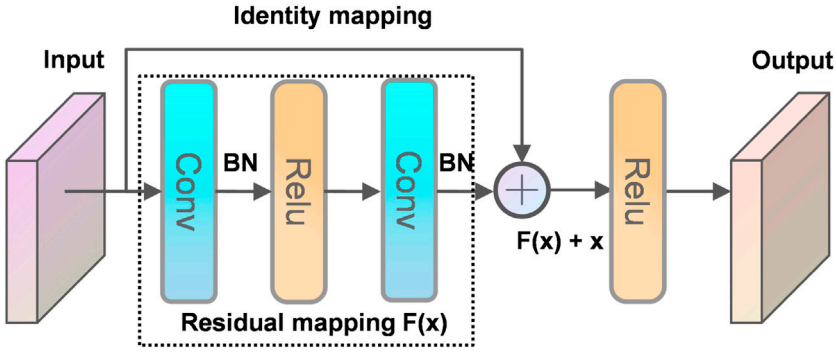

FIGURE 9
Residual structure.

When the deep network propagates forward, the information obtained by the network decreases layer by layer as the network deepens. In contrast, ResNet deals with this problem by identity mapping. The next layer includes not only the information x of that layer, but also the new information F(x) after the non-linear transformation of that layer. This treatment makes the information instead show an increasing trend layer by layer. This is so useful that you cannot worry about lossing data. Intuitively, the residual block protects the integrity of the information by directly passing the input information around to the output, and the whole network only needs that part of the input and output difference, simplifying the experimental goal and difficulty.

4 Experimental evaluation

4.1 Dataset

This paper uses heart sound datasets published on three different platforms, the PhysioNetChallenge 2016 heart sound database, the heart sound dataset from the kaggle platform, and the Yaseen heart sound dataset. In 2016, Physionet hosted the PhysioNet/Computing in Cardiology (CinC) Challenge 2016 and released the dataset Liu et al. (2016). Physionet is a resource platform for complex physiological signal research managed by the MIT Computational Physiology Laboratory. The dataset was collected by different research groups in clinical and non-clinical conditions. These heart sound data were sampled at the same frequency, with a large amount of data and low noise. The label classification of the dataset is relatively simple and is divided into two categories: normal and abnormal. There was a wide range of audio lengths, ranging from 5 s to 120 s. In this paper, the audio was cut before the classification task. The details of this dataset are shown in Table 1.

TABLE 1 PhysioNet/CinC Challenge dataset.

File name	Normal	Abnormal
Training-a	292	117
Training-b	104	386
Training-c	24	7
Training-d	28	27
Training-e	183	1958
Training-f	34	80
Total	665	2575

TABLE 2 Pascal dataset.

File name	Normal	Murmur	Extrahs	Artifact
Set-a	31	34	19	40
Set-b	320	95	None	None
Total	351	133	19	40

Kaggle is currently one of the largest data science platforms in the world, with many high-quality datasets. These datasets are often sponsored by large companies for data science competitions in 2016, Kaggle held a heart sound classification competition with a dataset that referenced the Pascal heart sound dataset Jiang and Choi. (2006) and attached several description files without any modifications to the audio files. For labeling purposes, the dataset used in this paper is the one published by Kaggle. The audio lengths in this dataset range from 1s to 30 s, and the details are shown in Table 2.

The third dataset was open-sourced by Herzig et al. (2014) on the GitHub platform, and the authors preprocessed the dataset. The audio was sampled at the same frequency, with the same

TABLE 3 Yaseen dataset.

File name	Normal	Aortic stenosis	Mitral stenosis	Mitral regurgitation
N	200	None	None	None
AS	None	200	None	None
MS	None	None	200	None
MR	None	None	None	200
MVP	None	None	None	None

TABLE 4 The parameters of deep learning architecture.

Model	Structure details	Params	Training time s)
LSTM	LSTM (64)-Drop (0.5)-FC(64)-FC (3)	30,979	75
GRU	GRU (64)-Drop (0.5)-FC(64)-FC (3)	24,515	55
CNNa	Conv [16, (3,3)]-MaxPooling (3,3)-Conv [32, (3,3)]-MaxPooling (3,3)-Conv [64, (3,3)]- MaxPooling (3,3)-Conv [128, (3,3)]-MaxPooling (3,3)-Drop (0.5)-GlobalAveragePooling ()-Dense (3)	97,539	55
CNNb	Conv [16, (3,3)]-MaxPooling (3,3)-Conv [32, (3,3)]-MaxPooling (3,3)-Conv [64, (3,3)]- MaxPooling (3,3)-Conv [128, (3,3)]-MaxPooling (3,3)-Drop (0.5)-GlobalAveragePooling ()-Dense (3)	40,979	200
Resnet	Conv [8, (3,3)]-BN-Conv [8, (3,3)]-residual {Conv [16, (1,1)]-BN}-SeparableConv [16, (3,3)]-BN-MaxPooling (3,3)-add-residual {Conv [32, (1,1)]-BN}-SeparableConv [32, (3,3)]-BN-SeparableConv [32, (3,3)]-BN-MaxPooling (3,3)-add-residual {Conv [64, (1,1)]-BN}-SeparableConv [64, (3,3)]-BN-SeparableConv [64, (3,3)]-BN-MaxPooling (3,3)-add- residual {Conv [128, (1,1)]-BN}-SeparableConv [128, (3,3)]-BN-MaxPooling (3,3)-add-Conv [3, (3,3)]-GlobalAveragePooling ()	52,339	320

length and less murmur. The data were labeled with five categories: normal, aortic stenosis, mitral valve insufficiency, mitral stenosis, and murmur, the latter four being abnormal heart sound signals in patients with cardiovascular disease, with the specific information shown in Table 3.

4.2 Experimental setup

In this study, we use Accuracy, Sensitivity, Specificity, and Precision to evaluate the proposed method. All of them are defined as follows

$$\text{Accuracy} = \frac{TP + TN}{TP + TN + FP + FN} \tag{13}$$

$$\text{Sensitivity} = \frac{TP}{TP + FN} \tag{14}$$

$$\text{Specificity} = \frac{TN}{TN + FP} \tag{15}$$

$$\text{Precision} = \frac{TP}{TP + FP} \tag{16}$$

To further illustrate the classification performance, we tested the proposed algorithm on two different deep learning network architectures by adding LSTM and GRU, whose structures are shown in Table 4. LSTM(x) represents an LSTM layer, and x is the dimension of the output space. GRU(x) represents a GRU layer, and x is the dimension of the output space. Drop(x) represents a Dropout layer, x is the possibility of dropping neurons. FC(x) represents a fully connected layer with x neurons. Conv [x, (y, z)] represents a convolution layer, x is the number of filters, y and z are the width and height of 2D filter window. BN represents a Batch Normalization layer Ioffe and Szegedy (2015). SeparableConv [x, (y, z)] is a deeply separable convolutional layer. MaxPooling (x, y) is a max pooling layer, and x and y are the pooling sizes. Residual (x) is a residual connectivity module, it is not a specific layer, it marks the position of the output layer. Add represents a residual connection layer, which takes the output of a previous layer as the input of a later one. GlobalAveragePooling() represents the global average pooling layer.

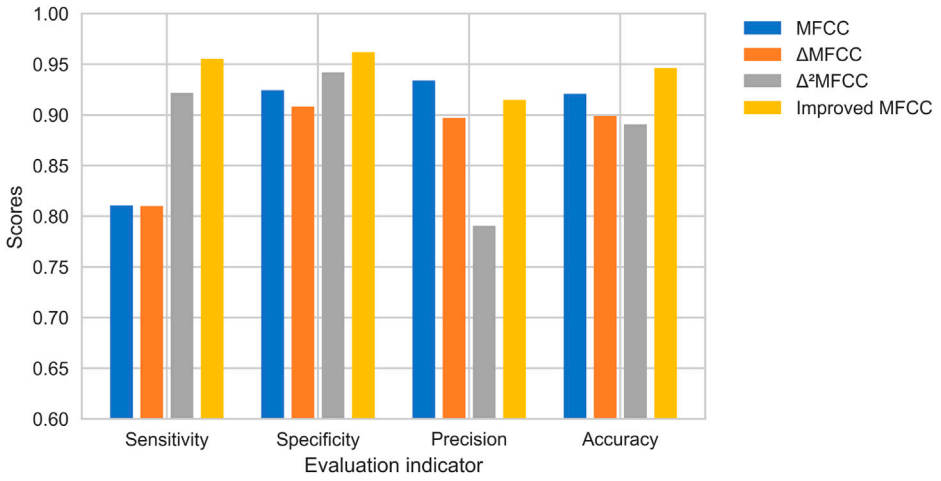

FIGURE 10
Comparison of heart sound features based on the proposed method.

4.3 Experimental results

To test the validation of the improved MFCC, we do comparison using the single features. MFCC, △MFCC, $\triangle^2$MFCC, and improved MFCC are trained on neural network separately, and the best epoch is taken as the result for comparison. The results of this experiment are shown in Figure 10. Improved MFCC's sensitivity, specificity, and accuracy are higher than other features, the precision is lower than MFCC. In medical signal recognition, higher sensitivity and specificity is a valid result. Especially for sensitivity, identifying more patients is a crucial thing.

Figure 11 shows the experimental results. It can be observed that the single Resnet, although the accuracy is higher, overfitting occurs very fast and overfitting occurs in the 10th round. Although LSTM can avoid overfitting better, has not yet reached the accuracy of Resnet in the 10th round, or even in the 30th round. This should be due to feature engineering, because the first-and second-order MFCC features are more reflective of relationships on time series, a property that is good for LSTM and GRU, but not friendly for networks like Resnet that extract locally relevant features. In addition, it can be seen that the accuracy of GRU is much lower than LSTM, but the average training time per round is 55 s for GRU and 75 s for LSTM. On the whole, Resnet can get better results.

Figure 12 shows the results of the comparison. CNNa has a shallow structure. In terms of performance, it is the least effective. The CNNb structure eliminates the residual connection of the Resnet. In comparison to CNNa, it performs better. In addition, it can be seen that the accuracy of GRU is lower than LSTM. The highest score is achieved by Resnet. As a result, it was determined that deep structure and residual connections are useful for classification of heart sounds. The results shows the training process of RNNs, CNNs and Resnet. It can be observed that the CNNs and Resnet, although the accuracy is higher, overfitting occurs very fast in the 10th round. Although LSTM can avoid overfitting better, has not yet reached the accuracy of CNNb and Resnet in the 10th round, or even in the 30th round. Overfitting exists in all machine learning problems. Obtaining more authoritative heart sound data is the best solution. Adjusting the capacity of the model is another solution. For a deep learning model, the number of parameters it can learn is called the capacity. If the model has a very large capacity, then the model can even achieve a dictionary-style mapping of the data, but this mapping does not have any recognition of new data, which is a serious overfitting. So this is when we need to improve the generalization ability of the model by decreasing the capacity of the model and compelling the model to learn the most important patterns. To reduce the influence of data partitioning on the experimental results, we use 5-fold cross-validation. The first step divides 20% on the whole dataset as the test set. The second step selects 80% of the remaining as the training set and 20% of the remaining as the validation set. It will reapeat the second step 5 times to allow the validation set to iterate, each time training a new neural network separately. Finally, taking the average of the accuracy of the five models on the test set as the study result.

Table 5 shows the comparison with the results of other studies. The essential difference between CNN and Resnet is that Resnet introduces a residual structure, which effectively mitigates the effect of degeneracy on the training of deep neural networks. Thus, it can be more applicable to the heart sound classification problem. In addition to the residual structure, the features are also essential. MFCC is inspired by

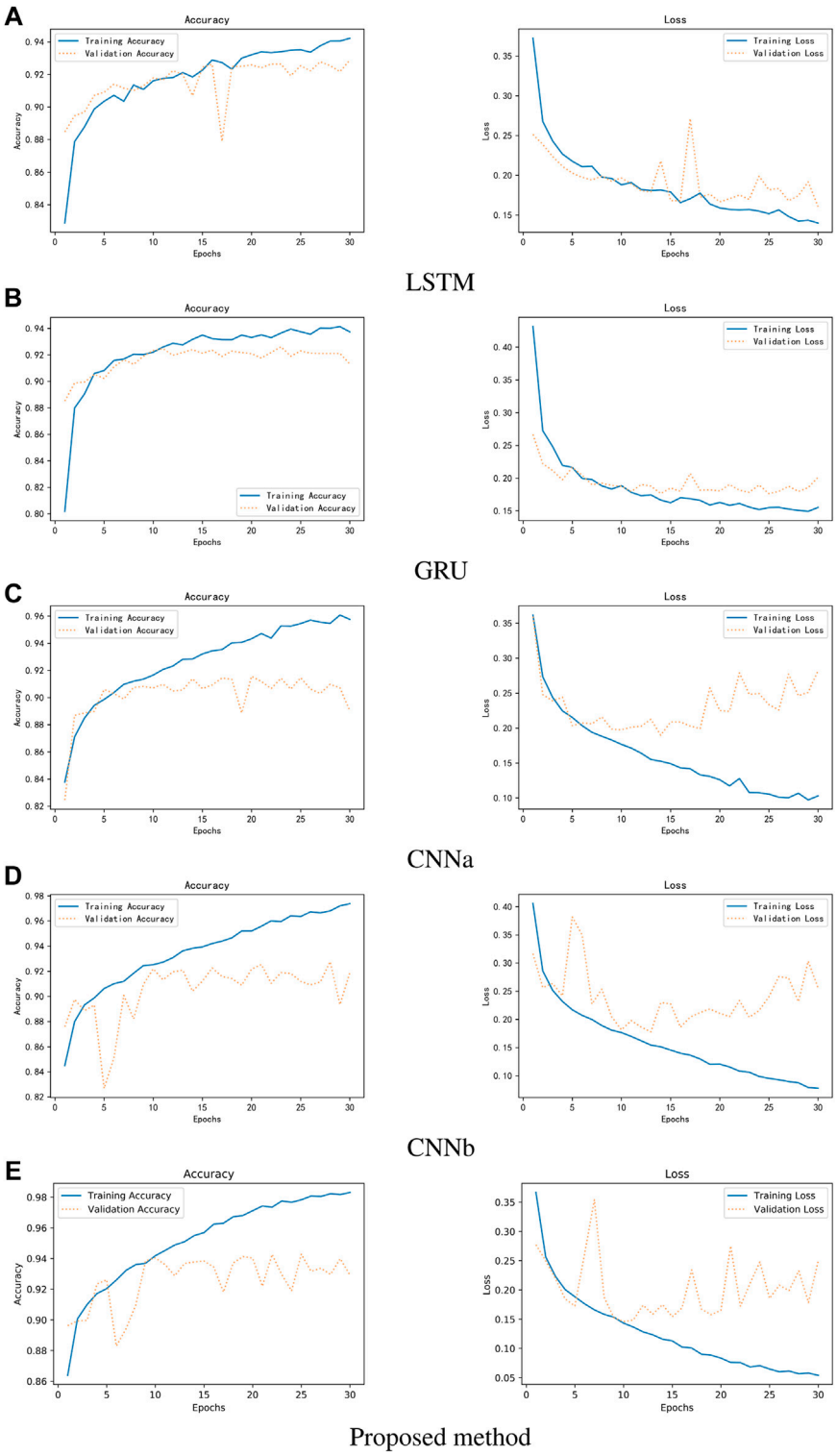

FIGURE 11
Comparison of three different networks between accuracy and loss. **(A)** LSTM **(B)** GRU **(C)** CNNa **(D)** CNNb **(E)** Proposed method.

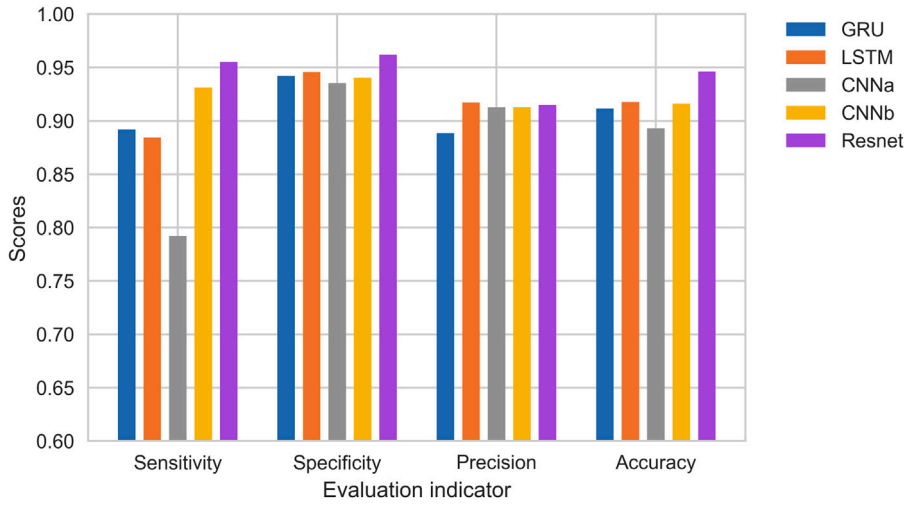

FIGURE 12
Comparison of RNNs and CNNs.

TABLE 5 Comparison of experimental results of different algorithms.

References	Algorithms	Sensitivity (%)	Specificity	Precision	Accuracy (%)
Li et al. (2021)	SFTF and CNN	88.70	86.40%	—	86.00
Wu et al. (2019)	MFCC and CNN	91.73	87.90%	—	89.81
Tschannen et al. (2016)	Wavelet and CNN	88.12	76.30%	—	82.12
Li F. et al. (2020)	497-features and CNN	87.00	72.10%	—	86.80
Er. (2021)	LBF and LTF	91.24	—	90.36%	91.66
Ours	Improved MFCC and Resnet	**92.32**	**95.47%**	**90.55%**	**94.43**

biology and simulates the non-linear changes of the human ear to sound, thus, extracting the physiological and pathological information in heart sounds, which can fully reflect the disease of the heart. Considering MFCC only reflects the static information of the heart sound signal, but the dynamic information of the heart sound signal also contains rich pathological features, which can be used to improve the classification accuracy further. We merge the extracted dynamic features with static features to more fully represent the physiological and pathological information in the heart sounds.

5 Conclusion

In this paper, we fused datasets from three different platforms for the lack of reliable heart sound datasets, which provided a solid foundation for neural network training. In addition, we used an enhanced feature extraction algorithm based on MFCC, and experiments show that using such features as input to the neural network can improve the model's performance well. The proposed method makes the neural network training faster and the model generalization enhanced, which effectively mitigates the negative effects of gradient disappearance and degradation phenomena on medical signal recognition and achieves an accuracy rate of 94.43% on the constructed dataset, which is higher than the state-of-the-art methods.

Data availability statement

The datasets presented in this study can be found in online repositories. The names of the repository/repositories and

accession number(s) can be found in the article/supplementary material.

Author contributions

FL improved dataset processing method, optimized neural network algorithm, manuscript writing. ZZ collected, processed the dataset, developed, implemented, and evaluated the neural network algorithm. LW analyzed the results and final approval of manuscript. WL revised it critically for important intellectual content. All author contributed to the article and approved the submitted version.

Funding

This work was supported in part by the Innovation Support Program for Returned Overseas Students in Anhui Province under Grant No. 2021LCX032 and National Natural Science Foundation of China under Grant No. 62202001.

Acknowledgments

We thank the reviewers and editors for their very constructive comments.

Conflict of interest

The authors declare that the research was conducted in the absence of any commercial or financial relationships that could be construed as a potential conflict of interest.

Publisher's note

References

Abduh, Z., Nehary, E. A., Wahed, M. A., and Kadah, Y. M. (2019). Classification of heart sounds using fractional Fourier transform based mel-frequency spectral coefficients and stacked autoencoder deep neural network. *J. Med. Imaging Health Inf.* 9, 1–8. doi:10.1166/jmihi.2019.2568

Astuti, W., Sediono, W., Aibinu, A., Akmeliawati, R., and Salami, M.-J. E. (2012). "Adaptive short time Fourier transform (stft) analysis of seismic electric signal (ses): A comparison of hamming and rectangular window," in *2012 IEEE symposium on industrial electronics and applications* (IEEE), 372–377.

Baghel, N., Dutta, M. K., and Burget, R. (2020). Automatic diagnosis of multiple cardiac diseases from pcg signals using convolutional neural network. *Comput. Methods Programs Biomed.* 197, 105750. doi:10.1016/j.cmpb.2020.105750

Baydoun, M., Safatly, L., Ghaziri, H., and El Hajj, A. (2020). Analysis of heart sound anomalies using ensemble learning. *Biomed. Signal Process. Control* 62, 102019. doi:10.1016/j.bspc.2020.102019

Bengio, Y. (2009). Learning deep architectures for ai. *Found. trends® Mach. Learn.* 2, 1–127. doi:10.1561/2200000006

Demir, F., Şengür, A., Bajaj, V., and Polat, K. (2019). Towards the classification of heart sounds based on convolutional deep neural network. *Health Inf. Sci. Syst.* 7, 16–19. doi:10.1007/s13755-019-0078-0

Deng, M., Meng, T., Cao, J., Wang, S., Zhang, J., and Fan, H. (2020). Heart sound classification based on improved mfcc features and convolutional recurrent neural networks. *Neural Netw.* 130, 22–32. doi:10.1016/j.neunet.2020.06.015

Er, M. B. (2021). Heart sounds classification using convolutional neural network with 1d-local binary pattern and 1d-local ternary pattern features. *Appl. Acoust.* 180, 108152. doi:10.1016/j.apacoust.2021.108152

Gomes, E. F., Bentley, P. J., Pereira, E., Coimbra, M. T., and Deng, Y. (2013). "Classifying heart sounds-approaches to the pascal challenge," in *Healthinf*, 337–340.

He, K., Zhang, X., Ren, S., and Sun, J. (2016). "Deep residual learning for image recognition," in *Proceedings of the IEEE conference on computer vision and pattern recognition*, 770–778.

Herzig, J., Bickel, A., Eitan, A., and Intrator, N. (2014). Monitoring cardiac stress using features extracted from S_1 heart sounds. *IEEE Trans. Biomed. Eng.* 62, 1169–1178. doi:10.1109/TBME.2014.2377695

Hinton, G. E., and Salakhutdinov, R. R. (2006). Reducing the dimensionality of data with neural networks. *science* 313, 504–507. doi:10.1126/science.1127647

Hinton, G., and Salakhutdinov, R. (2012). An efficient learning procedure for deep Boltzmann machines. *Neural Comput.* 24, 1967–2006. doi:10.1162/NECO_a_00311

Ioffe, S., and Szegedy, C. (2015). "Batch normalization: Accelerating deep network training by reducing internal covariate shift," in *International conference on machine learning* (Lille: PMLR), 448–456.

Iqtidar, K., Qamar, U., Aziz, S., and Khan, M. U. (2021). Phonocardiogram signal analysis for classification of coronary artery diseases using mfcc and 1d adaptive local ternary patterns. *Comput. Biol. Med.* 138, 104926. doi:10.1016/j.compbiomed.2021.104926

Ismail, S., Siddiqi, I., and Akram, U. (2022). Heart rate estimation in ppg signals using convolutional-recurrent regressor. *Comput. Biol. Med.* 145, 105470. doi:10.1016/j.compbiomed.2022.105470

Jiang, Z., and Choi, S. (2006). A cardiac sound characteristic waveform method for in-home heart disorder monitoring with electric stethoscope. *Expert Syst. Appl.* 31, 286–298. doi:10.1016/j.eswa.2005.09.025

Krishnan, P. T., Balasubramanian, P., and Umapathy, S. (2020). Automated heart sound classification system from unsegmented phonocardiogram (pcg) using deep neural network. *Phys. Eng. Sci. Med.* 43, 505–515. doi:10.1007/s13246-020-00851-w

Kui, H., Pan, J., Zong, R., Yang, H., and Wang, W. (2021). Heart sound classification based on log mel-frequency spectral coefficients features and convolutional neural networks. *Biomed. Signal Process. Control* 69, 102893. doi:10.1016/j.bspc.2021.102893

Lahmiri, S., and Bekiros, S. (2022). Complexity measures of high oscillations in phonocardiogram as biomarkers to distinguish between normal heart sound and pathological murmur. *Chaos, Solit. Fractals* 154, 111610. doi:10.1016/j.chaos.2021.111610

Li, F., Tang, H., Shang, S., Mathiak, K., and Cong, F. (2020). Classification of heart sounds using convolutional neural network. *Appl. Sci.* 10, 3956. doi:10.3390/app10113956

Li, S., Li, F., Tang, S., and Xiong, W. (2020). A review of computer-aided heart sound detection techniques. *BioMed Res. Int.* 2020, 5846191. doi:10.1155/2020/5846191

Li, T., Yin, Y., Ma, K., Zhang, S., and Liu, M. (2021). Lightweight end-to-end neural network model for automatic heart sound classification. *Information* 12, 54. doi:10.3390/info12020054

Liu, C., Springer, D., Li, Q., Moody, B., Juan, R. A., Chorro, F. J., et al. (2016). An open access database for the evaluation of heart sound algorithms. *Physiol. Meas.* 37, 2181–2213. doi:10.1088/0967-3334/37/12/2181

Mei, N., Wang, H., Zhang, Y., Liu, F., Jiang, X., and Wei, S. (2021). Classification of heart sounds based on quality assessment and wavelet scattering transform. *Comput. Biol. Med.* 137, 104814. doi:10.1016/j.compbiomed.2021.104814

Milani, M. M., Abas, P. E., and De Silva, L. C. (2022). A critical review of heart sound signal segmentation algorithms. *Smart Health* 24, 100283. doi:10.1016/j.smhl.2022.100283

Nair, V., and Hinton, G. E. (2010). "Rectified linear units improve restricted Boltzmann machines," in *Icml*.

Nogueira, D. M., Ferreira, C. A., Gomes, E. F., and Jorge, A. M. (2019). Classifying heart sounds using images of motifs, mfcc and temporal features. *J. Med. Syst.* 43, 168–213. doi:10.1007/s10916-019-1286-5

Oh, S. L., Jahmunah, V., Ooi, C. P., Tan, R.-S., Ciaccio, E. J., Yamakawa, T., et al. (2020). Classification of heart sound signals using a novel deep wavenet model. *Comput. Methods Programs Biomed.* 196, 105604. doi:10.1016/j.cmpb.2020.105604

Ranzato, M., Poultney, C., Chopra, S., and Cun, Y. (2006). Efficient learning of sparse representations with an energy-based model. *Adv. neural Inf. Process. Syst.* 19.

Ren, Z., Qian, K., Dong, F., Dai, Z., Nejdl, W., Yamamoto, Y., et al. (2022). *Deep attention-based neural networks for explainable heart sound classification*. Elsevier: Machine Learning with Applications, 100322.

Sakib, S., Ahmed, N., Kabir, A. J., and Ahmed, H. (2019). *An overview of convolutional neural network: Its architecture and applications*.

Silver, D., Huang, A., Maddison, C. J., Guez, A., Sifre, L., Van Den Driessche, G., et al. (2016). Mastering the game of go with deep neural networks and tree search. *nature* 529, 484–489. doi:10.1038/nature16961

Son, G.-Y., and Kwon, S. (2018). Classification of heart sound signal using multiple features. *Appl. Sci.* 8, 2344. doi:10.3390/app8122344

Tian, G., Lian, C., Zeng, Z., Xu, B., Su, Y., Zang, J., et al. (2022). *Imbalanced heart sound signal classification based on two-stage trained dsanet*. Springer: Cognitive Computation, 1–14.

Trang, H., Loc, T. H., and Nam, H. B. H. (2014). "Proposed combination of pca and mfcc feature extraction in speech recognition system," in *2014 international conference on advanced technologies for communications (ATC 2014)* (IEEE), 697–702.

Tschannen, M., Kramer, T., Marti, G., Heinzmann, M., and Wiatowski, T. (2016). "Heart sound classification using deep structured features," in *2016 computing in Cardiology conference (CinC)* (IEEE), 565–568.

Varghees, V. N., and Ramachandran, K. (2014). A novel heart sound activity detection framework for automated heart sound analysis. *Biomed. Signal Process. Control* 13, 174–188. doi:10.1016/j.bspc.2014.05.002

Vincent, P., Larochelle, H., Lajoie, I., Bengio, Y., Manzagol, P.-A., and Bottou, L. (2010). Stacked denoising autoencoders: Learning useful representations in a deep network with a local denoising criterion. *J. Mach. Learn. Res.* 11.

Wang, Z., Jin, Y., Zhao, L., and Liu, C. (2021). A heart sound classification method based on joint decision of extreme gradient boosting and deep neural network. *Sheng wu yi xue Gong Cheng xue za zhi= J. Biomed. Engineering= Shengwu Yixue Gongchengxue Zazhi* 38, 10–20. doi:10.7507/1001-5515.202006025

Wu, J. M.-T., Tsai, M.-H., Huang, Y. Z., Islam, S. H., Hassan, M. M., Alelaiwi, A., et al. (2019). Applying an ensemble convolutional neural network with savitzky–golay filter to construct a phonocardiogram prediction model. *Appl. Soft Comput.* 78, 29–40. doi:10.1016/j.asoc.2019.01.019

Yang, T.-c. I., and Hsieh, H. (2016). "Classification of acoustic physiological signals based on deep learning neural networks with augmented features," in *2016 computing in Cardiology conference (CinC)* (IEEE), 569–572.

Yu, K., Jia, L., Chen, Y., Xu, W., et al. (2013). Deep learning: Yesterday, today, and tomorrow. *J. Comput. Res. Dev.* 50, 1799–1804.

Zeinali, Y., and Niaki, S. T. A. (2022). Heart sound classification using signal processing and machine learning algorithms. *Mach. Learn. Appl.* 7, 100206. doi:10.1016/j.mlwa.2021.100206

Zhang, W., and Han, J. (2017). "Towards heart sound classification without segmentation using convolutional neural network," in *2017 computing in Cardiology (CinC)* (IEEE), 1–4.

frontiers | Frontiers in Physiology

TYPE Original Research
PUBLISHED 05 January 2023
DOI 10.3389/fphys.2022.1085530

OPEN ACCESS

EDITED BY
Lisheng Xu,
Northeastern University, China

REVIEWED BY
Chien-Hung Yeh,
Beijing Institute of Technology, China
Qingyun Wang,
Beihang University, China
Yangsong Zhang,
Southwest University of Science and Technology, China

*CORRESPONDENCE
Chunsheng Li,
lichunsheng@sut.edu.cn

SPECIALTY SECTION
This article was submitted to Computational Physiology and Medicine, a section of the journal Frontiers in Physiology

RECEIVED 31 October 2022
ACCEPTED 20 December 2022
PUBLISHED 05 January 2023

CITATION
Li C, Liu S, Wang Z and Yuan G (2023), Classifying epileptic phase-amplitude coupling in SEEG using complex-valued convolutional neural network.
Front. Physiol. 13:1085530.
doi: 10.3389/fphys.2022.1085530

Classifying epileptic phase-amplitude coupling in SEEG using complex-valued convolutional neural network

Chunsheng Li[1]*, Shiyue Liu[1], Zeyu Wang[1,2] and Guanqian Yuan[3]

[1]Department of Biomedical Engineering, School of Electrical Engineering, Shenyang University of Technology, Shenyang, China, [2]Department of Electrical Engineering and Information Systems, University of Pannonia, Veszprem, Hungary, [3]Department of Neurosurgery, General Hospital of Northern Theater Command, Shenyang, China

EEG phase-amplitude coupling (PAC), the amplitude of high-frequency oscillations modulated by the phase of low-frequency oscillations (LFOs), is a useful biomarker to localize epileptogenic tissue. It is commonly represented in a comodulogram of coupling strength but without coupled phase information. The phase-amplitude coupling is also found in the normal brain, and it is difficult to discriminate pathological phase-amplitude couplings from normal ones. This study proposes a novel approach based on complex-valued phase-amplitude coupling (CV-PAC) for classifying epileptic phase-amplitude coupling. The CV-PAC combines both the coupling strengths and the coupled phases of low-frequency oscillations. The complex-valued convolutional neural network (CV-CNN) is then used to classify epileptic CV-PAC. Stereo-electroencephalography (SEEG) recordings from nine intractable epilepsy patients were analyzed. The leave-one-out cross-validation is performed, and the area-under-curve (AUC) value is used as the indicator of the performance of different measures. Our result shows that the area-under-curve value is .92 for classifying epileptic CV-PAC using CV-CNN. The area-under-curve value decreases to .89, .80, and .88 while using traditional convolutional neural networks, support vector machine, and random forest, respectively. The phases of delta (1–4 Hz) and alpha (8–10 Hz) bands are different between epileptic and normal CV-PAC. The phase information of CV-PAC is important for improving classification performance. The proposed approach of CV-PAC/CV-CNN promises to identify more accurate epileptic brain activities for potential surgical intervention.

KEYWORDS

epilepsy, SEEG, complex-valued phase-amplitude coupling, complex-valued convolutional neural network, epileptogenic zone

1 Introduction

Epilepsy is the most common chronic disease in neurology. About 70% of patients with epilepsy can be cured by taking antiepileptic drugs, and other patients may develop drug-resistance epilepsy (DRE) (Kwan and Brodie, 2000). The epileptogenic zone (EZ) is the brain region responsible for seizure generation (Rosenow and Luders., 2001). Some patients with DRE can be treated by surgical intervention on EZ (Engel, 2019). Scalp electroencephalography (EEG) is one of these techniques which is fundamental for defining the EZ, frequently as a precursor to invasive recordings. Intracranial EEG (iEEG) signal provides anatomically precise information about the selective engagement of neuronal populations at the millimeter scale and about the temporal dynamics of their engagement at the millisecond scale (Parvizi and Kastner,

2018). Stereo-electroencephalography (SEEG) is one kind of iEEG and is widely used to study the spatiotemporal oscillatory dynamics of brain networks engaged in epileptogenic processes (Bartolomei et al., 2017). Some EEG features provide promise biomarkers for EZ, such as phase-amplitude coupling (PAC) (Weiss et al., 2015; Amiri et al., 2016; Jiang et al., 2019; Liu et al., 2021), and high-frequency oscillations (Worrell and Gotman, 2011). Currently, there is still a gap between those studies and their applications in the clinical setting. Machine learning can be used to close the gap in supporting clinical applications.

EEG PAC, where the amplitude of high-frequency oscillations (HFOs) is modulated by the phase of low-frequency oscillations (LFOs), is a useful biomarker to identify the activities of epileptogenic tissue (Guirgis et al., 2015). Cross-frequency push-pull dynamics contributed to the secondary generalization of focal seizures and potentially reflected impaired excitation-inhibition interactions of the epileptic network (Jiang et al., 2019). PAC feature of ictal EEG is used to determine the region of interest in epilepsy (Guirgis et al., 2015). The coupling phase was suggested as an interictal marker of the seizure-onset zone (SOZ) (Amiri et al., 2016). The PAC in the inter- and pre-seizure periods was weak and paroxysmal, and strong PAC channels were confined more to the SOZ and resection region (Ma et al., 2021). The theta—gamma PAC within the electrodes in the seizure region increased during the ictal period (Liu et al., 2021). In Parkinson's disease, the HFO (100–300 Hz) was found modulated by beta (13–30 Hz), and beta and gamma amplitudes were further modulated by their low-frequency components (Jin et al., 2022). Some studies have shown that cross-frequency coupling (CFC) plays a functional role in physiological functions, such as memory, and task performing (Lisman and Idiart, 1995; Canolty and Knight, 2010). It is difficult to apply those coupling patterns for identifying pathological brain tissues. To identify pathological PAC is critical for further applications in the clinical setting (von Ellenrieder et al., 2016). A multistage classifier based on the random forest was applied to classify CFC features and it successfully predicted seizures (Jacobs et al., 2018). Different kinds of algorithms have been applied in investigating epileptic EEG, such as principal component analysis (PCA) (Villar et al., 2017), Wavelet analysis (Wang et al., 2018), support vector machines (SVM), fuzzy logic systems (Jiang et al., 2016), and connectivity (Qin et al., 2020).

Convolutional neural networks (CNN) becomes more popular in neuroscience research after its success in some other fields, such as image recognition (Krizhevsky et al., 2012) and EEG analysis (Pan et al., 2022). CNN achieves automatic extraction of local features through its key component convolutional kernel and obtains high-level abstract features after a series of hierarchical processing. It may also avoid the problems of manual optimizing of traditional signal processing algorithms. In our preliminary study, a three-layer CNN was trained to identify pathological PAC in SEEG recordings (Wang and Li, 2020). The result showed that the area-under-curve (AUC) value reached .88 for classifying pathological PACs from normal ones (Wang and Li, 2020). However, the representation and operation of CNN in real values limit their applications in the field of complex-valued datasets. Complex-valued CNN (CV-CNN) has been developed and applied to various fields (Hirose, 2013; Tygert et al., 2016). Some studies have demonstrated that CV-CNN outperforms real-valued CNN after making full use of phase information in complex-valued data, such as magnetic resonance imaging (MRI) (Cole et al., 2021), steady-state visually evoked potentials (SSVEP) (Ravi et al., 2020).

In this study, we propose a novel approach for identifying pathological PAC in SEEG from patients with epilepsy. We first provide a method for generating complex-valued PAC (CV-PAC) with both the coupling strength and the coupled phase of LFO. The CV-CNN is then trained to discriminate the pathological PACs from normal ones. SEEG recordings from nine intractable epilepsy patients were further analyzed to validate our proposed approach.

2 Materials and methods

2.1 Data and subject description

SEEG data of 23 seizures from nine patients were used in this study. All patients had undergone surgery and achieved seizure-free outcomes (General hospital of northern theater command). The regions of surgical resection were used as the epileptogenic zone in this study. Informed consent was obtained from each patient, and the ethics committee of the hospital approved the study. The clinical information of each patient is outlined in Table 1. A neurologist marked the SEEG onset and termination of all seizures. To eliminate

TABLE 1 Clinical information of patients studied in this work.

Patients	Age/Sex	Duration (years)	Seizure (s)	MRI Findings	Pathology	Surgery
P1	16M	10	66, 61, 48	Left hippocampal abnormality	FCD/HS	Left: T
P2	37M	17	74, 76, 77	Normal	FCD	Left: T
P3	36M	23	75, 84	Normal	Gliosis	Right: T
P4	31M	30	42, 64, 120	Multiple region abnormality	Gliosis	Right: T
P5	25F	17	65, 97, 67	Normal	HS	Right: T
P6	38M	32	71	Left occipital abnormality	—	Left: O*
P7	11M	7	44, 54, 55	Left parietal and right occipital abnormality	Gliosis/FCD	Right: O
P8	54M	32	59, 60, 82	Right temporal abnormality	FCD	Right: FT
P9	22M	3	76, 80	both hippocampal abnormality	HS	Left: T

F, frontal; T, temporal; O, occipital; *, radio-frequency thermo-coagulation; —, unknown; FCD, focal cortical dysplasia; HS, hippocampal sclerosis.

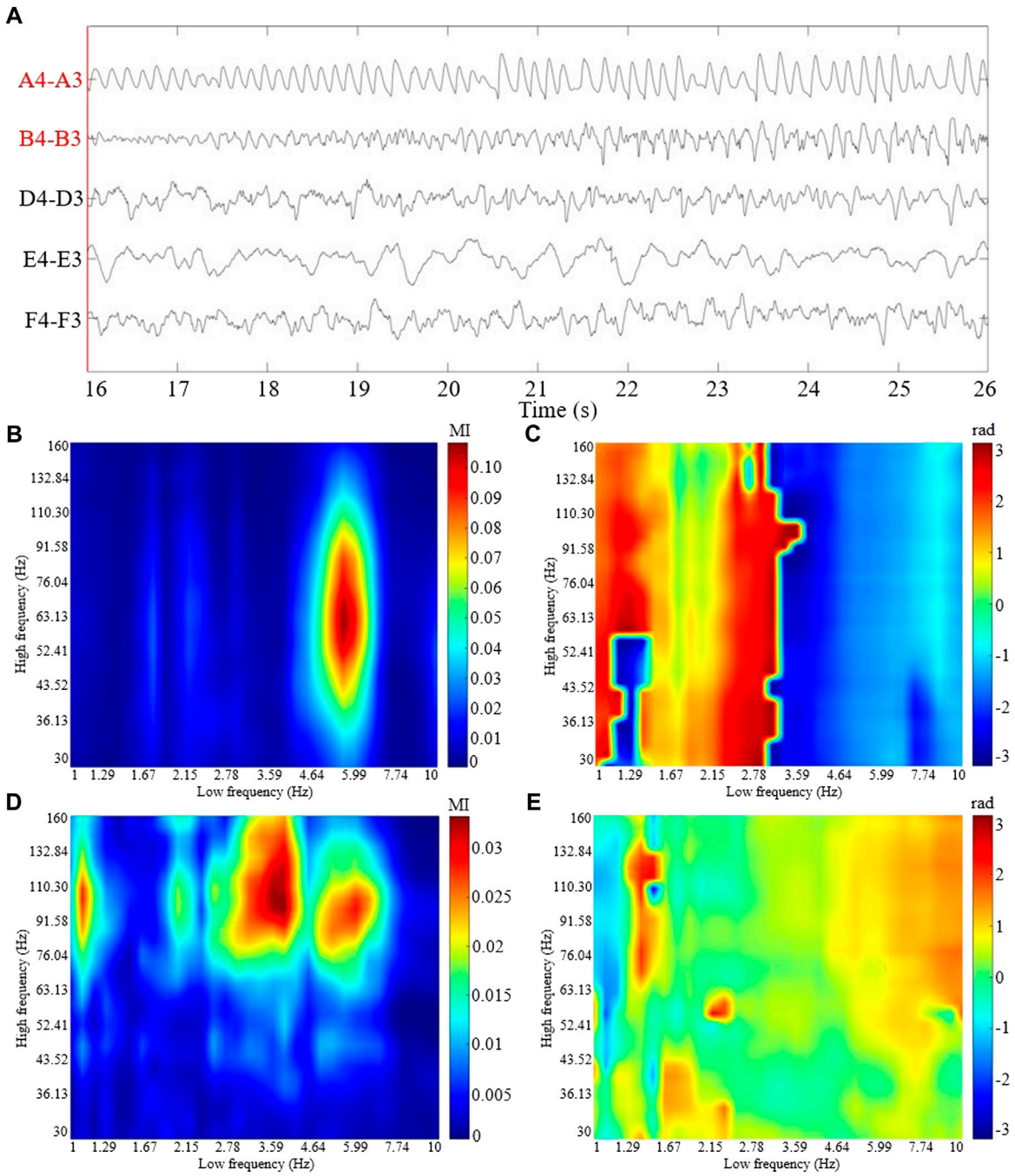

FIGURE 1
The ictal SEEG segment and the CV-PAC patterns from patient P1. **(A)** 10 s SEEG segment with selected channels 16 s after seizure onset. The labels of the SEEG channel in surgical resection are marked in red color. **(B)** The coupling strength of CV-PAC of channel A4-A3 in surgical resection. Red and blue colors indicate strong and weak coupling strengths, respectively. The value is between 0 and 1. **(C)** The coupled phase of CV-PAC of channel A4-A3 corresponding to **(B)**. The range of phase is between $-\pi$ and π rad. **(D)** The coupling strength of CV-PAC of channel D4-D3 in the normal brain region. Red and blue colors indicate strong and weak coupling strengths, respectively. **(E)** The coupled phase of CV-PAC of channel D4-D3 corresponding to **(D)**. The range of phase is between $-\pi$ and π rad.

the reference effect, we transform the SEEG recordings into a bipolar montage. Channels with obvious artifacts are removed based on visual inspection. EEG is a non-linear and non-stationary signal. It could be treated as a stable state within a short duration. A 10 s window was suggested for computing PAC (Guirgis et al., 2015; Shi et al., 2019). We used a 10 s sliding window on seizure with a step size of 2 s. The duration of each seizure is listed in Table 1. There are 38,751 CV-PACs generated. Each CV-PAC is represented as a complex-valued image. The CV-PAC is labeled as a pathological pattern if the corresponding SEEG channel resides in the surgical resection. Otherwise, the CV-PAC is labeled as normal. There are 10,289 CV-PACs marked as pathological, and the other 28,462 CV-PACs are marked as normal.

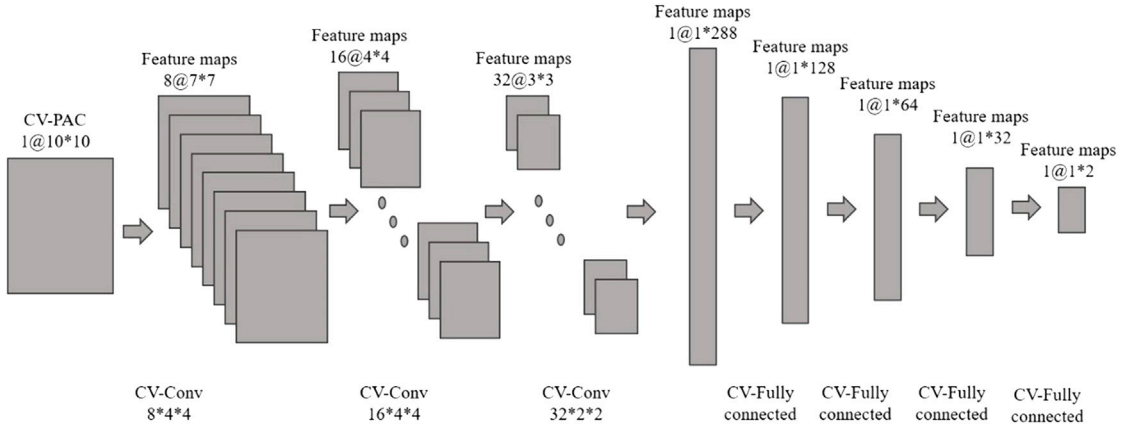

FIGURE 2
Complex-valued convolutional neural network (CV-CNN) with complex-valued phase-amplitude coupling (CV-PAC). There are three complex-valued convolutional layers and four complex-valued fully connected layers.

2.2 Complex-valued phase-amplitude coupling

The CV-PAC is generated based on the PAC measure (Guirgis et al., 2015). In this study, the low-frequency range is chosen as 1–10 Hz, and the high-frequency range is chosen as 30–160 Hz. Both low- and high-frequency ranges are further divided into 10 intervals equally in log space. We denote the selected low- and high-frequency signals as $x_{f_P}(t)$ and $x_{f_A}(t)$ (i.e.,$A_{f_A}(t)$) and the instantaneous phase of $x_{f_P}(t)$ (i.e., $\Phi_{f_P}(t)$) is extracted by using continuous wavelet transformation (CWT) in MATLAB (MathWorks, Natick, USA). The phases $\Phi_{f_P}(t)$ are binned and the mean of A_{f_A} over each phase bin is calculated, which denotes as $< A_{f_A} >_{\Phi_{f_P}}(j)$. The mean amplitude is then normalized by the sum of all mean amplitudes in each phase bin j, as follows

$$P(j) = \frac{< A_{f_A} >_{\Phi_{f_P}}(j)}{\sum_{k=1}^{N} < A_{f_A} >_{\Phi_{f_P}}(k)}, \quad (1)$$

where $N = 18$, and j is chosen from 1 to 18. The Kullback-Leibler (KL) distance between amplitude distribution p and uniform distribution U ($U(j) = 1/N$ for all bins j) is measured by following equation (Tort et al., 2010):

$$D_{KL}(P,U) = \sum_{j=1}^{N} P(j)^{*}\log\left[\frac{P(j)}{U(j)}\right]. \quad (2)$$

The strength of CV-PAC at low- and high-frequency pair is calculated as follows

$$S_{PAC} = \frac{D_{KL}(P,U)}{\log(N)}. \quad (3)$$

The phase bin at the peak of $P(j)$ is extracted as the coupling phase of the corresponding high and low frequency pair

$$\psi_{PAC} = \arg\max_{j} P(j)^{*}\frac{\pi}{9}. \quad (4)$$

The S_{PAC} is also called modulation index (MI) (Tort et al., 2010). The strength S_{PAC} and phase ψ_{PAC} are then used as the module and phase angle of complex-valued vector

$$C_{PAC} = S_{PAC}^{*}\cos(\psi_{PAC}) + i^{*}S_{PAC}^{*}\sin(\psi_{PAC}) \quad (5)$$

where i is the imaginary number. C_{PAC} forms one pixel in CV-PAC image.

The surrogate-tested CV-PAC (ST-CV-PAC) is also generated. The phases in each low frequency are shuffled 100 times. If the coupling strength of C_{PAC} in ST-CV-PAC is lower than the maximum 5% of the corresponding shuffled values, the C_{PAC} will be set to 0. The CV-PAC and CV-PAC-SA in 10 × 10 resolution are used in this study since our preliminary study shows that it is a good balance between performance and computational load (Wang and Li, 2020).

A 10 s SEEG segment during seizure is shown in Figure 1A. The coupling strengths and coupled phases of CV-PACs for pathological and normal activities are shown in Figures 1B–E, respectively. To compare the performance of CV-CNN with traditional CNN, SVM, and random forest, the real part of CV-PAC and the imaginary part of CV-PAC are used as two-layer images when using CNN to classify PAC patterns. The PAC with only coupling strength is also used to train traditional CNN for comparison.

2.3 Complex-valued convolutional neural network

In this study, we use CV-CNN to classify CV-PAC patterns. The structure of CV-CNN is shown in Figure 2. The activation function of CV-CNN is implemented using the rectified linear function (ReLU) in our study. The ReLU is applied on the real and the imaginary feature maps separately. In each complex-valued convolutional layer, the weights of the convolution kernel are complex values, and complex multiplication between weights and feature maps is implemented. To speed up the training convergence of the model and reduce the impact of the variation of the input, we define a complex batch normalization (BN) layer. The maximum number of iterations epoch set for training is 800, the batch size is 128, and the learning rate is .0025. In addition, the learning rate decays by a factor of .5 when the epoch is an integer multiple of 250. A dropout with a value of

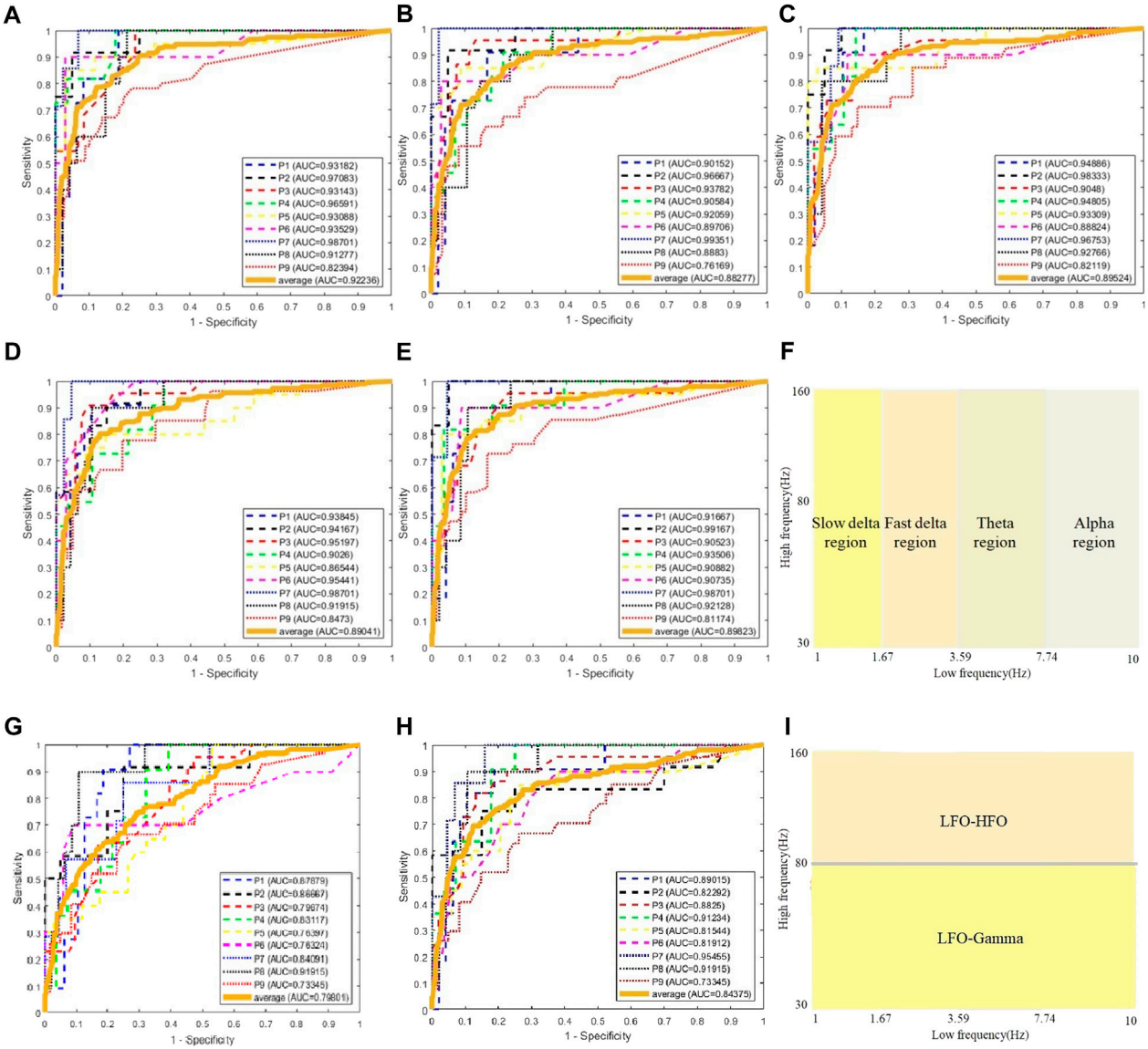

FIGURE 3
ROC curves of CV-CNN on CV-PAC dataset. **(A)** CV-PAC with full low-frequency band. **(B)** CV-PAC without slow delta. **(C)** CV-PAC without fast delta. **(D)** CV-PAC without theta **(E)** CV-PAC without alpha. **(F)** PAC regions are divided into four low-frequency bands. **(G)** CV-PAC with LFO-gamma. **(H)** CV-PAC with LFO-HFO. **(I)** PAC is divided into LFO-gamma and LFO-HFO regions.

.2 is used in the first layer of the fully connected layer, and the weights of all the complex convolution layers are regularized using L2 with $\lambda = .004$. The cross-entropy loss function is used to quantify the loss, and the stochastic gradient descent (SGD) algorithm is chosen as the optimization function. The training and testing of dataset are implemented using the PyTorch package.

3 Result

3.1 Identifying channel with pathological CV-PAC

We use the AUC value to evaluate the performance of classification. To classify one channel as pathological or normal is based on all CV-PAC generated from the channel. In the receiver operating characteristic (ROC) curve, if the percentage of pathological CV-PAC from one channel is higher than the optimal threshold, the channel will be classified as pathological. The leave-one-out cross-validation is performed. CV-PACs of eight patients are used as the training set to train the CNN model, and the remaining patient is used as a test. A total of nine rounds of training and verification are performed. By comparing with the ground truth of each CV-PAC, the ROC curve is obtained, as shown in Figure 3A. The AUC values of all patients are listed in the first column of Table 2. The average AUC value is .92 when applying CV-CNN on the CV-PAC dataset. The sensitivity and specificity are .82 and .83, respectively.

To further investigate the effects of each low-frequency band, the PAC is divided into four regions, as shown in Figure 3F. The

TABLE 2 AUC values using CV-CNN on CV-PAC.

Patients	CV-PAC	CV-PAC without slow delta	CV-PAC without fast delta	CV-PAC without theta	CV-PAC without alpha	CV-PAC with LFO-gamma	CV-PAC with LFO-HFO
P1	.93182	.90125	**.94886**	.93845	.91667	.87879	.89015
P2	.97083	.96667	.98333	.94167	**.99167**	.86667	.82292
P3	.93143	.93782	.90480	**.95197**	.90523	.79674	.88250
P4	**.96591**	.90584	.94805	.90260	.93506	.83117	.91234
P5	.93088	.92059	**.93309**	.86544	.90882	.76397	.81544
P6	.93529	.89706	.88824	**.95441**	.90735	.76324	.81912
P7	.98701	**.99351**	.96753	.98701	.98701	.84091	.95455
P8	.91277	.88830	**.92766**	.91915	.92128	.91915	.91915
P9	.82394	.76169	.82119	**.84730**	.81174	.73345	.73345
Average	**.92236**	.88277	.89524	.89041	.89823	.79801	.84375

Optimal values at each row are shown in bold.

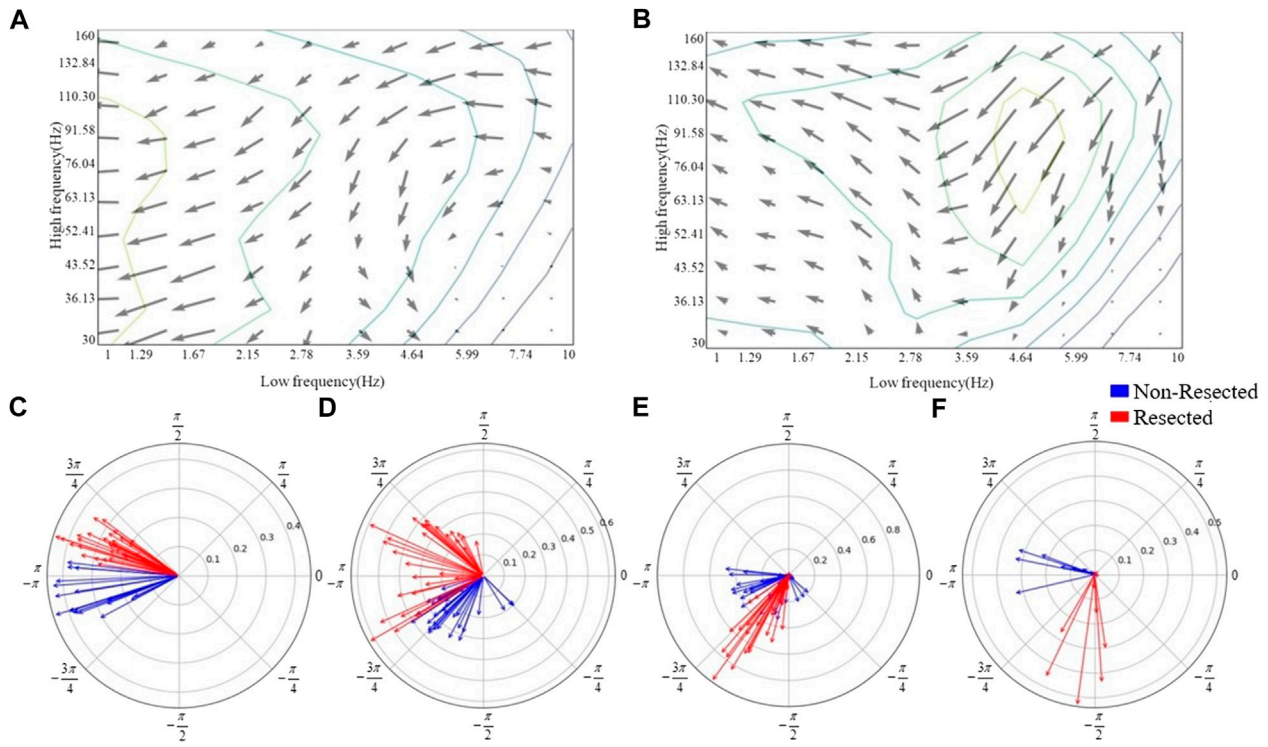

FIGURE 4
Phase distribution of low-frequency bands. **(A)** The quiver map of averaged strength and phase of CV-PACs in non-resected regions. Note that the length and angle of each gray arrow represent the coupling strength and coupled phase at each high- and low-frequency pair, respectively. **(B)** The quiver map of averaged strength and phase of CV-PACs in resected regions. The length and angle of each arrow represent the coupling strength and coupled phase, respectively. **(C)** The coupling with phases in slow-delta (1–2 Hz). The blue and red arrows indicate the coupling in the non-resected and resected regions, respectively. **(D)** The coupling with phases in delta (2–4 Hz). **(E)** The coupling with phases in theta (4–8 Hz). **(F)** The coupling with phases in alpha (8–10 Hz).

low-frequency bands include slow delta (1—2 Hz), fast delta (2—4 Hz), theta (4—8 Hz), and alpha (8—10 Hz). Each time we replace one of the CV-PAC regions with random values with the same mean and variance. The ROC curves are drawn in Figures 3B–E. The AUC values decrease to .882, .895, .890, and .898 for the slow delta, delta, theta, and alpha region replaced, respectively. The high-frequency band is then divided into gamma (30–80 Hz) and HFO (80—160 Hz), as shown in Figure 3I. The result shows that the AUC values decrease to .80 and .84 for using LFO-gamma and LFO-HFO regions (Figures 3G, H; Table 2), respectively. It is also interesting to notice that the test on original CV-PACs achieves the best performance on patient P4 only.

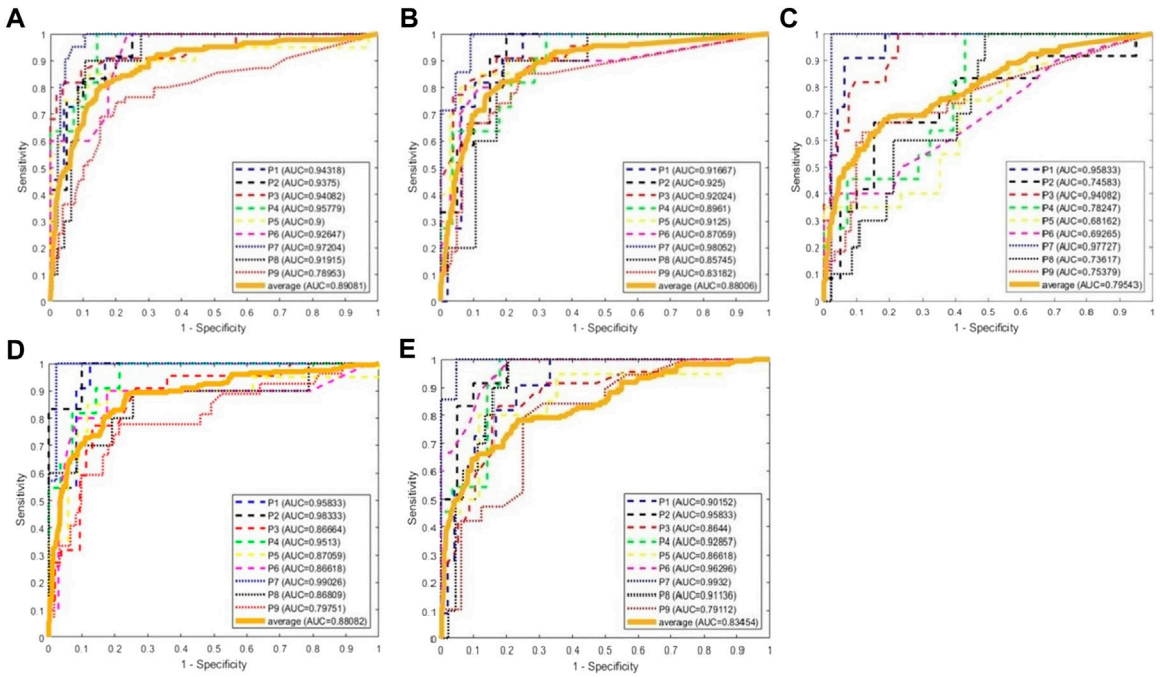

FIGURE 5
ROC curves of classification using CNN, SVM, random forest, and CV-CNN. **(A)** ROC curves using CNN. **(B)** ROC curves using SVM. **(C)** ROC curves using random forest. **(D)** ROC curves using CNN and PAC. **(E)** ROC curves using CV-CNN and ST-CV-PAC.

TABLE 3 Comparisons of AUC values by using CNN, SVM, RF, CNN(PAC), and CV-CNN(ST).

Patient	CNN	SVM	RF	CNN(PAC)	CV-CNN(ST)
P1	.94318	**.95833**	.91667	**.95833**	.90152
P2	.93750	.74583	.92500	**.98333**	.95833
P3	**.94082**	**.94082**	.92024	.86664	.86440
P4	**.95779**	.78247	.89610	.9513	.92857
P5	.90000	.68162	**.91250**	.87059	.86618
P6	.92647	.69265	.87059	.86618	**.96296**
P7	.97204	.97727	.98052	.99026	**.99320**
P8	**.91915**	.73617	.85745	.86809	.91136
P9	.78953	.75379	**.83182**	.79751	.79112
Average	**.89081**	.79543	.88006	.88082	.83454

Optimal values at each row are shown in bold.

The CV-PACs from non-resected regions and resected regions are averaged separately. The coupling strengths and coupled phases of pathological and normal CV-PAC are plotted in Figures 4A, B, respectively. The two patterns are different. The coupled phases in low-frequency bands are plotted in Figures 4C–F. The coupled phases in non-resected and resected regions are separable for slow delta, fast delta, and alpha bands. The phases in the non-resected and resected regions are overlapped for theta band, but the coupling strengths in the resected regions are stronger than the ones in non-resected regions. These features contribute to the capability of identifying pathological CV-PAC in the resected regions.

3.2 Comparison with CNN, SVM, and RF

We use traditional CNN, SVM, and random forest (RF) to train the model. The leave-one-out cross-validation is also performed. The real part and imaginary part of CV-PAC are extracted to form images with two layers. The obtained three-dimensional vectors are used as the features of the RF classifier. The number of trees searched is from 50 to 300. Since the performance does not improve after 100 trees, the number of trees is set to 100 in the remaining tests. The features used for SVM are the same as the RF. The SEEG of patient P1 is first trained and tested using the SVM method. A grid search over the parameters C (2^2, 2^6, . . ., 2^{20}) and γ(2^{-10}, 2^{-8}, . . ., 2^{10}) is performed to find optimal values. The parameter C is set to 2^{18}, and the parameter γ is set to 2^2. Those values of parameter C and γ are used for further analysis. The ROC curves are plotted in Figures 5A–C, and the AUC values are .890, .795, and .880 for traditional CNN, SVM, and RF, respectively. The performances of the above methods are lower than CV-CNN, as shown in Table 3. The PACs (without the coupled phases) are used to train the traditional CNN. The ROC curves are plotted in Figure 5D, and the AUC value is .88 (Table 3). We use the ST-CV-PAC to train the CV-CNN model with leave-one-out cross validation. The ROC curves are plotted in Figure 5E, and the averaged AUC value is .83 (Table 3).

4 Discussion

The PAC is commonly used to localize the epileptic tissue (Weiss et al., 2015; Liu et al., 2021), but the coupled phase of LFO in PAC is seldom used due to the complexity of the pattern. The proposed CV-PAC contains both the coupling strengths and the coupled phases.

Our result shows that the CV-PAC/CV-CNN approach outperforms PAC/CNN approach. The AUC values of the two approaches are .92 and .88, respectively (Tables 2, 3). When the real part and imaginary part of CV-PAC are extracted as two-layer input feature maps for traditional CNN, the AUC value decreases to .88. The performance will not improve if we just feed the CNN with real-value features. It implies that the coupling strengths and the coupled phases are correlated, and the complex-value operation in CV-CNN extracts the correlated information for identifying pathological PAC.

The coupled phases of LFOs are important in localizing the epileptogenic tissues (Amiri et al., 2016; Li et al., 2016). In our study, the delta band is divided into slow delta and fast delta (Amiri et al., 2016). Our result showed that the coupled phases of both slow delta and fast delta are different in pathological and normal PACs, as shown in Figures 4C, D. If the coupling in slow delta region was replaced by random values, the performance of classification dropped the most, as shown in Table 2. Our result also showed that the coupling in alpha region also contributes to the improvement of performance (Table 2; Figure 4F). The coupled phases in theta band are overlapped in pathological and normal PAC (Figure 4E). The coupling strengths of pathological PACs in delta band are stronger than the coupling strengths of normal PACs (Figures 4A, B). We infer that it is the main reason why the traditional PAC or MI can help us discriminate pathological brain tissues.

Some studies focused on the PAC in either LFO-gamma (30–80 Hz) or LFO-HFO (> =80) (Amiri et al., 2016; Liu et al., 2021). Our result shows that the AUC values scored only .80 and .84 when using CV-PAC of LFO-gamma (30–80 Hz) and LFO-HFO (80–160 Hz), respectively. Our result suggests that the CV-PAC of LFO-HFO (80–160 Hz) is more important than the CV-PAC of LFO-gamma (30–80 Hz) in classifying pathological patterns.

In our study, the PAC in the form of two-layer feature maps was used to train the SVM and RF. The performance of RF is comparable to PAC/CNN approach (Table 3). The AUC value of CV-PAC/CV-CNN approach is higher than all other methods, as listed in Table 3, which emphasizes the importance of the correlation between the coupling strength and coupled phase. The coupled phase is important, and it is more meaningful when combined with coupling strength. Since there are difficulties in analyzing the phase patterns of PAC, our proposed approach provides a tool for the classification of pathological PAC and normal PAC by introducing a complex-value image classification measure. Surrogate testing can be used to remove the spurious coupling in EEG signals (Shi et al., 2019; Li et al., 2021). In our study, the averaged AUC value using ST-CV-PAC is lower than the value using CV-PAC. Here, we adopt the image recognition measure by using CNN and CV-CNN. The ST-CV-PAC may become more complex and discontinuous due to removing some non-significant values. We think that is the main reason why the performance on ST-CV-PAC is lower than CV-PAC.

There are some limitations in this study. The ictal dataset is analyzed, and it still needs more study to extend it to inter-and pre-seizure data. Since the subdural is another widely used measure for recording brain electrical activity, it is necessary to include those types of data. In our study, most patients had temporal lobe epilepsy, and the location of SEEG implemented varied from patient to patient. It should be cautious to apply our method to all candidates for epilepsy surgery. Some studies have shown that PAC can be used to identify channels in SOZ, which is often much smaller than the area surgically removed. Comparing our results with traditional SOZ classification results still needs to be further explored. The non-linear decomposition methods for generating PAC may potentially improve the classification performance, which will be addressed in our future work.

5 Conclusion

The PAC pattern is a useful biomarker for identifying SEEG channels with pathological brain activities, and it is critical for presurgical evaluation of DRE patients. The proposed CV-PAC represents richer pathological patterns than PAC, which can be further analyzed by using image recognition measure. The CV-CNN achieves better performance than traditional machine learning measures in classification of pathological and normal PAC patterns. This study provides a new approach for localizing epileptogenic brain tissues.

Data availability statement

The raw data supporting the conclusion of this article will be made available by the authors, without undue reservation.

Ethics statement

The studies involving human participants were reviewed and approved by General Hospital of Northern Theater Command, Shenyang, China. Written informed consent to participate in this study was provided by the participants' legal guardian/next of kin.

Author contributions

CL and ZW contributed to design of the study. SL and ZW performed the data analysis. CL, SL, and ZW wrote the first draft of the manuscript. GY organized the dataset and interpreted the SEEG data. All authors approved the submitted version.

Funding

This work was supported by the National Natural Science Foundation of China (61771323) and Research Fund of Liaoning Provincial Natural Science (2021-KF-12-11), Program for Liaoning Innovative Talents in University, Research project of Liaoning Provincial Department of Education (LJGD20200012).

Acknowledgments

We would like to thank Dandan Gao for her help with collecting data.

Conflict of interest

The authors declare that the research was conducted in the absence of any commercial or financial relationships that could be construed as a potential conflict of interest.

Publisher's note

References

Amiri, M., Frauscher, B., and Gotman, J. (2016). Phase-amplitude coupling is elevated in deep sleep and in the onset zone of focal epileptic seizures. *Front. Hum. Neurosci.* 10, 387. doi:10.3389/fnhum.2016.00387

Bartolomei, F., Lagarde, S., Wendling, F., McGonigal, A., Jirsa, V., Guye, M., et al. (2017). Defining epileptogenic networks: Contribution of SEEG and signal analysis. *Epilepsia* 58 (7), 1131–1147. doi:10.1111/epi.13791

Canolty, R. T., and Knight, R. T. (2010). The functional role of cross-frequency coupling. *Trends Cogn. Sci.* 14 (11), 506–515. doi:10.1016/j.tics.2010.09.001

Cole, E., Cheng, J., Pauly, J., and Vasanawala, S. (2021). Analysis of deep complex-valued convolutional neural networks for MRI reconstruction and phase-focused applications. *Magn. Reson. Med.* 86, 1093–1109. doi:10.1002/mrm.28733

Engel, J., Jr. (2019). Evolution of concepts in epilepsy surgery. *Epileptic Disord.* 21, 391–409. doi:10.1684/epd.2019.1091

Guirgis, M., Chinvarun, Y., del Campo, M., Carlen, P. L., and Bardakjian, B. L. (2015). Defining regions of interest using cross-frequency coupling in extratemporal lobe epilepsy patients. *J. Neural Eng.* 12, 026011. doi:10.1088/1741-2560/12/2/026011

Hirose, A. (2013). *Complex-valued neural networks: Advances and applications*. Hoboken: Wiley-IEEE Press.

Jacobs, D., Hilton, T., Del Campo, M., Carlen, P. L., and Bardakjian, B. L. (2018). Classification of pre-clinical seizure states using scalp EEG cross-frequency coupling features. *IEEE Trans. Biomed. Eng.* 65 (11), 2440–2449. doi:10.1109/TBME.2018.2797919

Jiang, H., Cai, Z., Worrell, G. A., and He, B. (2019). Multiple oscillatory push-pull antagonisms constrain seizure propagation. *Ann. Neurol.* 86, 683–694. doi:10.1002/ana.25583

Jiang, Y., Deng, Z., Chung, F. L., Wang, G., Qian, P., Choi, K. S., et al. (2016). Recognition of epileptic EEG signals using a novel multiview TSK fuzzy system. *IEEE Trans. Fuzzy. Syst.* 25 (1), 3–20. doi:10.1109/TFUZZ.2016.2637405

Jin, L., Shi, W., Zhang, C., and Yeh, C. H. (2022). Frequency nesting interactions in the subthalamic nucleus correlate with the step phases for Parkinson's disease. *Front. Physiol.* 13, 890753. doi:10.3389/fphys.2022.890753

Krizhevsky, A., Sutskever, I., and Hinton, G. (2012). ImageNet classification with deep convolutional neural networks. *Commun. ACM* 60 (6), 84–90. doi:10.1145/3065386

Kwan, P., and Brodie, M. J. (2000). Early identification of refractory epilepsy. *N. Engl. J. Med.* 342, 314–319. doi:10.1056/NEJM200002033420503

Li, C., Jacobs, D., Hilton, T., del Campo, M., Chinvarun, Y., Carlen, P. L., et al. (2016). Epileptogenic source imaging using cross-frequency coupled signals from scalp EEG. *IEEE Trans. Biomed. Eng.* 63, 2607–2618. doi:10.1109/TBME.2016.2613936

Li, C., Sohrabpour, A., Jiang, H., and He, B. (2021). High-frequency hubs of the ictal cross-frequency coupling network predict surgical outcome in epilepsy patients. *IEEE Trans. Neural Syst. Rehabil. Eng.* 29, 1290–1299. doi:10.1109/TNSRE.2021.3093703

Lisman, J. E., and Idiart, M. A. (1995). Storage of 7 +/- 2 short-term memories in oscillatory subcycles. *Science* 267, 1512–1515. doi:10.1126/science.7878473

Liu, X., Han, F., Fu, R., Wang, Q., and Luan, G. (2021). Epileptogenic zone location of temporal lobe epilepsy by cross-frequency coupling analysis. *Front. Neurol.* 12, 764821. doi:10.3389/fneur.2021.764821

Ma, H., Wang, Z., Li, C., Chen, J., and Wang, Y. (2021). Phase-amplitude coupling and epileptogenic zone localization of frontal epilepsy based on intracranial EEG. *Front. Neurol.* 12, 718683. doi:10.3389/fneur.2021.718683

Pan, Y., Chen, J., Zhang, Y., and Zhang, Y. (2022). An efficient CNN-LSTM network with spectral normalization and label smoothing technologies for SSVEP frequency recognition. *J. Neural Eng.* 19 (5), 056014. doi:10.1088/1741-2552/ac8dc5

Parvizi, J., and Kastner, S. (2018). Promises and limitations of human intracranial electroencephalography. *Nat. Neurosci.* 21, 474–483. doi:10.1038/s41593-018-0108-2

Qin, Y., Zhang, N., Chen, Y., Zuo, X., Jiang, S., Zhao, X., et al. (2020). Rhythmic network modulation to thalamocortical couplings in epilepsy. *Int. J. Neural Syst.* 30 (11), 2050014. doi:10.1142/S0129065720500148

Ravi, A., Beni, N. H., Manuel, J., and Jiang, N. (2020). Comparing user-dependent and user-independent training of CNN for SSVEP BCI. *J. Neural Eng.* 17 (2), 026028. doi:10.1088/1741-2552/ab6a67

Rosenow, F., and Luders, H. (2001). Presurgical evaluation of epilepsy. *Brain* 124, 1683–1700. doi:10.1093/brain/124.9.1683

Shi, W., Yeh, C. H., and Hong, Y. (2019). Cross-frequency transfer entropy characterize coupling of interacting nonlinear oscillators in complex systems. *IEEE Trans. Biomed. Eng.* 66 (2), 521–529. doi:10.1109/TBME.2018.2849823

Tort, A. B., Komorowski, R., Eichenbaum, H., and Kopell, N. (2010). Measuring phase-amplitude coupling between neuronal oscillations of different frequencies. *J. Neurophysiol.* 104 (2), 1195–1210. doi:10.1152/jn.00106.2010

Tygert, M., Bruna, J., Chintala, S., LeCun, Y., Piantino, S., and Szlam, A. (2016). A mathematical motivation for complex-valued convolutional networks. *Neural comput.* 28, 815–825. doi:10.1162/NECO_a_00824

Villar, J. R., Menendez, M., de la Cal, E., Sedano, J., and Gonzalez, V. M. (2017). Identification of abnormal movements with 3D accelerometer sensors for seizure recognition. *J. Appl. Log.* 24, 54–61. doi:10.1016/j.jal.2016.11.024

von Ellenrieder, N., Frauscher, B., Dubeau, F., and Gotman, J. (2016). Interaction with slow waves during sleep improves discrimination of physiologic and pathologic high-frequency oscillations (80-500 Hz). *Epilepsia* 57, 869–878. doi:10.1111/epi.13380

Wang, D., Ren, D., Li, K., Feng, Y., Ma, D., Yan, X., et al. (2018). Epileptic seizure detection in long-term EEG recordings by using Wavelet-based directed transfer function. *IEEE Trans. Biomed. Eng.* 65 (11), 2591–2599. doi:10.1109/tbme.2018.2809798

Wang, Z., and Li, C. (2020). Classifying cross-frequency coupling pattern in epileptogenic tissues by convolutional neural network. *Annu. Int. Conf. IEEE Eng. Med. Biol. Soc.* 2020, 3440–3443. doi:10.1109/EMBC44109.2020.9175273

Weiss, S. A., Lemesiou, A., Connors, R., Banks, G. P., McKhann, G. M., Goodman, R. R., et al. (2015). Seizure localization using ictal phase-locked high gamma: A retrospective surgical outcome study. *Neurology* 84, 2320–2328. doi:10.1212/WNL.0000000000001656

Worrell, G., and Gotman, J. (2011). High-frequency oscillations and other electrophysiological biomarkers of epilepsy: Clinical studies. *Biomark. Med.* 5, 557–566. doi:10.2217/bmm.11.74

frontiers | Frontiers in Physiology

TYPE Original Research
PUBLISHED 19 January 2023
DOI 10.3389/fphys.2022.1068824

OPEN ACCESS

EDITED BY
Lisheng Xu,
Northeastern University, China

REVIEWED BY
Junichiro Hayano,
Heart Beat Science Lab Co., Ltd., Japan
Feifei Sun,
Sheng Jing Hospital of China Medical University, China

*CORRESPONDENCE
Xianda Wu,
xiandawu@m.scnu.edu.cn
Pengtao Sun,
sunpengtao@gzucm.edu.cn
Han Zhang,
zhanghan@scnu.edu.cn

SPECIALTY SECTION
This article was submitted to Computational Physiology and Medicine, a section of the journal Frontiers in Physiology

RECEIVED 13 October 2022
ACCEPTED 28 December 2022
PUBLISHED 19 January 2023

CITATION
Feng S, Wu X, Bao A, Lin G, Sun P, Cen H, Chen S, Liu Y, He W, Pang Z and Zhang H (2023), Machine learning-aided detection of heart failure (LVEF ≤ 49%) by using ballistocardiography and respiratory effort signals.
Front. Physiol. 13:1068824.
doi: 10.3389/fphys.2022.1068824

Machine learning-aided detection of heart failure (LVEF ≤ 49%) by using ballistocardiography and respiratory effort signals

Shen Feng[1,2], Xianda Wu[1,2]*, Andong Bao[1,2], Guanyang Lin[1,2], Pengtao Sun[3]*, Huan Cen[3], Sinan Chen[3], Yuexia Liu[3], Wenning He[4], Zhiqiang Pang[4] and Han Zhang[1,2]*

[1]Department of Electronics and Information Engineering, South China Normal University (SCNU), Foshan, China, [2]School of Physics and Telecommunication Engineering, South China Normal University (SCNU), Guangzhou, China, [3]Department of Ultrasonography, The Second Affiliated Hospital of Guangzhou University of Chinese Medicine, Guangzhou, China, [4]Guangzhou SENVIV Technology Co., Ltd., Guangzhou, China

Purpose: Under the influence of COVID-19 and the in-hospital cost, the in-home detection of cardiovascular disease with smart sensing devices is becoming more popular recently. In the presence of the qualified signals, ballistocardiography (BCG) can not only reflect the cardiac mechanical movements, but also detect the HF in a non-contact manner. However, for the potential HF patients, the additional quality assessment with ECG-aided requires more procedures and brings the inconvenience to their in-home HF diagnosis. To enable the HF detection in many real applications, we proposed a machine learning-aided scheme for the HF detection in this paper, where the BCG signals recorded from the force sensor were employed without the heartbeat location, and the respiratory effort signals separated from force sensors provided more HF features due to the connection between the heart and the lung systems. Finally, the effectiveness of the proposed HF detection scheme was verified in comparative experiments.
Methods: First, a piezoelectric sensor was used to record a signal sequences of the two-dimensional vital sign, which includes the BCG and the respiratory effort. Then, the linear and the non-linear features w.r.t. BCG and respiratory effort signals were extracted to serve the HF detection. Finally, the improved HF detection performance was verified through the LOO and the LOSO cross-validation settings with different machine learning classifiers.
Results: The proposed machine learning-aided scheme achieved the robust performance in the HF detection by using 4 different classifiers, and yielded an accuracy of 94.97% and 87.00% in the LOO and the LOSO experiments, respectively. In addition, experimental results demonstrated that the designed respiratory and cardiopulmonary features are beneficial to the HF detection (LVEF ≤49%).
Conclusion: This study proposed a machine learning-aided HF diagnostic scheme. Experimental results demonstrated that the proposed scheme can fully exploit the relationship between the heart and the lung systems to potentially improve the in-home HF detection performance by using both the BCG, the respiratory and the cardiopulmonary-related features.

KEYWORDS

heart failure, ballistocardiography, respiratory, classifier, home monitoring

1 Introduction

Heart failure (HF) is a kind of clinical syndrome caused by the abnormal cardiac structure or function, which leads to ventricular filling or ejection dysfunction. As the send-stage manifestation of all cardiovascular diseases, chronic HF brings serious burdens including the poor prognosis and the high mortality to many patients' families and our society (Hao et al., 2019). Also, as reporting in a global survey over 40 countries (Savarese et al., 2022), the reduced left ventricular ejection fraction (LVEF ≤49%) resulted by the HF can bring significant mortality rate. Therefore, early detection of HF is essentially important recently, especially for elderly patients with HF (LVEF ≤49%).

To better detect the body situation, some patients with hypertension and myocardial infarction and other heart diseases are suggested to perform regular medical checkups and early detection of HF in hospitals. For the dynamic management of chronic HF, regular review in hospitals to prevent the decompensation event is necessary (Society of Cardiology, 2018). Specifically, in the clinical diagnosis for the HF, echocardiography is regarded as one of the gold standards, and usually used to assess the systolic and diastolic capacity of the heart. In addition to the echocardiography, many techniques including X-rays, electrocardiogram (ECG) and brain natriuretic peptides (BNP) can be utilized as clinical key indicators to aid the HF diagnosis. However, the in-hospital HF diagnosis is challenging recently. On the one hand, under the influence of COVID-19, it may be inconvenient to the in-hospital routine check-ups related to the HF. On the other hand, many elderly patients are limited in the mobility, and unable to afford the high diagnostic cost for the inpatient check-ups. Therefore, it is worthy to develop the off-hospital/in-home HF detection scheme currently (Dickinson et al., 2018).

For the off-hospital/in-home HF detection, considering the benefits that the ballistocardiography (BCG) signals can conveniently monitor the body vibration caused by cardiac contraction and blood circulation, BCG is widely utilized for the in-home detection of various cardiac diseases recently (Wen et al., 2019). Specifically, Starr et al. first notified the clinical significance of BCG signals recorded by a mechanical bed, where the mathematical relationship between BCG and cardiac output (CO) was revealed (Starr et al., 1939), and the morphology difference between patients suffering from different types of cardio vascular (CV) diseases was analyzed (Starr and Schroeder, 1940), respectively. Also, the BCG signals were used to evaluate the cardiac contractility by the combined features with the ECG signals (Inan et al., 2009; Mozziyar et al., 2011; Ashouri et al., 2016). Since the correlation between the cardiac contractility and the heart functions, both the BCG and the ECG signals were applied to detect the HF decompensation (Giovangrandi et al., 2012; Etemadi et al., 2014; Aydemir et al., 2019). Similarly, Chang et al. calculated the waveform fluctuation metric at rest (WFMR) through the beat-to-beat features of the BCG signals to improve the quantitative analysis of the HF diseases (Chang et al., 2020). Generally, it was strongly demonstrated that the BCG per beat features can be effectively used for the HF detection in the above studies. However, considering the facts that many HF patients usually suffer from the weakened ventricular contractility, the mitral regurgitation and other symptoms, the resulted rhythm irregularity and the corresponding morphology diversity across different subjects bring a great challenge in the quality assessment of the BCG signals. Moreover, the respiratory effort signals, defined as the signals representing the energy consuming activity of the respiratory muscles (de Vries et al., 2018), and also is one of the important reference indicators for the clinical HF diagnosis (Siniorakis et al., 2018; Hamazaki et al., 2019), are rarely studied and developed in many existing works.

To overcome those above shortcomings, we proposed a non-contact sensing aided scheme for the in-home HF detection without quality assessment of BCG signals in this paper. Specifically, the piezoelectric sensing was used to acquire cardiopulmonary signs of various HF patients, where the signs contain the BCG and the respiratory effort information. Unlike the existing works, the proposed scheme performed the feature extractions from the BCG and the respiratory effort signals without the heartbeat location, where the extracted features finally identified the symptoms of the HF by using several typical classifiers. To validate the performance of the proposed HF detection scheme, the control experiments in terms of the leave-one-out (LOO) and the leave-one-subject-out (LOSO) rules were investigated. Experimental results demonstrated that the proposed scheme, in comparison with the existing studies, shows robust to HF (LVEF ≤ 49%) with low absolute global longitudinal strain (absolute GLS < 20%). Furthermore, the statistical analysis revealed that the respiratory and the cardiopulmonary features have the great diagnostic significance for the HF diseases.

2 Materials and methods

2.1 Experimental devices and protocol

The overall experimental procedure is shown in **Figure 1**, the non-contact sensing device consists of a vital sign acquisition module and a signal processing module. The vital sign acquisition module was made by a piezoelectric sensor with a sampling rate of $f_s = 1kHz$, and used to collect the vital signs under the head and neck. The aim of the signal processing module is to convert the collected signals as 12-bit analog-to-digital data. Furthermore, the echocardiography was recorded by EPIQ 7C (Philips).

Specifically, each subject was first asked to supine on an instrumented bed and keep soldier sleeping position for the 5 min baseline restoration and followed by vital sign signal

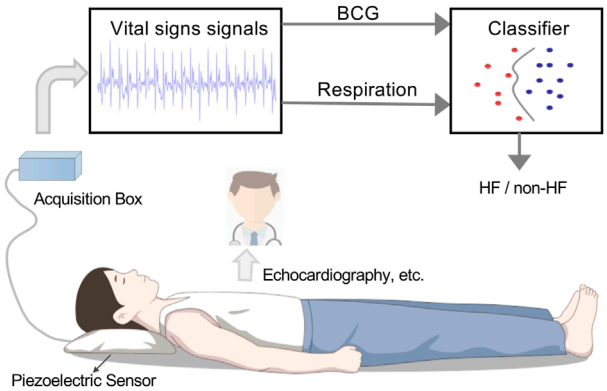

FIGURE 1
Heart failure detection by using non-contact recorded vital signs.

TABLE 1 A description of the subjects. BMI: body mass index. LVEF: left ventricular ejection fraction. GLS: global longitudinal strain. Value performance by mean ± standard deviation.

	Number	Gender (male /female)	Age (year)	Height (cm)	Weight (kg)	BMI (kg/m^2)	LVEF (%)	GLS (%)	Doppler ultrasonography
HF	30	20/10	61.80 ± 13.63	156.29 ± 8.24	61.63 ± 12.38	23.62 ± 4.02	38.99 ± 4.02	11.41 ± 3.76	Low, medium, and large volumes of regurgitation in 15, 6 and 9 cases, respectively
non-HF	24	19/5	45.79 ± 14.03	166.58 ± 8.65	67.29 ± 11.86	24.25 ± 3.29	69.21 ± 3.71	21.16 ± 2.40	No abnormal, small and moderate regurgitation in 9, 13 and 2 cases, respectively

acquisition. Before and during the 10 min period of the vital signs collection, all subjects did not have any exercise and kept the fixed positions. The recorded data are involved the non-contact sensing device and the echocardiography, where the collected vial signs contain the information of both the BCG and the respiratory effort from the head and necks of the subjects (Liu et al., 2021). After the data acquisition, some professional cardiologists made the HF diagnosis by the echocardiography signals, and other recorded data was selected by the above results. For a simpler interpretation, GLS was taken as absolute value in this study. Finally, the selected data from the non-contact sensing device was used in the following procedures of the proposed scheme.

2.2 Inclusion and exclusion criteria

To reduce the influence of other extraneous factors, the enrolled standards for the HF group are as follows.

- The HF diagnosis guidelines (Society of Cardiology, 2018).
- LVEF ≤49% and GLS <20% (Park et al., 2018).
- The diagnosed HF patients with complications of many heart diseases including the coronary artery disease, and the structural heart abnormalities resulted by the heart attack or the hypertension (all subjects received medications, and some of them has the coronary PCI or pacemakers.).

As a control group, the standards for the healthy group are as follows.

- Normal blood glucose, lipids, blood pressure, blood routine, liver function, and kidney function.
- Normal ECG (note: occasional atrial premature can be included as appropriate).
- No history of the medication affecting the cardiovascular system.
- No structural heart disease and normal cardiac function on the echocardiography (LVEF >50%), mild or less valvular regurgitation can be included. The criteria using the HFA-PEFF score is applied to classify the subjects with preserved LVEF (HFpEF) from all potential healthy candidates with LVEF >50% (Pieske et al., 2019).

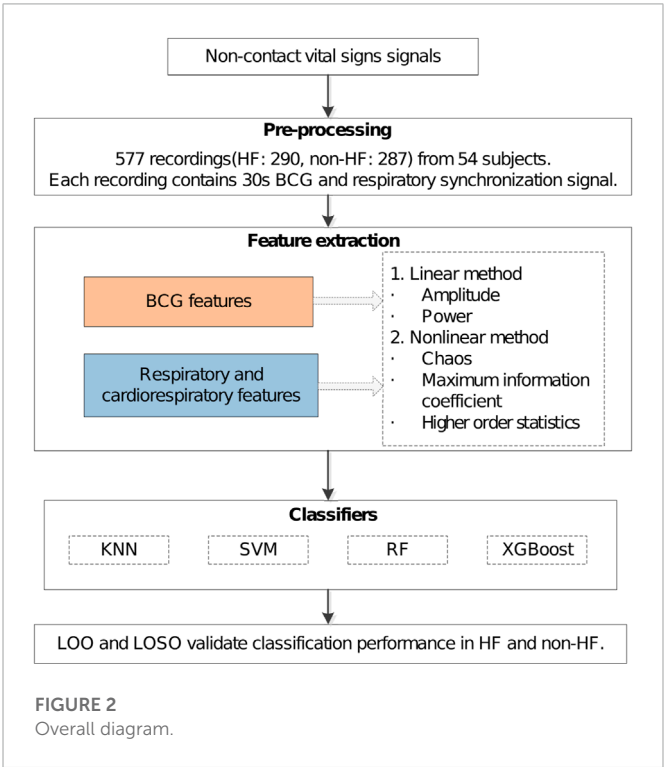

FIGURE 2
Overall diagram.

2.3 Study population

A total of 54 subjects in the age range of 23–92 years participated in the study, i.e., 24 healthy subjects and 30 HF (LVEF ≤49%) patients. The details of the subjects are listed in **Table 1**. All subjects who participated in this study were recruited by the Second Affiliated Hospital of Guangzhou University of Chinese Medicine (Guangdong Hospital of Chinese Medicine) in Guangzhou, China, including the volunteers, the routine physical examiners, and the HF patients. The study protocol has been reviewed and approved by the Ethics Committee of Guangdong Provincial Hospital of Traditional Chinese Medicine (ZE 2022–123). All subjects obtained the informed consent before their participation in this study. The flowchart diagram of the proposed non-contact HF diagnosis method is shown in **Figure 2**.

2.4 Pre-processing

The key purpose of performing the pre-processing is to process and divide the collected data into several data sets for the HF detection, where the first step is associated with the signal separation, and the second one is related to the sample grouping.

For the first step, similar to (Jingxian et al., 2020), the peak-to-mean ratio detection of the 1s time-scale signals was performed to remove the artifact interference and separate the BCG signals and the respirator effort contributions from the collected data. Specifically, the morphological and the low-pass filters were sequentially exploited to obtain the respiratory effort signals. Then we removed the separated respiratory effort signals from the collected signals and obtained the new vital sign sequences. Given such new sequences, a 4th-order Butterworth filter (2 Hz ~8.5 Hz) was applied to get the improved BCG signals. The results of the above signal separation can be found in **Figure 3**, where **Figure 3A** shows the 30s sign signals acquired *via* the piezoelectric sensing, and **Figures 3B, C** are the de-noised BCG and the respiratory effort signals, respectively.

Similar to (Chang et al., 2020), the BCG and the respiratory effort signals were first divided into multiple consecutive epochs of 30s in a non-overlapped manner. As a result, the total number of the recordings was 577, where each recording included the 30s synchronously BCG and the respiratory effort epoch. In details, 290 recordings were associated with the HF patients while others are related to the non-HF subjects. Among them, recordings were evenly distributed from each subject to ensure no bias in the data and furthermore the universality of the experimental results. In the traditional studies, the HF diseases can be easy detected by the typical waveforms of the BCG signals (Carlson et al., 2020; Liu et al., 2021). However, the corresponding BCG signals are usually irregular in rhythm and morphology due to disordered cardiac movement (HF patients with LVEF ≤49% and GLS <20%) (Siniorakis et al., 2018; Hamazaki et al., 2019; McDonagh et al., 2021). The irregular heartbeat waveforms of the BCG signals bring challenges for heartbeat location in the HF detection. By (Aydemir et al., 2019; Mai et al., 2022), we use signal-to-noise ratio (SNR) to access the signal quality of each BCG epoch. When SNR ≪ 4 dB, the whole (or part of) epoch of BCG signals are almost unable to identify. **Figures 3B, C, E–H** depicts the recorded BCG and the respiratory signals in terms of healthy subjects, HF patients with the heartbeat in BCG signals easily or difficult to be identified. It is noted that the heartbeat in BCG of 13 out of 30 HF patients was difficult to recognize due to the heart abnormality, as shown in **Figure 3D**, where the related existing methods are difficult to be applied (Aydemir et al., 2019; Chang et al., 2020). Therefore, to illustrate the robustness of our HF diagnostic method, we divided all 577 recordings into two groups in this experiment, i.e., Datasets 1 consists of 176 HF recordings (recognizable heartbeat in BCG) and 287 non-HF recordings, and Datasets 2 includes 114 HF recordings (unrecognizable heartbeat in BCG) and 287 non-HF recordings.

2.5 Feature extraction

2.5.1 BCG features

Unlike the existing HF detection methods depended on the heartbeat location of the BCG signals in (Etemadi et al., 2014; Aydemir et al., 2019; Chang et al., 2020), our proposed scheme focused on the large scale features of the BCG signals, i.e., the

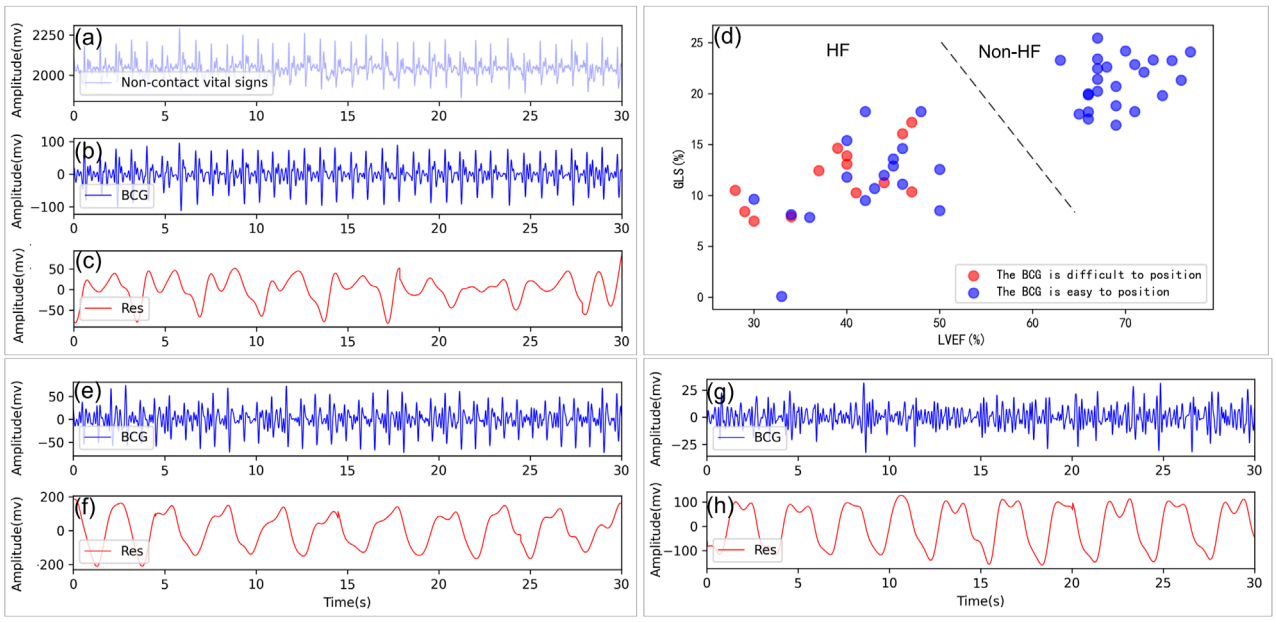

FIGURE 3
Non-contact vital sign signal processing and analysis. **(A)** Example of a non-contact vital sign signal collected. **(B, C)** Example of BCG and respiratory signals isolated from a healthy subject, GLS = 21.30%, LVEF = 76%. **(D)** Distribution of the J-peaks of the BCG for those who are difficult located (red circles) and those who are easier located (blue circles) in terms of LVEF, GLS. **(E, F)** Example of BCG and respiratory signals from a patient with HF with BCG can be located, GLS = 9.62%, LVEF = 30%. **(G, H)** Example of BCG and respiratory signals from a patient with HF with heartbeat are very difficult to locate, GLS = 16.07%, LVEF = 46%. Res: respiratory signal.

30 s epoch, where the hearbeat location was no longer needed. The corresponding features in the experiments were extracted in both linear and non-linear domains, as shown in **Table 2**.

2.5.1.1 Linear features

2.5.1.1.1 Amplitude

The amplitude coefficient of the given signal $x(n)$ can be expressed as

$$F(x(n)) = \frac{rms(x(n))}{max(x(n)) - min(x(n))} \tag{1}$$

where $rms(\cdot)$ is the root mean square function, $\max(\cdot)$ indicates the maximum value function, and $\min(\cdot)$ denotes the minimum value function. According to Eq. **1**, we obtained the amplitude features of each BCG epoch by $F(BCG(n))$ in the experiments, where the notation $BCG(n)$ was the separated BCG signals obtained from the above pre-progressing, and the amplitudes of the HF patient group were lower than that of the health subject group. This case is usually caused by that the HF patients suffer from the low myocardial contractility.

2.5.1.1.2 Power

Inspired by the morphological difference between HF patients and healthy subjects (Chang et al., 2020), the volatility and the irregularity of the BCG singals can be measured and analyzed in the power-domain. To eliminate individualized differences, in our experiments, the signal was normalized using Z-score before the power calculation (Shi et al., 2022). As (Li et al., 2020), the signals $x(n)$ was first divided into L segments x' by the sliding window as

$$x'_L = \{x'_1(i), x'_2(i), \ldots, x'_L(i), \quad i = 1, 2, \ldots, w * f_s\} \tag{2}$$

where $L = fix\left(\frac{N - w * f_s + t * f_s}{t * f_s}\right)$ represents the number of segments. N and w are the length of $x(n)$ and the sliding window (the segment length), respectively. t indicates the time moving factor of the sliding window, f_s denotes the sampling rate, and $fix(\cdot)$ is the rounding function. The power of each segment was computed as

$$Power_L(x') = \{\text{power}(x'_1(i)), \text{power}(x'_2(i)), \ldots, \text{power}(x'_L(i)), \\ i = 1, 2, \ldots, w * f_s\} \tag{3}$$

where $power(\cdot)$ is the power function. As a result, the statistics $Power_L(BCG(n))$ were used to characterize the volatility of the BCG signals.

2.5.1.2 Non-linear features

2.5.1.2.1 Chaos

Chaos is defined as an uncertain or unpredictable random phenomenon presented by a deterministic system under many certain conditions, which can evaluate the level of the time-series signal disorder (Gupta et al., 2019). As a result, the chaotic features of the BCG time series, including fuzzy entropy (FE), largest Lyapunov exponent (LLE) and correlation dimension (CD), can be extracted to evaluate the disorder degree in BCG.

Firstly, FE (Chen et al., 2007) not only reflects the similarity between two vectors in the phase space, but also represents the complexity of the chaos system, defined as

$$FE(x(n)) = -\ln\frac{C^{m+1}(r)}{C^m(r)} \tag{4}$$

where m is the embedding dimension, r indicates the similarity tolerance limit threshold, $C^m(r)$ denotes the average of all fuzzy affiliations except itself. The FE of a BCG epoch was obtained by $FE(BCG(n))$ in this study with the setting $m = 2$, and $r = 0.15$. In addition, similar to the calculation for the power volatility, the FE of each BCG segment, i.e., $FE_L(BCG(n))$, was computed by using Eqs. **2**, **4**, which characterize the volatility of the FE series.

Next, we used two features including the LLE and the CD to better analyze the BCG signals (Procacia et al., 1983; Rosenstein et al., 1993), where LLE is the exponential rate of the convergence between two adjacent trajectories, and CD indicates the correlation between two phase points in the phase space. Their definition can be respectively expressed as

$$LLE(x(n)) = \frac{1}{\Delta t} < \ln d_j(i) > \tag{5}$$

$$CD(x(n)) = \lim_{r \to 0} \frac{\ln C(r)}{\ln(r)} \tag{6}$$

where $< \cdot >$ denotes the mean value, Δt is the sampling interval, and $d_j(i)$ indicates the distance of the j-th pair of nearest neighbors after

TABLE 2 BCG features without localization assistance. sd: standard deviation. IQR: interquartile range.

Feature	Category	Name	Description
T1	Linear	$F(BCG(n))$	BCG amplitude coefficient
T2-T5		$Power_L(BCG(n)))$ $mean, sd, IQR, median$	Power volatility of BCG on a fixed time scale
T6	Non-linear	$FE(BCG(n))$	BCG fuzzy entropy
T7-T10		$FE_L(BCG(n))$ $mean, sd, IQR, median$	Fuzzy entropy volatility of BCG on fixed time scale
T11		$LLE(BCG(n))$	BCG largest liapunov exponent
T12		$CD(BCG(n))$	BCG correlation dimension
T13-T16		$MIC_{L-1}(BCG(n))$ $mean, sd, IQR, median$	MIC volatility of BCG on a fixed time scale
T17		$Skewness(BCG(n))$	BCG skewness
T18		$Kurtosis(BCG(n))$	BCG kurtosis

i discrete time steps. In the phase space, the function $C(r)$ is the proportion between the number of the point pairs locating within the given radius r of the hyper-sphere and the number of all point pairs. Therefore, according to Eqs. 5, 6, we computed the LLE and the CD by the maximum value of the parameter embedding dimension $m = 12$ and the maximum value of the time delay factor $\tau = 40$ ms as LLE ($BCG(n)$) and CD ($BCG(n)$), respectively.

2.5.1.2.2 Maximum information coefficient

The maximum information coefficient (MIC) (Reshef et al., 2011) is a generalization of mutual information. In order words, the MIC can describe the association degree between two series (0: no correlation, 1: strong correlation) by a maximum information-based non-parametric exploration. The MIC between two random variables x_1 and x_2 can be expressed as

$$MIC(x_1, x_2) = \max_{pq<B(s)} \{M(D)_{p,q}\} \tag{7}$$

where $B(s) = s^{0.6}$ is a function of the sample number. $M(D)$ is the mutual information on the grids p^*q. Using Eqs. 2, 7, the MIC values of the two adjacent segments can be calculated to form an $L-1$ sequence, i.e., MIC_{L-1} ($x(n)$). As a result, we computed the MIC parameter of the BCG signals as $MIC_{L-1}(BCG(n))$.

In the presence of the 4s sliding window and the 3s/2s/1s time moving factors, we calculated the mean, the standard deviation, and the interquartile range (IQR), and the median statistics for the above features, i.e., $Power_L(BCG(n))$, FE_L ($BCG(n)$), and $MIC_{L-1}(BCG(n))$), to serve the following experiments and analysis.

2.5.1.2.3 Higher order statistics

Similar to (Bruser et al., 2012), the skewness and the kurtosis of the given signals $x(n)$ can be respectively calculated as

$$Skewness(x(n)) = \frac{m_3(x(n))}{m_2(x(n))^{3/2}} \tag{8}$$

$$Kurtosis(x(n)) = \frac{m_4(x(n))}{m_2(x(n))^2} \tag{9}$$

where m_k ($x(n)$) denotes the kth sample moment around the mean of the signals $x(n)$.

2.5.2 Respiratory and cardiopulmonary features

Considering the facts that HF patients often suffer from the Respiratory aggravation symptoms, such as the chest tightness, the wheezing, the breath shortness, and the dyspnea due to the cardiac insufficiency (McDonagh et al., 2021), there are many connections between the respiration/cardiopulmonary-related features and the HF diseases. However, these features obtained from wearable devices lack attention recently and are rare to be applied into the HF detection. Motivated by this fact, in this study, we proposed to use these respiration-related features to improve the performance of the HF detection. These associated features can be found in Table 3. Similar to the above BCG-related features, many details of the respiration/cardiopulmonary-related feature calculation/extraction are presented as follows.

2.5.2.1 Respiratory features

Considering that the breath shortness in HF patients leads to the enhanced respiratory effort, we chooosed the amplitude coefficient of the respiratory signals, i.e., $F(Res(n))$, to characterize the respiratory strength in the proposed scheme, The corresponding feature details can be found in Eq. 1.

Similarly, the FE of the respiratory-related epochs, $FE(Res(n))$, was calculated by Eqs. 2, 4 to characterize the volatility of the respiratory-related signals. Specifically, the corresponding window length and the time moving factor were set at 6s and 1s, respectively. As mentioned in the BCG-related feature extractions, many typical statistics including the skewness and the kurtosis related to the respiratory FE were calculated for the classifiers.

2.5.2.2 Cardiopulmonary features

Similar to the respiratory effort, the connection between the heart and the lung systems can support that using the cardiopulmonary analysis to improve the heart detection performance. However, unlike the above feature extractions only relying on the BCG/respiratory signals, the cardiopulmonary features are associated with both the heart and the lung systems. As a result, the cardiopulmonary joint analysis can not only provide more benefits of reducing the effect caused by the occasional interference/noise in the BCG or the respiratory signals, but also eliminate the potential errors due to individual difference. The cardiopulmonary features, specifically,

TABLE 3 Respiratory and cardiopulmonary features. sd: standard deviation. IQR: interquartile range.

Feature	Category	Name	Description
T19	Respiratory	$F(Res(n))$	Respiratory effort amplitude coefficient
T20		$FE(Res(n))$	Respiratory effort fuzzy entropy
T21-T24		$FE_L(Res(n))$ $mean, sd, IQR, median$	Fuzzy entropy volatility of respiratory signals on fixed time scales
T25		$Skewness(Res(n))$	Respiratory effort skewness
T26		$Kurtosis(Res(n))$	Respiratory effort kurtosis
T27	Cardiopulmonary	$F^{ratio}(Res(n), BCG(n))$	Ratio of respiratory to BCG amplitude coefficient
T28		$Power^{ratio}(Res(n), BCG(n))$	Ratio of respiratory to BCG signal power
T29-T32		$Power_L^{ratio}(Res(n), BCG(n))$ $mean, sd, IQR, median$	Volatility of respiration to BCG power ratio on a fixed time scale
T33		$FE^{sum}(Res(n), BCG(n))$	Sum of respiratory and BCG signal fuzzy entropy

include the relative amplitude and power of respiratory effort and BCG, and quantify the overall complexity of these two kinds of signals.

According to the above considerations, the amplitude coefficient is defined as the ratio of the amplitude coefficients related to the respiratory and the BCG signals as

$$F^{ratio}(Res(n), BCG(n)) = \frac{F(Res(n))}{F(BCG(n))} = \frac{\frac{\mathrm{rms}(Res(n))}{\max(Res(n)) - \min(Res(n))}}{\frac{\mathrm{rms}(BCG(n))}{\max(BCG(n)) - \min(BCG(n))}} \quad (10)$$

Similarly, the corresponding power features and the corresponding chaos features was respectively calculated as

$$Power^{ratio}(Res(n), BCG(n)) = \frac{\sum_{n=1}^{N}(Res(n))^2/N}{\sum_{n=1}^{N}(BCG(n))^2/N} \quad (11)$$

$$FE^{sum}(Res(n), BCG(n)) = FE(Res(n)) + FE(BCG(n)) \quad (12)$$

Usually, HF patients have shortness of breath and a reduced volume per beat, which results in the larger values of $F^{ratio}(Res(n), BCG(n))$ and $Power^{ratio}(Res(n), BCG(n))$ than that of the healthy candidates. Consequently, it is thus expected that the above cardiopulmonary features (10)–(12) can complement the individual differences possibly induced by single-channel features of BCG or respiratory signals. Also, we calculated the relative power volatility of respiration and BCG using Eqs. **2**, **11**, the recommended window and time moving factor are recommended to be adjusted as 2s. The statistics of $Power_L^{ratio}(Res(n), BCG(n))$ were calculated for the following classifiers in the experiments.

2.6 Classifiers

Based on the above extracted features related to the BCG/respiratory/cardiopulmonary signals, we applied four supervised classifiers to evaluate the performance of the HF detection. The classifiers include the K-Nearest Neighbor (KNN), the Support Vector Machine (SVM), the Random Forest (RF) and the eXtreme Gradient Boosting (XGBoost), where the features require to be normalized within [0,1] before performing the classification (Shi et al., 2022).

Among these four classifiers, the KNN (Ertuğrul and Tağluk, 2017) algorithm is the fastest algorithm, where the principle is to classify the new data points by those nearest K classified data points. However, the KNN has the limited performance in the complex classification boundary. To achieve better classification in the complex data space, SVM (Palaniappan et al., 2014) utilizes the sparsity between classified data points, i.e., only a few of points play important role to the classification boundary. Unlike the iterative processing of the SVM may cost much system resources, the RF (Sun et al., 2020) algorithm is based on the multiple decision tress without iterations. By the gradient boosting in the optimization theory, the XGBoost (Chen and Guestrin, 2016) classifier is a distributed enhancement with many benefits including the low complexity and the high flexibility.

2.7 Performance metrics

Similar to (Magrelli et al., 2021), the performance metrics include accuracy (Acc), sensitivity (Sen), specificity (Spe), F1 score (F1) and area under the curve (AUC), defined as

$$Acc = \frac{TP + TN}{TP + TN + FP + FN} \quad (13)$$

$$Sen = \frac{TP}{TP + FN} \quad (14)$$

$$Spe = \frac{TN}{TN + FP} \quad (15)$$

$$F1 = \frac{2TP}{2TP + FP + FN} \quad (16)$$

where TP represents the number of correctly predicted positive samples, TN indicates the number of correctly predicted negative samples, FP is the number of negative samples predicted to be positive, and FN denotes the number of positive samples predicted to be negative. AUC is the area of receiver operating characteristic curve (ROC).

For the fairness in the evaluation, the LOO and the LOSO methods were used for the training and the testing phases, respectively. During the model training and testing phases, we also optimized each classifier by using the grid search method and obtained their highest classification accuracy.

3 Results

3.1 Performance of HF detection with different classifiers

Firstly, we examined the performance of the proposed HF detection scheme in the presence of 4 different classifiers by the BCG, the respiratory and the cardiopulmonary-related features. Specifically, the performance metrics including the accuracy, the sensitivity, the specificity, the F1 score, and the AUC, are presented in **Table 4** and **Figure 4**. These results showed that all 4 classifiers could provide the accuracy of over 91.16% under the LOO setting. Among them, the best performance was brought by the XGBoost classifier at 94.97% accuracy. In order to verify the stability of the performance, the LOSO cross-validation results were also given in **Table 4** to provide person independent classification results. Under the LOSO setting showing the generalization ability of the proposed scheme, the best accuracy results of the proposed HF detection scheme were provided by the XGBoost. In addition, for all 4 classifiers, the performance brought by the BCG and respiration-related (respiratory and cardiopulmonary) features outperformed that of the BCG features under both the LOO and the LOSO setting. The above results indicated that the proposed scheme, which is based on the BCG, the respiratory and the cardiopulmonary features, significantly improved the detection performance of the HF diseases.

Comparing with that one of the main limitations in the existing BCG-based HF detection algorithm is the additional quality assessment, our proposed detection scheme can avoid this limitation by using more linear and non-linear features of both the heart

10.3389/fphys.2022.1068824

TABLE 4 LOO and LOSO classification results for HF diagnostics based on BCG and respiratory-related features using 4 classifiers. Resp: Respiratory and cardiopulmonary features.

Classifiers	Features	LOO					LOSO				
		Acc(%)	Sen(%)	Spe (%)	F1 (%)	AUC(%)	Acc(%)	Sen(%)	Spe (%)	F1 (%)	AUC(%)
KNN	BCG	87.88	88.62	87.11	88.01	92.84	74.18	78.97	69.34	75.45	79.14
	BCG & Resp	92.20	92.07	92.33	92.23	97.78	81.63	82.76	80.49	81.91	90.25
SVM	BCG	87.88	88.97	86.76	88.05	94.20	75.56	80.00	71.08	76.69	83.33
	BCG & Resp	91.16	92.07	90.24	91.28	96.89	83.36	82.76	83.97	83.33	91.06
RF	BCG	85.10	87.59	82.58	85.52	93.19	74.18	76.55	71.78	74.87	81.94
	BCG & Resp	93.93	94.83	93.03	94.02	98.64	85.44	86.55	84.32	85.67	93.98
XGBoost	BCG	89.43	90.00	88.85	89.54	94.94	74.18	74.48	73.86	74.35	82.94
	BCG & Resp	94.97	96.55	93.38	95.08	99.05	87.00	86.21	87.80	86.96	94.37

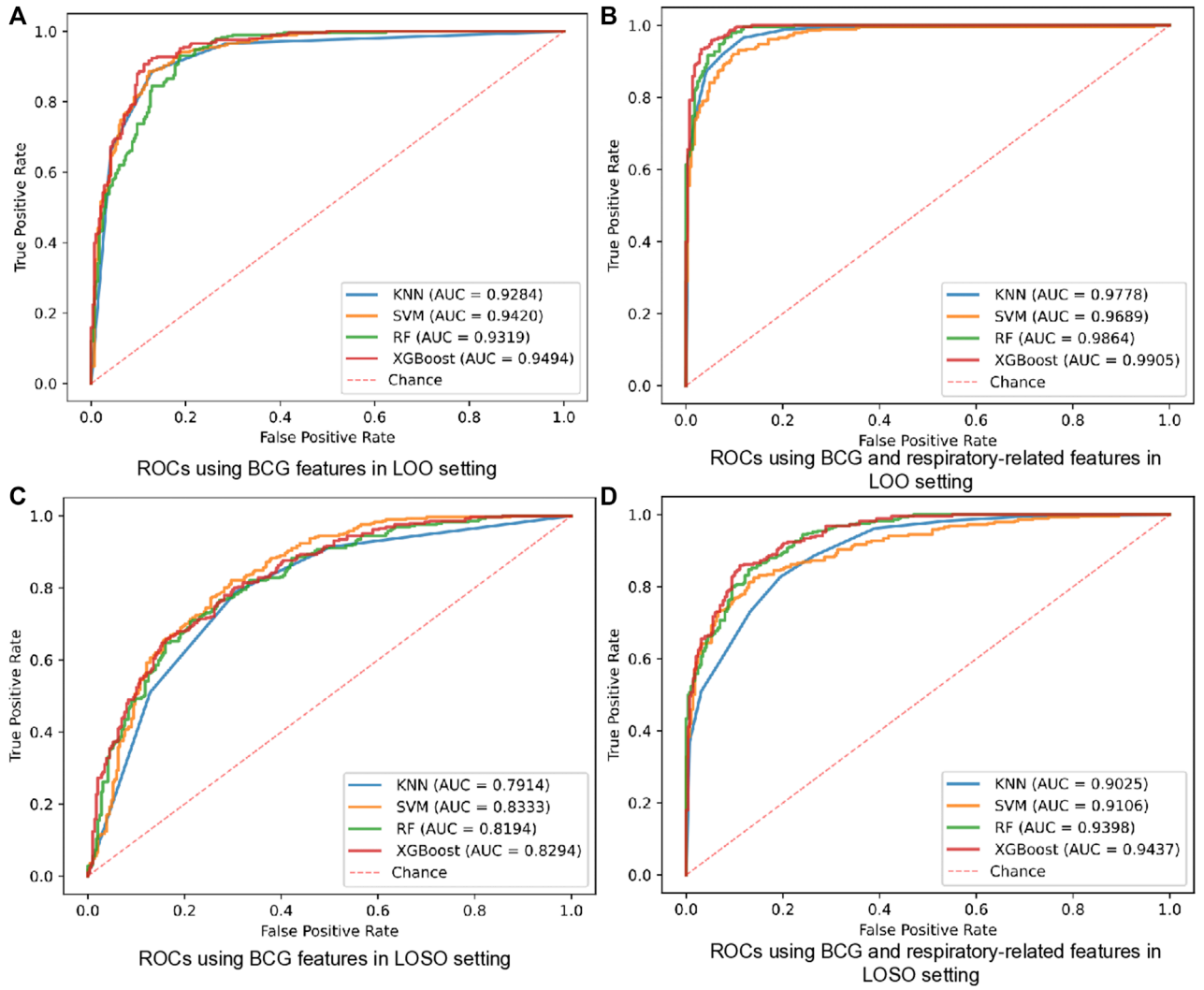

FIGURE 4
ROCs of HF diagnostics based on BCG and respiratory-related features using 4 classifiers in all datasets. **(A)** ROCs using BCG features in LOO setting. **(B)** ROCs using BCG and respiratory-related features in LOO setting. **(C)** ROCs using BCG features in LOSO setting. **(D)** ROCs using BCG and respiratory-related features in LOSO setting.

TABLE 5 LOO and LOSO classification results for HF diagnostics over 2 datasets using 4 classifiers. Datasets 1: HF patients of BCG easily localized and healthy subjects samples. Datasets 2: HF patients of BCG not easily localized and healthy subjects samples.

Classifiers	Datasets	LOO					LOSO				
		Acc(%)	Sen(%)	Spe(%)	F1(%)	AUC(%)	Acc(%)	Sen(%)	Spe(%)	F1(%)	AUC(%)
KNN	Datasets1	91.79	85.23	95.82	88.75	97.82	77.32	62.50	86.41	67.69	85.89
	Datasets2	95.76	93.86	96.52	92.64	99.21	91.02	81.58	94.77	83.78	96.65
SVM	Datasets1	88.55	81.82	92.68	84.46	94.77	79.05	71.02	83.97	72.05	86.33
	Datasets2	96.51	94.74	97.21	93.91	99.44	92.27	84.21	95.47	86.10	96.45
RF	Datasets1	90.71	86.36	93.38	87.61	98.12	82.94	72.16	89.55	76.28	91.70
	Datasets2	96.76	90.35	99.30	94.06	99.74	92.77	85.09	95.82	87.00	97.71
XGBoost	Datasets1	95.15	94.32	95.82	93.79	98.89	83.37	77.84	86.76	78.06	91.72
	Datasets2	99.00	99.12	98.95	98.26	99.73	94.01	86.84	96.86	89.19	98.59

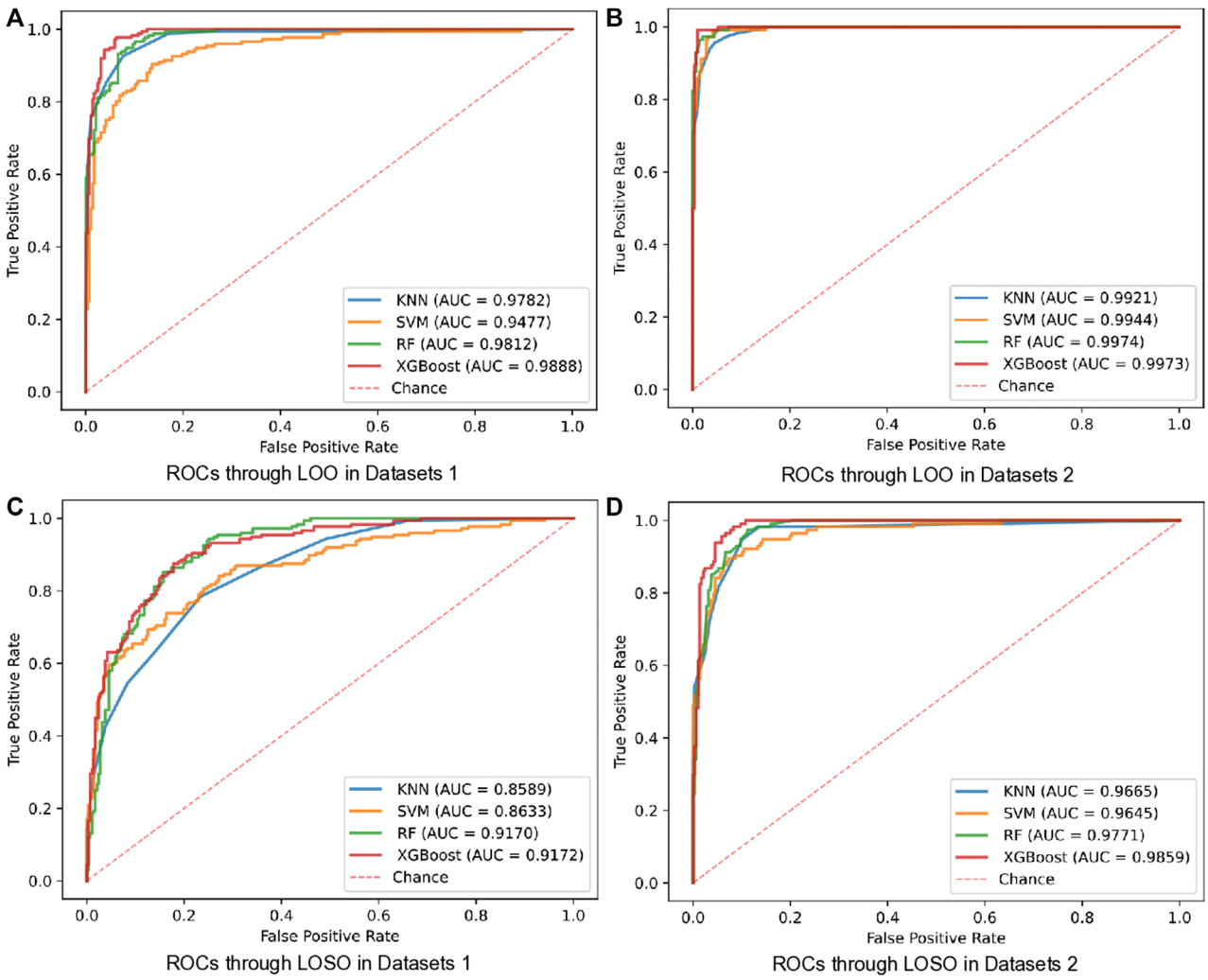

FIGURE 5
ROCs of LOO and LOSO for HF diagnostics over 2 datasets using 4 classifiers. **(A)** ROCs through LOO in Datasets 1. **(B)** ROCs through LOO in Datasets 2. **(C)** ROCs through LOSO in Datasets 1. **(D)** ROCs through LOSO in Datasets 2.

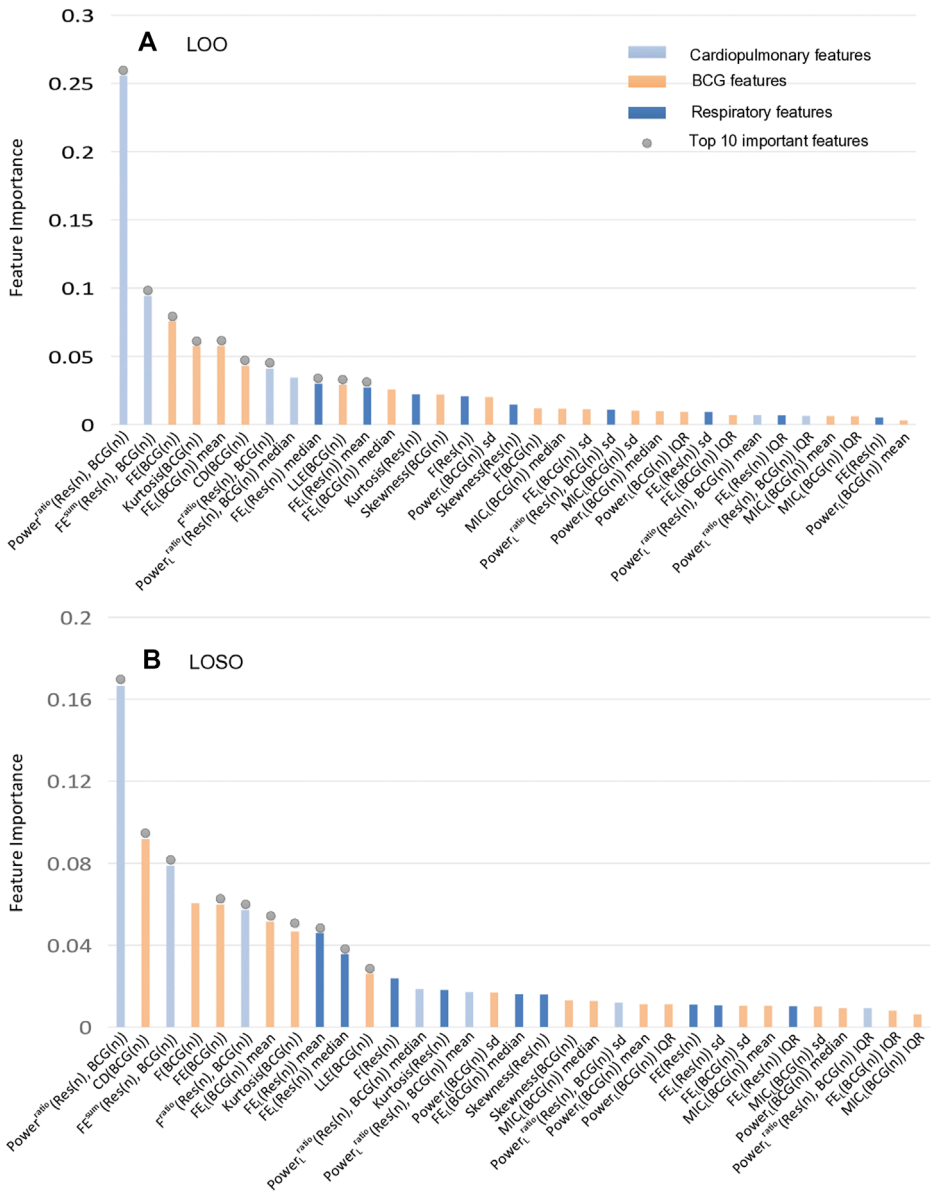

FIGURE 6
The importance ranking of all features in the XGBoost model under LOO and LOSO. The together top 10 important features contribute 71.00% and 65.88% to the classification, respectively. **(A)** The importance ranking of classifier features in LOO settings. **(B)** The importance ranking of classifier features in LOSO settings.

and the lung systems. To verify the corresponding effectiveness, two types of dataset, i.e., the Datasets 1 (recognizable heartbeat in BCG) and the Datasets 2 (unrecognizable heartbeat in BCG) were used in performing our proposed HF detection method. The detailed experiment results are shown in **Table 5** and **Figure 5**, which demonstrated that the Datasets 2 provided better classification performance than the Datasets 1 in all 4 classifiers under both the LOO and the LOSO settings. Among them, the best performance was brought by the XGBoost classifier at 99.00% and 94.01% under the LOO and the LOSO settings, respectively. All the above results showed that our proposed scheme addressed the limitation related to the heartbeat location in the existing BCG-based HF detection algorithms.

3.2 Feature importance of LOO and LOSO experiments

In the following experiments, we mainly focused on analyzing the features' contributions to the classification/detection of the HF diseases, where the XGBoost weights were used to evaluate the features' contributions. The details of the feature importance are shown in **Figure 6** under the LOO and the LOSO settings, respectively. Specifically, the importance scores of all features were firstly obtained from the XGBoost classifier after the training phase, and then the mean value of each feature's importance was computed. Similar to (Aydemir et al., 2019), the common top 10 features in the two experimental settings were analyzed. Among them, there are 5 features

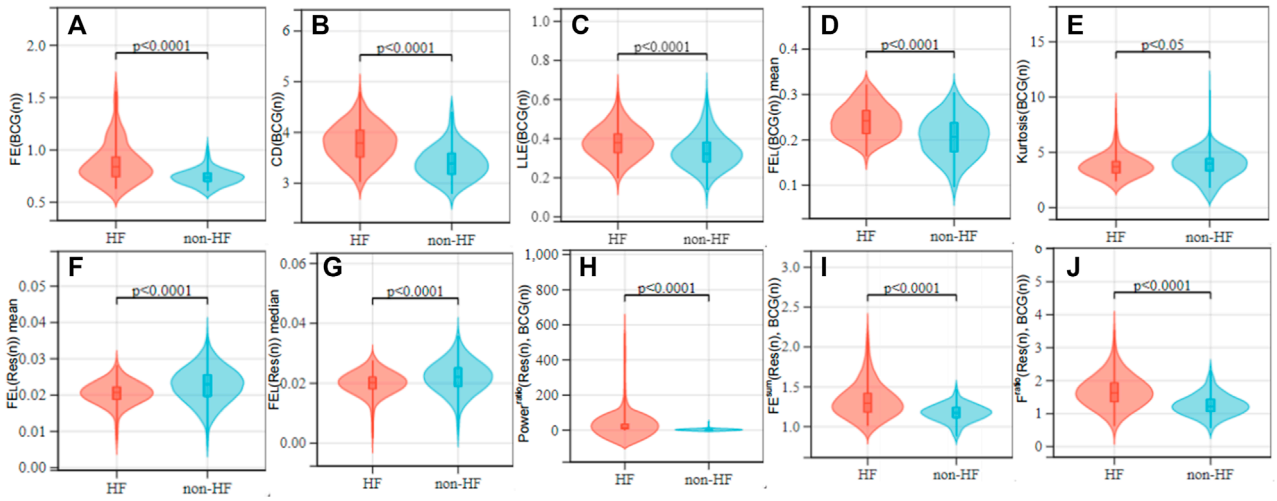

FIGURE 7
Value distribution of each feature over the HF and non-HF classes. **(A–E)** are BCG features; **(F, G)** are respiratory signal features; **(H–J)** are cardiopulmonary features. Non-parametric tests were used between groups.

about respiratory effort (there were 2 respiratory signal independent features and 3 cardiopulmonary features). Considering the facts that there are mostly non-linear features, implying that assessing the complexity, fluctuation of BCG and respiratory effort is key to assist in the detection of HF. More importantly, $Power^{ratio}\ (Res(n), BCG(n))$ features appear to be significantly more informative than the others, reflecting that a comprehensive assessment of individual relative power between respiratory effort and BCG signals is an important reference for the detection of HF.

4 Discussion

This study proposed a non-contact piezoelectric sensing-based HF detection scheme, which can provide the robust performance for HF (LVEF ≤ 49%) detection without the quality assessment of BCG signals. Considering that the HF is the end-stage of all cardiovascular diseases, many HF patients usually have mitral and tricuspid regurgitation and suffer from low vascular compliance (Cruickshank, 2007). These kinds of heart diseases may cause the irregularity in the beat-to-beat BCG morphology, and bring challenge in the HF detection (Aydemir et al., 2019; Chang et al., 2020). To reduce the above challenge, we proposed a HF detection method, which is available to the BCG signals with different complex morphologies by using many linear and non-linear features. From the viewpoint of the BCG feature extraction, it is considered that HF patients may have the reduced amplitude, the reduced power, the significant morphology diversity and the poor regularity due to the reduced ventricular systolic function and the unstable myocardial motor performance. To better exploit the signal morphology, we also extracted the non-linear BCG features including the FE, the LLE and the CD of the chaos, and the high order statistic kurtosis. As shown in **Figures 7A–E**, both of the four Chaos features ($FE\ (BCG(n))$, $CD\ (BCG(n))$, $LLE\ (BCG(n))$, $FE_L\ (BCG(n))mean$) had the low p-values ($p < 0.0001$) between the HF and the healthy cohorts, and the high order feature $Kurtosis\ (BCG(n))$ showed the p-values as $p < 0.05$. Therefore, by using more non-linear and high order statistic features, our proposed HF detection method is robust to the BCG signals.

On the other hand, HF patients with the lower CO usually result in the reduced gas exchange capacity of the lungs, that the human body compensates by accelerating the respiratory rate and amplitude to the regulate hypoxia. Consequently, the presence or the absence of the breath shortness is considered an important reference in the clinical diagnosis of the HF (McDonagh et al., 2021). However, there is a lack of analysis and usage of the respiratory characteristics in the existing HF detection studies related to the wearable devices. Motivated by that and considering that the HF patients are easy to show the breath shortness and the enhanced respiratory effort in the supine posture, the proposed HF detection algorithm was designed for the acquisition of sign data in the supine (soldier sleeping position) posture (Liu et al., 2015). **Figures 7F, G** shows that due to the HF patients have enhanced respiratory effort, respiratory signal complexity features ($FE_L\ (Res(n)))mean$, $FE_L\ (Res(n)))median$) were lower than the healthy group ($p < 0.0001$). According to the relationship between the heart and the lung systems, the used features are not only associated with the BCG signals, but also related to the respiratory effort signals including many cardiopulmonary features (the relative power $Power^{ratio}\ (Res(n), BCG(n))$, the relative amplitude $F^{ratio}\ (Res(n), BCG(n))$ and the overall complexity $FE^{sum}\ (Res(n), BCG(n))$). The detailed results are shown in **Figures 7H–J**, where the HF and the healthy cohorts had significant difference in statistic with the low p-values ($p < 0.0001$). They also demonstrated that the respiratory-related (respiratory and cardiopulmonary) features provide the key contribution and should be analyzed in the HF detection.

Compared with the existing studies of wearable sensor-aided HF detection, the proposed scheme has the advantage of automatic HF classification in a non-contact manner, and also performs feasible to the detection of HF patients with potential irregular heart rhythm (whose recorded BCG are unable to identify). It is thus expected that the proposed scheme has the potential for people with limited mobility carrying out in-home HF detection.

5 Conclusion

In this paper, a machine learning-based scheme was proposed for the HF detection by using the BCG, the respiratory and the cardiopulmonary features. Comparing with existing studies focusing on the BCG signals, our proposed scheme fully exploit the relationship between the heart and the lung systems. The experiment results verified that these above features can significantly improve the accuracy performance and the robustness of the HF detection. In the further step of our study, quantitative analysis for possible classification between HF patients with LVEF ≤ 40% and LVEF > 40% will be considered.

Data availability statement

The raw data supporting the conclusions of this article will be made available by the authors, without undue reservation.

Ethics statement

The studies involving human participants were reviewed and approved by Ethics Committee of Guangdong Provincial Hospital of Traditional Chinese Medicine. The patients/participants provided their written informed consent to participate in this study.

Author contributions

SF proposed the research idea, designed research, and completed the manuscript under the guidance of HZ. XW and PS provided professional advice on signal processing and medical knowledge respectively. AB and GL completed some signal processing and experimental testing. HC, SC, YL, WH, and ZP provided the hardware assistance and the vital data support for the experiments in this paper.

Funding

This work was supported in part by the Natural Science Foundation of Guangdong Province (Grant No. 2022A1515010104), in part by the Blue Fire Innovation Project of the Ministry of Education (Huizhou) under Grant No. CXZJHZ201803, in part by the Science and Technology Project of Guangzhou under Grant No. 202206010127 and 202102021114, in part by the Scientific Research Cultivation Project for Young Scholars of South China Normal University under Grant No. 21KJ07.

Conflict of interest

Authors WH and ZP are employed by Guangzhou SENVIV Technology Co., Ltd.

The remaining authors declare that the research was conducted in the absence of any commercial or financial relationships that could be construed as a potential conflict of interest.

Publisher's note

All claims expressed in this article are solely those of the authors and do not necessarily represent those of their affiliated organizations, or those of the publisher, the editors and the reviewers. Any product that may be evaluated in this article, or claim that may be made by its manufacturer, is not guaranteed or endorsed by the publisher.

References

Ashouri, H., Orlandic, L., and Inan, O. T. (2016). Unobtrusive estimation of cardiac contractility and stroke volume changes using ballistocardiogram measurements on a high bandwidth force plate. *Sensors* 16, 787. doi:10.3390/s16060787

Aydemir, V. B., Nagesh, S., Shandhi, M. M. H., Fan, J., Klein, L., Etemadi, M., et al. (2019). Classification of decompensated heart failure from clinical and home ballistocardiography. *IEEE Trans. Biomed. Eng.* 67, 1303–1313. doi:10.1109/tbme.2019.2935619

Bruser, C., Diesel, J., Zink, M. D., Winter, S., Schauerte, P., and Leonhardt, S. (2012). Automatic detection of atrial fibrillation in cardiac vibration signals. *IEEE J. Biomed. Health Inf.* 17, 162–171. doi:10.1109/titb.2012.2225067

Carlson, C., Turpin, V. R., Suliman, A., Ade, C., and Thompson, D. E. (2020). Bed-based ballistocardiography: Dataset and ability to track cardiovascular parameters. *Sensors* 21, 156. doi:10.3390/s21010156

Chang, I. S., Mak, S., Armanfard, N., Boger, J., Grace, S. L., Arcelus, A., et al. (2020). Quantification of resting-state ballistocardiogram difference between clinical and non-clinical populations for ambient monitoring of heart failure. *IEEE J. Transl. Eng. Health Med.* 8, 2700811–11. doi:10.1109/jtehm.2020.3029690

Chen, T., and Guestrin, C. (2016). "Xgboost: A scalable tree boosting system," in *Proceedings of the 22nd acm sigkdd international conference on knowledge discovery and data mining*, 785–794. doi:10.1145/2939672.2939785

Chen, W., Wang, Z., Xie, H., and Yu, W. (2007). Characterization of surface EMG signal based on fuzzy entropy. *IEEE Trans. Neural Syst. Rehabilitation Eng.* 15, 266–272. doi:10.1109/tnsre.2007.897025

Cruickshank, J. (2007). Are we misunderstanding beta-blockers. *Int. J. Cardiol.* 120, 10–27. doi:10.1016/j.ijcard.2007.01.069

de Vries, H., Jonkman, A., Shi, Z.-H., Spoelstra-de Man, A., and Heunks, L. (2018). Assessing breathing effort in mechanical ventilation: Physiology and clinical implications. *Ann. Transl. Med.* 6, 387–401. doi:10.21037/atm.2018.05.53

Dickinson, M. G., Allen, L. A., Albert, N. A., Salvo, T. D., Ewald, G. A., Vest, A. R., et al. (2018). Remote monitoring of patients with heart failure: A white paper from the heart failure society of America scientific statements committee. *J. Cardiac Fail.* 24, 682–694. doi:10.1016/j.cardfail.2018.08.011

Ertuğrul, Ö. F., and Tağluk, M. E. (2017). A novel version of k nearest neighbor: Dependent nearest neighbor. *Appl. Soft Comput.* 55, 480–490. doi:10.1016/j.asoc.2017.02.020

Etemadi, M., Hersek, S., Tseng, J. M., Rabbani, N., Heller, J. A., Roy, S., et al. (2014). "Tracking clinical status for heart failure patients using ballistocardiography and electrocardiography signal features," in 2014 36th Annual International Conference of the IEEE Engineering in Medicine and Biology Society, Chicago, IL, USA, 26-30 August 2014, 5188–5191. doi:10.1109/embc.2014.6944794

Giovangrandi, L., Inan, O. T., Banerjee, D., and Kovacs, G. T. (2012). Preliminary results from BCG and ECG measurements in the heart failure clinic. *Annu. Int. Conf. IEEE Eng. Med. Biol. Soc.* 2012, 3780–3783. doi:10.1109/embc.2012.6346790

Gupta, V., Mittal, M., and Mittal, V. (2019). R-peak detection using chaos analysis in standard and real time ecg databases. *Innovation Res. Biomed. Eng.* 40, 341–354. doi:10.1016/j.irbm.2019.10.001

Hamazaki, N., Masuda, T., Kamiya, K., Matsuzawa, R., Nozaki, K., Ichikawa, T., et al. (2019). 298Change in respiratory muscle strength predicts clinical events in patients with chronic heart failure. *Eur. Heart J.* 40, ehz747–0095. doi:10.1093/eurheartj/ehz747.0095

Hao, G., Wang, X., Chen, Z., Zhang, L., Zhang, Y., Wei, B., et al. (2019). Prevalence of heart failure and left ventricular dysfunction in China: The China hypertension survey, 2012–2015. *Eur. J. Heart Fail.* 21, 1329–1337. doi:10.1002/ejhf.1629

Inan, O. T., Etemadi, M., Paloma, A., Giovangrandi, L., and Kovacs, G. (2009). Non-invasive cardiac output trending during exercise recovery on a bathroom-scale-based ballistocardiograph. *Physiol. Meas.* 30, 261–274. doi:10.1088/0967-3334/30/3/003

Jingxian, L., Jialin, H., Liwei, M., Baoxian, Y., Pengbin, C., Zhiqiang, P., et al. (2020). An effective algorithm for beat-to-beat heart rate monitoring from ballistocardiograms. *J. Med. Imaging Health Inf.* 10, 633–640. doi:10.1166/jmihi.2020.2910

Li, M., Wang, R., and Xu, D. (2020). An improved composite multiscale fuzzy entropy for feature extraction of MI-EEG. *Entropy* 22, 1356. doi:10.3390/e22121356

Liu, J., Miao, F., Yin, L., Pang, Z., and Li, Y. (2021). A noncontact ballistocardiography-based IoMT system for cardiopulmonary health monitoring of discharged COVID-19 patients. *IEEE Internet Things J.* 8, 15807–15817. doi:10.1109/jiot.2021.3063549

Liu, X., Cao, J., Tang, S., Wen, J., and Guo, P. (2015). Contactless respiration monitoring via off-the-shelf wifi devices. *IEEE Trans. Mob. Comput.* 15, 2466–2479. doi:10.1109/tmc.2015.2504935

Magrelli, S., Valentini, P., De Rose, C., Morello, R., and Buonsenso, D. (2021). Classification of lung disease in children by using lung ultrasound images and deep convolutional neural network. *Front. Physiology* 12, 693448. doi:10.3389/fphys.2021.693448

Mai, Y., Chen, Z., Yu, B., Li, Y., Pang, Z., and Han, Z. (2022). Non-contact heartbeat detection based on ballistocardiogram using UNet and bidirectional long short-term memory. *IEEE J. Biomed. Health Inf.* 26, 3720–3730. doi:10.1109/jbhi.2022.3162396

McDonagh, T. A., Metra, M., Adamo, M., Gardner, R. S., Baumbach, A., Böhm, M., et al. (2021). 2021 ESC guidelines for the diagnosis and treatment of acute and chronic heart failure: Developed by the task force for the diagnosis and treatment of acute and chronic heart failure of the European society of cardiology (ESC) with the special contribution of the heart failure association (HFA) of the ESC. *Eur. Heart J.* 42, 3599–3726. doi:10.1093/eurheartj/ehab368

Mozziyar, E., T Omer, I., Laurent, G., and Ta Gregory, K. (2011). Rapid assessment of cardiac contractility on a home bathroom scale. *IEEE Trans. Inf. Technol. Biomed.* 15, 864–869. doi:10.1109/titb.2011.2161998

Palaniappan, R., Sundaraj, K., and Sundaraj, S. (2014). A comparative study of the SVM and K-nn machine learning algorithms for the diagnosis of respiratory pathologies using pulmonary acoustic signals. *BMC Bioinforma.* 15, 223. doi:10.1186/1471-2105-15-223

Park, J. J., Park, J.-B., Park, J.-H., and Cho, G.-Y. (2018). Global longitudinal strain to predict mortality in patients with acute heart failure. *J. Am. Coll. Cardiol.* 71, 1947–1957. doi:10.1016/j.jacc.2018.02.064

Pieske, B., Tschöpe, C., De Boer, R. A., Fraser, A. G., Anker, S. D., Donal, E., et al. (2019). How to diagnose heart failure with preserved ejection fraction: The HFA–PEFF diagnostic algorithm: A consensus recommendation from the heart failure association (HFA) of the European society of cardiology (ESC). *Eur. heart J.* 40, 3297–3317. doi:10.1093/eurheartj/ehz641

Procacia, I., and Procaccia, I. (1983). Measuring the strangeness of strange attractors. *Phys. D.* 9, 189–208. doi:10.1016/0167-2789(83)90298-1

Reshef, D. N., Reshef, Y. A., Finucane, H. K., Grossman, S. R., McVean, G., Turnbaugh, P. J., et al. (2011). Detecting novel associations in large data sets. *Science* 334, 1518–1524. doi:10.1126/science.1205438

Rosenstein, M. T., Collins, J. J., and De Luca, C. J. (1993). A practical method for calculating largest Lyapunov exponents from small data sets. *Phys. D. Nonlinear Phenom.* 65, 117–134. doi:10.1016/0167-2789(93)90009-p

Savarese, G., Becher, P. M., Lund, L. H., Seferovic, P., Rosano, G., and Coats, A. J. (2022). Global burden of heart failure: A comprehensive and updated review of epidemiology. *Cardiovasc. Res.* 00, 1–16. doi:10.1093/cvr/cvac013

Shi, Y., Yao, X., Xu, J., Hu, X., Tu, L., Lan, F., et al. (2022). A new approach of fatigue classification based on data of tongue and pulse with machine learning. *Front. Physiology* 12, 708742–712146. doi:10.3389/fphys.2021.708742

Siniorakis, E., Arvanitakis, S., Tsitsimpikou, C., Tsarouhas, K., Limberi, S., Panta, S., et al. (2018). Acute heart failure in the emergency department: Respiratory rate as a risk predictor. *Vivo* 32, 921–925. doi:10.21873/invivo.11330

Society of Cardiology, C. (2018). Chinese guidelines for the diagnosis and treatment of heart failure 2018. *Chin. J. Cardiovasc. Dis.* 46, 760–789. doi:10.3760/cma.j.issn.0253-3758.2018.10.004

Starr, I., Rawson, A. J., Schroeder, H. A., and Joseph, N. R. (1939). Studies on the estimation of cardiac output in man, and of abnormalities in cardiac function, from the heart's recoil and the blood's impacts; the ballistocardiogram. *Am. J. Physiology* 127, 1–28. doi:10.1152/ajplegacy.1939.127.1.1

Starr, I., and Schroeder, H. A. (1940). Ballistocardiogram. II. normal standards, abnormalities commonly found in diseases of the heart and circulation, and their significance. *J. Clin. Investigation* 19, 437–450. doi:10.1172/jci101145

Sun, J., Yu, H., Zhong, G., Dong, J., Zhang, S., and Yu, H. (2020). Random shapley forests: Cooperative game-based random forests with consistency. *IEEE Trans. Cybern.* 52, 205–214. doi:10.1109/tcyb.2020.2972956

Wen, X., Yanqi, H., Xiaomei, W., and Biyong, Z. (2019). A feasible feature extraction method for atrial fibrillation detection from BCG. *IEEE J. Biomed. Health Inf.* 24, 1093–1103. doi:10.1109/jbhi.2019.2927165

frontiers | Frontiers in Physiology

TYPE Original Research
PUBLISHED 23 February 2023
DOI 10.3389/fphys.2023.1097879

OPEN ACCESS

EDITED BY
Peng Li,
Harvard Medical School, United States

REVIEWED BY
Avinash Kondiboyina,
Murdoch Childrens Research Institute, Australia
Weiwei Jin,
King's College London, United Kingdom
Valerio Caleffi,
University of Ferrara, Italy
Francesco Piccioli,
University of Ferrara, Italy

*CORRESPONDENCE
Lisheng Xu,
xuls@bmie.neu.edu.cn

SPECIALTY SECTION
This article was submitted to Computational Physiology and Medicine, a section of the journal Frontiers in Physiology

RECEIVED 14 November 2022
ACCEPTED 13 February 2023
PUBLISHED 23 February 2023

CITATION
Sun H, Yao Y, Liu W, Zhou S, Du S, Tan J, Yu Y, Xu L and Avolio A (2023), Wave reflection quantification analysis and personalized flow wave estimation based on the central aortic pressure waveform. *Front. Physiol.* 14:1097879. doi: 10.3389/fphys.2023.1097879

Wave reflection quantification analysis and personalized flow wave estimation based on the central aortic pressure waveform

Hongming Sun[1], Yang Yao[2], Wenyan Liu[1], Shuran Zhou[1], Shuo Du[1], Junyi Tan[1], Yin Yu[1], Lisheng Xu[1,3,4]* and Alberto Avolio[5]

[1]College of Medicine and Biological and Information Engineering, Northeastern University, Shenyang, China, [2]School of Information Science and Technology, ShanghaiTech University, Shanghai, China, [3]Key Laboratory of Medical Image Computing, Ministry of Education, Shenyang, China, [4]Neusoft Research of Intelligent Healthcare Technology, Co. Ltd, Shenyang, China, [5]Macquarie Medical School, Faculty of Medicine, Health and Human Sciences, Macquarie University, Sydney, NSW, Australia

Pulse wave reflections reflect cardiac afterload and perfusion, which yield valid indicators for monitoring cardiovascular status. Accurate quantification of pressure wave reflections requires the measurement of aortic flow wave. However, direct flow measurement involves extra equipment and well-trained operator. In this study, the personalized aortic flow waveform was estimated from the individual central aortic pressure waveform (CAPW) based on pressure-flow relations. The separated forward and backward pressure waves were used to calculate wave reflection indices such as reflection index (RI) and reflection magnitude (RM), as well as the central aortic pulse transit time (PTT). The effectiveness and feasibility of the method were validated by a set of clinical data (13 participants) and the Nektar1D Pulse Wave Database (4,374 subjects). The performance of the proposed personalized flow waveform method was compared with the traditional triangular flow waveform method and the recently proposed lognormal flow waveform method by statistical analyses. Results show that the root mean square error calculated by the personalized flow waveform approach is smaller than that of the typical triangular and lognormal flow methods, and the correlation coefficient with the measured flow waveform is higher. The estimated personalized flow waveform based on the characteristics of the CAPW can estimate wave reflection indices more accurately than the other two methods. The proposed personalized flow waveform method can be potentially used as a convenient alternative for the measurement of aortic flow waveform.

KEYWORDS

wave reflection, wave separation analysis, personalized flow waveform, triangular flow waveform, arterial stiffness

Abbreviations: CAPW, Central aortic pressure waveform; CVD, Cardiovascular disease; DBP, Diastolic blood pressure; ET, Ejection time; FDA, Food and Drug Administration; MAP, Mean arterial pressure; P_b, Backward pressure wave; P_f, Forward pressure wave; PTT, Pulse transit time; Q_b, Back flow wave; Q_f, Forward flow wave; RI, Reflection index; RM, Reflection magnitude; RMSE, Root mean square error; SBP, Systolic blood pressure; T_{fb}, The time difference between P_f and P_b; Z_c, Characteristic impedance; Z_{in}, Input impedance.

1 Introduction

The central aortic pressure waveform (CAPW) contains information on the cardiovascular system and thus can be used to evaluate the cardiovascular system status and to predict and diagnose cardiovascular diseases (CVDs) (Suleman et al., 2017; Vallée et al., 2018; Sequi-Dominguez et al., 2020; Flores Geronimo et al., 2021). Central aortic pressure, unlike peripheral arterial pressure, is the blood pressure at the root of the ascending aorta, which is directly connected with the left ventricle (Pini et al., 2008). Hence, CAPW can more directly reflect the load on the left ventricle, coronary arteries, and cerebral vessels and more accurately predict the occurrence of cardiovascular events and damage of target organs in comparison with the peripheral arterial pressure waveform (Roman et al., 2007; McEniery et al., 2008; Zócalo and Bia, 2022). The separation analysis of CAPW can be used to predict cardiovascular events such as all-cause mortality and left ventricular failure (Manisty et al., 2010), which is more clinically significant.

When the heart pumps blood, the aortic valve opens, and the pressure in the aorta rises rapidly, resulting in pressure and flow waves called forward waves. Forward waves will undergo wave reflections at sites of impedance mismatch (vessel diameter reduction, vessel bifurcation or change in wall stiffness) during the propagation from the aorta to the distal segments, generating backward waves, and propagating back to the proximal segment (Westerhof et al., 1972; Yao et al., 2022). When the left ventricle contracts, blood flows through the aortic valve into the aorta. After the aortic valve closes, the ventricle enters diastole, when blood perfuses the heart through the coronary arteries. A small amount of diastolic blood occasionally flows backwards into the left ventricle (Thubrikar et al., 1979). The pressure and flow waveforms are formed by the superposition of backward and forward components. Pulse wave propagation and reflection are related to arteriosclerosis and also affect the hemodynamic characteristics of the cardiovascular system (Sofogianni and Tziomalos, 2019). In pulse wave analysis, pulse wave reflection indices can be derived from the decomposition of CAPW to quantify the degree of pulse wave reflections (Townsend et al., 2015). Based on the pressure-flow relations, the CAPW can be decomposed into backward (P_b) and forward (P_f) waves (Westerhof et al., 1972). The amplitude characteristics and time delay of P_f and P_b can effectively reflect the reflection and propagation time of the pulse wave from the aorta to the distal segments and branches, and the magnitude of the CAPW reflections affects cardiac afterload and perfusion (Davis et al., 2009; Laurent and Boutouyrie, 2020). More accurate wave reflection measurements can be obtained from P_f and P_b, mainly including the aortic pulse transit time (PTT), reflection index (RI), and reflection magnitude (RM). PTT can be calculated from the time delay between P_f and P_b, a valuable indicator for assessing arterial stiffness (Qasem and Avolio, 2008). RM, the ratio of P_b and P_f amplitudes, is an independent predictor of risk and can predict heart failure (Westerhof et al., 2006; Zamani et al., 2014). RI and RM contain physiological information about CAPW and are important indices that quantify pulse wave reflection. These metrics are not affected by timing of wave reflection and usually be used to access left ventricle afterload, which has clear physiological significance (Wang et al., 2010; Zamani et al., 2016).

Flow waveforms are essential for the decomposition and analysis of pulse waves. Clinically, the aortic flow velocity can usually be obtained directly and non-invasively by ultrasonic detection or magnetic resonance imaging (MRI). Combined with the cross-sectional area of blood vessels, the blood flow waveform can finally be calculated (Rivera et al., 2020; Stortz et al., 2020). Although this method is feasible and accurate, the operation is considered inconvenient because it requires specific types of equipment and skilled operators. Consequently, some proposed approaches use the CAPW morphology to generate an aortic flow waveform with an assumed triangular shape (Westerhof et al., 2006; Butlin and Qasem, 2016). In these methods, the wave separation analysis matches the start, peak, and end points of the triangular flow waveform with the foot, inflection, and dicrotic notch points of the CAPW using the time and amplitude characteristics of the CAPW. The triangular flow wave was first proposed in a proof-of-principle study to quantify aortic wave reflections from pressure alone by Westerhof et al. (Westerhof et al., 2006). This straightforward technique was utilized by the SphygmoCor MM3/CvMS system (AtCor Medical, Sydney, Australia) for the non-invasive acquisition of aortic flow (Ding et al., 2013; Carlsen et al., 2016; Yu et al., 2018). Later, they made improvements in the waveform decomposition of the CAPW by utilizing the triangular flow waveform as a novel way for determining the aortic pulse wave velocity (Qasem and Avolio, 2008). Although triangular flow waveform has been applied in several commercially available systems, this method poorly approximates the measured flow waveform, resulting in some errors in the decomposition of the CAPW.

Kip et al. demonstrated that in the participants of the Asklepios population study, the results for RM and aortic PTT based on the triangular flow waveform approximation method differed significantly from the values obtained from measured pressure and flow information (Verbeke et al., 2005; Rietzschel et al., 2007; Kips et al., 2009). In the Asklepios population study (Rietzschel et al., 2007), the measured flow waveforms were averaged and normalized to obtain more physiological aortic flow waveforms. The experimental results have demonstrated that the average flow method can evaluate RM better than triangular flow. However, there is still a significant deviation between the approximate and the actual values. This physiological flow method has been used to assess wave reflection indices in the multi-ethnic study of atherosclerosis (Zamani et al., 2015; Zamani et al., 2016). In this research, the pressure measured non-invasively by applanation tonometry at the common carotid artery was used as a substitute for central aortic pressure. Consequently, the difference persists and influences the experimental results.

Recently, Shenouda et al. proposed a new personalized physiological flow waveform method based on the CAPW morphology (Shenouda et al., 2021). The physiological flow waveform is more accurate than the triangle flow waveform for determining RM and Pb in the elderly. However, they did not examine children, healthy middle-aged individuals, or clinical populations such as cardiac disease patients. The sample set included only 49 young (18–42 years) and 29 older (51–77 years) adults. More recently, a novel lognormal flow wave method for separating the CAPW was proposed by Hao et al. (Hao et al., 2022).

TABLE 1 The hemodynamic characteristics of the Nektar1D-PWDB and clinical data for all subjects. Shown as mean ± standard deviation (Mean ± SD).

Variables	Nektar1D-PWDB	Clinical data
No. Of subjects	4,374	13
Age (years)	25–75	24–33
Aortic SBP (mmHg)	109.04 ± 11.58	103.52 ± 5.86
Aortic DBP (mmHg)	75.62 ± 6.74	80.24 ± 5.72
Aortic MAP (mmHg)	86.76 ± 5.98	86.66 ± 5.93

This study demonstrated that the lognormal flow wave improves CAPW separation analysis results both in time and frequency domains. Nevertheless, the lognormal flow waveform method must be compared in different populations and not limited to healthy and young participants. For the data set validated in this paper, there is still a gap between the estimated and the measured flow waveforms. In addition, the definition of variance σ of the lognormal function needs to be clarified, and how to determine the specific value is not well described. When accurate flow is inconvenient to measure, better non-invasive estimation of aortic flow is still needed to improve the results of pulse wave separation of the CAPW.

This research aims to propose a novel method to approximate the actual flow waveform with a personalized flow waveform and to examine the feasibility to decompose the CAPW and quantify wave reflection. We use the relationship between pressure and flow to separate and analyze the CAPW with triangular, lognormal, and personalized flow waveform methods, respectively, to explore the accuracy of the three methods in wave reflections. Based on the simulated pulse wave dataset and clinical data, the accuracy of the personalized flow wave method is further compared with the other two methods in deducing the reflection indices of RI, RM, and PTT.

2 Materials and methods

2.1 Data collection

In this study, we used two datasets to verify the feasibility and validity of the proposed method.

2.1.1 Nektar1D PWDB

The first dataset is the publicly accessible database (Nektar1D Pulse Wave Database, Nektar1D-PWDB), published by Alastruey et al. at King's College London, United Kingdom, based on the Nektar1D model. This model used the Nektar1D non-linear one-dimensional flow model, which has been fully clinically validated and used in several studies to simulate the hemodynamic characteristics of the human arterial tree, to ensure the validity of hemodynamic parameters of the 1D model and the generated data (Matthys et al., 2007; Alastruey et al., 2011; Xiao et al., 2014; Willemet et al., 2015). For more detailed information on this database, see the study by Charlton et al. (Charlton et al., 2019).

The database contains the arterial pulse waves from 4,374 virtual subjects, ranging from 25 to 75 years, at a sampling frequency of 500 Hz. A total of 537 out of the 4,374 subjects exhibited blood pressures outside of healthy norms (virtual subjects with abnormal blood pressure; without CVD), and 3,837 subjects are physiologically plausible. Table 1 contains basic population and hemodynamic statistics. SBP and DBP of the radial artery and central aortic are 95 mmHg–168 mmHg and 48 mmHg–87 mmHg, as shown in Figure 1.

2.1.2 Clinical data

In this section, we used clinical data to further validate the performance of personalized flow waves. There were 13 healthy participants in the study, seven male and six female, aged from 24 to 33 years old. The basic information of participants is summarized in Table 1. The Research Ethics Committee approved this study of Northeastern University (NO. NEU-EC-2021B022S), China, and all participants gave informed consent.

Each participant sat quietly and relaxed for 10 min in a quiet room before measuring their brachial systolic (SBP) and diastolic (DBP) blood pressures with the Yuwell Mercury sphygmomanometer (measurement accuracy of 2 mmHg). The pressure waveforms of the radial artery were measured non-invasively with the SphygmoCor device at a sampling rate of 128 Hz. In the SphygmoCor device, the corresponding CAPW was reconstructed using a generalized radial-to-aortic transfer function. The generalized transfer function (GTF) is the most widely used method to estimate the CAPW (Sharman et al., 2006), which is obtained by simultaneous measurement of aortic and peripheral pressure (Karamanoglu et al., 1993) to obtain the corresponding function between peripheral arterial pressure and central arterial pressure, then collecting new test samples, and validating the peripheral arterial pressure waveform signal by the trained transfer function to estimate the corresponding CAPW(Cameron et al., 1998; Payne et al., 2007). The corresponding CAPW is estimated by verifying the signal of the peripheral arterial pressure waveform with the trained transfer function. The flow velocity and diameter waveforms of the aortic root were concurrently captured and smoothed by a GE Vivid E95 US system. Flow waveforms were calculated by multiplying flow velocity waveforms with the aorta's cross-sectional area ($\pi \times (\text{diameter}/2)^2$). In the study of Zhou et al., the specifics of data collection are presented (Zhou et al., 2022).

2.2 Wave separation analysis and wave reflection

In the time domain, features can be calculated from the timing and amplitude of several fiducial points. The starting point of the pulse wave indicates the beginning of a pulse cycle and the end of the previous one. The time of the inflection point marks the arrival of the P_b (O'Rourke and Yaginuma, 1984). The notch is caused by aortic valve closure and blood reflux, representing the transition between the systolic and diastolic phases (Hartmann et al., 2019). The pulse wave systolic period is the duration between the starting point and the dicrotic notch point of the pulse wave, followed by the pulse wave diastolic period. Usually, the local maxima of the second derivative of the pulse waveforms are utilized to extract

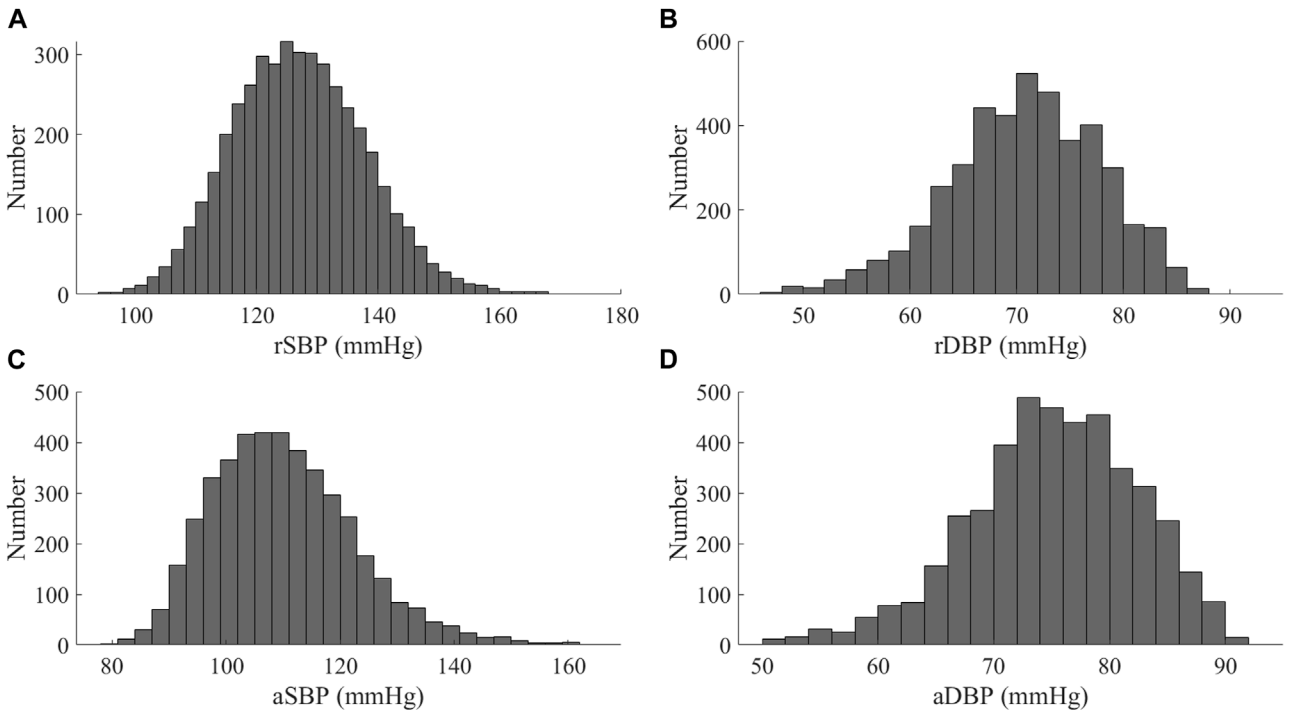

FIGURE 1
Distribution of blood pressure values for the Nektar1D-PWDB **(A)** SBP of at the radial artery (rSBP); **(B)** DBP of at the radial artery (rDBP); **(C)** SBP of at the aortic root (aSBP); **(D)** DBP of at the aortic root (aDBP).

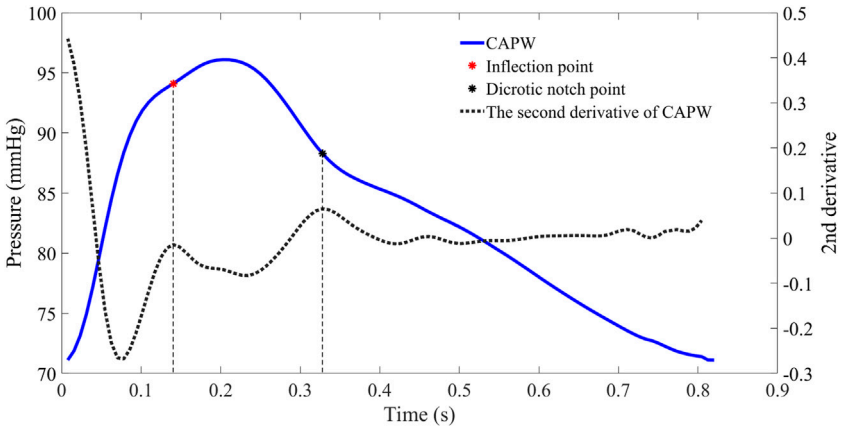

FIGURE 2
The CAPW feature points extraction. The red point represents the inflection point of the pulse wave (the moment when the P_b is generated), while the black point represents the dicrotic notch point (the end of the systolic phase or the beginning of the diastolic phase).

inflection points and dicrotic notch points (as in Figure 2 (Vlachopoulos et al., 2011)).

For some participants (e.g., those with severe atherosclerosis), the inflection point of the aortic pulse wave is difficult or even impossible to extract. In order to make this pulse wave decomposition method more practical, it has been proposed to use 30% of the systolic time as the location of the inflection point (Miyashita et al., 1994; Westerhof et al., 2006). In this paper, for pulse wave with inconspicuous inflection point, 30% of ejection time (ET) is used as the location of the inflection point to calculate the relevant features of pulse wave decomposition. The beginning of the pulse wave systole indicates the time of aortic valve opening and the start of ejection, and the notch time of the pulse wave is the time of aortic valve closure and the end of ejection. ET

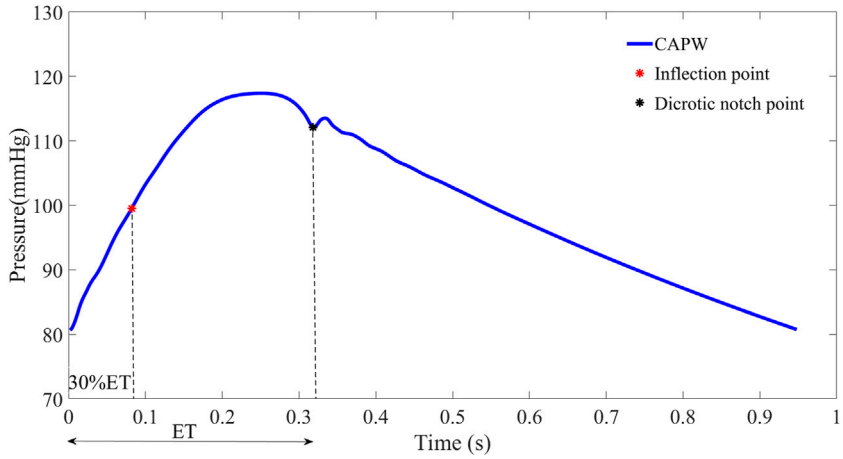

FIGURE 3
To facilitate wave separation analysis, the 30% ET is used as the location of the inflection point of the pulse wave.

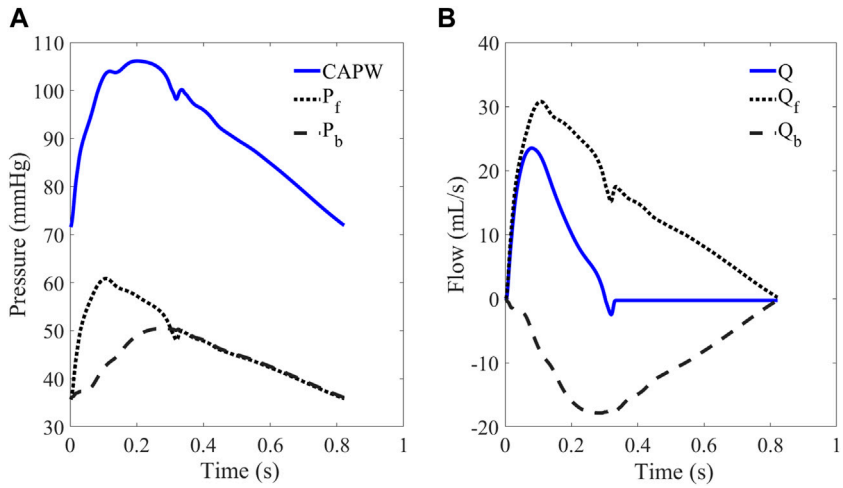

FIGURE 4
(A) CAPW and **(B)** flow waveform. The CAPW is decomposed into P_f and P_b, from which RM and RI can be calculated.

represents the systolic time of the pulse wave, which is determined by subtracting the beginning time from the end time of aortic flow (as in Figure 3).

In the arterial system, both aortic pressure and flow waveforms consist of forward waves (P_f, Q_f) and backward waves (P_b, Q_b). The CAPW mainly comprises forward and lower limb reflection waves (Westerhof et al., 1972). As shown in Figure 4, CAPW equals the sum of the P_f and P_b; and the flow wave equals the difference between the Q_f and Q_b, (as shown in Eq. 1, 2).

$$P = P_f + P_b \tag{1}$$

$$Q = Q_f + Q_b \tag{2}$$

The basic principle of pulse wave decomposition is as follows (Westerhof et al., 1972):

$$P_f = \frac{P + Z_c \times Q}{2} \tag{3}$$

$$P_b = \frac{P - Z_c \times Q}{2} \tag{4}$$

where, Q = U*A represents aortic flow; U is the flow velocity; A is blood vessels cross-sectional area; Z_c is the characteristic impedance.

Since the pulse waveform is not affected by the P_b in the early systolic phase, Z_c equals the ratio of blood pressure to flow (Li, 1986; Khir et al., 2001), and Z_c can also be calculated by high-frequency input impedance (Murgo et al., 1981; Miyashita et al., 1994). The input impedance (Z_{in}) is defined as follows:

$$Z_{in}(w) = P(w)/Q(w) \tag{5}$$

where P(w) and Q(w) are pressure and flow frequency components.

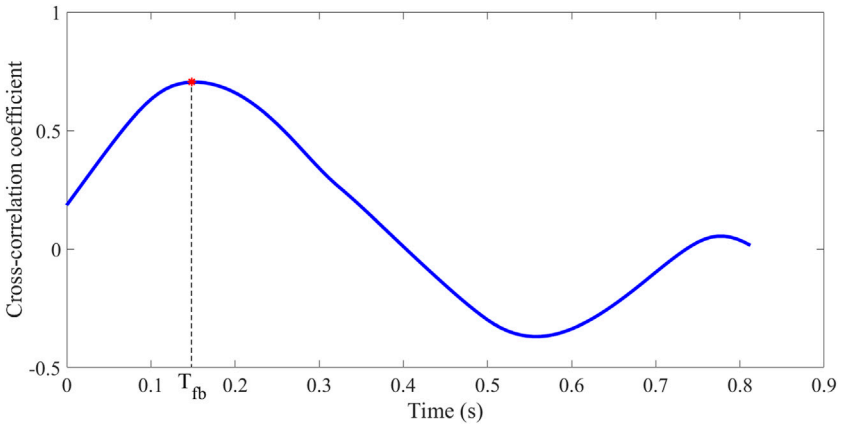

FIGURE 5
Calculation of T_{fb}: cross-correlation between P_f and P_b.

RI is the amplitude ratio of P_b to the sum of P_b and P_f, and the amplitude ratio of P_b to P_f is RM (Hametner et al., 2013). RM and RI are defined as follows:

$$RM = \frac{|P_b|}{|P_f|} \tag{6}$$

$$RI = \frac{|P_b|}{|P_b| + |P_f|} \tag{7}$$

PTT can be determined by pulse wave decomposition, an important index to assess arterial stiffness in the young and old (Qasem and Avolio, 2008). PTT can be calculated as half the time difference between P_f and P_b (T_{fb}), as in Eq. 8.

$$PTT = T_{fb}/2 \tag{8}$$

Qasem and Avolio calculated the cross-correlation coefficient of P_f and P_b to determine T_{fb} (Qasem and Avolio, 2008). The time of maximum cross-correlation coefficient is the T_{fb} between P_f and P_b (as in Figure 5).

2.2.1 Triangular and lognormal flow waveform

By measuring aortic flow velocities with Doppler ultrasound or magnetic resonance imaging (MRI) and combining them with the cross-sectional area of the aortic valves, the aortic flow can be calculated (Wang et al., 2010; Zamani et al., 2016). However, this requires specific medical equipment and skilled operators.

The triangular flow method is used in the SphygmoCor MM3/CVMS device, which is well clinically validated and certified by the Food and Drug Administration (FDA) and is frequently used as a non-invasive testing standard to validate other devices (Zuo et al., 2010; Ott et al., 2012; Laugesen et al., 2014). SphygmoCor MM3/CVMS system uses triangles to approximate the central aortic flow waveforms (Rivera et al., 2020). Specifically, as shown in Figure 6A, the systolic flow is approximated as a triangle, and the base of the triangle represents the total systolic ET. The peak of the triangle corresponds to the inflection point (timing and amplitude) of the CAPW. Furthermore, the beginning and ending points of the triangular flow waveform coincide with the CAPW foot and dicrotic notch points, respectively. Westerhof et al. have shown that it is feasible to construct the aortic flow waveform by a triangular wave (Westerhof et al., 2006).

As with the triangular flow waveform, there is a specific relationship between the characteristic points of the lognormal flow waveform and the characteristic points of CAPW. As shown in Figure 6B, the start, peak, and end points of the lognormal flow waveform correspond to the foot, the inflection point, and the dicrotic notch point of the CAPW, respectively (Plamondon et al., 2013; Hao et al., 2022).

2.2.2 Personalized flow waveform construction

The waveform of aortic flow can be estimated using a triangular wave. However, the P_f and P_b obtained directly using the triangular wave instead of the flow wave are not smooth and sometimes produce large P_b before the reflection point. The triangular flow waveform would also underestimate the degree of concavity of the flow waveforms. The lognormal approximate flow waveform has the same result, especially in early systole (as in Figure 8). Based on the above facts, we attempted to construct a flow waveform based on the characteristics of CAPW and explore the method's generalizability.

In early systole (before the inflection point), the CAPW is linear with flow waveform because wave reflections are almost unaffected by the P_b (Hughes et al., 2020). The P_f propagates from the proximal to the distal end, and at the end of the contraction, the pressure-flow waves encounter a high impedance location for continuous decay. At the end of systole, it is proposed to use the Hermite interpolation function to fit the flow waveforms during this period.

The Hermite interpolation function is a standard method for solving predictive problems in mathematical modeling, which can effectively solve the problem such as insufficient waveform data of aortic flow (Lorentz, 2000). Three points are required to satisfy the Hermitian interpolation function condition. Using segmented Hermite interpolation to obtain a smooth and continuous curve on the interval $[a, b]$. On node $a \le x_0 < x_1 < \cdots < x_n \le b, h_i = x_i - x_{i-1}\,(i = 1, 2, \cdots, n)$, the function value and derivative value of the given node are as follows:

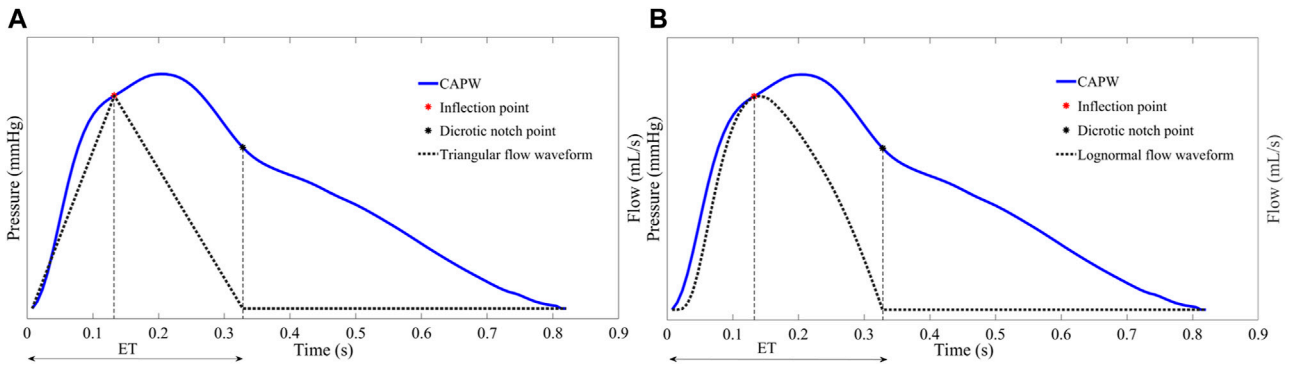

FIGURE 6
(A) The start, peak, and end of the triangle flow waveform correspond in time and amplitude to the foot, inflection point, and dicrotic notch point of the CAPW, respectively **(B)** Lognormal function approximation flow waveform.

$$y_i = f(x_i), y_i' = f'(x_i), i = 0, 1, \cdots, n \tag{9}$$

A piecewise cubic interpolation polynomial $H_3(x)$ is constructed on $[a, b]$, which satisfies the following interpolation conditions:

$$H_3(x_i) = y_i, H_3'(x_i) = y_i', i = 0, 1, \cdots, n \tag{10}$$

$H_3(x)$ on the interval $[x_{i-1}, x_i]$ is the cubic Hermite interpolation polynomial of $f(x)$ with x_{i-1}, x_i as nodes.

$$\begin{aligned} H_3(x) = \frac{1}{h_i^2}\Bigg[&\left(1 + 2\frac{x - x_{i-1}}{h_i}\right)(x - x_i)^2 y_{i-1} + \left(1 - 2\frac{x - x_i}{h_i}\right) \\ &(x - x_{i-1})^2 y_i \\ &+ (x - x_{i-1})(x - x_i)^2 y_{i-1}' + (x - x_{i-1})^2 (x - x_i) y_i'\Bigg] \end{aligned} \tag{11}$$

where $x \in [x_{i-1}, x_i]$ $(i = 1, 2, \cdots, n)$.

The process of constructing the personalized flow waveform based on CAPW features is divided into three steps.

1) The first part is the same as the CAPW before the inflection point.
2) We used the piecewise cubic Hermitian interpolation function at the end-systole to obtain the second part of the estimated flow waveform. Two points, a and b (see Figure 7), can be readily obtained, but a third point is still needed to perform the Hermite function operation. The third point was identified as c, because the magnitude of MAP and the time of SBP in CAPW are between a and b (Li et al., 2021; Parittotokkaporn et al., 2021), respectively. We combine the magnitudes of MAP and SBP and the time of SBP to obtain c for participating in the Hermitian interpolation calculation. The average value of arterial blood pressure during a cardiac cycle is called mean arterial pressure (MAP). MAP can be calculated by Eq. 12 (Papaioannou et al., 2016).

$$MAP = \frac{\int_T CAPW(t)\, dt}{T} \tag{12}$$

Where T represents a cardiac cycle. SBP and DBP are systolic and diastolic blood pressure, respectively. In the arterial system, the maximum peak and foot amplitudes of CAPW are SBP and DBP (as in Figure 7 (Avolio et al., 2009)), respectively.

3) The rest of the flow waveform is set to 0.

The waveforms of personalized flow, measured flow, triangular flow, and lognormal flow approximation are shown in Figure 8. The comparison of different flow waveforms reveals a prominent peak in the triangular estimated flow waveform, which has a considerable discrepancy with the measured flow waveform. In contrast, the estimated personalized flow waveform is closer in shape to the measured flow waveform. Additionally, there are also some variations between the lognormal flow waveform and the measured flow waveform, particularly in the initial part.

To further verify the viability of the proposed personalized flow wave, the three wave reflection indices RM, RI, and PTT of wave separation analysis are quantitatively compared based on triangular flow waveform, lognormal flow wave approximation, and personalized flow waveform, respectively (Table 2). We investigated the correlation and consistency of calculated RM, RI, and PTT on the Nektar1D PWDB dataset and clinical data using linear regression analysis (r-values) and Bland-Altman analysis (see Figures 10–15), respectively.

2.3 Evaluation and statistical analysis

In the experiment, we employed the root mean square error (RMSE) to quantitatively evaluate the deviation between measured and estimated flow waveform signals. Differences between wave reflection indices of the estimated and measured aortic flow waveforms were analyzed by two-tailed paired t tests (IBM SPSS Statistics, version-26) and reported as mean ± standard deviation (Mean ± SD) or 95% CI where appropriate. Linear regression and Pearson correlation coefficients were used to analyze the correlations between estimated and measured and aortic flow waveforms. Bland-Altman plots were constructed to assess the agreement between estimated and measured aortic flow

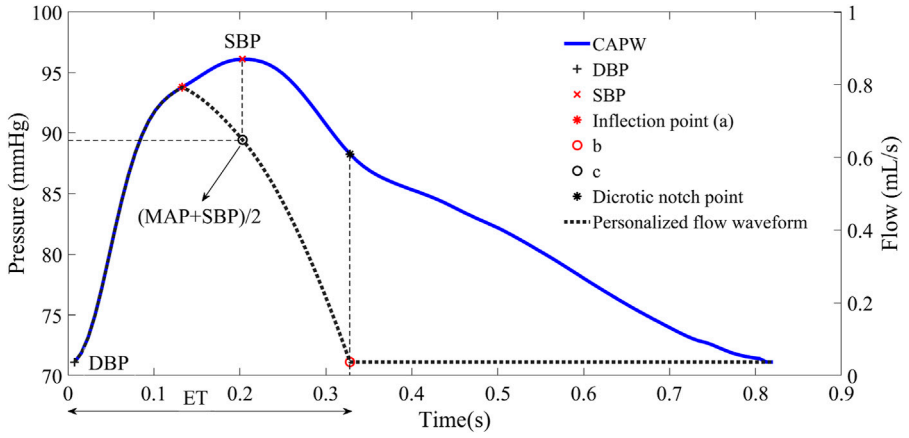

FIGURE 7
Personalized flow waveform constructed based on the feature points of CAPW.

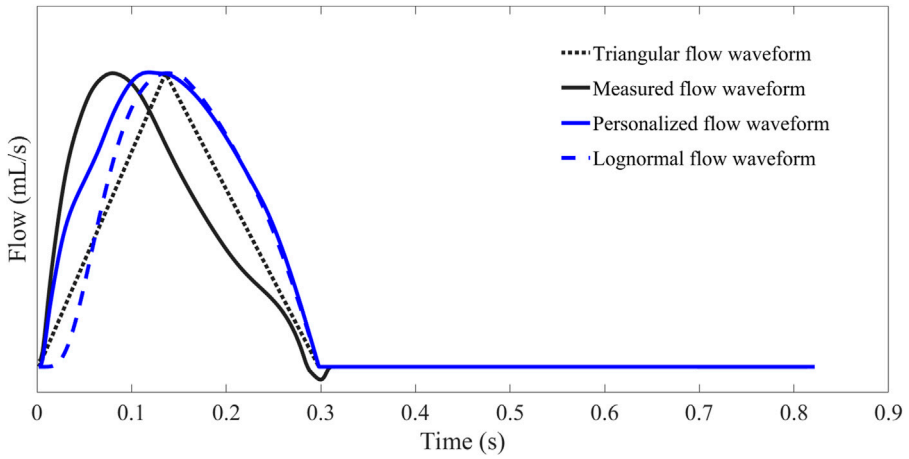

FIGURE 8
Comparison and contrast of flow waveforms obtained by Hermite interpolation function estimation, measurement, triangular estimation, and lognormal approximation.

waveforms. A *p*-value of 0.01 or less is regarded as statistically significant.

3 Results

3.1 Waveform analysis of P_f and P_b

In order to analyze the performance of the flow waveform estimation using the personalized flow method, the results are compared with the typical triangular flow method and lognormal flow wave approximation. Figure 9 shows an example of the P_f and P_b decomposed by four flow waves for CAPW, respectively. The results of CAPW separation show that both P_f and P_b have different degrees of triangular wave traces when separated by the triangular flow waveform. As shown in Figure 9C, the P_b decomposed by the triangular flow waveform appears as a sharp peak at its foot, like the triangular flow wave's triangular apex. However, this does not occur using personalized and lognormal flow waves, as shown in Figure 9B,D. Neither P_f nor P_b calculated by the measured flow wave in a practical situation exhibit traces of a triangle (Figure 9A). And there are no triangular features at the feet of P_f and P_b. Therefore, the decomposition of CAPW using a personalized flow wave is better than the triangular flow wave analysis. The personalized flow wave performs well in estimating the morphology of P_f and P_b, which is closer to the reference flow wave (Figure 9B).

3.2 Performance evaluation of wave reflection indices

The corresponding correlation graphs and Bland-Altman plots for comparing measured and estimated flow CAPW reflection indices using three flow wave methods as shown in Figures 10–15.

TABLE 2 Wave reflection indices (Mean ± SD) and biases statistics (RMSE: Root Mean Square Error).

Database	Variable	Wave reflection indices and biases (RMSE)			
		Measured flow	Personalized flow and | Measured-Personalized|	Lognormal flow and | Measured-Lognormal|	Triangular flow and | Measured-Triangular|
Nektar1D PWDB (n = 4,374)	Q (mL/s)	2.83 ± 5.62	**3.04 ± 4.98**	3.12 ± 5.20	4.22 ± 6.28
		—	**0.89**	0.92	2.33
	P_f amplitude (mmHg)	21.95 ± 8.49	**22.58 ± 7.99**	22.85 ± 9.47	20.8 ± 9.41
		—	**1.39**	2.01	2.38
	P_b amplitude (mmHg)	15.8 ± 6.81	**15.02 ± 5.94**	14.99 ± 5.98	16.06 ± 7.07
		—	**0.39**	1.19	1.24
	RM (%)	71.49 ± 9.55	**73.84 ± 4.14**	66.15 ± 3.66	63.88 ± 9.73
		—	**5.88**	9.06	10.17
	RI (%)	41.5 ± 3.4	**42.27 ± 1.57**	39.78 ± 1.34	38.94 ± 3.33
		—	**1.95**	3.09	3.47
	PTT (ms)	34.9 ± 13.1	**37.9 ± 14.3**	28.1 ± 15.9	23.7 ± 21.4
		—	**1.21**	1.23	1.52
Clinical data (n = 13)	Q (mL/s)	5.52 ± 8.07	**5.41 ± 8.12**	5.10 ± 8.00	4.43 ± 6.92
		—	**2.15**	3.20	2.84
	P_f amplitude (mmHg)	20.36 ± 5.16	**21.39 ± 5.7**	23.91 ± 7.41	35.14 ± 14.9
		—	**3.29**	4.16	7.35
	P_b amplitude (mmHg)	9.93 ± 2.9	**10.19 ± 2.8**	10.89 ± 2.9	11.79 ± 3.4
		—	**1.37**	1.59	2.15
	RM (%)	88.41 ± 2.62	**87.69 ± 2.76**	87.61 ± 3.6	83.34 ± 6.66
		—	**1.62**	2.25	3.76
	RI (%)	48.04 ± 1.16	**48.03 ± 1.55**	48.07 ± 1.47	46.46 ± 1.94
		—	**0.70**	0.93	2.26
	PTT (ms)	75.4 ± 15.9	**79.5 ± 15**	80.8 ± 18.7	80.4 ± 15.8
		—	**0.97**	1.13	1.86

The bold values in Table 2 are the wave reflection indices results of the personalized flow wave, which have the smallest biases with the measured flow wave.

The equation of the linear regression obtained between the measured and estimated RM using the personalized flow method based on Nektar1D PWDB is **y = 0.99x + 0.06** (**r = 0.97**, **p < 0.001**) as shown in Figure 10A; The corresponding equations obtained using the triangular flow approach and lognormal flow approximation (see Figure 10B,C) are y = 0.34x + 0.39 (r = 0.79, $p < 0.001$) and y = 0.28x +0.46 (r = 0.73, $p < 0.001$), respectively. A comparison (mean ± SD, **0.05 ± 0.03**) between the measured and estimated RM using the personalized flow method based on Nektar1D PWDB is shown in Figure 10D. The same comparison using the triangular flow approach and lognormal flow approximation (mean ± SD, −0.08 ± 0.07 and −0.05 ± 0.07) is shown in Figure 10E,F, respectively. The linear regression and Bland-Altman plots of RM calculated by three flow waveforms (Clinical data, 13 participants) are shown in Figure 11. The regression equations (panels A, B and C) are **y = 0.90x+0.08** (**r = 0.85**, **p < 0.001**), for the personalized flow wave method; y = 0.81x+0.11 (r = 0.32, $p = 0.28$) for the triangular flow wave approach; and y = 1.09x-0.08 (r = 0.79, $p = 0.0013$) for the lognormal flow wave approximation algorithm. The corresponding Bland-Altman plots (panels D, E and F) and their mean differences (± SD) for the personalized flow wave, triangular flow wave and lognormal flow wave methods respectively are (**− 0.01 ± 0.15**), (−0.05 ± 0.61) and (−0.01 ± 0.26).

The equation of the linear regression obtained between the measured and estimated RI using the personalized flow method based on Nektar1D PWDB is **y = 0.95x + 0.04** (**r = 0.97**, **p < 0.001**) as shown in Figure 12A; The corresponding equations obtained using the triangular flow method and lognormal flow approximation (see Figure 12B,C) are y = 0.37x + 0.24 (r = 0.80, $p < 0.001$) and y = 0.29x + 0.28 (r = 0.74, $p < 0.001$), respectively. A comparison (mean ± SD, **0.02 ± 0.01**) between the measured and estimated

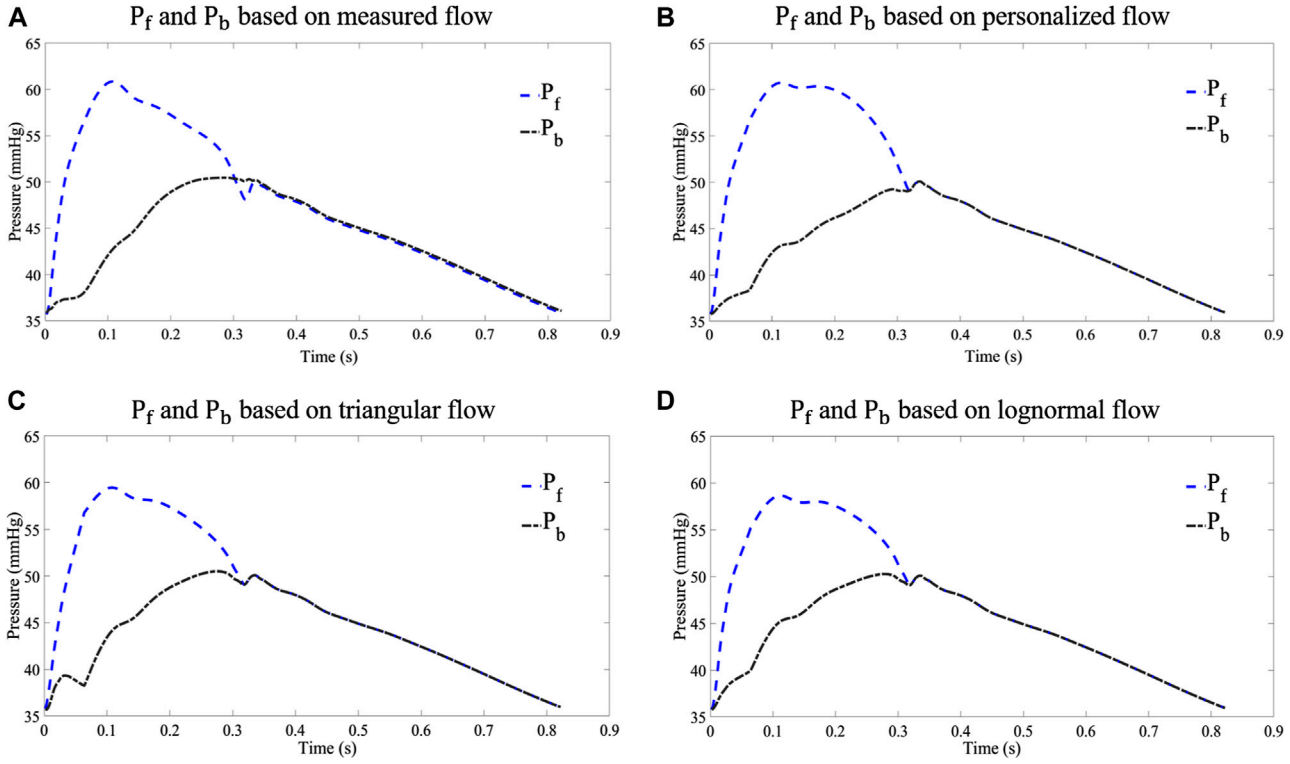

FIGURE 9
Comparison of P_f and P_b decomposed from different flow waves: **(A)** results of waveform separation based on measured flow wave; **(B)** results of waveform separation based on personalized flow wave; **(C)** results of waveform separation based on triangular flow wave; and **(D)** results of waveform separation based on lognormal flow wave approximation.

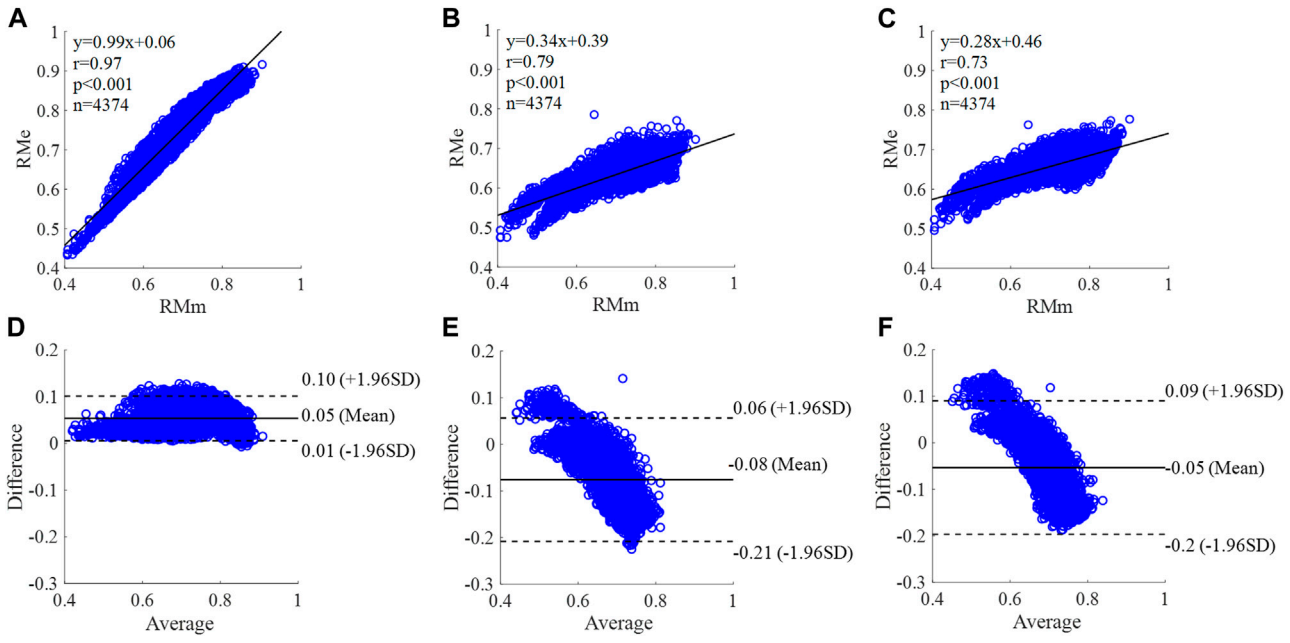

FIGURE 10
Correlation graphs and Bland-Altman plots of RM calculated by three flow waveforms **(A)** and **(D)** Results of the personalized flow wave (Nektar1D PWDB, 4,374 subjects); **(B)** and **(E)** Results of the triangular flow wave (Nektar1D PWDB, 4,374 subjects); **(C)** and **(F)** Results of the lognormal flow wave (Nektar1D PWDB, 4,374 subjects). RMm and RMe are measured and estimated RM, respectively. Difference: RMe - RMm; Average: (RMe + RMm)/2.

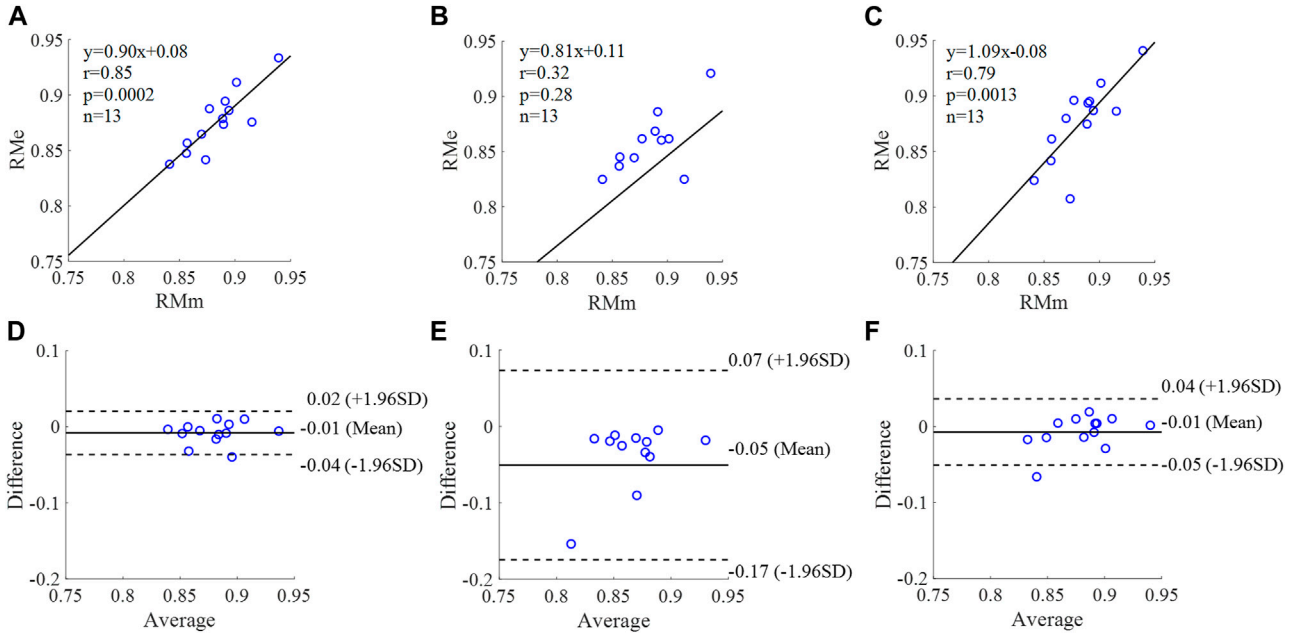

FIGURE 11
Correlation graphs and Bland-Altman plots of RM calculated by three flow waveforms **(A)** and **(D)** Results of the personalized flow wave (Clinical data, 13 participants); **(B)** and **(E)** Results of the triangular flow wave (Clinical data, 13 participants); **(C)** and **(F)** Results of the lognormal flow wave (Clinical data, 13 participants). RMm and RMe are measured and estimated RM, respectively. Difference: RMe - RMm; Average: (RMe + RMm)/2.

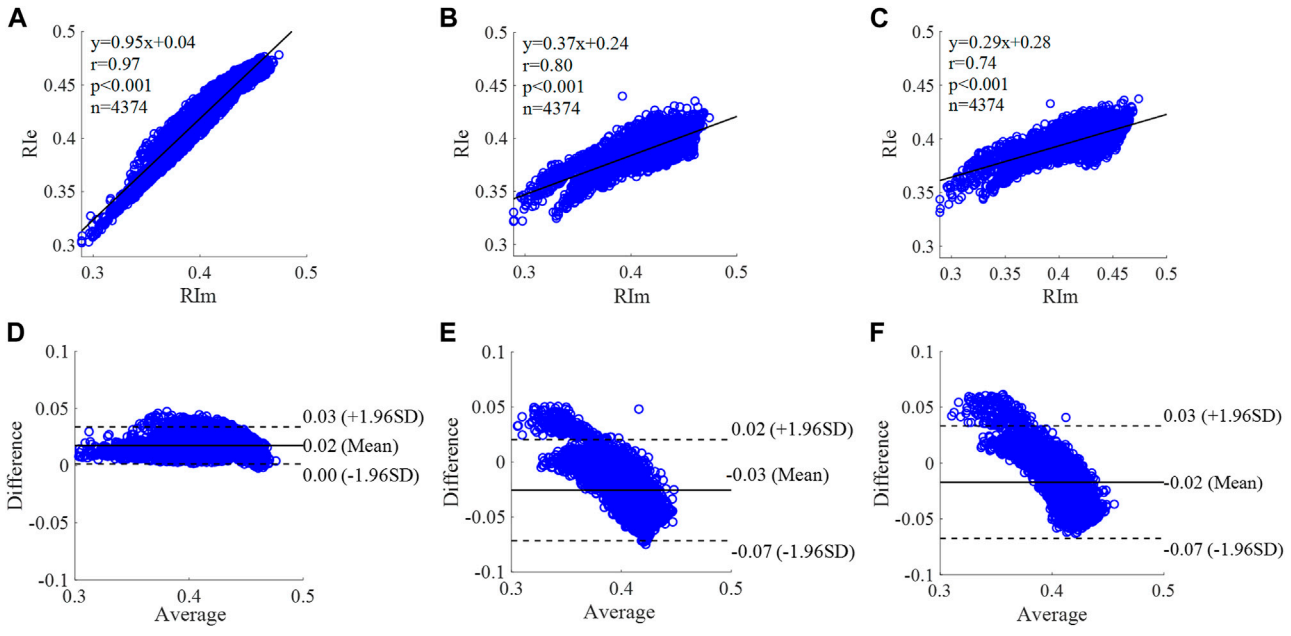

FIGURE 12
Correlation graphs and Bland-Altman plots of RI calculated by three flow waveforms. **(A)** and **(D)** Results of the personalized flow wave (Nektar1D PWDB, 4,374 subjects); **(B)** and **(E)** Results of the triangular flow wave (Nektar1D PWDB, 4,374 subjects); **(C)** and **(F)** Results of the lognormal flow wave (Nektar1D PWDB, 4,374 subjects). RIm and RIe are measured and estimated RI, respectively. Difference: RIe - RIm; Average: (RIe + RIm)/2.

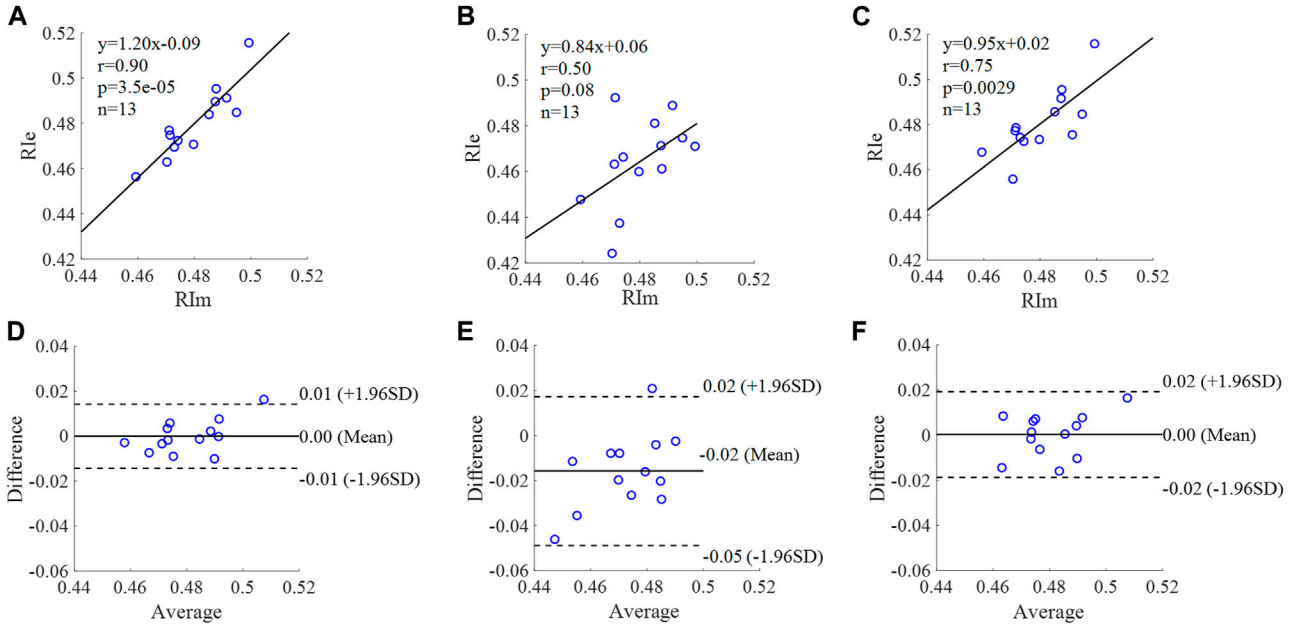

FIGURE 13
Correlation graphs and Bland-Altman plots of RI calculated by three flow waveforms. **(A)** and **(D)** Results of the personalized flow wave (Clinical data, 13 participants); **(B)** and **(E)** Results of the triangular flow wave (Clinical data, 13 participants); **(C)** and **(F)** Results of the lognormal flow wave (Clinical data, 13 participants). RIm and RIe are measured and estimated RI, respectively. Difference: RIe - RIm; Average: (RIe + RIm)/2.

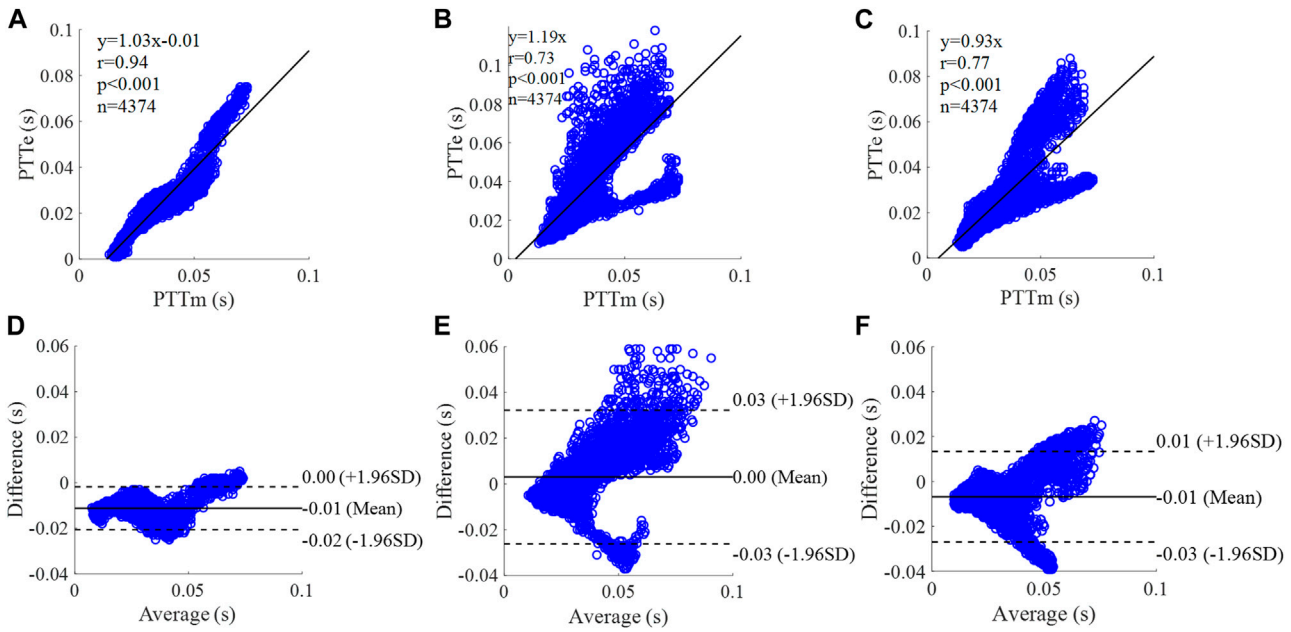

FIGURE 14
Correlation graphs and Bland-Altman plots of PTT calculated by three flow waveforms **(A)** and **(D)** Results of the personalized flow wave (Nektar1D PWDB, 4,374 subjects); **(B)** and **(E)** Results of the triangular flow wave (Nektar1D PWDB, 4,374 subjects); **(C)** and **(F)** Results of the lognormal flow wave (Nektar1D PWDB, 4,374 subjects). PTTm and PTTe are measured and estimated PTT, respectively. Difference: PTTe - PTTm; Average: (PTTe + PTTm)/2.

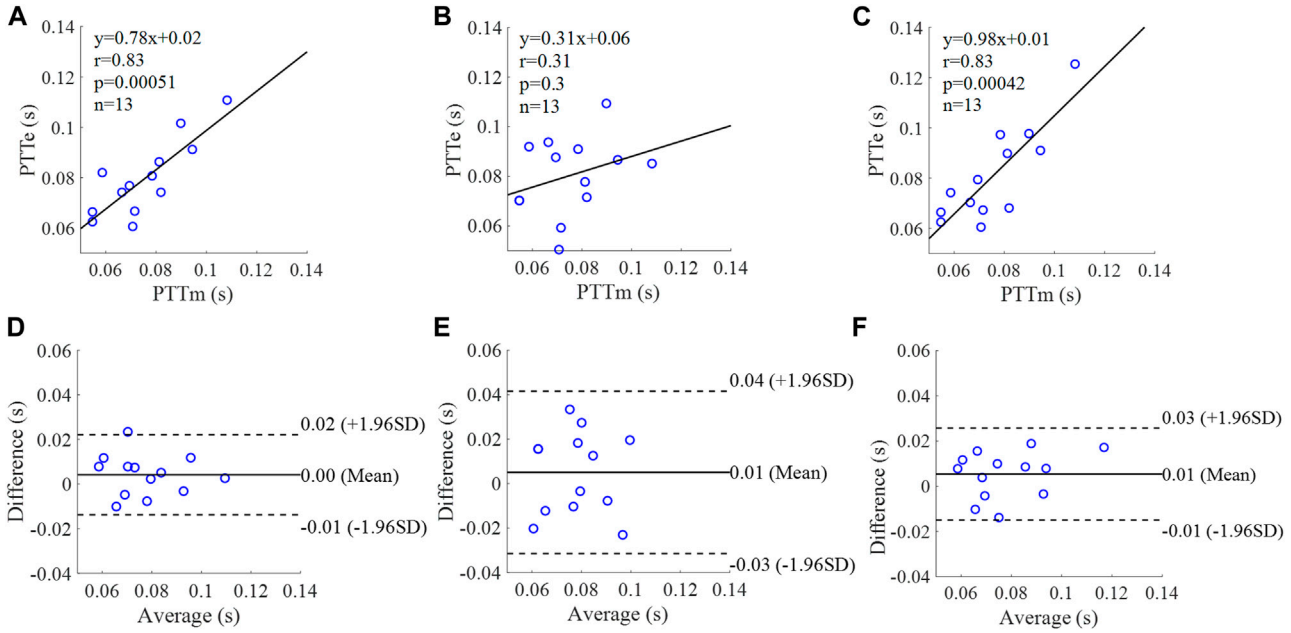

FIGURE 15
Correlation graphs and Bland-Altman plots of PTT calculated by three flow waveforms **(A)** and **(D)** Results of the personalized flow wave (Clinical data, 13 participants); **(B)** and **(E)** Results of the triangular flow wave (Clinical data, 13 participants); **(C)** and **(F)** Results of the lognormal flow wave (Clinical data, 13 participants). PTTm and PTTe are measured and estimated PTT, respectively. Difference: PTTe - PTTm; Average: (PTTe + PTTm)/2.

RI using the personalized flow method based on Nektar1D PWDB is shown in Figure 12D. The same comparison using the triangular flow method and lognormal flow approximation (mean ± SD, −0.03 ± 0.03 and −0.02 ± 0.03) is shown in Figure 12E,F, respectively. The linear regression and Bland-Altman plots of RI calculated by three flow waveforms (Clinical data, 13 participants) are shown in Figure 13. The regression equations (panels A, B and C) are **y = 1.20x-0.09** (**r = 0.90**, **p < 0.001**), for the personalized flow wave method; y = 0.84x+0.06 (r = 0.50, p = 0.08) for the triangular flow wave approach; and y = 0.95x+0.02 (r = 0.75, p = 0.0029) for the lognormal flow wave approximation algorithm. The corresponding Bland-Altman plots (panels D, E and F) and their mean differences (± SD) for the personalized flow wave, triangular flow wave and lognormal flow wave methods respectively are (**0 ± 0.01**), (−0.02 ± 0.02) and (0 ± 0.01).

The equation of the linear regression obtained between the measured and estimated PTT using the personalized flow method based on Nektar1D PWDB is **y = 1.03x - 0.01** (**r = 0.94**, **p < 0.001**) as shown in Figure 14A; The corresponding equations obtained using the triangular flow method and lognormal flow approximation (see Figure 14B,C) are y = 1.19x (r = 0.73, p < 0.001) and y = 0.93x (r = 0.77, p < 0.001), respectively. A comparison (mean ± SD, **-0.01 ± 0.01 s**) between the measured and estimated PTT using the personalized flow method based on Nektar1D PWDB is shown in Figure 14D. The same comparison using the triangular flow method and lognormal flow approximation (mean ± SD, 0 ± 0.02 s and −0.01 ± 0.01 s) is shown in Figure 14E,F, respectively. The linear regression and Bland-Altman plots of PTT calculated by three flow waveforms (Clinical data, 13 participants) are shown in Figure 15. The regression equations (panels A, B and C) are **y = 0.78x+0.02** (**r = 0.83**, **p < 0.001**), for the personalized flow wave method; y = 0.31x+0.06 (r = 0.31, p = 0.3) for the triangular flow wave approach; and y = 0.98x+0.01 (r = 0.83, p < 0.001) for the lognormal flow wave approximation algorithm. The corresponding Bland-Altman plots (panels D, E and F) and their mean differences (± SD) for the personalized flow wave, triangular flow wave and lognormal flow wave methods respectively are (**0 ± 0.01 s**), (0.01 ± 0.02 s) and (0.01 ± 0.01 s).

The coefficient of determination between the measured and estimated RM using the personalized flow method based on two datasets are **0.94** and **0.72**, and the results of using the triangular flow method are 0.62 and 0.10. The results of using the lognormal flow wave approximation are 0.53 and 0.62. The coefficient of determination between the measured and estimated RI using the personalized flow method based on two datasets are **0.94** and **0.81**, and the results of using the triangular flow method are 0.64 and 0.25. The results of using the lognormal flow wave approximation are 0.55 and 0.56. The coefficient of determination between the measured and estimated PTT using the personalized flow method based on two datasets are **0.88** and **0.69**, and the results of using the triangular flow method are 0.53 and 0.09. The results of using the lognormal flow wave approximation are 0.59 and 0.69. Therefore, the correlation of the reflection indices calculated by the personalized flow method is more robust than that of the triangular flow method and lognormal flow wave approximation (Figures 10–15). The results of personalized flow waveform method are the closest to one compared to the other methods, thus indicating a very good one to one correspondence. The personalized flow approximates the

measured flow and gives better estimates of RM, RI, and PTT. The quantitative and objective comparison of the three flow wave methods is summarized in Table 2. To further strengthen the validity of the proposed method in obtaining the flow waveform from CAPW, we also calculated the RMSE between the actual known flow and the approximated flow using three methods (i.e., personalized flow, lognormal flow, and triangular flow). The proposed personalized flow method gave the smallest values (as shown in Table 2). The small errors indicate that the personalized flow wave shape is a good approximation for applying waveform analysis and improves wave separation analysis results compared to the other two methods.

4 Discussion

In this study, we applied a personalized wave to estimate the aortic flow waveform in two data sets (Nektar1D PWDB and Clinical data) to investigate the feasibility of CAPW separation. Moreover, the CAPW reflection indices calculated using the personalized estimated flow waveform were compared with the results derived from the traditional triangular flow wave and the recently proposed lognormal flow wave approximation method. The CAPW was decomposed into P_f and P_b using pressure-flow relations, and wave reflections were quantitatively and qualitatively analyzed. By experimental analysis, the correlation and consistency of the wave reflection indices calculated based on the personalized and measured flow waves are higher than the other two methods (Figures 10–15). From the perspective of RI, RM, and PTT, the RMSE between the personalized flow waveform and measured flow waveform are smaller than the difference between the other two methods (Table 2). Moreover, the shape of the personalized estimation flow wave is better than that of the triangle and lognormal flow waves (see Figure 8).

Also, the P_f and P_b of the CAPW decomposition by personalized flow waveforms are closer to the actual results. The errors of the amplitudes of P_f and P_b decomposed by the personalized estimated flow wave and CAPW are smaller (Table 2). The waveform of personalized flow is more consistent with the actual flow waveform compared with the lognormal and triangular flow waveform (Figure 8). Moreover, the biases between wave reflection indices calculated by decomposing CAPW with the measured and personalized flow are smaller. Furthermore, the P_f and P_b of the CAPW decomposition by personalized flow waveform are closer to the actual results in amplitude and waveform morphology than the other two methods (Nektar1D PWDB; RMSEs = 1.39 and 0.39, Table 2 and Clinical data; RMSEs = 3.29 and 1.37; Table 2). Using a triangle to estimate the flow waveform will lead to spikes, and also P_f and P_b calculated by triangle flow waves will also appear as spikes (see Figure 8). This will not happen in the measured flow, and the personalized flow is more reliable.

Through linear regression equation and Bland-Altman diagram analysis, RM, RI, and PTT obtained from personalized flow waveform are highly correlated with RM, RI, and PTT obtained from the measured flow (Figures 10–15). These show that the wave reflection indices can be calculated by the personalized estimated flow wave when the real flow wave is not convenient to measure. As shown in Figures 10–15, Bland–Altman plots generally revealed smaller biases and narrower 95% LOA (Limits of agreement) for the personalized flow waveform, compared with the triangular and lognormal flow waveform approximation. Wave reflection indices derived using the truly measured flow waveform and estimated flow waveforms using three methods are reported in Table 2. Based on the comparison of the results between the Nektar1D PWDB and clinical data, the Pearson correlation coefficients between the personalized flow wave, lognormal flow, triangular flow wave, and the measured flow wave indicate that the accuracy of the personalized flow wave is higher. It was notable that over the pulse wave reflection indices, the biases of RM, RI, and PTT were lower for the personalized flow waveform than the triangular and lognormal flow waveform in most cases, thus confirming the superior performance of the personalized flow method. In addition, compared with the triangle flow wave, the personalized flow wave is more consistent with the measured flow wave in terms of RI, RM, and PTT. Besides, the personalized flow wave method does not require complex statistical calculations like the lognormal approximation, nor does it need to establish a variance value in advance.

The clinical data used for validation in this paper are limited to young, healthy participants only, which is one of the limitations of this study. There was no vascular or cardiac disease model included in the 1-D model when generating the virtual subjects. The 1-D database also only represents healthy subjects to the limitation. The proposed method should be validated in different populations (i.e., patients with heart disease) further to investigate the generalizability of the personalized flow waveform method. In addition, it is feasible that PTT is estimated only by calculating the time delay of P_f and P_b, but there is no comparison and correlation analysis with the measured carotid-femoral PTT and aortic pulse wave velocity. In order to better evaluate arterial stiffness, a comparison is necessary. The reliability of using the 30% ET as a surrogate of inflection point has not been rigorously proven, but it has just been used as a rule of thumb in previous studies. Typically, some degree of flow regurgitation occurs when the aortic valve closes, i.e., the actual aortic flow is negative at end-systole (shown in Figure 8). As with the triangular and the lognormal flow waves, the proposed personalized flow wave ignores this by setting the diastolic flow to 0 (Westerhof et al., 2006; Hao et al., 2022). Although the personalized flow wave improves the results of wave reflection and wave separation analysis compared to the other two methods, it is still necessary to further strengthen this research to implement this typical feature of aortic flow waveform. Furthermore, in early-systole, the flow peak obtained by the proposed personalized flow method is closer to the measured flow peak than the other methods, and occurs later in time compared to the measured waveform. Also, during the late-systolic part of the personalized flow waveform, the waveform overestimates the measured waveform (see Figure 8). There are still errors between the approximate personalized flow waveform and the measured flow waveform. Future research should focus on the three feature points (a, b, and c) involved in the Hermite interpolation operation in order to construct a flow wave that is more consistent with the measurement.

5 Conclusion

In this paper, a novel method of approximate estimation of flow waves based on the characteristics of the CAPW is proposed, and the feasibility of personalized flow separation in CAPW is evaluated. The results indicate that the personalized flow wave method generates more accurate aortic flow waveform. Experiments on Nektar1D PWDB and clinical data verify the feasibility of the proposed method. The personalized flow wave estimated by our proposed method is more consistent with the measured flow wave when used to calculate RM, RI, and PTT, compared to the triangle estimation and lognormal approximation. P_f and P_b decomposed from CAPW using personalized flow wave method have more accurate shapes and amplitudes than the other two methods. The personalized flow wave method improves CAPW separation results both in accuracy and reliability.

Data availability statement

The original contributions presented in the study are included in the article/supplementary material, further inquiries can be directed to the corresponding author.

Ethics statement

The studies involving human participants were reviewed and approved by the Research Ethics Committee of Northeastern University (NO. NEU-EC-2021B022S), China. The patients/participants provided their written informed consent to participate in this study.

Author contributions

HS: Conceptualization of this study, investigation, validation, visualization, writing–original draft preparation. YaY: Methodology of this study, writing–proof reading. WL: Conceptualization of this study, data curation, resources, software. SZ: Data curation, software. SD: Formal analysis, visualization, software. JT: Methodology, data analysis. YY: Investigation, visualization. AA: Writing–proof reading. LX: Supervision, writing–review and editing.

Funding

This work was supported by the National Natural Science Foundation of China (No. 62273082 and No. 61773110), the Natural Science Foundation of Liaoning Province (No. 20170540312 and No. 2021-YGJC-14), the Basic Scientific Research Project (Key Project) of Liaoning Provincial Department of Education (LJKZ00042021), and Fundamental Research Funds for the Central Universities (No. N2119008). This work was also supported by the Shenyang Science and Technology Plan Fund (No. 21-104-1-24, No. 20-201-4-10, and No. 201375), and the Member Program of Neusoft Research of Intelligent Healthcare Technology, Co. Ltd. (No. MCMP062002).

Acknowledgments

The authors thank the participants for their precious assistance during experiments. The authors would like to thank the Key Laboratory of Medical Image Computing, Ministry of Education, Shenyang, China.

Conflict of interest

Author LX was employed by Neusoft Research of Intelligent Healthcare Technology, Co. Ltd.

The remaining authors declare that the research was conducted in the absence of any commercial or financial relationships that could be construed as a potential conflict of interest.

Publisher's note

All claims expressed in this article are solely those of the authors and do not necessarily represent those of their affiliated organizations, or those of the publisher, the editors and the reviewers. Any product that may be evaluated in this article, or claim that may be made by its manufacturer, is not guaranteed or endorsed by the publisher.

References

Alastruey, J., Khir, A. W., Matthys, K. S., Segers, P., Sherwin, S. J., Verdonck, P. R., et al. (2011). Pulse wave propagation in a model human arterial network: Assessment of 1-D visco-elastic simulations against *in vitro* measurements. *J. biomechanics* 44 (12), 2250–2258. doi:10.1016/j.jbiomech.2011.05.041

Avolio, A. P., Butlin, M., and Walsh, A. (2009). Arterial blood pressure measurement and pulse wave analysis—Their role in enhancing cardiovascular assessment. *Physiol. Meas.* 31 (1), R1–R47. doi:10.1088/0967-3334/31/1/r01

Butlin, M., and Qasem, A. (2016). Large artery stiffness assessment using SphygmoCor technology. *Pulse* 4 (4), 180–192. doi:10.1159/000452448

Cameron, J. D., McGrath, B. P., and Dart, A. M. (1998). Use of radial artery applanation tonometry and a generalized transfer function to determine aortic pressure augmentation in subjects with treated hypertension. *J. Am. Coll. Cardiol.* 32 (5), 1214–1220. doi:10.1016/s0735-1097(98)00411-2

Carlsen, R. K., Peters, C. D., Khatir, D. S., Laugesen, E., Bøtker, H. E., Winther, S., et al. (2016). Estimated aortic blood pressure based on radial artery tonometry underestimates directly measured aortic blood pressure in patients with advancing chronic kidney disease staging and increasing arterial stiffness. *Kidney Int.* 90 (4), 869–877. doi:10.1016/j.kint.2016.05.014

Charlton, P. H., Mariscal Harana, J., Vennin, S., Li, Y., Chowienczyk, P., and Alastruey, J. (2019). Modeling arterial pulse waves in healthy aging: A database for *in silico* evaluation of hemodynamics and pulse wave indexes. *Am. J. Physiology-Heart Circulatory Physiology* 317 (5), H1062–H1085. doi:10.1152/ajpheart.00218.2019

Davis, S., Westerhof, B., Bogert, L., Westerhof, N., and van Lieshout, J. (2009). P9.10 pulse wave reflection in supine and standing healthy young and elderly. *Artery Res.* 3 (4), 169. doi:10.1016/j.artres.2009.10.130

Ding, F.-H., Li, Y., Zhang, R.-Y., Zhang, Q., and Wang, J.-G. (2013). Comparison of the SphygmoCor and Omron devices in the estimation of pressure amplification against the invasive catheter measurement. *J. Hypertens.* 31 (1), 86–93. doi:10.1097/hjh.0b013e32835a8eca

Flores Geronimo, J., Corvera Poire, E., Chowienczyk, P., and Alastruey, J. (2021). Estimating central pulse pressure from blood flow by identifying the main physical

determinants of pulse pressure amplification. *Front. Physiology* 90, 608098. doi:10.3389/fphys.2021.608098

Hametner, B., Wassertheurer, S., Kropf, J., Mayer, C., Holzinger, A., Eber, B., et al. (2013). Wave reflection quantification based on pressure waveforms alone—Methods, comparison, and clinical covariates. *Comput. methods programs Biomed.* 109 (3), 250–259. doi:10.1016/j.cmpb.2012.10.005

Hao, L., Zhang, Q., Chen, X., Yao, Y., and Xu, L. (2022). Feasibility of waveform separation of central aortic pressure pulse based on lognormal flow wave approximation. *Biomed. Signal Process. Control* 77, 103784. doi:10.1016/j.bspc.2022.103784

Hartmann, V., Liu, H., Chen, F., Qiu, Q., Hughes, S., and Zheng, D. (2019). Quantitative comparison of photoplethysmographic waveform characteristics: Effect of measurement site. *Front. physiology* 10, 198. doi:10.3389/fphys.2019.00198

Hughes, A. D., Park, C., Ramakrishnan, A., Mayet, J., Chaturvedi, N., and Parker, K. H. (2020). Feasibility of estimation of aortic wave intensity using non-invasive pressure recordings in the absence of flow velocity in man. *Front. physiology* 11, 550. doi:10.3389/fphys.2020.00550

Karamanoglu, M., O'Rourke, M. F., Avolio, A. P., and Kelly, R. P. (1993). An analysis of the relationship between central aortic and peripheral upper limb pressure waves in man. *Eur. heart J.* 14 (2), 160–167. doi:10.1093/eurheartj/14.2.160

Khir, A., O'brien, A., Gibbs, J., and Parker, K. (2001). Determination of wave speed and wave separation in the arteries. *J. biomechanics* 34 (9), 1145–1155. doi:10.1016/S0021-9290(01)00076-8

Kips, J. G., Rietzschel, E. R., De Buyzere, M. L., Westerhof, B. E., Gillebert, T. C., Van Bortel, L. M., et al. (2009). Evaluation of noninvasive methods to assess wave reflection and pulse transit time from the pressure waveform alone. *Hypertension* 53 (2), 142–149. doi:10.1161/HYPERTENSIONAHA.108.123109

Laugesen, E., Rossen, N. B., Peters, C. D., Mæng, M., Ebbehøj, E., Knudsen, S. T., et al. (2014). Assessment of central blood pressure in patients with type 2 diabetes: A comparison between SphygmoCor and invasively measured values. *Am. J. Hypertens.* 27 (2), 169–176. doi:10.1093/ajh/hpt195

Laurent, S., and Boutouyrie, P. (2020). Arterial stiffness and hypertension in the elderly. *Front. Cardiovasc. Med.* 7, 544302. doi:10.3389/fcvm.2020.544302

Li, J. K.-J. (1986). Time domain resolution of forward and reflected waves in the aorta. *IEEE Trans. Biomed. Eng.* 33 (8), 783–785. doi:10.1109/tbme.1986.325903

Li, Y., Guilcher, A., Charlton, P. H., Vennin, S., Alastruey, J., and Chowienczyk, P. (2021). Relationship between fiducial points on the peripheral and central blood pressure waveforms: Rate of rise of the central waveform is a determinant of peripheral systolic blood pressure. *Am. J. Physiology-Heart Circulatory Physiology* 320 (4), H1601–H1608. doi:10.1152/ajpheart.00818.2020

Lorentz, R. A. (2000). Multivariate hermite interpolation by algebraic polynomials: A survey. *J. Comput. Appl. Math.* 122 (1-2), 167–201. doi:10.1016/S0377-0427(00)00367-8

Manisty, C., Mayet, J., Tapp, R. J., Parker, K. H., Sever, P., Poulter, N. H., et al. (2010). Wave reflection predicts cardiovascular events in hypertensive individuals independent of blood pressure and other cardiovascular risk factors: An ASCOT (Anglo-Scandinavian cardiac outcome trial) substudy. *J. Am. Coll. Cardiol.* 56 (1), 24–30. doi:10.1016/j.jacc.2010.03.030

Matthys, K. S., Alastruey, J., Peiró, J., Khir, A. W., Segers, P., Verdonck, P. R., et al. (2007). Pulse wave propagation in a model human arterial network: Assessment of 1-D numerical simulations against *in vitro* measurements. *J. biomechanics* 40 (15), 3476–3486. doi:10.1016/j.jbiomech.2007.05.027

McEniery, C. M., YasminMcDonnell, B., Munnery, M., Wallace, S. M., Rowe, C. V., et al. (2008). Central pressure: Variability and impact of cardiovascular risk factors: The anglo-cardiff collaborative trial II. *Hypertension* 51 (6), 1476–1482. doi:10.1161/HYPERTENSIONAHA.107.105445

Miyashita, H., Ikeda, U., Tsuruya, Y., Sekiguchi, H., Shimada, K., and Yaginuma, T. (1994). Noninvasive evaluation of the influence of aortic wave reflection on left ventricular ejection during auxotonic contraction. *Heart vessels* 9 (1), 30–39. doi:10.1007/bf01744493

Murgo, J. P., Westerhof, N., Giolma, J., and Altobelli, S. (1981). Manipulation of ascending aortic pressure and flow wave reflections with the valsalva maneuver: Relationship to input impedance. *Circulation* 63 (1), 122–132. doi:10.1161/01.cir.63.1.122

O'Rourke, M. F., and Yaginuma, T. (1984). Wave reflections and the arterial pulse. *Archives Intern. Med.* 144 (2), 366–371. doi:10.1001/archinte.1984.00350140192026

Ott, C., Haetinger, S., Schneider, M. P., Pauschinger, M., and Schmieder, R. E. (2012). Comparison of two noninvasive devices for measurement of central systolic blood pressure with invasive measurement during cardiac catheterization. *J. Clin. Hypertens.* 14 (9), 575–579. doi:10.1111/j.1751-7176.2012.00682.x

Papaioannou, T. G., Protogerou, A. D., Vrachatis, D., Konstantonis, G., Aissopou, E., Argyris, A., et al. (2016). Mean arterial pressure values calculated using seven different methods and their associations with target organ deterioration in a single-center study of 1878 individuals. *Hypertens. Res.* 39 (9), 640–647. doi:10.1038/hr.2016.41

Parittotokkaporn, S., de Castro, D., Lowe, A., and Pylypchuk, R. (2021). Carotid pulse wave analysis: Future direction of hemodynamic and cardiovascular risk assessment. *JMA J.* 4 (2), 119–128. doi:10.31662/jmaj.2020-0108

Payne, R. A., Teh, C. H., Webb, D. J., and Maxwell, S. R. (2007). A generalized arterial transfer function derived at rest underestimates augmentation of central pressure after exercise. *J. Hypertens.* 25 (11), 2266–2272. doi:10.1097/hjh.0b013e3282ef96fa

Pini, R., Cavallini, M. C., Palmieri, V., Marchionni, N., Di Bari, M., Devereux, R. B., et al. (2008). Central but not brachial blood pressure predicts cardiovascular events in an unselected geriatric population: The ICARe dicomano study. *J. Am. Coll. Cardiol.* 51 (25), 2432–2439. doi:10.1016/j.jacc.2008.03.031

Plamondon, R., O'Reilly, C., Rémi, C., and Duval, T. (2013). The lognormal handwriter: Learning, performing, and declining. *Front. Psychol.* 4, 945. doi:10.3389/fpsyg.2013.00945

Qasem, A., and Avolio, A. (2008). Determination of aortic pulse wave velocity from waveform decomposition of the central aortic pressure pulse. *Hypertension* 51 (2), 188–195. doi:10.1161/hypertensionaha.107.092676

Rietzschel, E.-R., De Buyzere, M. L., Bekaert, S., Segers, P., De Bacquer, D., Cooman, L., et al. (2007). Rationale, design, methods and baseline characteristics of the Asklepios Study. *Eur. J. Prev. Cardiol.* 14 (2), 179–191. doi:10.1097/HJR.0b013e328012c380

Rivera, L. A., Eisenmenger, L., Cary, P., Johnson, S. C., and Johnson, K. M. (2020). Assessment of intracranial vascular flow oscillations in Alzheimer's disease using real time 4D flow MRI: Neuroimaging/New imaging methods. *Alzheimer's Dementia* 16, e044536. doi:10.1002/alz.044536

Roman, M. J., Devereux, R. B., Kizer, J. R., Lee, E. T., Galloway, J. M., Ali, T., et al. (2007). Central pressure more strongly relates to vascular disease and outcome than does brachial pressure: The strong heart study. *Hypertension* 50 (1), 197–203. doi:10.1161/HYPERTENSIONAHA.107.089078

Sequi-Dominguez, I., Cavero-Redondo, I., Alvarez-Bueno, C., Pozuelo-Carrascosa, D. P., Nunez de Arenas-Arroyo, S., and Martinez-Vizcaino, V. (2020). Accuracy of pulse wave velocity predicting cardiovascular and all-cause mortality. A systematic review and meta-analysis. *J. Clin. Med.* 9 (7), 2080. doi:10.3390/jcm9072080

Sharman, J. E., Lim, R., Qasem, A. M., Coombes, J. S., Burgess, M. I., Franco, J., et al. (2006). Validation of a generalized transfer function to noninvasively derive central blood pressure during exercise. *Hypertension* 47 (6), 1203–1208. doi:10.1161/01.hyp.0000223013.60612.72

Shenouda, N., Stock, J. M., Patik, J. C., Chirinos, J. A., and Edwards, D. G. (2021). Personalized physiologic flow waveforms improve wave reflection estimates compared to triangular flow waveforms in adults. *Am. J. Physiology-Heart Circulatory Physiology* 320 (5), H1802–H1812. doi:10.1152/ajpheart.00747.2020

Sofogianni, A., and Tziomalos, K. (2019). Ambulatory arterial stiffness evaluation: A step forward in the management of hypertension. *J. Clin. Hypertens.* 21 (8), 1169–1170. doi:10.1111/jch.13631

Stortz, G., Cahill, L. S., Chandran, A. R., Baschat, A., Sled, J. G., and Macgowan, C. K. (2020). Quantification of wave reflection in the human umbilical artery from asynchronous Doppler ultrasound measurements. *IEEE Trans. Med. imaging* 39 (11), 3749–3757. doi:10.1109/TMI.2020.3004511

Suleman, R., Padwal, R., Hamilton, P., Senthilselvan, A., and Alagiakrishnan, K. (2017). Association between central blood pressure, arterial stiffness, and mild cognitive impairment. *Clin. Hypertens.* 23 (1), 2–6. doi:10.1186/s40885-016-0058-5

Thubrikar, M., Bosher, L. P., and Nolan, S. P. (1979). The mechanism of opening of the aortic valve. *J. Thorac. Cardiovasc. Surg.* 77 (6), 863–870. doi:10.1016/s0022-5223(19)38191-7

Townsend, R. R., Wilkinson, I. B., Schiffrin, E. L., Avolio, A. P., Chirinos, J. A., Cockcroft, J. R., et al. (2015). Recommendations for improving and standardizing vascular research on arterial stiffness: A scientific statement from the American heart association. *Hypertension* 66 (3), 698–722. doi:10.1161/HYP.0000000000000033

Vallée, A., Yannoutsos, A., Temmar, M., Tubiana, C. D., Spinu, I., Zhang, Y., et al. (2018). Determinants of the aortic pulse wave velocity index in hypertensive and diabetic patients: Predictive and therapeutic implications. *J. Hypertens.* 36 (12), 2324–2332. doi:10.1097/HJH.0000000000001828

Verbeke, F., Segers, P., Heireman, S., Vanholder, R., Verdonck, P., and Van Bortel, L. M. (2005). Noninvasive assessment of local pulse pressure: Importance of brachial-to-radial pressure amplification. *Hypertension* 46 (1), 244–248. doi:10.1161/01.HYP.0000166723.07809.7e

Vlachopoulos, C., O'Rourke, M., and Nichols, W. W. (2011). *McDonald's blood flow in arteries: Theoretical, experimental and clinical principles*. London, United Kingdom: Hodder Arnold, CRC Press. doi:10.1111/j.1540-8175.1991.tb01207.x

Wang, K.-L., Cheng, H.-M., Sung, S.-H., Chuang, S.-Y., Li, C.-H., Spurgeon, H. A., et al. (2010). Wave reflection and arterial stiffness in the prediction of 15-year all-cause and cardiovascular mortalities: A community-based study. *Hypertension* 55 (3), 799–805. doi:10.1161/HYPERTENSIONAHA.109.139964

Westerhof, B. E., Guelen, I., Westerhof, N., Karemaker, J. M., and Avolio, A. (2006). Quantification of wave reflection in the human aorta from pressure alone: A proof of principle. *Hypertension* 48 (4), 595–601. doi:10.1161/01.HYP.0000238330.08894.17

Westerhof, N., Sipkema, P., Bos, G. V. D., and Elzinga, G. (1972). Forward and backward waves in the arterial system. *Cardiovasc. Res.* 6 (6), 648–656. doi:10.1093/cvr/6.6.648

Willemet, M., Chowienczyk, P., and Alastruey, J. (2015). A database of virtual healthy subjects to assess the accuracy of foot-to-foot pulse wave velocities for estimation of aortic stiffness. *Am. J. Physiology-Heart Circulatory Physiology* 309 (4), H663–H675. doi:10.1152/ajpheart.00175.2015

Xiao, N., Alastruey, J., and Figueroa, C. A. (2014). A systematic comparison between 1-D and 3-D hemodynamics in compliant arterial models. *Int. J. Numer. methods Biomed. Eng.* 30 (2), 204–231. doi:10.1002/cnm.2598

Yao, Y., Zhou, S., Alastruey, J., Hao, L., Greenwald, S. E., Zhang, Y., et al. (2022). Estimation of central pulse wave velocity from radial pulse wave analysis. *Comput. Methods Programs Biomed.* 219, 106781. doi:10.1016/j.cmpb.2022.106781

Yu, S., Xiong, J., Lu, Y., Chi, C., Teliewubai, J., Bai, B., et al. (2018). The prevalence of central hypertension defined by a central blood pressure type I device and its association with target organ damage in the community-dwelling elderly Chinese: The Northern Shanghai Study. *J. Am. Soc. Hypertens.* 12 (3), 211–219. doi:10.1016/j.jash.2017.12.013

Zamani, P., Bluemke, D. A., Jacobs, D. R., Jr, Duprez, D. A., Kronmal, R., Lilly, S. M., et al. (2015). Resistive and pulsatile arterial load as predictors of left ventricular mass and geometry: The multi-ethnic study of atherosclerosis. *Hypertension* 65 (1), 85–92. doi:10.1161/HYPERTENSIONAHA.114.04333

Zamani, P., Jacobs, D. R., Jr, Segers, P., Duprez, D. A., Brumback, L., Kronmal, R. A., et al. (2014). Reflection magnitude as a predictor of mortality: The multi-ethnic study of atherosclerosis. *Hypertension* 64 (5), 958–964. doi:10.1161/HYPERTENSIONAHA.114.03855

Zamani, P., Lilly, S. M., Segers, P., Jacobs, D. R., Jr, Bluemke, D. A., Duprez, D. A., et al. (2016). Pulsatile load components, resistive load and incident heart failure: The multi-ethnic study of atherosclerosis (MESA). *J. cardiac Fail.* 22 (12), 988–995. doi:10.1016/j.cardfail.2016.04.011

Zhou, S., Yao, Y., Liu, W., Yang, J., Wang, J., Hao, L., et al. (2022). Ultrasound-based method for individualized estimation of central aortic blood pressure from flow velocity and diameter. *Comput. Biol. Med.* 143, 105254. doi:10.1016/j.compbiomed.2022.105254

Zócalo, Y., and Bia, D. (2022). Central pressure waveform-derived indexes obtained from carotid and radial tonometry and brachial oscillometry in healthy subjects (2–84 Y): Age-Height-and sex-related profiles and analysis of indexes agreement. *Front. physiology* 2530, 774390. doi:10.3389/fphys.2021.774390

Zuo, J.-L., Li, Y., Yan, Z.-J., Zhang, R.-Y., Shen, W.-F., Zhu, D.-L., et al. (2010). Validation of the central blood pressure estimation by the SphygmoCor system in Chinese. *Blood Press. Monit.* 15 (5), 268–274. doi:10.1097/mbp.0b013e3283386866

frontiers | Frontiers in Physiology

TYPE Brief Research Report
PUBLISHED 15 March 2023
DOI 10.3389/fphys.2023.1137146

OPEN ACCESS

EDITED BY
Lisheng Xu,
Northeastern University, China

REVIEWED BY
Wenjun Tan,
Northeastern University, China
Yang Yao,
ShanghaiTech University, China
Hongbo Xie,
Queensland University of Technology, Australia

*CORRESPONDENCE
Zhiyuan Lu,
zhiyuan.lu@uor.edu.cn
Ping Zhou,
dr.ping.zhou@outlook.com

SPECIALTY SECTION
This article was submitted to Computational Physiology and Medicine, a section of the journal Frontiers in Physiology

RECEIVED 04 January 2023
ACCEPTED 27 February 2023
PUBLISHED 15 March 2023

CITATION
Huang C, Lu Z, Chen M, Klein CS, Zhang Y, Li S and Zhou P (2023), Muscle innervation zone estimation from monopolar high-density M-waves using principal component analysis and radon transform.
Front. Physiol. 14:1137146.
doi: 10.3389/fphys.2023.1137146

Muscle innervation zone estimation from monopolar high-density M-waves using principal component analysis and radon transform

Chengjun Huang[1], Zhiyuan Lu[2]*, Maoqi Chen[2], Cliff S. Klein[3], Yingchun Zhang[4], Sheng Li[5,6] and Ping Zhou[2]*

[1]Department of Neuroscience, Baylor College of Medicine, Houston, TX, United States, [2]School of Rehabilitation Science and Engineering, University of Health and Rehabilitation Sciences, Qingdao, Shandong, China, [3]Guangdong Work Injury Rehabilitation Center, Guangzhou, Guangdong, China, [4]Department of Biomedical Engineering, University of Houston, Houston, TX, United States, [5]Department of Physical Medicine and Rehabilitation, University of Texas Health Science Center at Houston, Houston, TX, United States, [6]TIRR Memorial Hermann Hospital, Houston, TX, United States

This study examined methods for estimating the innervation zone (IZ) of a muscle using recorded monopolar high density M waves. Two IZ estimation methods based on principal component analysis (PCA) and Radon transform (RT) were examined. Experimental M waves, acquired from the biceps brachii muscles of nine healthy subjects were used as testing data sets. The performance of the two methods was evaluated by comparing their IZ estimations with manual IZ detection by experienced human operators. Compared with manual detection, the agreement rate of the estimated IZs was 83% and 63% for PCA and RT based methods, respectively, both using monopolar high density M waves. In contrast, the agreement rate was 56% for cross correlation analysis using bipolar high density M waves. The mean difference in estimated IZ location between manual detection and the tested method was 0.12 ± 0.28 inter-electrode-distance (IED) for PCA, 0.33 ± 0.41 IED for RT and 0.39 ± 0.74 IED for cross correlation-based methods. The results indicate that the PCA based method was able to automatically detect muscle IZs from monopolar M waves. Thus, PCA provides an alternative approach to estimate IZ location of voluntary or electrically-evoked muscle contractions, and may have particular value for IZ detection in patients with impaired voluntary muscle activation.

KEYWORDS

innervation zone, monopolar, M wave, electrode array, principal component analysis, radon transform

1 Introduction

The innervation zone (IZ) of a muscle is the region where muscle fibers are innervated by motor axon terminals. The architecture of the IZ can influence electromyographic (EMG) signal characteristics recorded from the muscle surface (Nishihara et al., 2010; Rantalainen et al., 2012; Gallina et al., 2013; Ye et al., 2015; Smith et al., 2017; de Souza et al., 2022). The ability to detect the location of the IZ using EMG techniques has implications for understanding muscle function in health and disease. Thus, monitoring changes in IZ

location may provide valuable information about the processes of motor unit remodeling associated with aging, disease, and injury (Jahanmiri-Nezhad et al., 2015; Rasool et al., 2017; Dias et al., 2018; Li et al., 2021). In addition, the ability to detect the IZ has important clinical value. For example, one clinical application of IZ estimation is to guide botulinum toxin (BTX) injection more precisely for treating spasticity in patients with neurological injuries such as stroke and cerebral palsy (Van Campenhout and Molenaers, 2011; Guzmán-Venegas et al., 2014; Zhang et al., 2019; Chen et al., 2020; Zhang et al., 2021). The effectiveness of BTX treatment has been reported to depend on the distance between the injection site and the IZ (Shaari and Ira Sanders, 1993; Lapatki et al., 2011; Kaymak et al., 2018).

The IZ can be identified through EMG signals recorded by a linear electrode array or a matrix of electrodes placed over the muscle (Drost et al., 2006; Barbero et al., 2012; Piccoli et al., 2014; Campanini et al., 2022). Most investigators have estimated the location of the IZ based on surface EMG recordings of voluntary muscle contractions and processing the signals in a single differential or bipolar configuration (Ostlund et al., 2007; Mesin et al., 2009; Enck et al., 2010; Barbero et al., 2011; Beck et al., 2012; Ullah et al., 2014; Marateb et al., 2016; Liu et al., 2019; Mancebo et al., 2019; Liu et al., 2020; Zhang et al., 2020), whereas few have processed monopolar signals for IZ estimation (Rodriguez-Falces, 2017). When EMG signals are processed in a differential configuration the IZ location may correspond to either a reversal in EMG signal polarity between two adjacent channels along the muscle fibers, or the smallest amplitude in a single channel.

Although voluntary contractions are convenient for estimating the IZ, they may not be feasible in patients with significant paralysis or poor motor control. An alternative method for IZ location is to record compound muscle action potentials (or M waves) evoked by electrical stimulation of the motor nerve, but few have used this approach (Zhang et al., 2017). In two reports, the IZ location was found to be similar when based on M waves and voluntary EMG (Guzmán-Venegas et al., 2016) (Huang et al., 2019). When recording M waves using electrode arrays, a monopolar electrode configuration is often used because bipolar configuration may considerably attenuate M wave content (Tucker and Türker, 2005; Hadoush et al., 2009; Rodriguez-Falces and Place, 2018). There is a need to further develop appropriate methods to automatically estimate the IZ from M wave signals recorded in a monopolar configuration.

In this study we investigated two methods to estimate the IZ from monopolar M-wave recordings. One method was based on principal component analysis (PCA); specifically, the second principal component coefficients derived from PCA, which are related to time delays of different EMG channels. The method is suitable for analysis of monopolar signals and has been evaluated using high density voluntary surface EMG signals (Huang et al., 2022), but not on electrically-evoked signals. The other method is based on Radon transform (RT), which can be used to detect linear patterns in a two-dimensional signal and has been proved useful for IZ estimation (Cescon, 2006). Although IZ estimation based on RT was mainly applied to bipolar voluntary surface EMG signals (Li et al., 2021), (Cescon, 2006), (Li et al., 2022), theoretically, the RT method can also be applied on monopolar signals for estimation of IZ location.

The usefulness of PCA and RT methods for automated estimation of IZ location was explored in the current study using monopolar M waves recorded with surface electrode arrays from the biceps brachii (BB) muscles. The performance of automatic IZ detection was compared with manual detection based on visual inspection of the M waves. The objective was to provide an alternative approach to voluntary contraction for reliable and automatic estimation of muscle IZ.

2 Methods

2.1 Experiment

2.1.1 Participants and consent

Nine healthy male subjects (mean ± SD, 28.9 ± 4.8 years) without a history of neuromuscular or musculoskeletal disorders participated in the study. They were well informed of the experimental procedures, including possible risks and discomforts. All subjects gave written informed consent approved by the ethics committee of Guangdong Work Injury Rehabilitation Center (Guangzhou, China).

2.1.2 Experiment protocols

Two high density channel arrays (ELSCH064NM2, Bioelettronica, Torino, Italy) were placed parallel to the muscle fiber direction over the lateral side (Array 1) and the medial side (Array 2) of the BB after skin preparation and fixed with elastic straps (Figure 1A). Each channel matrix consists of 64 channels with an 8 mm inter electrode distance (IED) arranged in a grid of 5 columns by 13 rows (one column contained only 12 channels). A ground electrode was placed at the elbow. A constant-current stimulator (DS7A, Digitimer, Herthfordshire, UK) and standard bar electrode (3 cm inter-electrode spacing) were used to evoke BB M-waves. The bar electrode was placed over the musculocutaneous nerve at the proximal medial side of the BB (Figure 1B). Single pulses of 1 ms duration were applied every 5 s as the current intensity was increased until the maximal M-wave was recorded. The M waves were recorded by a signal amplifier (100x) in monopolar configuration (EMG-USB2, sampling frequency of 2048 Hz, 12-bit A/D converter, Bioelettronica, Torino, Italy).

2.2 Detection of muscle IZ from monopolar M waves

2.2.1 Muscle IZ estimation based on PCA

The rationale for using the 2nd principal component coefficients derived from PCA for IZ estimation was explained in detail (Huang et al., 2022). Briefly, PCA performs the eigen decomposition on the covariance matrix Σ of the standardized (zero mean, and unit variance) electrode array EMG signals X (M-by-N matrix, N samples and M channels), which is a M × M matrix where each element represents the covariance between two channels. The elements of each eigenvector are the coefficients of each principal component. It has been proven that the 2nd principal component coefficients are related with the time delays of different channels due to signal propagation from the IZ to the two ends of a muscle (Huang et al., 2022) (Laguna et al., 2018). As illustrated in Figure 1C, the channels located near the IZ are expected to have minimum time

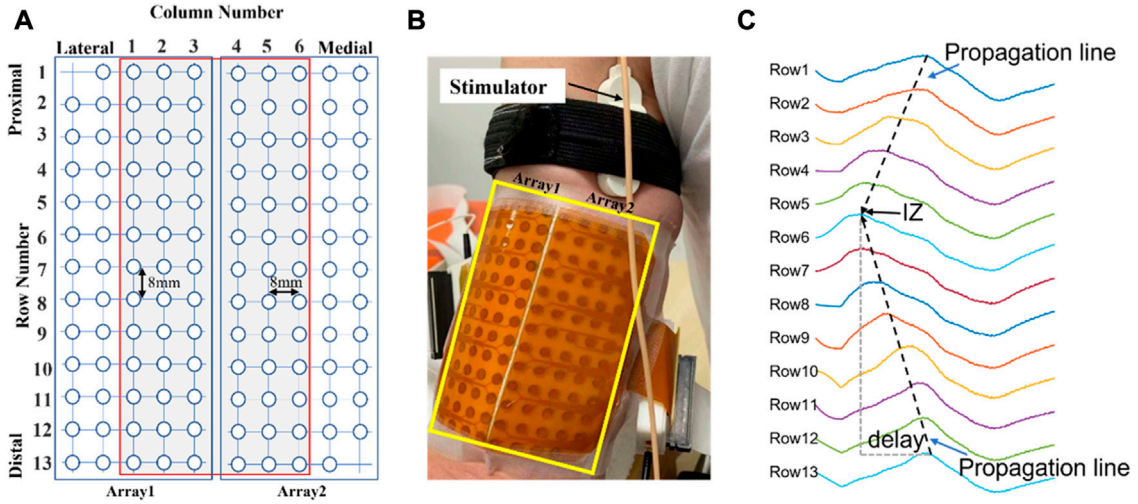

FIGURE 1
(A): Schematic representation of the two adhesive 2D matrices for recording experimental signals. **(B)**: High-density electrode array recording with columns positioned parallel to the muscle fiber direction. **(C)**: An example of monopolar M waves of 13 channels in one of the columns from a representative subject. The IZ is located close to row 6. Delay: time interval of the waveforms travelling distally from the IZ.

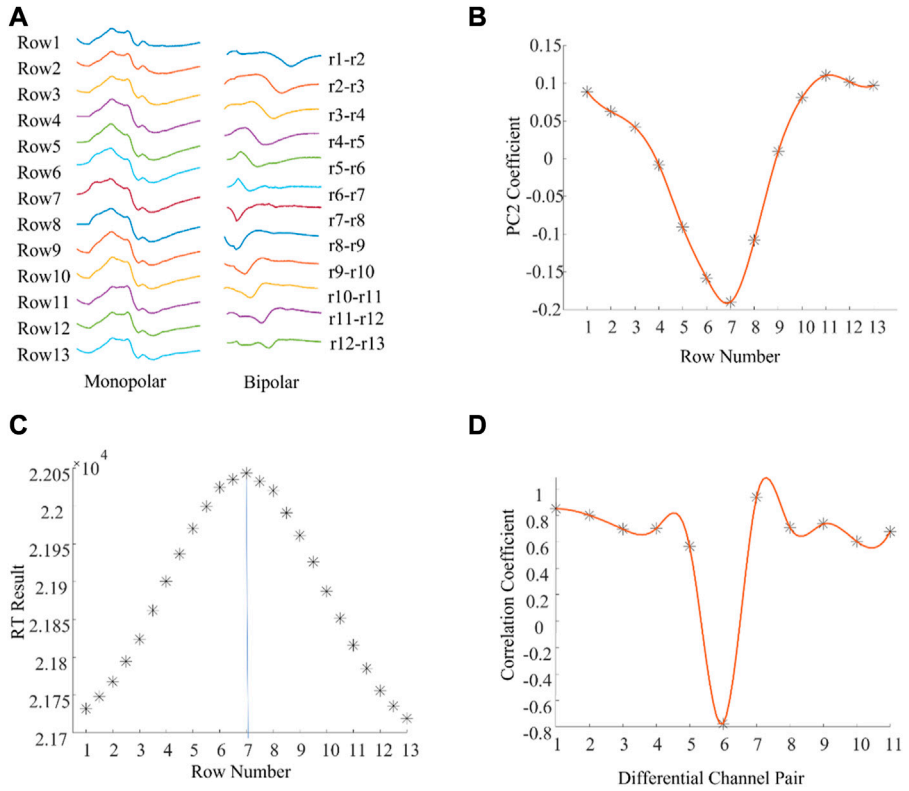

FIGURE 2
An example of muscle IZ estimation from experimental high density M waves where different methods reached the same results. **(A)**: A column of M waves of a tested subject. **(B)**: PCA based IZ estimation: the minimum coefficient was located at row 7 and the coefficients gradually increased along the fiber direction. **(C)**: RT based IZ estimation: the distribution of RT results across all the rows, and between rows. **(D)**: Cross correlation based IZ estimation: the distribution of the correlation coefficients between adjacent bipolar signals.

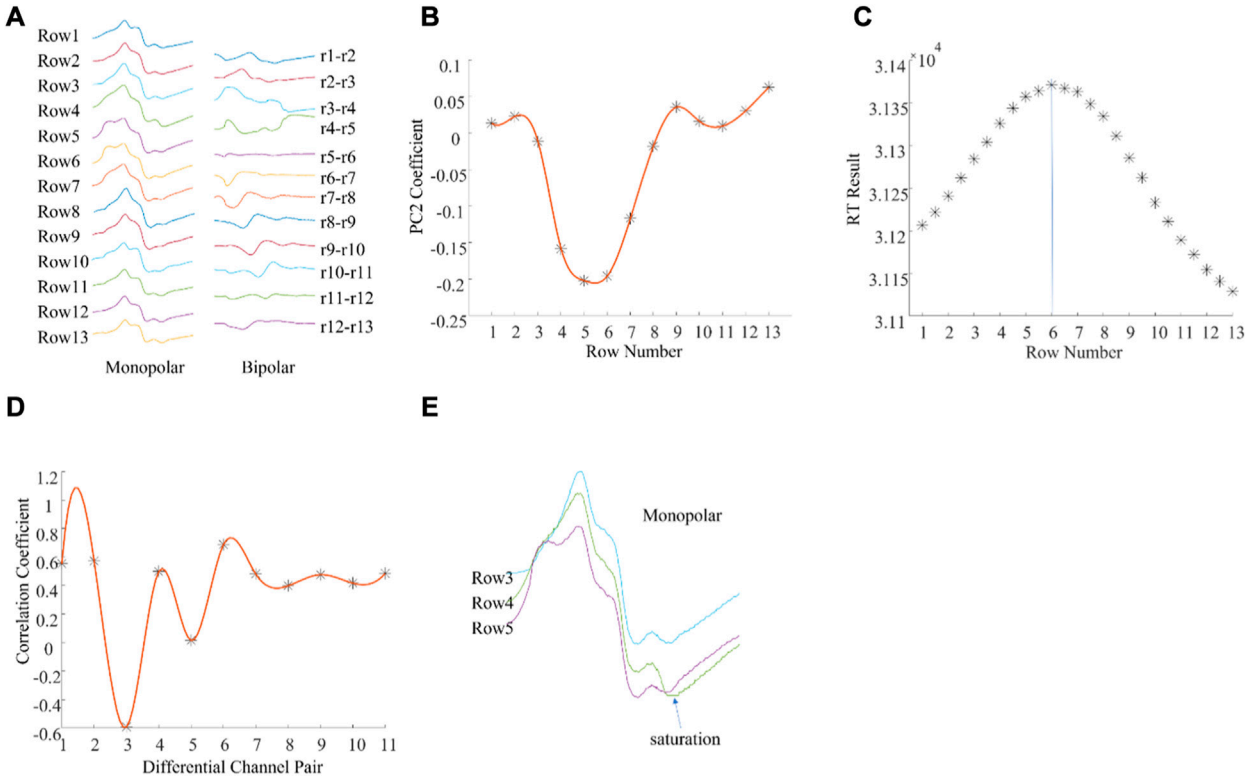

FIGURE 3
An example of muscle IZ estimation from experimental high density M waves where different methods produced different results. **(A)**: A column of M waves of a single subject. **(B)**: PCA based IZ estimation; **(C)**: RT based IZ estimation; **(D)**: Cross correlation based IZ estimation; **(E)**: Enlarged view of the monopolar M waves from rows 3, 4, and 5. See text for details.

delay. Therefore, analysis of the 2nd principal component coefficients can provide useful information pertaining to IZ location.

2.2.2 Muscle IZ estimation based on RT

The procedures of the RT based IZ identification have been described in detail (Cescon, 2006). For a column of signals, starting from the first row, the RT was implemented to search for the optimal propagation lines from signals at either side of a row i (i = 1,2,3 . . . 13), or between row j and row j + 1 (j = 1,2,3 . . . 12). A total of 25 RT results were obtained. As illustrated in Figure 1C, the potentials in the spatiotemporal surface EMG signal appear along inclined lines as they travel from the IZ to the tendon regions at a certain velocity. Therefore, the IZ location can be estimated by the maximum RT result.

2.3 Performance evaluation

The M-waves of the two most lateral and most two medial side columns were excluded from IZ identification as they were close to margin of the muscle. This left 6 columns for IZ estimation for each subject (Figure 1A). For each M wave, stimulation artifact was identified and suppressed as described previously (Liu et al., 2014). The signal duration was 0.2 s. For the PCA-based method, the signals were standardized (zero mean and unit variance). The spline interpolation was applied to the 2nd component coefficients along the rows to determine the IZ location for each column. For the RT based method, the signals were rectified. The output of the IZ detection was the channel number if the IZ was located on a specific channel or the average of neighboring channels if the IZ was located between two channels. In addition, the IZ was estimated from a conventional cross correlation method applied on bipolar M wave signals constructed from monopolar signals. The identified IZs from each of the methods were compared with those estimated manually based on visual inspection of the M waves by at least two experienced investigators. These investigators reached an agreement on IZ location prior to automated processing. The IZ location from manual inspection was used as the reference for quantifying the performance of the automated methods.

3 Results

Figure 2A shows one column of M waves in both monopolar and bipolar configurations for a single subject. Visually, the IZ was located near the channel at row 7. Figure 2B shows spatial distribution of the 2nd component coefficients. Notice that the position of the smallest coefficients was at row 7. The RT method also identified the IZ at row 7 (Figure 2C). The minimum correlation coefficient was between bipolar pair row6—row7 and row 7—row8 (Figure 2D), which also indicated that the IZ was located at row 7 based on the monopolar

configuration. These results reveal that IZ location was similar across the three methods.

There were also examples where the different methods produced different IZ locations (Figure 3). Figure 3A shows a column of M waves in both monopolar and bipolar configurations from a different subject. The IZ was located between row 5 and row 6 according to the 2nd principal component coefficients (Figure 3B) and at row 6 according to the maximum RT (Figure 3C). In contrast, the IZ was located at row 4 (between bipolar pair row 3—row 4, and row 4—row 5) according to the minimum correlation coefficient (Figure 3D). To explore possible reasons for the different estimates, the associated M waves were visually examined. As shown in Figure 3E, at the second phase of the M wave from row 4, there was a very short segment of saturation, which caused an artificial phase reversal between the bipolar pair row3—row4, and row4—row5, leading to misidentification of the IZ. Visual inspection of the M waves revealed that the IZ was located between row 5 and row 6. This was also confirmed from the differential signals as the amplitude between row 5 and row 6 was close to 0.

In total, 54 columns of experimental signals were processed for IZ estimation. Among them, 45 IZs (83%) estimated from the PCA, 34 IZs (63%) from the RT, and 30 IZs (56%) from the cross correlation were the same as estimations based on visual inspection. Compared with the visual estimations (reference IZs), the mean difference in estimated IZ location was 0.12 ± 0.28 IED for PCA, 0.33 ± 0.41 IED for RT, and 0.39 ± 0.74 IED for cross correlation.

4 Discussion

The ability to estimate muscle IZ through high density surface EMG signals using linear or 2-dimensional electrode arrays may be important clinically. A typical application is to guide BTX injection as close as possible to the IZ for spasticity treatment (Lapatki et al., 2011), (Kaymak et al., 2018). Voluntary contraction and electrical stimulation of the motor nerve are two common ways to generate surface EMG signals. The advantage of using electrical stimulation for IZ estimation is that it can be applied in patients who are paralyzed or lack the necessary voluntary control. M waves are commonly recorded in a monopolar mode, which provides informative content of action potential generation, propagation, and extinction (Rodriguez-Falces and Place, 2018). Compared with a differential configuration, monopolar recording can capture EMG signals from a larger muscle volume. The loss of M wave signal due to phase cancellation was more pronounced in bipolar than monopolar recording (Tucker and Türker, 2005). Although M waves provide a valuable signal source, its application for muscle IZ estimation has been rarely explored in the literature.

The current study examined two methods of estimating IZ location (PCA and RT) from monopolar M waves of the BB muscles. The BB was chosen as it is often affected by spasticity in patients with neurological disorders and is thus often a target muscle for treatment. Compared with manual IZ detection by an experienced investigator, the PCA based method achieved more consistent performance than one based on RT. PCA and RT use different computational approaches for IZ estimation. In PCA, a simplified time misaligned data model shows that the 2nd principal component coefficients are linearly related with the time delay of different channels (Laguna et al., 2018). Therefore, the 2nd principal component can be used for IZ estimation. The rationale of RT is that it can be used to measure the projections of the line-scan image at a range of angles and determine the propagation of waveforms. When the RT is applied for IZ estimation, it is assumed that waveforms propagate at a constant velocity on both sides of the IZ (Cescon, 2006). However, this is not always the case experimentally, as illustrated from examples of the 2nd principal component coefficients distributions (Figures 2, 3). This might be one reason that the performance of RT is not as consistent as PCA.

The IZ was also estimated from cross correlation analysis applied to bipolar M waves constructed from the monopolar signals, and its performance was the least consistent relative to the visual inspected IZ. In the correlation coefficient method, if one monopolar channel is of poor signal quality, the constructed bipolar configuration may be affected leading to errors in IZ location (Figure 3). This was also demonstrated in our previous study (Huang et al., 2022).

The experimental data sets used for evaluating IZ estimation performance were limited to the BB of healthy subjects. Recordings from other muscles in the future is desirable. It would be clinically relevant to test patients with neurological disorders such as stroke. The IED of the electrode array used in this study was 8 mm. This limited the spatial resolution for IZ detection, but can be increased by using a smaller IED. In addition, this study only considered a single IZ in a muscle. The effects of possible multiple IZs on recorded M waves needs further investigation, as they may compromise accuracy of the estimated IZ (Piccoli et al., 2014), (Huang et al., 2021) (Lateva et al., 2010).

In summary, the current study explored the feasibility of estimating IZ using monopolar high density BB M waves. The PCA based method was able to automatically detect muscle IZs from monopolar M waves, demonstrating a performance most consistent with manual detection by human operators. The findings provide an alternative approach to voluntary contractions for estimating the IZ, which has practical clinical value for patients with compromised ability to voluntarily activate their skeletal musculature.

Data availability statement

The raw data supporting the conclusion of this article will be made available by the authors, without undue reservation.

Ethics statement

The studies involving human participants were reviewed and approved by the ethics committee of Guangdong Work Injury Rehabilitation Center. The patients/participants provided their written informed consent to participate in this study.

Author contributions

Conceptualization: PZ, CK, YZ, and SL; methodology: CH, ZL, MC, and PZ; data collection: CH and CK; data analysis and

interpretation: CH, ZL, MC, YZ, SL, CK, and PZ; writing—original draft preparation: CH; writing—review and editing: PZ, CK, YZ, and SL; Study supervision: CK and PZ All authors have read and agreed to the published version of the manuscript.

Funding

This work was supported by Shandong Provincial Natural Science Foundation (ZR2020KF012, ZR2021QH267, and ZR2021QH053), National Natural Science Foundation of China (82102179), and the Guangzhou Science and Technology Program (201904010256).

Conflict of interest

The authors declare that the research was conducted in the absence of any commercial or financial relationships that could be construed as a potential conflict of interest.

Publisher's note

References

Barbero, M., Merletti, R., and Rainoldi, A. (2012). *Atlas of muscle innervation zones: Understanding surface electromyography and its applications*. Berlin/Heidelberg, Germany: Springer Science & Business Media.

Barbero, M., Gatti, R., Lo Conte, L., Macmillan, F., Coutts, F., and Merletti, R. (2011). Reliability of surface EMG matrix in locating the innervation zone of upper trapezius muscle. *J. Electromyogr. Kinesiol.* 21 (5), 827–833. doi:10.1016/j.jelekin.2011.05.013

Beck, T. W., DeFreitas, J. M., and Stock, M. S. (2012). Accuracy of three different techniques for automatically estimating innervation zone location. *Comput. Methods Programs Biomed.* 105 (1), 13–21. doi:10.1016/j.cmpb.2010.07.003

Campanini, I., Merlo, A., Disselhorst-Klug, C., Mesin, L., Muceli, S., and Merletti, R. (2022). Fundamental concepts of bipolar and high-density surface EMG understanding and teaching for clinical, occupational, and sport applications: Origin, detection, and main errors. *Sensors (Basel)* 22 (11), 4150. doi:10.3390/s22114150

Cescon, C. (2006). "Automatic location of muscle innervation zones from multi-channel surface EMG signals," in IEEE International Workshop on Medical Measurement and Applications, Benevento, Italy, 20-21 April 2006 (IEEE), 87–90.

Chen, Y.-T., Zhang, C., Liu, Y., Magat, E., Verduzco-Gutierrez, M., Francisco, G. E., et al. (2020). The effects of botulinum toxin injections on spasticity and motor performance in chronic stroke with spastic hemiplegia. *Toxins (Basel).* 12 (8), 492. doi:10.3390/toxins12080492

de Souza, L. M. L., Cabral, H. V., de Oliveira, L. F., and Vieira, T. M. (2022). Differences between vastus medialis and lateralis excitation onsets are dependent on the relative distance of surface electrodes placement from the innervation zone location. *J. Electromyogr. Kinesiol* 67, 102713. doi:10.1016/j.jelekin.2022.102713

Dias, N., Li, X., Zhang, C., and Zhang, Y. (2018). Innervation asymmetry of the external anal sphincter in aging characterized from high-density intra-rectal surface EMG recordings. *Neurourol. Urodyn.* 37 (8), 2544–2550. doi:10.1002/nau.23809

Drost, G., Stegeman, D. F., van Engelen, B. G., and Zwarts, M. J. (2006). Clinical applications of high-density surface EMG: A systematic review. *J. Electromyogr. Kinesiol* 16 (6), 586–602. doi:10.1016/j.jelekin.2006.09.005

Enck, P., Franz, H., Davico, E., Mastrangelo, F., Mesin, L., and Merletti, R. (2010). Repeatability of innervation zone identification in the external anal sphincter muscle. *Neurourol. Urodyn.* 29 (3), 449–457. doi:10.1002/nau.20749

Gallina, A., Merletti, R., and Gazzoni, M. (2013). Innervation zone of the vastus medialis muscle: Position and effect on surface EMG variables. *Physiol. Meas.* 34 (11), 1411–1422. doi:10.1088/0967-3334/34/11/1411

Guzmán-Venegas, R. A., Araneda, O. F., and Silvestre, R. A. (2014). Differences between motor point and innervation zone locations in the biceps brachii. An exploratory consideration for the treatment of spasticity with botulinum toxin. *J. Electromyogr. Kinesiol* 24 (6), 923–927. doi:10.1016/j.jelekin.2014.07.012

Guzmán-Venegas, R. A., Bralic, M. P., Cordero, J. J., Cavada, G., and Araneda, O. F. (2016). Concordance of the location of the innervation zone of the tibialis anterior muscle using voluntary and imposed contractions by electrostimulation. *J. Electromyogr. Kinesiol.* 27, 18–23. doi:10.1016/j.jelekin.2016.01.002

Hadoush, H., Tobimatsu, Y., Nagatomi, A., Kimura, H., Ito, Y., and Maejima, H. (2009). Monopolar surface electromyography: A better tool to assess motoneuron excitability upon passive muscle stretching. *J. Physiol. Sci.* 59 (3), 243–247. doi:10.1007/s12576-009-0027-9

Huang, C., Chen, M., Li, X., Zhang, Y., Li, S., and Zhou, P. (2021). Neurophysiological factors affecting muscle innervation zone estimation using surface EMG: A simulation study. *Biosensors* 11 (10), 356. doi:10.3390/bios11100356

Huang, C., Chen, M., Zhang, Y., Li, S., Klein, C. S., and Zhou, P. (2022). A novel muscle innervation zone estimation method using monopolar high density surface electromyography. *IEEE Trans. Neural Syst. Rehabil. Eng.* 31, 2022–2030. doi:10.1109/TNSRE.2022.3215612

Huang, C., Klein, C. S., Meng, Z., Zhang, Y., Li, S., and Zhou, P. (2019). Innervation zone distribution of the biceps brachii muscle examined using voluntary and electrically-evoked high-density surface EMG. *J. Neuroeng. Rehabil.* 16 (1), 73–79. doi:10.1186/s12984-019-0544-6

Jahanmiri-Nezhad, F., Barkhaus, P. E., Rymer, W. Z., and Zhou, P. (2015). Innervation zones of fasciculating motor units: Observations by a linear electrode array. *Front. Hum. Neurosci.* 9, 239. doi:10.3389/fnhum.2015.00239

Kaymak, B., Kara, M., Yağiz On, A., Soylu, A. R., and Özçakar, L. (2018). Innervation zone targeted botulinum toxin injections. *Eur. J. Phys. Rehabil. Med.* 54 (1), 100–109. doi:10.23736/S1973-9087.17.04663-9

Laguna, P., Garde, A., Giraldo, B. F., Meste, O., Jané, R., and Sörnmo, L. (2018). Eigenvalue-based time delay estimation of repetitive biomedical signals. *Digit. Signal Process.* 75, 107–119. doi:10.1016/j.dsp.2018.01.007

Lapatki, B. G., Van Dijk, J. P., Van De Warrenburg, B. P. C., and Zwarts, M. J. (2011). Botulinum toxin has an increased effect when targeted toward the muscle's endplate zone: A high-density surface EMG guided study. *Clin. Neurophysiol.* 122 (8), 1611–1616. doi:10.1016/j.clinph.2010.11.018

Lateva, Z. C., McGill, K. C., and Johanson, M. E. (2010). The innervation and organization of motor units in a series-fibered human muscle: The brachioradialis. *J. Appl. Physiol.* 108, 1530–1541. doi:10.1152/japplphysiol.01163.2009

Li, X., Huang, C., Lu, Z., Wang, I., Klein, C. S., Zhang, L., et al. (2022). Distribution of innervation zone and muscle fiber conduction velocity in the biceps brachii muscle. *J. Electromyogr. Kinesiol.* 63, 102637. doi:10.1016/j.jelekin.2022.102637

Li, X., Lu, Z., Wang, I., Li, L., Stampas, A., and Zhou, P. (2021). Assessing redistribution of muscle innervation zones after spinal cord injuries. *J. Electromyogr. Kinesiol.* 59, 102550. doi:10.1016/j.jelekin.2021.102550

Liu, J., Li, S., Jahanmiri-Nezhad, F., Zev Rymer, W., and Zhou, P. (2019). Motor unit innervation zone localization based on robust linear regression analysis. *Comput. Biol. Med.* 106, 65–70. doi:10.1016/j.compbiomed.2019.01.007

Liu, J., Li, S., Li, X., Klein, C., Rymer, W. Z., and Zhou, P. (2014). Suppression of stimulus artifact contaminating electrically evoked electromyography. *NeuroRehabilitation* 34 (2), 381–389. doi:10.3233/NRE-131045

Liu, Y., Zhang, C., Dias, N., Chen, Y. T., Li, S., Zhou, P., et al. (2020). Transcutaneous innervation zone imaging from high-density surface electromyography recordings. *J. Neural Eng.* 17 (1), 016070. doi:10.1088/1741-2552/ab673e

Mancebo, F. D., Cabral, H. V., de Souza, L. M. L., de Oliveira, L. F., and Vieira, T. M. (2019). Innervation zone locations distribute medially within the pectoralis major muscle during bench press exercise. *J. Electromyogr. Kinesiol* 46, 8–13. doi:10.1016/j.jelekin.2019.03.002

Marateb, H. R., Farahi, M., Rojas, M., Mañanas, M. A., and Farina, D. (2016). Detection of multiple innervation zones from multi-channel surface EMG recordings with low signal to noise ratio using graph-cut segmentation. *PLoS One* 11 (12), e0167954. doi:10.1371/journal.pone.0167954

Mesin, L., Gazzoni, M., and Merletti, R. (2009). Automatic localisation of innervation zones: A simulation study of the external anal sphincter. *J. Electromyogr. Kinesiol.* 19 (6), e413–e421. e413–e421. doi:10.1016/j.jelekin.2009.02.002

Nishihara, K., Chiba, Y., Suzuki, Y., Moriyama, H., Kanemura, N., Ito, T., et al. (2010). Effect of position of electrodes relative to the innervation zone on surface EMG. *J. Med. Eng. Technol.* 34 (2), 141–147. doi:10.3109/03091900903480754

Ostlund, N., Gerdle, B., and Stefan Karlsson, J. (2007). Location of innervation zone determined with multichannel surface electromyography using an optical flow technique. *J. Electromyogr. Kinesiol.* 17 (5), 549–555. doi:10.1016/j.jelekin.2006.06.002

Piccoli, M. B., Rainoldi, A., Heitz, C., Wuthrich, M., Boccia, G., Tomasoni, E., et al. (2014). Innervation zone locations in 43 superficial muscles: Toward a standardization of electrode positioning. *Muscle Nerve* 49, 413–421. doi:10.1002/mus.23934

Rantalainen, T., Kłodowski, A., and Piitulainen, H. (2012). Effect of innervation zones in estimating biceps brachii force-EMG relationship during isometric contraction. *J. Electromyogr. Kinesiol* 22 (1), 80–87. doi:10.1016/j.jelekin.2011.09.012

Rasool, G., Afsharipour, B., and Suresh, N. L. (2017). Spatial analysis of multichannel surface EMG in hemiplegic stroke. *IEEE Trans. Neural Syst. Rehabil. Eng.* 25 (10), 1802–1811. doi:10.1109/TNSRE.2017.2682298

Rodriguez-Falces, J. (2017). A new method for the localization of the innervation zone based on monopolar surface-detected potentials. *J. Electromyogr. Kinesiol. Off. J. Int. Soc. Electrophysiol. Kinesiol.* 35, 47–60. doi:10.1016/j.jelekin.2017.05.004

Rodriguez-Falces, J., and Place, N. (2018). Determinants, analysis and interpretation of the muscle compound action potential (M wave) in humans: Implications for the study of muscle fatigue. *Eur. J. Appl. Physiol.* 118 (3), 501–521. doi:10.1007/s00421-017-3788-5

Shaari, C. M., and Ira Sanders, M. D. (1993). Quantifying how location and dose of botulinum toxin injections affect muscle paralysis. *Muscle Nerve* 16 (9), 964–969. doi:10.1002/mus.880160913

Smith, C. M., Housh, T. J., Zuniga, J. M., Camic, C. L., Bergstrom, H. C., Smith, D. B., et al. (2017). Influences of interelectrode distance and innervation zone on electromyographic signals. *Int. J. Sports Med.* 38 (2), 111–117. doi:10.1055/s-0042-119398

Tucker, K. J., and Türker, K. S. (2005). A new method to estimate signal cancellation in the human maximal M-wave. *J. Neurosci. Methods* 149 (1), 31–41. doi:10.1016/j.jneumeth.2005.05.010

Ullah, K., Cescon, C., Afsharipour, B., and Merletti, R. (2014). Automatic detection of motor unit innervation zones of the external anal sphincter by multichannel surface EMG. *J. Electromyogr. Kinesiol.* 24 (6), 860–867. doi:10.1016/j.jelekin.2014.05.003

Van Campenhout, A., and Molenaers, G. (2011). Localization of the motor endplate zone in human skeletal muscles of the lower limb: Anatomical guidelines for injection with botulinum toxin. *Dev. Med. Child. Neurol.* 53 (2), 108–119. doi:10.1111/j.1469-8749.2010.03816.x

Ye, X., Beck, T. W., and Wages, N. P. (2015). Relationship between innervation zone width and mean muscle fiber conduction velocity during a sustained isometric contraction. *J. Musculoskelet. Neuronal Interact.* 15 (1), 95–102.

Zhang, C., Chen, Y. T., Liu, Y., Zhou, P., Li, S., and Zhang, Y. (2019). Three dimensional innervation zone imaging in spastic muscles of stroke survivors. *J. Neural Eng.* 16 (3), 034001. doi:10.1088/1741-2552/ab0fe1

Zhang, C., Dias, N., He, J., Zhou, P., Li, S., and Zhang, Y. (2020). Global innervation zone identification with high-density surface electromyography. *IEEE Trans. Biomed. Eng.* 67 (3), 718–725. doi:10.1109/TBME.2019.2919906

Zhang, C., Peng, Y., Liu, Y., Li, S., Zhou, P., Rymer, W. Z., et al. (2017). Imaging three-dimensional innervation zone distribution in muscles from M-wave recordings. *J. Neural Eng.* 14 (3), 036011. doi:10.1088/1741-2552/aa65dd

Zhang, C., Gutierrez-Verduzco, M., Francisco, G. E., Ping, Z., Sheng, L., Yingchun, Z., et al. (2021). Improving botulinum toxin efficiency in treating post-stroke spasticity using 3D innervation zone imaging. *Int. J. Neural Syst.* 31, 2150007. doi:10.1142/S0129065721500076

frontiers | Frontiers in Physiology

TYPE Original Research
PUBLISHED 16 March 2023
DOI 10.3389/fphys.2023.1085871

OPEN ACCESS

EDITED BY
Lucas Omar Müller,
University of Trento, Italy

REVIEWED BY
Wenjun Tan,
Northeastern University, China
Alexander Ruesch,
Carnegie Mellon University, United States

*CORRESPONDENCE
Junfeng Feng,
fengjfmail@163.com
Dingchang Zheng,
dingchang.zheng@coventry.ac.uk

SPECIALTY SECTION
This article was submitted to Computational Physiology and Medicine, a section of the journal Frontiers in Physiology

RECEIVED 31 October 2022
ACCEPTED 24 February 2023
PUBLISHED 16 March 2023

CITATION
Liu H, Pan F, Lei X, Hui J, Gong R, Feng J and Zheng D (2023), Effect of intracranial pressure on photoplethysmographic waveform in different cerebral perfusion territories: A computational study. *Front. Physiol.* 14:1085871. doi: 10.3389/fphys.2023.1085871

Effect of intracranial pressure on photoplethysmographic waveform in different cerebral perfusion territories: A computational study

Haipeng Liu[1], Fan Pan[2], Xinyue Lei[2], Jiyuan Hui[3], Ru Gong[3], Junfeng Feng[3]* and Dingchang Zheng[1]*

[1]Research Centre for Intelligent Healthcare, Coventry University, Coventry, United Kingdom, [2]College of Electronics and Information Engineering, Sichuan University, Chengdu, China, [3]Brain Injury Center, Renji Hospital, School of Medicine, Shanghai Jiao Tong University, Shanghai, China

Background: Intracranial photoplethysmography (PPG) signals can be measured from extracranial sites using wearable sensors and may enable long-term non-invasive monitoring of intracranial pressure (ICP). However, it is still unknown if ICP changes can lead to waveform changes in intracranial PPG signals.

Aim: To investigate the effect of ICP changes on the waveform of intracranial PPG signals of different cerebral perfusion territories.

Methods: Based on lump-parameter Windkessel models, we developed a computational model consisting three interactive parts: cardiocerebral artery network, ICP model, and PPG model. We simulated ICP and PPG signals of three perfusion territories [anterior, middle, and posterior cerebral arteries (ACA, MCA, and PCA), all left side] in three ages (20, 40, and 60 years) and four intracranial capacitance conditions (normal, 20% decrease, 50% decrease, and 75% decrease). We calculated following PPG waveform features: maximum, minimum, mean, amplitude, min-to-max time, pulsatility index (PI), resistive index (RI), and max-to-mean ratio (MMR).

Results: The simulated mean ICPs in normal condition were in the normal range (8.87–11.35 mm Hg), with larger PPG fluctuations in older subject and ACA/PCA territories. When intracranial capacitance decreased, the mean ICP increased above normal threshold (>20 mm Hg), with significant decreases in maximum, minimum, and mean; a minor decrease in amplitude; and no consistent change in min-to-max time, PI, RI, or MMR (maximal relative difference less than 2%) for PPG signals of all perfusion territories. There were significant effects of age and territory on all waveform features except age on mean.

Conclusion: ICP values could significantly change the value-relevant (maximum, minimum, and amplitude) waveform features of PPG signals measured from different cerebral perfusion territories, with negligible effect on shape-relevant features (min-to-max time, PI, RI, and MMR). Age and measurement site could also significantly influence intracranial PPG waveform.

KEYWORDS

intracranial pressure (ICP), photoplethysmography (PPG), windkessel effect, computational simulation, artery network, cerebral microcirculation

1 Introduction

Intracranial pressure (ICP), defined as the pressure within the craniospinal compartment, is an important physiological parameter that reflects the biomechanical status of the brain. ICP is derived from cerebral blood and cerebrospinal fluid (CSF) circulatory dynamics. ICP can be significantly changed in many neurological diseases (Czosnyka and Pickard, 2004). For decades, ICP monitoring has been a cornerstone of traumatic brain injury (TBI) management (Stocchetti et al., 2014). Currently, external ventricular drain (EVD) is considered as the gold standard of ICP monitoring due to its accuracy with additional function of CSF drainage (Harary et al., 2018). In EVD measurement, the ICP is transmitted into an external saline-filled tube through a strain-gauge transducer for pressure measurement. The insertion of the tube is invasive with a 5%–7% risk of hemorrhage, and is difficult to perform in some patients with inherently small ventricles size (Harary et al., 2018). To ease the postoperative ICP monitoring especially in TBI patients, it is essential to develop non-invasive methods of ICP monitoring.

The photoplethysmography (PPG) technology has been applied in the daily monitoring of many physiological parameters and may enable non-invasive long-term ICP monitoring. The cyclic fluctuations of a PPG signal reflect volumetric changes in the microcirculation, which is regulated by many physiological factors, e.g., respiratory pattern, arterial stiffness, and the mechanical properties of surrounding tissues. Therefore, PPG signals derived from the distal area of intracranial arteries might reflect ICP-related changes in cerebral microcirculation. The infra-red PPG signals measured from extracranial skin surface could reflect the intracranial microcirculation in different cerebral perfusion territories (Viola et al., 2013). A recent pilot study showed that the PPG signal recorded non-invasively from forehead can detect apnea-induced cerebral blood flow oscillations (Alex et al., 2019). In a pilot study on 14 subjects, Morgan et al. (2021) estimated ICP using retinal vein PPG signal and achieved clinically acceptable accuracy (−0.35 ± 3.6 mmHg). These studies indicated that intracranial PPG signals measured from extracranial areas might be a promising tool for non-invasive ICP monitoring. However, it is uncertain if ICP changes could generate waveform changes of intracranial PPG signals, with a lack of theoretical basis and in-depth analysis from a physiological perspective.

Computational modelling and simulation based on biomechanical and hemodynamic theories have been widely applied in the investigation of intracranial blood flow and ICP (Liu et al., 2020b). Especially, the Windkessel model is a highly simplified one where the resistance and compliance in the circulatory system are simulated as resistors and capacitors in a circuit (Alastruey et al., 2007). The unidirectional flow in the CSF circulation can be simulated using diode elements (Ursino and Di Giammarco, 1991). Recently, data-driven algorithms were proposed to improve the accuracy of ICP simulation. It was suggested that ICP can be computationally estimated from the cerebral blood flow and blood pressure (Kashif et al., 2012). However, the biomechanical properties of arteries are non-linear and age-dependent, which was not fully considered in existing models of ICP simulation. Moreover, the hemodynamic data in existing models were from invasive measurement. The relationship between non-invasively measured intracranial PPG and ICP has not been comprehensively investigated using computational modelling.

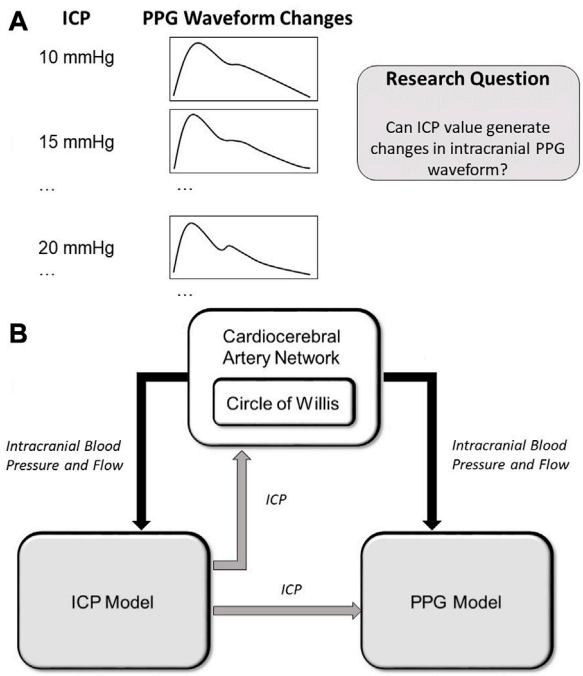

FIGURE 1
(A) Scientific hypothesis of this paper: changes in ICP values can lead to PPG waveform changes which can be computationally simulated. **(B)** Structure of the computational model. The arrows show the data flows. ICP: intracranial pressure; PPG: photoplethysmography.

To fill this research gap, we aim to develop a computational model of intracranial PPG signals and investigate if the changes in ICP could lead to the changes in intracranial PPG signals of different cerebral perfusion territories (Figure 1).

2 Methods

2.1 Overview of the computational model

As shown in Figure 1A, we hypothesize that the changes in ICP can lead to waveform changes in intracranial PPG signals. To verify this hypothesis, we developed a computational model to simulate the PPG signals of different cerebral perfusion territories in different ICP conditions. The computational model consists of three parts: A cardiocerebral artery network, an ICP model, and a PPG model (Figure 1B). The cardiocerebral artery network simulated the blood flow of intracranial arteries and the local blood pressure, which were transmitted to the ICP and PPG models as model input. The ICP signal derived from the ICP model was transmitted back to the cardiocerebral artery networks to generate the boundary conditions. At the same time, the ICP model generates the input of the PPG model at microcirculatory level. In summary, the three parts are interactive. All the components of the three parts are based on lump-parameter Windkessel models. The computational models are

TABLE 1 Data sources of the parameters in the computational models.

Models	Data sources and references of the parameters
Cardiocerebral artery network	Anatomic parameters of arteries: Table 1 of (Alastruey et al., 2007); Calculation of parameters of Windkessel elements: Eqs 1–3 and Table 1 of (Zhang et al., 2014)
Age-dependent non-linear arterial capacitance	Parameters in age-dependent capacitance of aorta: Table 1 and Eq. 5 of (Wesseling et al., 1993); Parameters of age-dependent capacitance of CCA: basic function from Table 1 and Eq. 1 of (Kopustinskas et al., 2010), References pressure (mean pressure of healthy adults) from the subsection "Theoretical Background" and Eq. 1 of (Giudici et al., 2022), age-dependent capacitance changes from Figure 2 of (Vriz et al., 2017)
ICP model	Parameters of circuit elements in the ICP model: Table 1 of (Lee et al., 2015); Piecewise ICP function: References ICP value (5 mmHg) from (Ryding, 2017) and (Alperin et al., 2000); parameter in the inverse proportional function from the subsection "Assignment of Parameter Basal Values" of (Ursino and Lodi, 1997) and Figure 8 of (Ursino and Di Giammarco, 1991)
PPG model	Values of distal resistance and capacitance: same as those in cardiocerebral artery network; Ratios between different components: Table 1 of (Tanaka, 2022)

CCA, common carotid artery; ICP, intracranial pressure; PPG, photoplethysmography.

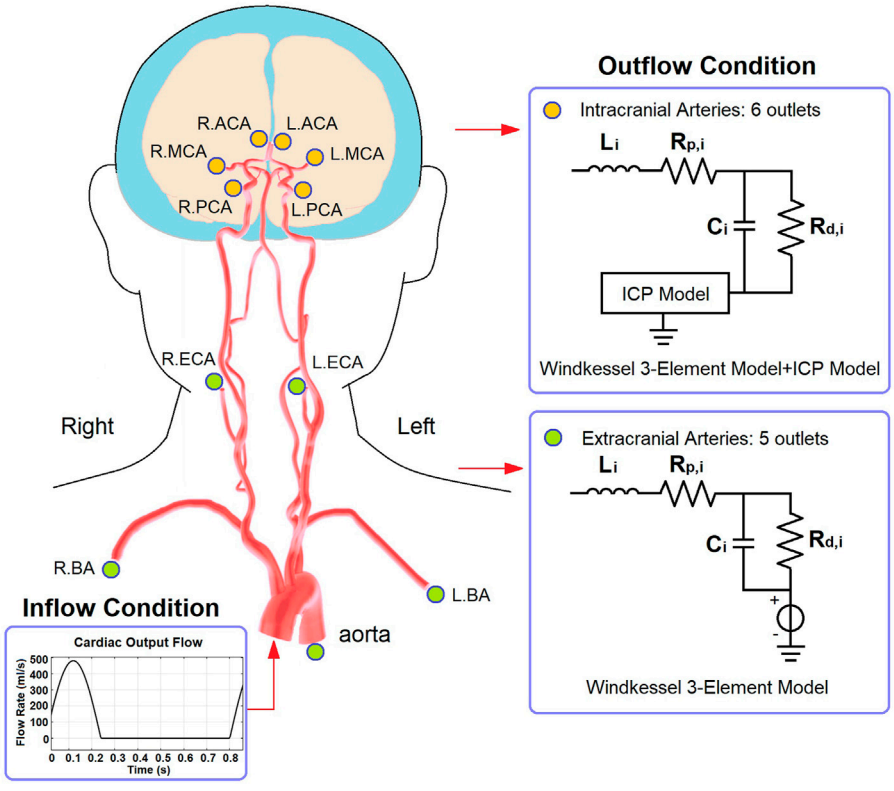

FIGURE 2
The structure of cardiocerebral artery network and the boundary conditions. The illustration of artery structure is adapted from Figure 2 of (Kang et al., 2021).

detailed in the following subsections. The parameters in the models are listed in Table 1.

2.2 Cardiocerebral artery network

The cardiocerebral arterial network was based on the classic brain circulation model proposed by Alastruey et al. (2007), with outlet boundary conditions of intracranial arteries modified to include the effect of ICP on cerebral microcirculation. The cardiac output flow (i.e., the inflow of the aorta) was used as the inlet boundary condition. The structure of the artery network starts from the aorta and includes the major branches of intracranial arteries (Figure 2). The intermediate (i.e., connecting other artery segments without any inlet or outlet) branches included: ascending aorta, aortic arch (in two segments), brachiocephalic artery, common carotid arteries (left and right), subclavian arteries (left and right), vertebral arteries (left and right), internal carotid arteries

(left and right, both in two segments), basilar artery, as well as the connecting arteries in the Circle of Willis, i.e., posterior communicating arteries (left and right), anterior communicating artery, and the first segments of anterior and posterior cerebral arteries (left and right, for both). Each intermediate artery was simulated using a three-element Windkessel model which consisted of a resistor, a capacitor, and an inductor that reflected the resistance, capacitance, and inductance of an elastic artery wall, respectively (Figure 2). The anatomic properties of the arteries and the methods of calculating the values of circuit elements can be found in Alastruey et al. (2007) and Zhang et al. (2014) (Table 1).

Regarding the outlets, the extracranial ones included thoracic aorta, brachial arteries (left and right), and external carotid arteries (left and right). These arteries were connected to a 3-element Windkessel model (Figure 2). The resistance included peripheral and distal ones which denoted the flow resistances in the artery and microcirculation, respectively. The outlet pressure was the venous pressure (5 mmHg) which was simulated by a voltage source. For the intracranial arteries (anterior, middle, and posterior cerebral arteries, left and right for all), the outlet pressure at microvascular level (i.e., prearteriole pressure) was derived from the ICP value generated by the ICP model.

2.3 Age-dependent non-linear arterial capacitance

To simulate the artery blood flow in different age groups, we used age-dependent parameters in the Windkessel models of aorta and common carotid arteries.

In the aorta model, we used the pressure-dependent Windkessel capacitance element proposed by Wesseling et al. (1993). The capacitance value depends non-linearly on the pressure:

$$C_A(P) = \frac{A_{max} \cdot L}{\pi P_1 \left[1 + \left(\frac{P-P_0}{P_1}\right)^2\right]} \tag{1}$$

where A_{max} is the maximal cross-sectional area, approximated as 5.8 cm^2 for male adults, L is the length of aorta, P denotes the local blood pressure, whilst parameter P_0 and P_1 are age-dependent reference pressure values.

$$P_0 = (76 - 0.98^{*}age)\, mmHg \quad age \in [20, 70] \tag{2}$$

$$P_1 = (57 - 0.44^{*}age)\, mmHg \quad age \in [20, 70] \tag{3}$$

The biomechanical relationship between the capacitance of common carotid artery and local blood pressure is described by a non-linear exponential function:

$$C_{CCA}(P) = a \cdot e^{-b \cdot P(t)} \tag{4}$$

where $a = 3.14\, ml^{*}mmHg^{-1}$, $b = 0.018\, mmHg^{-1}$, and $P(t)$ denotes transient value of blood pressure in common carotid artery which is a major source of the capacitance effect on intracranial blood flow (Kopustinskas et al., 2010).

$$C_{CCA}(P) = C_{CCA}\left(P_{ref}\right) \cdot e^{-b \cdot \left[P(t) - P_{ref}\right]} \cdot \left[1.3 - 0.012^{*}(age - 20)\right] \quad age \in [20, 70] \tag{5}$$

where $P_{ref} = 100\, mmHg$ is an established value for mean pressure of healthy adults and has been used in computational simulation studies (Giudici et al., 2022). The age-dependent function is based on a large-scale physiological measurement of common carotid artery stiffness in 900 healthy subjects (Vriz et al., 2017).

2.4 ICP model

The computational model for continuous ICP simulation was based on the classic model proposed by Ursino and Di Giammarco (1991) which has been widely used in ICP estimation (Lee et al., 2015). The model includes resistors and capacitors to simulate the overall resistance and capacitance of intracranial arteries, microcirculation, and veins, respectively (Figure 3). Two diodes were used to simulate the unidirectional flow in the CSF circulation.

The intracranial capacitance is a piecewise function of ICP, which is a constant when $ICP < 5\, mmHg$ (venous pressure) and depends non-linearly on ICP when $ICP \geq 5\, mmHg$:

$$C = \begin{cases} 7.502^{*}10^{-9}{}^{*}Ratio_{CD} & ICP \in [0, 666.5) \\ \dfrac{5^{*}10^{-6}}{ICP}{}^{*}Ratio_{CD} & ICP \in [666.5, +\infty) \end{cases} \tag{6}$$

where the unit of ICP and intracranial capacitance are Pa and m^3/Pa, respectively. $Ratio_{CD}$ denotes the ratio of intracranial capacitance decrease, which is used to simulate the pathological conditions due to the brain injury with acute increase of brain tissue volume where ICP increases. The connection point of the two subintervals (5 mmHg) was modified from the reference pressure of 6 mmHg in (Ryding, 2017) to match the reference venous pressure. The reference ICP value of 5 mmHg is also in accordance with the clinical observation after the withdrawal of CSF (Alperin et al., 2000). Both normal and pathological situations were simulated, therefore, the parameter in the inverse proportional function ($5^{*}10^{-6}$ m^3, or 5 ml) was set marginally below the normal range (6.66–20 ml) derive from (Ursino and Lodi, 1997) and within the range used in the simulation of pathological situations (1.92–6.41 ml) (Ursino and Di Giammarco, 1991).

2.5 PPG model

The PPG model was based on a cerebral microcirculation model including arteriole, capillary, and venule components (Figure 4) (Tanaka, 2022). The ratios of element values among the different components were from physiological measurement results of human cerebral circulation (Mandeville et al., 1999). The inputs of the model include prearteriole pressure and ICP generated by the cardiocerebral artery network and ICP model, respectively. The PPG signals were generated from distal perfusion territories of anterior, middle, and posterior cerebral arteries (ACA, MCA, and PCA) on the left side. For the territory of a cerebral artery (e.g., MCA), the arteriovenous anastomoses in brain tissues were simulated by a resistance between the middle points of arteriole and venule components (RAVA-MCA in Figure 4). The PPG signal was simulated as the voltage along the capacitance elements in the Windkessel model (Figure 4). Therefore, the simulation result

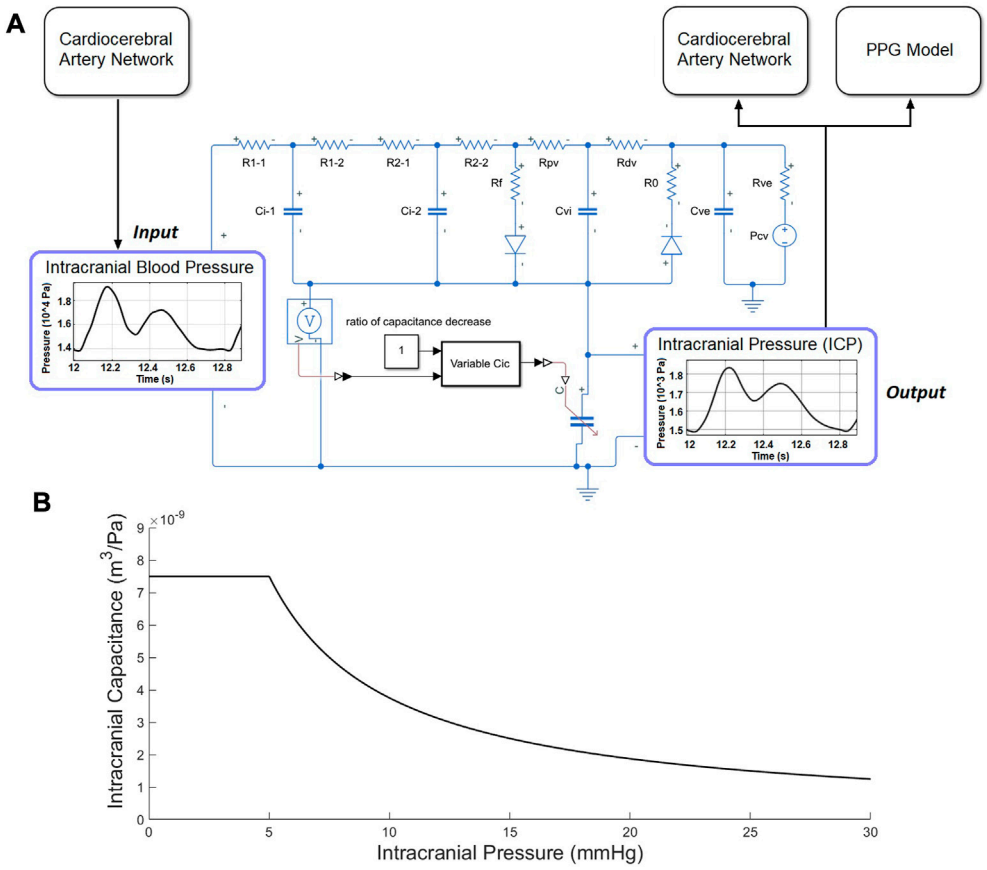

FIGURE 3
ICP model. **(A)** Electric analog of the human intracranial hydrodynamics for ICP simulation. R1-1, R1-2, and Ci-1: hydraulic resistance and compliance of the proximal arterial cerebrovascular bed (basal brain arteries and large pial arteries), respectively; R2-1, R2-2, and Ci-2: hydraulic resistance and compliance of the distal arterial cerebrovascular bed (medium and small pial arteries), respectively; Cic: intracranial tissue compliance; Cvi: intracranial venous compliance; Rpv: hydraulic resistance of the proximal venous cerebrovascular bed; Rdv: hydraulic resistance of the distal venous cerebrovascular bed (lateral lacunae and bridge veins); Rf: CSF formation resistance; Ro: CSF outflow resistance; Rve and Cue: hydraulic resistance and compliance of the extracranial venous pathways; Pcv: central venous pressure. **(B)** The piecewise function between ICP and intracranial capacitance.

("simulated PPG") reflects the pressure drop on microvascular level induced by the volumetric changes from which the PPG signal originates, whereas the unit is in Pa instead of V or mV.

2.6 PPG waveform features

To quantitatively investigate the ICP-induced changes of PPG waveform, we used five waveform features, as shown in Figure 5. Besides the maximum and minimum (i.e., baseline) values, we calculated the mean value as the integration of the PPG signal in a cardiac cycle divided by the length of a cardiac cycle (T): $\frac{\int_0^T PPG(t)dt}{T}$, where *PPG(t)* is the transient value of simulated PPG signal, and $T = 0.8s$. The amplitude was defined as the difference between the maximum and the minimum: $Amplitude = PPG_{max} - PPG_{min}$. The min-to-max period was defined as the length of the period from minimum to maximum, which was named as rising time in existing studies on finger PPG signals where the systolic period was clearly observable (Khalid et al., 2020).

Based on the directly measured basic waveform features, we calculated three secondary waveform features which have been applied in hemodynamic research: pulsatility index (PI): $PI = \frac{PPG_{max} - PPG_{min}}{PPG_{mean}}$; resistive index (RI): $RI = \frac{PPG_{max} - PPG_{min}}{PPG_{max}}$, and the ratio between maximum and mean values of PPG signal, i.e., max-to-mean ratio (MMR): $MMR = \frac{PPG_{max}}{PPG_{mean}}$. The definitions of PI and RI were in accordance with those in 4D flow magnetic resonance imaging (MRI) observation of cerebral microcirculation based on flow velocity (Rivera-Rivera et al., 2015).

2.7 Simulation and evaluation

The simulation was performed on MATLAB-Simulink (Version: r2021a, MathWorks, Natick, MA, United States). We simulated the ICP and PPG signals in male subjects of three ages: 20, 40, and 60 years old. The simulation was repeated in four pathophysiological conditions of intracranial

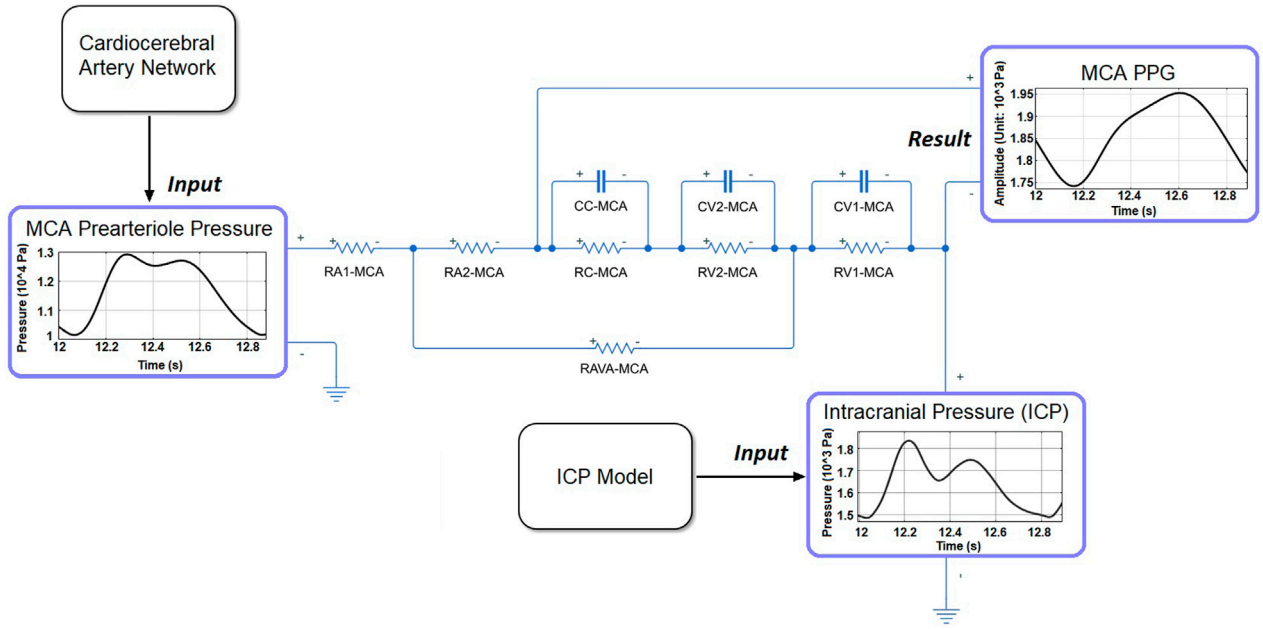

FIGURE 4
The structure of microcirculatory model to generate the PPG signal in MCA territory. RA1-MCA and RA2-MCA: equally divided arteriole resistances. RC-MCA: capillary resistance. RV2-MCA and RV1-MCA: equally divided venule resistances. CC-MCA: capillary capacitance. CV1-MCA and CV2-MCA: equally divided venular capacitances.

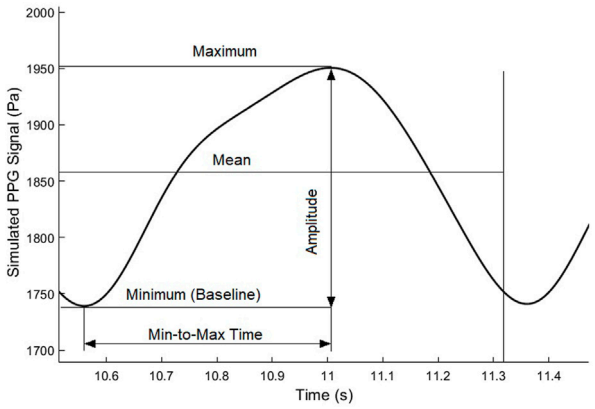

FIGURE 5
Basic waveform features of a simulated PPG signal in a cardiac cycle.

capacitance decrease: 0 (i.e., normal status), 25%, 50%, and 75%. To verify the model, the ICP values simulated at normal condition were compared with the results of existing physiological measurement. Each simulation lasted 30 s. To avoid any initial effect, the features were measured in the first cardiac cycle after 10 s when the signal was stable. The PPG waveform features derived were quantitatively compared between different intracranial capacitance conditions to investigate if ICP changes could lead to the waveform changes of intracranial PPG signals.

3 Results

3.1 Model validation: ICP and PPG waveforms in different ages

As shown in Figure 6, the simulated ICP signals of 20, 40, and 60 years old subjects with normal intracranial capacitance have minor differences in waveform but are similar in range: 9.31–11.12, 9.13–11.35, and 8.87–11.68 mmHg, with nearly identical mean values of 11.12, 11.35, and 11.68 mmHg (Figure 7). These mean ICP values were within the normal range of healthy adults: 10–15 mmHg (Rangel-Castillo et al., 2008).

As to the PPG waveform, it can be observed that PPG signals of ACA, MCA, and PCA territories are similar in amplitude and baseline, but different in waveform (Figure 6). There is no sharp fluctuations in the PPG waveform, which is in accordance with the fact that high-frequency components (i.e., sharp fluctuations) are absorbed by the capacitance of large arteries before arriving arterioles. The results of simulated PPG waveform features in Table 2 are in accordance with the 4D MRI flow observations that PI is large in PCA compared with MCA, and in older subjects (Rivera-Rivera et al., 2015).

As a more general case of all the simulations, Figure 7 shows the simulated waveforms of arterial blood pressure, PPG, and ICP of a 40 years old subject with 25% decrease of intracranial capacitance. It can be observed that the dicrotic notch and secondary peak are blurred with a flat systolic peak in the arterial blood pressure of intracranial arteries, which reflects the buffering effect of intracranial capacitance on the pulse wave (i.e., neutralization of backward wave) and is basically in accordance with existing modelling studies (Blanco et al., 2017; Schollenberger et al., 2021).

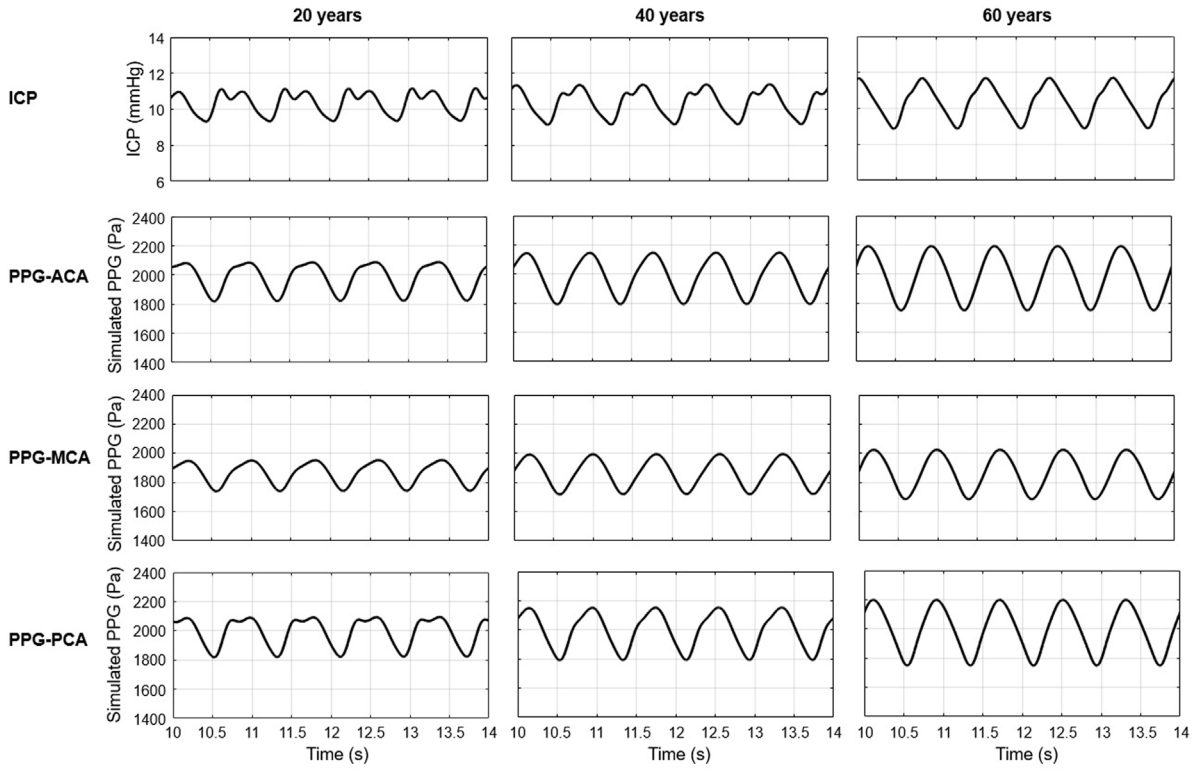

FIGURE 6
Simulated ICP and PPG waveforms during five cardiac cycles (10–14s) in 20, 40, and 60 years old healthy male subjects with normal intracranial capacitance.

Therefore, the model can reliably simulate the ICP values in subjects with different ages, and reflect the waveform features of human cerebral microcirculation in different perfusion territories.

3.2 ICP values in different intracranial capacitance conditions

As shown in Figure 8, ICP increases when intracranial capacitance decreases. Between different ages, the differences in maximum and minimum of ICP are very limited, while the difference in mean ICP is even negligible. With 50% decrease of intracranial capacitance, the mean values of ICP in all three ages are above 15 mmHg (16–16.1 mmHg), which is beyond the normal range (7–15 mmHg). With 75% decrease of intracranial capacitance, the mean values of ICP in all three ages are marginally beyond 20 mmHg (20.2–20.3 mmHg) where clinical intervention is recommended (Rangel-Castillo et al., 2008).

3.3 PPG waveform features in different intracranial capacitance conditions

Figure 9 and Figure 10 illustrate the effects of age and intracranial capacitance condition on the basic and secondary PPG features in different cerebral perfusion territories.

In Figure 9, the maximum, minimum, and mean values significantly decrease with intracranial capacitance, while the ICP increases from <11.5 mmHg to hypertensive condition (>20 mmHg). Meanwhile, there is a minor decrease in amplitude. In contrast, there is no consistent changes in min-to-max time or any secondary waveform feature (Figure 10) where the maximal relative difference is less than 2% among all intracranial capacitance conditions.

On the other hand, we observed significant effects of age and cerebral perfusion territory on all the waveform features. When age increases, maximum, amplitude, PI, RI, and MMR are higher, while the minimum and min-to-max time are lower, with negligible changes of the mean. Compared with PCA and ACA territories, MCA territory has lower maximum, minimum, amplitude, PI, RI, and MMR, with lower age-relevant differences in min-to-max time (Figure 9 and Figure 10).

4 Discussion

4.1 Summary of results

In this study, based on lump-parameter Windkessel models with age-dependent non-linear elements, we simulated the effect of ICP increase due to intracranial capacitance decrease on the waveform features of PPG signals of different cerebral perfusion territories in subjects of different ages. The simulation results showed that ICP changes could significantly influence the maximum, minimum, and amplitude of PPG signals, with limited effect on min-to-max

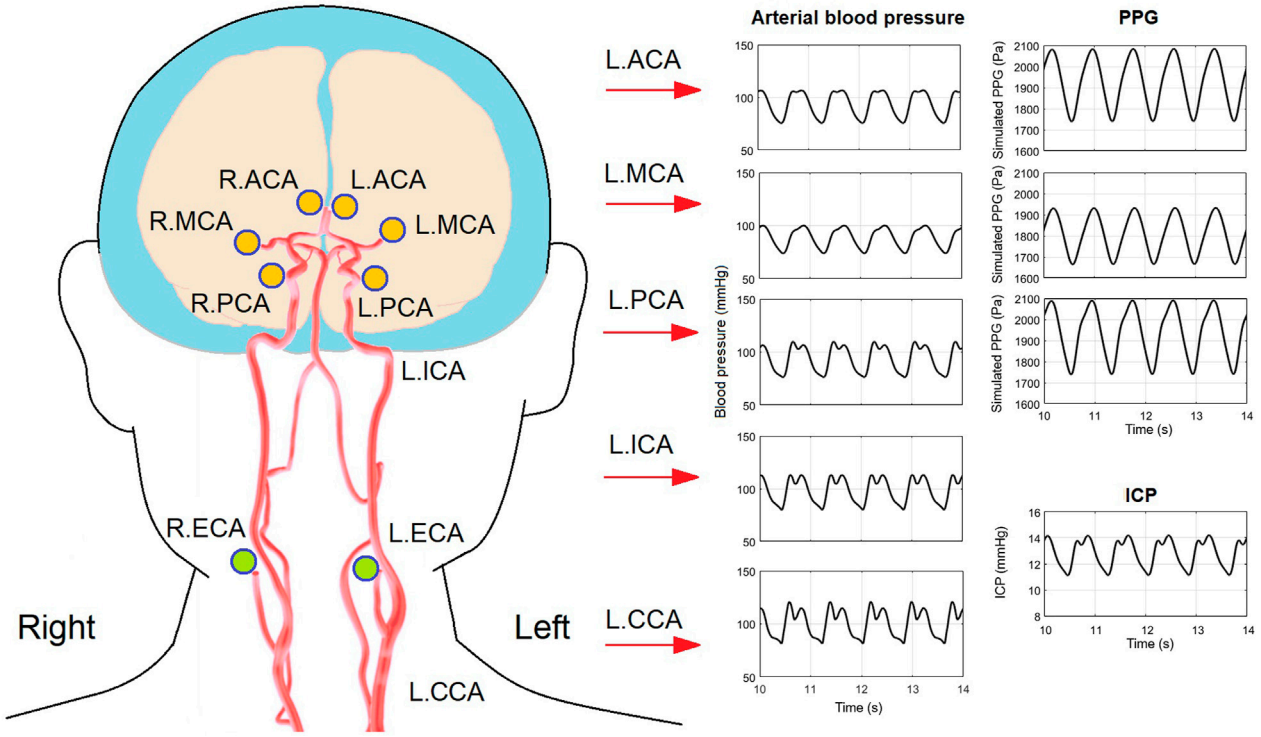

FIGURE 7
Arterial blood pressure, PPG, and ICP waveforms in a 40-years old subject with 20% decrease of intracranial capacitance. The illustration of artery structure is adapted from (Kang et al., 2021).

TABLE 2 Simulated PPG waveform features in normal intracranial capacitance.

	ACA			MCA			PCA		
Age (years)	20	40	60	20	40	60	20	40	60
PI	0.134	0.178	0.222	0.114	0.147	0.182	0.137	0.181	0.226
RI	0.127	0.165	0.201	0.108	0.138	0.167	0.130	0.167	0.205
MMR	1.052	1.081	1.104	1.047	1.069	1.085	1.050	1.079	1.104

PI, pulsatility index; RI, resistive index; MMR, max-to-mean ratio.

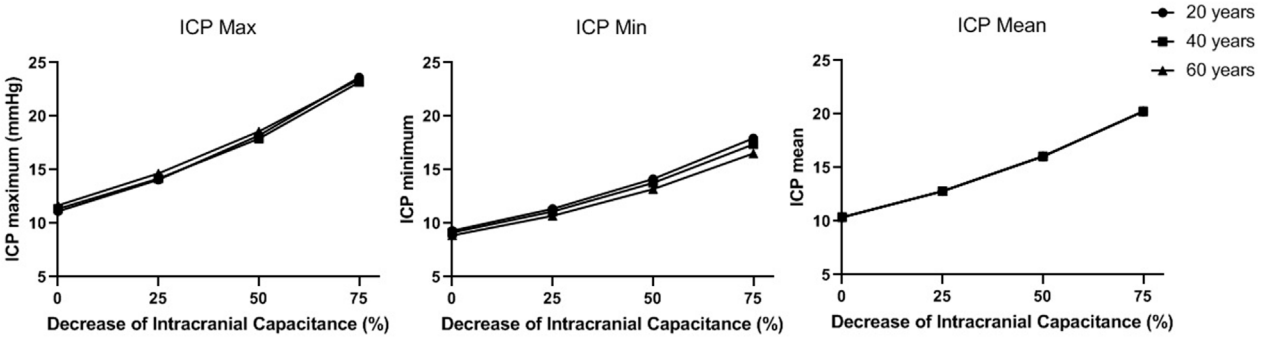

FIGURE 8
The maximum, minimum, and mean values of ICP in a cardiac cycle in different intracranial capacitance conditions.

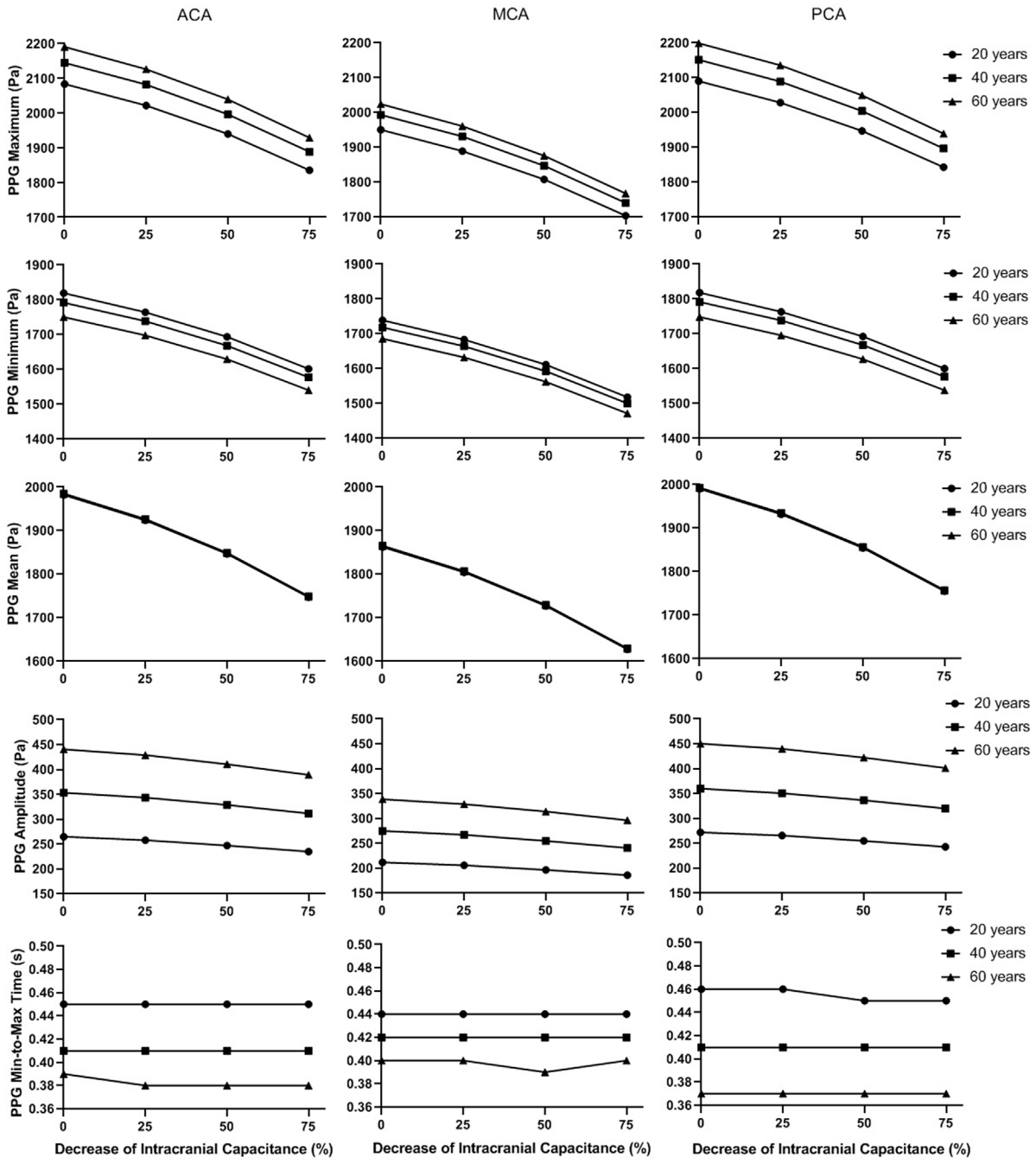

FIGURE 9
The basic waveform features of the simulated PPG signals in different intracranial capacitance conditions.

time, PI, RI, and MMR. As far as we know, this is the first study that quantitatively investigates the effect of ICP on the waveform features of intracranial PPG signals using computational simulation.

4.2 Clinical need on non-invasive ICP monitoring: A wearable pathway *via* PPG?

Recent years have witnessed the development of non-invasive ICP monitoring technologies, including transcranial Doppler measurement of cerebral blood flow, near-infrared spectroscopy (NIRS), tympanic membrane displacement (TMD) (Lee et al., 2020), ophthalmodynamometry (Nag et al., 2019), optic nerve sheath diameter (ONSD) analysis based on ultrasound (i.e., transcranial Doppler) or radiological [e.g., computed tomography (CT), MRI, and optical coherence tomography (OCT)] data, and other imaging-based methods (e.g., analysis of CT-derived ratio of CSF volume to the total intracranial volume) (Harary et al., 2018; Nag et al., 2019). These techniques enable the non-invasive measurement of ICP in clinical practice. However, these methods depend on expensive

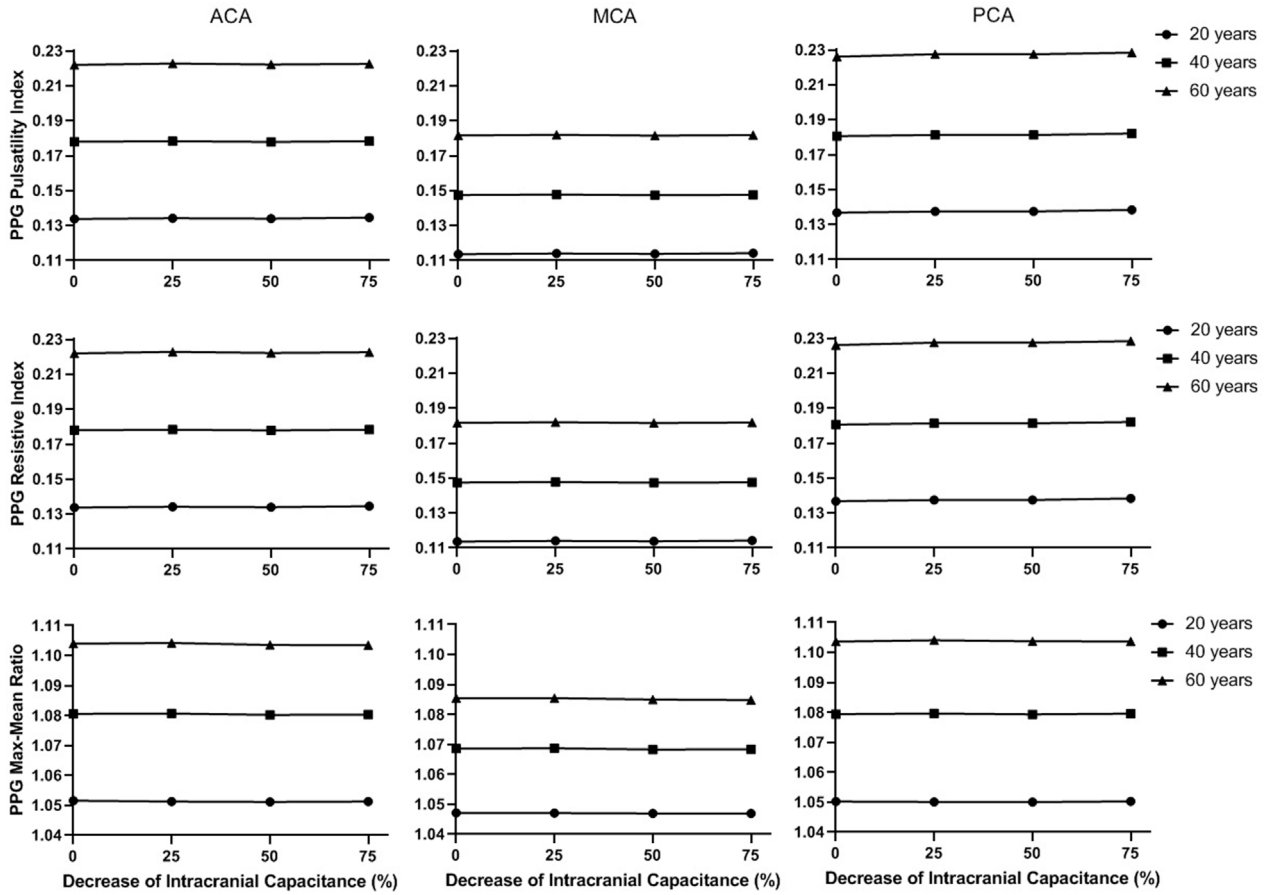

FIGURE 10
The secondary waveform features of the simulated PPG signals in different intracranial capacitance conditions.

devices or clinical imaging data, which require professional skills of operation and data processing. Considering the risk of infection and limited medical resources, the postoperative ICP monitoring was often performed for a couple of days or a week for invasive and non-invasive methods, respectively, despite its clinical significance (Chang et al., 2019; Chang et al., 2021). To achieve better postoperative management of TBI patients, there is a high clinical need for easy-to-perform and low-cost techniques of non-invasive long-term ICP monitoring.

Compared with existing techniques, PPG signals can be detected from different body sites using low-cost wearable sensors without any need for expertise or training. PPG technology has been widely used in healthcare monitoring and early detection of cardiovascular diseases (Allen, 2007; Liu et al., 2019). Transcranial Doppler ultrasonography (TCD) and servo-controlled finger PPG have been applied in continuous bedside monitoring of cerebral blood flow and blood pressure, as well as the evaluation of cerebral autoregulation (Aries et al., 2010). Some pilot studies showed that PPG waveform features may indicate pathological hemodynamic changes in cerebral circulation on which ICP has a strong influence. The amplitude of PPG signals measured from bilateral index fingers is associated with cerebral artery stenosis (Kang et al., 2018). The TCD-derived PI and PPG waveform are associated with cerebrovascular hemodynamic changes in the patients with the disorder of consciousness (Liu et al., 2016). Morgan et al. (2014) developed a modified PPG system using video recordings taken through an ophthalmodynamometer and timed to the cardiac cycle to investigate the phase lag between retinal venous and arterial pulses. Based on this modified PPG system, Abdul-Rahman et al. (2020) recently estimated ICP value from retinal vascular pulse wave attenuation. Abnormal morphological and biomechanical properties of retinal veins have been proven to be biomarkers to guide diagnosis and management of elevated ICP (Moss, 2021). In accordance with existing studies, our results provided new evidence that waveform features (i.e., maximum, minimum, mean, and amplitude) of intracranial PPG signals could reflect the changes in ICP. Therefore, PPG technology may enable the non-invasive long-term ICP monitoring.

Meanwhile, the majority of existing studies on PPG-assisted ICP monitoring are based on the PPG signals of fingers, retina, or other extracranial sites. The transcranial brain PPG technology was developed to study the venules of cerebral cortex (Viola et al., 2013) but has not been applied in ICP monitoring. Our results provide new reference on ICP estimation based on intracranial PPG signals which directly reflect the status of cerebral microcirculation.

4.3 ICP-relevant PPG waveform features

We observed that ICP significantly influenced the value-related waveform features (i.e., maximum, minimum, mean, and amplitude), with negligible effect on shape-related ones (i.e., min-to-max time, PI, RI, and MMR). Especially, the ICP changes did not generate any consistent differences in PI, which is in accordance with Fernando et al.'s observation in a recent systematic review that PI derived from TCD signal (TCD-PI) has poor accuracy in estimating ICP (range of area under the receiver operating characteristic curve: .550–.718) (Fernando et al., 2019). Here we try to provide an initial explanation on this phenomenon from a physiological perspective based on our computational model. The changes in intracranial capacitance influence the ICP, thus the boundary conditions of intracranial arteries in the cardiocerebral artery network. However, the fluctuations of ICP signals in a cardiac cycle are limited (amplitude<5 mmHg, Figure 6 and Figure 8). Thus, the increase of ICP changes the value of outlet pressure in the model, without generating much pulsatility at the outlets. On the other hand, ICP is much lower in value than the blood pressure, which does not change the biomechanical properties of the vessel wall on both macro- and microvascular levels. Therefore, ICP can significantly change the value-related PPG waveform features of ICP with minor effect on the shape-related ones.

4.4 Role of other physiological factors in ICP-induced PPG waveform changes

We observed strong effects of age and measurement site (i.e., cerebral perfusion territory) on intracranial PPG waveform features. The PPG waveform depends on many physiological features including age, measurement site, blood pressure, respiratory pattern, and neural activities (Liu et al., 2020a). The biomechanical properties of the cardiovascular system (e.g., arterial stiffness) depends on the age. In Figure 9, age-related changes in PPG waveform features are more significant than ICP-related ones. Age-adjusted analysis can be considered in PPG-based ICP estimation. However, the effect of age on the mean is negligible, which indicates that the normal intensity of cerebral microcirculation is unaffected by age (Cidis Meltzer et al., 2000).

PPG waveform also strongly depends on the blood pressure value and can be used for blood pressure estimation (Allen, 2007). The combination of TCD and blood pressure showed much higher accuracy than the TCD-PI method in estimating ICP (Fernando et al., 2019). Ruesch et al. (2020) investigated the estimation of ICP based on cerebral blood flow measured by diffuse correlation spectroscopy, and found an obvious improvement in accuracy when mean arterial blood pressure was included (R-squared values: .82 and .92). Furthermore, the ICP-induced dysfunction of cardiorespiratory system and cerebral autoregulation can lead to complex changes in cerebral microcirculation and resultant PPG waveform (Winklewski et al., 2019). Therefore, other physiological factors and their interactions deserve further consideration in investigating the relationship between ICP and PPG waveform features.

4.5 Towards better accuracy: Individualization of arterial parameters and venous model

The proposed model consists of 33 artery segments from aorta to the Circle of Willis. To generate reliable simulation results for clinical application, the biomechanical properties of the arteries need to be evaluated individually in different subjects. In this model, the biomechanical and anatomic properties of the arteries were derived from some earlier physiological measurement results (Stergiopulos et al., 1992; Fahrig et al., 1999; Moore et al., 2006) where the properties distributed in wide ranges. We noted that the parameters of vascular anatomy in Alastruey et al. (2007) and Zhang et al. (2014) models were not exactly the same. All the values fell in the normal ranges, whilst the differences in anatomic parameters provided a chance to observe the effect of individual vascular anatomy on the simulated ICP and PPG signals. Figure 11 shows the simulation results of a 40-year old male subject with 25% decrease in intracranial capacitance based on Alastruey et al. (2007) and Zhang et al. (2014) arterial models (scenarios 1 and 2, respectively), with the parameters of other parts identical. The ICPs of both scenarios are similar in range but different in waveform. The PPG signals of both scenarios are different in range and waveform, whereas, similar trends can be observed, i.e., the PPG of MCA territory is lower in amplitude, maximum, and minimum compared with those of ACA and PCA territories. Therefore, this model initially indicated the possibility of PPG-based ICP estimation, while there is a long way to explore towards individualization of the model where patient-specific anatomic data are essential.

In addition, the simulated ICP has one or two peaks, while *in vivo* ICP often has three peaks in a cardiac cycle: P1 (percussion wave), P2 (tidal wave), and P3 (dicrotic wave) (Harary et al., 2018). This might partly due to the simplification of venous circulation and its interaction with ICP. Although the precise origin of ICP peaks is not fully understood yet, P2 and P3 are often thought relevant to the retrograde venous pulse of the jugular against the cortical veins (Rodríguez-Boto et al., 2015). In the classic ICP model which we adopted, the cerebral venous system was simplified as a unilateral flow dependent on ICP (Ursino and Di Giammarco, 1991; Lee et al., 2015). Some advanced mathematical models have been proposed to describe the non-linear hemodynamic properties of cerebral veins (Toro, 2016). However, these models have not been fully validated on patients with different ICP levels. Considering the complexity and individual difference of cerebral venous system, patient-specific hemodynamic data (e.g., MRI-derived flow) are essential in the individualization of the cerebral circulation model measurement (Müller and Toro, 2014). A computationally efficient model that reflects the interaction between ICP and intracranial venous system is essential for improving the accuracy of ICP waveform estimation.

4.6 Limitations and future directions

There are some limitations in this pilot study. First, as aforementioned, the model was an idealized one where the values of elements and boundary conditions were derived from literature. Considering the individual difference in waveform which may

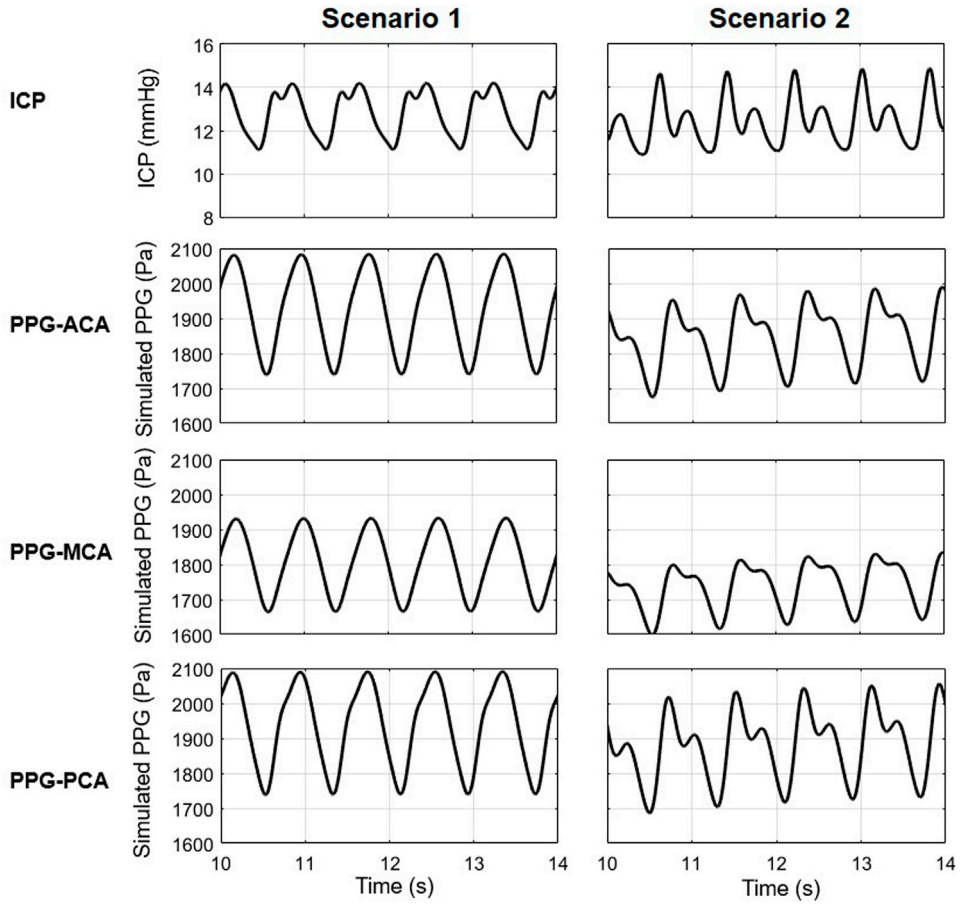

FIGURE 11
The ICP and PPG signals simulated in two scenarios with different values of the elements in cardiocerebral artery network.

involve other confounders, we did not include the analysis of focal waveform features, e.g., the location of maximal/minimal first or second derivatives. These features may reflect important physiological information including neural activities (Khalid et al., 2022) and cardiovascular pathophysiological changes (Elgendi et al., 2018). Second, the Windkessel models were highly simplified where the local hemodynamic changes within an arterial segment or a perfusion territory could not be reflected. For simplification, the aging effect was only considered in aorta and big arteries. The aging effects on cerebral vasculature (Oudegeest-Sander et al., 2014; Graff et al., 2021) and veins (Fulop et al., 2019; Huang et al., 2021) were not included in the proposed model due to the lack of comprehensive measurement results among subjects with different ages and ICP levels. Cerebral autoregulation and respiration can also significantly influence the dynamics of ICP (Budohoski et al., 2012; Vinje et al., 2019). In addition, the ICP model was simplified as a unidirectional flow system where the interactions between cerebral ventricles were not included. The PPG signals was also highly simplified as the pressure drop due to volumetric changes. The optical and electronic components were not included. In real-world scenarios, the PPG signals are sensitive to many physiological and technical factors, e.g., motion artefact, contact pressure, *etc.*, which can significantly deform the PPG signals (Fine et al., 2021). It needs further validation whether the ICP-related changes can be reliably detected from the real-world noisy PPG signals. Most importantly, the ICP values were generated by setting different intracranial capacitance decrease levels, while an elevated ICP could be generated by different pathological mechanisms where multiple physiological factors are involved.

In future studies, by introducing patient-specific biomechanical parameters and hemodynamic parameters as boundary conditions, using more advanced biomechanical models (e.g., venous valves, starling resistors) especially in cerebral venous system (Toro et al., 2022), adding optical sensing components, and including more physiological factors (e.g., respiratory regulation), the relationship between ICP and the waveform features of intracranial PPG signal could be further investigated in different pathological conditions.

5 Conclusion

ICP values could significantly change the value-relevant (maximum, minimum, mean, and amplitude) waveform features of PPG signals measured from different cerebral perfusion territories, with negligible effect on shape-relevant features (min-to-max time, PI, RI,

and MMR). In addition, age and measurement site significantly influence all PPG waveform features except the mean.

Data availability statement

The original contributions presented in the study are included in the article/Supplementary Material, further inquiries can be directed to the corresponding authors.

Author contributions

HL conceived and planned the study, performed the computational simulation, and drafted the manuscript. DZ supervised the project that led to production of the results. All authors contributed to the discussion and revision of the manuscript and concur with the current submitted version.

Funding

This study was supported by NSFC (82071358), Program of Shanghai Academic Research Leader (21XD1422400), Project of Shanghai Medical And Health Development Foundation (20224Z0012) and Key Research and Development Program of Sichuan (2022YFG0045).

Acknowledgments

We acknowledge Muhammad Usama Noorani from Coventry University for his proofreading work and suggestions in improving the language.

Conflict of interest

The authors declare that the research was conducted in the absence of any commercial or financial relationships that could be construed as a potential conflict of interest.

Publisher's note

References

Abdul-Rahman, A., Morgan, W., and Yu, D.-Y. (2020). Measurement of normal retinal vascular pulse wave attenuation using modified photoplethysmography. *PLOS ONE* 15, e0232523. doi:10.1371/journal.pone.0232523

Alastruey, J., Parker, K. H., Peiró, J., Byrd, S. M., and Sherwin, S. J. (2007). Modelling the circle of Willis to assess the effects of anatomical variations and occlusions on cerebral flows. *J. Biomechanics* 40, 1794–1805. doi:10.1016/j.jbiomech.2006.07.008

Alex, R. M., Zhang, R., Watenpaugh, D. E., and Behbehani, K. (2019). "Dynamic estimation of cerebral blood flow using photoplethysmography signal during simulated apnea," in 41st Annual International Conference of the IEEE Engineering in Medicine and Biology Society (EMBC) (IEEE), 5727–5730.

Allen, J. (2007). Photoplethysmography and its application in clinical physiological measurement. *Physiol. Meas.* 28, R1–R39. doi:10.1088/0967-3334/28/3/R01

Alperin, N. J., Lee, S. H., Loth, F., Raksin, P. B., and Lichtor, T. (2000). MR-intracranial pressure (ICP): A method to measure intracranial elastance and pressure noninvasively by means of mr imaging: Baboon and human study. *Radiology* 217, 877–885. doi:10.1148/radiology.217.3.r00dc42877

Aries, M. J. H., Elting, J. W., De Keyser, J., Kremer, B. P. H., and Vroomen, P. C. a. J. (2010). Cerebral autoregulation in stroke: A review of transcranial Doppler studies. *Stroke* 41, 2697–2704. doi:10.1161/STROKEAHA.110.594168

Blanco, P. J., Müller, L. O., and Spence, J. D. (2017). Blood pressure gradients in cerebral arteries: A clue to pathogenesis of cerebral small vessel disease. *Stroke Vasc. Neurology* 2, 108–117. doi:10.1136/svn-2017-000087

Budohoski, K. P., Czosnyka, M., De Riva, N., Smielewski, P., Pickard, J. D., Menon, D. K., et al. (2012). The relationship between cerebral blood flow autoregulation and cerebrovascular pressure reactivity after traumatic brain injury. *Neurosurgery* 71 (3), 652–660. doi:10.1227/NEU.0b013e318260

Chang, T., Li, L., Yang, Y., Li, M., Qu, Y., and Gao, L. (2019). Transcranial Doppler ultrasonography for the management of severe traumatic brain injury after decompressive craniectomy. *World Neurosurg.* 126, e116–e124. doi:10.1016/j.wneu.2019.02.005

Chang, T., Yan, X., Zhao, C., Zhang, Y., Wang, B., and Gao, L. (2021). Noninvasive evaluation of intracranial pressure in patients with traumatic brain injury by transcranial Doppler ultrasound. *Brain Behav.* 11, e2396. doi:10.1002/brb3.2396

Cidis Meltzer, C., Cantwell, M. N., Greer, P. J., Ben-Eliezer, D., Smith, G., Frank, G., et al. (2000). Does cerebral blood flow decline in healthy aging? A pet study with partial-volume correction. *J. Nucl. Med.* 41, 1842–1848.

Czosnyka, M., and Pickard, J. D. (2004). Monitoring and interpretation of intracranial pressure. *J. Neurology, Neurosurg. & Psychiatry* 75, 813. doi:10.1136/jnnp.2003.033126

Elgendi, M., Liang, Y., and Ward, R. (2018). Toward generating more diagnostic features from photoplethysmogram waveforms. *Diseases* 6, 20. doi:10.3390/diseases6010020

Fahrig, R., Nikolov, H., Fox, A. J., and Holdsworth, D. W. (1999). A three-dimensional cerebrovascular flow phantom. *Med. Phys.* 26, 1589–1599. doi:10.1118/1.598672

Fernando, S. M., Tran, A., Cheng, W., Rochwerg, B., Taljaard, M., Kyeremanteng, K., et al. (2019). Diagnosis of elevated intracranial pressure in critically ill adults: Systematic review and meta-analysis. *BMJ* 366, l4225. doi:10.1136/bmj.l4225

Fine, J., Branan, K. L., Rodriguez, A. J., Boonya-Ananta, T., AjmalRamella-Roman, J. C., Mcshane, M. J., et al. (2021). Sources of inaccuracy in photoplethysmography for continuous cardiovascular monitoring. *Biosensors* 11, 126. doi:10.3390/bios11040126

Fulop, G. A., Tarantini, S., Yabluchanskiy, A., Molnar, A., Prodan, C. I., Kiss, T., et al. (2019). Role of age-related alterations of the cerebral venous circulation in the pathogenesis of vascular cognitive impairment. *Am. J. Physiology-Heart Circulatory Physiology* 316, H1124–H1140. doi:10.1152/ajpheart.00776.2018

Giudici, A., Palombo, C., Kozakova, M., Morizzo, C., Cruickshank, J. K., and Khir, A. W. (2022). Subject-specific pressure normalization of local pulse wave velocity: Separating intrinsic from acute load-dependent stiffening in hypertensive patients. *Front. Physiology* 12, 783457. doi:10.3389/fphys.2021.783457

Graff, B. J., Payne, S. J., and El-Bouri, W. K. (2021). The ageing brain: Investigating the role of age in changes to the human cerebral microvasculature with an *in silico* model. *Front. Aging Neurosci.* 13, 632521. doi:10.3389/fnagi.2021.632521

Harary, M., Dolmans, R. G. F., and Gormley, W. B. (2018). Intracranial pressure monitoring—review and avenues for development. *Sensors* 18, 465. doi:10.3390/s18020465

Huang, Z., Tu, X., Lin, Q., Zhan, Z., Tang, L., and Liu, J. (2021). Increased internal cerebral vein diameter is associated with age. *Clin. Imaging* 78, 187–193. doi:10.1016/j.clinimag.2021.03.027

Kang, H. G., Lee, S., Ryu, H. U., and Shin, Y. (2018). Identification of cerebral artery stenosis using bilateral photoplethysmography. *J. Healthc. Eng.* 2018, 3253519. doi:10.1155/2018/3253519

Kang, T., Mukherjee, D., Kim, J.-M., Park, K.-Y., and Ryu, J. (2021). Effects of progressive carotid stenosis on cerebral haemodynamics: Aortic-cerebral 3D patient-specific simulation. *Eng. Appl. Comput. Fluid Mech.* 15, 830–847. doi:10.1080/19942060.2021.1916601

Kashif, F. M., Verghese, G. C., Novak, V., Czosnyka, M., and Heldt, T. (2012). Model-based noninvasive estimation of intracranial pressure from cerebral blood flow velocity and arterial pressure. *Sci. Transl. Med.* 4, 129ra44. 129ra144-129ra144. doi:10.1126/scitranslmed.3003249

Khalid, S. G., Ali, S. M., Liu, H., Qurashi, A. G., and Ali, U. (2022). Photoplethysmography temporal marker-based machine learning classifier for anesthesia drug detection. *Med. Biol. Eng. Comput.* 60, 3057–3068. doi:10.1007/s11517-022-02658-1

Khalid, S. G., Liu, H., Zia, T., Zhang, J., Chen, F., and Zheng, D. (2020). Cuffless blood pressure estimation using single channel photoplethysmography: A two-step method. *IEEE Access* 8, 58146–58154. doi:10.1109/access.2020.2981903

Kopustinskas, A., Kupciunas, I., and Marcinkeviciene, J. (2010). Estimation of arterial nonlinear compliance using ultrasound images. *Elektron. Ir. Elektrotechnika* 105, 93–96.

Lee, J. H., Grace, E. J., Sieker, J., Hargens, A., Petersen, J. C. G., and Petersen, L. G. (2020). Intracranial pressure after soccer heading. *FASEB J.* 34, 1. doi:10.1096/fasebj.2020.34.s1.02273

Lee, K. J., Park, C., Oh, J., and Lee, B. (2015). Non-invasive detection of intracranial hypertension using a simplified intracranial hemo- and hydro-dynamics model. *Biomed. Eng. OnLine* 14, 51. doi:10.1186/s12938-015-0051-3

Liu, H., Allen, J., Zheng, D., and Chen, F. (2019). Recent development of respiratory rate measurement technologies. *Physiol. Meas.* 40, 07TR01. doi:10.1088/1361-6579/ab299e

Liu, H., Chen, F., Hartmann, V., Khalid, S. G., Hughes, S., and Zheng, D. (2020a). Comparison of different modulations of photoplethysmography in extracting respiratory rate: From a physiological perspective. *Physiol. Meas.* 41, 094001. doi:10.1088/1361-6579/abaaf0

Liu, H., Wang, D., Leng, X., Zheng, D., Chen, F., Wong, L. K. S., et al. (2020b). State-of-the-art computational models of circle of willis with physiological applications: A review. *IEEE Access* 8, 156261–156273. doi:10.1109/access.2020.3007737

Liu, Z., Zhou, Y., Yi, R., He, J., Yang, Y., Luo, L., et al. (2016). Quantitative research into the deconditioning of hemodynamic to disorder of consciousness carried out using transcranial Doppler ultrasonography and photoplethysmography obtained via finger-transmissive absorption. *Neurol. Sci.* 37, 547–555. doi:10.1007/s10072-015-2429-1

Mandeville, J. B., Marota, J. J. A., Ayata, C., Zaharchuk, G., Moskowitz, M. A., Rosen, B. R., et al. (1999). Evidence of a cerebrovascular postarteriole windkessel with delayed compliance. *J. Cereb. Blood Flow Metabolism* 19, 679–689. doi:10.1097/00004647-199906000-00012

Moore, S., David, T., Chase, J. G., Arnold, J., and Fink, J. (2006). 3D models of blood flow in the cerebral vasculature. *J. Biomechanics* 39, 1454–1463. doi:10.1016/j.jbiomech.2005.04.005

Morgan, W. H., Hazelton, M. L., Betz-Stablein, B. D., Yu, D.-Y., Lind, C. R. P., Ravichandran, V., et al. (2014). Photoplethysmographic measurement of various retinal vascular pulsation parameters and measurement of the venous phase delay. *Investigative Ophthalmol. Vis. Sci.* 55, 5998–6006. doi:10.1167/iovs.14-15104

Morgan, W. H., Khoo, Y. J., Kermode, A. G., Lind, C. R., Hazelton, M. L., Parsons, K. E., et al. (2021). Utilisation of retinal vein photoplethysmography to measure intracranial pressure. *J. Neurology, Neurosurg. & Psychiatry* 92, 104. doi:10.1136/jnnp-2019-321072

Moss, H. E. (2021). *Retinal Vein Changes as a Biomarker to Guide Diagnosis and Management of Elevated Intracranial Pressure*, 12.

Müller, L. O., and Toro, E. F. (2014). Enhanced global mathematical model for studying cerebral venous blood flow. *J. Biomechanics* 47, 3361–3372. doi:10.1016/j.jbiomech.2014.08.005

Nag, D. S., Sahu, S., Swain, A., and Kant, S. J. W. J. O. C. C. (2019). Intracranial pressure monitoring: Gold standard and recent innovations. *Gold Stand. recent innovations* 7, 1535–1553. doi:10.12998/wjcc.v7.i13.1535

Oudegeest-Sander, M. H., Van Beek, A. H. E. A., Abbink, K., Olde Rikkert, M. G. M., Hopman, M. T. E., and Claassen, J. a. H. R. (2014). Assessment of dynamic cerebral autoregulation and cerebrovascular CO2 reactivity in ageing by measurements of cerebral blood flow and cortical oxygenation. *Exp. Physiol.* 99, 586–598. doi:10.1113/expphysiol.2013.076455

Rangel-Castillo, L., Gopinath, S., and Robertson, C. S. (2008). Management of intracranial hypertension. *Neurol. Clin.* 26, 521–541. doi:10.1016/j.ncl.2008.02.003

Rivera-Rivera, L. A., Turski, P., Johnson, K. M., Hoffman, C., Berman, S. E., Kilgas, P., et al. (2015). 4D flow MRI for intracranial hemodynamics assessment in Alzheimer's disease. *J. Cereb. Blood Flow Metabolism* 36, 1718–1730. doi:10.1177/0271678x15617171

Rodríguez-Boto, G., Rivero-Garvía, M., Gutiérrez-González, R., and Márquez-Rivas, J. (2015). Basic concepts about brain pathophysiology and intracranial pressure monitoring. *Neurol. Engl. Ed.* 30, 16–22. doi:10.1016/j.nrl.2012.09.002

Ruesch, A., Yang, J., Schmitt, S., Acharya, D., Smith, M. A., and Kainerstorfer, J. M. (2020). Estimating intracranial pressure using pulsatile cerebral blood flow measured with diffuse correlation spectroscopy. *Biomed. Opt. Express* 11, 1462–1476. doi:10.1364/BOE.386612

Ryding, E. (2017). The relationship between intracranial pressure increase and volume of brain compression. *J. Neurology Neurophysiology* 8, 1–4. doi:10.4172/2155-9562.1000436

Schollenberger, J., Osborne, N. H., Hernandez-Garcia, L., and Figueroa, C. A. (2021). A combined computational fluid dynamics and arterial spin labeling MRI modeling strategy to quantify patient-specific cerebral hemodynamics in cerebrovascular occlusive disease. *Front. Bioeng. Biotechnol.* 9, 722445. doi:10.3389/fbioe.2021.722445

Stergiopulos, N., Young, D. F., and Rogge, T. R. (1992). Computer simulation of arterial flow with applications to arterial and aortic stenoses. *J. Biomechanics* 25, 1477–1488. doi:10.1016/0021-9290(92)90060-e

Stocchetti, N., Picetti, E., Berardino, M., Buki, A., Chesnut, R. M., Fountas, K. N., et al. (2014). Clinical applications of intracranial pressure monitoring in traumatic brain injury: Report of the milan consensus conference. *Acta Neurochir.* 156, 1615–1622. doi:10.1007/s00701-014-2127-4

Tanaka, A. (2022). Analysis of a microcirculatory windkessel model using photoplethysmography with green light: A pilot study. *IEICE Electron. Express advpub* 19 (21), 20220371. doi:10.1587/elex.19.20220371

Toro, E. F. (2016). Brain venous haemodynamics, neurological diseases and mathematical modelling. A review. *Appl. Math. Comput.* 272, 542–579. doi:10.1016/j.amc.2015.06.066

Toro, E. F., Celant, M., Zhang, Q., Contarino, C., Agarwal, N., Linninger, A., et al. (2022). Cerebrospinal fluid dynamics coupled to the global circulation in holistic setting: Mathematical models, numerical methods and applications. *Int. J. Numer. Methods Biomed. Eng.* 38, e3532. doi:10.1002/cnm.3532

Ursino, M., and Di Giammarco, P. (1991). A mathematical model of the relationship between cerebral blood volume and intracranial pressure changes: The generation of plateau waves. *Ann. Biomed. Eng.* 19, 15–42. doi:10.1007/BF02368459

Ursino, M., and Lodi, C. A. (1997). A simple mathematical model of the interaction between intracranial pressure and cerebral hemodynamics. *J. Appl. Physiology* 82, 1256–1269. doi:10.1152/jappl.1997.82.4.1256

Vinje, V., Ringstad, G., Lindstrøm, E. K., Valnes, L. M., Rognes, M. E., Eide, P. K., et al. (2019). Respiratory influence on cerebrospinal fluid flow – A computational study based on long-term intracranial pressure measurements. *Sci. Rep.* 9, 9732. doi:10.1038/s41598-019-46055-5

Viola, S., Viola, P., Fiorelli, L., Buongarzone, M. P., and Litterio, P. (2013). Transcranial brain photoplethysmography to study the venules of cerebral cortex in patients with multiple sclerosis. *Phlebology* 30, 119–126. doi:10.1177/0268355513515650

Vriz, O., Aboyans, V., Minisini, R., Magne, J., Bertin, N., Pirisi, M., et al. (2017). Reference values of one-point carotid stiffness parameters determined by carotid echo-tracking and brachial pulse pressure in a large population of healthy subjects. *Hypertens. Res.* 40, 685–695. doi:10.1038/hr.2017.24

Wesseling, K. H., Jansen, J. R., Settels, J. J., and Schreuder, J. J. (1993). Computation of aortic flow from pressure in humans using a nonlinear, three-element model. *J. Appl. Physiology* 74, 2566–2573. doi:10.1152/jappl.1993.74.5.2566

Winklewski, P. J., Wolf, J., Gruszecki, M., Wszedybyl-Winklewska, M., and Narkiewicz, K. (2019). Current understanding of the effects of inspiratory resistance on the interactions between systemic blood pressure, cerebral perfusion, intracranial pressure, and cerebrospinal fluid dynamics. *J. Appl. Physiology* 127, 1206–1214. doi:10.1152/japplphysiol.00058.2019

Zhang, C., Li, S., Pu, F., Fan, Y., and Li, D. (2014). The effect of anatomic variations of circle of willis on cerebral blood distribution during posture change from supination to standing: A model study. *Bio-Medical Mater. Eng.* 24, 2371–2380. doi:10.3233/BME-141050

frontiers | Frontiers in Physiology

TYPE Original Research
PUBLISHED 22 August 2023
DOI 10.3389/fphys.2023.1138257

OPEN ACCESS

EDITED BY
Linwei Wang,
Rochester Institute of Technology (RIT), United States

REVIEWED BY
Daniel Baum,
Zuse Institute Berlin, Germany
Alireza Gholipour,
Massachusetts General Hospital and Harvard Medical School, United States

*CORRESPONDENCE
Lu Wang,
wanglu@cse.neu.edu.cn
Stephen E. Greenwald,
s.e.greenwald@qmul.ac.uk

RECEIVED 05 January 2023
ACCEPTED 01 August 2023
PUBLISHED 22 August 2023

CITATION
Wang Q, Xu L, Wang L, Yang X, Sun Y, Yang B and Greenwald SE (2023), Automatic coronary artery segmentation of CCTA images using UNet with a local contextual transformer.
Front. Physiol. 14:1138257.
doi: 10.3389/fphys.2023.1138257

Automatic coronary artery segmentation of CCTA images using UNet with a local contextual transformer

Qianjin Wang[1], Lisheng Xu[2], Lu Wang[1]*, Xiaofan Yang[1], Yu Sun[2,3,4], Benqiang Yang[3,4] and Stephen E. Greenwald[5]*

[1]School of Computer Science and Engineering, Northeastern University, Shenyang, China, [2]College of Medicine and Biological and Information Engineering, Northeastern University, Shenyang, China, [3]Department of Radiology, General Hospital of Northern Theater Command, Shenyang, China, [4]Key Laboratory of Cardiovascular Imaging and Research of Liaoning Province, Shenyang, China, [5]Blizard Institute, Barts and the London School of Medicine and Dentistry, Queen Mary University of London, London, United Kingdom

Coronary artery segmentation is an essential procedure in the computer-aided diagnosis of coronary artery disease. It aims to identify and segment the regions of interest in the coronary circulation for further processing and diagnosis. Currently, automatic segmentation of coronary arteries is often unreliable because of their small size and poor distribution of contrast medium, as well as the problems that lead to over-segmentation or omission. To improve the performance of convolutional-neural-network (CNN) based coronary artery segmentation, we propose a novel automatic method, DR-LCT-UNet, with two innovative components: the Dense Residual (DR) module and the Local Contextual Transformer (LCT) module. The DR module aims to preserve unobtrusive features through dense residual connections, while the LCT module is an improved Transformer that focuses on local contextual information, so that coronary artery-related information can be better exploited. The LCT and DR modules are effectively integrated into the skip connections and encoder-decoder of the 3D segmentation network, respectively. Experiments on our CorArtTS2020 dataset show that the dice similarity coefficient (DSC), Recall, and Precision of the proposed method reached 85.8%, 86.3% and 85.8%, respectively, outperforming 3D-UNet (taken as the reference among the 6 other chosen comparison methods), by 2.1%, 1.9%, and 2.1%.

KEYWORDS

coronary artery segmentation, 3D-Unet, local contextual transformer, dense residual connection, convolutional neural network

1 Introduction

Cardiovascular disease is a major cause of death worldwide and its most common manifestation is coronary artery disease (CAD) (Jayaraj et al., 2019). Early diagnosis of CAD, especially coronary artery stenosis and atherosclerosis, is essential for subsequent treatment. As a non-invasive screening method, Computed Tomography Angiography (CTA) has been widely used for this purpose (Raff, 2007). However, coronary CTA (CCTA) images have the typical shortcomings of medical images, such as unbalanced foreground-background distribution, small targets, and unstable image quality (Kroft et al., 2007). This instability

results from differences in scanning equipment and variations in patient motion during scanning, which affect the consistency of image quality. Radiologists can manually assess the site of stenosis and plaque in coronary arteries, but this is not only time-consuming but also prone to misdiagnosis and omission (Ghekiere et al., 2017). Furthermore, clinical workforce resources are limited, so there is a drive to employ computers to help physicians analyze coronary artery images. Segmentation of coronary arteries in these images is a prerequisite for automating the diagnosis and analysis these tissues. (Mihalef et al., 2011; Tesche et al., 2018). Given the current difficulties in automated diagnosis of CCTA images, there is a need to develop more effective methods for segmenting the coronary arteries contained therein.

In previous research, traditional methods have achieved some notable success in the field of vessel segmentation. These methods include techniques based on image processing, morphological operations, and traditional machine learning algorithms. More than 10 years ago, Lesage et al. (2009) provided further insights into vessel segmentation approaches, which do not involve deep learning. These include the use of region-based methods, edge detection, and active contour models, among others. Orujov et al. (2020) proposed a contour detection algorithm for retinal blood vessels using Mamdani (Type-2) fuzzy rules; the method enhanced contrast with contrast-limited adaptive histogram equalization, removed noise using a median filter, calculated image gradients, and classified pixels as edges based on fuzzy rules considering gradient magnitude and direction, ultimately obtaining segmentation of the blood vessels. Yang et al. (2020) proposed an improved multi-scale enhancement method based on Frangi filtering to enhance the contrast between vessels and other objects in the image, and used an improved level set model to segment vessels from both the enhanced and original grayscale images. Cheng et al. (2015) applied thresholding and morphological operations to preprocessed images, obtaining an initial outline of blood vessels, which were then segmented using an active contour framework based on a B-snake model with a constraint force to prevent leakage into adjacent structures. Kerkeni et al. (2016) proposed a multiscale region growing (MSRG) technique for segmenting coronary arteries in 2D X-ray angiography images, beginning with image enhancement using a multi-scale vascularity filter and a contrast enhancement technique, followed by identifying initial seed points by thresholding and manually selecting points with a high density of vascularity, and finally employing an iterative region growing approach to obtain the segmentation. Although these methods have to some extent helped address vessel segmentation tasks, they still have shortcomings, such as sensitivity to noise, dependency on manual intervention, and difficulty in handling complex vessel structures or poor contrast images.

Recently, deep learning methods have performed extremely well in the segmentation of medical images and have been shown to significantly outperform traditional methods in accuracy. Artificial intelligence has also found extensive applications in cardiothoracic fields, particularly in diagnostic imaging (Sharma et al., 2020). UNet (Ronneberger et al., 2015) is a classical network in the field of biomedical image segmentation and has become a benchmark in this domain (Liu et al., 2020). The network has a U-shaped structure consisting of an encoder, a decoder, and skip connections, which allow it to acquire both spatial and semantic information simultaneously. 3D-UNet (Çiçek et al., 2016), as an extension of UNet, is used for 3D image segmentation. The input is a volume instead of a slice so that interslice information can be exploited, and the convolution operation is changed from 2D to 3D accordingly. A typical 3D-UNet consists of four stages for both the encoder and the decoder. VNet (Milletari et al., 2016), which has also been proposed for processing 3D medical images, is similar to 3D-UNet in terms of network structure. The differences are that it uses convolution operations instead of pooling operations for upsampling and downsampling, and it also introduces residual connections in both the encoder and decoder.

Due to its excellent performance, many studies have employed 3D-UNet as a baseline network and improved upon it. As to the encoding and decoding path, some variants of 3D-UNet add residual connections to the convolution and deconvolution operations in the encoding and decoding stages (Lee et al., 2017; Qamar et al., 2020). Furthermore, some variants of 3D-UNet introduce dense connections between the fine and coarse feature maps to improve the transfer of feature information (Li et al., 2018; Bui et al., 2019; Zhang Y et al., 2020; Pan et al., 2021). Song et al. (2022) incorporated dense blocks into the encoder for effective feature extraction and applied residual blocks to the decoder for feature rectification. Several works have introduced attention mechanisms into UNet (Islam et al., 2020; Jin et al., 2020; Li et al., 2021). For example, channel attention (Li et al., 2021) and spatial attention (Islam et al., 2020) have been added to the decoder. Spatial attention focuses more on the target region, while channel attention estimates the importance of individual features. However, accurate segmentation of medical images requires rich contextual information to resolve ambiguities, and these methods do not make effective use of such information.

The Transformer model (Vaswani et al., 2017) proposed in the Natural Language Processing field has fundamentally changed the way that machines work with text data. Inspired by this, many recent studies have adapted the Transformer model for computer vision applications. For instance, Vision Transformer (Dosovitskiy et al., 2021) divides images into fixed-size patches, and these patches are regarded as words and fed into the Transformer for image recognition. Related works that utilize the Transformer for medical image segmentation have also performed well. VT-UNet (Peiris et al., 2022) uses window-based Transformers as encoders and decoders to construct a U-shaped network for 3D Tumor Segmentation. UNETR (Hatamizadeh et al., 2022) applies the original Transformers as encoders in a U-shaped network to learn the input representation and capture global multi-scale information, while the decoders remain as traditional convolutional modules. UCTransNet (Wang et al., 2022a) introduces the channel Transformer to replace the skip connection of U-Net for more effective encoder-decoder feature connection and hence more accurate segmentation of medical images. AFTer-UNet (Yan et al., 2022) replaces the convolution with a Transformer in the last layer of the UNet. MT-UNet (Wang et al., 2022b) proposes a mixed Transformer and embeds it into the deeper layers of UNet. The mixed Transformer first calculates self-affinities using an efficient local-global self-attention mechanism and then exploits the relations between data samples with an external attention.

Besides the improvements in UNet and the introduction of the attention mechanism, several other network architectures have been employed for coronary artery segmentation. Lei Y et al. (2020) introduced an improved 3D attention into a fully convolution network (FCN) to automatically segment the coronary arteries in CCTA images. Tian et al. (2021) used VNet for initial segmentation and then used region growing to further segment the image, thus obtaining complete and smooth-edged coronary arteries. Gao et al. (2021) conducted coronary centerline extraction and lumen segmentation jointly on CCTA images to address the breakage issue, employing a Graph Convolutional Network (GCN) for the segmentation of the coronary lumen. Some studies use specific features of coronary vessels for segmentation. For instance, Kong et al. (2020) focused more on the anatomical structure of coronary arteries and proposed incorporating a tree-structured convolutional gated recurrent unit into the fully convolutional neural network. Ma et al. (2020) are more concerned with the continuity of the vessels and used a novel region growing method to segment coronary arteries, which considers a variable sector search area within each region. Wolterink et al. (2019) focused more on tubular surfaces and employed graph convolutional networks to forecast the spatial coordinates of vertices within a tubular surface mesh, thus segmenting the lumen of the coronary artery. Other studies have adopted a two-stage framework to achieve coronary artery segmentation in CCTA images. For instance, in the first stage, cardiac segmentation is performed, followed by slicing the cardiac region and segmenting the coronary arteries within the local sliced region. This procedure can alleviate the foreground-background imbalance problem (Dong et al., 2022). Wang et al. (2022c) adopted a similar approach in which the first stage involves a rough segmentation of the 3D image and in the second, the segmentation network is fed with the original 2D images and the 2D images resulting from slicing the 3D segmentation.

However, these existing methods still have shortcomings and we aim at tackling some of them in this work. First, as a proportion of the coronary arteries are of small diameter and thus appear as very thin lines in images, simply increasing the number of convolutional layers in the encoding or decoding blocks of UNet would not improve the segmentation accuracy, because the information in the shallow-layer features, which is necessary for segmenting details, may be lost when the convolution operation goes deeper. Although the traditional residual module (He et al., 2016) can complement the shallow-layer information, it is not sufficient for coronary artery segmentation (as demonstrated in Table 4 in the results and discussion section). Existing research has explored the idea of combining residual learning and dense connections to enhance feature extraction and fusion capabilities in 2D image recognition tasks (Zhang Z et al., 2020; Zhang et al., 2021). However, these approaches are tailored for specific tasks and datasets, and directly applying them to 3D-UNet could result in a large network due to its dense concatenation. Therefore, there is a need to adapt this concept and we have consequently proposed a module specifically designed for 3D coronary artery image segmentation. Second, with similar Hounsfield Unit (HU) values, the feature representations of coronary arteries in the inner layers of a CNN network are likely to be similar to those of other blood vessels such as veins and the ascending aorta. To deal with this, the attention mechanism can be used to enhance the weighting of the coronary regions. However, traditional self-attention computes an attention matrix based on isolated query-key pairs, which may focus more on segmenting the main part of coronary artery and ignore the ends and regions with low concentrations of contrast medium. There has been research on transformers that focus on local context information (Li et al., 2022), and this has been used for 2D image recognition. However, this approach does not simultaneously extract local context information for Q and V, which may limit its feature representation ability. There is a need for a module suitable for 3D-UNet networks for segmentation tasks and to improve the attention mechanism to better capture the local context information of Q and V. This will enhance the feature representation ability of the network.

Therefore, we aim to extract and fuse a greater number of deep and shallow features than the residual module. To this end, we propose the Dense Residual (DR) module, which is continuously supplemented with preceding convolution features during the convolution process, thus improving the encoding and decoding block of UNet. Then, aiming to concentrate more on the local characteristics of the coronary arteries and reduce the noise information from other organs, we propose the Local Contextual Transformer (LCT) module, which focuses more on the local contextual information by obtaining an attention matrix based on query and contextual-information-enhanced key pairs. In particular, we apply the LCT module after each encoding block to provide more informative features to the decoding block, instead of simply using the skip connection, so that the decoding procedure can focus more on the region's neighboring the coronary arteries. Using these modules, we have conducted extensive experiments on our CorArtTS2020 dataset and compared the results to the most widely used image segmentation method 3D-UNet and six other segmentation networks commonly used in coronary artery segmentation studies. The code of the proposed method is available at https://github.com/qianjinmingliang/Coronary-Artery-segmentation-with-LCTUnet.

2 Materials and methods

2.1 Dataset

The dataset used for the experiment (CorArtTS 2020) was provided by the General Hospital of the Northern Theater Command in China. It is a modified version of the one used in our previous work (Song A. et al.) and was acquired using a Philips iCT 256 Scanner, running a 120 kVp protocol. Each slice had a width and height of 512 pixels, and the interval between adjacent slices was 0.45 mm. Each case consisted of between 310 and 390 slices. As shown in Table 1, the CorArtTS2020 dataset consists of 81 cases, of which the numbers of normal subjects and patients were 40 and 41, respectively. The data were randomly divided into training, validation, and test sets in the ratio of 6:1:3, respectively.

TABLE 1 The CorArtTS2020 dataset.

	Training set	Validation set	Testing set
Normal subjects	24 cases	4 cases	12 cases
Patients	25 cases	4 cases	12 cases

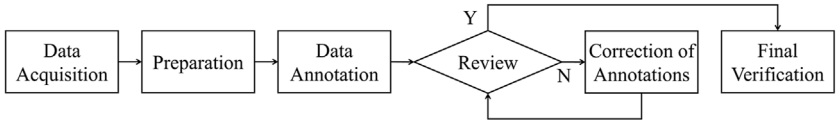

FIGURE 1
Outline of the annotation process.

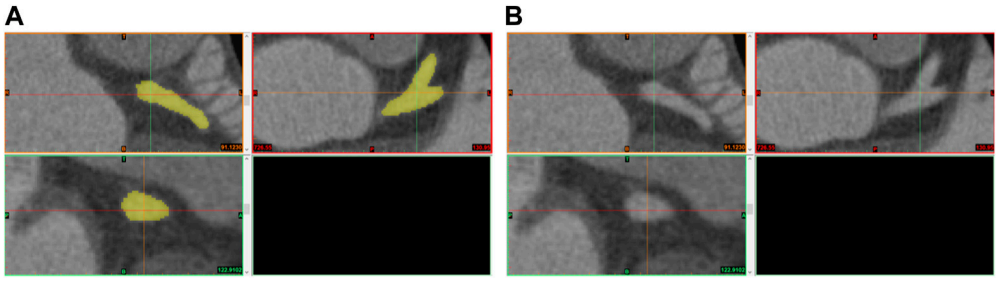

FIGURE 2
Illustration of the annotation process **(A)** and original CCTA images **(B)**.

The annotation process, summarized in Figure 1, was performed by three experienced radiologists from the same hospital. Initially, data were acquired from the radiology department of the hospital, and the radiologists underwent training to familiarize themselves with the anatomical features and distribution of coronary arteries in CCTA images (Data Acquisition and Preparation). Utilizing specialized medical image processing software, Mimics (Materialise), they carefully annotated the visible contours and branches of the right coronary artery, the left coronary artery, and their branches using the coronal, sagittal, and axial planes (Data Annotation). Upon completion of the annotation process, another experienced cardiovascular imaging radiologist from the same hospital reviewed the annotations (Review). If inaccuracies were found, they were corrected under the guidance of the reviewing radiologist (Correction of Annotations). This iterative and collaborative review process helped to ensure the accuracy of the final labels. Finally, a last check was made to confirm the correctness of all annotations (Final Verification).

Figure 2A provides an example of the annotation process conducted on the Mimics medical image processing software interface, with the annotated regions of the coronary arteries highlighted in yellow. Correspondingly, Figure 2B displays the original CCTA images prior to the annotation process.

The CCTA data require pre-processing before being fed into the segmentation network, because different tissues have different radio-densities, giving rise to a wide range of HU values. Highlighting the coronary arteries can improve the segmentation result. However, there is no clear definition of the exact range of HU values for coronary arteries (Marquering et al., 2005; Liu et al., 2013). For our dataset, we therefore conservatively limit the range of HU values in the CCTA data to be within the interval [−260,760] HU, under the guidance of the physicians, and we note that it may not be generalizable to other medical imaging modalities. The result of the data pre-processing is shown in Figure 3. It is notable that the pre-processing effectively removes irrelevant tissues and some noise, as shown in the green box, while making the coronary arteries (red arrows) more distinct. To ensure fair comparison we also used the pre-processed data for all the other comparison methods (Milletari et al., 2016; Çiçek et al., 2016; Lee et al., 2017; Li et al., 2018; Islam et al., 2020; Wang et al., 2022a; Hatamizadeh et al., 2022).

2.2 Structure of the DR-lct-unet

The proposed network structure for coronary artery segmentation is based on the 3D-UNet, to which we have made three modifications. Firstly, the LCT module, which is a novel Transformer-style attention module, is developed to bridge the gap between the features of the encoding and decoding stages before combining them. Secondly, the DR module, which is a mix of residual and dense connections of convolutions, is developed to extract multi-level features for both the encoding and decoding stages. Thirdly, deep supervision is exploited to facilitate the training process of the network. The architecture of the proposed DR-LCT-UNet is shown schematically in Figure 4.

Specifically, in the encoding process, the pre-processed image is fed into the network, and its size is $1 \times 16 \times 512 \times 512$, where 1 is the channel size, 16 is the thickness (i.e., the number of slices) of the input volume, and the height and width are 512. There are four layers in the encoding stage, in each of the first three layers, the features are first extracted and then downsampled, while the fourth layer only performs feature extraction. In order to extract rich feature representations for the coronary arteries, the DR module is used in the encoding path, as it is able to extract deeper features while retaining more detailed ones than traditional convolution.

For the decoding process, as the decoding features are quite different from the encoding features after several sampling and

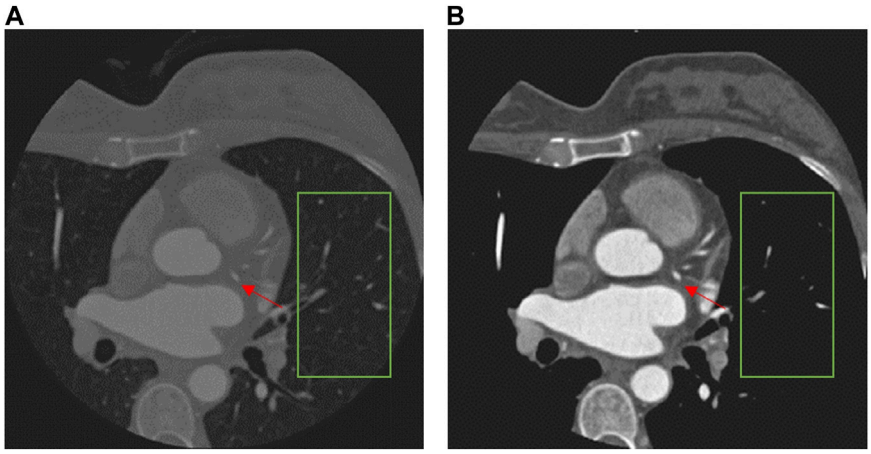

FIGURE 3
Comparison of a CCTA image before **(A)** and after pre-processing **(B)**.

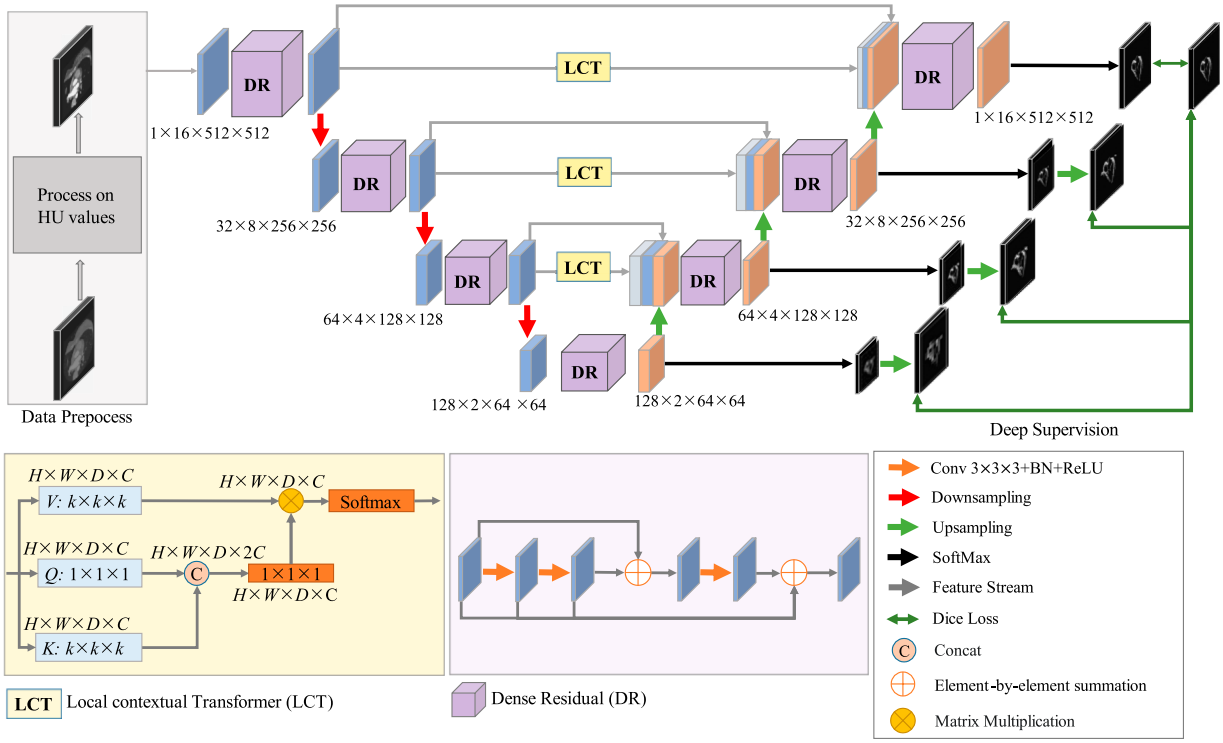

FIGURE 4
Schematic of the architecture of the proposed DR-LCT-UNet network.

convolution operations, the LCT module is used before performing decoding to fill the semantic gap between the features from the encoding and decoding stages of the same resolution level. Consequently, the input to each decoding layer consists of three parts, i.e., the features from the LCT module of the same level, the features from the encoding layers and the features from the previous decoding layers. These features are first concatenated and then decoded by the proposed DR module in each decoding layer.

Finally, we use a deep supervision strategy (Lee et al., 2015) in the training process to prevent the gradient from disappearing in the early stage of training. To be specific, the SoftMax function is applied at the end of each decoding layer to obtain the feature map used for deep supervision. To compute the segmentation loss for deep supervision, each feature map is upsampled to the same size as the input and then the Dice loss is calculated based on the similarity between the feature map and the ground truth.

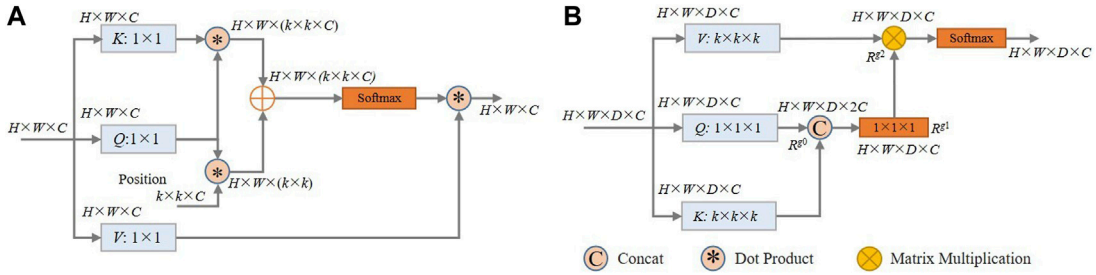

FIGURE 5
(A) Schematic of the architecture of the traditional self-attention model; **(B)** Schematic of the proposed LCT module.

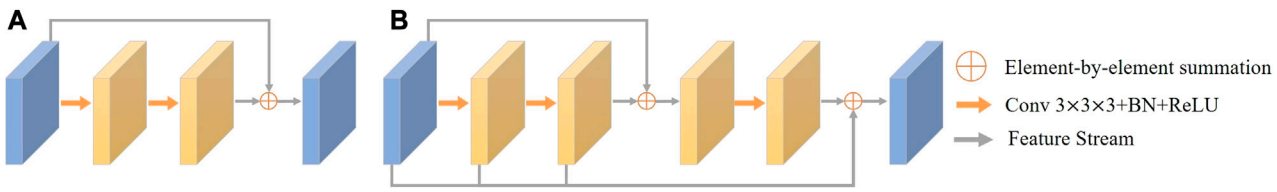

FIGURE 6
(A) Schematic of the architecture of the traditional Residual Module; **(B)** Description of the architecture of the proposed Dense Residual Module.

2.3 Structure of the LCT module

In CCTA images, as coronary arteries are smaller compared with nearby structures, and the appearance of coronary arteries and coronary veins is similar, it is necessary to exploit more local contextual information for accurate coronary artery segmentation.

Self-attention (Vaswani et al., 2017) computes an attention matrix based on isolated query-key pairs, as is shown in Figure 5A. Q, K, and V are obtained by 1×1 convolution, which only uses the information of each individual location without considering any neighbourhood information. Such operation limits the visual feature representation ability of the resulting embeddings. To deal with this, we propose a local contextual Transformer (LCT) module, the structure of which is shown in Figure 5B).

Specifically, for an input X of size $H \times W \times D \times C$ (H, W, D and C are respectively the height, width, thickness and the number of channels), it is first transformed into queries (Q), keys (K), and values (V) using embedding matrices W_q, W_k, and W_v, respectively. This transformation is represented by $Q = XW_q$, $K = XW_k$, and $V = XW_v$. Instead of using $1 \times 1 \times 1$ convolution to encode each key and value as in traditional self-attention, the LCT module uses $k \times k \times k$ group convolution over all the neighbouring keys and values within a $k \times k \times k$ grid to take advantage of local contextual information. That is, the matrices W_k and W_v are set to $k \times k \times k$ in size, while the matrix W_q is maintained at $1 \times 1 \times 1$ to retain the information of each location in Q.

Then, the contextualized keys K are concatenated with the queries Q. This combined information is then fed into a $1 \times 1 \times 1$ convolution with the ReLU activation function to obtain the attention matrix $R^{g1} \in R^{H \times W \times D \times C}$, thereby learning a feature that integrates local context information with global information.

After that, in a manner similar to traditional self-attention, the values of V, which contains the local context information, are multiplied element-by-element with the attention matrix R^{g1} to obtain $R^{g2} \in R^{H \times W \times D \times C}$:

$$R^{g2} = R^{g1} \otimes V \tag{1}$$

Finally, a softmax function is applied to R^{g2} to yield the output of the LCT module.

In general, the proposed LCT makes use of the local contextual information to enhance the effectiveness of the self-attention calculation, and it can thus adaptively put emphasis on the more relevant regions of the coronary arteries for segmentation. In our implementation, k is set to 3 and the optimality of this setting was experimentally validated (see Table 7).

2.4 Structure of the DR module

Traditional residual connection is proposed to solve the degradation problem of deep neural networks. Its structure is shown in Figure 6A, and consists of two consecutive convolution operations and a residual connection. The residual connection is implemented by adding up the features before and after the convolutions. The mathematical description of the original residual connection is

$$Y = X + \mathrm{H}^2(X) \tag{2}$$

where X is the input feature, $\mathrm{H}(X)$ denotes the convolution operation on X followed by a ReLU operation, and accordingly, $\mathrm{H}^k(X)$ denotes k successive convolution operations on X, each followed by the ReLU operation. Although the residual

connection has the effect of preserving the original features, some coronary artery regions in the images are not clear and the corresponding features are not obvious due to the prevalence of narrow areas, such as their distal ends, stenotic regions, and areas with uneven distribution of contrast. Such information may easily get lost during the convolution operation. Therefore, we need to preserve more of the information which might subsequently be lost during the convolution process. To this end, we propose a dense residual (DR) module, as shown in Figure 6B).

Specifically, the DR module has two residual connections which work synergistically to fuse the multi-level features from successive convolution operations. The first residual connection adds the input features to the features obtained after the second convolution operation. After that, one more convolution operation is used to extract additional deeper features. The second residual connection then sums all the previous feature maps, i.e., the input features and the feature maps generated by each of the convolution operations. Thus, the DR module is able to retain features at different convolution levels and extract rich features without information loss. In this way, the features extracted by the DR module can more completely represent the characteristics of coronary arteries. The DR module is defined by the equation:

$$Y = \mathrm{H}[X + \mathrm{H}^2(X)] + X + \mathrm{H}(X) + \mathrm{H}^2(X) \tag{3}$$

With the DR module, features in regions with narrow vessels and along low contrast boundaries are enhanced, making more accurate coronary artery segmentation possible.

2.5 Loss function

As coronary arteries are of small diameter in comparison with nearby tissues such as the heart, ascending aorta, and the pulmonary artery, the coronary artery segmentation task suffers greatly from the foreground-background imbalance problem. Dice Loss was proposed in 2017 to deal with the imbalance problem in segmentation (Ghekiere et al., 2017). It is well suited to the demands of this study, and has therefore been employed to train our network. The computation of Dice loss is based on the Dice similarity coefficient (DSC), which measures the overlap between two samples, producing results in the range [0,1], i.e., a higher DSC value indicates a higher degree of overlap. The DSC is defined by Eq. 8, and Dice Loss is computed as.

$$Dice\ Loss = 1 - \mathrm{DSC} \tag{4}$$

2.6 Deep supervision

For deep supervision, a separate loss is calculated for each decoding layer, which also plays the role of regularization. This strategy, known as deep supervision, leverages the intermediate outputs of the decoding process to guide the training, helping to mitigate the vanishing gradient problem and leading to more discriminative features being learned at all levels. These intermediate losses provide additional guidance to the learning process, which often results in faster convergence.

TABLE 2 Parameter settings for the training process.

Parameters	Values
Batch size	3
Epochs	180
Learning rate (0< epochs< 100)	10^{-5}
Learning rate (100≤ epochs< 160)	10^{-6}
Learning rate (160≤ epochs≤ 180)	10^{-7}
weight decay factor	5×10^{-4}
α (0< epochs< 40)	1
α (40≤ epochs< 80)	0.8
α (80≤ epochs< 120)	0.8^2
α (120≤ epochs< 160)	0.8^3
α (160≤ epochs≤ 180)	0.8^4

The loss function used for deep supervision is defined in Eq. 5, where L_k denotes the loss at the decoding layer of depth k, and the Dice Loss is defined by Eq. 4. As the output of the first decoding layer has the greatest effect on the performance of the network, we set smaller weights for the losses of the other decoding layers, i.e., $\alpha < 1$. The weight α for deep supervision is also gradually decreased during the training process so that at the end of the training the loss reflects the segmentation quality of the last decoding layer.

$$L = L_1 + \alpha(L_2 + L_3 + L_4) \tag{5}$$

3 Experiments and results

3.1 Experimental settings

All the experiments were carried out on a GeForce RTX 3090 GPU. The experimental environment was Pytorch 1.7 and the same training process was used for the proposed network and the other compared methods. The input was a volume of size 16 × 512 × 512. The Adam optimizer which uses adaptive moment estimation to speed up convergence was employed to update the network parameters. Due to GPU memory limitations, we chose a batch size of 3 to avoid out-of-memory errors. The parameter settings for the training process are shown in Table 2.

3.2 Evaluation metrics

We applied five commonly used evaluation metrics, i.e., the Dice similarity coefficient (DSC), Recall, Precision, Average Symmetric Surface Distance (ASSD), and Hausdorff Distance (HD), to evaluate the effectiveness of the different methods (Kirişli et al., 2013). DSC describes the similarity between two samples. Recall is the ratio of the number of correctly predicted positive voxels to the actual number of positive voxels. Precision is the proportion of correctly predicted positive voxels to all the voxels predicted to

TABLE 3 Comparison of segmentation results between various methods (Optimal value for each evaluation metric is shown in bold. In the top row of this and subsequent tables, up arrows indicate that an increase in the evaluation metric implies better performance, the reverse being the case for the down arrows).

Method	DSC↑	Recall↑	Precision↑	ASSD↓	HD↓
3D-UNet (Çiçek et al., 2016)	0.837	0.844	0.837	0.613	30.076
VNet (Milletari et al., 2016)	0.837	0.810	0.872	0.538	33.519
ResUNet (Lee et al., 2017)	0.841	0.832	**0.882**	0.533	29.054
DenseUNet (Li et al., 2018)	0.839	0.826	0.859	0.514	37.413
AttUNet (Islam et al., 2020)	0.843	0.835	0.857	0.506	32.642
UNETR (Hatamizadeh et al., 2022)	0.827	0.784	0.884	0.551	44.071
UCTransNet (Wang et al., 2022a)	0.818	0.821	0.813	1.205	59.128
DR-LCT-UNet (Ours)	**0.858**	**0.863**	0.858	**0.425**	**28.215**

TABLE 4 Comparison of the number of parameters and inference time for the different methods.

Method	Parameters (M)	Inference Time (s/case)
3D-UNet (Çiçek et al., 2016)	8.61	17.21
VNet (Milletari et al., 2016)	16.80	18.65
ResUNet (Lee et al., 2017)	9.50	18.50
DenseUNet (Li et al., 2018)	18.10	16.35
AttUNet (Islam et al., 2020)	8.65	17.23
UNETR (Hatamizadeh et al., 2022)	92.58	20.65
UCTransNet (Wang et al., 2022a)	65.60	19.55
DR-LCT-UNet (Ours)	10.70	18.60

be positive. ASSD describes the average surface distance between two samples. HD describes the maximum distance from a point in the label to a nearest point in the predicted image. The five evaluation metrics were computed according to the following expressions:

$$\text{Recall} = \frac{TP}{TP + FN} \tag{6}$$

$$\text{Precision} = \frac{TP}{TP + FP} \tag{7}$$

$$\text{DSC} = \frac{2TP}{2TP + FN + FP} \tag{8}$$

$$\text{ASSD} = \frac{\sum_{S(TP+FP)} d[S(TP+FP), S(TP+FN)] + \sum_{S(TP+FN)} d[S(TP+FN), S(TP+FP)]}{|S(TP+FP)| + |S(TP+FN)|} \tag{9}$$

$$\text{HD} = max\left(\max_{a \in S(TP+FP)} \left\{ \min_{b \in S(TP+FN)} \|a-b\| \right\}, \max_{b \in S(TP+FN)} \left\{ \min_{a \in S(TP+FP)} \|b-a\| \right\} \right) \tag{10}$$

where TP (True Positives) represents samples correctly identified as coronary arteries; FN (False Negatives) denotes samples predicted to be background, but which actually belong to coronary arteries; FP (False Positives) indicates samples predicted to be coronary arteries, but which actually belong to the background. $S\,(TP + FN)$ is the set of actual surface voxels of the coronary arteries, and $S\,(TP + FP)$ is the set of predicted surface voxels of the coronary arteries. d [$sample^1$, $sample^2$] refers to the shortest distance from $sample^1$ to $sample^2$. The values of DSC, Recall, and Precision are all in the range of [0,1], and larger values indicate better performance; while for ASSD and HD, smaller values are better.

3.3 Experimental results and discussion

3.3.1 Comparison of the different segmentation networks

To assess the quality of the proposed network structure, we have reproduced and retrained some classical and state-of-art methods commonly used for medical image segmentation from scratch. It is noteworthy that our model's final scores on the test set are not dependent on a single run. Instead, they are computed as the average results from multiple runs, thus enhancing the robustness and stability of our model and preventing the results from being influenced by a specific initialization of the model.

A comparison of the proposed DR-LCT-UNet with the other networks is shown in Tables 3, 4. The proposed network achieves better results than the baseline 3D-UNet in terms of all five evaluation metrics. Specifically, compared with the 3D-UNet, DR-LCT-UNet improves DSC by 2.1%, Recall by 1.9%, Precision by 2.1%, reduces ASSD by 0.188, and reduces HD by 1.861. DR-LCT-UNet also outperforms other networks in terms of DSC, Recall,

TABLE 5 Results of the ablation experiments (Optimal value for each evaluation metric is in bold). Legend: SA: self-attention module; LCT: local contextual Transformer; DR: Dense Residual module; R: Residual block. The ticks indicate which modules are included in each model.

Method	SA	LCT	DR	R	DSC↑	Recall↑	Precision↑	ASSD↓	HD↓
3D-UNet					0.837	0.844	0.837	0.613	30.076
SA-UNet	✓				0.843	0.835	0.857	0.506	32.642
LCT-UNet		✓			0.852	0.846	0.869	0.480	29.057
R-UNet				✓	0.841	0.832	**0.882**	0.533	29.054
DR-UNet			✓		0.852	0.863	0.847	0.494	29.821
DR-LCT-UNet		✓	✓		**0.858**	**0.863**	0.858	**0.425**	**28.215**

TABLE 6 Comparison of the number of parameters and inference time for the different modules.

Baseline	Module	Parameters (M)	Inference Time (s/case)
3D-UNet	—	8.61	17.21
	SA	8.65	17.23
	LCT	8.80	17.23
	R	9.50	18.50
	DR	10.28	18.55
	LCT + DR	10.70	18.60

ASSD, and HD. These results can be seen in Figure 8 which shows the final 3D reconstruction of the segmented coronary arterial tree.

The improvements in the various evaluation metrics achieved by the proposed DR-LCT-UNet indicate its superiority in the task of coronary artery segmentation. The improvement of Recall indicates that more coronary arteries are correctly segmented, the improvement of ASSD indicates that the segmentation result differs less from the ground truth, and the improvement of DSC indicates that the overall segmentation is better and closer to the ground truth label. Although the Precision of the networks ResNet, VNet and UNETR, is higher than that achieved by the network proposed here, indicating that they have fewer background voxels mistakenly segmented as coronary arteries, their Recall and DSC scores are much lower than the proposed network, meaning that their segmentation results miss more coronary artery voxels.

3.3.2 Ablation experiments

First, to demonstrate the performance improvement associated with each proposed module of our DR-LCT-UNet, we carried out an ablation study, the results of which are shown in Table 5. It can be seen that, compared with UNet, both the proposed LCT and DR modules consistently improve the five evaluation metrics. Specifically, the LCT module markedly improves the Precision (3.2%), while the DR module substantially improves the Recall (1.9%).

The ablation study results demonstrate the effectiveness of the individual LCT and DR modules in enhancing the segmentation performance. The LCT module contributes to a marked improvement in Precision, while the DR module has a considerable impact on Recall. By combining the advantages of both the LCT and DR modules, the DR-LCT-UNet achieves superior performance in terms of DSC, Recall, ASSD, and HD, highlighting the complementary benefits of the two modules.

Second, we have compared the number of parameters and the average inference time for the different modules. As shown in Table 6, the LCT and DR modules only slightly increase the number of parameters and the inference time compared with the SA and Residual modules.

This result demonstrates that, despite the minor increase in the number of parameters and inference time, the LCT and DR modules achieve much better segmentation accuracy compared to the SA and Residual modules. This demonstrates the effectiveness of the proposed LCT and DR modules in improving segmentation performance without significantly impacting computational complexity.

Third, to support our claim that setting the convolutional kernel W_k and W_v to the same size, i.e., $k \times k \times k$, in the LCT module is optimal, we investigated three different strategies for setting the kernel size, the results of which are shown in Table 7. We see that although every kernel size setting strategy improves the segmentation performance compared to that of using the self-attention module (i.e., SA-UNet in Table 5), the first option led to the best performance, i.e., using convolution kernels of the same size for K and V. In addition, Table 7 shows that using $k = 3$ produces the best segmentation accuracy.

This result demonstrates that the sizes of local regions for spatial context extraction of K and V should be matched. This shows that, contrary to our intuition, obtaining the contextual information from a larger neighbourhood, which will accordingly increase the number of parameters of the LCT module, does not necessarily result in a better segmentation accuracy. It is likely that this is because a larger neighbourhood may introduce more irrelevant information into the segmentation process and thus degrade the segmentation accuracy.

3.3.3 Deep supervision

We used deep supervision to prevent gradient disappearance and explosion. As can be seen from Figure 7, with an increase in the number of training epochs, the training is clearly accelerated at the beginning of the process and the DSC value of the validation set also improves. Table 8 confirms this and also shows that deep supervision leads to a slight improvement of the other segmentation metrics.

The results obtained from incorporating deep supervision demonstrate its benefits in both the network training and the

TABLE 7 Different structural designs of LCT modules (Optimal values shown in bold).

Q	K	V	DSC↑	Recall↑	Precision↑	ASSD↓	HD↓
1 × 1 × 1	1 × 1 × 1	1 × 1 ×1	0.847	0.842	0.850	0.511	30.015
	3 × 3 ×3	1 × 1 × 1	0.851	0.846	0.867	0.491	29.381
	3 × 3 × 3	3 × 3 × 3	**0.852**	**0.846**	**0.869**	**0.480**	**29.057**
	1 × 1 × 1	3 × 3 × 3	0.849	0.844	0.853	0.509	29.108
	5 × 5 × 5	1 × 1 × 1	0.845	0.840	0.855	0.513	29.277
	5 × 5 × 5	5 × 5 × 5	0.845	0.841	0.854	0.515	29.351
	1 × 1 × 1	5 × 5 × 5	0.844	0.842	0.852	0.520	29.330
	7 × 7 × 7	1 × 1 × 1	0.844	0.843	0.851	0.522	30.164
	7 × 7 × 7	7 × 7 × 7	0.844	0.842	0.849	0.522	30.097
	1 × 1 × 1	7 × 7 × 7	0.843	0.841	0.847	0.525	30.172

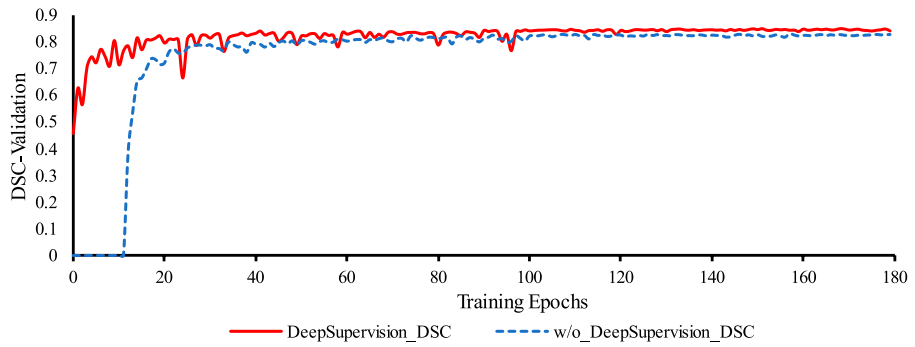

FIGURE 7
Comparison of the training process of the proposed network with and without Deep Supervision. Legend: w/o: without.

TABLE 8 Results comparison of the proposed method without and with Deep Supervision.

Method	DSC↑	Recall↑	Precision↑	ASSD↓	HD↓
DR-LCT-UNet_w/o_ Deep_Supervision	0.856	0.861	0.855	0.438	28.220
DR-LCT-UNet_ Deep_Supervision	0.858	0.863	0.858	0.425	28.215

prediction accuracy of the coronary artery segmentation task. By accelerating the training process and enhancing the DSC value of the validation, deep supervision proves to be a valuable technique in optimizing the proposed segmentation network.

3.3.4 Effect of data pre-processing

To show the effectiveness of data pre-processing on the segmentation results, we used the data with and without pre-processing, to train and test the UNet and our DR-LCT-UNet. As shown in Table 9, the segmentation metrics DSC, Recall, Precision ASSD and HD are all clearly improved.

The improvements in the segmentation metrics can be attributed to the fact that truncating the range of HU values can increase the contrast along the boundaries of the coronary arteries, remove some irrelevant tissues from the images and eliminate some noise as well, thus making the network learning and inference more effective.

4 Visual illustration of the segmentation results

Figure 8 shows 3D reconstructions of the segmentation results using UNet, UNETR, and the proposed DR-LCT-UNet. Four cases were randomly chosen from the test set, with the first two from normal subjects and the latter two belonging to patients with cardiovascular disease. The segmentation results of our proposed method are better than those of the other two methods, resulting in

TABLE 9 The impact of data pre-processing on the network.

Method	DSC↑	Recall↑	Precision↑	ASSD↓	HD↓
UNet_w/o_Data_preprocess	0.820	0.826	0.820	1.195	60.412
UNet_Data_preprocess	0.837	0.844	0.837	0.613	30.076
DR-LCT-UNet_w/o_Data_preprocess	0.841	0.848	0.840	0.597	29.024
DR-LCT-UNet_Data_preprocess	0.858	0.863	0.858	0.425	28.215

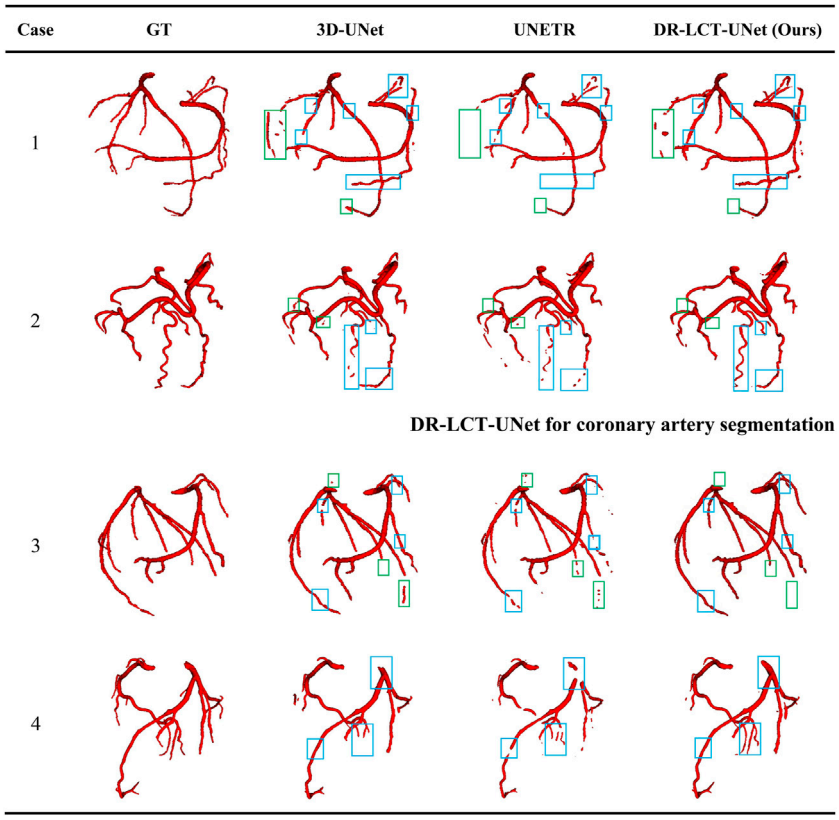

FIGURE 8
Visualization of the segmentation results from the different methods. Legend: Green boxes: locations where over-segmentation occurs for at least one of the compared methods; blue boxes: locations with under-segmentation.

fewer discontinuities and more complete segmentation at the ends of the coronary arteries.

This performance improvement can be attributed to the Dense Residual (DR) and Local Contextual Transformer (LCT) modules in our model. Specifically, the DR module, through its feature preservation capability at various convolution levels, is key to this enhancement. This module supplements shallow information layers, such as spatial structures and gray-scale features, thereby improving the network's sensitivity. This enhanced sensitivity facilitates the segmentation of a greater number of coronary arteries. Furthermore, the DR module excels in extracting deeper-level features without compromising the retention of these shallow features, contributing to a more comprehensive feature map for segmentation tasks. On the other hand, the LCT module, serving as an attention mechanism, focuses predominantly on the vicinity of the coronary arteries. It effectively distinguishes these arteries from other vessels with similar CT intensities. When implemented post the encoding block, the LCT module enhances the skip connections, thereby improving the model's feature representation ability. This enhancement leads to the provision of richer, more diversified features for the decoder, optimizing the feature extraction and representation in our deep learning model. Consequently, the combined operation of the DR and LCT modules results in fewer discontinuities and a more complete and precise segmentation at the ends of the coronary arteries.

While our method does produce fewer false positives compared to the UNet, it has shown a tendency for occasional over-segmentation compared to the UNETR, as demonstrated in case 1 (specifically, the area within the green box). In-depth analysis reveals that this is due to the sensitivity of the Dense Residual (DR)

module to shallow information, which occasionally results in the misidentification of structures similar to the coronary arteries, such as veins. This over-sensitivity and the resulting over-segmentation suggest areas of improvement. We acknowledge this limitation and plan to refine our model in follow-up studies, to better distinguish between similar structures.

5 Conclusion

The proposed method for coronary artery segmentation, DR-LCT-UNet, alleviates the omission and over-segmentation problems of previous methods for several reasons. Firstly, the data preprocessing enhances the contrast at the boundaries of the coronary arteries and reduces some of the noise in the image, hence improving the segmentation to some extent. Secondly, the proposed Transformer-style LCT module can pay more attention to local contextual information, reducing the semantic gap between the encoding and decoding features, significantly improving the segmentation Precision. Furthermore, the proposed DR module for the encoding stage can preserve multi-level features, reducing the loss of shallow-layer information due to the convolution process. As a result, this improves the Recall of the segmentation. Finally, introducing Deep Supervision to the network improves the efficiency of the training process and also has the effect of regularizing feature extraction for the different decoding layers. The final DSC, Recall, and Precision of the proposed method are 85.8%, 86.3%, and 85.8%, respectively, which are 2.1%, 1.9%, and 2.1% better than the corresponding values for 3D-UNet, the most widely used image segmentation method and the baseline based on which our approach has been developed.

Data availability statement

The original contributions presented in the study are included in the article/Supplementary Material, further inquiries can be directed to the corresponding authors.

Author contributions

Conceptualization, QW, LX, YS, and BY; methodology, QW and LW; software, QW and XY; validation, QW and LX; formal analysis, QW, LX, LW, and YS and BY; investigation, QW, LX, LW, and XY; resources, YS, BY, LX, and LW; data curation, YS, BY, and LX; writing—original draft preparation, QW, LX, and LW; writing—review and editing, LX, LW, and SG; visualization, QW and XY; supervision, LX and LW; project administration, LX; funding acquisition, LX and LW. All authors contributed to the article and approved the submitted version.

Funding

This research was funded by the National Natural Science Foundation of China (No. 62273082, 61773110, and U21A20487), the Natural Science Foundation of Liaoning Province (Grant 2021-YGJC-14), the Basic Scientific Research Project (Key Project) of The Educational Department of Liaoning Province, (LJKZ00042021), the Fundamental Research Funds for the Central Universities (No. N2119008 and N181906001), and the Liaoning Provincial "Selecting the Best Candi-dates by Opening Competition Mechanism" Science and Technology Program (2022JH1/10400004). It was also supported by the Shenyang Science and Technology Plan Fund (No. 21-104-1-24, 20-201-4-10, and 201375) and the Member Program of Neusoft Research of Intelligent Healthcare Technology, Co., Ltd. (No. MCMP062002). The authors declare that this study received funding from Intelligent Healthcare Technology, Co., Ltd. The funder was not involved in the study design, collection, analysis, interpretation of data, the writing of this article, or the decision to submit it for publication.

Acknowledgments

The authors thank the participants for their greatly valued assistance during experiments.

Conflict of interest

The authors declare that the research was conducted in the absence of any commercial or financial relationships that could be construed as a potential conflict of interest.

Publisher's note

Supplementary material

The Supplementary Material for this article can be found online at: https://www.frontiersin.org/articles/10.3389/fphys.2023.1138257/full#supplementary-material

SUPPLEMENTARY IMAGE 1
Segmentation result of the DR-LCT-UNet (ours) method on CCTA data of case 4.

SUPPLEMENTARY IMAGE 2
Segmentation result of the UNETR method on CCTA data of case 4.

SUPPLEMENTARY IMAGE 3
Segmentation result of the 3D-UNet method on CCTA data of case 4.

SUPPLEMENTARY IMAGE 4
Ground Truth segmentation result on CCTA data of case 4.

SUPPLEMENTARY IMAGE 5
Segmentation result of the DR-LCT-UNet (ours) method on CCTA data of case 1.

SUPPLEMENTARY IMAGE 6
Ground Truth segmentation result on CCTA data of case 2.

SUPPLEMENTARY IMAGE 7
Segmentation result of the 3D-UNet method on CCTA data of case 2.

SUPPLEMENTARY IMAGE 8
Segmentation result of the UNETR method on CCTA data of case 2.

SUPPLEMENTARY IMAGE 9
Segmentation result of the DR-LCT-UNet (ours) method on CCTA data of case 2.

SUPPLEMENTARY IMAGE 10
Ground Truth segmentation result on CCTA data of case 3.

SUPPLEMENTARY IMAGE 11
Segmentation result of the 3D-UNet method on CCTA data of case 3.

SUPPLEMENTARY IMAGE 12
Segmentation result of the UNETR method on CCTA data of case 3.

SUPPLEMENTARY IMAGE 13
Segmentation result of the DR-LCT-UNet (ours) method on CCTA data of case 3.

SUPPLEMENTARY IMAGE 14
Ground Truth segmentation result on CCTA data of case 1.

SUPPLEMENTARY IMAGE 15
Segmentation result of the 3D-UNet method on CCTA data of case 1.

SUPPLEMENTARY IMAGE 16
Segmentation result of the UNETR method on CCTA data of case 1.

References

Bui, T. D., Shin, J., and Moon, T. (2019). Skip-connected 3D DenseNet for volumetric infant brain MRI segmentation. *Biomed. Signal Process. Control* 54, 101613. doi:10.1016/j.bspc.2019.101613

Cheng, Y., Hu, X., Wang, J., Wang, Y., and Tamura, S. (2015). Accurate vessel segmentation with constrained B-snake. *IEEE Trans. Image Process.* 24 (8), 2440–2455. doi:10.1109/TIP.2015.2417683

Çiçek, Ö., Abdulkadir, A., Lienkamp, S. S., Brox, T., and Ronneberger, O. (2016). "3D U-net: learning dense volumetric segmentation from sparse annotation," in *International conference on medical image computing and computer-assisted intervention* (Cham: Springer), 424–432. doi:10.1007/978-3-319-46723-8_49

Dong, C., Xu, S., and Li, Z. (2022). A novel end-to-end deep learning solution for coronary artery segmentation from CCTA. *Med. Phys.* 49 (11), 6945–6959. doi:10.1002/mp.15842

Dosovitskiy, A., Beyer, L., Kolesnikov, A., Weissenborn, D., Zhai, X., Unterthiner, T., et al. (2021). *An image is worth 16x16 words: Transformers for image recognition at scale*. ICLR. doi:10.48550/arXiv.2010.11929

Gao, R., Hou, Z., Li, J., Han, H., Lu, B., and Zhou, S. K. (2021). "Joint coronary centerline extraction and lumen segmentation from ccta using cnntracker and vascular graph convolutional network," in Proceeding of the 2021 IEEE 18th International Symposium on Biomedical Imaging (ISBI), Nice, France, April 2021 (IEEE), 1897–1901. doi:10.1109/ISBI48211.2021.9433764

Ghekiere, O., Salgado, R., Buls, N., Leiner, T., Mancini, I., Vanhoenacker, P., et al. (2017). Image quality in coronary CT angiography: challenges and technical solutions. *Br. J. radiology* 90 (1072), 20160567. doi:10.1259/bjr.20160567

Hatamizadeh, A., Tang, Y., Nath, V., Yang, D., Myronenko, A., Landman, B., et al. (2022). "Unetr: transformers for 3d medical image segmentation," in *Proceedings of the IEEE/CVF winter conference on applications of computer vision*, 574–584. doi:10.48550/arXiv.2103.10504

He, K., Zhang, X., Ren, S., and Sun, J. (2016). "Deep residual learning for image recognition," in *Proceedings of the IEEE conference on computer vision and pattern recognition*, 770–778. doi:10.1109/CVPR.2016.90

Islam, M., Vibashan, V. S., Jose, V., Wijethilake, N., Utkarsh, U., and Ren, H. (2020). "Brain tumor segmentation and survival prediction using 3D attention UNet," in *International MICCAI brainlesion workshop* (Cham: Springer), 262–272. doi:10.1007/978-3-030-46640-4_25

Jayaraj, J. C., Davatyan, K., Subramanian, S. S., and Priya, J. (2019). Epidemiology of myocardial infarction. *Myocard. Infarct.* 3 (10). doi:10.5772/intechopen.74768

Jin, Q., Meng, Z., Sun, C., Cui, H., and Su, R. (2020). RA-UNet: a hybrid deep attention-aware network to extract liver and tumor in CT scans. *Front. Bioeng. Biotechnol.* 1471, 605132. doi:10.3389/fbioe.2020.605132

Kerkeni, A., Benabdallah, A., Manzanera, A., and Bedoui, M. H. (2016). A coronary artery segmentation method based on multiscale analysis and region growing. *Comput. Med. Imaging Graph.* 48, 49–61. doi:10.1016/j.compmedimag.2015.12.004

Kirişli, H. A., Schaap, M., Metz, C. T., Dharampal, A. S., Meijboom, W. B., Papadopoulou, S. L., et al. (2013). Standardized evaluation framework for evaluating coronary artery stenosis detection, stenosis quantification and lumen segmentation algorithms in computed tomography angiography. *Med. image Anal.* 17 (8), 859–876. doi:10.1016/j.media.2013.05.007

Kong, B., Wang, X., Bai, J., Lu, Y., Gao, F., Cao, K., et al. (2020). Learning tree-structured representation for 3D coronary artery segmentation. *Comput. Med. Imaging Graph.* 80, 101688. doi:10.1016/j.compmedimag.2019.101688

Kroft, L. J. M., De Roos, A., and Geleijns, J. (2007). Artifacts in ECG-synchronized MDCT coronary angiography. *Am. J. Roentgenol.* 189 (3), 581–591. doi:10.2214/AJR.07.2138

Lee, C. Y., Xie, S., Gallagher, P., Zhang, Z., and Tu, Z. (2015). "Deeply-supervised nets," in *Artificial intelligence and statistics* (San Diego, CA: PMLR), 562–570.

Lee, K., Zung, J., Li, P., Jain, V., and Seung, H. S. (2017). Superhuman accuracy on the SNEMI3D connectomics challenge. *arXiv preprint*. doi:10.48550/arXiv.1706.00120

Lei, Y., Guo, B., Fu, Y., Wang, T., Liu, T., Curran, W., et al. (2020). Automated coronary artery segmentation in coronary computed tomography angiography (CCTA) using deep learning neural networks. *Med. Imaging 2020 Imaging Inf. Healthc. Res. Appl.* 11318, 279–284. doi:10.1117/12.2550368

Lesage, D., Angelini, E. D., Bloch, I., and Funka-Lea, G. (2009). A review of 3D vessel lumen segmentation techniques: models, features and extraction schemes. *Med. image Anal.* 13 (6), 819–845. doi:10.1016/j.media.2009.07.011

Li, X., Chen, H., Qi, X., Dou, Q., Fu, C. W., and Heng, P. A. (2018). H-DenseUNet: hybrid densely connected UNet for liver and tumor segmentation from CT volumes. *IEEE Trans. Med. imaging* 37 (12), 2663–2674. doi:10.1109/TMI.2018.2845918

Li, W., Qin, S., Li, F., and Wang, L. (2021). MAD-UNet: a deep U-shaped network combined with an attention mechanism for pancreas segmentation in CT images. *Med. Phys.* 48 (1), 329–341. doi:10.1002/mp.14617

Li, Y., Yao, T., Pan, Y., and Mei, T. (2022). Contextual transformer networks for visual recognition. *IEEE Trans. Pattern Analysis Mach. Intell.* 45, 1489–1500. doi:10.1109/TPAMI.2022.3164083

Liu, J., Gao, J., Wu, R., Zhang, Y., Hu, L., and Hou, P. (2013). Optimizing contrast medium injection protocol individually with body weight for high-pitch prospective ECG-triggering coronary CT angiography. *Int. J. Cardiovasc. imaging* 29 (5), 1115–1120. doi:10.1007/s10554-012-0170-x

Liu, L., Cheng, J., Quan, Q., Wu, F. X., Wang, Y. P., Wang, J., et al. (2020). Randomized, multicenter, open-label trial of autologous cytokine-induced killer cell immunotherapy plus chemotherapy for squamous non-small-cell lung cancer: nCT01631357. *Neurocomputing* 409, 244–258. doi:10.1038/s41392-020-00337-x

Ma, G., Yang, J., and Zhao, H. (2020). A coronary artery segmentation method based on region growing with variable sector search area. *Technol. Health Care* 28 (1), 463–472. doi:10.3233/thc-209047

Marquering, H. A., Dijkstra, J., de Koning, P. J., Stoel, B. C., and Reiber, J. H. (2005). Towards quantitative analysis of coronary CTA. *Int. J. Cardiovasc. imaging* 21 (1), 73–84. doi:10.1007/s10554-004-5341-y

Materialise (2020). *Mimics*. Retrieved from https://www.materialise.com/en/medical/mimics-innovation-suite/mimics.

Mihalef, V., Ionasec, R. I., Sharma, P., Georgescu, B., Voigt, I., Suehling, M., et al. (2011). Patient-specific modelling of whole heart anatomy, dynamics and haemodynamics from four-dimensional cardiac CT images. *Interface Focus* 1 (3), 286–296. doi:10.1098/rsfs.2010.0036

Milletari, F., Navab, N., and Ahmadi, S. A. (2016). "V-net: fully convolutional neural networks for volumetric medical image segmentation," in Proceeding of the 2016 fourth international conference on 3D vision (3DV), Stanford, CA, USA, October 2016 (IEEE), 565–571. doi:10.1109/3DV.2016.79

Orujov, F., Maskeliūnas, R., Damaševičius, R., and Wei, W. J. A. S. C. (2020). Fuzzy based image edge detection algorithm for blood vessel detection in retinal images. *Appl. Soft Comput.* 94, 106452. doi:10.1016/j.asoc.2020.106452

Pan, L. S., Li, C. W., Su, S. F., Tay, S. Y., Tran, Q. V., and Chan, W. P. (2021). Coronary artery segmentation under class imbalance using a U-Net based architecture on computed tomography angiography images. *Sci. Rep.* 11 (1), 14493–14497. doi:10.1038/s41598-021-93889-z

Peiris, H., Hayat, M., Chen, Z., Egan, G., and Harandi, M. (2022). "A robust volumetric transformer for accurate 3d tumor segmentation," in *International conference on medical image computing and computer-assisted intervention* (Cham: Springer), 162–172. doi:10.1007/978-3-031-16443-9_16

Qamar, S., Jin, H., Zheng, R., Ahmad, P., and Usama, M. (2020). A variant form of 3D-UNet for infant brain segmentation. *Future Gener. Comput. Syst.* 108, 613–623. doi:10.1016/j.future.2019.11.021

Raff, G. L. (2007). Interpreting the evidence: how accurate is coronary computed tomography angiography? *J. Cardiovasc. Comput. Tomogr.* 1 (2), 73–77. doi:10.1016/j.jcct.2007.04.014

Ronneberger, O., Fischer, P., and Brox, T. (2015). "U-net: convolutional networks for biomedical image segmentation," in *International Conference on Medical image computing and computer-assisted intervention* (Cham: Springer), 234–241. doi:10.1007/978-3-319-24574-4_28

Sharma, P., Suehling, M., Flohr, T., and Comaniciu, D. (2020). Artificial intelligence in diagnostic imaging: status quo, challenges, and future opportunities. *J. Thorac. Imaging* 35, S11–S16. doi:10.1097/RTI.0000000000000499

Song, A., Xu, L., Wang, L., Wang, B., Yang, X., Xu, B., et al. (2022). Automatic coronary artery segmentation of CCTA images with an efficient feature-fusion-and-rectification 3D-UNet. *IEEE J. Biomed. Health Inf.* 26 (8), 4044–4055. doi:10.1109/JBHI.2022.3169425

Tesche, C., De Cecco, C. N., Baumann, S., Renker, M., McLaurin, T. W., Duguay, T. M., et al. (2018). Coronary CT angiography–derived fractional flow reserve: machine learning algorithm versus computational fluid dynamics modeling. *Radiology* 288 (1), 64–72. doi:10.1148/radiol.2018171291

Tian, F., Gao, Y., Fang, Z., and Gu, J. (2021). Automatic coronary artery segmentation algorithm based on deep learning and digital image processing. *Appl. Intell.* 51 (12), 8881–8895. doi:10.1007/s10489-021-02197-6

Vaswani, A., Shazeer, N., Parmar, N., Uszkoreit, J., Jones, L., Gomez, A. N., et al. (2017). Attention is all you need. *Adv. neural Inf. Process. Syst.* 30. doi:10.48550/arXiv.1706.03762

Wang, L., Yang, X., Wang, Q., and Xu, L. (2022a). Two-stage U-net coronary artery segmentation based on CTA images. J. Northeast. Univ. *Nat.* Sci. 43 (6), 792. doi:10.12068/j.issn.1005-3026.2022.06.005

Wang, H., Cao, P., Wang, J., and Zaiane, O. R. (2022b). Uctransnet: rethinking the skip connections in u-net from a channel-wise perspective with transformer. *Proc. AAAI Conf. Artif. Intell.* 36 (3), 2441–2442. doi:10.1021/acs.biochem.2c00621

Wang, H., Xie, S., Lin, L., Iwamoto, Y., Han, X. H., Chen, Y. W., et al. (2022c). "Mixed transformer u-net for medical image segmentation," in ICASSP 2022-2022 IEEE International Conference on Acoustics, Speech and Signal Processing (ICASSP), Singapore, Singapore, May 2022 (IEEE), 2390–2394. doi:10.1109/ICASSP43922.2022.9746172

Wolterink, J. M., Leiner, T., and Išgum, I. (2019). "Graph convolutional networks for coronary artery segmentation in cardiac CT angiography," in Graph Learning in Medical Imaging: First International Workshop, GLMI 2019, Held in Conjunction with MICCAI 2019, Shenzhen, China, October 17, 2019 (Springer International Publishing), 62–69. Proceedings 1.

Yan, X., Tang, H., Sun, S., Ma, H., Kong, D., and Xie, X. (2022). "After-unet: axial fusion transformer unet for medical image segmentation," in *Proceedings of the IEEE/CVF winter conference on applications of computer vision*, 3971–3981. doi:10.48550/arXiv.2110.10403

Yang, J., Lou, C., Fu, J., and Feng, C. (2020). Vessel segmentation using multiscale vessel enhancement and a region based level set model. *Comput. Med. Imaging Graph.* 85, 101783. doi:10.1016/j.compmedimag.2020.101783

Zhang, Z., Tang, Z., Wang, Y., Zhang, Z., Zhan, C., Zha, Z., et al. (2021). Dense Residual Network: enhancing global dense feature flow for character recognition. *Neural Netw.* 139, 77–85. doi:10.1016/j.neunet.2021.02.005

Zhang, Y., Tian, Y., Kong, Y., Zhong, B., and Fu, Y. (2020). Residual dense network for image restoration. *IEEE Trans. Pattern Analysis Mach. Intell.* 43 (7), 2480–2495. doi:10.1109/TPAMI.2020.2968521

Zhang, Z., Wu, C., Coleman, S., and Kerr, D. (2020). DENSE-INception U-net for medical image segmentation. *Comput. methods programs Biomed.* 192, 105395. doi:10.1016/j.cmpb.2020.105395

frontiers | Frontiers in Physiology

TYPE Original Research
PUBLISHED 21 November 2023
DOI 10.3389/fphys.2023.1157787

OPEN ACCESS

EDITED BY
Dingchang Zheng,
Coventry University, United Kingdom

REVIEWED BY
Philipp Berg,
Otto Von Guericke University Magdeburg, Germany
Omid Amili,
University of Toledo, United States

*CORRESPONDENCE
Yuanyuan Liu,
liuyuanyuan@csu.edu.cn
Chuntao Li,
chuntao.li@csu.edu.cn

†These authors have contributed equally to this work

RECEIVED 03 February 2023
ACCEPTED 25 September 2023
PUBLISHED 21 November 2023

CITATION
Chen B, Huang S, Zhang L, Yang L, Liu Y and Li C (2023), Global tendencies and frontier topics in hemodynamics research of intracranial aneurysms: a bibliometric analysis from 1999 to 2022.
Front. Physiol. 14:1157787.
doi: 10.3389/fphys.2023.1157787

Global tendencies and frontier topics in hemodynamics research of intracranial aneurysms: a bibliometric analysis from 1999 to 2022

Bo Chen[1,2,3†], Siting Huang[4†], Liyang Zhang[1,3,5], Liting Yang[1,3,5], Yuanyuan Liu[3*] and Chuntao Li[1,3,5*]

[1]Department of Neurosurgery, Xiangya Hospital, Central South University, Changsha, Hunan, China, [2]Department of Surgery, LKS Faculty of Medicine, School of Clinical Medicine, Queen Mary Hospital, The University of Hong Kong, Pokfulam, Hong Kong SAR, China, [3]National Clinical Research Center for Geriatric Disorders, Xiangya Hospital, Central South University, Changsha, Hunan, China, [4]Department of Dermatology, Xiangya Hospital, Central South University, Changsha, Hunan, China, [5]Hypothalamic-Pituitary Research Center, Xiangya Hospital, Central South University, Changsha, Hunan, China

Background: Hemodynamics plays a crucial role in the initiation, enlargement, and rupture of intracranial aneurysms (IAs). This bibliometric analysis aimed to map the knowledge network of IA hemodynamic research.

Methods: Studies on hemodynamics in IAs published from 1999 to 2022 were retrieved from the Web of Science Core Collection (WoSCC). The contributions of countries, institutions, authors, and journals were identified using VOSviewer, Scimago Graphica, and Microsoft Excel. Tendencies, frontier topics, and knowledge networks were analyzed and visualized using VOSviewer and CiteSpace.

Results: We identified 2,319 publications on hemodynamics in IAs. The annual number of publications exhibited an overall increasing trend. Among these, the United States, Japan, and China were the three major contributing countries. Capital Medical University, State University of New York (SUNY) Buffalo University, and George Mason University were the three most productive institutions. Meng H ranked first among authors regarding the number of articles and citations, while Cebral JR was first among co-cited authors. The *American Journal of Neuroradiology* was the top journal in terms of the number of publications, citations, and co-citations. In addition, the research topics can be divided into three clusters: hemodynamics itself, the relationship of hemodynamics with IA rupture, and the relationship of hemodynamics with IA treatment. The frontier directions included flow diverters, complications, morphology, prediction, recanalization, and four-dimensional flow magnetic resonance imaging (4D flow MRI).

Abbreviations: AUC, Area under the curve; C/P, Citations/papers; CFD, Computational fluid dynamics; FSI, Fluid-structure interaction; 4D flow MRI, four-dimensional flow magnetic resonance imaging; IF, Impact factor; IA, Intracranial aneurysms; LS, link strength; LSA%, Low shear index%; N, Number; OSI, Oscillatory shear index; PIV, Particle image velocimetry; PTV, Particle tracking velocimetry; TC, Total citation; TLS, Total link strength; WSS, Wall shear stress; WoSCC, Web of Science Core Collection; WFNS, World Federation of Neurosurgical Societies; WSSG, WSS gradient.

Conclusion: This study drew a knowledge map of the top countries, institutions, authors, publications, and journals on IA hemodynamics over the past 2 decades. The current and future hotspots of IA hemodynamics mainly include hemodynamics itself (4D flow MRI), its relationship with IA rupture (morphology and prediction), and its relationship with IA treatment (flow diverters, complications, and recanalization).

KEYWORDS

intracranial aneurysm, hemodynamics, bibliometric, knowledge map, hotspot

1 Introduction

Intracranial aneurysm (IA) is a pathologically saccular or fusiform dilatation of the cerebral arteries that occurs in approximately 2%–5% of the population and can be life-threatening upon rupture (Brown and Broderick, 2014; Zhu et al., 2022). Because of the inevitable impingement of blood flow to the arterial wall, IA is closely related to hemodynamics. Once hemodynamic damage exceeds the structural strength of the arterial wall, the arterial wall is injured, and IA may occur. Hemodynamics interacts with other complex biological factors that contribute to IA initiation, development, growth, and potential stability or rupture (Frösen et al., 2012; Morel et al., 2021). However, in the early years, technical limitations made the measurement of hemodynamic parameters in humans difficult. The advent of computational and radiographic modeling has allowed for hemodynamic research on IAs. Studies have found that blood flow pulsation affects both the arterial wall surface (such as the wall shear stress and oscillatory shear index) (Soldozy et al., 2019) and inner structures (such as the medial gap and intimal pad) (Kataoka et al., 2020; Chen et al., 2022a), which can contribute to IA initiation, enlargement, and rupture. Hemodynamics also affects the biological signals of the arterial wall and can serve as a tool to understand the molecular pathogenesis of IAs (Levitt et al., 2019; Chen et al., 2022b; Chen et al., 2023). In addition, computational fluid dynamics (CFD) can be used to predict IA rupture (Tang et al., 2021), inform stent design (Suzuki et al., 2017; Bisighini et al., 2023), and allow surgical improvement (Bao et al., 2021). Overall, hemodynamic research in IAs is rich, diverse, and valuable. Clarifying the current status and hot topics may benefit new researchers in this field and permit better research.

Bibliometrics is a widely accepted method for reviewing numerous articles in a specific field through quantitative analysis (Donthu et al., 2021). Through bibliometrics, we can identify crucial contributors (e.g., authors, institutions, and countries), collaborative networks, and frontier research topics (Zhang et al., 2022). Several bibliometric studies on IAs have been conducted. Chen et al. (2022) investigated the research trends and hotspots of stent application in acutely ruptured IAs. Lu et al. (2021) described a research shift of unruptured IAs, especially in terms of endovascular treatment. Zhang et al. (2022) explored the application of animal models in IA research and found that mice were the optimal model (Chen et al., 2022). However, no bibliometric analyses of hemodynamic research in IAs have been reported to date. Accordingly, based on the Web of Science Core Collection (WoSCC) from 1999 to 2022, this study applied bibliometric tools (VOSviewer, CiteSpace, and Scimago Graphica) to uncover publication trends, influential contributors, top collaborators, and emerging frontier topics in the field of hemodynamic research in IAs.

2 Materials and methods

2.1 Data source and search strategy

The literature search was performed on the WoSCC website (https://www.webofscience.com/wos/woscc/advanced-search) to identify publications indexed between 1 January 1999, and 31 December 2022. The specific search formula was as follows: Topic (TS) = ("intracranial aneurysm*" OR "cerebral aneurysm*" OR "brain aneurysm*" OR "intracerebral aneurysm*" OR "cranial aneurysm*") AND TS = ("hemodynamic*" OR "haemodynamic*" OR "computational fluid dynamic*" OR "CFD" OR "4D-Flow MRI" OR "optical imaging modalities" OR "particle image velocimetry" OR "PIV" OR "particle tracking velocimetry" OR "PTV" OR "shear stress" OR "flow velocity" OR "flow rate"). To avoid bias, two independent investigators (B Chen and LY Zhang) performed the literature search and filtering and a senior researcher (CT Li) resolved any discrepancies in findings between these investigators.

2.2 Inclusion and exclusion criteria

This analysis included original review articles on the hemodynamics of IAs indexed in the WoSCC database between 1 January 1999, and 31 December 2022. The exclusion criteria were 1) unpublished papers, 2) articles requiring manual research, and 3) articles written in languages other than English. Of the 2,815 publications initially identified, 496 were excluded, and 2,319 were finally included in the analyses.

2.3 Data extraction and bibliometric analysis

The extracted bibliometric parameters included journal names, publication times, titles, countries/regions, institutions, authors, keywords, references, and citations. Journal impact factors (IFs) were collected from the most recent Journal Citation Reports (2022). In addition, VOSviewer (version 1.6.18), CiteSpace (version 6.1 R6), Scimago Graphica (version 1.0.26), and Microsoft Excel 2019 were used to perform the bibliometric analysis and visualization.

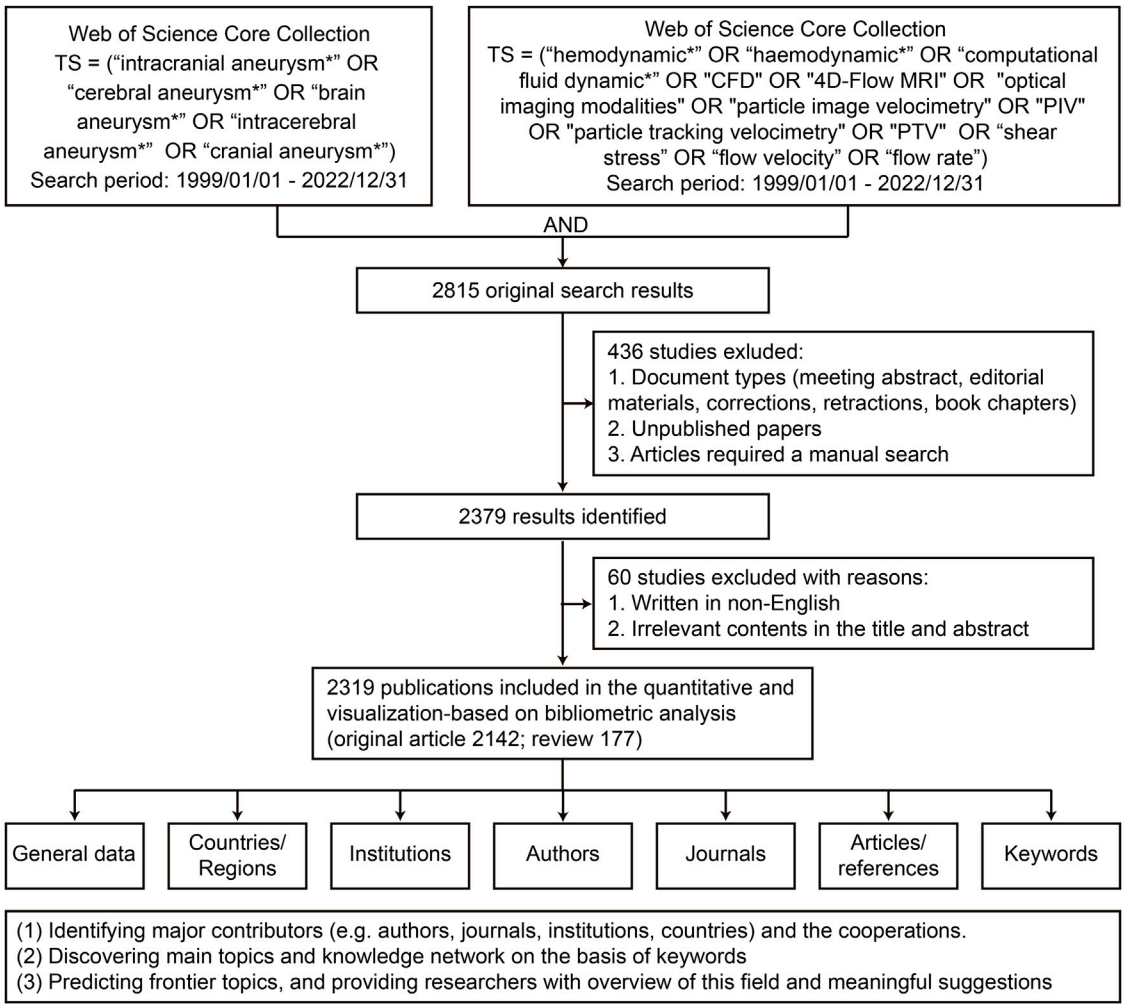

FIGURE 1
Flow chart of data collection, screening, and bibliometric analysis.

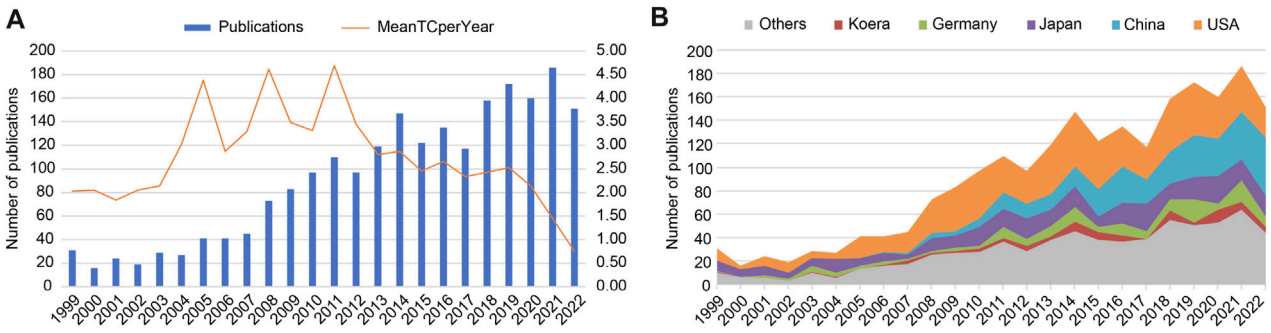

FIGURE 2
Trends of publications and citations on intracranial aneurysm (IA) hemodynamics. **(A)** Numbers of publications and mean total citations (TCs). **(B)** Annual publications of the top five countries/regions.

Microsoft Excel was used for the time and contribution analyses. Scimago Graphica was used for the country collaboration analysis. VOSviewer was used to visualize the institutional cooperation map, author cooperation map, author co-citation network, and keyword co-occurrence network. CiteSpace was used to visualize the keyword and reference burst figures and reference co-citation network.

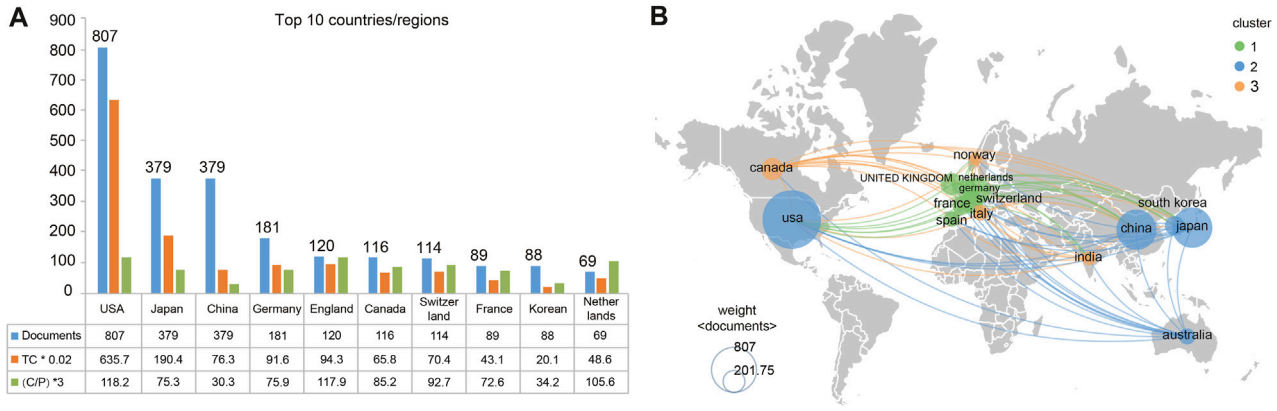

FIGURE 3
Top 10 most productive countries and international collaborations on IA hemodynamics. **(A)** Numbers of publications, TCs, and citations per paper (C/P). **(B)** International collaboration map. Node size, number of produced articles; color, clusters.

3 Results

3.1 Overall characteristics

A total of 2,319 publications on the hemodynamics of IAs indexed between 1 January 1999, and 31 December 2022, were finally identified, including 2,142 (92.4%) original articles and 177 (7.6%) reviews (Figure 1). Although there were some slight fluctuations, the number of published articles showed an overall upward trend from 31 in 1999 to 151 in 2022, peaking at 186 in 2021. Additionally, the timing of the mean total citations (TC) per year could be divided into three periods: Phase I, 1999–2003 (remaining stable); Phase II, 2003–2013 (showing dramatic fluctuations); and Phase III, 2013–2022 (declining) (Figure 2A). Figure 2B shows the annual publications from the top five countries in this field. Among these, the US contributed the most publications. China began publishing articles in 2006, relatively late but has developed rapidly, surpassing the US in the number of published articles in 2021.

3.2 Countries/regions

More than 60 countries/regions have contributed to this field, the top ten of which are listed in Figure 3. Among these, the US was first, with 807 publications, followed by Japan (379 publications) and China (379 publications). Regarding TC, the US again ranked first (31,785 TC), followed by Japan (9520 TC) and England (4716 TC). The US also ranked first in citations per paper (C/P) (39.4 C/P), followed by England (39.3 C/P) and the Netherlands (35.2 C/P) (Figure 3A). An international collaboration map drawn using VOSviewer with the minimum number of publications set at 40 included 15 countries/regions that met the criteria. Of these, the US, Japan, and China appeared as center nodes, with the closest cooperations between the US and Japan (link strength, LS = 69) and the US and China (LS = 52) (Figure 3B).

3.3 Institutions

In total, 861 institutions participated in the publication of articles on hemodynamics in IAs. Among the top ten productive institutions, five were located in the US, two in China, and one each in Canada, Germany, and Japan. Capital Medical University contributed the most publications (105 publications), followed by the State University of New York (SUNY) Buffalo (88 publications) and George Mason University (88 publications). Regarding TC and C/P, the top three institutions were SUNY Buffalo University (TC = 5,911, C/p = 67.2), George Mason University (TC = 5,364, C/p = 61), and Inova Fairfax Hospital (TC = 3,798, C/p = 99.9) (Figure 4A). Figure 4B illustrates the cooperation among the 54 institutions with >15 publications. Of these, George Mason University had the widest cooperation (total link strength, TLS = 108), followed by Capital Medical University (TLS = 60) and Tohoku University (TLS = 60) (Figure 4B).

3.4 Authors and co-authors

Table 1 shows the top ten prolific authors and the most co-cited authors, most of whom were from the US. Author co-citation was defined as ≥2 authors meanwhile cited in ≥1 publication. Among the authors, Meng, H published the most articles (69 articles, 4,326 citations), followed by Yang, Xj (50 articles, 929 citations) and Cebral, Jr (38 articles, 1,047 citations). The top three co-cited authors were Cebral, Jr (1902 co-citations), Meng, H (743 co-citations), and Xiang, Jp (532 co-citations). The visualized map analysis revealed that widely cooperating authors, including Meng, H (TLS = 173) and Yang Xj (TLS = 192), were active in the relatively early phase (average publication years 2013–2016), while recently active authors, such as Ishibashi, T and Berg, P (average publication year 2019) had relatively narrow cooperation networks ($TLS_{Ishibashi}$ = 70, TLS_{Berg} = 30) (Figure 5A). The map of the top 34 co-cited authors with >200 co-citations showed the highest number of co-citations between Torii, R and Tezduyar, Te (LS = 2,443) (Figure 5B).

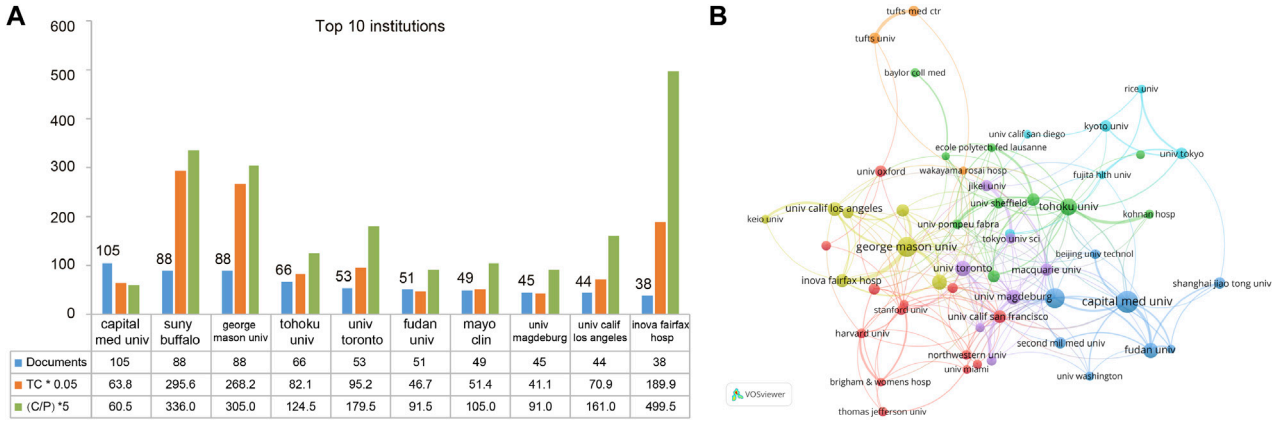

FIGURE 4
Top 10 most prolific institutions and inter-institution cooperations on IA hemodynamics. **(A)** Numbers of publications, TCs, and C/P. **(B)** Inter-institution cooperation network. Node size, number of produced articles; line thickness, cooperated strength; color, clusters.

TABLE 1 Top 10 prolific authors and co-cited authors on hemodynamics research in IAs.

Rank	Author	Publications	Citations	Country	Co-cited author	Co-citations	Country
1	Meng, H	69	4,326	United States	Cebral, Jr	1,902	United States
2	Yang, Xj	50	929	China	Meng, H	743	United States
3	Cebral, Jr	38	1,047	United States	Xiang, Jp	532	China
4	Siddiqui, Ah	36	2,020	United States	Shojima, M	489	Japan
5	Xiang, Jp	34	1,332	China	Wiebers, D	455	United States
6	Zhang, Y	33	703	China	Aoki, T	453	Japan
7	Liu, J	32	491	China	Jou, Ld	417	United States
8	Berg, P	29	394	Germany	Ujiie, H	380	Japan
9	Mut, F	28	602	United States	Steinman, Da	368	Canada
10	Malek, Am	28	801	United States	Castro, Ma	358	United States

3.5 Journals, co-cited journals, and impact factors

Altogether, 461 journals published articles on hemodynamics research in IAs. The top ten active journals and co-cited journals are listed in Table 2. Journal co-citation was defined as ≥2 journals being cited simultaneously in ≥1 publications. In terms of publication quantity, the *American Journal of Neuroradiology* was first, with 155 publications, followed by *Neurosurgery* (94 publications) and *World Neurosurgery* (92 publications). Regarding citations and co-citations, the *American Journal of Neuroradiology* ranked first (7,906 citations, 8,108 co-citations), followed by *Stroke* 4,722 citations, 7,166 co-citations) and *Journal of Neurosurgery* (4,030 citations, 5,499 co-citations). In addition, among these ten journals and co-cited journals, the highest and lowest IFs were 8.3 (*Stroke*) and 1.7 (*Interventional Neuroradiology* and *J Biomech Eng-T Asme*), respectively.

3.6 Keywords

Figure 6A illustrates a visualization of keywords that co-occurred at least 50 times in hemodynamics research in IAs. A total of 66 keywords were identified and grouped into three clusters. Cluster #1 (red) indicates research on hemodynamics itself, with keywords including "computational fluid dynamics," "wall shear stress," and "fluid-structure interaction". Cluster #2 (blue) represents research on aneurysm rupture, with keywords including "arachnoid hemorrhage," "rupture risk," and "prediction". Cluster 3 (green) indicates research on aneurysm treatment, with keywords including "endovascular treatment," "stent pipeline," and "coil embolization". In addition, the keywords in Figure 6B are colored based on the average publication years. The concepts of "saccular aneurysms," "carotid artery," and "subarachnoid hemorrhage" appeared early (blue), while frontier topics including "inflammation" and "flow

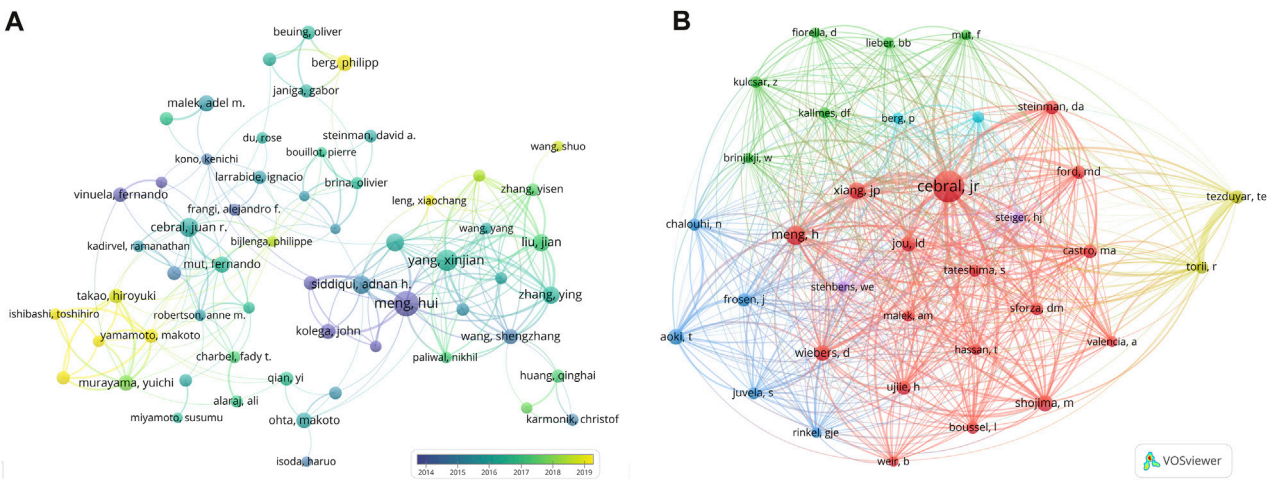

FIGURE 5
Author collaboration and co-cited author networks on IA hemodynamics. **(A)** Collaborated map of productive authors from 2014 to 2019. **(B)** Co-cited author map. Node size, number of produced articles; line thickness, cooperated strength; color, **(A)** average publication year, **(B)** clusters.

TABLE 2 Top 10 prolific journals and co-cited journals on hemodynamics research in IAs.

Rank	Journal	Publications	Citations	IF	Co-cited journal	Co-citations	IF
1	*Am J Neuroradiol*	155	7,906	3.5	*Am J Neuroradiol*	8,108	3.5
2	*Neurosurgery*	94	3,877	4.8	*Stroke*	7,166	8.3
3	*World Neurosurg*	92	992	2.0	*J Neurosurg*	5,499	4.1
4	*J Neurosurg*	86	4,030	4.1	*Neurosurgery*	5,138	4.8
5	*J Neurointerv Surg*	83	1,519	4.8	*J Biomech*	2,341	2.4
6	*J Biomech*	78	1,975	2.4	*Ann Biomed Ang*	1,993	3.8
7	*Interv Neuroradiol*	53	254	1.7	*J Neurointerv Surg*	1,700	4.8
8	*Stroke*	47	4,722	8.3	*J Biomech Eng-T Asme*	1,539	1.7
9	*Ann Biomed Eng*	46	2,265	3.8	*Neuroradiology*	1,275	2.8
10	*Int J Numer Method Biomed Eng*	44	843	2.1	*Acta Neurochir*	1,174	2.4

IF, impact factor.

diverter," appeared recently (yellow). Next, the CiteSpace burst module was applied to identify the research tendencies and shifts in central topics. Bursts refer to sudden increases over time. The 25 keywords with the strongest citation bursts are shown in Figure 6C. Among them, the topics gradually shifted from "saccular aneurysm," "Guglielmi detachable coil," and "internal carotid artery" to "angiography, complex hemodynamics, fluid-structure interaction" and "morphology, prediction, diversion, complication, recanalization, and four-dimensional flow magnetic resonance imaging (4D flow MRI)".

3.7 Top cited articles and co-cited references

Table 3 lists the top 10 most-cited papers in hemodynamics research on IAs, with the number of citations ranging from 351 to 566. Among these, nine were original articles and one was a review article. Four studies were published in *Stroke* and two in the *American Journal of Neuroradiology*. An article by Shojima et al. (2004) had the highest number of citations (566), followed by articles from Helgadottir et al. (2008) (550 citations) and Cebral et al. (2005) (514 citations). In addition, we performed a burst analysis of the reference co-citations. Reference co-citations are defined as two or more references cited in one or more papers simultaneously. Figure 7A shows the reference co-citation map colored by publication year from 1999 to 2022, in which the burst co-cited references were mainly concentrated in the middle period. Figure 7B displays the 20 references with the strongest citation bursts. Of them, "Meng et al., 2014, AM J NEURORADIOL, V35, P1254" had the highest burst strength (54.42), followed by "Cebral et al., 2005, AM J NEURORADIOL, V26, P2550" (strength = 45.15) and "Shojima et al., 2004, STROKE, V35, P2500" (strength = 42.86). The citation burst of "Cebral et al., 2017, AM J NEURORADIOL, V38, P119" ended in 2022, indicating high attention in recent years.

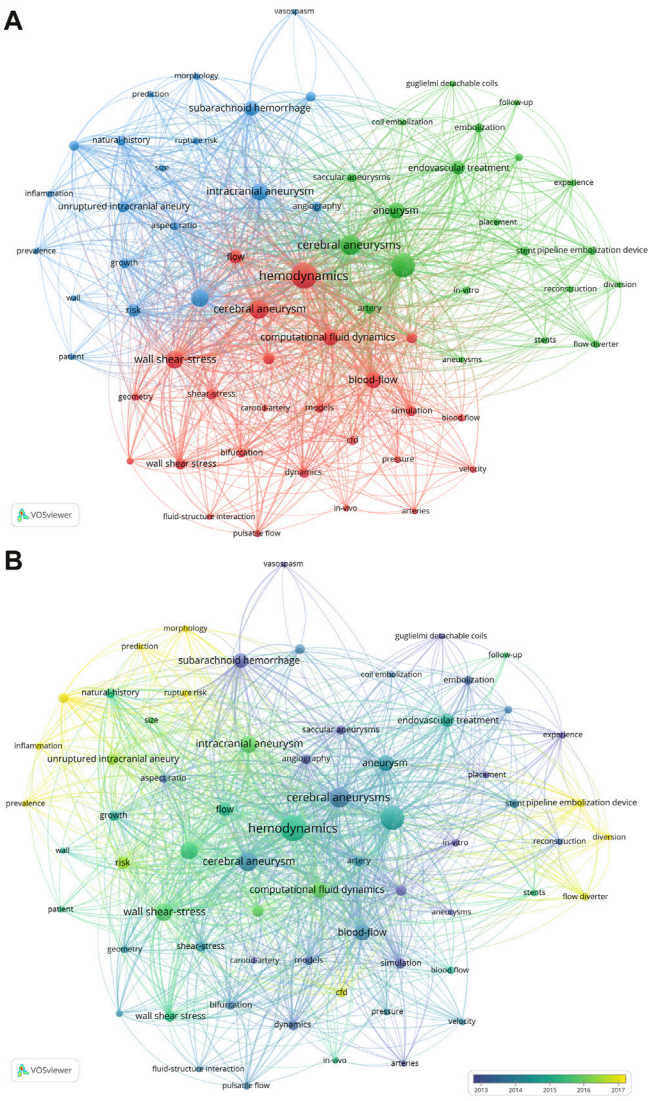

FIGURE 6
Analysis of keywords on IA hemodynamics. **(A)** Keyword co-occurrence network colored by clusters. **(B)** Keyword co-occurrence network colored by average publication years. Node size, keyword frequency. **(C)** Top 25 keywords with the strongest citation bursts. Red segment, burst duration.

4 Discussion

Hemodynamics is widely involved in IA formation, enlargement, and rupture (Soldozy et al., 2019; Liu et al., 2023). Hemodynamics can also be used to predict the prognosis and improve therapeutic approaches for patients with IA (Suzuki et al., 2017; Bao et al., 2021; Tang et al., 2021). In the current study, we performed a bibliometric analysis of publications on hemodynamics in IAs. This analysis identified publication trends, influential contributors (e.g., authors, journals, institutions, and countries), corresponding cooperation networks, and emerging frontier topics. Importantly, the results of this study may help new researchers to quickly learn about this field and perform better research in the future.

4.1 Overall trends and major contributing countries

The number of published articles reflects the interest of researchers in the field (Durieux and Gevenois, 2010; Huang et al., 2023). Overall, the number of publications on hemodynamics in IA displayed an upward tendency from 1999 to 2022, indicating the increasing interest of researchers in this field. Of these, the US was the most productive country, while China was an emerging country, with a steeper increase in the number of publications. Several factors may explain the increase in IA hemodynamics in China. First, China has a large population and a high prevalence of unruptured IA (7% among Chinese adults aged 35–75 years) (Li et al., 2013). Second, the number of neurosurgeons and the level of IA detection have grown strikingly in recent years.

TABLE 3 Top 10 most cited publications related to hemodynamics research in intracranial aneurysms.

Rank	Title	Journal	Document type	Corresponding author	Affiliation	Year	Citations
1	Magnitude and role of wall shear stress on cerebral aneurysm: computational fluid dynamic study of 20 middle cerebral artery aneurysms	*Stroke*	Article	Kirino, T	University of Tokyo	2004	566
2	The same sequence variant on 9p21 associates with myocardial infarction, abdominal aortic aneurysm and intracranial aneurysm	*Nat Genet*	Article	Stefansson, K	deCODE Genet	2008	550
3	Characterization of cerebral aneurysms for assessing risk of rupture by using patient-specific computational hemodynamics models	*AJNR Am J Neuroradiol*	Article	Putman, CM	Inova Fairfax Hospital	2005	514
4	Hemodynamic-morphologic discriminants for intracranial aneurysm rupture	*Stroke*	Article	Meng, H	State University of New York (SUNY_ Buffalo	2011	481
5	High WSS or low WSS? Complex interactions of hemodynamics with intracranial aneurysm initiation, growth, and rupture: toward a unifying hypothesis	*AJNR Am J Neuroradiol*	Review	Siddiqui, A	SUNY Buffalo	2014	465
6	Efficient pipeline for image-based patient-specific analysis of cerebral aneurysm hemodynamics: technique and sensitivity	*IEEE Trans Med Imaging*	Article	Frangi, AF	George Mason University	2005	434
7	Complex hemodynamics at the apex of an arterial bifurcation induces vascular remodeling resembling cerebral aneurysm initiation	*Stroke*	Article	Kolega, J	SUNY Buffalo	2007	408
8	Prospective evaluation of surgical microscope-integrated intraoperative near-infrared indocyanine green video angiography during aneurysm surgery	*J Neurosurg*	Article	Spetzler, RF	Barrow Neurological Institute	2005	384
9	Aneurysm Growth Occurs at Region of Low Wall Shear stress patient-specific correlation of hemodynamics and growth in a longitudinal study	*Stroke*	Article	Saloner, D	Vet Adm Med Ctr	2008	366
10	Morphology parameters for intracranial aneurysm rupture risk assessment	*Neurosurgery*	Article	Kassell, NF	SUNY Buffalo	2008	351

According to the reports of the World Federation of Neurosurgical Societies (WFNS), China has possessed the most neurosurgeons (around 11,000) worldwide since 2016 (Yu et al., 2019). Third, the Chinese government has recently expanded its funding in the field of basic research. However, an increased number of publications does not necessarily represent highly influential affiliations, authors, and articles. For example, China accounted for only two of the top ten productive institutions, one of the top prolific co-cited authors, and none of the top ten most cited articles.

The number of citations represents the performance of a publication (Durieux and Gevenois, 2010; Liang et al., 2023). In our study, the timing of the mean TCs on hemodynamics in IAs could be divided into three periods. Phase II (2003–2013) had a dramatically higher number of citations than the other two periods, reflecting better publication performance. During this Phase II, some representative keywords with high research value showed bursts, including "parent vessel," "angiography," and "fluid-structure interaction". In addition, the top ten cited publications emerged during this Phase. Therefore, we conclude that Phase II was a crucial stage for research on hemodynamics in IAs, which laid the major foundation for current research. In addition, one reason for the declining citation phase of Phase III (2013–2022) might be the non-standardized acquisition of relevant hemodynamic parameters. Excessive assumptions, simplifications, and imprecise pre- and post-simulation steps may lead to incorrect findings in this field (Berg et al., 2019a) and could partially explain why hemodynamics have not yet been widely implemented for the investigation of IAs in clinical practice.

4.2 Active institutions, authors, journals, and co-cited journals

Identifying influential authors and institutions may help researchers choose their collaborating partners. Meng H (SUNY Buffalo University) was the most productive and cited author of hemodynamic research on IAs. She and her team performed CFD histology mapping on a dog IA model and found that high wall shear stress (WSS) and a high WSS gradient (WSSG) were dangerous hemodynamic conditions for IA initiation (Meng et al., 2007). Later, based on clinical imaging data, she built a combined model of hemodynamics and morphology to

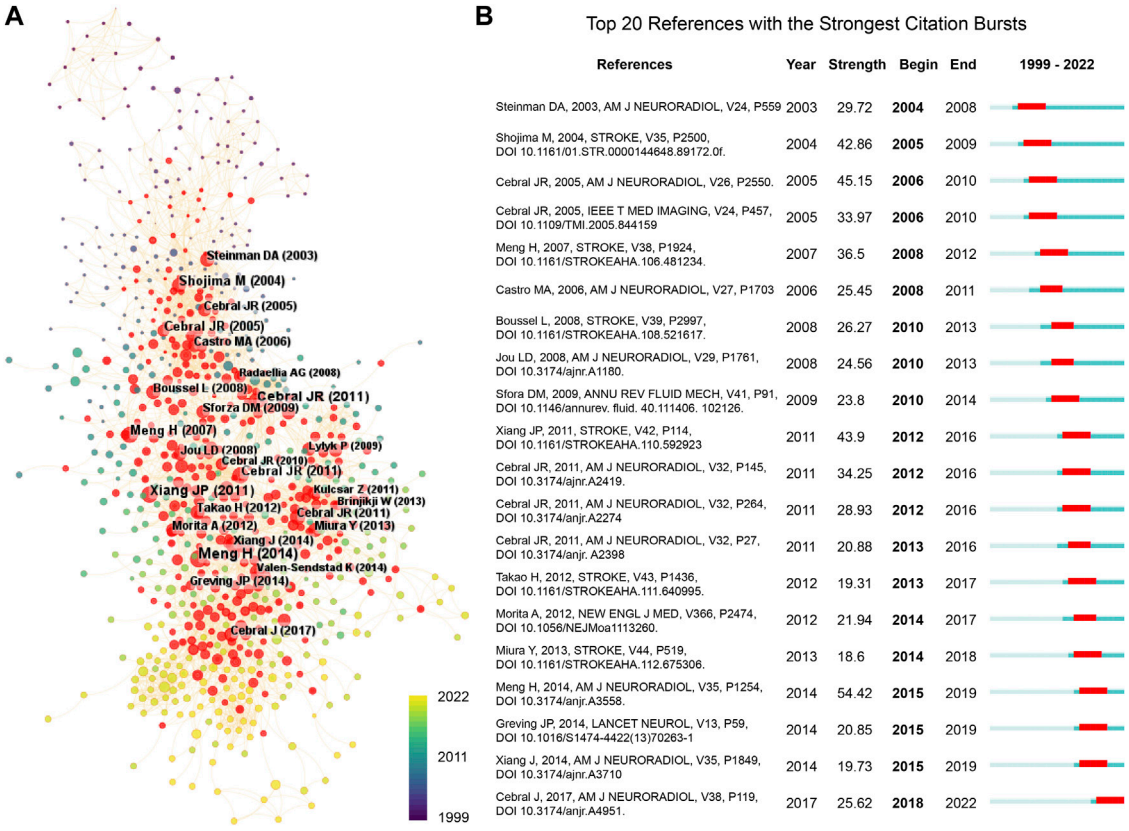

FIGURE 7
Analysis of co-cited reference on IA hemodynamics. **(A)** Reference co-citation network visualized using CiteSpace. Node size, citation number; red nodes, burst references. **(B)** Top 20 references with the strongest citation bursts. Red segment, burst duration.

predict IA rupture (Xiang et al., 2011). These studies were the most cited publications and references with the strongest citation bursts, laying the foundation for subsequent research. Regarding prolific affiliations, Capital Medical University in China ranked first but ranked low in citations per paper. Several reasons may account for the contradiction between quantity and quality in China. First, the number of publications in China will surpass that in the US for the first time in 2021, indicating that Chinese publications might need more time to be cited. Second, compared to the US, a lower percentage of Chinese studies are published in high-IF journals such as *Stroke* (IF = 8.3).

Journal productivity represents the interest of a journal in a specific field; thus, the top co-cited journals can be regarded as authoritative journals. In research on hemodynamics in IA, the *American Journal of Neuroradiology*, *Neurosurgery*, and *World Neurosurgery* are the most productive journals, while the *American Journal of Neuroradiology*, *Stroke*, and *Journal of Neurosurgery* were the most frequently cited journals. If Chinese researchers want to improve their influence on IA hemodynamics, they should deepen their studies and select more influential target journals.

4.3 Research hotspots and frontier trends

Quick learning in a field can be obtained through keyword co-occurrence analysis (Ai et al., 2023). In our study, the major keywords could be divided into three clusters representing different topics and frontier trends.

Cluster 1 (red): Research on hemodynamics itself. Hemodynamic analyses in IA are mainly performed through approaches including CFD, 4D-Flow MRI, and optical imaging. CFD calculates the blood flow by solving the governing equations of fluid mechanics; therefore, the flow field in CFD is slightly virtual. 4D-Flow MRI measures blood flow *in vivo* and *in vitro*; thus, the flow field is more real (Kamada et al., 2022). Previous studies have reported a strong correlation between 4D flow MRI and CFD for the inflow hemodynamics of IA (Misaki et al., 2021). Despite being more consistent with the real hemodynamics in the human body, 4D flow MRI also has shortcomings, including relatively low spatiotemporal resolutions and limited accuracy due to imaging noise (Wu et al., 2022). Moreover, optical imaging techniques are commonly utilized for the *in vitro* hemodynamic validation of CFD and 4D flow MRI, as they offer well-controlled and high-resolution flow fields and do not require the use of ionizing radiation (Wu et al., 2022). The common optical imaging techniques research on hemodynamics in IA include particle image velocimetry (PIV), particle tracking velocimetry (PTV), and others (Liou et al., 2007; Medero et al., 2020). Some international studies on IA hemodynamics have reported that the accuracy of hemodynamic calculation is affected by model segmentation, boundary conditions, hemodynamic parameters, solver algorithms, and others

(Steinman et al., 2013; Berg et al., 2015; Berg et al., 2018; Valen-Sendstad et al., 2018; Berg et al., 2019b; Voß et al., 2019). Researchers should combine actual clinical situations to evaluate IA hemodynamics and use optical imaging techniques to validate the results. Furthermore, to enhance the reliability of research on hemodynamics in IA, Berg et al. (2019a) proposed flow analysis standardization in comparison studies, as well as numerical investigations in uncertainty quantification and validation studies.

Cluster 2 (blue): Research on the relationship between hemodynamics and IA rupture. IA rupture comprises 80%–85% of non-traumatic subarachnoid hemorrhages and can lead to high mortality (Brown and Broderick, 2014). Considering the long-term impingement of blood flow on the arterial wall, IA rupture is closely related to hemodynamics such as WSS, WSSG, oscillatory shear index (OSI), flow patterns, and others (Soldozy et al., 2019). One meta-analysis identified average WSS as a protective hemodynamic parameter, whereas OSI and low shear index% (LSA%) were harmful hemodynamic parameters of IA rupture (Han et al., 2021). However, hemodynamics are complex and the role of WSS in IA rupture remains controversial. Zhang et al. (2018) found that an excessively high WSS in the parent artery could predict rupture of anterior communicating artery aneurysms. Accordingly, regarding the "high-versus-low WSS" controversy, Meng et al. (2014) proposed a widely accepted unifying hypothesis that low WSS and high OSI contributed to the rupture of large and atherosclerotic IA phenotypes, while high WSS and positive WSSG facilitated the rupture of small or secondary bleb IA phenotype. In addition, compared to unruptured IAs, ruptured IAs have more complex and unstable flow patterns (Byrne et al., 2014) such as a higher number of vortices (Xiang et al., 2011) and more complex inflow jet patterns (Futami et al., 2017). Some retrospective cohort studies have shown that hemodynamics can be integrated with geometric and clinically relevant information, such as IA site and focal wall enhancement, to predict IA rupture (Janiga et al., 2015a; Berg et al., 2019b; Larsen et al., 2020). The area under the curve (AUC) value for predicting IA rupture accuracy can reach 0.820–0.910 (Chen et al., 2020; Shi et al., 2021). However, prospective, large-sample, multicenter cohort studies are needed to compare hemodynamics and IA rupture.

Cluster 3 (green): Research on the relationship between hemodynamics and IA treatment. Over the past 30 years, multiple therapeutic approaches have been developed for IA, including clipping and endovascular treatment (coils, stents, and flow diverters). These treatments commonly change the hemodynamic status. Both coil embolization and flow diverters decrease intra-aneurysmal blood flow velocity and WSS, which explains their protection against rupture (Goubergrits et al., 2014; Jing et al., 2016). When treatments fail, the high WSS at the neck remnant could require recanalization, while a lack of decreased flow velocity and undiminished high-WSS areas might lead to postoperative rupture (Goubergrits et al., 2014; Chen et al., 2021). Moreover, hemodynamic research may be an effective tool to improve IA treatment. Janiga et al. (2015b) used CFD to identify an optimal flow-diverting stent for patient-specific IAs. Chen et al. (2021) employed CFD to propose the proximal densification of flow diverters to reduce IA rupture risk. The combination of CFD and structural analysis can optimize flow diverter design, including the weave angle and wire thickness (Suzuki et al., 2017). Notably, in our study, the keyword "diversion" appeared in the average time of 2017, indicating that the flow diverter received more attention in IA treatments. However, flow diverters still have limitations and complications such as in-stent stenosis (John et al., 2016), thromboembolic complications (Leung et al., 2012), and others. Future hemodynamic research on IA treatment should focus on these topics.

5 Limitations

This study had several limitations. First, we only collected literature from the WoSCC, which provided the most suitable data format for CiteSpace and VOSviewer. Other databases such as Scopus and PubMed were also used to confirm our findings. Second, our study only included publications written in English and excluded non-English publications, which may have caused a selection bias. Third, record updates in the WoSCC may have led to retrieval disparities.

6 Conclusion

In conclusion, this study drew a knowledge map of the top countries, institutions, authors, publications, and journals on IA hemodynamics over the past 2 decades. The current and future hotspots of IA hemodynamics mainly include hemodynamics itself (4D flow MRI), its relationship with IA rupture (morphology and prediction), and its relationship with IA treatment (flow diverters, complications, and recanalization).

Data availability statement

The original contributions presented in the study are included in the article/Supplementary material, further inquiries can be directed to the corresponding authors.

Author contributions

BC, LY, SH, and CL designed and drafted the manuscript; BC, LZ, and CL organized figures and edited legends. BC, LZ, SH, CL, LY, and YL revised the article; BC, LY, and LZ conducted the data analysis; All authors contributed to the article and approved the submitted version.

Funding

This study was supported by the Fundamental Research Funds for the Central Universities of Central South University (No. 2021zzts1036).

Conflict of interest

The authors declare that the research was conducted in the absence of any commercial or financial relationships that could be construed as a potential conflict of interest.

Publisher's note

References

Ai, S., Li, Y., Tao, J., Zheng, H., Tian, L., Wang, Y., et al. (2023). Bibliometric visualization analysis of gut-kidney axis from 2003 to 2022. *Front. Physiol.* 14, 1176894. doi:10.3389/fphys.2023.1176894

Bao, Q., Meng, X., Hu, M., Xing, J., Jin, D., Liu, H., et al. (2021). Simulation analysis of aneurysm embolization surgery: hemorheology of aneurysms with different embolization rates (CTA). *Bio-Med. Mat. Eng.* 32, 295–308. doi:10.3233/bme-211225

Berg, P., Roloff, C., Beuing, O., Voss, S., Sugiyama, S., Aristokleous, N., et al. (2015). The computational fluid dynamics rupture challenge 2013--phase II: variability of hemodynamic simulations in two intracranial aneurysms. *J Biomech Eng.* 137, 121008. doi:10.1115/1.4031794

Berg, P., Saalfeld, S., Voß, S., Beuing, O., and Janiga, G. (2019a). A review on the reliability of hemodynamic modeling in intracranial aneurysms: why computational fluid dynamics alone cannot solve the equation. *Neurosurg. Focus* 47, E15. doi:10.3171/2019.4.Focus19181

Berg, P., Voß, S., Janiga, G., Saalfeld, S., Bergersen, A. W., Valen-Sendstad, K., et al. (2019b). Multiple Aneurysms AnaTomy CHallenge 2018 (MATCH)-phase II: rupture risk assessment. *Int. J. Comput. Assist. Radiol. Surg.* 14, 1795–1804. doi:10.1007/s11548-019-01986-2

Berg, P., Voß, S., Saalfeld, S., Janiga, G., Bergersen, A. W., Valen-Sendstad, K., et al. (2018). Multiple aneurysms AnaTomy CHallenge 2018 (MATCH): phase I: segmentation. *Cardiovasc. Eng. Technol.* 9, 565–581. doi:10.1007/s13239-018-00376-0

Bisighini, B., Aguirre, M., Biancolini, M. E., Trovalusci, F., Perrin, D., Avril, S., et al. (2023). Machine learning and reduced order modelling for the simulation of braided stent deployment. *Front. Physiol.* 14, 1148540. doi:10.3389/fphys.2023.1148540

Brown, R. D., Jr., and Broderick, J. P. (2014). Unruptured intracranial aneurysms: epidemiology, natural history, management options, and familial screening. *Lancet Neurol.* 13, 393–404. doi:10.1016/s1474-4422(14)70015-8

Byrne, G., Mut, F., and Cebral, J. (2014). Quantifying the large-scale hemodynamics of intracranial aneurysms. *AJNR Am. J. Neuroradiol.* 35, 333–338. doi:10.3174/ajnr.A3678

Cebral, J. R., Castro, M. A., Burgess, J. E., Pergolizzi, R. S., Sheridan, M. J., and Putman, C. M. (2005). Characterization of cerebral aneurysms for assessing risk of rupture by using patient-specific computational hemodynamics models. *AJNR Am. J. Neuroradiol.* 26, 2550–2559.

Cebral, J., Ollikainen, E., Chung, B. J., Mut, F., Sippola, V., and Jahromi, B. R. (2017). Flow conditions in the intracranial aneurysm lumen are associated with inflammation and degenerative changes of the aneurysm wall. *AJNR Am. J. Neuroradiol.* 38, 119–126. doi:10.3174/ajnr.A4951

Chen, B., Tao, W., Li, S., Zeng, M., Zhang, L., Huang, Z., et al. (2022a). Medial gap: a structural factor at the arterial bifurcation aggravating hemodynamic insult. *J. Neuropathol. Exp. Neurol.* 81, 282–290. doi:10.1093/jnen/nlac017

Chen, B., Xie, K., Zhang, J., Yang, L., Zhou, H., Zhang, L., et al. (2023). Comprehensive analysis of mitochondrial dysfunction and necroptosis in intracranial aneurysms from the perspective of predictive, preventative, and personalized medicine. *Apoptosis* 28, 1452–1468. doi:10.1007/s10495-023-01865-x

Chen, B., Zhou, H., Zhou, X., Yang, L., Xiong, Y., and Zhang, L. (2022b). Comprehensive analysis of endoplasmic reticulum stress in intracranial aneurysm. *Front. Cell. Neurosci.* 16, 865005. doi:10.3389/fncel.2022.865005

Chen, G., Lu, M., Shi, Z., Xia, S., Ren, Y., Liu, Z., et al. (2020). Development and validation of machine learning prediction model based on computed tomography angiography-derived hemodynamics for rupture status of intracranial aneurysms: a Chinese multicenter study. *Eur. Radiol.* 30, 5170–5182. doi:10.1007/s00330-020-06886-7

Chen, J., Liu, J., Liu, X., Zeng, C., Chen, Z., Li, S., et al. (2022c). Animal model contributes to the development of intracranial aneurysm: a bibliometric analysis. *Front. Vet. Sci.* 9, 1027453. doi:10.3389/fvets.2022.1027453

Chen, R., Wei, Y., Zhang, G., Zhang, R., Zhang, X., Dai, D., et al. (2022d). Worldwide productivity and research trends of publications concerning stent application in acutely ruptured intracranial aneurysms: a bibliometric study. *Front. Neurol.* 13, 1029613. doi:10.3389/fneur.2022.1029613

Chen, S., Bai, B., Lv, N., Cheng, Y., and Ji, B. (2021). Hemodynamic analysis and implantation strategies of delayed intracranial aneurysm rupture after flow diverter treatment. *Ann. Transl. Med.* 9, 1735. doi:10.21037/atm-21-5939

Donthu, N., Kumar, S., Mukherjee, D., Pandey, N., and Lim, W. M. (2021). How to conduct a bibliometric analysis: an overview and guidelines. *J. Bus. Res.* 133, 285–296. doi:10.1016/j.jbusres.2021.04.070

Durieux, V., and Gevenois, P. A. (2010). Bibliometric indicators: quality measurements of scientific publication. *Radiology* 255, 342–351. doi:10.1148/radiol.09090626

Frösen, J., Tulamo, R., Paetau, A., Laaksamo, E., Korja, M., Laakso, A., et al. (2012). Saccular intracranial aneurysm: pathology and mechanisms. *Acta Neuropathol.* 123, 773–786. doi:10.1007/s00401-011-0939-3

Futami, K., Nambu, I., Kitabayashi, T., Sano, H., Misaki, K., Uchiyama, N., et al. (2017). Inflow hemodynamics evaluated by using four-dimensional flow magnetic resonance imaging and the size ratio of unruptured cerebral aneurysms. *Neuroradiology* 59, 411–418. doi:10.1007/s00234-017-1801-7

Goubergrits, L., Schaller, J., Kertzscher, U., Woelken, T., Ringelstein, M., and Spuler, A. (2014). Hemodynamic impact of cerebral aneurysm endovascular treatment devices: coils and flow diverters. *Expert Rev. Med. Devices* 11, 361–373. doi:10.1586/17434440.2014.925395

Han, P., Jin, D., Wei, W., Song, C., Leng, X., Liu, L., et al. (2021). The prognostic effects of hemodynamic parameters on rupture of intracranial aneurysm: a systematic review and meta-analysis. *Int. J. Surg.* 86, 15–23. doi:10.1016/j.ijsu.2020.12.012

Helgadottir, A., Thorleifsson, G., Magnusson, K. P., Grétarsdottir, S., Steinthorsdottir, V., Manolescu, A., et al. (2008). The same sequence variant on 9p21 associates with myocardial infarction, abdominal aortic aneurysm and intracranial aneurysm. *Nat. Genet.* 40, 217–224. doi:10.1038/ng.72

Huang, X., Zheng, J., Ma, Y., Hou, M., and Wang, X. (2023). Analysis of emerging trends and hot spots in respiratory biomechanics from 2003 to 2022 based on CiteSpace. *Front. Physiol.* 14, 1190155. doi:10.3389/fphys.2023.1190155

Janiga, G., Berg, P., Sugiyama, S., Kono, K., and Steinman, D. A. (2015a). The computational fluid dynamics rupture challenge 2013—phase I: prediction of rupture status in intracranial aneurysms. *AJNR Am. J. Neuroradiol.* 36, 530–536. doi:10.3174/ajnr.A4157

Janiga, G., Daróczy, L., Berg, P., Thévenin, D., Skalej, M., and Beuing, O. (2015b). An automatic CFD-based flow diverter optimization principle for patient-specific intracranial aneurysms. *J. Biomech.* 48, 3846–3852. doi:10.1016/j.jbiomech.2015.09.039

Jing, L., Zhong, J., Liu, J., Yang, X., Paliwal, N., Meng, H., et al. (2016). Hemodynamic effect of flow diverter and coils in treatment of large and giant intracranial aneurysms. *World Neurosurg.* 89, 199–207. doi:10.1016/j.wneu.2016.01.079

John, S., Bain, M. D., Hui, F. K., Hussain, M. S., Masaryk, T. J., Rasmussen, P. A., et al. (2016). Long-term follow-up of in-stent stenosis after pipeline flow diversion treatment of intracranial aneurysms. *Neurosurgery* 78, 862–867. doi:10.1227/neu.0000000000001146

Kamada, H., Nakamura, M., Ota, H., Higuchi, S., and Takase, K. (2022). Blood flow analysis with computational fluid dynamics and 4D-flow MRI for vascular diseases. *J. Cardiol.* 80, 386–396. doi:10.1016/j.jjcc.2022.05.007

Kataoka, H., Yagi, T., Ikedo, T., Imai, H., Kawamura, K., Yoshida, K., et al. (2020). Hemodynamic and histopathological changes in the early phase of the development of an intracranial aneurysm. *Neurol. Med. Chir. (Tokyo)* 60, 319–328. doi:10.2176/nmc.st.2020-0072

Larsen, N., Flüh, C., Saalfeld, S., Voß, S., Hille, G., Trick, D., et al. (2020). Multimodal validation of focal enhancement in intracranial aneurysms as a surrogate marker for aneurysm instability. *Neuroradiology* 62, 1627–1635. doi:10.1007/s00234-020-02498-6

Leung, G. K., Tsang, A. C., and Lui, W. M. (2012). Pipeline embolization device for intracranial aneurysm: a systematic review. *Clin. Neuroradiol.* 22, 295–303. doi:10.1007/s00062-012-0178-6

Levitt, M. R., Mandrycky, C., Abel, A., Kelly, C. M., Levy, S., Chivukula, V. K., et al. (2019). Genetic correlates of wall shear stress in a patient-specific 3D-printed cerebral aneurysm model. *J. Neurointerv. Surg.* 11, 999–1003. doi:10.1136/neurintsurg-2018-014669

Li, M. H., Chen, S. W., Li, Y. D., Chen, Y. C., Cheng, Y. S., Hu, D. J., et al. (2013). Prevalence of unruptured cerebral aneurysms in Chinese adults aged 35 to 75 years: a cross-sectional study. *Ann. Intern. Med.* 159, 514–521. doi:10.7326/0003-4819-159-8-201310150-00004

Liang, G., Wang, W., and He, Z. (2023). Sepsis associated with acute lung injury over the period 2012-2021: a bibliometric analysis. *Front. Physiol.* 14, 1079736. doi:10.3389/fphys.2023.1079736

Liou, T. M., Li, Y. C., and Juan, W. C. (2007). Numerical and experimental studies on pulsatile flow in aneurysms arising laterally from a curved parent vessel at various angles. *J. Biomech.* 40, 1268–1275. doi:10.1016/j.jbiomech.2006.05.024

Liu, Z., Yuan, Y., Jiang, R., Zhao, B., Gu, J., He, X., et al. (2023). How to create a nervous system aneurysm model in canines? ligation of the lingual artery is a simple and effective method. *Front. Physiol.* 14, 1137564. doi:10.3389/fphys.2023.1137564

Lu, V. M., Chen, S. H., Young, C. C., and Starke, R. M. (2021). Nature, content and shifts over time of the most impactful unruptured intracranial aneurysms articles: a bibliometric analysis. *J. Neurointerv. Surg.* 13, 177–181. doi:10.1136/neurintsurg-2020-016238

Medero, R., Falk, K., Rutkowski, D., Johnson, K., and Roldán-Alzate, A. (2020). *In vitro* assessment of flow variability in an intracranial aneurysm model using 4D flow MRI and tomographic PIV. *Ann. Biomed. Eng.* 48, 2484–2493. doi:10.1007/s10439-020-02543-8

Meng, H., Tutino, V. M., Xiang, J., and Siddiqui, A. (2014). High WSS or low WSS? Complex interactions of hemodynamics with intracranial aneurysm initiation, growth, and rupture: toward a unifying hypothesis. *AJNR Am. J. Neuroradiol.* 35, 1254–1262. doi:10.3174/ajnr.A3558

Meng, H., Wang, Z., Hoi, Y., Gao, L., Metaxa, E., Swartz, D. D., et al. (2007). Complex hemodynamics at the apex of an arterial bifurcation induces vascular remodeling resembling cerebral aneurysm initiation. *Stroke* 38, 1924–1931. doi:10.1161/strokeaha.106.481234

Misaki, K., Futami, K., Uno, T., Nambu, I., Yoshikawa, A., Kamide, T., et al. (2021). Inflow hemodynamics of intracranial aneurysms: a comparison of computational fluid dynamics and 4D flow magnetic resonance imaging. *J. Stroke Cerebrovasc. Dis.* 30, 105685. doi:10.1016/j.jstrokecerebrovasdis.2021.105685

Morel, S., Schilling, S., Diagbouga, M. R., Delucchi, M., Bochaton-Piallat, M. L., Lemeille, S., et al. (2021). Effects of low and high aneurysmal wall shear stress on endothelial cell behavior: differences and similarities. *Front. Physiol.* 12, 727338. doi:10.3389/fphys.2021.727338

Shi, Z., Chen, G. Z., Mao, L., Li, X. L., Zhou, C. S., Xia, S., et al. (2021). Machine learning-based prediction of small intracranial aneurysm rupture status using CTA-derived hemodynamics: a multicenter study. *AJNR Am. J. Neuroradiol.* 42, 648–654. doi:10.3174/ajnr.A7034

Shojima, M., Oshima, M., Takagi, K., Torii, R., Hayakawa, M., Katada, K., et al. (2004). Magnitude and role of wall shear stress on cerebral aneurysm: computational fluid dynamic study of 20 middle cerebral artery aneurysms. *Stroke* 35, 2500–2505. doi:10.1161/01.STR.0000144648.89172.0f

Soldozy, S., Norat, P., Elsarrag, M., Chatrath, A., Costello, J., Sokolowski, J., et al. (2019). The biophysical role of hemodynamics in the pathogenesis of cerebral aneurysm formation and rupture. *Neurosurg. Focus* 47, E11. doi:10.3171/2019.4.Focus19232

Steinman, D. A., Hoi, Y., Fahy, P., Morris, L., Walsh, M. T., Aristokleous, N., et al. (2013). Variability of computational fluid dynamics solutions for pressure and flow in a giant aneurysm: the ASME 2012 Summer Bioengineering Conference CFD Challenge. *J. Biomech. Eng.* 135, 021016. doi:10.1115/1.4023382

Suzuki, T., Takao, H., Fujimura, S., Dahmani, C., Ishibashi, T., Mamori, H., et al. (2017). Selection of helical braided flow diverter stents based on hemodynamic performance and mechanical properties. *J. Neurointerv. Surg.* 9, 999–1005. doi:10.1136/neurintsurg-2016-012561

Tang, X., Zhou, L., Wen, L., Wu, Q., Leng, X., Xiang, J., et al. (2021). Morphological and hemodynamic characteristics associated with the rupture of multiple intracranial aneurysms. *Front. Neurol.* 12, 811281. doi:10.3389/fneur.2021.811281

Valen-Sendstad, K., Bergersen, A. W., Shimogonya, Y., Goubergrits, L., Bruening, J., Pallares, J., et al. (2018). Real-world variability in the prediction of intracranial aneurysm wall shear stress: the 2015 international aneurysm CFD challenge. *Cardiovasc. Eng. Technol.* 9, 544–564. doi:10.1007/s13239-018-00374-2

Voß, S., Beuing, O., Janiga, G., and Berg, P. (2019). Multiple aneurysms AnaTomy CHallenge 2018 (MATCH)-Phase ib: effect of morphology on hemodynamics. *PLoS One* 14, e0216813. doi:10.1371/journal.pone.0216813

Wu, X., Gürzing, S., Schinkel, C., Toussaint, M., Perinajová, R., van Ooij, P., et al. (2022). Hemodynamic study of a patient-specific intracranial aneurysm: comparative assessment of tomographic PIV, stereoscopic PIV, *in vivo* MRI and computational fluid dynamics. *Cardiovasc. Eng. Technol.* 13, 428–442. doi:10.1007/s13239-021-00583-2

Xiang, J., Natarajan, S. K., Tremmel, M., Ma, D., Mocco, J., Hopkins, L. N., et al. (2011). Hemodynamic-morphologic discriminants for intracranial aneurysm rupture. *Stroke* 42, 144–152. doi:10.1161/strokeaha.110.592923

Yu, J., Gao, J., Chen, J., and Sun, Y. (2019). Academic versus non-academic neurosurgeons in China: a national cross-sectional study on workload, burnout and engagement. *BMJ Open* 9, e028309. doi:10.1136/bmjopen-2018-028309

Zhang, Q., Chen, J., and Liu, J. (2022). Global trends and hot-spots in research on virtual simulation in nursing: a bibliometric analysis from 1999 to 2021. *Front. Public Health* 10, 890773. doi:10.3389/fpubh.2022.890773

Zhang, X., Karuna, T., Yao, Z. Q., Duan, C. Z., Wang, X. M., Jiang, S. T., et al. (2018). High wall shear stress beyond a certain range in the parent artery could predict the risk of anterior communicating artery aneurysm rupture at follow-up. *J. Neurosurg.* 131, 868–875. doi:10.3171/2018.4.Jns173179

Zhu, G., Luo, X., Yang, T., Cai, L., Yeo, J. H., Yan, G., et al. (2022). Deep learning-based recognition and segmentation of intracranial aneurysms under small sample size. *Front. Physiol.* 13, 1084202. doi:10.3389/fphys.2022.1084202

Frontiers in Physiology

Understanding how an organism's components work together to maintain a healthy state

The second most-cited physiology journal, promoting a multidisciplinary approach to the physiology of living systems - from the subcellular and molecular domains to the intact organism and its interaction with the environment.

Discover the latest Research Topics

See more →

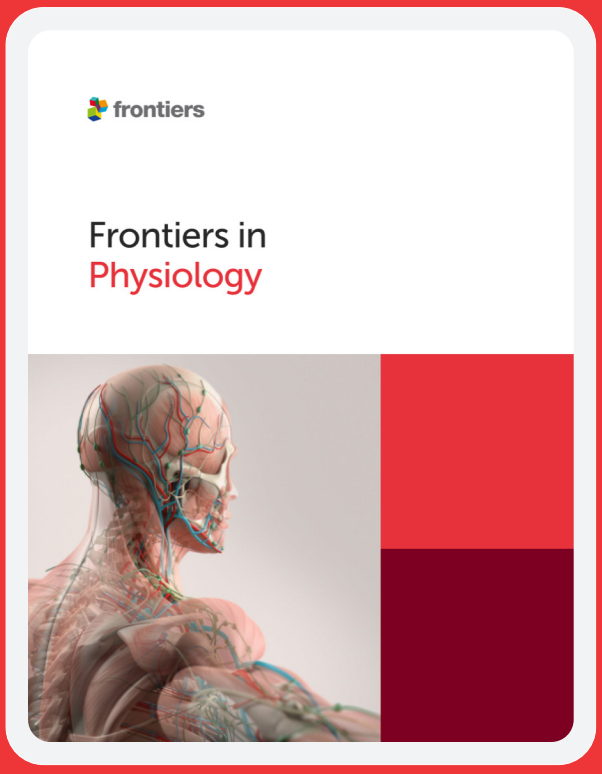

Frontiers

Avenue du Tribunal-Fédéral 34
1005 Lausanne, Switzerland
frontiersin.org

Contact us

+41 (0)21 510 17 00
frontiersin.org/about/contact